

UNIVERSITÉ LILLE 1 - SCIENCES ET TECHNOLOGIES

Habilitation à Diriger des Recherches

Présentée par

Roman Motiyenko

Spectroscopie térahertz à haute résolution : développements expérimentaux et études des molécules manifestant des mouvements de grande amplitude

Soutenance le 20 décembre 2017 devant le jury composé de :

Rapporteurs :

V. Boudon	Directeur de Recherches CNRS	Université de Bourgogne
A. Maestrini	Maître de Conférences	Observatoire de Paris
S. Schlemmer	Professeur	Université de Cologne

Examinateurs :

L. Coudert	Directeur de Recherches CNRS	Université Paris 11
M. Douay	Professeur	Université Lille 1
G. Mouret	Professeur	Université du Littoral Côte d'Opale

Directeur de Recherche :

L. Margulès	Professeur	Université Lille 1
-------------	------------	--------------------

Table des matières

Introduction	3
1 Développement du spectromètre térahertz à balayage rapide	5
1.1 Introduction	5
1.2 Réalisation du synthétiseur térahertz	7
1.2.1 Synthétiseur numérique direct : points forts et faibles	7
1.2.2 Synthétiseur térahertz à base de carcinotrons	9
1.2.3 Synthétiseur térahertz à base de sources solides	13
1.3 Spectromètre térahertz à balayage rapide	16
1.3.1 La synchronisation et le rôle du microcontrôleur	16
1.3.2 Fonctionnement du spectromètre à balayage rapide à base de sources solides	18
1.3.3 Caractéristiques du spectromètre à balayage rapide	22
1.4 Publications	28
2 Spectroscopie de molécules manifestant la rotation interne d'une toupie C_{3v}	51
2.1 Molécules non rigides	51
2.2 La rotation interne d'une toupie de symétrie C_{3v}	52
2.2.1 Modèles théoriques	52
2.2.2 Les codes	56
2.3 Résultats	59
2.3.1 Formiate de méthyle	59
2.3.2 Acétaldéhyde	62
2.3.3 N-méthylformamide	63
2.3.4 Méthacroléine	64
2.4 Publications	67
3 Spectroscopie de molécules avec la vibration de type inversion	145
3.1 Introduction	145
3.2 L'étude du formiate de méthyle déuteré	149

3.2.1 L'application du « formalisme du dimère de l'eau » au formiate de méthyle déuteré	149
3.2.2 Résultats	150
3.3 La méthode d'axes réduits	151
3.3.1 Modèle théorique	151
3.3.2 2-hydroxyacetonitrile	153
3.3.3 1,3-propanediol	155
3.4 Publications	158
4 Études des molécules manifestant deux mouvements de vibration de grande amplitude de nature différentes	191
4.1 Introduction	191
4.2 Étude du spectre de la méthylamine	193
4.2.1 Modèle théorique	193
4.2.2 Analyse du spectre	196
4.3 Étude du spectre de l'aminomalononitrile	198
4.4 Étude du spectre du Diméthyléther deutéré	201
4.5 Publications	204
Conclusions et perspectives	237
Bibliographie	240
Curriculum vitae synthétique	249

Introduction

Les travaux présentés dans cette habilitation à diriger des recherches ont pour objet deux axes principaux : (i) développement instrumental d'un spectromètre dans la région térahertz et (ii) des études de spectre de rotation de molécules organiques complexes non rigides dans la région térahertz

Le domaine térahertz qui s'étend entre 100 GHz et 30THz est connu par ses difficultés pour générer et contrôler le rayonnement surtout en deçà de 3 THz environ. Ce domaine de fréquences représente un intérêt particulier pour la détection de molécules en phase gaz grâce à leurs spectres de rotation. Historiquement les sources les plus performantes en terme de couverture, puissance et pureté spectrale dans ce domaine étaient les tubes électroniques carcinotrons. Cependant ces dix dernières années des progrès considérables ont été fait dans le développement des nouvelles sources solides basées sur le principe de génération d'harmoniques par des diodes Schottky. Dans le chapitre 1, je présente la mise en œuvre du spectromètre térahertz qui utilise comme sources de rayonnement des chaines de multiplication de fréquence à la base de diodes Schottky. Outre les sources de rayonnement, la particularité du spectromètre est l'application du synthétiseur numérique direct qui permet de balayer la source de façon très rapide tout en gardant la précision de mesure de la fréquence ainsi que sa sensibilité.

En ce qui concerne les études de spectres moléculaires, mes travaux portent principalement sur l'analyse de spectres de rotation de molécules ayant un ou deux mouvements de vibration grande amplitude (MVGA). Ces molécules souvent représentent un intérêt pour la télédétection dans le milieu interstellaire ou dans l'atmosphère planétaire. Pour assurer la détection sans ambiguïté d'une nouvelle espèce, ceci doit être précédée d'une étude en amont en laboratoire avec une résolution et précision suffisante.

En ce qui concerne les molécules d'intérêt astrophysiques, les résultats des études spectroscopiques permettent de générer des prévisions spectrales qui peuvent être utilisés dans l'analyse des données des radiotéléscopes dans le domaine millimétrique et submillimétrique, tels que ALMA, SOFIA, IRAM 30 m et de l'interféromètre du plateau de Bure (NOEMA). A ce jour, presque 200 molécules ont été détectées dans le milieu

interstellaire.¹ La grande majorité de ces molécules a été détecté via leurs signatures spectrales de rotation.

Les moyens d'observation dans l'atmosphère terrestre dans le domaine térahertz sont plus rares. Ici, on peut mentionner les projets de NASA de satellites MLS et EOS-MLS. Le plus souvent, dans l'atmosphère, les molécules sont observées et caractérisées dans le domaine infrarouge, dans la fenêtre autour de 900 cm^{-1} . Ceci implique l'utilisation des spectres de vibration. Néanmoins, pour la caractérisation des ces derniers par la méthode de différences combinées, on a besoin d'avoir des informations très précises sur l'état fondamental, que l'on obtient via la spectroscopie térahertz.

J'ai choisi de présenter les études des molécules non-rigides par type de MVGA. Le chapitre 2 porte sur les molécules manifestant la rotation interne d'une toupie de symétrie C_{3v} . Le chapitre 3 est consacré aux molécules ayant des doublements dans les spectres suite au mouvement de type inversion. Enfin, dans le quatrième chapitre, les cas des molécules présentant deux MVGA de natures différentes sont traités. Pour chaque type de MVGA je présente les modèles théoriques les plus performantes en termes de précision de l'analyse. J'ai appliqué ces modèles dans l'analyse des spectres des différentes molécules J'ai pu également établir les cas limites, où les méthodes théoriques actuelles ne permettent plus de reproduire le spectre à la précision expérimentale.

1. <http://www.astro.uni-koeln.de/cdms/molecules>

Chapitre 1

Développement du spectromètre térahertz à balayage rapide

1.1 Introduction

L'objectif principal de toute analyse spectroscopique est de mesurer les fréquences de raies, d'attribuer de nombres quantiques à des raies observées et de déterminer les paramètres de l'hamiltonien moléculaire. Cela est facilité si les spectres sont enregistrés dans une large gamme de fréquences avec très haute résolution et précision de mesure de fréquence. L'enregistrement des spectres de rotation large bande en continu est devenu possible grâce aux développements des sources de rayonnement telles que les carcinotrons puis les chaines de multiplication de fréquence. Les spectres large bande sont particulièrement utiles pour débuter l'analyse lorsque l'information sur la position des raies n'est pas très précise ou lorsque aucune étude n'existe pas pour une molécule. Ils permettent également d'obtenir une vue d'ensemble pour pouvoir identifier les zones les plus importantes pour la future analyse. L'enregistrement spectral dans une large gamme de fréquences rend possible l'application de la technique des diagrammes Loomis-Wood qui facilite grandement l'interprétation des spectres et permet de détecter de nouvelles caractéristiques qui ne pouvaient pas être prévues dans le cadre du modèle initial.

En spectroscopie d'absorption la grande majorité des spectromètres est construite selon le schéma typique suivant : le rayonnement d'une source à balayage monochromatique passe à travers une cellule contenant un gaz et arrive par la suite sur un récepteur qui peut détecter la diminution du signal en cas d'absorption résonante. Parmi nombreux spectromètres, ceux basés sur les synthétiseurs de fréquence comme source de rayonnement assurent la plus grande précision de la mesure de fréquence ainsi que de la forme de raie d'absorption. La synthèse de fréquence consiste à générer à partir d'un signal

fourni par un oscillateur de référence, un signal de fréquence différente. La stabilité de fréquence de l'oscillateur de référence est alors transférée au signal généré dont la fréquence correspond aux besoins de l'utilisateur. Le terme synthétiseur désigne aussi bien l'instrument complet que le module élémentaire qui en constitue le cœur.

Il existe également une technique qui permet d'enregistrer les spectres d'absorption par balayage extrêmement rapide sans la synthèse de fréquence : FASSST [[Petkie et al. 1997](#); [Medvedev et al. 2004](#)]. Le principal default du spectromètre FASSST est la détérioration de la précision de mesure due à l'absence de la synthèse de fréquence. En spectroscopie d'émission la technique de génération de pulsation à dérive de fréquence (en anglais : chirped pulse) permet d'enregistrer des larges intervalles spectraux dans le domaine térahertz en très peu de temps [[Brown et al. 2008](#); [Park et al. 2011](#); [Gerecht et al. 2011](#); [Steber et al. 2012](#); [Zaleski et al. 2012](#); [Neill et al. 2013](#)]. Cependant la très courte durée de pulsation (jusqu'à 2 μ s) et l'absence de sources de rayonnement puissantes dans le domaine térahertz rend cette technique pour l'instant moins sensible sur une simple acquisition par rapport à la spectroscopie d'absorption. Par conséquent, pour obtenir des spectres moléculaires avec un rapport signal/bruit satisfaisant il faut accumuler des acquisitions pendant une longue période. Au final, les temps d'enregistrement d'un large intervalle spectral avec un bon rapport signal/bruit en absorption et en émission par pulsation à dérive de fréquence sont comparables. On peut constater que la question très importante liée à la spectroscopie large bande est le temps nécessaire pour acquérir le spectre. L'enregistrement rapide de spectre est un outil indispensable lors des études de molécules instables, rares, ou bien dans les cas d'expérience de courte durée, par exemple pour les mesures en jet moléculaire supersonique.

Dans ce chapitre je présente le résumé de mes activités de recherches liées au développement du spectromètre d'absorption térahertz. Mon objectif principal était de construire un spectromètre :

- couvrant une large gamme de fréquences ;
- ayant la capacité d'enregistrement rapide de spectre ;
- assurant la haute précision de mesure de fréquence de raie.

En ce qui concerne la gamme de fréquence, à mon arrivée au laboratoire PhLAM, le spectromètre utilisait les tubes électroniques - carcinotrons couvrant la gamme jusqu'à 660 GHz. Entre 2008 et 2013, nous avons remplacé progressivement les tubes électroniques par des sources dites « solides » basées sur la technique de génération d'harmoniques ou multiplication de fréquence dans les diodes Schottky. Cela nous a permis également d'éteindre la gamme du spectromètre jusqu'à 1.5 THz. Les deux types de sources font partie du synthétiseur térahertz utilisé dans le spectromètre pour assurer une très grande précision de réglage de fréquence. Parallèlement avec le travaux sur l'extension de la

gamme, en collaboration avec Eugen Alekseev de l’Institut de Radioastronomie de l’ANS de l’Ukraine j’ai développé et mis en place le système de balayage rapide en fréquence. L’enregistrement rapide de spectre est devenu possible grâce à des nouveaux synthétiseurs numériques directes (DDS, de anglais : Direct Digital Synthesizer) que nous avons implémentés au sein du synthétiseur térahertz. Le chapitre présente en ordre chronologique le développement des synthétiseurs térahertz à balayage rapide en fréquence suivi par la description assez détaillée du spectromètre à balayage rapide et les performances du nouveau spectromètre.

1.2 Réalisation du synthétiseur térahertz

1.2.1 Synthétiseur numérique direct : points forts et faibles

La *synthèse numérique directe* est une méthode de génération du signal analogique à une fréquence fixe à l’aide d’un système numérique qui produit une séquence temporelle et transforme celle-ci par un convertisseur numérique-analogique (CNA).

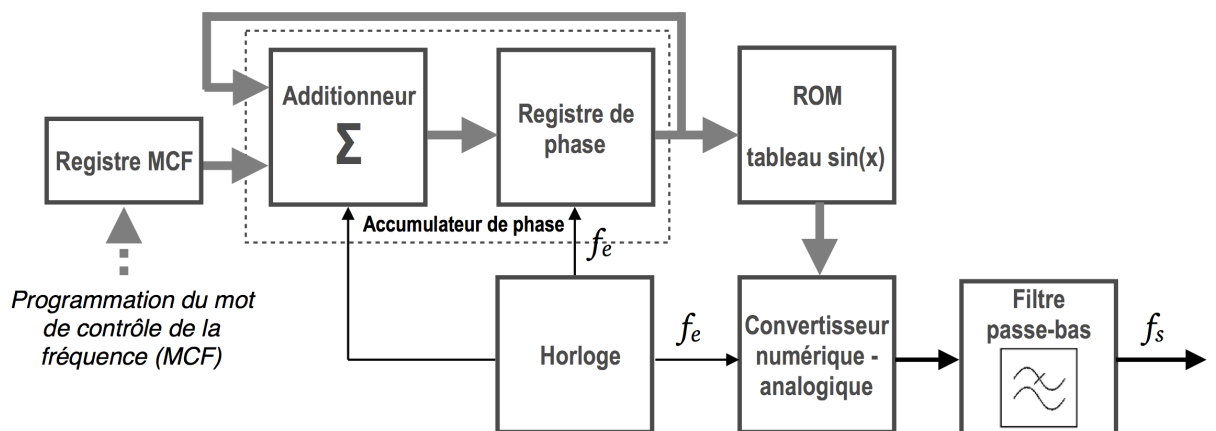


FIGURE 1: Le schéma de principe du synthétiseur numérique direct

Le schéma simplifié du synthétiseur numérique direct est représenté sur la Fig. 1. La séquence numérique temporelle est générée par prélèvement de la valeur de la fonction $\sin(x)$ dans la mémoire ROM à chaque cadence de l’horloge. L’argument de la fonction $\sin(x)$, ou bien la phase $[0, 2\pi]$, représente une adresse dans ROM codée sur N bits $[0, 2^N]$. Cette adresse provient de l’accumulateur de phase réalisé à partir d’un additionneur et d’un registre de phase. La valeur de l’argument est obtenue à chaque cadence de l’horloge en rajoutant le mot de contrôle de la fréquence (MCF) à la valeur précédemment sauvegardée dans le registre de phase. La séquence numérique temporelle formée de cette façon est ensuite convertie en valeur de courant ou de tension par CNA. Après le

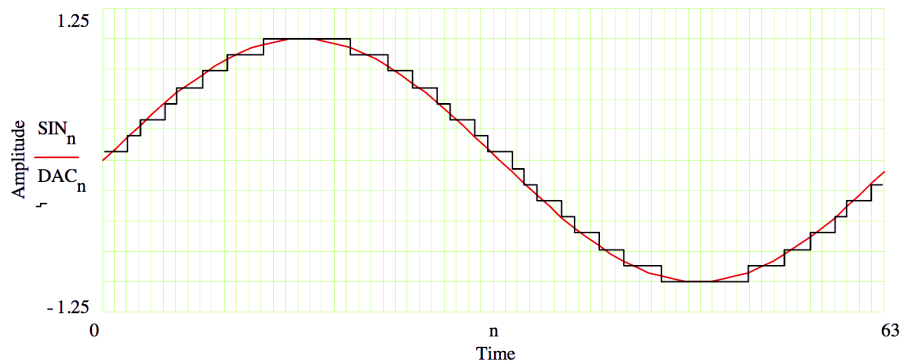


FIGURE 2: La séquence numérique temporelle représentant la fonction $\sin(x)$ (en noir) et le signal analogique après la filtration (en rouge). La figure prise du tutoriel technique sur la synthèse numérique.¹

filtrage on obtient ainsi un signal analogique dont la fréquence dépend de la fréquence de l'horloge, de la valeur du MCF et du nombre de bits N de l'accumulateur de phase :

$$f_s = \frac{f_e}{2^N} \text{MCF} \quad (1.1)$$

Un exemple d'une séquence numérique générée par un SDN et le résultat de la conversion numérique – analogique avec la filtration successive est présenté sur la Fig. 2. Le signal analogique obtenu par SDN correspond à l'échantillonnage de la fonction $\sin 2\pi f_s$. Par conséquent, le théorème d'échantillonnage (Nyquist-Shannon) limite la fréquence maximale du signal analogique : $f_{s(max)} = \frac{f_e}{2}$. En pratique on utilise plutôt le facteur $\frac{1}{2.5}$. Par exemple, la fréquence maximale du signal synthétisé par le microcircuit SDN AD9915 est $f_s = 1000$ MHz avec la fréquence de l'horloge $f_e = 2500$ MHz. Le palier minimal de fréquence est obtenu pour MCF = 1

$$\Delta f_s = \frac{f_e}{2^N} \quad (1.2)$$

Pour le microcircuit AD9915 avec $f_e = 2500$ MHz et $N = 32$ cette valeur est de 0.5820766... Hz. Elle représente également la plus petite fréquence synthétisable.

Les synthétiseurs SDN ont plusieurs points forts qui favorisent leur application en spectroscopie à haute résolution :

- Le changement de la valeur du MCF entraîne le changement presque instantané de la fréquence synthétisée. La vitesse de la commutation de fréquence est définie par les caractéristiques de l'interface de contrôle du microcircuit DDS et très souvent elle ne dépasse pas quelques périodes d'horloge.

1. <http://www.ieee.li/pdf/essay/dds.pdf>

- La commutation de fréquence s'effectue de façon continue sans des processus transitoires. Ce point ainsi que le point précédent rendent possible le balayage extrêmement rapide en fréquence d'un synthétiseur à base de DDS.
- La stabilité du signal et la précision de fréquence de la DDS sont complètement déterminés par les caractéristiques de l'horloge. Ainsi la DDS permet de synthétiser la fréquence avec une très grande précision si l'on utilise comme horloge un standard de fréquence atomique ou contrôlé par GPS.
- De même, le bruit de phase du synthétiseur DDS dépend uniquement du bruit de phase de l'horloge. Par rapport au bruit de phase d'horloge celui du synthétiseur DDS est amélioré par $20 \log \frac{f_s}{f_e}$.
- Le microcircuits DDS sont réalisés avec différentes interfaces de communication (en série et en parallèle) ce qui permet de les contrôler à distance avec facilité.

Les synthétiseurs DDS ont donc des nombreux avantages mais possèdent également quelques points faibles qui peuvent limiter leurs application en spectroscopie et plus précisément en spectroscopie térahertz :

- La fréquence maximale du signal du synthétiseur DDS commercial ne dépasse pas 1500 MHz actuellement. Or, les spectres de rotation se trouvent bien au delà de 1500 MHz et pour atteindre le domaine spectral voulu avec la DDS on a besoin d'appliquer la multiplication de fréquence.
- Le spectre du signal de DDS contient plusieurs composantes parasites. Elles sont dues à plusieurs phénomènes liés à la structure du DDS dont les principaux sont : l'échantillonnage, la quantification, la troncature de la phase. Notons qu'avec la multiplication de la fréquence on multiplie également le nombre de composantes parasites.

Par conséquent, sans des mesures particulières, le signal de sortie d'un synthétiseur DDS devient inexploitable pour la spectroscopie à haute résolution. Le problème de composantes parasites dans le spectre peut être résolu par la filtration à bande étroite du signal. Pour couvrir une large gamme de fréquences, la filtration doit également être adaptative, i.e. avec la bande passante de filtre réglable. Ci-dessous on va présenter des différents réalisations de synthétiseurs térahertz à base de DDS avec la filtration ayant une application en spectroscopie THz à haute résolution.

1.2.2 Synthétiseur térahertz à base de carcinotrons

La première version du synthétiseur à balayage rapide a été construite en intégrant le DDS dans la boucle de verrouillage en phase de carcinotron. Les carcinotrons (où

BWO du terme anglais Backward Wave Oscillator) sont des tubes à faisceaux d'électrons dont la fréquence générée dépend des interactions entre les électrons, la structure périodique à onde lente et le rayonnement électromagnétique se propageant le long de la structure périodique. La vitesse des électrons joue le rôle prépondérant dans ces interactions et pour cette raison la fréquence de sortie du carcinotron dépend fortement du potentiel électrique entre la cathode et la structure à onde lente. La pureté spectrale instantanée du carcinotron peut atteindre la valeur de 10 kHz [Dryagin 1970], mais plus généralement les variations temporelles de la fréquence du carcinotron sont de l'ordre de quelques MHz en quelques minutes, ce qui est bien au-delà de la résolution spectrale limitée par l'effet Doppler ou la précision de mesure de la fréquence d'une raie. Pour cette raison, dans les applications à la spectroscopie haute résolution, on utilise les carcinotrons verrouillés en phase [Lewen *et al.* 1998; McElmurry *et al.* 2003; Alekseev *et al.* 2012]. À noter que la technique de balayage rapide FASSST [Petkie *et al.* 1997] est basée sur la bonne pureté spectrale instantanée de BWO.

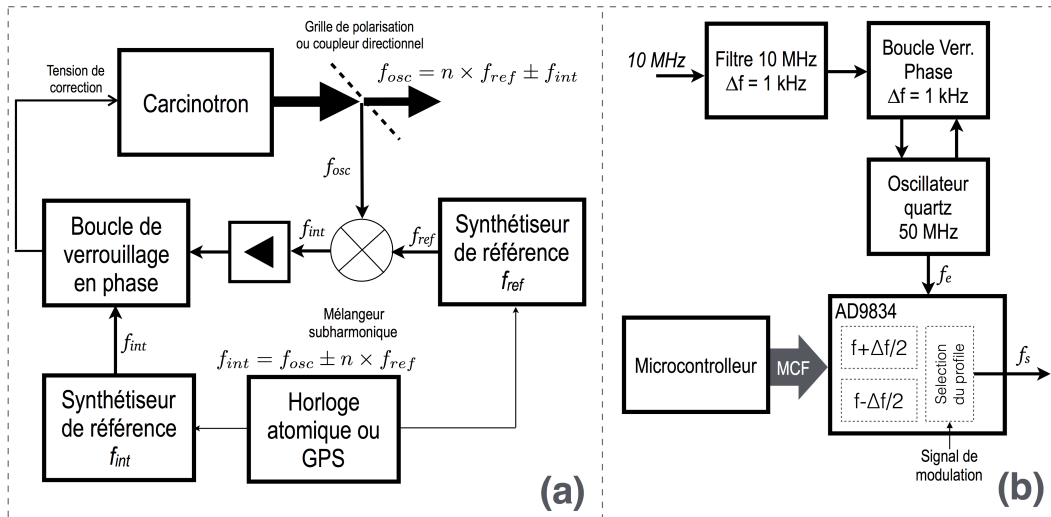


FIGURE 3: Schéma de la stabilisation de fréquence du carcinotron par une boucle de verrouillage en phase avec deux synthétiseurs de référence.

Le schéma de la stabilisation de fréquence du carcinotron par une boucle de verrouillage en phase est présenté sur la Fig. 3a. Dans ce schéma le carcinotron est verrouillé à l'harmonique n du synthétiseur de référence 1 (SR1). La boucle de verrouillage en phase fonctionne à la fréquence f_{int} délivrée par le synthétiseur de référence 2 (SR2). La fréquence synthétisée peut être exprimée comme :

$$f_{osc} = n \times f_{SR1} \pm f_{SR2} \quad (1.3)$$

Comme on peut constater à partir de l'Eq. 1.3 le balayage en fréquence peut être réalisé par l'un de deux SRs. La gamme de fréquence de balayage du SR1 est limitée

uniquement par ses caractéristiques physique, alors que pour le SR2 elle est limitée par la bande passante de la boucle de verrouillage en phase. Dans cette configuration, l'on peut appliquer le synthétiseur DDS en tant que SR1 ou SR2, mais vu la fréquence maximale de DDS et par conséquent un très important facteur de multiplication pour SR1, nous avons préféré d'utiliser un synthétiseur DDS en tant que SR2.

Dans le cas du spectromètre à base de carcinotron, la fréquence intermédiaire (FI) produite par le mélangeur subharmonique varie entre 278 et 378 MHz. Avant d'arriver dans la boucle de verrouillage en phase le signal de la FI est divisé par 32. Ainsi, pour balayer la fréquence de carcinotron, la fréquence de SR2 doit varier entre 8.7 et 11.8 MHz. Pour cette gamme de fréquences, nous avons réalisé un synthétiseur DDS à balayage rapide à base de microcircuit AD9834. Le schéma du synthétiseur est présenté sur la Fig. 3b. Le signal de référence pour le microcircuit est formé par un oscillateur quartz 50 MHz qui à son tour est verrouillé en phase à la référence 10 MHz produite par un horloge atomique. En plus, le signal d'entrée 10 MHz et le signal de sortie 50 MHz sont filtrés par les filtres quartz à grand facteur Q. Ces mesures assurent une excellente stabilité et pureté spectrale du signal de synthétiseur DDS. Le faible facteur de multiplication (32), la gamme de fréquences beaucoup plus petite par rapport à la fréquence de référence du DDS et le filtre passe-bande 8.7 – 11.8 MHz permettent d'éviter les composantes parasites dans le spectre du synthétiseur. Le microcircuit DDS est piloté par un microcontrôleur via l'interface en série SPI. Pour programmer les deux valeurs du MCF pour deux profiles de fréquence, la communication par SPI prend environ 20 µs. Le réglage de la fréquence synthétisée s'effectue en quelques cycles d'horloge (50 MHz) et de ce fait il est négligeable par rapport au temps de communication.

Vu la bande passante de la boucle de verrouillage en phase, le synthétiseur de fréquence à base de carcinotron et de synthétiseur DDS construit d'après le schéma sur la Fig. 3a procure le balayage rapide et continu dans la gamme de 100 MHz environ entre $f_{s_{min}} \times 32$ et $f_{s_{max}} \times 32$, où $f_{s_{min}} = 8.7$ MHz $f_{s_{max}} = 11.8$ MHz. Cela correspond au balayage continu entre :

$$f_{osc_{min}} = n \times f_{SR1} + f_{s_{min}} \text{ et } f_{osc_{max}} = n \times f_{SR1} + f_{s_{max}} \quad (1.4)$$

si l'on choisit le signe « + » dans l'Eq. 1.3. Pour continuer le balayage au-delà de $f_{osc_{max}}$ l'on rétabli la fréquence à $f_{s_{min}}$ et l'on change la fréquence du SR1 :

$$f'_{SR1} = f_{SR1} + \frac{32}{n} \times (f_{s_{max}} - f_{s_{min}}) + \delta f \quad (1.5)$$

A ce moment le synthétiseur térahertz peut être balayé entre :

$$f'_{osc_{min}} = n \times f'_{SR1} + f_{s_{min}} \text{ et } f'_{osc_{max}} = n \times f'_{SR1} + f_{s_{max}} \quad (1.6)$$

avec $f'_{osc_{min}}$ dans 1.6 égale $f_{osc_{max}}$ dans 1.4. Le terme δf dans l'Eq. 1.5 représente une correction de la fréquence due à l'erreur d'arrondi de la fréquence DDS. En effet comme l'on peut constater à partir d'Eq. 1.1 le MCF pour AD9834 ($N = 28$) est calculé comme :

$$MCF = 2^{28} \frac{f_s}{f_e} \quad (1.7)$$

Le rapport $\frac{f_s}{f_e}$ est inférieur à 1 et plus généralement peut être un nombre irrationnel, or le MCF doit être un nombre entier codé sur 28 bits. La nécessité d'arrondir le résultat dans la partie gauche de l'Eq. 1.7 entraîne une erreur dans la valeur de la fréquence synthétisée. Cette erreur bien évidemment est inférieure à la fréquence minimale synthétisable, mais au cours du balayage en fréquence elle peut s'accumuler. Le facteur δf est calculé en fonction du palier de fréquence du synthétiseur DDS et du nombre de points à balayer et il permet de corriger l'erreur d'arrondi avec la précision de 1 mHz environ.

Ainsi, la variation de la fréquence du synthétiseur DDS fournit une vue détaillée du spectre. Pour couvrir une large gamme de fréquences, on doit également varier la fréquence de SR1 par des paliers égaux à $\frac{32}{n} \times (f_{s_{max}} - f_{s_{min}}) + \delta f$. Notons, que la fréquence de SR1 doit être établie une seule fois par balayage de SR2 et pour cette raison comme SR1 l'on peut utiliser un synthétiseur avec une faible vitesse de commutation de fréquence. En même temps le synthétiseur SR1 doit avoir une grille de fréquences assez détaillée (1 Hz minimum) pour pouvoir corriger efficacement l'erreur d'arrondi du synthétiseur DDS.

La modulation de fréquence du synthétiseur térahertz est réalisée à partir de la modulation du synthétiseur DDS. Le microcircuit AD9834 possède quatre profils de fréquence qui peuvent être programmés simultanément. La modulation de fréquence de type rectangulaire est réalisée par commutation de deux de ces profils par un signal extérieur à la fréquence de modulation f_m . L'un de deux profils est configuré à la fréquence $f_s + \frac{\Delta f}{2}$ et l'autre à la fréquence $f_s - \frac{\Delta f}{2}$, où Δf est l'amplitude de modulation ou la déviation de fréquence. La commutation de la fréquence de DDS est accompagnée par des perturbations mineures et symétriques de courte durée, environ 1 – 2 μ s dans le système PLL [Alekseev 2011], de sorte que le signal MF ainsi obtenu fournit la distorsion minimale possible dans les formes des raies moléculaires. La particularité de ce type de modulation est la possibilité de détection synchrone uniquement en harmoniques impaires, le signal en harmoniques paires étant très faible.

Le synthétiseur à balayage rapide à base de carcinotrons a été utilisé dans le spectromètre térahertz entre 2008 et 2013 et nous a permis d'étudier plusieurs molécules peu stables ou réactives [Motiyenko *et al.* 2010a; Motiyenko *et al.* 2010b; Goubet *et al.* 2012; Motiyenko *et al.* 2012a; Motiyenko *et al.* 2012b]. Le succès de cette version

à base de carcinotrons est devenu une bonne base nécessaire à la transformation du spectromètre à sources solides.

1.2.3 Synthétiseur térahertz à base de sources solides

L'évolution technique des diodes Schottky planaires a permis le développement des chaînes de multiplication de fréquence du domaine de microondes vers térahertz [Drouin et al. 2005 ; Maestrini et al. 2010 ; Pearson et al. 2011] dont les caractéristiques en terme de puissance de sortie, de pureté spectrale ou de gamme d'accordabilité sont devenus comparables à celles des carcinotrons. Les sources solides térahertz basées sur les diodes Schottky ont également plusieurs avantages devant les carcinotrons : leurs caractéristiques spectrales dépendent essentiellement de celles de la source microonde et ce sont des éléments compacts, assez robustes et consomment très peu de la puissance électrique, ils ne nécessitent pas de champ magnétique intense et pas de refroidissement par eau.

Pour toutes ces raisons, ainsi qu'à cause d'une certaine extinction progressive de la technologie des carcinotrons, les chaînes de multiplication de fréquence sont devenues les sources principales de notre spectromètre térahertz. Toutes les chaînes utilisent au premier étage le synthétiseur commercial Agilent E8257D. Le balayage de la source térahertz en fréquence est ainsi produit par le balayage du synthétiseur du premier étage. La particularité du synthétiseur est le bruit de phase très faible obtenu grâce à plusieurs boucles de correction. Les processus transitoires dans ces boucles ainsi que dans les boucles de verrouillage en phase ont une influence directe sur le temps de commutation entre deux valeurs de fréquence. Pour E8257D, le temps de commutation minimum est de 11 ms, cependant dans la configuration de balayage large bande il est de l'ordre de 20 ms.

Suite au succès du projet de synthétiseur DDS pour la source térahertz à base de carcinotrons, l'étape suivante était de réaliser une source à balayage rapide avec les chaînes de multiplication de fréquence. Comme il a été indiqué ci-dessus, la fréquence maximale du synthétiseur DDS commercial ne dépasse pas 1.5 GHz, or d'après les caractéristiques techniques, le premier étage de la chaîne de multiplication doit fournir le signal dans la gamme 10 – 18.5 GHz avec la puissance de sortie de +10 dBm (10 milliwatts). Pour satisfaire ces conditions nous avons réalisé une conversion montante vers la gamme 10 – 18.5 GHz par le mélange radiofréquentiel (RF) du signal du synthétiseur DDS f_s et du synthétiseur Agilent E8257D f_{RF} avec la filtration et l'amplification successive. Le schéma de la nouvelle source microonde à balayage rapide est présenté sur la Fig. 4.

Le mélange RF produit les signaux principaux : $f_{RF} - f_s$, f_{RF} et $f_{RF} + f_s$. La conversion montante consiste à isoler l'un des deux signaux $f_{RF} - f_s$ ou $f_{RF} + f_s$. Pour cette raison

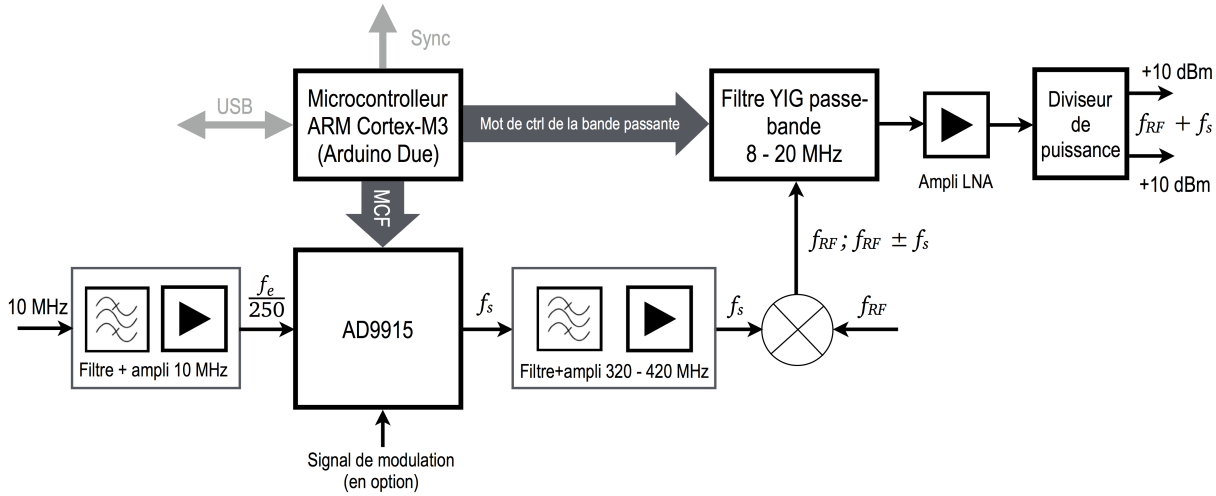


FIGURE 4: Schéma du synthétiseur RF basé sur le principe de la conversion montante.

f_{RF} et l'un des deux signaux de la conversion doivent être suffisamment espacés sur l'échelle des fréquences pour que la filtration soit efficace. Par conséquent, nous avons choisi un synthétiseur DDS dont la fréquence peut atteindre la valeur de quelques centaines de MHz. Le microcircuit choisi est AD9915 dont la fréquence maximale de sortie est 1000 MHz. Le signal 10 MHz est multiplié en interne dans le microcircuit par le facteur 250 pour produire l'horloge du système DDS à la fréquence $f_e = 2.5$ GHz. Pour éviter la présence des composantes parasites dans le spectre du synthétiseur DDS nous avons choisi en première étape de restreindre sa gamme d'accordabilité effective par l'intervalle 320 – 420 MHz. Le signal de sortie de microcircuit DDS est filtré par le filtre passe-bande fixe et amplifié par la suite. Le résultat du mélange radiofréquentiel de f_s et f_{RF} est filtré par le filtre passe-bande YIG (de l'anglais : yttrium iron garnet, le filtre basé sur le principe de résonance magnétique) accordable sur la gamme de fréquences 8 – 20 GHz. Le filtre YIG permet d'une part d'isoler la composante RF utile et d'autre part représente une seconde étape dans la lutte contre les composantes parasites dans le spectre du synthétiseur DDS. La bande passante du filtre (réjection à 3dB) varie de 30 MHz en bas de la gamme jusqu'à 60 – 70 MHz en haut. En outre, nous avons limité le balayage du synthétiseur DDS au sein de la bande passante du filtre YIG par une intervalle ne dépassant pas 15 MHz. Cela permet d'éviter les variations de la puissance du signal à la sortie du filtre YIG à cause des ondulations dans la bande passante et également de limiter le nombre de composantes parasites.

Après le filtre YIG le signal est amplifié par un amplificateur RF de très faible facteur de bruit pour atteindre le niveau de puissance 10 dBm nécessaire pour alimenter le multiplicateur actif (x6) à l'étage suivant. Le choix de ce type d'amplificateur est dicté

par la nécessité de multiplier la fréquence du signal du système produisant la conversion montante. Avec la multiplication de fréquence par un facteur N , le bruit de phase augmente typiquement par le facteur $20 \log N$. De ce fait, il est indispensable d'avoir au premier étage de la chaîne de multiplication un synthétiseur ayant le bruit de phase minimum possible. C'était la raison principale du choix du synthétiseur Agilent E8257D comme le premier étage de la chaîne de multiplication. La sortie de l'amplificateur est envoyée sur le diviseur de puissance qui sépare la voie du signal en deux parties équivalentes chacune ayant la puissance de +10 dBm environ. L'une des deux voies peut être utilisée pour contrôler le signal produit par le système de conversion montante. Des variations légères de la puissance à la sortie du synthétiseur RF de l'ordre de quelques pour cent sont possibles à cause de l'onde stationnaire dans le système. Pour réduire l'effet de l'onde stationnaire nous avons placé un atténuateur 3 dB entre le mélangeur et le filtre YIG. Puisque le deuxième étage de la chaîne de multiplication de fréquence fonctionne en mode de saturation, les variations de puissance à la sortie du synthétiseur RF n'influencent pas la puissance de sortie du deuxième étage.

Le résultat du mélange RF $f_{RF} \pm f_s$ est par la suite multiplié par des différents facteurs de multiplication, n_m : 6, 12, 18, 30, 36, 54 et 108. Ceci permet de couvrir plus de 80% de la gamme 75 - 1520 GHz. Ainsi la fréquence synthétisée par le nouveau synthétiseur térahertz à balayage rapide peut être exprimée comme :

$$f_{out} = n_m \times (f_{RF} \pm f_s) \quad (1.8)$$

Le balayage détaillé et rapide est assuré par le synthétiseur DDS et pour couvrir une large gamme de fréquence l'on doit également varier la fréquence du synthétiseur RF. Par analogie avec les Eqs. 1.4 – 1.6 l'on peut établir que le palier de la fréquence RF dans ce cas est égal à $f_{s_{max}} - f_{s_{min}} + \delta f$, où $f_{s_{min}}$ et $f_{s_{max}}$ d'après les caractéristiques techniques doivent se trouver entre 320 et 420 MHz et à l'intérieur de la bande passante du filtre YIG. Le terme de correction δf est également nécessaire pour corriger l'erreur d'arrondi du synthétiseur DDS.

La modulation de fréquence dans le système à conversion montante peut être réalisée de deux manières différentes. La première est la modulation rectangulaire de même type que pour le synthétiseur à base de carcinotrons décrite ci-dessus. La seconde version consiste à moduler en fréquence ou en amplitude le synthétiseur Agilent E8257D. Dans ce cas, il est possible de programmer une seule valeur de MCF du synthétiseur DDS. En outre, on peut également profiter de la fonctionnalité du microcircuit AD9915 pour programmer la fréquence sans l'erreur d'arrondi. Le microcircuit AD9915 peut fonctionner en mode de « module programmable » permettant d'implémenter des fractions qui ne sont pas limités 2^N dans le dénominateur d'Eq. 1.1 et ainsi de programmer la valeur de

la fréquence exacte avec un pas minimal de 1 Hz. La fréquence synthétisée dans le mode de « module programmable » est exprimée comme :

$$f_s = f_e \frac{\text{MCF} + A/B}{2^N} \quad (1.9)$$

L'algorithme du calcul de valeurs de paramètres A et B de l'Eq. 1.9 est décrit dans la fiche technique du microcircuit AD9915.² On remarque juste que cet algorithme est couteux en terme de temps de calcul, car il demande de calculer deux fois le diviseur commun de deux nombres entiers long. Pour cette raison, pour piloter le microcircuit AD9915 j'ai choisi le microcontrôleur basé sur le microprocesseur ARM Cortex-M3 32-bit avec la fréquence d'horloge 84 MHz.

1.3 Spectromètre térahertz à balayage rapide

1.3.1 La synchronisation et le rôle du microcontrôleur

L'enregistrement d'un spectre d'absorption se fait typiquement en mode étagé en variant la fréquence de la source par des paliers équidistants et en mesurant la réponse du détecteur à chaque valeur de fréquence de la source. Pour que la réponse du détecteur soit unique il faut synchroniser les deux processus. Une solution simple dans ce cas consiste à contrôler la source et le détecteur par un seul instrument - microcontrôleur. Les microcontrôleurs sont et continueront à être largement utilisés pour les applications de régulation et de commande de processus. Ce sont de véritables micro-ordinateurs intégrés dans un microcircuit qui comportent une unité centrale, la mémoire ou une interface à la mémoire externe, des ports d'entrée-sortie, plusieurs interfaces de communications ce qui leur permet d'établir une connexion avec un ordinateur (typiquement via le port série tels que USB ou COM) et les instruments périphériques (typiquement via l'interface SPI ou I2C), ainsi qu'une unité de gestion de temps et d'événements. Les microcircuits DDS (AD9834 et AD9915) utilisés dans les synthétiseurs térahertz sont configurés et programmés par des microcontrôleurs via l'interface SPI. Les microcontrôleurs à leur tour reçoivent des commandes d'utilisateur via le port en série depuis un ordinateur.

Dans le cas du synthétiseur à base de carcinotrons, le microcontrôleur contrôle également le synchronisme de boucle de verrouillage en phase du carcinotron. Le microcontrôleur peut arrêter les mesures et envoyer une commande d'interruption vers l'ordinateur si le synchronisme est perdu. Par la suite, l'ordinateur lance une procédure de

2. <http://www.analog.com/media/en/technical-documentation/data-sheets/AD9915.pdf>

verrouillage du carcinotron en phase et en cas de succès envoie vers le microcontrôleur une commande pour reprendre les mesures.

Dans le cas du synthétiseur à base de sources solides, le microcontrôleur est également utilisé pour piloter la bande passante du filtre YIG. La fréquence centrale de la bande passante du filtre varie en fonction du courant dans le solénoïde qui entoure le cristal YIG. Le filtre choisi MLFP-70820 est doté d'une source de courant continu pilotée de façon numérique via l'interface SPI. Le pilotage s'effectue d'une manière simple en envoyant un mot de contrôle codé sur 16 bits. Ainsi, la valeur minimale du courant et de la fréquence centrale (8 GHz) correspond au code 0 et la valeur maximale du courant et de la fréquence (20 GHz) correspond au code $2^{16} - 1 = 65535$. Le pilotage numérique permet l'ajustement très fine et continu de la fréquence centrale car le pas minimal $\Delta f_{YIG} = \frac{20000 - 8000}{2^{16}} = 0.1831$ MHz est bien inférieur à la bande passante du filtre (30 – 70 MHz).

De même, pour synchroniser le synthétiseur térahertz et le détecteur il est logique de confier cette tâche à un microcontrôleur. Cette solution permet de réaliser des mesures spectrales à des taux très élevés car le microcontrôleur fonctionne sous un système de temps réel contrairement aux ordinateurs modernes fonctionnant en grande majorité sous des systèmes d'exploitation multitâches. Par exemple, sous Windows ou Linux il est très difficile et contraignant de réaliser avec une grande précision des mesures d'intervalles temporels inférieurs à 1 ms. Alors que l'unité de gestion de temps d'un microcontrôleur permet de générer des interruptions de très faible « jitter » avec un taux égal à quelques cycles de microprocesseur, à savoir de quelques centaines de nanosecondes à quelques microsecondes suivant le modèle.

En résumé, dans les deux systèmes à balayage rapide en fréquence, le microcontrôleur joue le rôle d'intermédiaire entre l'ordinateur et les instruments du spectromètre. Pour des mesures à des taux très élevés, l'interfaçage par un microcontrôleur est indispensable. En revanche, puisque le microcontrôleur fonctionne sous un système de temps réel, sa communication avec l'ordinateur doit être minimisée car l'on ne peut pas effectuer deux tâches (communication avec l'ordinateur et les instruments) simultanément. La solution la plus simple consiste à réduire le temps de communication en séparant les tâches effectuées par l'ordinateur et le microcontrôleur. Le microcontrôleur effectue les tâches les plus importantes des mesures spectrales : la programmation de la fréquence du synthétiseur térahertz et la synchronisation de la détection. L'ordinateur n'est utilisé que pour initialiser et configurer les mesures. La communication entre l'ordinateur et le microcontrôleur a lieu deux fois : au début du processus des mesures pour initialiser et configurer les instruments et à la fin du cycle des mesures pour récupérer les données mesurées.

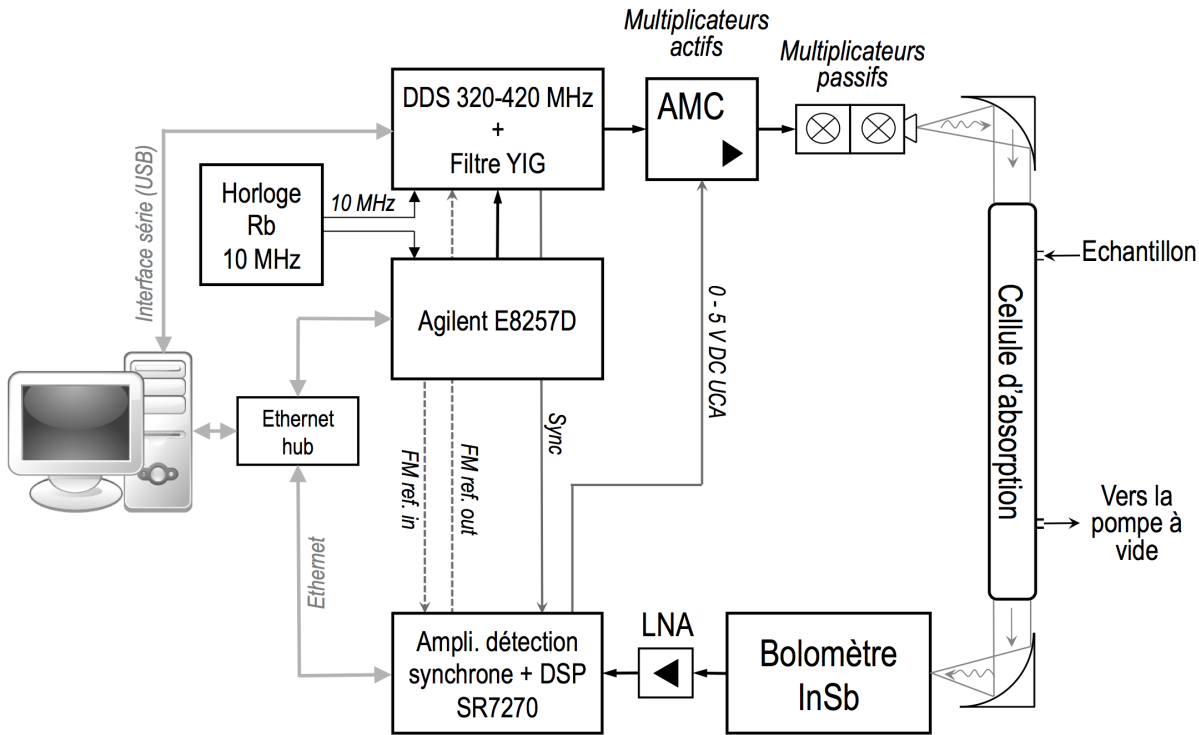


FIGURE 5: Le schéma du spectromètre térahertz à balayage rapide basé sur des sources solides.

1.3.2 Fonctionnement du spectromètre à balayage rapide à base de sources solides

Le spectromètre à balayage rapide à base des carcinotrons est décrit en détail dans l'article [Alekseev *et al.* 2012]. Par conséquent, dans cette habilitation je ne présente que les développements les plus récents du spectromètre à balayage rapide à base de sources solides. Celui-ci a été développé comme une extension du spectromètre décrit dans l'article [Zakharenko *et al.* 2015].

Le schéma du nouveau spectromètre est présenté sur la Fig. 5. La modification principale est l'intégration du nouveau synthétiseur à balayage rapide décrit en détail dans Sec. 1.2.3. Le signal RF f_{RF} pour le nouveau synthétiseur dans la gamme 10 - 18.5 GHz est fourni par le synthétiseur Agilent E8257D. Le synthétiseur Agilent E8257D et le système de détection synchrone sont contrôlés via le réseau Ethernet avec le débit de 10 Mbit/s. La communication entre l'ordinateur et le synthétiseur à balayage rapide est établi via l'interface série (USB) avec le débit en baud de 57.6 kbit/s.

Pour les mesures spectrales de grande sensibilité le synthétiseur térahertz est modulé en fréquence et l'on utilise la détection synchrone en back-end. Comme il était expliqué dans Sec. 1.2.3 la modulation en fréquence est possible par la modulation du synthétiseur RF en interne ou par la commutation de deux profils de fréquence du synthétiseur DDS. Dans le premier cas, le signal de référence pour la détection synchrone est fourni

1.3. Spectromètre térahertz à balayage rapide

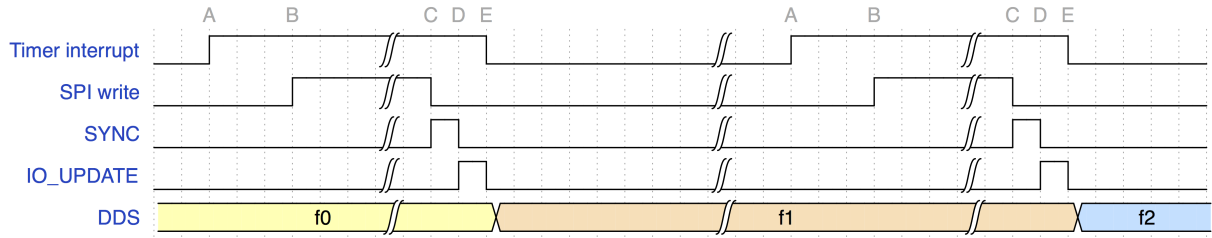


FIGURE 6: Le diagramme de temps du cycle de mesure

par le connecteur LF OUT du synthétiseur RF (*FM ref. in* sur la Fig. 5). Dans le second cas, le signal de référence est produit en interne dans le système de la détection synchrone et envoyé vers l'entrée du commutateur installé devant le microcircuit DDS (*FM ref. out* sur la Fig. 5).

Le système de la détection synchrone SR 7270 contient l'amplificateur à détection synchrone mais également un système d'acquisition rapide de données : un convertisseur analogique - numérique rapide, un processeur du signal numérique et une mémoire tampon rapide. La mémoire tampon permet d'acquérir et stocker jusqu'à 10^5 points avec une vitesse d'acquisition jusqu'à $1 \mu\text{s}/\text{point}$. Dans le spectromètre à balayage rapide, on utilise cette mémoire tampon pour l'acquisition de données. L'acquisition de chaque point expérimental est initiée par un signal TTL extérieur. Ce signal (*Sync* sur la Fig. 5) est généré par le microcontrôleur et envoyé vers le connecteur TRIG IN du SR 7270. Ainsi l'on arrive à satisfaire la condition de synchronisation entre la source et le détecteur et à obtenir une réponse unique à chaque valeur de la fréquence de la source.

Suite à la configuration initiale de tous les instruments du spectromètre, le processus d'enregistrement de spectre est composé de deux étapes qui se succèdent en répétition :

- série d'acquisitions de données spectrales ;
- configuration des instruments et visualisation de données.

Une série d'acquisitions contient un certain nombre de cycles, chacun représentant une mesure de réponse du détecteur à une fréquence de la source THz. Le cycle d'acquisition est illustré par le diagramme de temps sur la Fig. 6. Chaque cycle est initié par une interruption de l'horloge (timer) du microcontrôleur. Suite à l'interruption de l'horloge, le microcontrôleur invoque la procédure de gestion d'interruption et toute les commandes du cycle sont effectuées en interne dans cette procédure.

La première étape du cycle est le calcul de la nouvelle valeur de fréquence du synthétiseur DDS. Tout d'abord on calcule la valeur de la fréquence par l'addition du palier de fréquence à la valeur actuelle. La fréquence et le palier de fréquence sont exprimés en unité de MCF en mode « profile » et en Hz en mode « module programmable ». Par la suite, en mode « profile » on calcule les fréquences de deux profils P0 et P1 comme

$f - \frac{\Delta f}{2}$ et $f + \frac{\Delta f}{2}$, où $\frac{\Delta f}{2}$ est également exprimé en unité de MCF. Pour le microcontrôleur à base de micropocesseur ARM Cortex-M3, dont la fréquence d'horloge f_{ACLK} est de 84 MHz, ces deux opérations simples prennent moins de 1 μ s. En mode « module programmable » le calcul de la nouvelle valeur de fréquence comprend également : le calcul de la valeur de MCF et de paramètres A et B de l'Eq. 1.9 selon l'algorithme décrit dans la fiche technique du microcircuit DDS AD9915. Comme il était indiqué dans Sec. 1.2.3, l'algorithme comprend le calcul de diviseur commun de deux nombres entiers codés sur 32 bits. Dans le cas général, cette opération peut être assez fastidieuse. Mes estimations montrent qu'en moyenne, pour le microprocesseur ARM Cortex-M3 de la carte Arduino Due, le temps maximal de calcul de la nouvelle valeur de fréquence en mode « module programmable » varie entre 10 et 15 μ s.

L'étape suivante du cycle est la programmation du microcircuit du synthétiseur via l'interface en série SPI. L'interface fonctionne à la fréquence de 21 MHz ($f_{ACLK}/4$). Chaque instruction envoyée vers le microcircuit comprend 5 octets : 1 octet de l'adresse du registre à programmer et 4 octets de données. Le temps nécessaire à envoyer une instruction via l'interface en série est de 6.5 μ s environ. En mode « profile » on programme deux registres P0 et P1 correspondant à deux profiles de fréquence. Au total, avec les délais entre les instructions, le temps nécessaire pour programmer le microcircuit DDS est de 14 μ s. En mode « module programmable » on programme trois registres MCF, A et B, et avec les délais entre les instructions, le temps total de programmation est de 19.5 μ s environ.

Les instructions envoyées dans le microcircuit DDS via l'interface en série sont initialement stockées dans la mémoire tampon du microcircuit. Ces instructions sont transférées vers les registres correspondants suite au basculement de la broche IO_UPDATE du microcircuit. Avant la pulsation TTL de basculement de IO_UPDATE le microcontrôleur produit une pulsation TTL de synchronisation (SYNC sur la Fig. 6) pour déclencher l'acquisition d'un point expérimental correspondant à la réponse du détecteur à la valeur actuelle de la fréquence de la source THz. Le basculement de IO_UPDATE et la programmation des registres du microcircuit entraînent le changement de la valeur de fréquence synthétisée. D'après la fiche technique du microcircuit, en mode « profile » la latence de données (délai de changement de fréquence) est de 222 cycles d'horloge (environ 89 ns). On peut supposer qu'en mode « module programmable » il s'agit d'une valeur de même ordre de grandeur que celle du mode « profile ». Ainsi, le temps entre l'acquisition d'un point du spectre et le prochain changement de fréquence est inférieur à 1 μ s.

Le basculement de IO_UPDATE est la dernière opération effectuée dans la procédure de gestion d'interruption. On appelle l'intervalle de temps occupé par la procédure le temps de *commutation* de fréquence Δt_f . Comme l'on peut constater Δt_f dépend du

mode de fonctionnement du microcircuit du synthétiseur. En mode « profile », le temps de traitement est de 16 μs tandis que en mode « module programmable » celui-ci varie entre 35 et 45 μs .

L'intervalle entre l'instant de la commutation de fréquence et l'instant de la mesure d'un point du spectre (point E du cycle précédent et point D du cycle suivant) doit être supérieur ou égale à cinq fois la constante de temps de la détection synchrone. Ce délai est nécessaire pour bien distinguer les réponses du détecteur à deux fréquences différentes de la source. La constante τ caractérise le temps d'intégration du signal dans le filtre RC à la sortie du circuit de la détection synchrone. Le temps d'intégration assez court par rapport à la constante τ entraîne l'apparition dans la réponse du détecteur d'une contribution due à la fréquence de la source qui précédait la fréquence actuelle. Ceci a pour conséquence le décalage de la fréquence mesurée d'une raie spectrale. Les estimations théoriques [Rohart *et al.* 2014 ; Rohart 2017] montrent qu'avec $\Delta t_d = 5\tau$ l'erreur de mesure de la fréquence de raie est de l'ordre de $0.019\Delta f$, où Δf est le palier de fréquence de la source. En même temps l'erreur devient égale à $1.5\Delta f$ si $\Delta t_d = \tau$. On peut réduire davantage cette erreur en augmentant Δt_d et par conséquent en réduisant la vitesse d'enregistrement, mais le délai égal à 5τ est un bon compromis entre la vitesse de mesure et l'erreur induite. En pratique, nous n'avons jamais détecté le décalage de la fréquence de raie mesurée à 5τ , même dans le domaine au-delà de 1 THz ou le palier de fréquence devient supérieur à 150 kHz et d'après les estimations théoriques le décalage devrait avoisiner 3.5 kHz.

Puisque l'instant de mesure de la réponse du détecteur et l'instant de changement de fréquence du synthétiseur térahertz sont séparés par un intervalle de temps très court, on peut utiliser tout le temps occupé par la procédure de gestion d'interruption comme le délai minimum équivalent à 5τ . De ce fait, en rajoutant au temps de commutation de fréquence le délai d'invocation de la procédure (très court $\approx 1\ \mu\text{s}$) on obtient le temps minimal entre deux mesures consécutives à deux fréquence différentes de la source térahertz $\Delta t_m^{(min)}$. On estime que ce temps $\Delta t_m^{(min)}$ est de l'ordre de 20 $\mu\text{s}/\text{point}$ en mode « profile » et de 50 $\mu\text{s}/\text{point}$ en mode « module programmable ».

Typiquement, une série d'acquisitions comprend un enregistrement de 2000 à 10000 points. Cette limitation est dictée par la nécessité de restreindre la gamme d'accordabilité du synthétiseur DDS, qui ne doit pas dépasser la bande passante du filtre YIG. Par exemple, une acquisition de 2000 points par paliers de fréquence de 0.03 MHz représente une gamme effective de la source THz de 60 MHz. Avec le facteur de multiplication égal à 12, la gamme d'accordabilité effective du synthétiseur DDS doit être $\frac{60}{12} = 5\ \text{MHz}$. Avec 10000 points, la gamme d'accordabilité effective dépasse la limite imposée par les caractéristiques techniques du synthétiseur DDS et du filtre YIG.

Une fois l'enregistrement de la série d'acquisitions terminé, toutes les données enregistrées sont envoyées de la mémoire tampon de SR7270 vers l'ordinateur. L'ordinateur, à son tour, reconfigure les instruments du spectromètre pour continuer les mesures :

- i. change la fréquence RF par un palier égal à $f_{s_{max}} - f_{s_{min}}$;
- ii. réinitialise la mémoire tampon de SR7270 ;
- iii. rétablit la fréquence du synthétiseur DDS à $f_{s_{min}}$;
- iv. envoie une commande pour démarrer une nouvelle série d'acquisitions au micro-contrôleur.

Les mesures en temps réel montrent que l'exécution de cette étape d'enregistrement du spectre prend environ 400 ms. La moitié de ce temps est occupée par la préparation de données de la mémoire tampon au transfert via le protocole Ethernet.

Ainsi, le processus de mesures spectrales est complètement automatisé et il s'effectue sans aucune intervention de l'utilisateur. Cela permet d'atteindre la vitesse d'enregistrement de spectre maximale.

1.3.3 Caractéristiques du spectromètre à balayage rapide

La vitesse d'enregistrement de spectre. La vitesse maximale théorique d'enregistrement de spectre peut être estimée par rapport à la largeur de la raie spectrale observée $\Delta\nu$, dont la valeur est inversement proportionnelle au temps de relaxation de l'état d'énergie τ_r . Avec la modulation de la source de rayonnement et la détection synchrone on peut également appliquer « la règle de 5τ » par rapport au temps de relaxation, en stipulant que pour atteindre le régime stationnaire de mesures, l'intervalle entre deux mesures successives doit être supérieur à $5\tau_r$. Dans ce cas, $5\tau_r$ est la valeur minimale d'une période de la modulation T_{mod} . Ainsi

$$T_{mod} \geq 5\tau_r \text{ ou } f_{mod} \leq \frac{\Delta\nu}{5} \quad (1.10)$$

En même temps il existe une seconde limitation par rapport à la valeur de la fréquence de modulation. La constante de temps de la détection synchrone τ détermine également la fréquence de coupure du filtre passe-bas : $f_c = \frac{1}{\tau}$. Pour bien isoler le signal de modulation du signal détecté, la fréquence de modulation doit être au moins trois fois supérieure à f_c :

$$f_{mod} \geq 3f_c \text{ ou } T_{mod} \leq \frac{\tau}{3} \quad (1.11)$$

Le facteur devant f_c dans Eq. 1.11 dépend essentiellement de l'ordre de filtre passe-bas. La valeur 3 que l'on a adopté ici est valable pour les filtres du deuxième ordre dont

TABLE 1.1: Constante de temps de la détection synchrone et le temps minimum de mesure en fonction de la largeur de raie.

$\Delta\nu$ (MHz)	τ (μ s)	$\Delta t_m^{(min,th)}$ (μ s)
0.2	75	375
0.5	30	150
1	15	75
2	7.5	37.5

la pente est 12 dB/octave. En combinant 1.10 et 1.11 on obtient le rapport entre la constante de temps de la détection synchrone et le temps de relaxation (largeur de raie spectrale) :

$$\tau \geq 15\tau_r \quad (1.12)$$

Le rapport 1.12 est purement qualitatif et le facteur devant τ_r peut varier en fonction de la qualité du détecteur synchrone et de son filtre passe-bas. Néanmoins ce rapport nous permet de faire une estimation de la vitesse maximale d'enregistrement de spectre. Avec la règle de 5τ introduite dans Sec. 1.3.2 et l'Eq. 1.12 le temps de mesure d'un point de spectre devient :

$$\Delta t_m^{(min,th)} \geq 75\tau_r \quad (1.13)$$

En respectant le rapport 1.12 l'on n'ajoute pas des bruits supplémentaires et l'on ne déforme pas la raie spectrale, ce qui est très important pour la précision de mesure de la fréquence de celle-ci.

En pratique on peut utiliser les Eqs. 1.12 et 1.13 pour estimer la vitesse maximale d'enregistrement de spectre en fonction de la largeur de raie. La largeur de raie spectrale dépend essentiellement des conditions expérimentales. Dans le domaine térahertz les deux phénomènes principaux qui influencent la largeur de raie sont : l'élargissement par l'effet Doppler ($\Delta\nu_D$) et l'élargissement par collisions ($\Delta\nu_L$). Typiquement, le meilleur rapport signal/bruit est obtenu lorsque les contributions des deux phénomènes sont comparables : $\Delta\nu_D \simeq \Delta\nu_L$. Dans ce cas la largeur totale de raie peut être estimée comme : $\Delta\nu = \sqrt{2}\Delta\nu_D$. La largeur Doppler dépend de la fréquence de la raie ν_0 , de la température T et de la masse moléculaire M :

$$\Delta\nu = 7.162 \times 10^{-7} \nu_0 \sqrt{\frac{T}{M}} \quad (1.14)$$

avec T exprimée en K et M en g/mol. A la température ambiante, la valeur de $\Delta\nu$ de 0.2 – 0.5 MHz est caractéristique pour les mesures dans le domaine millimétrique jusqu'à 300 GHz environ, tandis que les valeurs de $\Delta\nu$ supérieures à 0.5 MHz sont caractéris-

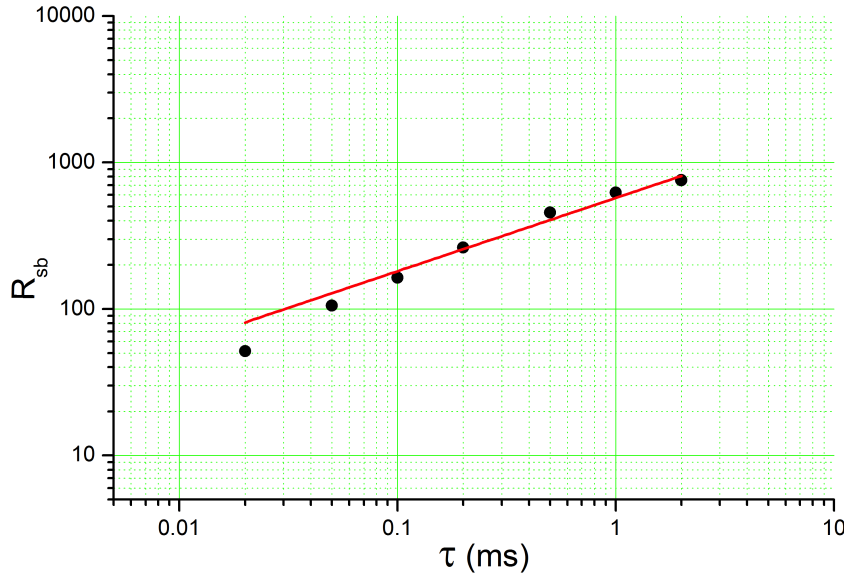


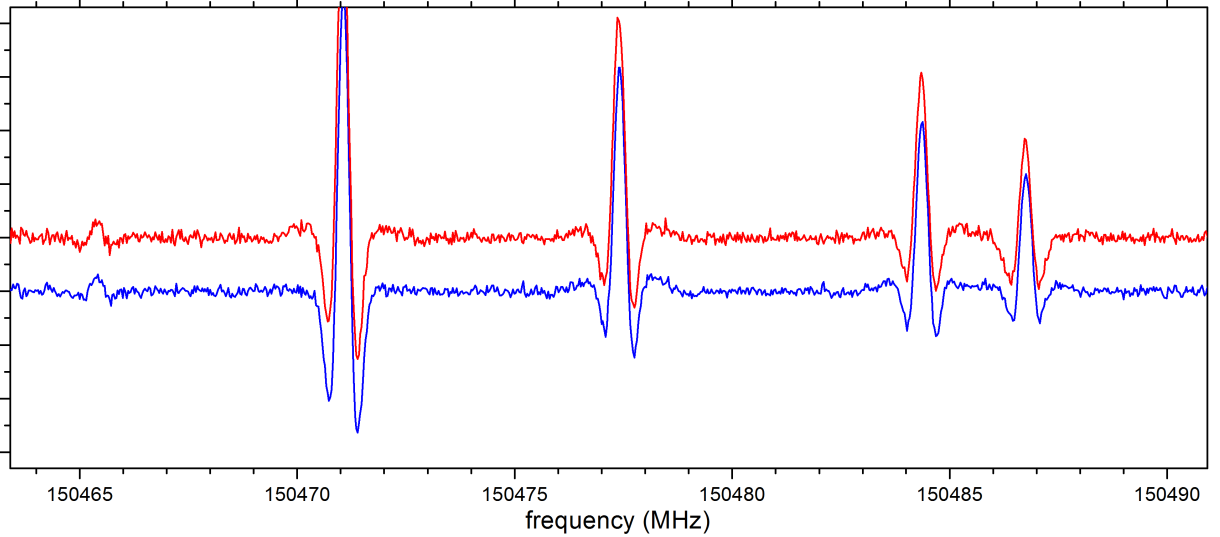
FIGURE 7: Le rapport signal/bruit en fonction de la constante de temps de la détection synchrone.

tiques pour le domaine submillimétrique. La Table 1.1 représente les différentes valeurs typiques de la largeur de raie, de la constante de temp de la détection synchrone et de la vitesse maximale d'enregistrement de spectre estimée avec l'Eq. 1.13.

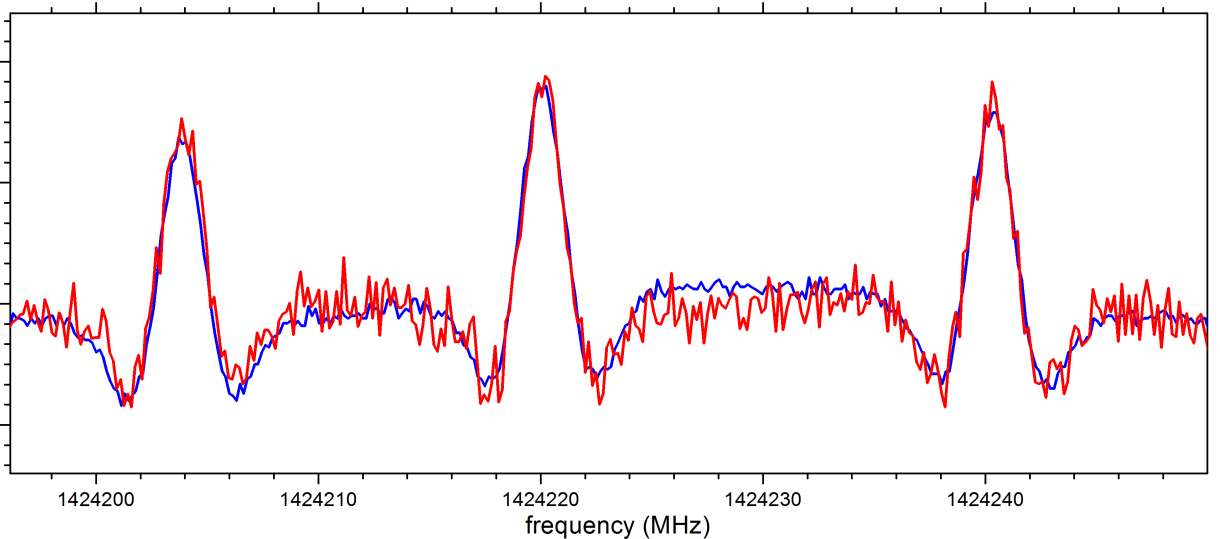
Comme il était constaté dans Sec. 1.3.2, le temps minimal de mesure $\Delta t_m^{(min)}$ avec le synthétiseur de balayage rapide est de 20 $\mu\text{s}/\text{point}$ en mode « profile ». Cette valeur du $\Delta t_m^{(min)}$ correspond à la valeur de la constante de temps $\tau \leq 4 \mu\text{s}$ et par conséquent à la largeur maximale de raie de 3.75 MHz. Celle-ci est comparable avec la largeur Doppler des raies du dimère de l'eau (H_2O)₂ à 1.7 THz. Dans la gamme de fréquences en dessous de 1 THz la largeur Doppler de raie des molécules avec la masse supérieure à 16 u.a. ne dépasse pas 3 MHz. Ainsi on peut constater que l'implémentation du synthétiseur à balayage rapide nous a permis d'atteindre la *limite physique* dans la vitesse d'enregistrement de spectre pour les mesures spectrales à la température ambiante au moins dans la gamme de fréquences jusqu'à 1 THz.

En ce qui concerne la capacité du spectromètre à balayage rapide de couvrir larges portions de spectre, on peut estimer qu'avec le temps minimal de 20 $\mu\text{s}/\text{point}$ et compte tenu du délai pour reconfigurer les instruments du spectromètre, il est possible d'enregistrer 10000 points en 1 s et par conséquent plus de 3×10^6 points par heure. Par exemple, cela représente un enregistrement de spectre dans l'intervalle de 500 MHz en 1 s, avec le palier de fréquence de 0.05 MHz. Typiquement le palier de fréquence de 0.05 MHz permet de bien résoudre une raie moléculaire dont la largeur est supérieure à 10 points spectraux (0.5 MHz).

1.3. Spectromètre térahertz à balayage rapide



(a) Les spectres du méthanol CH_3OH . Les spectres sont enregistrés dans les mêmes conditions expérimentales ($\tau = 5 \text{ ms}$, $\Delta t_m = 35 \text{ ms}$). En rouge : le spectre enregistré avec le synthétiseur THz à balayage rapide, en bleu : le spectre enregistré avec la version « lente » du synthétiseur THz.



(b) Les spectres du méthanol CH_3DOH . En rouge : le spectre enregistré avec le synthétiseur THz à balayage rapide ($\tau = 200 \mu\text{s}$, $\Delta t_m = 1 \text{ ms}$), en bleu : le spectre enregistré avec la version « lente » du synthétiseur THz ($\tau = 5 \text{ ms}$, $\Delta t_m = 35 \text{ ms}$).

FIGURE 8: Les spectres du méthanol utilisés pour comparer les deux versions du spectromètre THz.

Sensibilité. Il est évident que l'augmentation de la vitesse d'enregistrement de spectre et la réduction de la constante de temps de la détection synchrone ont pour conséquence la réduction du rapport signal/bruit des raies observées et de la sensibilité de spectromètre. Dans le cas idéal, le rapport signal/bruit augmente ou diminue de façon proportionnelle à la racine carrée du temps d'observation.

La Fig. 7 représente le rapport signal/bruit R_{sb} mesuré en fonction de τ pour la

raie de transition $J = 37 \leftarrow 36$ à 448319.4 MHz de O¹³CS, en abondance naturelle. Les mesures ont été réalisées avec le synthétiseur THz à balayage rapide à base de sources solides. Tous les points expérimentaux ont été mesurés dans les mêmes conditions, température : 298 K, pression de gaz dans la cellule d'absorption : 6 µbar, fréquence de modulation : 0.1515 MHz, déviation de fréquence : 0.51 MHz, détecteur : bolomètre à électrons chauds InSb. La ligne continue est le résultat d'approximation par la méthode de moindres carrés de l'ensemble des points expérimentaux par une fonction de type : $R_{sb} = A\sqrt{\tau}$, avec $A = 572 \pm 20$.

Comme l'on peut constater, dans l'ensemble l'évolution des points expérimentaux suit la proportion à $\sqrt{\tau}$. Ceci confirme le fait que l'implémentation du synthétiseur à balayage rapide et le respect de la condition 1.13 ne rajoute pas de bruit supplémentaire ni dans la source de rayonnement ni dans la chaîne de détection. Nos estimations ultérieures montrent que la sensibilité du spectromètre THz sans le synthétiseur à balayage rapide est de l'ordre de 10⁻⁶ cm⁻¹. Cette valeur correspond au temps minimal de mesure d'un point spectral de 25 ms/point. Dans la nouvelle configuration avec le synthétiseur DDS, si la priorité de mesures spectrales est la couverture de large bande de fréquence en minimum de temps, on peut augmenter la vitesse d'enregistrement d'un facteur 100 en réduisant ainsi la sensibilité d'un ordre de grandeur seulement. Ainsi avec le temps de mesure d'un point spectral de 250 µs/point et la constante de temps de la détection synchrone de 50 µs, la sensibilité du spectromètre est de l'ordre de 10⁻⁵ cm⁻¹ ce qui est en accord avec l'observation de la raie $J = 37 \leftarrow 36$ de O¹³CS. Le coefficient d'absorption de cette raie, en tenant compte de l'abondance naturelle de l'isotope ¹³C, est de 6.6×10^{-4} cm⁻¹ et le rapport signal/bruit pour cette raie à $\tau = 50$ µs est de 100 environ.

Les figures 8a permettent de comparer les performances des deux versions du spectromètre THz : la version précédente « classique », où le balayage en fréquence s'effectuait par le synthétiseur Agilent E8257D, et la version actuelle, avec le système de balayage en fréquence rapide. La Fig. 8a compare les enregistrements des spectres effectués dans les mêmes conditions expérimentales. S'il n'y a pas de différences importantes entre les deux spectres, le synthétiseur THz à balayage rapide peut être appliqué en spectroscopie à haute résolution sans dégradation de la sensibilité du spectromètre. L'analyse détaillée montre que l'écart entre les variances du bruit dans les deux cas ne dépasse pas 10%. Le niveau de bruit de phase du nouveau synthétiseur THz à balayage rapide est comparable à celui de la version « classique » du spectromètre. La Fig. 8b représente les spectres du méthanol CH₂DOH à 1.4 THz. Notons que les deux spectres ont été obtenus par multiplication de la fréquence du synthétiseur de référence par un grand facteur de multiplication $N = 108$. L'analyse montre que le rapport des variances de bruit entre la

version « classique » du synthétiseur et la version à balayage rapide est de 6.16 ce qui est comparable avec la valeur théorique idéale de $\sqrt{35} = 5.92$.

Précision des mesures. La manière la plus précise de déterminer la fréquence d'une raie spectrale est d'ajuster le profile de celle-ci en utilisant la méthode des moindres carrés par une fonction mathématique dont l'un des paramètres est la fréquence de la raie. En plus de la fréquence, la liste typique des paramètres ajustés comprend également l'amplitude et la largeur de la raie. Ainsi la précision de l'ajustement dépend essentiellement de la forme de la raie observée, à condition que la fonction mathématique ait été choisie de façon appropriée et qu'elle tient compte des conditions expérimentales.

Comme il était indiqué ci-dessus, en mode « profile » le synthétiseur à balayage rapide est modulé en fréquence par commutation entre deux profiles de fréquence. Ce type de modulation fournit la déviation de fréquence avec très grande précision car elle est définie de façon numérique et reste donc inchangée lors du balayage du synthétiseur. Par conséquent ce type de modulation fournit également l'erreur la plus faible possible, dans la détermination de la fréquence de raie. De plus, la bonne définition des paramètres de modulation permet de prendre ceux-ci en compte dans la modélisation des profiles de raies moléculaires et d'exclure toute l'influence de la fonction d'appareil dans la forme des raies.

Comme l'on peut également constater à partir de la Fig. 8b, le balayage rapide en fréquence ne déforme pas la raie, et le respect de la condition 1.13 garantit également la distorsion minimale dans la forme de raie dans le circuit du détecteur synchrone. Ainsi, on peut estimer que la précision de mesure de fréquence du spectromètre THz à balayage rapide est la même que pour le spectromètre dans sa configuration « classique » : 0.02 à 0.03 MHz pour une raie spectrale isolée et intense. Cette estimation se confirme par les études en masse des spectres moléculaires enregistrés avec le nouveau spectromètre à balayage rapide. En réduisant le temps d'acquisition de spectre par un facteur 10 en moyenne, nous n'avons pas remarqué des changements dans les déviations standards issues des ajustements des fréquences des raies spectrales par rapport aux études des spectres enregistrés avec la version « classique ».

1.4 Publications

1. E. A. Alekseev, R. A. Motiyenko & L. Margulès. **Millimiter- and Submillimeter-Wave Spectrometers on the Basis of Direct Digital Frequency Synthesizers.** *Radio Phys. Radio Astron.* 3, 75–88, 2012.
2. O. Zakharenko, R. A. Motiyenko, L. Margulès & T. R. Huet. **Terahertz spectroscopy of deuterated formaldehyde using a frequency multiplication chain.** *J. Mol. Spec.* 317, 41–46, 2015

MILLIMETER- AND SUBMILLIMETER-WAVE SPECTROMETERS ON THE BASIS OF DIRECT DIGITAL FREQUENCY SYNTHESIZERS

E. A. Alekseev¹, R. A. Motiyenko², & L. Margulès²

¹*Institute of Radio Astronomy, National Academy of Sciences of Ukraine,
4, Chervonopravorna St., Kharkiv, 61002, Ukraine*

²*Laboratoire de Physique des Lasers, Atomes et Molécules, UMR CNRS 8523,
Université de Lille 1,
F-59655 Villeneuve d'Ascq, France*

*Address all correspondence to E. A. Alekseev E-mail: ealekseev@rian.kharkov.ua

Original Manuscript Submitted: 5/19/2011

Two new spectrometers based on the direct digital frequency synthesizers are presented. The instruments are characterized by a high rate (up to 100 GHz/hr) of molecular spectrum recording with a high accuracy of measuring transition frequencies (the measurement error for isolated spectral lines lies within ± 0.002 MHz provided that the signal-to-noise ratio is 50 or greater). Frequency modulation of the radiation source is provided by direct digital frequency synthesizers that guarantees high stability and determinancy of frequency-modulated signal parameters and makes it possible to minimize the spectral lineshape distortions.

KEY WORDS: *spectrometer, rotational spectrum, millimeter and submillimeter wavelength ranges, direct digital frequency synthesizer*

1. INTRODUCTION

As is known, wide range records of molecular spectra represent a good basis for comprehensive investigation of spectral lines making essentially easier their assignment at the initial stage of study. The time required to obtain such records plays an important role especially during investigation of unstable or rare molecules. That is the reason why researchers were looking for a long time for possibilities to build spectrometers that would allow obtaining wide-range records for a minimum possible time. In the infrared range the obtaining of such records has become usual long ago

(see e.g. [1, 2]), and spectrometers of the kind are already produced commercially [3].

By the present time, two basic approaches to the construction of wide-range spectrometers have been developed in the microwave molecular spectroscopy. The first one is based on frequency synthesizers, while the second on the use of optical calibration technique.

Currently, the overwhelming majority of spectrometers are built on the basis of frequency synthesizers [4–11]. This is not per accident since this is exactly the approach that provides the highest measurement accuracy of central frequencies and shapes of spectral lines. Today, most spectrometers are built around various

versions of the phase-locked loop (PLL) synthesizers produced by the Agilent Technologies, Inc., whose output frequency is multiplied into millimeter- or sub-millimeter-wave range. However, application of frequency synthesizers is associated with principal limitations on the spectrum recording rate. The reason is that due to a comparatively long frequency switching time the time interval between adjacent samples in the majority of cases is about 100 ms.

At present, the family of spectrometers with optical calibration is represented by two instruments [12, 13]. In the late eighties, a novel approach to constructing wide-range spectrometers without using the frequency synthesis technique was suggested in Nizhni Novgorod (Russia) [12]. The emission source is a backward-wave oscillator (BWO) whose frequency is stabilized using a reference Fabry–Perot resonator. The wide-range frequency scanning is provided by mechanical adjustment of the reference resonator frequency. Within this approach, the molecular line frequencies are estimated through comparison with the well-studied SO₂ molecule spectrum [14, 15] using a special optical calibration system. The spectrometer was named RAD-3, which means radio spectrometer with acoustic detector of the third generation. The current status of the spectrometer is presented in detail in paper [16]. The indisputable advantage of the spectrometer is the absence of a complicated system of frequency synthesis. However, the optical calibration system has proved to be no less complicated in comparison with the frequency synthesis system, simultaneously providing poorer measurement accuracy of molecular line frequencies (errors reaching ± 0.5 MHz). In addition, the mechanical adjustment of the reference resonator frequency limits essentially the spectrum recording rate.

A similar approach has been used as a basis for the well-known spectrometer of the Ohio State University (USA) [11, 13, 17] named FASSST (FAst Scan Submillimeter Spectroscopic Technique). A BWO was also used in the spectrometer as the radiation source. By application of parametric stabilization of the BWO and without using the reference resonator the designers have obtained record rate of molecular spectrum recording (for a single frequency scan it reaches 10 GHz/s). The measurement of molecular line frequency is provided by SO₂ molecule spectrum and a special optical calibration system, which occurred to be much more complicated than that used in Nizhni Novgorod. Nevertheless, the acceptable accuracy can be obtained only

as a result of processing of at least 200 independent upward frequency scans and additionally of 200 independent downward frequency scans [11, 13]. Thus, the actual recording rate for molecule spectra proves to be lower approximately by three orders of magnitude and is about 100 GHz/hr. In addition, the extremely high rate of single realization recording is accompanied by essential lineshape distortions, and the accuracy proves to be poorer by about two orders of magnitude in comparison with the spectrometers based on the frequency synthesis. Any attempts to improve the frequency measurement accuracy missed the desired result. Some improvement was possible for those frequency ranges only where a preliminary calibration had been performed using a spectrometer with frequency synthesis [18].

As was already mentioned above, the spectrum recording rate of the spectrometers built on the basis of frequency synthesizers is primarily limited by the switching time of the reference synthesizers. However, over the recent years, a great advancement is observed in the development of Direct Digital Synthesizers (DDS) [19], which are capable to provide extremely fast (up to 10 ns) frequency switching. These devices have a number of advantages, especially such as the high precision and rate of frequency setting. In addition, these synthesizers possess a unique property to allow changing the frequency from one value to another with continuous phase. The grave disadvantage of the DDS is the presence of spurious spectral components in the output signal which leads to considerable limitations of their application in the systems with frequency multiplication. Despite the fact that in order to suppress spurious spectral components, the newest DDSs include a spurkiller device [20] for their selective suppression, this technology proves to be inefficient in the fast frequency scan systems. The reason is that the selective suppression is provided through introduction of a compensating signal and hence, precise adjustment of the frequency, amplitude and phase of the signal is required for each spectral component. The impact of spurious spectral components can be essentially reduced through minimizing the frequency multiplication factor, and also using a narrowband adaptive filtration technique [21]. Alekseev and Zakharenko [21] and Motiyenko et al. [22] succeeded in constructing a millimeter wave spectrometer based on a DDS. However, the authors have used a sole advantage of these synthesizers consisting of high precision

of frequency setting. The problem of increasing the rate of molecular spectrum recording was not analyzed in these studies.

By now there are two more spectrometers known to be constructed with the use of DDS. One of these has been developed in Nizhni Novgorod [23, 24]. This is a cavity spectrometer intended primarily for precise measurements of the lineshape at the atmospheric pressure. For this reason the instrument cannot be used for high- and ultra-high resolution spectroscopy. Moreover, because of a large width of a spectral line at the atmospheric pressure and narrowness of the cavity modes there is no need in providing a continuous recording of the spectrum. It is sufficient just to minutely record the cavity modes within the operation frequency range [24]. Such a solution, being optimum for atmospheric optics, is unacceptable for spectroscopy of high- and ultra-high resolution in which case a continuous recording of the spectrum is required.

Another DDS-based spectrometer has been constructed in the Texas University in Austin (USA) [25-27]. It is basically intended for spectroscopy of molecules in a pulsed supersonic jet. The instrument is capable of very fast recording of narrow spectral ranges and is not used for wide-range recording of molecular spectra.

In the present paper we have made an attempt to develop a DDS-based spectrometer which would provide a molecular recording rate comparable with that of the FASSST, while retaining advantages of the spectrometers built on the basis of frequency synthesizers.

2. ON THE POSSIBILITY OF INCREASING THE RECORDING RATE OF THE FREQUENCY SYNTHESIZER-BASED SPECTROMETERS

It is evident that the spectrometer capable of highly accurate measurements of absorption line frequencies can be constructed only on the basis of frequency synthesizers. The high rate of molecular spectrum recording can be obtained using the direct digital frequency synthesis. Since the maximum value of the DDS operation frequency today does not exceed 500 MHz, in order to operate at millimeter and submillimeter waves it is necessary to use the frequency multiplication. However here, there is a rather grave obstacle since the DDS output signal contains a number of spurious products in addition to the synthesized useful compo-

nent [19]. The discussion of the nature of these spurious components lies beyond the scope of the present paper. Moreover, all these points have been already considered in detail in the literature [19].

The most efficient way to reduce spurious components is the adaptive filtration based on a phase-locked loop (PLL) system along with minimizing the frequency multiplication factor [21, 22]. This is the reason why the response of the PLL system to switching of the DDS frequency, is one of the most important problems. As was shown earlier [28], the duration of such transient processes does not exceed 1–2 μ s, which offers good possibility to essentially increase (by one or two orders of magnitude) the molecular spectrum recording rate.

It should be noted that, except purely technical problems, there are also real physical limitations for increasing the spectrum recording rate. These limitations stem from reaction time of molecular systems, i.e. they are associated with the finite time of excitation and relaxation of molecular state. If the spectrum recording rate is too high, then the finite reaction time leads to severe lineshape distortions and also to a noticeable shift of the line central frequency. These problems are well demonstrated in the case of the FASSST spectrometer [11, 13, 17]. The designers selected deliberately the extremely high recording rate for single scans (about 10 GHz/s), which leads to considerable lineshape distortions. However, this is a forced measure since in order to reach the acceptable accuracy during an optical calibration cycle it is necessary to “freeze” the BWO frequency instability (here we use terminology of the authors of paper [13]).

In order to avoid the above mentioned problems and keep the measurement accuracy, it is necessary to estimate the maximum admissible rate of molecular spectrum recording. The simplest way to make the estimate is based on the use of the experimentally observed linewidth Δv , whose value is reciprocal to the state relaxation time τ (as a rule, the measurements are carried out for observations of the Voigt contour of the spectral line with comparable contributions of the Doppler and collision broadening effects). As is known, in order to provide a completely steady-state mode, the time interval between adjacent measurements should exceed 5τ . Since molecular spectra are recorded with the use of a frequency-modulated probe radiation with subsequent lock-in detection, our time estimates relate first of all to limitations on the selection of the modulation frequency magnitude. In this case, the time inter-

val 5τ is the minimum acceptable value of the one half of the modulation period T_{mod} , and hence $T_{\text{mod}} \geq 10\tau$ or $T_{\text{mod}} \geq 10/(\Delta\nu)$. To provide efficient operation of the lock-in detector, the observation time Δt at each point should be greater by at least one order of magnitude than the signal modulation cycle, i.e. $\Delta t \geq 10T_{\text{mod}}$ or $\Delta t \geq 100/(\Delta\nu)$. For the spectral line width of 0.5 MHz, the modulation frequency should not exceed 0.05 MHz, while the time interval between adjacent samples Δt , which provide no distortions of the lineshape and no additional noise, should be essentially greater than 0.2 ms. The line width in the millimeter wavelength range may reach 0.2 MHz. In this case, the time interval Δt between adjacent samples should exceed 0.5 ms. Taking into account the evaluation character of the above consideration, we have limited the minimum observation time Δt to 1 ms.

Hereafter, we present practical results obtained during modernization of two spectrometers. One of these is the millimeter wave spectrometer developed in Kharkiv (Ukraine) at the Institute of Radio Astronomy, National Academy of Sciences of Ukraine (IRA NASU) [21, 22]. The other one has been constructed at the Laboratory for the Physics of Lasers, Atoms and Molecules of the University of Science and Technology in Lille (France) [8].

3. THE IRA NASU MICROWAVE SPECTROMETER

The millimeter wave spectrometer developed at the IRA NASU (Kharkiv, Ukraine) [21, 22] has been successfully used for investigation of molecular spectra for many years (see e.g. [14, 22, 29–31]). Since after the papers [21, 22] had been published, the spectrometer was essentially modified, below we present its current status. The functional diagram of the spectrometer is shown in Fig. 1. This is an absorption spectrometer. The radiation from the frequency synthesizer at 49000 to 250000 MHz is transmitted through the absorption cell containing the gas to be investigated and then is detected by the receiving system.

A DDS AD9851 [32] is used in the spectrometer as the reference synthesizer. Its output frequency is converted into the frequency range 385 to 430 MHz using an up-converter (see Fig. 1). The frequency of the reference synthesizer is multiplied in two PLL circuits. In order to increase the signal-to-noise ratio for the

subsequent frequency multiplication and also to efficiently filter out spurious components in the DDS signal, a klystron operating within the 3400–5200 MHz frequency range with a narrowband (~ 1 kHz) PLL system is used at the first stage of frequency multiplication. A special electromechanical lock system is intended to provide automatic synchronization of this PLL, as well as its wide-range tracking. At the second multiplication stage, the BWO is locked by a PLL system using a harmonic of the klystron radiation. Application of the three BWOs allows covering the frequency range 49000 to 149000 MHz. A comparatively high level of the BWO output signal power (10–30 mW) makes it possible to use a passive frequency multiplier to extend the operation frequency range to 250000 MHz. The maximum measurement accuracy is achieved by synchronizing all the signals by a rubidium frequency standard.

The sample of gas to be analyzed is contained in a quasi-optical dielectric cell of 3 m length and internal diameter 56 mm. The cell-waveguide section matching is provided by waveguide-to-quasioptic adaptors. The vacuum windows are made of Teflon. To minimize the standing wave level their thickness does not exceed 1 mm.

The detector of radiation represents a Schottky diode working at room temperature. The detector output signal is amplified by a low-noise amplifier based on AD8331 [33] (LNA, see Fig. 1). This is an ultra low-noise gain-controlled amplifier which allows the spectrometer to be easily adapted to different measurement conditions.

The spectrometer hardware is connected to the control computer through a standard serial interface RS-232. The interface section of the spectrometer has been constructed on the basis of an ADuC834 micro-converter (Analog devices, Inc.) [34], which contains high-quality analog-to-digital and digital-to-analog converters, a rather powerful microprocessor with a diversity of standard interfaces (RS-232, SPI, I²C) and many other components. Such a solution makes it possible to create a compact-size, flexible and highly efficient data-processing and measuring system.

3.1. Features of Frequency Modulation and Lock-in Detection

The majority of modern frequency synthesizer-based spectrometers involves frequency modulation of the radiation source signal and lock-in detection in the re-

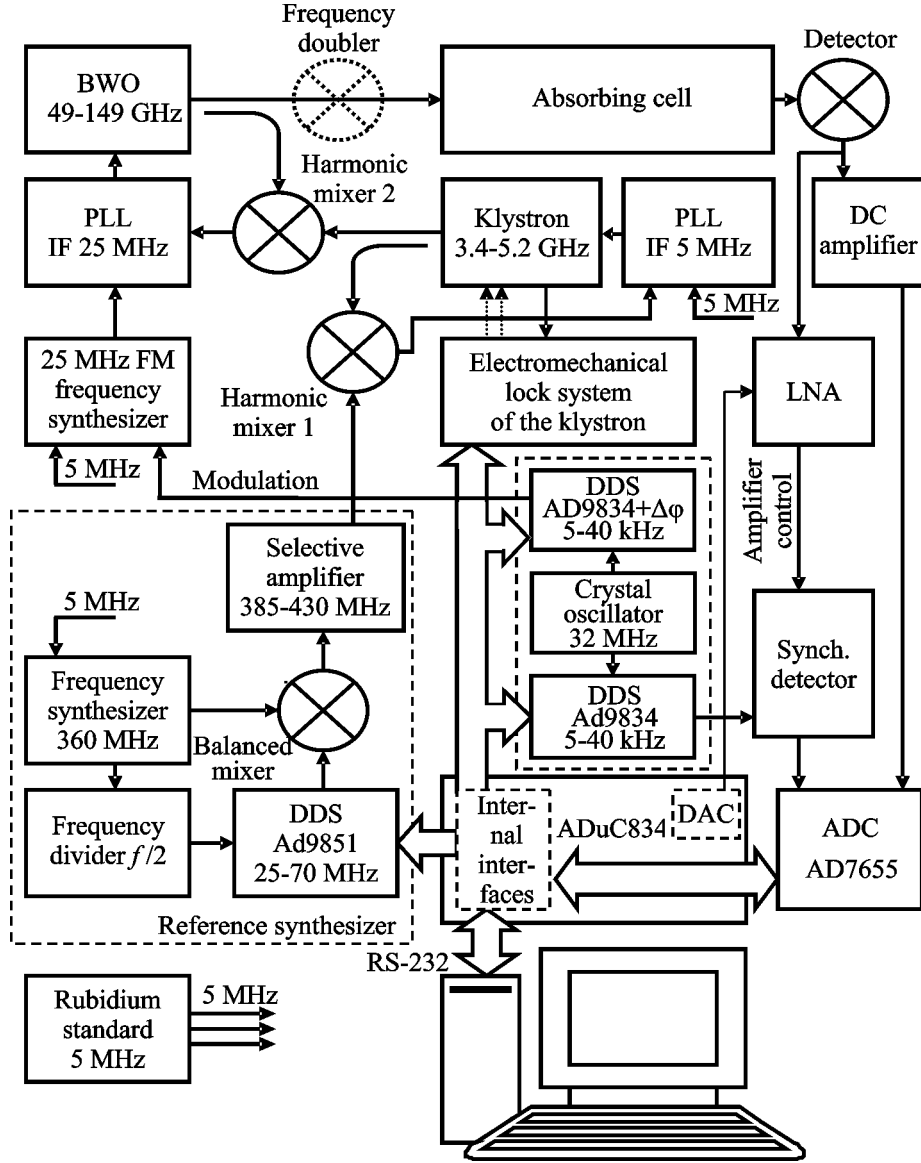


FIG. 1: Functional diagram of the spectrometer developed in Kharkiv

ceiving system. Therefore absorption lines are detected as the first-order frequency derivative of their shape. It is quite natural that any variations in the modulation index result finally in lineshape distortions and consequently in errors of determining the transition central frequencies. Moreover, it is well-known [35, 36] that the highest accuracy of measuring the absorption line central frequencies is provided with minimal distortions of modulation signal. As was shown earlier [28], appli-

cation of DDSs is the most suitable way to form frequency-modulated signals. Unfortunately, today it seems impossible to implement in our spectrometer this method of obtaining frequency-modulated signals. The main impediment is the narrowband PLL intended for filtering out spurious components of the DDS output signal. This is the reason why we have used another method where the modulated signal is formed by a frequency synthesizer operating at fixed frequency. First

of all, this solution guarantees invariability of the frequency deviation (and hence, of the modulation index) in the process of molecular spectrum recording. In addition, by properly selecting the operating point on the operational characteristic of the voltage-controlled oscillator included in the 25 MHz synthesizer we have achieved minimum distortions of the modulating signal waveform. In the case of operation at a fixed frequency, this can be achieved in some reasonable ways. The modulating and reference signals for synchronous detection are both formed by a pair of additional synchronously operating DDS based on the AD9834 [37] with programmable phase shift (see Fig. 1). The synthesizer of the frequency-modulated signal at the 25 MHz carrier frequency is used as a reference oscillator in the PLL system that provides the BWO phase locking. As a result, the BWO output radiation is also frequency-modulated.

3.2. Full-Power Channel

As is known, application of frequency modulation in spectrometers with subsequent lock-in detection makes it impossible to measure level of the constant power of the radiation passed through the absorbing cell. At the same time, estimation of this power level is necessary in many situations, for example, while measuring absorption factors, in the case of ambiguous assignment of transitions, etc. In order to measure this signal level we have included in the spectrometer an additional channel with a DC amplifier. Since the detectors operate with a bias, we have provided a compensation for this bias. At present, a two-channel reception of the detector signal has been implemented in the spectrometer which implies conventional reception at the modulation frequency and registration of the DC signal level (see Fig. 1).

It should be noted that only rather strong lines could be observed in the full power channel. To improve the sensitivity and intensity estimation accuracy it is necessary to recover the full power channel on the basis of the high-precision measuring channel that records the first-order frequency derivative of the lineshape. The basic problem in this case is the amplitude relation between the channels. Below we will consider this problem in detail.

As is known, the spectroscopy technique is based on the measurement of variations of the intensity of electromagnetic radiation passed through the absorbing cell with the gas sample to be investigated. For a

cell of length l such variation is described by the Bouguer–Lambert law [36]. In terms of the detector current it can be represented as follows (in case of low absorption the exponential function can be expanded into a Taylor series truncated to the linear term)

$$i(v) = i_0(v) \exp(-\gamma(v)l) = i_0(v)(1 - \gamma(v)l). \quad (1)$$

Here $\gamma(v)$ describes the lineshape (depending on measurement conditions $\gamma(v)$ can correspond to Doppler, Lorentz or Voigt profile [38]), and $i_0(v)$ is the initial current through the detector in the absence of molecular absorption, i.e. when the cell is empty. It is worthy of note that $i_0(v)$ describes possible variation of the detector current due to the frequency dependence of its sensitivity, unhomogeneity of the source radiation power characteristic, and standing wave effects. If the frequency deviation is sufficiently small, the output signal of the lock-in detector can be considered as the first-order frequency derivative of Eq. (1) when the first harmonic detection is applied, or as the second derivative correspondingly at the second harmonic detection (in the square brackets we emphasized the terms responsible for lineshape distortions), viz.

$$i'(v) = [i'_0(v)(1 - \gamma(v)l)] - i_0(v)l\gamma'(v), \quad (2)$$

$$i''(v) = [i''_0(v)(1 - \gamma(v)l) - 2i'_0(v)\gamma'(v)l] - i_0(v)l\gamma''(v). \quad (3)$$

Usually in experiments we record the signal given by the expression Eq. (2). This formula includes an unknown empirical function $i_0(v)$ whose form is determined by conditions of specific measurements. In order to estimate the molecular line intensity, it is necessary to determine this function. The function cannot be obtained a priori since even small temperature variations or mechanical vibrations can essentially affect its form. Hence it should be determined immediately in the process of measurements. The full power channel implemented in the spectrometer is intended exactly for this purpose.

A typical record of the spectrum obtained in the two-channel technique is presented in Fig. 2. The solid curves here correspond to experimental records, with $S(v)$ and $P(v)$ being associated with the measuring and full-power channels, respectively. One notes that $P(v) \sim i(v)$. The function $P(v)$ can be obtained from $S(v)$ using the following relation

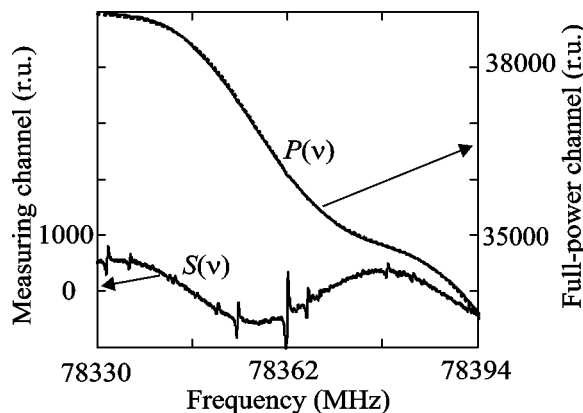


FIG. 2: Reconstruction of the full-power channel using the measuring channel $S(v)$. The full-power channel $P(v)$ is represented by the solid curve. The result of reconstruction using the measuring channel is shown by the dotted curve. As can be seen, it is completely coincident with $P(v)$

$$P(v) = A \int S(v) dv + Bv + C.$$

Here, parameters A , B and C are to be fitted by the least-squares method. The coefficient A represents a scaling factor describing the channel-to-channel conformity, the linear term Bv is used to compensate the inaccuracy of the lock-in detector adjustment to zero, and C is associated with the constant power level, i.e. being the parameter which is lost during lock-in detection (as a result of differentiation).

Parameters A , B and C are determined by applying the least-squares method to experimental data obtained in the measuring and full-power channels. This allows sufficiently accurate recovering the function $i(v)$. The recovered function is shown by the dotted curve in Fig. 2. To reconstruct the empirical function $i_0(v)$ it is sufficient either to filter the function $i(v)$ or to approximate it by a suitable analytic expression, for example, by a polynomial. The full-power level recovered in such a way along with the channel conformity factor makes it possible to estimate the molecular line intensity.

The constructed two-channel system has one more advantage. As was mentioned above, the terms in the square brackets in the expressions Eqs. (2) and (3) describe distortions in the shape of experimentally measured molecular spectral lines. These distortions finally result

in errors of estimating the line central frequencies. It is absolutely evident that these distortions and errors are minimum when $i'_0(v) = 0$, i.e. in the case when $i_0(v) = \text{const}$. However by virtue of various factors, first of all due to the effects produced by the standing wave in the absorbing cell, this condition is not met. As was shown above, the implementation of the full-power channel makes it possible to recover the empirical function $i_0(v)$ and hence, to make use of a more accurate expression for the shape of the recorded line, namely, the expression Eq. (2). This allows minimizing the errors in determining the absorption line frequencies associated with the frequency dependence of the empirical function $i_0(v)$.

3.3. Increasing the Spectrum Recording Rate

The main objective of the study is to essentially increase the spectrum recording rate without loss of the measurement accuracy. The spectrum recording rate of the previous version of the spectrometer [21, 22] was mainly limited by the conversion time of the measuring $\Sigma - \Delta$ ADC (analog-to-digital converter). As a result, the time interval between adjacent samples was equal to 40 ms. To overcome this obstacle, we have applied a 16-bit fast multichannel ADC AD7655 with the conversion time about 1 μ s.

Another essential limitation is the bidirectional data exchange through a serial interface. To minimize the data exchange time we have used the maximum rate of asynchronous data transmission equal to 38400 bit/s. In addition, we have minimized the amount of the data to be transmitted having transferred the function of calculating the current value of the DDS frequency to a controller. The initial magnitudes of frequency and step are transferred from the control computer into the controller once per one thousand of samples, and at each acquisition the computer only sends the command that starts the measurements. The changes described above allowed reducing the acquisition time to 10 ms. Hence we have succeeded to increase the spectrum recording rate by a factor of four.

The obtained value of the spectrum recording rate is mostly limited by the capabilities of data transfer through the serial interface (RS-232). Here the main obstacles are the data transfer rate and regular alternation of the data transfer direction. The reason is that this interface serves for transmitting both the frequency control instructions from the computer to the spectrometer and the measured data from the spectrometer

into the computer. These obstacles can be removed by means of data stream separation, for example, through arranging transferring instructions to the spectrometer via one interface and reading measured data through another one. At present, we are in search for an acceptable engineering solution which would allow further increasing the spectrum recording rate of the spectrometer constructed in Kharkiv.

The performances of the new spectrometer are illustrated by the wide-range record of the methyl formate molecule (HCOOCH_3) spectrum presented in Fig. 3(a). The record has been obtained with the step 0.02 MHz and contains about 325000 samples. For better visualization, a fragment of the record is shown in more detail in Fig. 3(b). The spectrum covering the 6.5 GHz frequency range has been obtained during approximately 55 min, that corresponds the molecular spectrum recording rate equal to about 7 GHz/hr. With the frequency step 0.03 MHz (in most cases it is the maximum allowed step value for our spectrometer) the recording rate is increased up to

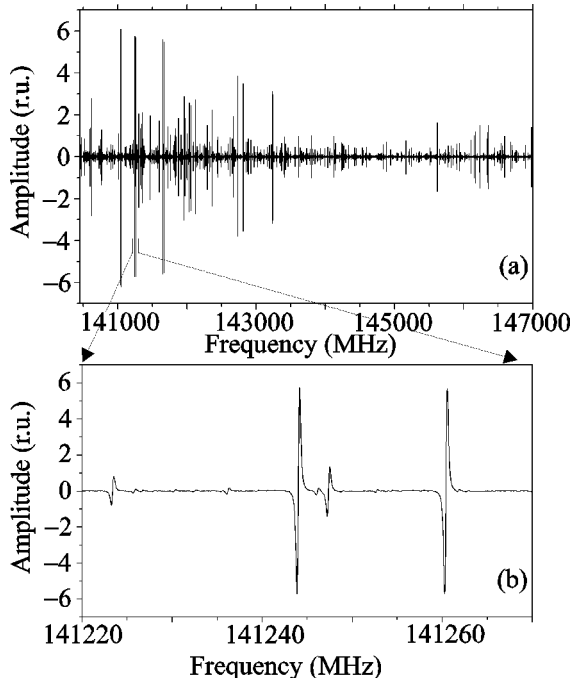


FIG. 3: A fragment of a record of the methyl formate molecule (HCOOCH_3) spectrum. The record has been obtained for 55 minutes

10 GHz/hr. Hence we may speak about the essential increase of the spectrum recording rate since the operation frequency range of each BWO can be recorded during 3 or 4 hours. It should be noted that the obtained fourfold increase of the spectrum recording rate is not accompanied by any loss of the accuracy of transition frequency measurements.

Evidently, the increase of the spectrum recording rate is accompanied by the respective loss in sensitivity. However the high rate makes it possible to provide the synchronous integration mode to increase the signal-to-noise ratio. This procedure can now be applied to realizations, i.e. to spectral scans containing a few hundreds of points. The advantage of this mode consists in efficient averaging of low-frequency noise. Conventionally, the noise-limited sensitivity of spectrometers is estimated from the record of the weakest absorption line obtained with the detector time constant τ equal to 1 s. With $\tau=1$ s, it is possible to effectively average noise components whose correlation length is less than 1 s. To provide the steady-state mode for $\tau=1$ s, the time interval between adjacent samples should be $\Delta t=5\tau$. Hence a scan of e.g. 100 points would be recorded during 500 s. For the time interval between samples equal to 10 ms, a 100 point scan in the case of a fast scan spectrometer would take 1 s. Hence we can record 500 scans during 500 s. Since in this case the maximum time interval between samples at each frequency point reaches almost 500 s, all noises with the correlation length less than 500 s would be averaged. It is evident that such a way to increase the signal-to-noise ratio proves to be more efficient in comparison with simply increasing the detector time constant.

4. MICROWAVE SPECTROMETER OF THE LABORATOIRE DE PHYSIQUE DE LASERS, ATOMES ET MOLÉCULES

A functional diagram of the spectrometer constructed at the University Lille 1 is shown in Fig. 4. Like the instrument developed in Kharkiv, it is an absorption spectrometer with a BWO-based radiation source. The operation frequency range of the spectrometer is determined by frequency ranges of the applied BWOs which are 100–190, 170–250 and 580–660 GHz. The BWO phase locking is provided using a harmonic

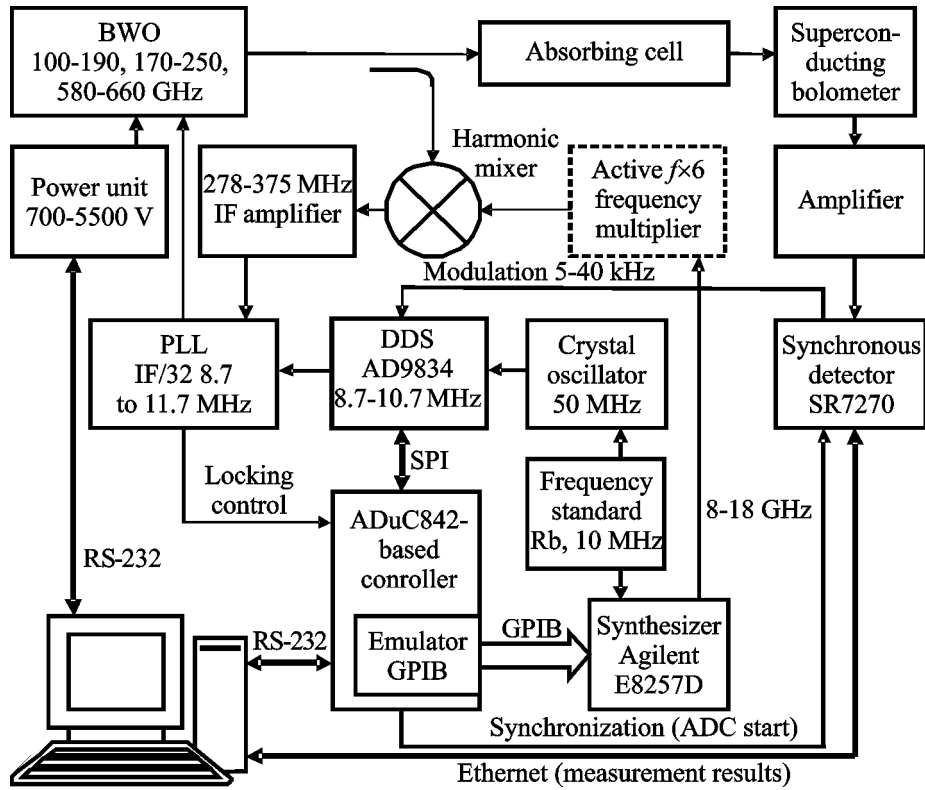


FIG. 4: Functional diagram of the spectrometer developed in Lille

of the commercial frequency synthesizer Agilent E8257D. In the frequency range 580 to 660 GHz in order to obtain an acceptable signal-to-noise ratio in the PLL system the E8257D output signal frequency is multiplied by a factor of six with the use of an active frequency multiplier (see Fig. 4).

The fast frequency scanning is achieved through scanning the reference frequency of the PLL system which provides the BWO phase locking. The signal of reference frequency is generated by a DDS (AD9834 [37]). To reduce the DDS spurious spectral components, the frequency multiplication factor has been selected comparatively low (specifically, 32), while the operation frequency range has been limited to 8.7–11.7 MHz. The multiplication factor of 32 corresponds to the value of PLL system intermediate frequency of 278–375 MHz. As is known, the spectral purity of the DDS output signal depends on purity of reference signal (50 MHz in the present case). Since the absolute frequency stability is provided by 10 MHz signal of high-stability

either from a rubidium frequency standard or from a GPS-receiver, we have focused a special attention on the formation of the 50 MHz reference signal. First, this signal is generated by a controllable crystal oscillator stabilized by a narrow-band PLL system using signals either from the rubidium standard or from the GPS-receiver. In this case the PLL system plays a role of an additional narrow-band filter reducing the influence of spurious spectral components in the 10 MHz reference signal. Second, the 10 MHz reference signal and the output signal of the 50 MHz synthesizer are both filtered by passive high-Q crystal filters.

The absorbing cell made of stainless steel is 2.2 m long with the internal diameter equal to 56 mm. The vacuum windows are arranged in the same way as in the spectrometer of the IRA NASU (see Section 3). A superconducting bolometer (QMC Instruments, Ltd.) is used as a broadband radiation detector. This allows one to use efficiently the whole operating frequency range of the spectrometer.

4.1. Increasing the Spectrum Recording Rate

The spectrometer hardware is controlled using an ADuC842 controller [39] which allows applying a standard RS-232 interface for communication. In addition, this design solution provides an opportunity to program the DDS via the SPI interface and perform emulation of the GPIB interface to control the E8257D synthesizer.

As was shown above, the principal obstacle to further increase the spectrum recording rate is the time of bidirectional data transfer through the RS-232 interface. To remove this obstacle, we have performed two important modifications of the spectrometer.

First, we have organized the process of molecular spectrum recording by fragments of ~ 100 MHz. By passing some part of calculation and control functions to the controller we were able to significantly reduce the amount of data transferred. In the new system, only in the beginning of frequency scan the computer sends to the controller a code of initial frequency value, a code of frequency step and a number of frequency steps. Then the whole segment of 100 MHz is measured without any data transfer between controller and computer. Each frequency value is calculated and set by controller. It should be noted that at each step of measurements these operations take about 4 μ s and thus do not influence the rate of molecular spectrum recording.

Second, we were almost able to avoid the bidirectional data transfer through the RS-232 interface during measurements due to application in the recording system of the newest commercial lock-in detector with a digital signal processor SR7270 (AMETEK, Inc.). A specific feature of this lock-in detector is the embedded memory buffer capable of storing up to 100000 samples at the acquisition rate up to 1 μ s per point. In this case, the data from the SR7270 can be transferred into computer through the Ethernet interface, which is much more faster against the RS-232. In fact, we have separated the measurement stage and the stage of data transfer into the computer. During the measurement stage, a spectrum segment of 100 MHz is scanned. The measurement process is synchronized by the controller. Specifically, after each new value of the DDS frequency is set the controller yields a start signal for the ADC with storing the result in the buffer memory. The measured data are stored in the recording system buffer, and they are transferred to the computer after comple-

tion of ~ 100 MHz scan. The controller is also intended for checking up lock-in mode of the PLL.

The typical molecular line width in submillimeter-wave range is 0.5 MHz or greater. In order to provide an acceptable accuracy and spectral resolution of measurements, one needs to obtain at least 10 samples per absorption line. For this reason, the frequency step is selected to be about 0.05 MHz. With this value of step in order to record the spectrum range of 100 MHz one needs 2000 points. Taking into account all the modifications performed, the typical scanning rate is 1 ms per point. Hence 2000 points would be recorded for 2 s. To transfer the data into the computer and visualize them, 1 s is needed. In addition 0.3 s are required to set new values of the reference synthesizer frequencies and correct voltages in the BWO slow-wave system. Thus, the total cycle of recording a 100 MHz segment of spectrum with a 0.05 MHz step takes about 3.3–4 s. Under these conditions for 1 hr one can record a spectrum in the range of 90–110 GHz. In the lower frequency range the frequency step has to be decreased since the absorption line width decreases. For example, the typical value of the frequency step for the frequency range 100–200 GHz is 0.025 MHz. Therefore, for 1 hr one can record a segment of spectrum of 45–55 GHz wide.

4.2. Frequency Modulation Features.

Wide-Range Recording. Estimated Accuracy

The spectrometer of the University Lille 1 operates with the frequency modulated radiation source and lock-in detection in the receiving system. The DDS is used as a reference source for the PLL system, which provides phase locking of the BWO. The frequency-modulated signal is produced by means of periodical variations of the DDS frequency (the architecture of AD9834 allows to set two values of the frequency with a possibility of rapid switching between them). A modulator of this type allows one to determine almost ideally the deviation since the frequency alternates between two values set with high accuracy. This means that the frequency deviation is set digitally and hence, remains unchanged in the process of molecular spectrum recording. Switching the DDS frequency is accompanied by an insignificant symmetric perturbations of short duration (~ 1 – 2 μ s) in the PLL system [28]. For this reason, the frequency-modulated signal obtained this way produces minimum possible, symmetric and predictable distortions of the molecular line shape and

hence, minimum possible errors in its frequency measurement. Moreover, the high determinacy of the parameters of the frequency-modulated signal would allow in future to account for the effect of modulation on the lineshape and exclude all possible distortions.

A characteristic feature of this technique of generating frequency-modulated signals is that molecular spectra can be recorded only in the form of the first frequency derivative of the lineshape. If desired, the second derivative of the lineshape can be obtained through numerical differentiation of the scan.

One of the most important problems is the measurement accuracy of the central frequencies of absorption lines, namely, the question how the increase in spectrum recording rate has affected this accuracy. As an example of the new spectrometer operation, Fig. 5(a) presents a record of the rotational spectrum of aziridine molecule (methyleneimine, C_2H_4NH) within the

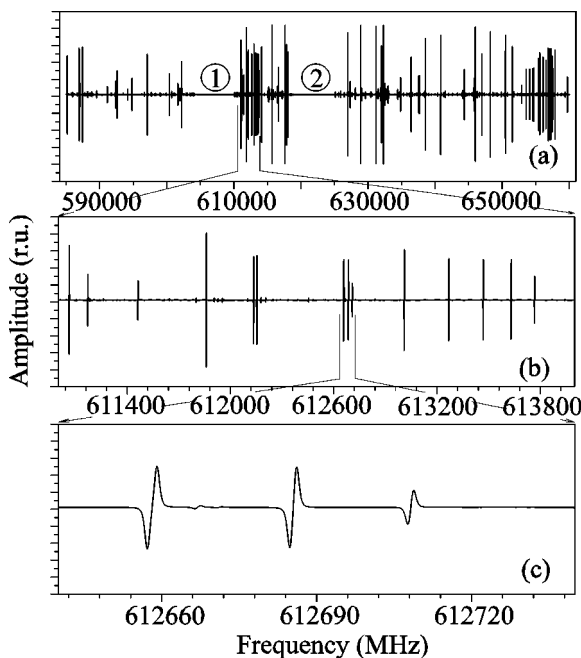


FIG. 5: A wide-range (585 to 660 GHz) record of the aziridine molecule (C_2H_4NH) spectrum. The record has been obtained for 49 minutes. Figures 1 and 2 label frequency ranges within which frequency synthesis was impossible because of an unsatisfactory value of the signal-to-noise ratio in the PLL system due to the low level of the output signal of the active frequency multiplier

frequency range 585–660 GHz. Using our spectrometer this fragment of spectrum has been obtained in 49 minutes with the frequency step 0.05 MHz. The record shown in the Figure contains short intervals (labeled by figures 1 and 2) where frequency synthesis was impossible because of an unsatisfactory value of the signal-to-noise ratio in the PLL system due to a low level of the output signal of the active frequency multiplier (see Fig. 4). The fragments of the spectrum presented in Fig. 5(a) are shown in Fig. 5(b) and 5(c) in more detail. As follows from Fig. 5(c), the selected value of the frequency step allows to define well the shape of absorption line. Transition frequency can be measured with high accuracy by treating the spectrum records containing sufficient number of samples per absorption line width. In the case under consideration, we measured frequencies of 298 rotational transitions of aziridine within the frequency range 585–660 GHz [40]. As follows from the processing of these data, the root-mean-square deviation in the experimental spectrum is 0.017 MHz. Hence the measurement accuracy in submillimeter waves in the case of routine observations in the fast spectrum recording mode can be estimated to be 0.02 MHz.

The measurement accuracy of rotational transition frequencies for isolated lines with a high signal-to-noise ratio (50 or greater) in submillimeter waves may be even better by an order of magnitude. Fig. 6 presents a record of the $J = 52 \leftarrow 51$ transition of OCS molecule characterized by a great dipole moment and hence, by intensive spectrum. This is a linear molecule with a sufficiently sparse spectrum such that practically all spectral lines can be treated as isolated ones. The record of the $J = 52 \leftarrow 51$ line has been obtained in two operation modes of the spectrometer which are i) sub-Doppler resolution mode, i.e. Lamb dip recording (curve 1 in Fig. 6), and ii) in the fast spectrum recording mode with Doppler broadening (curve 2 in Fig. 6). As is known, observation of the Lamb dip allows to essentially improve the frequency measurement accuracy since in this case one observes the natural linewidth which does not exceed a few tens of kilohertz. This is the reason why the frequency measurement accuracy for molecular lines with the Lamb dip is estimated to be about ± 0.001 MHz. The value of the $J = 52 \leftarrow 51$ transition frequency we have measured from the Lamb dip is (631743.0104 ± 0.0004) MHz, while in the fast scan mode it is (631743.010 ± 0.002) MHz. The frequency of this line in the Cologne Database for Molecular Spectro-

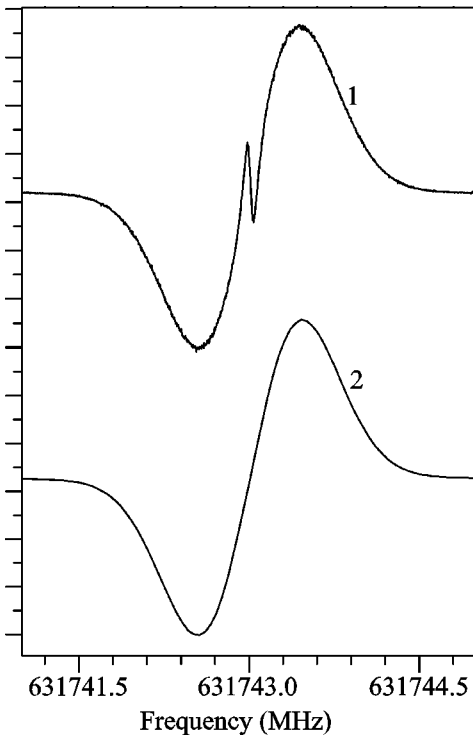


FIG. 6: A record of the $J = 52 \leftarrow 51$ transition line of the OCS molecule obtained in the sub-Doppler resolution mode, i.e. in the course of recording the Lamb shift (curve 1) and in the fast spectrum recording mode (curve 2)

scopy [41, 42] is (631743.0116 ± 0.001) MHz. The obtained results show that the measurement accuracy of the transition frequencies for isolated molecular lines observed in the fast recording mode with the signal-to-noise ratio exceeding 50 is estimated to be ± 0.002 MHz.

5. CONCLUSIONS

Based on DDS, the two wide-range fast scan spectrometers have been constructed. The maximum obtainable recording rate is comparable with that of the well-known FASSST spectrometer and reaches 100 GHz/hr. The high recording rate is not accompanied by reducing the frequency measurement accuracy. Specifically, the error of measurement of the absorption line central frequencies in the case of routine wide-range measurements does not exceed ± 0.02 MHz. The measurement

error for isolated lines recorded with the signal-to-noise ratio greater than 50 does not exceed ± 0.002 MHz which is better by two orders of magnitude in comparison with the FASSST spectrometer. It should be noted that the spectrum recording rate we have obtained is close to the limiting one. Below this limiting threshold deterioration of the frequency measurement accuracy yet occurs.

Naturally, the cost for the high recording rate is the respective reduction of sensitivity. To improve the sensitivity, a mode of synchronous integration consisting in multiple recording of a spectrum by fragments with further averaging is provided. This technique makes the averaging of low-frequency noise more efficient as compared with simply increasing the detector time constant.

ACKNOWLEDGMENTS

The authors express their gratitude to Professor S. F. Dyubko for constructive perusal and fruitful discussion of the manuscript.

REFERENCES

1. Carlotti, M., Di Lonardo, G., Fusina, L., Carli, B., and Mencaraglia, F., The submillimeter-wave spectrum and spectroscopic constants of SO_2 in the ground state, *J. Mol. Spectrosc.*, 106(2):235-244, 1984.
2. Lolck, J.-E., Poussigue, G., Pascaud, E., and Guelachvili, G., The Pentad Rotation-Vibrational States of $^{12}\text{CD}_4$: Wavenumber analysis of infrared and raman spectra of the v_1 , v_3 , $2v_2$, $v_2 + v_4$, and $2v_4$ bands, *J. Mol. Spectrosc.*, 111(2):235-274, 1985.
3. Available from: <http://www.brukeroptics.com/>
4. Lewen, F., Gendriesch, R., Pak, I., Paveliev, D. G., Hepp, M., Schieder, R., and Winnewisser, G., Phase locked backward wave oscillator pulsed beam spectrometer in the submillimeter wave range, *Rev. Sci. Instrum.*, 69(1):32-39, 1998.
5. Winnewisser, G., Spectroscopy in the terahertz region, *Vibrational spectroscopy*, 8(2):241-253, 1995.
6. Brünken, S., Fuchs, U., Lewen, F., Urban, Š., Giesen, T., and Winnewisser, G., Sub-Doppler and Doppler spectroscopy of DCN isotopomers in the terahertz region: ground and first excited bending states $(v_1 v_2 v_3) = (01^{e,f})$, *J. Mol. Spectrosc.*, 225(2):152-161, 2004.
7. Colmont, J.-M., Bakri, B., Rohart, F., Włodarczak, G., Demaison, J., Cazzoli, G., Dore, L., and Puzzarini, C.,

- Intercomparison between ozone-broadening parameters retrieved from millimetre-wave measurements by using different techniques, *J. Mol. Spectrosc.*, 231(2):171-187, 2005.
8. Nguyen, L., Buldyreva, J., Colmont, J.-M., Rohart, F., Włodarczak, G., and Alekseev, E. A., Detailed profile analysis of millimetre 502 and 602 GHz N₂O-N₂(O₂) lines at room temperature for collisional linewidth determination, *Mol. Phys.*, 104(16-17):2701-2710, 2006.
 9. Cazzoli, G., Dore, L., Puzzarini, C., Bakri, B., Colmont, J.-M., Rohart, F., and Włodarczak, G., Experimental determination of air-broadening parameters of pure rotational transitions of NHO₃: intercomparison of measurements by using different techniques, *J. Mol. Spectrosc.*, 229(2):158-169, 2005.
 10. Kania, P., Stříteská, L., Šcimečková, M., and Urban, Š., Pressure shifts of acetonitrile ground state parameters, *J. Mol. Struct.*, 795(1-3):209-218, 2006.
 11. Medvedev, I., Winnewisser, M., De Lucia, F. C., Herbst, E., Bialkowska-Jaworska, E., Pszczorłkowski, L., and Kisiel, Z., The millimeter- and submillimeter-wave spectrum of the trans-gauche conformer of diethyl ether, *J. Mol. Spectrosc.*, 228(2):314-328, 2004.
 12. Belov, S. P., Demkin, V. M., Puchenin, V. I., and Tretyakov, M. Y., *A submillimeter gas spectrometer RAD of the third generation*, Preprint # 201, Gorki: Institute of Applied Physics, USSR Academy of Sciences, 1988, (in Russian).
 13. Petkie, D. T., Goyette, T. M., Bettens, R. P. A., Belov, S. P., Albert, S., Helminger, P., and De Lucia, F. C., A fast scan submillimeter spectroscopic technique, *Rev. Sci. Instrum.*, 68(4):1675-1683, 1997.
 14. Alekseev, E. A., Dyubko, S. F., Ilyushin, V. V., and Podnos, S. V., The high-precision millimeter-wave spectrum of ³²SO₂, ³²SO₂(v₂), and ³⁴SO₂, *J. Mol. Spectrosc.*, 176(2):316-320, 1996.
 15. Belov, S. P., Tretyakov, M. Y., Kozin, I. N., Klisch, E., Winnewisser, G., Lafferty, W. J., and Flaud, J.-M., High frequency transitions in the rotational spectrum of SO₂, *J. Mol. Spectrosc.*, 191(1):17-27, 1998.
 16. Belov, S. P., Demkin, V. M., Zobov, N. F., Karyakin, E. N., Krupnov, A. F., Kozin, I. N., Polyansky, O. L., and Tretyakov, M. Yu., Microwave study of the submillimeter spectrum of the H₂O-HF dimmer, *J. Mol. Spectrosc.*, 241(2):124-135, 2007.
 17. De Lucia, F. C., The submillimeter: A spectroscopist's view, *J. Mol. Spectrosc.*, 261(1):1-17, 2010.
 18. Kisiel, Z., Dorosh, O., Winnewisser, M., Behnke, M., Medvedev, I. R., and De Lucia, F. C., Comprehensive analysis of the FASSST rotational spectrum of S(CN)₂, *J. Mol. Spectrosc.*, 246(1):39-56, 2007.
 19. Available from: <http://www.analog.com> and <http://www.ieee.li/pdf/essay/dds.pdf>
 20. Available from: http://www.analog.com/static/imported-files/data_sheets/AD9912.pdf
 21. Alekseev, E. A. and Zakharenko, V. V., A direct digital frequency synthesizer for microwave spectroscopy applications, *Radiofizika i Radioastronomia*, 12(2):205-213, 2007, (in Russian).
 22. Motiyenko, R. A., Alekseev, E. A., Dyubko, S. F., and Lovas, F. J., Microwave Spectrum and Structure of Furfural, *J. Mol. Spectrosc.*, 240(1):93-101, 2006.
 23. Krupnov, A. F., Tretyakov, M. Yu., Parshin, V. V., Shannin, V. N., and Myasnikova, S. E., Modern Millimeter-Wave Resonator Spectroscopy of Broad Lines, *J. Mol. Spectrosc.*, 202(1):107-115, 2000.
 24. Tretyakov, M. Yu., Parshin, V. V., Koshelev, M. A., Shkaev, A. P., and Krupnov, A. F., Extension of the range of resonator scanning spectrometer into submillimeter band and some perspectives of its further developments, *J. Mol. Spectrosc.*, 238(1):91-97, 2006.
 25. McElmurry, B. A., Lucchese, R. R., Bevan, J. W., Leonov, I. I., Belov, S. P., and Legon, A. C., Studies of Ar:HBr using fast scan submillimeter-wave and microwave coaxial pulsed jet spectrometers with sub-kHz precision, *J. Chem. Phys.*, 119:10687-10695, 2003.
 26. Belov, S. P., McElmurry, B. A., Lucchese, R. R., Bevan, J. W., and Leonov, I. I., Testing the morphed potential of Ar:HBr using frequency and phase stabilized FASSST with a supersonic jet, *Chem. Phys. Lett.*, 370(3-4):528-534, 2003.
 27. Couder, L. H., Belov, S. P., Wilraert, F., McElmurry, B. A., Bevan, J. W., and Hougen, J. T., Submillimeter spectrum and analysis of vibrational and hyperfine coupling effects, *Chem. Phys. Lett.*, 482(4-6):180-188, 2009.
 28. Alekseev, E. A., Direct digital frequency synthesizers: Potentialities and limitations for microwave spectroscopy applications, *Radio Physics and Radio Astronomy*, 2(4):369-378, 2011.
 29. Ilyushin, V. V., Alekseev, E. A., Dyubko, S. F., Motiyenko, R. A., and Lovas, F. J., Millimeter wave spectrum of glycine, *J. Mol. Spectrosc.*, 231(1):15-22, 2005.
 30. Ilyushin, V. V., Alekseev, E. A., Demaison, J., and Kleiner, I., The ground and first excited torsional states of methyl carbamate, *J. Mol. Spectrosc.*, 240(1):127-132, 2006.
 31. Kryvda, A. V., Gerasimov, V. G., Dyubko, S. F., Motiyenko, R. A., and Alekseev, E. A., New measurements of the microwave spectrum of formamide, *J. Mol. Spectrosc.*, 254(1):28-32, 2009.
 32. Available from: http://www.analog.com/static/imported-files/data_sheets/AD9851.pdf
 33. Available from: http://www.analog.com/static/imported-files/data_sheets/AD8331_8332_8334.pdf
 34. Available from: http://www.analog.com/static/imported-files/data_sheets/ADUC834.pdf
 35. De Vreede, J. P. M., Gillis, M. P. W., and Dijkerman, H. A., Linewidth, lineshift, and lineshape measurements on rotational transitions of OCS using frequency modulation, *J. Mol. Spectrosc.*, 128(2):509-520, 1988.

36. Cazzoli, G. and Dore, L., Lineshape measurements of rotational lines in the millimeter-wave region by second harmonic detection, *J. Mol. Spectrosc.*, 141(1):49-58, 1990.
37. Available from: http://www.analog.com/static/imported-files/data_sheets/AD9834.pdf
38. Bykov, A. D., Sinitsa, L. N., and Starikov, V. I., *Experimental and theoretical methods in the spectroscopy of water vapor molecules*, Novosibirsk: SB RAS Publ., 1999, (in Russian).
39. Available from: http://www.analog.com/static/imported-files/data_sheets/ADUC841_842_843.pdf
40. Motiyenko, R. A., Margulès, L., Alekseev, E. A., Guillemin, J.-C., and Demaison, J., Centrifugal distortion analysis of the rotational spectrum of aziridine : Comparison of different Hamiltonians, *J. Mol. Spectrosc.*, 264(2):94-99, 2010.
41. Müller, H. S. P., Schlöder, F., Stutzki, J., and Winnewisser, G., The Cologne Database for Molecular Spectroscopy, CDMS: a useful tool for astronomers and spectroscopists, *J. Mol. Struct.*, 742(1-3):215-227, 2005.
42. Available from: <http://www.astro.uni-koeln.de/cgi-bin/cdmssearch?file=c060503.cat>



Terahertz spectroscopy of deuterated formaldehyde using a frequency multiplication chain



Olena Zakharenko, Roman A. Motienko*, Laurent Margulès, Thérèse R. Huet

Laboratoire de Physique des Lasers, Atomes et Molécules, UMR8523 CNRS – Université Lille 1, 59655 Villeneuve d'Ascq Cedex, France

ARTICLE INFO

Article history:

Received 19 August 2015

In revised form 10 September 2015

Available online 16 September 2015

Keywords:

Formaldehyde

Deuterated isotopologue

Terahertz spectroscopy

Frequency multiplication

ABSTRACT

The rotational spectra of deuterated formaldehyde HDCO and D₂CO were recorded between 1.1 and 1.52 THz in order to benchmark new terahertz frequency multiplication chain used in the Lille spectrometer. Important spectrometer parameters such as sensitivity, measurement accuracy, and harmonic composition of the radiation source have been tested using the newly measured spectra. For each of the main deuterated isotopic species of formaldehyde the existent datasets from high resolution measurements were augmented by more than 300 new distinct transition frequencies. Most of these frequencies were measured with an accuracy better than 30 kHz. In addition, the high sensitivity of the spectrometer provided by the new frequency multiplication chain allowed observation, assignment and analysis of ¹³C, ¹⁷O, ¹⁸O, and ¹³C¹⁸O isotopic species of HDCO and D₂CO. For some of these isotopologues the rotational parameters were determined for the first time.

© 2015 Elsevier Inc. All rights reserved.

1. Introduction

Formaldehyde (H₂CO) is a simple organic molecule that plays an important role in atmospheric chemistry. It is the product of combustion of many carbon compounds like methane and methanol, and it is also formed in the atmosphere as a result of the oxidation of different volatile organic compounds. Formaldehyde is eliminated from the atmosphere mainly through photolysis and reaction with hydroxyl radical. The photodissociation of H₂CO leading to the formation of H₂ and CO is responsible for over half of the atmospheric H₂ [1]. Recently, deuterated isotopic species of formaldehyde, and especially HDCO, received increasing attention owing to their importance as tracers in the atmospheric hydrogen cycle [1–3].

Different techniques have been used to measure H₂CO concentrations in the atmosphere [4] including the spectroscopy in the terahertz region [5]. The laboratory terahertz spectroscopy of formaldehyde has been an object of many studies and includes the measurements of the parent isotopic species as well as of the singly and doubly deuterated isotopologues in the frequency range up to 2 THz [6–9]. The deuterated species of formaldehyde have been also studied using Fourier transform far infrared spectroscopy [10,11]. For the parent isotopic species a good measurement accuracy of 0.02–0.05 MHz has been achieved throughout all the

frequency range of the experiment up to 2 THz. Whereas the transition frequencies for HDCO and D₂CO in the frequency range above 1 THz were measured with the accuracy of 0.3–1 MHz. In weighted least squares fit used for adjustment of the rotational Hamiltonian parameters, the weights are estimated as reciprocals of measurement accuracy squared. Combined with high accuracy measurements (0.005–0.2 MHz) in the frequency range below 1 THz, the measurements in the frequency range above 1 THz have much smaller weights and thus they does not cause any significant influence on the Hamiltonian parameters.

Relatively low measurement accuracy for the lines above 1 THz is mainly caused by difficulties in recording molecular rotational spectra in this frequency range. The spectral region above 1 THz and probably up to 10 THz represents the so-called «terahertz gap», the frequency range where both electronic and photonic sources exhibit difficulties in generation and control of radiation. For the purposes of high-resolution molecular rotational spectroscopy the spectrometer should be based on a source that is coherent, powerful, and has low phase noise, narrow instant bandwidth, and good tuning capabilities. Up to now, in the frequency range above 1 THz, two main approaches have been used to at least partially satisfy these conditions. The first one consists in producing a sideband source by photomixing of two [12] or three lasers, or by mixing a FIR laser with a microwave source like frequency synthesizer, phase-locked klystron, and backward-wave oscillator [13–15]. The second approach consists in cascaded frequency multiplication, or up conversion, of a fundamental microwave source

* Corresponding author.

E-mail address: roman.motienko@univ-lille1.fr (R.A. Motienko).

like frequency synthesizer [16,17], phase-locked klystron or BWO [18], or Gunn oscillator [19]. Between these two techniques, the photomixing provides larger continuous bandwidth coverage, being at the same difficult to tune and having low output power. Whereas the sources based on frequency multiplication have higher output power, good spectral purity and phase noises, but they are limited in the frequency range to 3 THz. At the same time one should note that the rotational spectra of molecules with masses higher than 25 a.m.u. typically fall within 0–3 THz frequency range, and therefore, the technique of frequency multiplication is more commonly used in laboratory high-resolution molecular spectroscopy.

In this paper we present the results of new high-resolution study of the rotational spectra of deuterated formaldehyde that has two main objectives: (i) to characterize our new frequency multiplication chain in the 1.1–1.5 THz frequency range, and (ii) to provide very accurate transition frequencies and to improve the rotational Hamiltonian parameters. The latter is also very important for astrophysical applications since formaldehyde is ubiquitous molecule in the interstellar medium and its both deuterated isotopologues were detected in different astronomical sources. In particular, the improvement of the frequency predictions accuracy for deuterated formaldehyde above 1 THz should represent an interest for Herschel telescope mission.

2. Experiment

2.1. Spectrometer overview

The spectrometer scheme is shown in Fig. 1. It is built according to typical absorption spectrometer layout: radiation source – absorption cell – detector. The spectrometer covers with a few gaps the frequency range between 0.075 THz and 1.52 THz using two different frequency multiplication chains (see Table 1). As a reference source in the both chains we use an Agilent E8257D synthesizer that may be continuously tuned with 1 Hz frequency step between 100 kHz and 20 GHz. The synthesizer is locked onto Rubidium frequency standard that provides very high accuracy of frequency setting. The sub-terahertz frequency chain consists of an active frequency multiplier by the factor of 6, AMC-10 from Virginia Diodes, Inc. (VDI) producing frequencies in the 75–110 GHz frequency range, and a series of passive multipliers with factors varying from 2 up to 9. The new terahertz frequency chain is composed of four active frequency multipliers by the factor of 12, AMC-350 to AMC-353 (VDI), covering the 120–170 GHz frequency range, and a passive cascaded multiplier with the total factor of 9 (VDI). Table 1 summarizes the elements used in the frequency multiplica-

Table 1
Active (AMC) and passive elements used in the frequency multiplication chain.

Device	Multiplication factor	Frequency range (GHz)	Typical output power (mW)
AMC-10	6	75–100	30
AMC-350	12	122–134	150
AMC-351	12	134–145	150
AMC-352	12	145–156	150
AMC-353	12	156–167	150
VDI 5.1×2	2	150–220	3
VDI 3.4×3	3	225–330	1
VDI 1.9×5	5	400–520	0.05
VDI 1.5×2×3	6	500–660	0.03
VDI 1.0×3×3	9	750–990	0.01
VDI 0.65×3×3	9	1100–1520	0.02

tion chains according to the frequency range, typical output power provided by the manufacturer, and multiplication factor.

A hot-electron bolometer (QMC Instruments, Ltd.) is used as a broadband radiation detector. In the 75–330 GHz frequency range a series of Schottky diode zero biased detectors (WR10ZBD, WR5.1ZBD, and WR3.4ZBD) may also be used. To increase the sensitivity of the spectrometer, frequency modulation of the reference source and lock-in detection are used. The detector output signal is amplified by a low noise amplifier and fed into a DSP lock-in amplifier SR 7270. The frequency modulation is provided by the internal low frequency generator of the reference source. The modulation signal is also fed up to the lock-in amplifier that demodulates the detected signal. Typical modulation frequency falls within the 10–25 kHz frequency range. The demodulation of the detected signal may be performed either at 1f or 2f, but 2f demodulation is preferred because of simpler presentation of observed spectrum in this case. The value of frequency deviation or modulation amplitude takes into account the molecular line width. A frequency deviation significantly higher than line width results in broad spectral features, lost of spectral resolution and lineshape distortions. Whereas low frequency deviation leads to decrease in the signal-to-noise ratio (SNR), and to the lost of sensitivity.

One of the digital-to-analog (DAC) outputs of the lock-in amplifier is used for controlling the output power level of active multipliers AMC. For this purpose the DC signal 0–5 V from DAC is supplied into user controlled attenuation input of AMC. In the sub-terahertz frequency multiplication chain, the output power level control is additionally provided by a variable attenuator installed between AMC-10 and one of the passive multipliers.

The spectrum is acquired in a step-by-step manner by tuning the reference synthesizer. To obtain minimum frequency switching time and continuous-phase frequency switching the reference synthesizer is used in the stepped sweep mode. In this mode the minimum time interval between setting two successive frequencies is about 25 ms. The radiation source is swept only in one direction from lower to higher frequencies. In order to avoid permanent frequency shift in observed spectral lines, a 5τ relation between the frequency switching time and the time constant of the lock-in amplifier is preserved. For example, for 25 ms of the frequency switching time, the maximum possible value of the time constant is 5 ms. The frequency step of the radiation source depends on molecular line width. To measure the line frequency with high accuracy we perform least-squares fitting of the observed profile. In simple case of a single isolated spectral feature we fit the line peak using the Gaussian function. In the case of several partially resolved spectral features, we use a more complex model that includes Voigt or Galatry profiles. The quality of the fit depends on the number of experimental points, and consequently the frequency step is chosen in order to measure at least ten spectral points within molecular line full width half maximum interval.

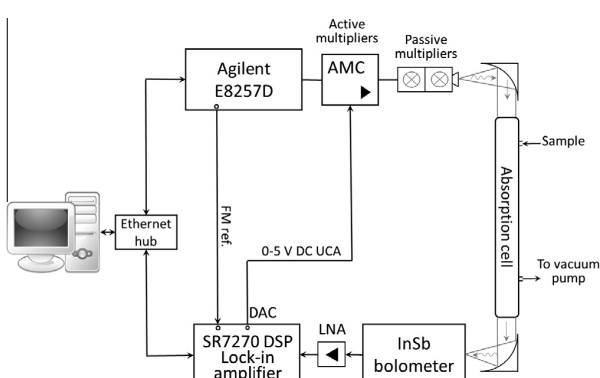


Fig. 1. The scheme of the Lille terahertz spectrometer based on solid state sources.

Typical frequency step varies from 0.03 MHz at 150 GHz to 0.16 MHz at 1.5 THz, and, for example, the spectrum acquired between 150 and 220 GHz contains about 2.3 millions of sample points. With 25 ms seconds of frequency switching time, and taking into account additional time delays used for programming the reference synthesizer in stepped sweep mode, the 150–220 GHz frequency range may be acquired in about 16.5 h. The whole frequency ranger of the spectrometer (0.075–1.5 THz) may be acquired in about 160 h.

The spectrometer hardware communicates with the control computer through a standard Ethernet protocol. The computer uses homemade software to send commands to, and to receive and visualize data from the hardware. The spectral acquisition process is fully automated.

2.2. Terahertz frequency multiplication chain

High-resolution molecular spectroscopy is a useful tool to test and to characterize the radiation source used in spectrometer. For example, it can provide the information on spectral characteristics, accuracy and sensitivity. The terahertz frequency multiplication chain (FMC) was first tested on the benchmark molecule of carbon monoxide, CO, which rotational frequencies are well known [20]. Table 2 represents a comparison between the CO rotational frequencies measured in this work and the measurements with 5–13 kHz uncertainties from [20]. However, owing to its low line density, the rotational spectrum of CO may not be well

suitied for benchmarking broadband characteristics of the source. For this purpose we measured and studied much denser rotational spectra of two deuterated isotopologues of formaldehyde, HDCO and D₂CO. Commercial samples of HDCO and D₂CO of 99% of purity were used. The spectra of both isotopic species recorded using the terahertz FMC between 1.1 and 1.52 THz are shown in Fig. 2. In these measurements, the absorption cell of 2 m path length was used. The absorbing gas pressure in the cell was close to 30 µbar. The spectra were recorded using frequency modulation of the source with a frequency deviation of 1.08 MHz, with a 0.168 MHz frequency step, and a 5 ms time constant of lock-in amplifier (25 ms/point acquisition time).

As it may be seen from Fig. 2 the strongest lines in the spectra are distorted, as their lineshape minima and maxima do not correspond to usual 1/2 ratio. The distortion is caused by the saturated absorption under experimental conditions indicated above. Fig. 3a illustrates a close look at one of the saturated lines of D₂CO that corresponds to the $J_{KaKc} = 24_{2,22}-23_{2,21}$ transition, having high absorption coefficient of $1.22 \times 10^{-1} \text{ cm}^{-1}$. To provide high dynamic range of the measurements, all the saturated transitions were further re-measured using the same 2 m length absorption cell, and at a gas pressure close to 1 µbar. The unsaturated absorption line with correct lineshape is shown in Fig. 3b.

The sensitivity of the spectrometer based on the new terahertz frequency multiplication chain was tested in two ways. First, in the recorded spectra we searched for the transitions with the lowest absorption coefficients. The weakest lines observed for HDCO, 35_{3,32}–35_{2,33}, and for D₂CO 27_{8,19}–28_{6,22} are shown in Fig. 4. Their corresponding absorption coefficients are $1.1 \times 10^{-5} \text{ cm}^{-1}$ and $1.0 \times 10^{-5} \text{ cm}^{-1}$. Based on the signal-to-noise ratio of the weakest transitions and their absorption coefficients, the minimum absorption sensitivity is at least $3.0 \times 10^{-6} \text{ cm}^{-1}$. One should note that the lines shown in Fig. 4 were measured in single acquisition cycle, with an acquisition rate of 25 ms/point and a time constant of 5 ms. Better SNR and consequently better sensitivity may be achieved by slowing the measurement rate and increasing the integration time. Thus the value of $3.0 \times 10^{-6} \text{ cm}^{-1}$ may be considered as the upper limit of minimum absorption sensitivity with the fastest spectral acquisition rate. For the second test of the spectrome-

Table 2

Comparison between the rotational frequencies of carbon monoxide measured in this work and the results of the Ref. [20].

Transition $J''-J'$	ν_{exp} (MHz) Ref. [20]	$\Delta\nu_{\text{exp}}$ (kHz) Ref. [20]	ν_{exp} (MHz) This work	$\Delta\nu_{\text{exp}}$ (kHz) This work
10–9	1151985.452	11	1151985.438	20
11–10	1267014.486	5	1267014.483	20
12–11	1381995.105	13	1381995.099	20
13–12	1496922.909	12	1496922.911	20

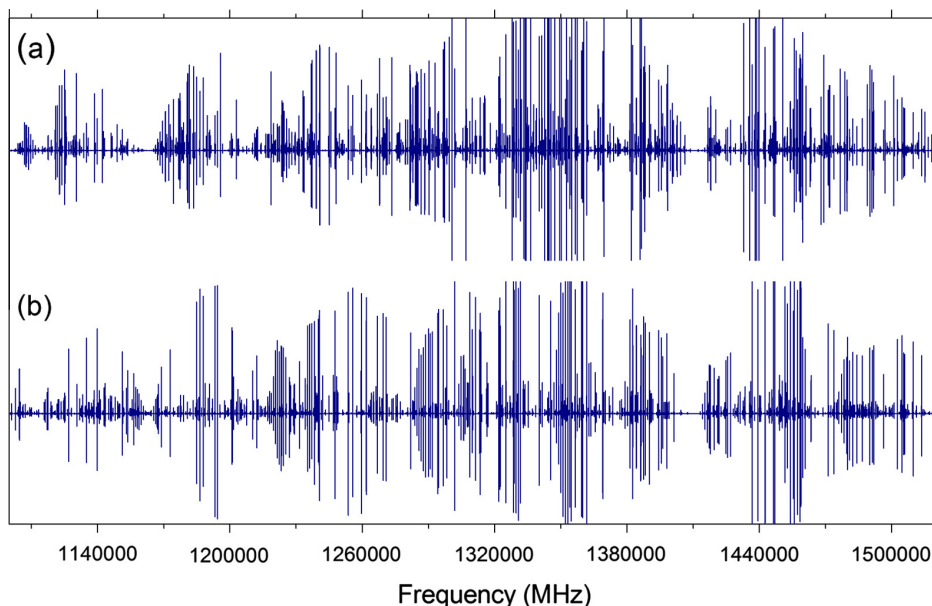


Fig. 2. Overview of the terahertz spectra of HDCO (a) and D₂CO (b) recorded using the Lille spectrometer in the frequency range 1.1–1.52 THz.

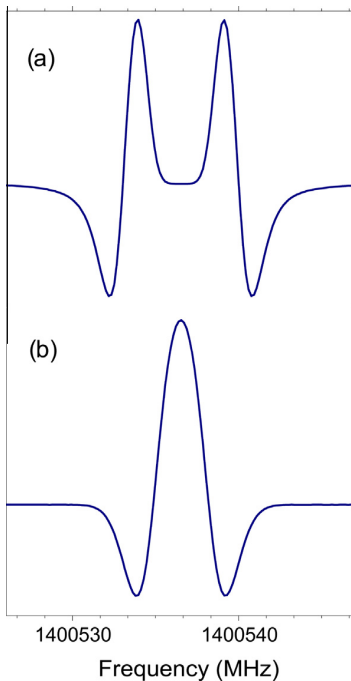


Fig. 3. (a) An example of saturated absorption for the $24_{2,22}-23_{2,21}$ transition of D₂CO observed in a 2 m length absorption cell with a sample pressure of 30 μ bar. (b) The same transition without saturation recorded at a reduced sample pressure of 1 μ bar.

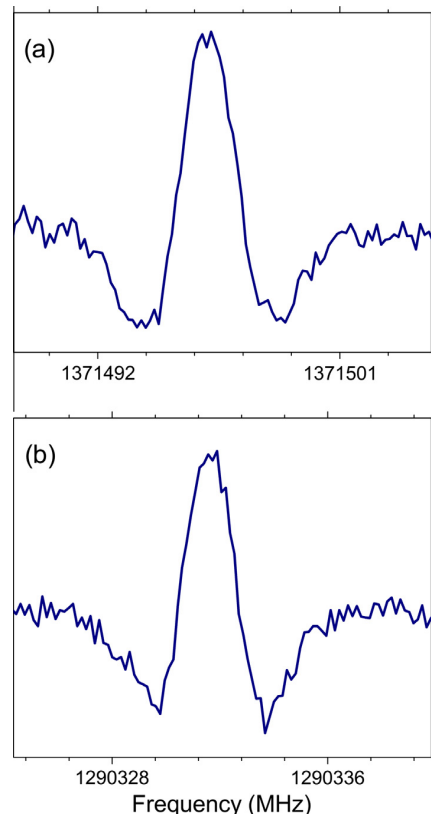


Fig. 4. Examples of weak transitions of deuterated formaldehyde, recorded in a single scan, acquisition rate: 25 ms/point, time constant: 5 ms. (a) $27_{8,19}-28_{6,22}$ transition of D₂CO, $\alpha_{\max} = 1.0 \times 10^{-5} \text{ cm}^{-1}$ and (b) $35_{3,32}-35_{2,33}$ transition of HDCO, $\alpha_{\max} = 1.1 \times 10^{-5} \text{ cm}^{-1}$.

ter sensitivity, in the recorded spectra we assigned the lines of singly substituted ¹³C, ¹⁸O, ¹⁷O, and doubly substituted ¹³C¹⁸O isotopic species of HDCO and D₂CO in natural abundance of 1%, 0.2%, 0.037%, and 0.002% respectively.

Using molecular spectra one can explore the harmonic composition of the signal emitted by the radiation source provided that a broadband detector such as a hot electron bolometer is used in the receiving system. In general, the radiation source in spectrometer should be single harmonic. However, in reality higher or lower order harmonics may also be present. Polyharmonic composition of the output spectrum of the radiation source is beneficial in a limited number of applications. As an example, one may cite the pioneering works of Gordy and co-workers on harmonics generation in the millimeter-wave range that allowed accurate measurements of the rotational transitions of diatomic and simple polyatomic molecules [21]. In the case of the molecules having complex rotational spectra, higher order harmonics of the radiation source would cause additional absorption features in the spectrum making its analysis more laborious. The new terahertz frequency multiplication chain is composed of three stages of multiplication with corresponding factors of 12, 3, and 3, and a total multiplication factor of 108. In assumption that the radiation propagates at the dominant TEM₁₀ mode, higher order harmonics from the first and the second stages of multiplication would be effectively cut off owing to rectangular waveguide sizes. Thus, we concentrated our effort on searching for unwanted harmonics generated by the last frequency tripler in the chain. Apart from the main harmonics x3, the most probable unwanted harmonics in this case are x2, x4, and x5. In the observed spectra we found very weak features that can be attributed to the absorptions at frequencies that corresponds to multiplication factors of 2 or 4 at the last stage of the chain. For example, due to the presence of the second harmonics at the last stage, $15_{0,15}-14_{0,14}$ transition of HDCO at

919557.056 MHz was observed as a line at “false” frequency of 1379335.649 MHz. The fourth harmonics in the source emission spectrum gave an absorption feature at “false” frequency of 1129365.239 MHz, whereas it was attributed to the transition $25_{0,25}-24_{0,24}$ of HDCO at 1505820.319 MHz. In total, in the rotational spectrum of HDCO we found about 30 spectral features that could be attributed to absorption due to unwanted harmonics. All these features were found to be very weak, typically with SNR lower than 3.

3. Assignment and analysis

For the main isotopic species HDCO and D₂CO, the initial analysis of the ground state rotational transitions was based on the results of Bocquet et al. [9] where all previous studies were also summarized. The useful information on centrifugal distortion constants for D₂CO and D₂¹³CO was taken from the results of far infrared studies [10,11]. In the paper [9], the final fits were done using the A reduction of the Watson’s Hamiltonian. In later publications [6,22] on the rotational spectrum of H₂¹³CO and H₂CO it was shown that in the S-reduction Hamiltonian, the convergence of the J-dependent diagonal distortion constants may be achieved faster than in the A-reduction Hamiltonian, and therefore the S-reduction should be preferred for predicting the rotational spectra. Following this suggestion, at the first stage of the analysis, we fitted all available transitions of HDCO and D₂CO using the S-reduction Hamiltonian. With the new set of rotational and centrifugal distortion constants we calculated the initial frequency

Table 3

Ground state rotational parameters for various isotopic species of HDCO.

Parameters	HDCO	HD ¹³ CO	HDC ¹⁸ O	HDC ¹⁷ O	HD ¹³ C ¹⁸ O
A (MHz)	198118.35720(75) ^a	197648.2097(65)	198003.909(84)	198057.58(25)	197532.02(32)
B (MHz)	34909.10614(15)	34191.19978(57)	33139.7634(26)	33971.9858(56)	32399.1137(64)
C (MHz)	29562.87141(16)	29035.85954(63)	28281.2325(21)	28886.4781(50)	27730.3965(38)
DJ (kHz)	58.25351(27)	55.45941(43)	52.9590(49)	55.4195(49)	50.2909(33)
DJK (kHz)	760.9743(35)	761.6398(79)	693.736(17)	725.233(18)	692.45(12)
DK (kHz)	11052.942(35)	11034.75(66)	11115.(17)	11131.(28)	10887.(40)
d ₁ (kHz)	-11.720560(57)	-10.89698(90)	-10.1469(19)	-10.8658(54)	-9.4045(24)
d ₂ (kHz)	-2.841587(23)	-2.66709(36)	-2.36857(81)	-2.5844(14)	-2.2105(34)
H _J (Hz)	0.04072(16)	0.04072 ^b	0.0384(33)	0.0416(36)	0.04072 ^b
H _{JK} (Hz)	5.2060(71)	4.8333(78)	4.298(17)	4.654(19)	4.08(11)
H _{KJ} (Hz)	-42.765(26)	-39.408(85)	-40.481(69)	-41.20(14)	-38.3(10)
H _K (Hz)	2093.95(68)	2072.(16)	2093.95 ^b	2093.95 ^b	2093.95 ^b
h ₁ (Hz)	0.049922(40)	0.04557(89)	0.0410(16)	0.0434(42)	0.049922 ^b
h ₂ (Hz)	0.060485(31)	0.05550(55)	0.04789(98)	0.0520(15)	0.0571(42)
h ₃ (Hz)	0.0199820(81)	0.017907(67)	0.01459(46)	0.01558(78)	0.0199820 ^b
L _{JK} (mHz)	-0.0811(43)				
L _{JK} (mHz)	-0.427(25)				
L _{KKJ} (mHz)	18.768(63)	18.62(30)			
L _K (mHz)	-551.2(41)				
l ₃ (mHz)	-0.000716(10)				
l ₄ (mHz)	-0.0001789(23)				
η ^c	158	67	210	280	56
N ^d	675	278	129	102	65
rms	0.053	0.063	0.044	0.029	0.104
Weighted rms	0.74	0.88	0.93	0.71	0.54

^a Numbers in parentheses are one standard deviation uncertainties and apply to the last digits.^b Fixed to the corresponding value for HDCO.^c Condition number.^d Number of distinct frequency lines in fit.**Table 4**Ground state rotational parameters for various isotopic species of D₂CO.

Parameters	D ₂ CO	D ₂ ¹³ CO	D ₂ C ¹⁸ O	D ₂ C ¹⁷ O	D ₂ ¹³ C ¹⁸ O
A (MHz)	141653.59272(66) ^a	141668.485(10)	141649.244(22)	141651.326(91)	141663.01(12)
B (MHz)	32282.50636(17)	31732.2674(11)	30594.8006(11)	31388.6733(39)	30023.1748(55)
C (MHz)	26186.34731(16)	25823.4993(10)	25064.1628(10)	25594.7836(32)	24679.5441(31)
DJ (kHz)	45.73244(25)	43.7604(20)	41.6042(17)	43.5223(32)	39.7359(38)
DJK (kHz)	662.5698(22)	659.5129(33)	603.5287(51)	631.173(10)	599.93(30)
DK (kHz)	4449.479(34)	4455.12(99)	4507.7(12)	4483.8(49)	4420.5(75)
d ₁ (kHz)	-11.446664(54)	-10.73340(49)	-9.90990(80)	-10.6146(29)	-9.2643(17)
d ₂ (kHz)	-3.528474(25)	-3.33548(15)	-2.92700(29)	-3.20084(78)	-2.7564(15)
H _J (Hz)	0.02749(11)	0.0185(12)	0.0284(10)	0.0265(19)	0.02749 ^b
H _{JK} (Hz)	3.1105(42)	3.004(20)	2.5961(39)	2.8238(91)	3.04(28)
H _{KJ} (Hz)	13.1813(77)	13.808(64)	10.128(11)	11.608(30)	13.1813 ^b
H _K (Hz)	482.01(43)	494.(24)	482.01 ^b	482.01 ^b	482.01 ^b
h ₁ (Hz)	0.045289(39)	0.04111(41)	0.04034(55)	0.0419(18)	0.045289 ^b
h ₂ (Hz)	0.065636(30)	0.06083(25)	0.05249(37)	0.05837(93)	0.0630(12)
h ₃ (Hz)	0.024448(12)	0.022233(39)	0.018514(92)	0.02058(38)	0.024448 ^b
L _{JK} (mHz)	-0.0363(22)				
L _{KKJ} (mHz)	0.788(15)				
l ₃ (mHz)	-0.000695(13)				
l ₄ (mHz)	-0.0002307(24)				
η ^c	80	241	165	301	122
N ^d	686	241	191	143	62
rms	0.235	0.055	0.036	0.028	0.069
Weighted rms	0.72	0.69	0.68	0.70	0.64

^a Numbers in parentheses are one standard deviation uncertainties and apply to the last digits.^b Fixed to the corresponding value for D₂CO.^c Condition number.^d Number of distinct frequency lines in fit.

predictions for both isotopologues. The assignment process was straightforward and easy, as the predicted frequencies fell within 0.1–0.5 MHz interval from the observed line positions.

For the ¹³C, ¹⁷O, and ¹⁸O isotopic species of HDCO and D₂CO measured in natural abundance, the initial frequency predictions were calculated in the following way. For previously studied isotopologues, the starting set was composed by the rotational constants available in literature, and centrifugal distortion constants

up to the sixth order from the results of our analysis of HDCO and D₂CO. We did not find in literature any information on the rotational spectra of H¹⁷C¹⁷O, D₂C¹⁷O, HD¹³C¹⁸O, D₂C¹⁸O. Therefore the initial values of the rotational constants for these species were calculated with the assumption that isotopic substitution does not alter the structure of the molecule. We used the structure of formaldehyde determined by Takagi and Oka [23]. By taking into account zero-point vibration correction for each of the principal

inertia moments and for each of the isotopologues, we calculated the values of B and C rotational constants with 1–5 MHz precision, and the value of A rotational constant with 10–20 MHz precision depending on isotopic species. The predictions based on these constants combined with centrifugal distortion parameters from D₂CO and HDCO allowed relatively easy assignment of the rotational lines in the terahertz range.

The final sets of high resolution measurements for the main isotopic species HDCO and D₂CO consist of 675 and 686 lines respectively. Compared to 219 and 312 distinct transition frequencies of HDCO and D₂CO available from [9], the current study represents a significant extension in the high accuracy rotational transitions datasets for deuterated formaldehyde. In the final fits of others isotopic species all the assigned lines were also combined with previous measurements when available [24]. The fits were performed using a modified version of the ASFIT program [25]. The results of the fits are presented in Tables 3 and 4. Tables with line assignments, measured frequencies their uncertainties and deviations are provided as a Supplementary material to this paper. Tables 3 and 4 that contain the values of fitted parameters, their standard deviations, number of lines in each dataset, including number of lines measured in this study, rms, weighted rms deviation of the fits, and condition number [26]. The latter was obtained as a result of one of several statistical tests performed to support the choice of fitted and fixed parameters, and to check for inconsistencies in datasets. For rare isotopic species like both ¹³C¹⁸O, the limited number of assigned rotational lines does not allow accurate determination of sextic centrifugal distortion constants. At the same time, the results of the fit without sextic parameters were significantly poorer, and with high condition numbers. Therefore, in the fits of the two ¹³C¹⁸O species we decided to fix the sixth order centrifugal distortion constants to their corresponding values of the main isotopologues.

4. Conclusions

The capability of electronic sources to efficiently cover the THz gap was previously demonstrated in Refs. [16,17]. The results of the present study may serve as an additional argument in favor of using frequency multiplication chains in high-resolution, highly sensitive broadband terahertz spectroscopy. Relatively high output power of the terahertz frequency multiplication chain, its high stability and excellent spectral purity, in combination with He-cooled bolometer provide high signal-to-noise ratio, minimum distortions of the absorption lineshape, and consequently high measurement accuracy. The latter may be supported by the comparison between the CO ground state transition frequencies measured in the present study and high-precision measurements in Ref. [20]. As an indirect evidence for high accuracy in the case of broadband measurements in the THz gap region, we may use the results of the least-squares fit of HDCO and D₂CO rotational transitions. For 376 lines of HDCO and 292 lines of D₂CO with SNR better than 20, the rms deviations of the fits are respectively 0.0186 MHz and 0.019 MHz.

Acknowledgments

The present work was funded by the French CPER “IRENI”, by the French ANR “Labex CaPPA” through the PIA under contract

“ANR-11-LABX-0005-01”, by the Regional Council “Nord-Pas de Calais” and the “European Funds for Regional Economic Development (FEDER)”, by the CNES, and by the French CNRS-INSU programme “PCMI”. O.Z. also acknowledges the support of CNRS-INP.

Appendix A. Supplementary material

Supplementary data for this article are available on ScienceDirect (www.sciencedirect.com) and as part of the Ohio State University Molecular Spectroscopy Archives (http://library.osu.edu/sites/msa/jmsa_hp.htm). Supplementary data associated with this article can be found, in the online version, at <http://dx.doi.org/10.1016/j.jms.2015.09.005>.

References

- [1] E.J.K. Nilsson, J.A. Schmidt, M.S. Johnson, *Atmos. Chem. Phys.* 14 (2014) 551–558.
- [2] E.J.K. Nilsson, V.F. Andersen, H. Skov, M.S. Johnson, *Atmos. Chem. Phys.* 10 (2010) 3455–3462.
- [3] H. Hu, T.S. Dibble, G.S. Tyndall, J.J. Orlando, *J. Phys. Chem. A* 116 (2012) 6295–6302.
- [4] A. Perrin, D. Jacquemart, F. Kwabia Tchana, N. Lacome, *J. Quant. Spectrosc. Radiat. Transfer* 110 (2009) 700–716.
- [5] P. Ricaud, D. Alexandre, B. Barret, E. Le Flochmoën, E. Motte, G. Berthet, et al., *J. Quant. Spectrosc. Radiat. Transfer* 107 (2007) 91–104.
- [6] S. Brünken, H.S.P. Müller, F. Lewen, G. Winnewisser, *Phys. Chem. Chem. Phys.* 5 (2003) 1515–1518.
- [7] R. Bocquet, J. Demaison, L. Poteau, M. Liedtke, S. Belov, K.M.T. Yamamada, G. Winnewisser, C. Gerke, J. Gripp, T. Köhler, *J. Mol. Spectrosc.* 177 (1996) 154–159.
- [8] S. Eliet, A. Cuisset, M. Guinet, F. Hindle, G. Mouret, R. Bocquet, J. Demaison, *J. Mol. Spectrosc.* 279 (2012) 12–15.
- [9] R. Bocquet, J. Demaison, J. Cosléou, A. Friedrich, L. Margulès, S. Macholl, H. Mäder, M.M. Beaky, G. Winnewisser, *J. Mol. Spectrosc.* 195 (1999) 345–355.
- [10] J. Lohilahti, V.-M. Horneman, *J. Mol. Spectrosc.* 228 (2004) 1–6.
- [11] J. Lohilahti, H. Mattila, V.-M. Horneman, F. Pawłowski, *J. Mol. Spectrosc.* 234 (2005) 279–285.
- [12] A.S. Pine, R.D. Suenram, E.R. Brown, K.A. McIntosh, *J. Mol. Spectrosc.* 175 (1996) 37–47.
- [13] G.A. Blake, K.B. Laughlin, R.C. Cohen, K.L. Busarow, D.-H. Gwo, C.A. Schmuttenmaer, D.W. Steyert, R.J. Saykally, *Rev. Sci. Instrum.* 62 (1991) 1701.
- [14] P. Verhoeve, E. Zwart, M. Versluis, J. Ter Meulen, W.L. Meerts, A. Dymanus, D. McLay, *Rev. Sci. Instrum.* 61 (1990) 1612.
- [15] R. Gendriesch, F. Lewen, G. Winnewisser, J. Hahn, *J. Mol. Spectrosc.* 203 (2000) 205–207.
- [16] B.J. Drouin, F.W. Maiwald, J.C. Pearson, *Rev. Sci. Instrum.* 76 (2005) 093113.
- [17] J.C. Pearson, B.J. Drouin, A. Maestrini, I. Mehdi, J. Ward, R.H. Lin, S. Yu, J.J. Gill, B. Thomas, C. Lee, G. Chattopadhyay, E. Schlecht, F.W. Maiwald, P.F. Goldsmith, P. Siegel, *Rev. Sci. Instrum.* 82 (2011) 093105.
- [18] F. Lewen, R. Gendriesch, I. Pak, D.G. Paveliev, M. Hepp, R. Schieder, G. Winnewisser, *Rev. Sci. Instrum.* 69 (1998) 32.
- [19] C. Puzzarini, G. Cazzoli, J. Gauss, *J. Chem. Phys.* 137 (2012) 154311.
- [20] G. Winnewisser, S.P. Belov, Th. Klaus, R. Schieder, *J. Mol. Spectrosc.* 184 (1997) 468.
- [21] W.C. King, W. Gordy, *Phys. Rev.* 93 (1954) 407.
- [22] H.S.P. Müller, R. Gendriesch, L. Margulès, F. Lewen, G. Winnewisser, R. Bocquet, J. Demaison, U. Wötzl, H. Mäder, *Phys. Chem. Chem. Phys.* 2 (2000) 3401–3404.
- [23] K. Takagi, T. Oka, *J. Phys. Soc. Jpn.* 18 (1963) 1174.
- [24] D. Dangoisse, E. Willemot, J. Bellet, *J. Mol. Spectrosc.* 71 (1978) 414–429.
- [25] Z. Kisiel, J. Demaison, et al. (Eds.), *Spectroscopy from Space*, Kluwer Academic Publishers, Dordrecht, 2001. <<http://info.ifpan.edu.pl/~kisiel/prospe.htm>>.
- [26] L. Margulès, R.A. Motiyenko, E.A. Alekseev, J. Demaison, *J. Mol. Spectrosc.* 260 (2010) 23–29.

Chapitre 2

Spectroscopie de molécules manifestant la rotation interne d'une toupie C_{3v}

2.1 Molécules non rigides

Dans ce chapitre ainsi que dans les deux chapitres suivants j'aborde le sujet de traitement de spectres des molécules non-rigides manifestant différents MVGA. Ces molécules représentent le plus souvent un intérêt astrophysique ou atmosphérique, pour obtenir la description de leurs spectres avec la bonne précision, on doit appliquer des modèles spécifiques. Ce chapitre est consacré aux molécules avec une toupie présentant une symétrie C_{3v} .

La définition d'une molécule non rigide peut se faire de deux points de vue étroitement liés, tout d'abord celui de la surface d'énergie potentielle, puis celui du déplacement de coordonnées de vibration par rapport à l'état d'équilibre. En terme de déplacements, la molécule est considérée comme non rigide si les déplacements Δr_i de noyaux des atomes de la molécules pour une coordonnée de vibration sont comparables avec les longueurs des liaisons atomiques dans la molécule à l'état d'équilibre $\Delta r_i \sim r_i^e$ [Kroto 1992]. Du point de vue de la surface d'énergie potentielle, la molécule peut être considérée comme non rigide si sa surface d'énergie potentielle dans un état électronique donné possède plusieurs minima séparés par des barrières relativement basses [Bunker and Jensen 2006]. Dans ce cas l'effet tunnel entre les configurations équivalentes entraîne le décalage et la séparation des raies spectrales à plusieurs composantes. Pour les deux cas présentés ci-dessus on peut également parler d'une molécule manifestant un ou plusieurs *mouvements de vibration de grande amplitude* (MVGA).

Les hamiltoniens utilisés pour traiter les différents MVGA peuvent être séparés en

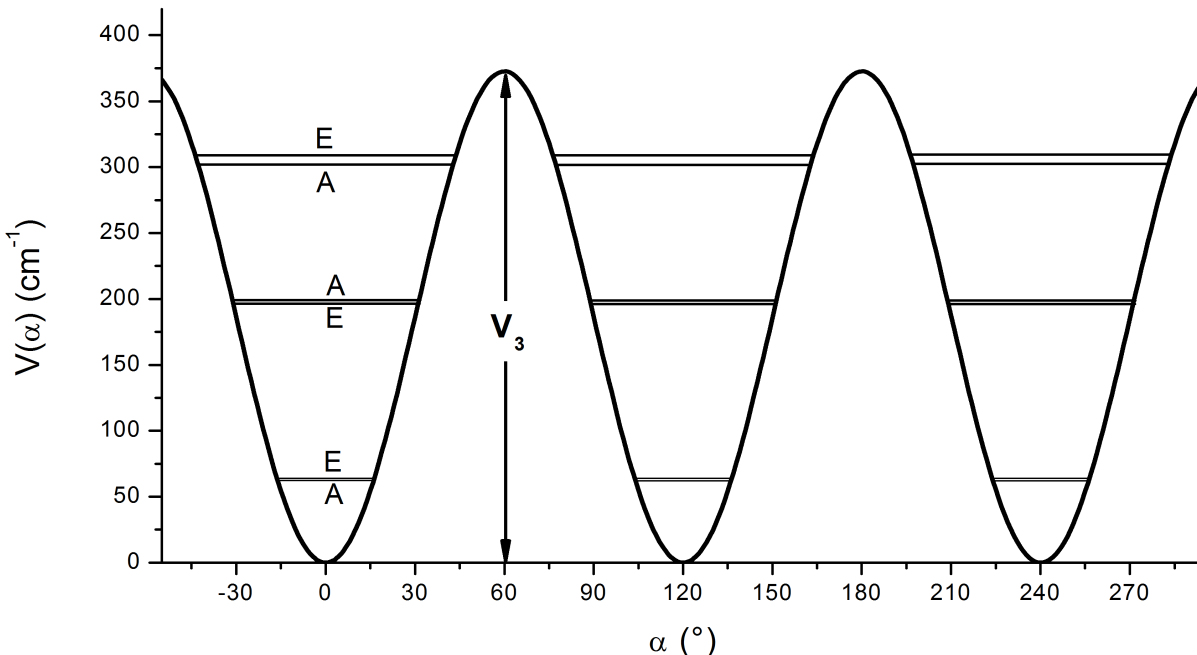


FIGURE 9: La fonction de potentiel de rotation interne $V(\alpha)$ pour le formiate de méthyle.

deux groupes : les modèles « locaux » et « globaux » [Kleiner 2010]. Les premiers considèrent un certain sous-groupe de tous les états d'énergie associés avec un MVGA et traitent ceux-ci par un hamiltonien dédié. La division en sous-groupes se fait par la symétrie ou par l'ordre énergétique. Les secondes peuvent traiter la totalité des états par un seul ensemble de paramètres. L'avantage des modèles « globaux » est qu'ils peuvent prendre en compte les perturbations dans le spectre liées aux interactions entre les différents états de vibration associés avec MVGA. De plus, les paramètres issus des modèles globaux ont souvent un lien direct avec les paramètres de la structure ou avec le champ de force de la molécule. L'avantage des modèles « locaux » est la convergence relativement rapide suite à l'absence de fortes corrélations entre les paramètres.

2.2 La rotation interne d'une toupie de symétrie C_{3v}

2.2.1 Modèles théoriques

De manière générale, pour traiter la rotation interne, on commence par séparer la molécule en deux parties : le cadre et la toupie, dont le mouvement de torsion par rapport au cadre est entravé par une barrière de potentiel de hauteur finie. Les toupies de type CH_3 , CB_3 , CF_3 possèdent une symétrie interne de type C_{3v} par rapport à l'axe de la torsion. En raison de la symétrie, il existe trois positions équivalentes de la toupie et la fonction du potentiel prend une forme présentée sur la Fig. 9 Ici l'énergie potentielle

dépend de l'angle dièdre α entre la toupie et le cadre. Ainsi, le potentiel peut s'écrire par un développement en série :

$$V(\alpha) = \frac{V_3}{2} (1 - \cos 3\alpha) + \frac{V_6}{2} (1 - \cos 6\alpha) + \dots \quad (2.1)$$

Dans le cas de la barrière V_3 de hauteur infinie chaque niveau de torsion est triplement dégénéré. Dans le cas de la barrière finie, l'effet tunnel entraîne la séparation de chaque niveau de torsion en deux sous-niveaux : doublement dégénéré (type E du groupe C_{3v}) et non-dégénéré (type A du groupe C_{3v}). Ceci se traduit par l'observation dans le spectre de rotation des dédoublements des transitions.

Dans le système d'axes principaux d'inertie on peut établir l'hamiltonien qui prend en compte la rotation de la molécule dans l'ensemble, la torsion de la toupie C_{3v} exprimée via les termes d'énergie potentielle et cinétique et l'interaction entre la rotation et la torsion [Lin and Swalen 1959 ; Kleiner 2010] :

$$H = F (p_\alpha - \rho_x P_x - \rho_y P_y - \rho_z P_z)^2 + V(\alpha) + AP_z^2 + BP_x^2 + CP_y^2 \quad (2.2)$$

où p_α est le moment angulaire du groupement méthyle conjugué à l'angle de torsion α ; $V(\alpha)$ est la fonction d'énergie potentielle de la rotation interne; P_x, P_y, P_z sont les composantes du vecteur de moment angulaire dans le système d'axes moléculaires; A, B, C sont les constantes de rotation. Les composantes du vecteur ρ sont définies de façon suivante :

$$\rho_g = \frac{\lambda_g I_\alpha}{I_g}, \quad g = x, y, z \quad (2.3)$$

où λ_g sont les cosinus directeurs de l'axe de rotation interne; I_α est le moment d'inertie du rotateur interne (le groupement méthyle, par exemple) par rapport à l'axe de rotation interne; I_g sont les moments d'inertie principaux de la molécule; F est le moment d'inertie réduit du groupement méthyle, exprimé comme :

$$F = \frac{\hbar^2}{2rI_\alpha}, \quad r = 1 - \sum_g \lambda_g^2 \frac{I_\alpha}{I_g} \quad (2.4)$$

Dans le système d'axes principaux l'hamiltonien 2.2 contient des termes non-diagonaux ($P_i P_j + P_j P_i$) et trois termes $p_\alpha P_g$ qui décrivent l'interaction de type Coriolis entre la rotation interne de la toupie et la rotation de la molécule. Pour une molécule avec un plan de symétrie, la composante du vecteur ρ perpendiculaire au plan est nulle et ainsi l'est sa composante correspondante $p_\alpha P_g$. Plusieurs méthodes permettent de traiter le problème de la rotation interne et proposent différentes voies de solution de l'hamiltonien 2.2. Ci-dessous je décris brièvement les méthodes principales utilisées.

Méthode d'axes principaux (MAP). L'approche de base utilisée dans la méthode d'axes principaux est de considérer les termes $p_\alpha P_g$ (qui ne sont pas diagonaux selon le nombre quantique de la torsion v_t et connectent ainsi des différents états de torsion) comme une perturbation à laquelle on applique une série de transformations de van Vleck [Herschbach 1959]. Les transformations réduisent les éléments non diagonaux générés par les termes $p_\alpha P_g$ à un niveau où l'on peut négliger ces éléments dans une première approximation. Après ces transformations, la matrice de l'hamiltonien peut être séparée en blocs, chacun correspondant à un état de torsion v_t et à un sous-état de symétrie $\sigma = 0$ (A) ou $\sigma = \pm 1$ (E). En conséquence, cette approche d'aborder le problème devrait être considérée comme « locale » dans la terminologie de Kleiner [Kleiner 2010]. Dans le cadre de MAP l'hamiltonien pour un état de torsion et un sous-état de symétrie a la forme suivante :

$$H_{v_t, \sigma}^{PAM} = AP_z^2 + BP_x^2 + CP_y^2 + F \sum_n W_{v_t, \sigma}^{(n)} \sum_g (\rho_g J_g)^n \quad (2.5)$$

où $W_{v_t, \sigma}^{(n)}$ sont les coefficients de développement en série obtenus de la transformation de van Vleck. Les valeurs des coefficients sont inversement proportionnelles à la hauteur de la barrière réduite $s = \frac{4V_3}{9F}$. Pour cette raison, la MAP peut être appliquée plutôt dans les cas où les barrières à la rotation interne sont relativement hautes. De plus, comme l'on peut constater à partir de l'Eq. 2.5, la convergence de l'hamiltonien dépend de la valeur du paramètre ρ , ce qui limite l'application de la MAP à des molécules à des faibles valeurs de ρ .

Les méthodes suivantes utilisent des systèmes d'axes différents des axes principaux. Ceci permet d'obtenir certains avantages dans la solution du problème des valeurs propres et des fonctions d'onde de torsion-rotation.

Méthode de l'axe rho (MAR). L'idée principale de la méthode de l'axe rho consiste à orienter l'axe moléculaire z parallèlement au vecteur ρ [Herbst *et al.* 1984; Hougen *et al.* 1994]. Dans ce cas parmi les trois termes de type Coriolis $p_\alpha P_g$, seulement $p_\alpha P_z$ reste non nul et l'hamiltonien 2.2 prend la forme suivante :

$$H = F(p_\alpha - \rho P_z)^2 + V(\alpha) + A_{RAM} P_z^2 + B_{RAM} P_x^2 + C_{RAM} P_y^2 + D_{zx}(J_z J_x + J_x J_z) + D_{zy}(J_z J_y + J_y J_z) \quad (2.6)$$

avec $\rho = \sqrt{\rho_x^2 + \rho_y^2 + \rho_z^2}$. Puisque le nouveau système d'axes en général ne coïncide pas avec les axes principaux, on voit apparaître dans l'Eq. 2.6 deux termes non diagonaux :

$D_{zx}(J_z J_x + J_x J_z)$ et $D_{zy}(J_z J_y + J_y J_z)$. Pour une molécule avec un plan de symétrie, l'un de deux termes est nul. La MAR n'a pas les limitations caractéristiques de la MAP au niveau des valeurs des paramètres V_3 et ρ et elle peut être appliquée aux molécules avec des très basses barrières et avec les valeurs élevées de ρ proches de 1. En outre, cette méthode est une méthode « globale » qui utilise un seul ensemble de paramètres pour traiter la totalité des états de torsion.

Un autre avantage de la MAR est que les paramètres de l'Hamiltonien 2.6 peuvent être déterminés à partir de la structure et le champ de force moléculaire. Pour une molécule de type allongé (en anglais : prolate) avec un plan de symétrie (ab) on choisit typiquement la représentation I^r de coordonnées : $z = a, x = b, y = c$, et le terme $D_{zy} = D_{ac}$ dans l'Eq. 2.6 devient nul. L'optimisation de la structure de la molécule par une des méthodes de chimie quantique permet de calculer les moments d'inertie dans le système d'axes principaux, le moment d'inertie du groupement méthyle par rapport à l'axe de la rotation interne, ainsi que les cosinus directeurs λ_g . Ces données sont nécessaires pour calculer les coordonnées du vecteur ρ et les constantes A, B, C et F . Ensuite, pour passer du système d'axe principaux au système de l'axe rho il faut effectuer la rotation des axes x et z par un angle $\theta = \tan^{-1}(\frac{\rho_x}{\rho_z})$. En utilisant la matrice de rotation dans le plan (ab) :

$$\mathbb{R}(\theta) = \begin{pmatrix} \cos \theta & -\sin \theta \\ \sin \theta & \cos \theta \end{pmatrix}$$

le lien entre les constantes de rotation dans les systèmes MAR et MAP peut s'écrire :

$$\mathbb{R}(\theta) \begin{pmatrix} A & 0 \\ 0 & B \end{pmatrix} \mathbb{R}(\theta)^T \Rightarrow \begin{aligned} A_{RAM} &= A \cos^2 \theta + B \sin^2 \theta \\ B_{RAM} &= A \sin^2 \theta + B \cos^2 \theta \\ D_{ab} &= -(A - B) \cos \theta \sin \theta \end{aligned} \quad (2.7)$$

De même, on doit appliquer la rotation par un angle θ au vecteur du moment dipolaire : $\mu_{RAM} = \mathbb{R}\mu$. La matrice de rotation peut être appliquée pour faire le calcul dans le sens inverse c.à.d. pour passer du système de l'axe rho au système d'axes principaux en effectuant la rotation $\mathbb{R}(-\theta)$. Cela donne :

$$\begin{aligned} A &= \frac{A_{RAM} \cos^2 \theta - B_{RAM} \sin^2 \theta}{\cos 2\theta} \\ B &= \frac{-A_{RAM} \sin^2 \theta - B_{RAM} \cos^2 \theta}{\cos 2\theta} \end{aligned} \quad (2.8)$$

où l'angle θ est calculé comme : $\theta = \frac{1}{2} \tan^{-1} \left(\frac{2D_{ab}}{A_{RAM} - B_{RAM}} \right)$.

Finalement, la façon la plus simple pour calculer le premier terme V_3 du dévelop-

pement en série de l'énergie potentielle $V(\alpha)$ consiste à optimiser les structures de la molécule correspondants à la configuration stable ($\alpha = 0^\circ$ sur la Fig. 9) et à l'état de transition ($\alpha = 60^\circ$ sur la Fig. 9). La différence d'énergies entre deux configurations donne une bonne estimation de la hauteur de barrière à la rotation interne.

Méthode d'axes internes (MAI). Contrairement aux systèmes MAP et MAR qui sont fixes par rapport au cadre de la molécule, le système d'axes internes tourne autour du cadre. L'axe z reste toujours parallèle au vecteur ρ et la rotation du système d'axes se fait de manière à ce que le moment angulaire généré par la rotation de la molécule dans ce système compense le moment angulaire généré par la rotation du groupement méthyle. La MAI n'a pas trouvé une application pratique en raison de nombreux problèmes liés à l'interprétation de cette approche en termes de la théorie des groupes et de la symétrie moléculaire [Hougen *et al.* 1994].

Méthode combinée. La méthode combinée [Woods 1966 ; Woods 1967] utilise les approches de MAP et de MAR. La méthode sépare le problème de torsion-rotation en deux parties : la rotation de la molécule et la torsion de toupie C_{3v} . La seconde partie prend en compte l'interaction de type Coriolis entre la rotation interne et la rotation de la molécule. Pour la partie de la rotation pure on utilise le système des axes principaux, tandis que pour la partie de la torsion on utilise le système de l'axe rho. L'idée principale de la méthode est de combiner la solution du problème de la torsion transformée préalablement vers le système de la MAP avec la solution de la partie de rotation. Dans le cas de plusieurs toupies C_{3v} dans la molécule, l'approche de la méthode combinée consiste à résoudre la partie de torsion du problème séparément pour chaque toupie (pour chacune on utilise son propre système de l'axe rho). Ensuite, toutes les solutions obtenues sont converties dans le système des axes principaux d'inertie, où toutes les solutions sont combinées et complétées par les éléments de la matrice de la partie du problème de rotation.

2.2.2 Les codes

La revue détaillée des différentes approches théoriques et des programmes utilisés pour aborder le problème de la rotation interne de toupie C_{3v} est disponible dans l'article [Kleiner 2010]. Ci-dessous je présente la description de deux programmes que j'ai utilisé dans les études des spectres moléculaires. L'analyse des différentes méthodes présentées dans l'article [Kleiner 2010] montre que la méthode la plus prometteuse en termes de la précision et d'applicabilité est la MAR. Elle n'a pas de limitation ni au niveau de la

hauteur de la barrière V_3 ni au niveau de la constante de couplage entre la rotation interne et la rotation globale ρ .

XIAM. Le programme XIAM [Hartwig and Dreizler 1996] est basé sur la méthode combinée. XIAM permet de traiter les spectres de molécules ayant jusqu'à trois toupies C_{3v} . L'approche utilisée dans XIAM est « locale » car chaque état de torsion est considéré séparément et de ce fait, le programme ne permet pas de prendre en compte les interactions entre les différents états de torsion. XIAM ne convient pas aux molécules avec une basse barrière à la rotation interne. Le manque de paramètres de torsion-rotation d'ordre quatre et plus limite également le domaine d'application du programme. Néanmoins, XIAM reste très efficace surtout à l'étape initiale de l'analyse spectrale des molécules avec une moyenne ou haute barrière et avec $\rho < 0.1$. Ceci est dû notamment à la rapidité de calculs et à la convergence rapide de la méthode. Un autre avantage de XIAM est que la rotation de la molécule dans l'ensemble est traité dans le système d'axes principaux ce qui permet d'obtenir les constantes de rotation sans l'influence de la partie de torsion-rotation de l'Hamiltonien [Demaison et al. 2010]. Ceci est très important dans la détermination de la structure moléculaire à partir de l'analyse spectrale.

RAM36. Le programme RAM36 est basé sur la méthode de l'axe rho et permet de traiter les spectres des molécules avec une toupie de symétrie C_{3v} et avec le cadre de symétrie C_s dont la fonction de l'énergie potentielle possède trois ou six minima équivalents [Ilyushin et al. 2010]. L'hamiltonien 2.6 est défini dans l'approximation du rotateur rigide. Le modèle qui tient compte de la flexibilité de la toupie et du cadre a été développé dans l'article [Kirtman 1962] où il a été démontré que les termes d'ordre supérieur ont une forme d'une expansion en série des puissances des opérateurs de rotation et de torsion. Dans ce cas, l'hamiltonien 2.6 peut être représenté en forme suivante :

$$H = \frac{1}{2} \sum_{knpqrs} B_{knpqrs0} [P^{2k} P_z^n P_x^p P_y^q p_\alpha^r \cos(3s\alpha) + \cos(3s\alpha) p_\alpha^r P_y^q P_x^p P_z^n P^{2k}] \\ \frac{1}{2} \sum_{knqrst} B_{knqr0t} [P^{2k} P_z^n P_x^p P_y^q p_\alpha^r \sin(3t\alpha) + \sin(3t\alpha) p_\alpha^r P_y^q P_x^p P_z^n P^{2k}] \quad (2.9)$$

où $B_{knpqrst}$ sont les paramètres à ajuster. Par exemple $B_{0000200}$ correspond à F dans l'Eq. 2.6, $B_{0110000}$ à $2D_{xz}$, $B_{0200000}$ à A_{RAM} etc. Dans le cas d'une toupie C_{3v} et d'un cadre C_s , les termes autorisés dans l'hamiltonien 2.9 doivent être totalement symétriques dans le groupe de symétrie moléculaire G_6 et doivent également être hermitiens et invariants

TABLE 2.1: Lien entre le nombre quantique m du rotateur libre, le nombre quantique de l'oscillateur harmonique v_t et le type de symétrie A, E .

v_t	A	E
0	$m = 0$	$m = 1$
1	$m = -3$	$m = -2$
2	$m = 3$	$m = 4$
3	$m = -6$	$m = -5$
4	$m = 6$	$m = 7$

à l'opération d'inversion du temps. Le groupe de symétrie moléculaire G_6 est composé de toutes les opérations de permutation-inversion des noyaux équivalents réalisables grâce à la torsion du groupement méthyle. L'invariance d'inversion du temps entraîne une restriction sur les valeurs possibles des indices des coefficients B_{knqrst} : la somme de $n + q + p + r$ doit être paire. Le groupe G_6 impose également la restriction suivante : la somme de $n + p + r$ doit être paire si $t = 0$ et impaire si $t \neq 0$.

Le programme RAM36 permet d'introduire dans le modèle de l'hamiltonien n'importe quel terme satisfaisant les conditions sur la symétrie de combinaison des opérateurs P^{2k} , P_z^n , P_x^p , P_y^q , p_α^r , $1 - \cos(3s\alpha)$, $\sin(3t\alpha)$ et correspondant aux opérateurs dont la puissance totale maximale est de 12. En plus de combinaisons (produits et anticommutateurs) des termes de l'Eq. 2.9 le programme RAM36 permet d'introduire des opérateurs de type $P_x^2 + P_y^2$, $P_x^4 - P_y^4$, $P_x^6 - P_y^6$, ... et de les combiner avec les opérateurs individuels mentionnés ci-dessus à condition de satisfaire la symétrie du problème. De même, la définition de terme de type $P_+^{2n} + P_-^{2n}$ (par exemple pour les éléments non-diagonaux de la partie de rotation pure en réduction S) se fait par l'expression de celui-là comme $(P_x + iP_y)^{2n} + (P_x - iP_y)^{2n}$ et par développement en une expression polynomiale contenant les opérateurs P_x^p et P_y^q .

Une autre particularité du code RAM36 est l'utilisation du nombre quantique m du rotateur libre pour l'attribution des niveaux de torsion. L'énergie du rotateur libre correspondant au nombre quantique m est donnée comme Fm^2 , où F est défini dans l'Eq. 2.4. De manière générale, la torsion de la toupie C_{3v} doit être considérée comme une vibration anharmonique s'il s'agit des niveaux bien en-dessous de la barrière et comme une rotation quasi-libre pour les niveaux au-dessus de la barrière. Ainsi, l'utilisation du nombre quantique v_t de l'oscillateur harmonique/anharmonique est appropriée dans le cas où les séparations entre les niveaux de torsion sont bien supérieures par rapport aux séparation $A - E$ à cause de l'effet tunnel. Le programme RAM36 permet de traiter les cas de barrières basses et très basses, et de ce fait, l'attribution avec le nombre quantique m est plus pertinente. Le schéma de l'attribution en m est basé sur l'ordre des niveaux d'énergie de la torsion [Ilyushin et al. 2010]. Pour une molécule avec une barrière à

la rotation interne à trois minimas, les deux niveaux les plus bas sont attribués comme $m = \sigma$, où $\sigma = 0$ pour les états de symétrie A et $\sigma = 1$ pour les états de symétrie E . Les niveaux suivants sur l'échelle de l'énergie sont attribués comme $m = \sigma - 3$, $m = \sigma + 3$, $m = \sigma - 6$, etc. Ainsi, dans les cas de moyennes et hautes barrières on peut établir le lien entre m et v_t . Ce lien est présenté dans la Table 2.1

Le programme RAM36 représente un outil versatile et polyvalent dans l'analyse spectrale des molécules avec une toupie C_{3v} . La seule limitation est la symétrie du cadre de la molécule. Cependant, la majorité des molécules organiques avec un rotateur interne C_{3v} que j'ai étudié dans le cadre de la présente habilitation satisfont la condition du symétrie C_s du cadre moléculaire. Ceci m'a permis d'obtenir la description de spectres de ces molécules avec la précision de l'expérience au moins pour les états fondamentaux de vibration.

2.3 Résultats

2.3.1 Formiate de méthyle

Le formiate de méthyle est l'une des plus abondantes molécules organiques dans le milieu interstellaire (MIS). Depuis sa première détection dans Sgr B2 en 1975 [Brown *et al.* 1975 ; Churchwell and Winnewisser 1975] presque un millier de transitions de rotation de l'état fondamental de vibration ont été identifiés dans le milieu interstellaire (MIS). L'abondance particulièrement importante du formiate de méthyle dans l'Orion-KL rend possible la détection de ses raies à 900 GHz [Comito *et al.* 2005] ce qui est loin sur l'échelle de fréquence par rapport au maximum d'absorption dans cette source situé autour de 300 GHz. La rotation interne du groupement méthyle dans HCOOCH_3 est entravée par une barrière moyenne de 400 cm^{-1} ce qui entraîne des séparations $A - E$ assez larges plusieurs MHz, même dans l'état $v_t = 0$. Cela demande l'utilisation d'une méthode adapté au problème, telle que la MAR.

Il est également possible de détecter les transition de rotation du formiate de méthyle dans les états excités de torsion $v_t = 1$ [Kobayashi *et al.* 2007] et $v_t = 2$ [Takano *et al.* 2012]. De plus, les estimations des astrophysiciens montrent qu'il est possible de détecter des transitions de l'état $v_t = 3$. Cependant, les transitions de rotation de cet état n'ont toujours pas été identifiées en laboratoire. La cause principale est la forte interaction entre l'état $v_t = 3$ et les premiers états excités du mode de pliage COC dans le plan de symétrie à 318 cm^{-1} et du mode de pliage hors du plan de symétrie à 332 cm^{-1} . L'analyse de ces trois états représente un vrai défi spectroscopique. D'une part, le spectre du formiate de méthyle est assez dense et les raies de ces trois états sont bien moins

intenses par rapport aux raies de l'état fondamental. D'autre part, l'état $v_t = 3$ correspond à la rotation presque libre du groupement méthyle et, en conséquence, les séparations $A - E$ sont très grandes et elles ne permettent pas de les attribuer de façon explicite. En plus, l'interaction entre les trois états se propage également à l'état $v_t = 2$ dont l'analyse est très limité en nombre de transitions. De ce fait, l'utilisation de la méthode globale telle que la MAR pour traiter les états $vt = 0, 1, 2$ ne permet pas de prédire les transitions de $v_t = 3$ avec une précision suffisante pour l'analyse initiale.

L'abondance importante dans le MIS est la raison principale des études des espèces isotopiques du formiate de méthyle. D'un point point de vue, les résultats de telles études donnent des informations sur le rapport entre les abondances isotopique dans les conditions bien différentes des conditions terrestres. De l'autre point de vue, il est important de nettoyer les spectres interstellaires des espèces connues afin de pouvoir détecter des nouvelles molécules. Le formiate de méthyle, ainsi que le méthanol, l'acétone, l'acétal-déhyde, le propionitrile et l'acétonitrile ont été désignés comme les « mauvais herbes » du MIS et doivent être traités en priorité.

En ce qui concerne les espèces isotopiques du formiate de méthyle, ici il est d'usage de séparer la substitution isotopique en deux catégories : les substitutions sur des atomes lourds et sur l'hydrogène du groupement aldéhyde et les substitutions sur les hydrogènes du groupement méthyle. Ceci est nécessaire car dans le cas des hydrogènes du groupement méthyle remplacés par deutérium la symétrie C_{3v} n'est plus valable et le spectre moléculaire nécessite un traitement différent du modèle MAR. Cette question est abordée dans le chapitre suivant.

Pour ce qui est de la substitution des atomes lourds, j'ai étudié deux espèces différentes : ^{18}O et ^{13}C . Pour les deux espèces $\text{HC}^{18}\text{OOCH}_3$ et $\text{HCO}^{18}\text{OCH}_3$, l'information spectroscopique disponible dans la littérature [[Curl Jr 1959](#)] était très limitée en termes de la gamme de fréquences et des valeurs des nombres quantiques. De ce fait, il était impossible d'avoir des bonnes prévisions spectrales pour les recherches dans le MIS. Pour l'espèce $\text{HCOO}^{13}\text{CH}_3$, une étude [[Carvajal et al. 2009](#)] a permis la détection de celle-ci dans le MIS. Cependant cette étude ne comportait que l'analyse de l'état fondamental de vibration tandis que l'abondance du formiate de méthyle indiquait la possibilité de détection des raies de son état $v_t = 1$. De plus, les mesures spectrales dans l'étude [[Carvajal et al. 2009](#)] ont été réalisées avec des tubes électroniques dans la gamme jusqu'à 660 GHz et en totale la couverture spectrale était inférieure à 50% de la gamme 150–660 GHz. Dans notre nouvelle étude, le spectromètre à base de sources solides a permis l'enregistrement de nouveaux spectres dans la gamme étendue jusqu'à 930 GHz avec la couverture de l'ordre de 80% de l'intervalle spectrale 150–930 GHz. La nouvelle analyse a été réalisée globalement pour les états $v_t = 0$ et $v_t = 1$ avec la méthode RAM. En ce qui

concerne l'état fondamental, par rapport à l'étude précédente, le nombre de transitions attribuées a été augmenté par un ordre de grandeur.

L'un des problèmes principaux liés à l'utilisation de la méthode RAM est la corrélation entre les paramètres F , ρ et V_3 de l'hamiltonien. On peut montrer que le moment d'inertie I_α de la toupie C_{3v} peut être exprimé indépendamment comme une fonction de ρ ou de F [Ilyushin 2012]. Dans ce cas, il est possible de réécrire l'hamiltonien 2.6 avec un paramètre de moins, en remplaçant F et ρ par I_α . Cette approche que l'on peut appeler MAR (I_α) donne des résultats similaires aux résultats du modèle avec F et ρ MAR (F, ρ) lorsque l'ensemble de données ne contient que les transitions de l'état fondamental [Ilyushin 2012]. Cependant, l'analyse de données contenant les transitions des états excités de torsion nécessite l'insertion dans le modèle des termes de type $V_{3m} \{1 - \cos 3\alpha, p_\alpha^2\}$ et $\rho_{3m} \{1 - \cos 3\alpha, p_\alpha P_z\}$ pour obtenir le même niveau de précision. Ces termes décrivent la différence entre la structure et l'orientation de la toupie C_{3v} au minimum et au maximum de la fonction de l'énergie potentielle $V(\alpha)$ [Xu *et al.* 1999; Ilyushin 2012]. Ainsi les transitions des états excités de torsion permettent de dé-corréler les paramètres F , ρ et V_3 . Les programmes BELGI et RAM36 utilisés dans l'analyse spectrale sont basés sur le modèle MAR(F, ρ). Dans le cas où l'analyse de données ne contient que des transitions de l'état fondamental et où la barrière à la rotation interne est relativement haute, on fixe l'un de deux paramètres (typiquement F) à une valeur raisonnable, par exemple, obtenue par les calculs de chimie quantique. Dans le cas des espèces isotopiques ^{18}O du formiate de méthyle, le paramètre F a été fixé à la valeur 5.49038 cm^{-1} obtenue lors l'analyse des données de l'espèce isotopique principale [Carvajal *et al.* 2007]. Dans l'étude précédente de l'espèce $\text{HCOO}^{13}\text{CH}_3$ la valeur F a été fixée à 5.69168 cm^{-1} estimée à partir de la structure *ab initio* à l'équilibre. L'analyse globale de $v_t = 0$ et $v_t = 1$ de $\text{HCOO}^{13}\text{CH}_3$ dans la nouvelle étude a été réalisé avec le paramètre F varié. Sa valeur finale de $5.478521(46) \text{ cm}^{-1}$ est assez proche de la valeur de l'espèce isotopique principale.

Pour toutes les espèces isotopiques du formiate de méthyle étudiées, l'application de la MAR a permis d'obtenir des ensembles des paramètres qui reproduisent les spectres avec très grande précision. Grâce aux résultats des analyses spectroscopiques des deux espèces ^{18}O et de l'espèce ^{13}C avec la substitution sur le carbone du groupement méthyle il était possible de détecter 80 raies spectrales de $\text{HC}^{18}\text{OOCH}_3$ et $\text{HCO}^{18}\text{OCH}_3$ [Tercero *et al.* 2012] et 135 raies spectrales de l'état $v_t = 1$ de $\text{HCOO}^{13}\text{CH}_3$ [Haykal *et al.* 2014] dans Orion-KL.

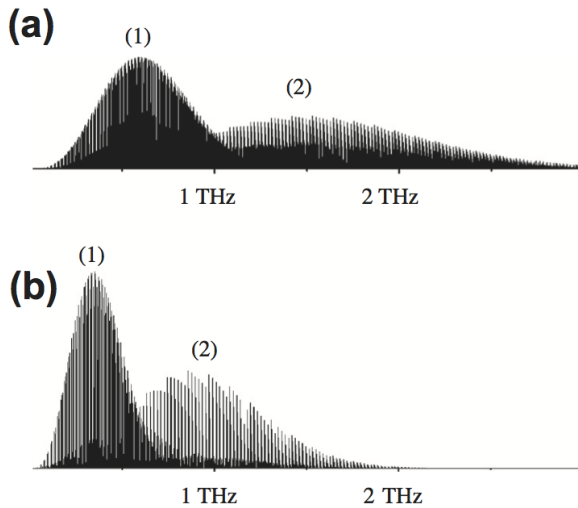


FIGURE 10: Les spectres de rotation de l'acétaldéhyde calculés à des températures $T = 300\text{ K}$ (a) et $T = 100\text{ K}$ (b). Les spectres contiennent deux maxima distincts : (1) correspond aux transitions de type ${}^aR_{0,1}$ et (2) correspond aux transitions de type ${}^bR_{1,\pm 1}$.

2.3.2 Acétaldéhyde

Le développement du programme RAM36 a marqué un certain progrès dans l'analyse des cas compliqués de la rotation interne de toupie C_{3v} . C'est le cas notamment de l'acétaldéhyde dont le paramètre de couplage entre la rotation interne du groupement méthyle et la rotation d'ensemble de la molécule est assez élevé : $\rho = 0.32$. L'avantage principal du programme RAM36 est l'absence de limitations en termes d'ordre supérieur de l'hamiltonien 2.6.

Le spectre de rotation de l'acétaldéhyde a été l'objet de nombreuses études. Parmi les dernières articles il faut mentionner la publication de prévisions spectrales pour cette molécule dans la gamme de fréquences jusqu'à 500 GHz et $J \leq 26$ et $K_a \leq 14$ [Kleiner et al. 1996]. L'acétaldéhyde est une molécule relativement légère, ayant un spectre intense qui s'étend au-delà de 2 THz à la température ambiante grâce notamment à la valeur élevée du moment dipolaire μ_b . Fig. 10 représente les spectres de rotation de l'acétaldéhyde calculés pour la température ambiante et pour la température caractéristique au MIS (100 K). Sur les deux figures on voit clairement deux maxima d'absorption : le premier dû aux transitions de type ${}^aR_{0,1}$, avec les faibles valeurs de K_a , et le second dû aux transitions de type ${}^bR_{1,\pm 1}$, avec les valeurs de K_a proches des valeurs de J . A la température de 100 K le second maximum se trouve autour de 1 THz, d'où vient la nécessité d'étendre l'analyse spectrale de l'acétaldéhyde par rapport aux données existantes. Pour les espèces isotopiques ${}^{13}\text{C}$, les données précédentes étaient extrêmement limitées avec 10 transitions mesurées pour chaque espèce dans le domaine centimétrique.

Nos nouvelles études de l'espèce isotopique principale et des espèces ${}^{13}\text{C}$ de l'acé-

taldéhyde comprennent les mesures et l'analyse dans la gamme de fréquences jusqu'à 1 THz. Le modèle final, permettant la description du spectre des états $v_t = 0, 1, 2$ de HCOCH_3 , contient 109 paramètres y compris trois paramètres d'ordre 10 de l'hamiltonien 2.9 [Smirnov *et al.* 2014]. Pour les espèces isotopiques $\text{H}^{13}\text{COCH}_3$ et $\text{HCO}^{13}\text{CH}_3$, le nombre de paramètres est de 87 et 91 respectivement [Margulès *et al.* 2015]. Tous les paramètres sont déterminés statistiquement et ils sont tous nécessaires pour reproduire les transitions analysées à la précision de l'expérience. A ce stade de l'analyse, on peut se poser la question si les modèles de cette taille dans le cadre de l'hamiltonien de la MAR sont appropriés pour l'analyse des transitions avec les valeurs de J relativement élevées. En terme de nombres de paramètres par état d'une toupie asymétrique simple, pour l'espèce isotopique principale de l'acétaldéhyde, on obtient $109/(3 \times 2) = 18.2$ paramètres. Les valeurs dans le dénominateur correspondent à trois états excités et deux sous-états de symétrie A et E . De même on obtient 14.5 et 15.2 paramètres pour les deux espèces isotopiques ^{13}C . Ce nombre paraît complètement normal lorsque il s'agit d'un état isolé d'une toupie symétrique relativement légère et l'ensemble de données contient les transitions avec les valeurs de J et K_a élevées. Ce nombre correspond notamment à la détermination de tous les paramètres d'ordre 4 et 6 et de quelques paramètres d'ordre 8. Ainsi le modèle MAR qui nécessite 109 paramètres pour analyser les états $v_t = 0, 1, 2$ de HCOCH_3 semble être pertinent. Il faut également souligner que cette analyse à la précision de l'expérience serait quasiment impossible sans le programme RAM36.

2.3.3 N-méthylformamide

L'étude du spectre de rotation de la N-méthyleformamide (CH_3NHCHO) démontre l'avantage de la MAR dans le cas d'une basse barrière à la rotation interne. La molécule N-méthylformamide possède deux conformations : *trans* et *cis*. La conformation *trans* est la plus stable et représente un plus grand intérêt d'un point de vue astrophysique. Cette même conformation est également caractérisée par la barrière relativement basse à la rotation interne $V_3 = 51.7 \text{ cm}^{-1}$. De ce fait, les séparations $A - E$ dans le spectre de la molécule peuvent atteindre plusieurs GHz même pour l'état fondamental de vibration, en compliquant significativement l'analyse spectrale. Dans la première étude du spectre de rotation de la conformation *trans*, seules les transitions de symétrie A de l'état fondamental ont été identifiées dans le domaine centimétrique [Fantoni and Caminati 1996]. L'étude suivante a révélé également les transitions de symétrie E [Fantoni *et al.* 2002]. Dans cette étude, les différentes méthodes, y compris la méthode combinée, ont été utilisées pour l'ajustement de données expérimentales, cependant, la précision de l'ajustement restait chaque fois loin de celle de l'expérience. La dernière publication en date [Kawashima *et al.* 2010] évoque l'application de la méthode proche de la MAP

TABLE 2.2: Comparaison de valeurs résiduelles issues des ajustements des fréquences des transitions de la N-méthylformamide. Dans l'étude [Kawashima et al. 2010] la méthode proche de MAP a été utilisée. Nos résultats ont été obtenus avec la méthode MAR et le code RAM36.

m'	F'	J'	K'_a	K'_c	m''	F''	J''	K''_a	K''_c	Fréq. obs. (MHz)	Incertitude (MHz)	O.-c. (MHz) MAR	O.-c. (MHz) MAP
0	6	6	2	4	0	6	6	2	5	7374.5866	0.004	0.0014	0.6448
0	7	6	2	4	0	7	6	2	5	7375.4781	0.004	-0.0012	0.6424
0	5	6	2	4	0	5	6	2	5	7375.6331	0.004	0.0028	0.6465
1	4	5	1	4	1	3	4	2	2	8535.0632	0.004	0.0014	1.1206
1	6	5	1	4	1	5	4	2	2	8535.1198	0.004	0.0000	1.1189
1	5	5	1	4	1	4	4	2	2	8535.4241	0.004	-0.0001	1.1173
1	5	6	2	5	1	4	5	3	3	13190.0141	0.004	-0.0080	5.3670
1	7	6	2	5	1	6	5	3	3	13190.0767	0.004	-0.0043	5.3704
1	6	6	2	5	1	5	5	3	3	13190.4059	0.004	-0.0030	5.3697

et représente également une extension de mesures jusqu'à 120 GHz. Cependant, suite aux limitations de la méthode utilisée dans cette étude, il n'était possible d'ajuster que les transitions avec $J \leq 11$. De plus, ont été exclus de l'ajustement 60 de 467 transitions attribuées car leurs valeurs résiduelles étaient beaucoup plus élevées par rapport à la précision de l'expérience (trois à quatre ordres de grandeurs pour certaines transitions).

Les problèmes avec l'ajustement du spectre de la N-méthylformamide trans ont été résolus avec l'application de la MAR. La puissance de la méthode peut être démontrée par la Table 2.2, où l'on compare les valeurs résiduelles des ajustements des fréquences obtenues avec la MAR et le code RAM36 dans notre dernière étude [Belloche et al. 2017] et avec MAP dans l'article [Kawashima et al. 2010]. Notons que les raies indiquées dans la Table 2.2 concernent les transitions avec des faibles valeurs de J . Cependant, à cause de la basse barrière à la rotation interne et forte interaction de torsion-rotation, ces raies n'ont pas pu être ajustées avec la méthode PAM dans l'article [Kawashima et al. 2010]. En contrepartie, dans notre nouvelle étude, toutes ces raies ont été ajustées à la précision de l'expérience et l'analyse a été étendue pour inclure les transitions des états $v_t = 0, 1, 2$ pour des nombres quantiques jusqu'à $J \leq 62$ et $K_a \leq 21$. Le modèle RAM utilisé contient 103 paramètres, ce qui paraît raisonnable vu les arguments présentés ci-dessus et vu que l'ensemble de données est similaire à celui de l'acétaldéhyde en termes des valeurs de nombres quantiques.

2.3.4 Méthacroléine

La MAR peut être appliquée aux molécules ayant une ou plusieurs toupies de symétrie C_{3v} . En conséquence, cette méthode a une application assez limitée dans le cas d'une molécule ayant deux ou plusieurs MVGA de natures différentes. Typiquement, dans

ce cas une analyse satisfaisante ne peut être obtenue que pour l'état fondamental de vibration ou pour les transitions de K_a faibles de l'état fondamental. Cela est dû à l'absence des modèles permettant de prendre en compte de façon efficace les interactions de torsion-rotation-vibration entre les états excités des modes représentants les MVGA ou entre l'état fondamental et les états excités.

C'est le cas notamment de la conformation *trans* de la méthacroléine, manifestant deux MVGA : la torsion du groupement méthyle v_{27} , et la torsion du squelette v_{26} . Il convient de noter que la torsion du squelette convertit la conformation *trans* en conformation *cis*. Par conséquent, de point de vue de la conformation *trans*, la torsion de squelette ne rajoute pas de minimas supplémentaires sur la surface de l'énergie potentielle. La méthacroléine $\text{CH}_3\text{C}(\text{CHO})\text{CH}_2$ représente plutôt un intérêt atmosphérique, en étant l'un des produits d'oxydation de l'isoprène, un composé organique volatil biogénique. Pour la méthacroléine, nous avons pu obtenir l'ajustement des paramètres des l'hamiltonien MAR à la précision de l'expérience pour l'ensemble de données composé de toutes les raies de l'état fondamental attribuées dans les spectres et d'un nombre limité de raies de l'état excité de torsion $v_{27} = 1$ [Zakharenko *et al.* 2016]. La restriction en nombre raies de l'état $v_{27} = 1$ a été faite pour éviter l'ajustement trop effectif avec les paramètres éloignés de valeurs réalistes. En effet, l'interaction entre les deux modes a une influence directe sur ceux-ci. Pour l'état $v_{27} = 1$ l'interaction peut être prise en compte en partie par les termes de l'hamiltonien MAR. L'attribution et l'analyse de raies de l'état $v_{26} = 1$ était bien plus compliquée, en particulier, à cause de l'ordre inversé de transitions de symétrie *A* et *E*. L'information sur l'attribution de la symétrie de la transition vient du modèle MAR. Typiquement, pour l'état fondamental, la transition de type *E* est décalée vers les fréquences basses et celle de type *A* vers les fréquences hautes par rapport à la position de la raie sans séparation *A* – *E* dans le cas de très haute barrière. Cette ordre est inversé pour le premier état excité de torsion. Pour tous les autres modes de vibration en absence de couplage avec le mode de torsion, l'ordre de transitions dans le doublet *A* – *E* doit être le même que celui de l'état fondamental. Ceci n'est pas le cas pour le mode $v_{27} = 1$ comme on peut constater à partir de la Fig. 11. Lors de l'attribution des raies avec les faibles valeurs de K_a il est impossible de distinguer les transitions de symétrie *A* et *E* car elles ont la même intensité relative. Cela devient possible pour les transitions avec les grandes valeurs de K_a , pour lesquelles la dégénérescence en K_a est enlevée pour les transitions de type *E* à cause de l'interaction de type Coriolis. On peut constater à partir de la Fig. 11 que pour les mêmes transitions de rotation les séparation *A* – *E* de l'état $v_{27} = 1$ sont un ordre de grandeurs plus élevées que celles de l'état fondamental. Ceci est également une manifestation de l'interaction entre les deux modes de torsion.

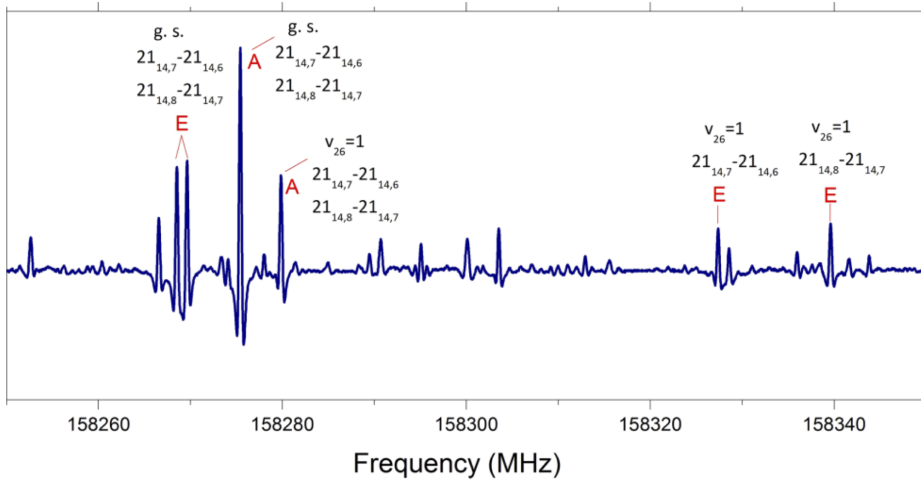


FIGURE 11: Une portion de spectre de rotation de la méthacroléine illustrant la séquence inversé de transitions A – E pour l'état $v_{27} = 1$ par rapport à l'état fondamental (g.s.).

De point de vu de calculs de chimie quantique, l'optimisation du champ de force harmonique de la méthacroléine démontre que les deux MVGA impliquent les déplacements de mêmes coordonnées des noyaux atomiques, cependant en différentes proportions et en opposition de phase. En d'autres termes, les deux modes v_{27} et v_{26} représentent un mélange de la torsion de CH_3 et de la torsion du squelette, ou la torsion de CH_3 entraîne le mouvement de torsion de squelette et vice versa.

A ce jour il n'existe pas de modèle permettant de traiter une interaction de type torsion-vibration avec la précision de l'expérience. Parmi les différents approches théoriques utilisées pour décrire ce phénomène d'interaction, je voudrais mettre un accent sur les modèles flexibles et le code informatique développé par R. Meyer à la fin des années 1970 [Meyer 1979]. Le traitement numérique avec les modèles flexibles a permis notamment de prendre en compte le couplage entre deux [Meyer and Bauder 1982] ou trois MVGA [Meyer et al. 1989] et d'obtenir les paramètres de la surface d'énergie potentielle multidimensionnelle avec relativement bonne précision. Dans ces travaux, il a été également démontré que le couplage entre les modes de MVGA peut être traité à l'aide des termes de l'énergie cinétique ou des termes d'énergie potentielle, ce qui a conduit à l'apparition des expressions « couplage cinétique » et « couplage d'engrenage » respectivement. Cependant, le code informatique développé par Meyer est limité aux niveaux d'énergie de rotation $J = 0$ et $J = 1$ et ne peut pas être utilisé pour le traitement de l'ensemble des données spectrales. Cette limitation est due principalement aux restrictions de calculs numériques à grande échelle suite aux capacités limitées des ordinateurs de l'époque. Dans des conditions modernes des tels calculs ne posent pas des difficultés et l'extension des modèles flexibles reste une piste intéressante à explorer.

2.4 Publications

1. B. Tercero, L. Margulès, M. Carvajal, R. A. Motiyenko, T. Huet, E. Alekseev, I. Kleiner, J.-C. Guillemin, H. Mollendal & J. Cernicharo. **Microwave and submillimeter spectroscopy and first ISM detection of ^{18}O -methyl formate.** *Astronomy & Astrophysics*, 538, A119, 2012.
2. I. Haykal, M. Carvajal, B. Tercero, I. Kleiner, A. López, J. Cernicharo, R. Motiyenko, T. R. Huet, J. Guillemin & L. Margulès. **THz spectroscopy and first ISM detection of excited torsional states of ^{13}C -methyl formate.** *Astronomy & Astrophysics*, 568, A58, 2014.
3. I. Smirnov, E. Alekseev, V. Ilyushin, L. Margulès, R. Motiyenko & B. Drouin. **Spectroscopy of the ground, first and second excited torsional states of acetaldehyde from 0.05 to 1.6 THz.** *J. Mol. Spec.*, 295, 44-50, 2014
4. L. Margulès, R. Motiyenko, V. Ilyushin et J. Guillemin. **Millimeter and submillimeter wave spectra of mono- ^{13}C -acetaldehydes.** *Astronomy & Astrophysics*, 579, A46, 2015.
5. A. Belloche, A. Meshcheryakov, R. Garrod, V. Ilyushin, E. Alekseev, R. Motiyenko, L. Margulès, H. Müller & K. Menten. **Rotational spectroscopy, tentative interstellar detection, and chemical modeling of N-methylformamide.** *Astronomy & Astrophysics*, 601, A49, 2017.
6. O. Zakharenko, R. Motiyenko, J.-R. Aviles Moreno, A. Jabri, I. Kleiner & T. Huet. **Torsion-rotation-vibration effects in the ground and first excited states of methacrolein, a major atmospheric oxidation product of isoprene.** *The Journal of Chemical Physics*, 144, 024303, 2016.

Microwave and submillimeter spectroscopy and first ISM detection of ^{18}O -methyl formate[★]

B. Tercero¹, L. Margulès², M. Carvajal³, R. A. Motiyenko², T. R. Huet², E. A. Alekseev⁴, I. Kleiner⁵, J. C. Guillemin⁶, H. Møllendal⁷, and J. Cernicharo¹

¹ Centro de Astrobiología (CSIC-INTA). Laboratory of Molecular Astrophysics. Department of Astrophysics. Ctra de Ajalvir, Km 4, 28850 Torrejón de Ardoz, Madrid, Spain

² Laboratoire de Physique des Lasers, Atomes, et Molécules, UMR CNRS 8523, Université de Lille I, 59655 Villeneuve d'Ascq Cedex, France

e-mail: laurent.margules@univ-lille1.fr

³ Departamento de Física Aplicada, Facultad de Ciencias Experimentales, Universidad de Huelva, 21071 Huelva, Spain

⁴ Institute of Radio Astronomy of NASU, Chernovonoporna Str., 4, 61002 Kharkov, Ukraine

⁵ Laboratoire Interuniversitaire des Systèmes Atmosphériques, UMR CNRS/IPSL 7583, Université Paris 7 et Université Paris Est, 61 Av. Charles de Gaulle, 94010 Créteil Cedex, France

⁶ Sciences Chimiques de Rennes, École Nationale Supérieure de Chimie de Rennes, CNRS, UMR 6226, Avenue du Général Leclerc, CS 50837, 35708 Rennes Cedex 7, France

⁷ Centre for Theoretical and Computational Chemistry (CTCC), Department of Chemistry, University of Oslo, PO Box 1033, Blindern, 0315 Oslo, Norway

Received 13 April 2011 / Accepted 3 October 2011

ABSTRACT

Context. Astronomical survey of interstellar molecular clouds needs a previous analysis of the spectra in the microwave and sub-mm energy range to be able to identify them. We obtained very accurate spectroscopic constants in a comprehensive laboratory analysis of rotational spectra. These constants can be used to predict transition frequencies that were not measured in the laboratory very precisely.

Aims. We present an experimental study and a theoretical analysis of two ^{18}O -methyl formate isotopologues, which were subsequently detected for the first time in Orion KL.

Methods. The experimental spectra of both methyl formate isotopologues recorded in the microwave and sub-mm range from 1 to 660 GHz. Both spectra were analysed by using the rho-axis method (RAM) which takes into account the CH_3 internal rotation.

Results. We obtained spectroscopic constants of both ^{18}O -methyl formate with high accuracy. Thousands of transitions were assigned and others predicted, which allowed us to detect both species in the IRAM 30 m line survey of Orion KL.

Key words. astrochemistry – ISM: molecules – submillimeter: ISM – line: identification – astronomical databases: miscellaneous – ISM: individual objects: Orion KL

1. Introduction

Complex organic molecules are relatively heavy and therefore have their maximum absorptions in the millimeter domain at about 300 GHz. But the most abundant compounds, like methyl formate, can be detected in the ISM up to 900 GHz (Comito et al. 2005). Since the first detection of this compound in 1975 (Brown et al. 1975; Churchwell et al. 1975), nearly one thousand lines were detected in the ground torsional state $v_t = 0$ (Lovas 2004) in star-forming regions (Sakai et al. 2007, and references therein). The column density depends on the object, it goes from 8.8×10^{15} in NGC 2264 MMS 3 (Sakai et al. 2007) to $3.4 \times 10^{17} \text{ cm}^{-2}$ in G19.61-0.23 (Remijan et al. 2004). Because of this fairly high column density, some lines from the first torsional state were also detected in Orion KL (Kobayashi et al. 2007) and in W51e2 (Demyk et al. 2008).

The spectra of the complex organic molecules are dense, and when a compound is abundant, for example methyl formate, one can detect the lines from the lower energy excited states, but also those from isotopic species. They can only be unambiguously detected if laboratory measurements and theoretical modelling are performed. Accurate line-by-line predictions for the positions and intensities were obtained for this purpose. Laboratory spectroscopic studies are therefore very important to be able to satisfactorily treat the spectra that are or will be obtained with submillimeter wave facilities *Herschel*, ALMA, and SOFIA.

Consequently, we decided to study the entire mono-isotopic species of methyl formate (Willaert et al. 2006; Carvajal et al. 2007, 2009, 2010; Margulès et al. 2009a, 2010; Demaison et al. 2010). These studies allowed the detection of more than 400 lines of both ^{13}C isotopologues and 100 lines of DCOOCH_3 in Orion KL.

The first laboratory measurements of the rotational spectra of methyl formate were made by Curl (1959). But the first general analysis of the internal rotation splitting (A and E) was made in 1999 (Oesterling et al. 1999). A more complete summary of the

* Full Tables A.1 et A.2 are available at the CDS via anonymous ftp to cdsarc.u-strasbg.fr (130.79.128.5) or via <http://cdsarc.u-strasbg.fr/viz-bin/qcat?J/A+A/538/A119>

spectroscopic history can be found in Carvajal et al. (2009). The only measurements of the ^{18}O isotopologues, available are those made in the centimeter-wave range by Curl (1959).

A few of the ^{18}O species have been detected up to now. The only isotopic species detected so far in SgrB2 are C^{18}O , $^{13}\text{C}^{18}\text{O}$, HC^{18}O^+ , $\text{CH}_3^{18}\text{OH}$, S^{18}O , and SO^{18}O (Belloche, priv. comm.), besides $^{28}\text{Si}^{18}\text{O}$ maser lines in Orion KL. Studying these is important for two main reasons: first, they give information about the isotopic ratio, as in the case of the detections of ^{18}OH (Morino et al. 1995), HC^{18}O^+ (Guélin et al. 1979), or H_2^{18}O (Neufeld et al. 2000). The ^{18}O species were also useful to determine the isotopic ratio of ^{12}C - ^{13}C in the case of CO (Langer et al. 1990). The second reason is that the ISM spectra should be cleaned of the lines from “weed’s” isotopic species to detect new species.

2. Experiments

2.1. Lille – FTMW spectrometer

The 1–20 GHz spectra were observed using the new molecular beam Fourier transform microwave spectrometer of Lille. The basic principles and technical details remain unchanged (Kassi et al. 2000). The main improvement of the new spectrometer consists of two new mirrors (diameter of 0.7 m compared to 0.4 m previously) to improve the signal-to-noise ratio at low frequencies (diffraction losses). Signals were recorded in the 4–18 GHz spectral region. Methyl formate vapors at a pressure of 20 mbars were mixed with neon carrier gas at a backing pressure of 1.5 bar. The mixture was introduced into a Fabry-Perot cavity at a repetition rate of 1.5 Hz. Molecules were polarized within the supersonic expansion by a 2 μs pulse and the free induction decay signal was detected and digitized at a repetition rate of 120 MHz. After transformation of the time domain signal into the frequency domain, molecular lines were observed as Doppler doublets, with a signal point every 0.92 kHz, resulting from the average of about 100 coded signals. Transition frequency was measured as an average of the two Doppler components and for most of the lines the uncertainty of the measurements is estimated to be less than 2 kHz.

2.2. Oslo – Stark centimeter wave spectrometer

The spectra of $\text{HC}^{18}\text{OOCH}_3$ and of $\text{HCO}^{18}\text{OCH}_3$ were recorded in the 7–80 GHz spectral region using the Stark-modulated microwave spectrometer of the University of Oslo. Details of the construction and operation of this spectrometer have been given elsewhere (Møllendal et al. 2005, 2006). The spectrum was taken at room temperature, or at roughly -20°C at a pressure of approximately 10 Pa, employing a Stark field strength of about 1100 V/cm. The frequency of individual transitions has an estimated accuracy of ≈ 0.15 MHz.

2.3. Lille – Submillimeter wave (SMM) spectrometer

The submillimeter-wave measurements (150–660 GHz) were performed using the Lille spectrometer (Motiyenko et al. 2010). In the frequency ranges: 150–322 and 400–533 GHz the solid state sources were used. The frequency of the Agilent synthesizer (12.5–17.5 GHz) was first multiplied by six and amplified by a Spacek active sextupler, providing the output power of +15 dBm in the W-band range (75–110 GHz). This power is high enough to use passive Schottky multipliers (X2, X3, X5) from Virginia Diodes Inc. in the next stage of the frequency multiplication chain.

In the frequency range from 580 to 660 GHz our new fast-scan spectrometer was applied. In general this is a usual absorption spectrometer. As a radiation source we applied the Istok backward wave oscillator (BWO). It was phase-locked to a harmonic of Agilent E8257D synthesizer which provided in our design large-step (~ 100 MHz) frequency control. A high-resolution fast frequency scan provided by a direct digital synthesizer, which is used as a reference source of BWO’s PLL (phase-locked loop). This solution allows us to reach a very high speed of spectra records of up to 100 GHz per hour. As a detector we used an InSb liquid He-cooled bolometer from QMC Instruments Ltd. To improve the sensitivity of the spectrometer, the sources were frequency-modulated at 10 kHz. The absorption cell was a stainless-steel tube (6 cm diameter, 220 cm long). The sample pressure during measurements was about 2.5 Pa and the linewidth was limited by Doppler broadening. The measurement accuracy for isolated line is estimated to be better than 30 kHz. However, if the lines were blended or had a poor signal-to-noise ratio they were given a weight of 100 or even 200 kHz.

2.4. Synthesis of ^{18}O -formic acid, methyl ester

Material. Formic acid, methanol and sulfuric acid (reagent grade, 95–98%) were purchased from Aldrich. ^{18}O -methanol and $^{18}\text{O}_2$ -formic acid, sodium salt were purchased from the Eurisotop Company.

$\text{H}_3\text{COC}^{(18)\text{O}}\text{H}$. In a flask were introduced $^{18}\text{O}_2$ -formic acid, sodium salt (0.72 g, 10 mmol) and methanol (0.48 g, 15 mmol). The solution was cooled to about -80°C and we added sulfuric acid (1.0 g, 10 mmol). The mixture was then cooled in a liquid nitrogen bath and evacuated (0.1 mbar). The stopcock was closed and the solution was heated up to 40°C and stirred overnight at this temperature. The cell was then adapted to a vacuum line equipped with two traps. The solution was distilled and higher boiling compounds were trapped in the first trap immersed in a bath cooled at -70°C and the methyl formate $\text{H}_3\text{COC}^{(18)\text{O}}\text{H}$ (0.57 g, 9.2 mmol) was condensed in the second trap immersed in a liquid nitrogen bath (-196°C). Yield: 92% but the methanol was quite difficult to remove completely and only 0.4 g of the pure product was isolated after a second trap-to-trap distillation with a first trap cooled at -90°C (with another sample containing about 20% of methanol).

$\text{H}_3\text{C}^{18}\text{OC(O)H}$. The synthesis reported for the ^{13}C derivative (Carvajal et al. 2009) was used starting from formic acid (2.0 g, 43 mmol) and ^{18}O -methanol (1.0 g, 29 mmol). Yield: 97% (1.7 g, 28 mmol).

^1H and ^{13}C NMR spectra of $\text{H}_3\text{C}^{18}\text{OC(O)H}$ and $\text{H}_3\text{COC}^{(18)\text{O}}\text{H}$ are identical to those of the ^{16}O derivative.

3. Theoretical model

The theoretical model and the so-called RAM method (rho-axis method) used for the present spectral analyses and fits of the $\text{HC}^{18}\text{OOCH}_3$ and $\text{HCO}^{18}\text{OCH}_3$ species have also been used previously for a number of molecules containing an internal methyl rotor (see for example Ilyushin et al. 2003, 2008) and in particular for the normal species of the cis-methyl formate (Carvajal et al. 2007; Ilyushin et al. 2009), for the $\text{H}^{13}\text{COOCH}_3$ and $\text{HCOO}^{13}\text{CH}_3$ species (Carvajal et al. 2009, 2010) and for DCOOCH_3 (Margulès et al. 2010). The RAM Hamiltonian used in the present study is based on previous works (Kirtman 1962; Lees & Baker 1968; Herbst et al. 1984). This method takes

its name from the choice of the axis system that allows one to minimize the coupling between internal rotation and global rotation in the Hamiltonian, at least to zeroth order. Because this method has been presented in great details in the literature (Lin & Swalen 1959; Hougen et al. 1994; Kleiner 2010), we will not describe it here.

The principal advantage of the RAM global approach used in our code BELGI, which is publicly available¹, is its general approach that simultaneously takes into account the A- and E-symmetry species in our fit. All the torsional levels that originated from one given vibrational state and the interactions within those rotation-torsion energy levels are also included in the rotation-torsion Hamiltonian matrix elements. The various rotational, torsional and coupling terms between rotation and torsion that we used for the fit of the $\text{HC}^{18}\text{OOCH}_3$ and of $\text{HCO}^{18}\text{OCH}_3$ species were defined previously for the normal methyl formate species (Carvajal et al. 2007). The labelling scheme of the energy levels and transitions used for methyl formate was also described in the same reference, as was the connection with the more traditional J_{K_a, K_c} labelling.

The $\text{HC}^{18}\text{OOCH}_3$ and $\text{HCO}^{18}\text{OCH}_3$ species share a number of spectroscopic characteristics with the other isotopologues of the cis-methyl formate molecule that are summarized in Demaison et al. (2010). The potential that hinders the internal rotation has an intermediate height, $V_3 = 391.569$ (6) cm^{-1} and 391.356 (4) cm^{-1} for $\text{HC}^{18}\text{OOCH}_3$ and $\text{HCO}^{18}\text{OCH}_3$, respectively; thus, it produces fairly large splittings of the rotational transitions even in the ground torsional state. Its A rotational constant is fairly small (about 0.56 cm^{-1}), which permits the measurement of many transitions, including high- J transitions ($J \leq 80$). The different isotopologues of methyl formate are all fairly asymmetric near-prolate rotors ($\kappa \sim -0.78$) and this leads to the observation of a clustering of lines with the same K_c quantum number at high J and low K_a . Finally the density of the ^{18}O -methyl formate species spectrum is increased, like the case of the other isotopologues of methyl formate, by the existence of several low-lying vibrations (for the $\text{H}^{12}\text{COO}^{12}\text{CH}_3$ molecule the torsion mode is around 130 cm^{-1} , the COC bend at 318 cm^{-1} , and an out-of-plane C-O torsion mode at 332 cm^{-1}) (Chao et al. 1986). But like the other isotopologues of methyl formate we studied, no perturbation was observed in the ground state $v_t = 0$ data, and this was assumed in the present fit of the ^{18}O species.

4. Assignments and fit

We started the present analysis by including transitions corresponding to low values of the rotational quantum number J in the fit, floating the lower order terms, i.e. the rotational parameters A, B, C and D_{ab} used in the RAM non principal axis system, the potential barrier V_3 and ρ , the coupling term between the internal rotation angular momentum and the global rotation angular momentum. The internal rotation constant F was kept fixed to its value determined in a fit of the ground and first torsional states $v_t = 0$ and 1 of the normal species of methyl formate (Carvajal et al. 2007). After fitting transitions corresponding to low J values, we gradually included transitions with higher J values.

¹ The source code for the fit, an example of input data file and a readme file are available at the web site (<http://www.ifpan.edu.pl/~kisiel/introt/introt.htm#belgi>) managed by Dr. Zbigniew Kisiel. Extended versions of the code made to fit transitions with higher J and K are also available the authors (I. Kleiner and M.C.).

For the $\text{HCO}^{18}\text{OCH}_3$ species, a total of 4430 A and E type transitions belonging to the ground torsional state were fitted using 31 parameters (floating 30 parameters and fixing parameter F) with a unitless standard deviation of 0.60 (47.8 kHz). The spectral ranges covered by our laboratory analysis were the following: 1–19 GHz (FTMW Lille spectrometer), 7–80 GHz (Oslo Stark spectrometer), 150–322 GHz, 400–533 GHz and 583–650 GHz (Lille SMM-spectrometer). The maximum values of J and K analyzed were 62 and 30 respectively. In the dataset, the 30 transition lines measured with the FTMW were weighted 3 kHz, the 4148 unblended transitions measured by the millimeter spectrometer at Lille were weighted 30 or 50 kHz depending on the broadening of the lines, 4 blended transitions from the same spectrometer were weighted 100 kHz and the 248 transitions measured in Oslo were weighted 150 kHz.

The fit included 3258 lines for the $\text{HC}^{18}\text{OCH}_3$ species, using 30 parameters (floating 29 parameters and again fixing the internal rotation parameter F). The unitless standard deviation for this other ^{18}O species of methyl formate is 0.82 (44.8 kHz). The same spectral ranges as for the other ^{18}O species were covered, and the weights distribution in the dataset was similar. Eleven lines measured with the FTMW spectrometer were weighted 3 kHz. Some 262 and 2628 unblended transitions measured very precisely by the millimeter spectrometer at Lille were weighted 30 or 50 kHz depending on the line broadening, 179 blended transitions from the same spectrometer were weighted 100 kHz, and 137 transitions measured in Oslo were weighted 150 kHz. Some 3 and 38 blended transitions measured in Oslo and Lille respectively were weighted 200 kHz. Tables 1 and 2 show the quality of the fit for the $\text{HCO}^{18}\text{OCH}_3$ and $\text{HC}^{18}\text{OOCH}_3$ species, respectively, with the root-mean-square deviations for the transitions according to their measurement uncertainty.

The dataset corresponding to the A-symmetry and to the E-symmetry for both $^{18}\text{O}-\text{HCOOCH}_3$ species, that were simultaneously taken into account in the theoretical model, fit with similar root-mean-square deviations of 51 kHz and 44 kHz for $\text{HCO}^{18}\text{OCH}_3$, and 48 kHz and 41 kHz for $\text{HC}^{18}\text{OOCH}_3$, showing the quality of the fit. The unitless standard deviations obtained for the $\text{HCO}^{18}\text{OCH}_3$ and $\text{HC}^{18}\text{OOCH}_3$ species are 0.60 and 0.82, respectively, similar to those obtained for the other isotopologues of methyl formate (Ilyushin et al. 2009; Carvajal et al. 2009; Margulès et al. 2009a; Carvajal et al. 2010). Table 3 compares the results of the fits using the code BELGI for the various isotopologues of methyl formate, using the same RAM method.

Table 3 gives the values of the internal rotation parameters (V_3 , F and the reduced height $s = 4V_3/9F$ and ρ), the angle θ_{RAM} between the RAM a axis and the principal axis, the angle $\angle(i, a)$ between the direction of the methyl group and the principal a axis, the maximum values of J_{\max} , K_{\max} , $v_{t\max}$ reached in the analysis, the number of lines included in the fit, the number of floated parameters, and the unitless standard deviations. One comment should be made on the internal rotation constant F and barrier height V_3 values appearing in Table 3. As already mentioned in Carvajal et al. (2009), an analysis of rotational transitions belonging to the excited torsional states have not been performed for any of the isotopologues of methyl formate (except for the normal species $\text{H}^{12}\text{COO}^{12}\text{CH}_3$ and $\text{H}^{13}\text{COO}^{12}\text{CH}_3$ for which we recently fitted rotational lines belonging to $v_t = 1$ Carvajal et al. 2010). The two torsion parameters V_3 (the height of the barrier) and F (the internal rotation parameter) are therefore highly correlated in this case and cannot be fitted simultaneously. The value of the F parameter of $\text{HCOO}^{13}\text{CH}_3$ species

Table 1. Root-mean-square (rms) deviations from the global fit^a of transitions involving $v_t = 0$ torsional energy levels of $\text{HCO}^{18}\text{OCH}_3$ methyl formate.

	Number of parameters	30 (+1fixed)
	Number of lines	4430
	rms of the 4430 MW $v_t = 0$ –0 lines	0.0478 MHz
	rms of the 2256 A symmetry lines	0.051 MHz
	rms of the 2174 E symmetry lines	0.044 MHz
Source ^b	Range ^c (GHz)	$v_t, J_{\max}, K_{\max}^d$
FTMW-LILLE	1–20	0, 7, 2
SMM-LILLE ^h	150–660	0, 62, 30
SMM-LILLE ^h	150–660	0, 25, 6
OSLO	7–80	0, 36, 9
		Number of lines ^e
		Uncertainties ^f (MHz)
		rms ^g (MHz)

Notes. ^(a) Parameter values are given in Table 4. The observed minus calculated residuals are given in the supplementary Table S1. ^(b) Sources of data: FTMW-LILLE, SMM-LILLE and OSLO data comes from present work, see experimental section. ^(c) Range containing the measurements in a given row. ^(d) v_t state and maximum J and K_a for each group of measurements. ^(e) Number of MW lines in each uncertainty group. ^(f) One-sigma standard uncertainty in MHz used in the fit. ^(g) Root-mean-square deviation in MHz for each group. ^(h) The SMM-LILLE spectrometer spectral ranges for these measurements are: 150–322 GHz, 400–533 GHz and 583–660 GHz.

Table 2. Root-mean-square (rms) deviations from the global fit^a of transitions involving $v_t = 0$ torsional energy levels of $\text{HC}^{18}\text{OOCH}_3$ methyl formate.

	Number of parameters	29 (+1fixed)
	Number of lines	3258
	rms of the 3258 MW $v_t = 0$ –0 lines	0.0448 MHz
	rms of the 1720 A symmetry lines	0.048 MHz
	rms of the 1538 E symmetry lines	0.041 MHz
Source ^b	Range ^c (GHz)	$v_t, J_{\max}, K_{\max}^d$
FTMW-LILLE	1–20	0, 4, 1
SMM-LILLE ^h	150–660	0, 63, 30
SMM-LILLE ^h	150–660	0, 52, 29
OSLO	7–80	0, 33, 8
OSLO	7–80	3
SMM-LILLE ^h	150–660	0, 38, 29
		Number of lines ^e
		Uncertainties ^f (MHz)
		rms ^g (MHz)

Notes. ^(a) Parameter values are given in Table 5. The observed minus calculated residuals are given in the supplementary Table S2. ^(b) Sources of data: FTMW-LILLE, SMM-LILLE and OSLO data comes from present work, see experimental section. ^(c) Range containing the measurements in a given row. ^(d) v_t state and maximum J and K_a for each group of measurements. ^(e) Number of MW lines in each uncertainty group. ^(f) One-sigma standard uncertainty in MHz used in the fit. ^(g) Root-mean-square deviation in MHz for each group. ^(h) The SMM-LILLE spectrometer spectral ranges for these measurements are 150–322 GHz, 400–533 GHz and 583–660 GHz.

Table 3. Comparison of results of the fits using the code BELGI for the various isotopologues of methyl formate, using the same RAM method.

Molecules	V_3	F	s^a	ρ^b	θ_{RAM}^c	$\langle(i, a)^d\rangle$	J_{\max}	K_a^{\max}	v_t^{\max}	N^e	N_p^f	rms ^g	Ref.
$\text{HC}^{18}\text{OOCCH}_3$	392	5.5 ^{fixed}	32	0.0798	26	55	63	30	0	3258	29	0.82	Present work
$\text{HCO}^{18}\text{OCH}_3$	391	5.5 ^{fixed}	32	0.0806	26	54	62	30	0	4430	30	0.60	Present work
$\text{HCOO}^{13}\text{CH}_3$	407	5.7 ^{fixed}	32	0.0845	24	52	63	34	0	936	27	1.08	Carvajal et al. (2009)
DCOOCH_3	389	5.5 ^{fixed}	31	0.0813	24	51	64	36	0	1703	24	1.11	Margulès et al. (2010)
$\text{H}^{12}\text{COO}^{12}\text{CH}_3$	373	5.5	30	0.0842	25	53	62	26	1	10533	55	0.71	Ilyushin et al. (2009)
$\text{H}^{13}\text{COOCH}_3$	372	5.5	30	0.0841	25	52	59	27	1	7445	45	0.55	Carvajal et al. (2010)

Notes. ^(a) Reduced height $s = 4V_3/9F$ (unitless). ^(b) Coupling constant between internal and global rotation (unitless). ^(c) Angle between the rho-axis system and the principal axis system, for C_s molecules, in degrees. ^(d) Angle between the methyl top symmetry axis and the a principal axis, in degrees. ^(e) Number of lines included in the fit. ^(f) Number of parameters used in the fit. ^(g) Unitless Root-mean-square deviations, which should be 1.0 if the fit were good to experimental uncertainty.

is fixed to its ab initio value calculated in the equilibrium structure at the CCSD(T)/cc-pV5Z + core-correction level of theory (5.69 cm^{-1}), whereas for DCOOCH₃ and the two ¹⁸O-methyl formate species, F is fixed to the ground state $v_t = 0$ value of the normal species (5.49 cm^{-1}). Finally, for the ¹³C₂-methyl

formate, DCOOCH₃ and the ¹⁸O isotopologues, the V_6 parameter, which is the second term in the torsional potential Fourier series

$$V(\gamma) = \frac{V_3}{2} \times (1 - \cos 3\gamma) + \frac{V_6}{2} \times (1 - \cos 6\gamma) + \dots$$

Table 4. Torsion-rotation parameters needed for the global fit of transitions involving $v_t = 0$ torsional energy levels of $\text{HCO}^{18}\text{OCH}_3$ methyl formate.

nlm ^a	Operator ^b	Parameter	$\text{HCO}^{18}\text{OCH}_3^c$	nlm	Operator	Parameter	$\text{HCO}^{18}\text{OCH}_3^c$
220	$(1 - \cos 3\gamma)/2$	V_3	391.35594(377)	404	$-P^4$	D_J	$-0.1781(240) \times 10^{-7}$
	P_γ^2	F	5.49038 ^d		$-P_a^2 P_a^2$	D_{JK}	$-0.13188(145) \times 10^{-5}$
211	$P_\gamma P_a$	ρ	0.08057980(284)		$-P_a^4$	D_K	$0.50871(198) \times 10^{-5}$
202	P_a^2	A^{RAM}	0.56177506(636)		$-2P_b^2(P_b^2 - P_c^2)$	δ_J	$-0.4338(120) \times 10^{-7}$
	P_b^2	B^{RAM}	0.30985885(512)		$-\{P_a^2, (P_b^2 - P_c^2)\}$	δ_K	$0.2660(229) \times 10^{-7}$
	P_c^2	C^{RAM}	0.174524916(392)		$P^2(P_a P_b + P_b P_a)$	D_{abJ}	$-0.93534(382) \times 10^{-6}$
	$(P_a P_b + P_b P_a)$	D_{ab}	-0.16362225(395)		$(P_a^3 P_b + P_b P_a^3)$	D_{abK}	$0.153543(349) \times 10^{-5}$
422	$\sin 3\gamma (P_b P_c + P_c P_b)$	D_{bc}	0.00197000(784)	624	$(1 - \cos 3\gamma) P_a^4$	k_{5K}	$-0.2211(122) \times 10^{-6}$
	$(1 - \cos 3\gamma) P^2$	F_v	-0.00248015(206)	606	P^6	H_J	$0.3554(355) \times 10^{-12}$
	$(1 - \cos 3\gamma) P_a^2$	k_5	0.0127104(136)		$P^4 P_a^2$	H_{JK}	$0.6789(118) \times 10^{-11}$
	$(1 - \cos 3\gamma)(P_a P_b + P_b P_a)$	d_{ab}	-0.00627264(369)		P_a^6	H_K	$0.52885(929) \times 10^{-10}$
413	$P_\gamma P_a^3$	k_1	0.48356(550)	10^{-5}	$2P^4(P_b^2 - P_c^2)$	h_J	$0.1855(169) \times 10^{-12}$
	$P_\gamma P_a P^2$	L_v	0.17553(349)	10^{-5}	$\{P_a^4(P_b^2 - P_c^2)\}$	h_K	$0.17745(887) \times 10^{-11}$
	$P_\gamma \{P_a, (P_b^2 - P_c^2)\}$	c_4	0.13412(118)	10^{-5}	$P^2(P_a^3 P_b + P_b P_a^3)$	D_{abJK}	$0.3103(210) \times 10^{-11}$
	$P_\gamma (P_a^2 P_b + P_b P_a^2)$	δ_{ab}	-0.18642(438)	10^{-5}	$P^4(P_a P_b + P_b P_a)$	D_{abJJ}	$-0.17323(825) \times 10^{-11}$
				615	$P^2 P_\gamma P_a^3$	k_{1J}	$-0.39079(975) \times 10^{-9}$

Notes. ^(a) Notation from Ilyushin et al. (2008); $n = l + m$, where n is the total order of the operator, l is the order of the torsional part and m is the order of the rotational part. ^(b) Notation from Ilyushin et al. (2008). $\{A, B\} = AB + BA$. The product of the parameter and operator from a given row yields the term actually used in the vibration-rotation-torsion Hamiltonian, except for F , ρ and A^{RAM} , which occur in the Hamiltonian in the form $F(P_\gamma - \rho P_a)^2 + A^{\text{RAM}} P_a^2$. ^(c) Present work. ^(d) Value of the internal rotation constant F was kept fixed to the HCOOCH_3 value from Carvajal et al. (2007).

cannot be determined. This V_6 term is fairly high for normal methyl formate (23.9018(636) cm^{-1}) and we expect its value to be of the same magnitude for the other methyl formate species. However, in the absence of excited torsional transitions we cannot fit V_6 parameter in the cases of $^{13}\text{C}_2$ -methyl formate, DCOOCH_3 or for the ^{18}O isotopologues; we fixed its value to zero. For these reasons, the values of V_3 determined for these methyl formate isotopologues can only be considered as effective values that contain the contribution of V_6 .

The two ^{18}O -methyl formate species show excellent root-mean-square deviations (rms). For $\text{HC}^{18}\text{OOCCH}_3$, however, many lines were overlapped by transitions originated from the methanol molecule used during the synthesis and was still present in very small amounts in the sample even though it was purified (see experimental section). Therefore less lines were available for the analysis of the $\text{HC}^{18}\text{OOCCH}_3$ isotopologue than for the $\text{HCO}^{18}\text{OCH}_3$ isotopologue. Tables 4 and 5 show the 31 and 30 parameters (including the fixed parameter F) used in our fit of the ground torsional state of the $\text{HCO}^{18}\text{OCH}_3$ and $\text{HC}^{18}\text{OOCCH}_3$ species. The two sets of parameters are similar.

5. Line strengths

The intensity calculations for the two ^{18}O species of methyl formate were performed using the same method as described in Hougen et al. (1994); Ilyushin et al. (2008), and applied for the normal species by Carvajal et al. (2007), the ^{13}C species (Carvajal et al. 2009, 2010) and for DCOOCH_3 (Margulès et al. 2010). For this reason we will not repeat it here. The line strength calculation for the ^{18}O species was performed using the same value for the dipole moment as for the parent methyl formate (Margulès et al. 2010). This assumption was made because the angle between the internal axis of the methyl top and

the principal a-axis does not change much upon substitution (see the $\langle i, a \rangle$ angle values in Table 6). All other structural parameters such as the angle between RAM and PAM axes (θ_{RAM}) and the ρ parameter do not change much upon substitution (see Table 6). Because the changes in the structure in the various isotopomers are not important, we assumed that the dipole moment does not change considerably from one species to another. The dipole moment components of $\text{HCO}^{18}\text{OCH}_3$ and $\text{HC}^{18}\text{OOCCH}_3$ in RAM axis system that we used for the intensity calculations are $\mu_a^{\text{RAM}} = 1.790 \text{ D}$; $\mu_b^{\text{RAM}} = -0.094 \text{ D}$ and $\mu_a^{\text{RAM}} = 1.791 \text{ D}$; $\mu_b^{\text{RAM}} = -0.081 \text{ D}$, respectively.

We provided Tables A1 and A2, which are part of the supplementary Tables S1 and S2 (available on CDS) in the appendix. They contain all included lines from our fit for the $\text{HCO}^{18}\text{OCH}_3$ and $\text{HC}^{18}\text{OOCCH}_3$ methyl formate species. They show the line assignments, the observed frequencies with measurement uncertainty (in parenthesis), the computed frequencies, observed-calculated values, the line strength for the $v_t = 0$ transitions, and the lower-state energy relative to the $J = K = 0$ A-species level taken as zero-energy level.

6. $^{18}\text{O-HCOOCH}_3$ detection in Orion KL

Thanks to the new laboratory frequencies provided above, we have detected the two ^{18}O isotopologues of HCOOCH_3 in the IRAM 30 m line survey of Orion KL presented in Tercero et al. (2010, 2011). After summarizing the observations, data reduction, and overall results of that line survey (Sect. 6.1), we concentrated on the detection of the two ^{18}O isotopologues of HCOOCH_3 and their analysis (Sect. 6.2). This is the last of a series of papers dedicated to the different isotopologues of methyl formate (laboratory frequencies and detection in Orion KL, see Carvajal et al. 2009; and Margulès et al. 2010).

Table 5. Torsion-rotation parameters needed for the global fit of transitions involving $v_t = 0$ torsional energy levels of $\text{HC}^{18}\text{OOCH}_3$ methyl formate.

nlm ^a	Operator ^b	Parameter	$\text{HC}^{18}\text{OOCH}_3^c$	nlm	Operator	Parameter	$\text{HC}^{18}\text{OOCH}_3^c$
220	$(1 - \cos 3\gamma)/2$	V_3	391.56929 (646)	404	$-P^4$	D_J	$0.2097(211) \times 10^{-7}$
	P_γ^2	F	5.49038 ^d		$-P_a^2 P_a^2$	D_{JK}	$-0.180042(857) \times 10^{-5}$
211	$P_\gamma P_a$	ρ	0.07977981(403)		$-P_a^4$	D_K	$0.532763(931) \times 10^{-5}$
202	P_a^2	A^{RAM}	0.56776348 (810)		$-2P_b^2(P_b^2 - P_c^2)$	δ_J	$-0.2519(106) \times 10^{-7}$
	P_b^2	B^{RAM}	0.30216119(677)		$\{-P_a^2, P_b^2 - P_c^2\}$	δ_K	$-0.35754(981) \times 10^{-7}$
	P_c^2	C^{RAM}	0.170313544(770)		$P^2(P_a P_b + P_b P_a)$	D_{abJ}	$-0.90979(301) \times 10^{-6}$
	$(P_a P_b + P_b P_a)$	D_{ab}	-0.16731097(526)		$(P_a^3 P_b + P_b P_a^3)$	D_{abK}	$0.144807(244) \times 10^{-5}$
422	$\sin 3\gamma(P_b P_c + P_c P_b)$	D_{bc}	0.0017299(105)	624	$(1 - \cos 3\gamma)P^2 P_a^2$	k_{5J}	$-0.14491(670) \times 10^{-6}$
	$P_\gamma^2 P_a^2$	k_2	0.35429(548) 10^{-4}		$P^2 P_\gamma^2 P_a^2$	k_{2J}	$-0.28717(908) \times 10^{-8}$
	$(1 - \cos 3\gamma) P^2$	F_v	-0.00203120(379)	606	$P^4 P_a^2$	H_{JK}	$0.6870(113) \times 10^{-11}$
	$(1 - \cos 3\gamma) P_a^2$	k_5	0.0140399(189)		$P^2 P_a^4$	H_{KJ}	$-0.23719(718) \times 10^{-10}$
	$(1 - \cos 3\gamma)(P_a P_b + P_b P_a)$	d_{ab}	-0.00613830(453)		P_a^6	H_K	$0.68402(464) \times 10^{-10}$
	$P_\gamma^2 P^2$	G_V	0.118883(538) 10^{-4}		$2P_b^4(P_b^2 - P_c^2)$	h_J	$0.935(9) \times 10^{-14}$
413	$P_\gamma \{P_a, (P_b^2 - P_c^2)\}$	c_4	0.11880(160) 10^{-5}		$P^2(P_a^3 P_b + P_b P_a^3)$	D_{abJK}	$0.5012(136) \times 10^{-11}$
	$P_\gamma (P_a^2 P_b + P_b P_a^2)$	δ_{ab}	-0.21412 (315) 10^{-5}		$P^4(P_a P_b + P_b P_a)$	D_{abJJ}	$-0.8718(390) \times 10^{-12}$

Notes. ^(a) Notation from Ilyushin et al. (2008); $n = l + m$, where n is the total order of the operator, l is the order of the torsional part and m is the order of the rotational part. ^(b) Notation from Ilyushin et al. (2008). $\{A, B\} = AB + BA$. The product of the parameter and operator from a given row yields the term actually used in the vibration-rotation-torsion Hamiltonian, except for F , ρ and A^{RAM} , which occur in the Hamiltonian in the form $F(P_\gamma - \rho P_a)^2 + A^{\text{RAM}} P_a^2$. ^(c) Present work. ^(d) Value of the internal rotation constant F was kept fixed to the HCOOCH_3 value from Carvajal et al. (2007).

Table 6. Rotational constants in the RHO axis system (RAM) and in the principal axis system (PAM) for $\text{HC}^{18}\text{OOCH}_3$ and $\text{HCO}^{18}\text{OCH}_3$.

	$\text{HC}^{18}\text{OOCH}_3$		$\text{HCO}^{18}\text{OCH}_3$	
	(RAM) ^a	(PAM) ^b	(RAM) ^a	(PAM) ^b
$A(\text{MHz})$	17021.121(243)	19443.700(236)	16841.593(191)	19255.846(182)
$B(\text{MHz})$	9058.565(203)	6635.985(211)	9289.335(153)	6875.081(160)
$C(\text{MHz})$	5105.8716 (231)	5105.8716 (231)	5232.1254(118)	5232.1254(118)
$D_{ab}(\text{MHz})$	-5015.857 (158)		-4905.272(118)	
$\angle(i, a)$		54.754(2)		54.042 (1)
$\angle(i, b)$		35.246(2)		35.958 (1)
$\angle(i, c)$		90.000		90.000
θ_{RAM}^c		25.7798(7)		26.2053(6)

Notes. Angles between the principal axis and the methyl top axis. ^(a) Rotational constants obtained in our work for RAM-axis system (see Tables 4 and 5 for $\text{HCO}^{18}\text{OCH}_3$ and $\text{HC}^{18}\text{OOCH}_3$). ^(b) Rotational constants of our work transformed to the principal axis system and angles in degrees between the principal axis (a, b, c) and the methyl top axis (i). ^(c) The angle θ_{RAM} angle between the a-principal axis and the a-RAM axis is given in degrees and obtained from Eq. (1) of Carvajal et al. (2007) with the parameters A^{RAM} , B^{RAM} , C^{RAM} , and D_{ab} of Tables 4 and 5.

6.1. Observations, data reduction, and overall results of the line survey

The observations were carried out using the IRAM 30m radio telescope during September 2004 (3 mm and 1.3 mm windows), March 2005 (full 2 mm window), April 2005 (completion of 3 mm and 1.3 mm windows), and January 2007 (maps and pointed observations at particular positions). Four SiS receivers operating at 3, 2, and 1.3 mm were used simultaneously with image sideband rejections within 20–27 dB (3 mm receivers), 12–16 dB (2 mm receivers) and ≈ 13 dB (1.3 mm receivers). System temperatures were in the range 100–350 K for the 3 mm receivers, 200–500 K for the 2 mm receivers, and 200–800 K for the 1.3 mm receivers, depending on the particular frequency, weather conditions, and source elevation. For frequencies in

the range 172–178 GHz, the system temperature was significantly higher, 1000–4000 K, owing to proximity of the atmospheric water line at 183.31 GHz. The intensity scale was calibrated using two absorbers at different temperatures and the atmospheric transmission model (ATM, Cernicharo 1985; Pardo et al. 2001).

Pointing and focus were regularly checked on the nearby quasars 0420–014 and 0528+134. Observations were made in the balanced wobbler-switching mode, with a wobbling frequency of 0.5 Hz and a beam throw in azimuth of $\pm 240''$. No contamination from the off-position affected our observations except for a marginal one at the lowest elevations ($\sim 25^\circ$) for molecules showing low J emission along the extended ridge.

Two filter banks with 512×1 MHz channels and a correlator providing two 512 MHz bandwidths and 1.25 MHz resolution

were used as backends. We pointed towards the IRc2 source at $\alpha_{2000.0} = 5^{\text{h}}35^{\text{m}}14.5^{\text{s}}$, $\delta_{2000.0} = -5^{\circ}22'30.0''$ (J2000.0).

Although we had a good receiver image-band rejection, each setting was repeated at a slightly shifted frequency (10–20 MHz) to manually identify and remove all features arising from the image side band. The spectra from different frequency settings were used to identify all potential contaminating lines from the image side band. In some cases it was impossible to eliminate the contribution of the image side band and we removed the signal in those contaminated channels, leaving holes in the data. The total frequencies blanked this way represent less than 0.5% of the total frequency coverage. We removed most of the features from the image side band above a 0.05 K threshold.

Within the 168 GHz bandwidth covered (80–115.5, 130–178, and 196–281 GHz), we detected more than 14 600 spectral features of which $\sim 10\,200$ were already identified and attributed to 43 molecules, including 148 different isotopologues and vibrationally excited states. Any feature covering more than 3–4 channels and of intensity greater than 0.02 K is above 3σ and was considered to be a line in our survey. In the 2 mm and 1.3 mm windows the features weaker than 0.1 K have not yet been systematically analysed, except when searching for isotopic species with good laboratory frequencies. We therefore expect to considerably increase the number of both identified and unidentified lines. We note that the number of U lines was initially much larger. Identification of some isotopologues of most abundant species allowed us to reduce the number of U-lines at a rate of ~ 500 lines per year (see, as examples, Demyk et al. 2007; Margulès et al. 2009b; Carvajal et al. 2009; and Margulès et al. 2010). We used standard procedures to identify lines above 0.2 K including all possible contributions (taking into account the energy of the transition and the line strength) from different species. Thanks to the wide frequency coverage of our survey, many rotational lines were observed for each species, hence it is possible to estimate the contribution of a given molecule to the intensity of a spectral feature where several lines from different species are blended.

In agreement with previous works, four different spectral cloud components were defined in the analysis of low angular resolution line surveys of Orion KL where different physical components overlap in the beam. These components are characterized by different physical and chemical conditions (Blake et al. 1987; Blake et al. 1996; Tercero et al. 2010, 2011): (i) a narrow or “spike” ($\sim 4 \text{ km s}^{-1}$ line-width) component at $v_{\text{LSR}} \approx 9 \text{ km s}^{-1}$ delineating a north-to-south *extended ridge* or ambient cloud ($T_k \approx 60 \text{ K}$, $n(\text{H}_2) \approx 10^5 \text{ cm}^{-3}$); (ii) a compact and quiescent region, the *compact ridge*, ($v_{\text{LSR}} \approx 8 \text{ km s}^{-1}$, $\Delta v \approx 3 \text{ km s}^{-1}$, $T_k \approx 110 \text{ K}$, $n(\text{H}_2) \approx 10^6 \text{ cm}^{-3}$) identified for the first time by Johansson et al. (1984); (iii) the *plateau*, a mixture of outflows, shocks, and interactions with the ambient cloud ($v_{\text{LSR}} \approx 6\text{--}10 \text{ km s}^{-1}$, $\Delta v \gtrsim 25 \text{ km s}^{-1}$, $T_k \approx 150 \text{ K}$, $n(\text{H}_2) \approx 10^6 \text{ cm}^{-3}$); (iv) a *hot core* component ($v_{\text{LSR}} \approx 5 \text{ km s}^{-1}$, $\Delta v \sim 10 \text{ km s}^{-1}$, $T_k \approx 225 \text{ K}$, $n(\text{H}_2) \approx 5 \times 10^7 \text{ cm}^{-3}$) first detected in ammonia emission Morris et al. (1980). Methyl formate (in general, organic saturated O-rich molecules) emission comes mainly from the compact ridge component.

6.2. Detection and astronomical modelling

We have detected the ^{18}O isotopologues of HCOOCH_3 in states A and E through 80 emission lines of the line survey. Despite the large number of line blends in the 80–280 GHz domain, we were able to assign these 80 lines to $\text{HCO}^{18}\text{OCH}_3$

and $\text{HC}^{18}\text{OOCH}_3$. Table 7 gives the observed line intensities and frequencies together with the predicted frequencies from the rotational constants derived in this paper for all lines of these isotopologues that are not strongly blended with other lines from other species. All emission lines expected to have a T_{MB} above 0.1 K (those lines that correspond with the overlap of different a -type transitions with $K_a = 0, 1$ in the 1.3 mm domain) were detected. Unfortunately, several of them are blended with strong emission lines from other molecules; Table 7 gives information on these contaminating lines. There is no strong line expected that is not observed in the astronomical spectra. In addition, Table 7 gives the line intensity derived from the model predictions (see below). The observed brightness temperature for the lines in Table 7 has been obtained from the peak emission channel in the spectra. To quantify the contribution of possible blending, all contaminating species should be modelled. Hence, we limited ourselves in Table 7 to those lines that are practically free of blending or that only are affected by other weak lines. Consequently, our observed main beam temperatures have to be considered as upper limits for these weakly blended lines. The predicted intensities agree quite well with the observations of the 80 spectral lines detected, with 40 lines practically free of blending with other species.

All together these observations ensure the detection of ^{18}O -methyl formate in Orion KL.

Figures 1 and 2 show selected detected lines at 3 and 2 mm and at 1.3 mm, respectively, together with our best model (see below). In those figures we have tried to display no strongly contaminated lines (at least one per box). The overlaps with other species are quoted in Table 7. In addition, both figures show many detected lines without blending with other species, which support the first detection in space of both ^{18}O methyl formate isotopologues.

Following the models made by Margulès et al. (2010), we consider that the line profiles of methyl formate display the four components of Orion KL quoted above. We added an additional component for the compact ridge with a kinetic temperature of 250 K to better reproduce the line profiles of all isotopologues of HCOOCH_3 in all spectral windows of the 30-m survey (this inner and hotter component of the compact ridge is required for fitting the emission lines of different molecules in the HIFI domain on-board the *Herschel Space Observatory*; Tercero et al. and Marcelino et al. both in prep.). Because of the weakness of ^{18}O methyl formate lines, the plateau component is not needed to reproduce the observations of these isotopologues. Therefore, in this case, we assume that the emission of ^{18}O methyl formate comes from the compact ridge, “hot” compact ridge, extended ridge, and hot core.

We used LTE approximation in all cases (for the extended ridge, both compact ridges, and hot core). The lack of collisional rates for this molecule prevents a more detailed analysis of the emission of methyl formate. Nevertheless, taking into account the physical conditions of the different cloud components, we expect that this approximation works reasonably well. Only for the extended ridge we were able to obtain non LTE conditions. However, the lines affected by this cloud component are those involving low-energy levels, for which its contribution is less than 50%. Its effect on the lines associated with high-energy levels is negligible.

For each cloud component we assumed uniform physical conditions for the kinetic temperature, density, radial velocity, and line width (see parameters quoted in Sect. 6.1). We adopted these values from the data analysis (Gaussian fits and an attempt to simulate the line profiles for several molecules with LTE

Table 7. Detected lines of $^{18}\text{O}-\text{HCOOCH}_3$.

Species	Transition J_{K_a,K_c}	Rest freq. (MHz)	E_u (K)	S_{ij}	Observed freq. (MHz)	Observed T_{MB} (K)	Modeled T_{MB} (K)
A-HCO $^{18}\text{OCH}_3$	7 _{2,6} -6 _{2,5}	83327.49	18.7	6.40	83327.5	0.012	0.013
E-HC $^{18}\text{OOCH}_3$	8 _{1,8} -7 _{1,7}	85805.17	19.4	7.86	85802.4 ¹	0.030	0.016
A-HC $^{18}\text{OOCH}_3$	8 _{1,8} -7 _{1,7}	85807.01	19.4	7.86	85807.4	0.033	0.016
E-HCO $^{18}\text{OCH}_3$	8 _{2,7} -7 _{2,6}	94754.73	23.2	7.49	94755.5	0.037	0.017
E-HC $^{18}\text{OOCH}_3$	8 _{3,5} -7 _{3,4}	95996.47	26.4	6.90	95996.5	0.025	0.016
E-HC $^{18}\text{OOCH}_3$	8 _{1,7} -7 _{1,6}	96466.39	21.8	7.79	96466.5	0.025	0.017
A-HCO $^{18}\text{OCH}_3$	8 _{3,6} -7 _{3,5}	97429.39	26.7	6.87	97430.0 ¹	0.031	0.016
E-HCO $^{18}\text{OCH}_3$	8 _{4,5} -7 _{4,4}	97569.09	31.2	5.76	97569.5	0.028	0.013
E-HCO $^{18}\text{OCH}_3$	9 _{0,9} -8 _{0,8}	99039.16	24.5	8.86	99040.0	0.025	0.022
A-HCO $^{18}\text{OCH}_3$	9 _{0,9} -8 _{0,8}	99040.86	24.5	8.86	²
A-HCO $^{18}\text{OCH}_3$	8 _{2,6} -7 _{2,5}	102414.82	24.3	7.53	102415.0	0.029	0.019
E-HCO $^{18}\text{OCH}_3$	9 _{2,8} -8 _{2,7}	106025.11	28.3	8.52	106025.5	0.025	0.023
E-HC $^{18}\text{OOCH}_3$	9 _{5,4} -8 _{5,3}	106251.00	41.8	6.24	106251.0	0.037	0.014
A-HC $^{18}\text{OOCH}_3$	9 _{5,4} -8 _{5,3}	106265.60	41.8	6.24	106265.4	0.050	0.013
E-HC $^{18}\text{OOCH}_3$	9 _{3,7} -8 _{3,6}	106295.64	31.6	8.01	106295.5	0.044	0.020
A-HC $^{18}\text{OOCH}_3$	9 _{3,7} -8 _{3,6}	106302.47	31.4	8.01	106302.5	0.025	0.021
E-HC $^{18}\text{OOCH}_3$	9 _{4,6} -8 _{4,5}	106576.35	36.0	6.86	106576.5	0.019	0.017
E-HC $^{18}\text{OOCH}_3$	9 _{1,8} -8 _{1,7}	107284.86	27.0	8.75	107284.4	0.038	0.025
A-HC $^{18}\text{OOCH}_3$	9 _{1,8} -8 _{1,7}	107292.37	27.0	8.75	107292.5	0.038	0.023
E-HC $^{18}\text{OOCH}_3$	9 _{3,6} -8 _{3,5}	108822.96	31.9	8.01	108823.5	0.038	0.023
E-HCO $^{18}\text{OCH}_3$	10 _{1,10} -9 _{1,9}	109037.62	29.8	9.85	109037.5	0.038	0.027
A-HCO $^{18}\text{OCH}_3$	10 _{1,10} -9 _{1,9}	109039.39	29.8	9.85	109040.6 ¹	0.057	0.027
E-HCO $^{18}\text{OCH}_3$	10 _{0,10} -9 _{0,9}	109365.53	29.8	9.85	109365.5 ¹	0.032	0.028
E-HCO $^{18}\text{OCH}_3$	9 _{1,8} -8 _{1,7}	109988.47	27.7	8.71	109988.5	0.038	0.026
A-HC $^{18}\text{OOCH}_3$	9 _{2,7} -8 _{2,6}	111644.35	29.0	8.58	111644.5	0.025	0.024
E-HC $^{18}\text{OOCH}_3$	10 _{2,9} -9 _{2,8}	114108.78	33.1	9.56	114108.5	0.025	0.026
E-HCO $^{18}\text{OCH}_3$	12 _{0,12} -11 _{0,11}	130114.40	42.7	11.9	130115.1 ¹	0.012	0.038
A-HCO $^{18}\text{OCH}_3$	12 _{0,12} -11 _{0,11}	130115.91	41.7	11.9	²
E-HC $^{18}\text{OOCH}_3$	12 _{2,11} -11 _{2,10}	135472.80	45.6	11.6	135472.7	0.026	0.036
E-HC $^{18}\text{OOCH}_3$	13 _{0,13} -12 _{0,12}	137256.72	48.6	12.9	137256.3	0.080	0.044
A-HC $^{18}\text{OOCH}_3$	13 _{0,13} -12 _{0,12}	137258.10	47.4	12.9	²	...	0.044
E-HCO $^{18}\text{OCH}_3$	11 _{3,8} -10 _{3,7}	139979.02	45.1	10.2	139978.6	0.046	0.031
A-HCO $^{18}\text{OCH}_3$	11 _{3,8} -10 _{3,7}	139995.37	45.1	10.2	139995.7	0.026	0.031
E-HCO $^{18}\text{OCH}_3$	13 _{1,13} -12 _{1,12}	140452.90	49.9	12.9	140453.3	0.073	0.045
A-HCO $^{18}\text{OCH}_3$	13 _{1,13} -12 _{1,12}	140454.43	48.5	12.9	²	...	0.043
E-HC $^{18}\text{OOCH}_3$	13 _{2,12} -12 _{2,11}	145979.69	52.6	12.6	145980.5 ¹	0.12	0.038
A-HC $^{18}\text{OOCH}_3$	13 _{2,12} -12 _{2,11}	145985.77	52.6	12.6	145985.6 ³	0.055	0.037
E-HCO $^{18}\text{OCH}_3$	12 _{7,6} -11 _{7,5}	146004.17	76.6	7.93	146004.1	0.040	0.049
A-HCO $^{18}\text{OCH}_3$	12 _{7,6} -11 _{7,5}	146004.24	76.6	7.93	²
A-HCO $^{18}\text{OCH}_3$	12 _{7,5} -11 _{7,4}	146004.47	77.2	7.93	²
E-HC $^{18}\text{OOCH}_3$	12 _{2,10} -11 _{2,9}	147364.51	48.6	11.6	147363.8	0.085	0.038
E-HC $^{18}\text{OOCH}_3$	14 _{1,14} -13 _{1,13}	147369.38	56.2	13.9	147371.3 ⁴	0.11	0.048
A-HC $^{18}\text{OOCH}_3$	14 _{1,14} -13 _{1,13}	147370.78	54.4	13.9	²	...	0.049
A-HC $^{18}\text{OOCH}_3$	12 _{2,10} -11 _{2,9}	147377.44	54.4	11.6	147377.0	0.11	0.038
E-HC $^{18}\text{OOCH}_3$	14 _{0,14} -13 _{0,13}	147423.20	56.2	13.9	147423.8 ¹	0.22	0.050
A-HC $^{18}\text{OOCH}_3$	14 _{0,14} -13 _{0,13}	147424.53	54.4	13.9	²
E-HCO $^{18}\text{OCH}_3$	14 _{0,14} -13 _{0,13}	150934.10	57.7	13.9	150934.6	0.11	0.052
A-HCO $^{18}\text{OCH}_3$	14 _{0,14} -13 _{0,13}	150935.51	55.7	13.9	²
E-HC $^{18}\text{OOCH}_3$	13 _{4,10} -12 _{4,9}	154549.58	62.4	11.8	154550.1	0.062	0.038
E-HCO $^{18}\text{OCH}_3$	13 _{3,11} -12 _{3,10}	156545.98	58.7	12.6	156546.5	0.056	0.039
E-HCO $^{18}\text{OCH}_3$	13 _{7,7} -12 _{7,6}	158334.49	84.2	9.26	158335.0	0.034	0.053
A-HCO $^{18}\text{OCH}_3$	13 _{7,7} -12 _{7,6}	158334.52	84.2	9.26	²
E-HCO $^{18}\text{OCH}_3$	13 _{7,6} -12 _{7,5}	158335.25	84.2	9.26	²
A-HC $^{18}\text{OOCH}_3$	14 _{10,5} -13 _{10,4}	164877.29	124.8	6.86	164877.6	0.058	0.018
A-HC $^{18}\text{OOCH}_3$	14 _{10,4} -13 _{10,3}	164877.29	124.8	6.86	²
A-HCO $^{18}\text{OCH}_3$	13 _{3,10} -12 _{3,9}	166681.88	60.5	12.4	166819.5 ¹	0.070	0.042
E-HC $^{18}\text{OOCH}_3$	16 _{0,16} -15 _{0,15}	167776.18	72.9	15.9	167778.5 ¹	0.10	0.066
A-HC $^{18}\text{OOCH}_3$	16 _{0,16} -15 _{0,15}	167777.40	70.0	15.9	²
E-HCO $^{18}\text{OCH}_3$	14 _{6,8} -13 _{6,7}	171239.76	84.3	11.4	171240.1	0.021	0.029
E-HCO $^{18}\text{OCH}_3$	16 _{1,16} -15 _{1,15}	171768.46	74.8	15.9	171769.5	0.10	0.067
A-HCO $^{18}\text{OCH}_3$	16 _{1,16} -15 _{1,15}	171769.77	71.7	15.9	²
E-HCO $^{18}\text{OCH}_3$	14 _{5,9} -13 _{5,8}	172580.99	77.5	12.2	172580.5	0.13	0.034
A-HCO $^{18}\text{OCH}_3$	14 _{5,9} -13 _{5,8}	172605.81	77.5	12.2	172606.5	0.14	0.034

Table 7. continued.

Species	Transition J_{K_a,K_c}	Rest freq. (MHz)	E_u (K)	S_{ij}	Observed freq. (MHz)	Observed T_{MB} (K)	Modeled T_{MB} (K)
E-HC $^{18}\text{OOCCH}_3$	19 _{1,19} -18 _{1,18}	198318.71	101.5	18.9	198321.1	0.10	0.080
A-HC $^{18}\text{OOCCH}_3$	19 _{1,19} -18 _{1,18}	198319.77	97.1	18.9	2
E-HC $^{18}\text{OOCCH}_3$	19 _{0,19} -18 _{0,18}	198321.96	101.5	18.9	2	0.082	...
A-HC $^{18}\text{OOCCH}_3$	19 _{0,19} -18 _{0,18}	198323.01	97.1	18.9	2
E-HC $^{18}\text{OOCCH}_3$	17 _{2,15} -16 _{2,14}	198878.18	91.5	16.4	198877.3 ¹	0.069	0.046
A-HC $^{18}\text{OOCCH}_3$	17 _{2,15} -16 _{2,14}	198886.46	91.5	16.4	198888.5 ⁵	0.060	0.046
A-HC $^{18}\text{OOCCH}_3$	17 _{6,11} -16 _{6,10}	202607.55	110.5	14.9	202608.1 ⁶	0.076	0.031
E-HCO $^{18}\text{OCH}_3$	19 _{1,19} -18 _{1,18}	203058.14	104.1	18.9	203059.4	0.16	0.11
A-HCO $^{18}\text{OCH}_3$	19 _{1,19} -18 _{1,18}	203059.27	99.5	18.9	2
E-HCO $^{18}\text{OCH}_3$	19 _{0,19} -18 _{0,18}	203060.03	104.1	18.9	2
A-HCO $^{18}\text{OCH}_3$	19 _{0,19} -18 _{0,18}	203061.15	99.5	18.9	2
E-HC $^{18}\text{OOCCH}_3$	20 _{1,20} -19 _{1,19}	208502.31	112.0	19.9	7	...	0.11
A-HC $^{18}\text{OOCCH}_3$	20 _{1,20} -19 _{1,19}	208503.31	107.1	19.9	2
E-HC $^{18}\text{OOCCH}_3$	20 _{0,20} -19 _{0,19}	208504.12	112.0	19.9	2
A-HC $^{18}\text{OOCCH}_3$	20 _{0,20} -19 _{0,19}	208505.12	107.1	19.9	2
A-HC $^{18}\text{OOCCH}_3$	18 _{1,18} -17 _{1,17}	212218.60	175.8	11.3	212219.8	0.071	0.025
A-HC $^{18}\text{OOCCH}_3$	18 _{1,17} -17 _{1,16}	212218.60	175.8	11.3	2
E-HCO $^{18}\text{OCH}_3$	20 _{1,20} -19 _{1,19}	213485.36	114.8	19.9	1	...	0.16
E-HCO $^{18}\text{OCH}_3$	20 _{0,20} -19 _{0,19}	213486.38	114.8	19.9	2
A-HCO $^{18}\text{OCH}_3$	20 _{1,20} -19 _{1,19}	213486.42	109.7	19.9	2
A-HCO $^{18}\text{OCH}_3$	20 _{0,20} -19 _{0,19}	213487.44	109.7	19.9	2
E-HC $^{18}\text{OOCCH}_3$	18 _{7,11} -17 _{7,10}	213740.59	129.0	15.2	213741.1	0.045	0.052
A-HC $^{18}\text{OOCCH}_3$	18 _{7,12} -17 _{7,11}	213741.50	129.0	15.3	2
E-HC $^{18}\text{OOCCH}_3$	18 _{6,13} -17 _{6,12}	214582.20	120.8	15.9	214583.6 ¹	0.15	0.065
A-HC $^{18}\text{OOCCH}_3$	18 _{6,13} -17 _{6,12}	214582.20	120.7	16.0	2
E-HC $^{18}\text{OOCCH}_3$	21 _{1,21} -20 _{1,20}	218684.67	122.9	20.9	8	...	0.16
A-HC $^{18}\text{OOCCH}_3$	21 _{1,21} -20 _{1,20}	218685.61	117.6	20.9	2
E-HC $^{18}\text{OOCCH}_3$	21 _{0,21} -20 _{0,20}	218685.68	122.9	20.9	2
A-HC $^{18}\text{OOCCH}_3$	21 _{0,21} -20 _{0,20}	218686.61	117.6	20.9	2
E-HCO $^{18}\text{OCH}_3$	21 _{1,21} -20 _{1,20}	223911.47	126.0	20.9	9	...	0.18
E-HCO $^{18}\text{OCH}_3$	21 _{0,21} -20 _{0,20}	223912.01	126.0	20.9	2
A-HCO $^{18}\text{OCH}_3$	21 _{1,21} -20 _{1,20}	223912.48	120.5	20.9	2
A-HCO $^{18}\text{OCH}_3$	21 _{0,21} -20 _{0,20}	223913.02	120.5	20.9	2
A-HC $^{18}\text{OOCCH}_3$	19 _{8,12} -18 _{8,11}	225191.38	149.5	15.7	225194.9	0.15	0.028
E-HC $^{18}\text{OOCCH}_3$	19 _{8,12} -18 _{8,11}	225194.04	149.5	15.7	2	...	0.048
A-HC $^{18}\text{OOCCH}_3$	19 _{8,11} -18 _{8,10}	225194.84	149.5	15.7	2
A-HC $^{18}\text{OOCCH}_3$	21 _{2,20} -20 _{2,19}	228083.06	126.5	20.6	228083.6 ¹⁰	0.16	0.043
E-HC $^{18}\text{OOCCH}_3$	22 _{1,22} -21 _{1,21}	228865.84	134.4	21.9	11	...	0.18
E-HC $^{18}\text{OOCCH}_3$	22 _{0,22} -21 _{0,21}	228866.40	134.4	21.9	2
A-HC $^{18}\text{OOCCH}_3$	22 _{1,22} -21 _{1,21}	228866.72	128.6	21.9	2
A-HC $^{18}\text{OOCCH}_3$	22 _{0,22} -21 _{0,21}	228867.27	128.6	21.9	2
E-HCO $^{18}\text{OCH}_3$	18 _{4,14} -17 _{4,13}	231398.96	112.9	17.2	231402.3 ¹²	0.11	0.045
E-HC $^{18}\text{OOCCH}_3$	19 _{5,14} -18 _{5,13}	232102.19	125.3	17.7	232103.0	0.11	0.038
E-HCO $^{18}\text{OCH}_3$	20 _{3,18} -19 _{3,17}	232673.55	126.1	19.3	232673.9 ¹³	0.14	0.037
E-HCO $^{18}\text{OCH}_3$	19 _{6,14} -18 _{6,13}	234214.48	134.5	17.1	234215.5	0.049	0.035
A-HCO $^{18}\text{OCH}_3$	19 _{6,14} -18 _{6,13}	234226.53	134.4	17.1	234227.5	0.052	0.034
E-HCO $^{18}\text{OCH}_3$	22 _{1,22} -21 _{1,21}	234336.48	137.7	21.9	234337.6 ¹	1.00	0.19
E-HCO $^{18}\text{OCH}_3$	22 _{0,22} -21 _{0,21}	234336.77	137.7	21.9	2
A-HCO $^{18}\text{OCH}_3$	22 _{1,22} -21 _{1,21}	234337.43	131.7	21.9	2
A-HCO $^{18}\text{OCH}_3$	22 _{0,22} -21 _{0,21}	234337.72	131.7	21.9	2
E-HC $^{18}\text{OOCCH}_3$	22 _{1,21} -21 _{1,20}	238283.08	140.9	21.6	238281.4 ¹⁴	0.14	0.043
A-HC $^{18}\text{OOCCH}_3$	22 _{1,21} -21 _{1,20}	238288.08	137.9	21.6	238290.1 ¹⁵	0.11	0.042
E-HC $^{18}\text{OOCCH}_3$	20 _{5,16} -19 _{5,15}	238745.64	136.1	18.8	238746.7	0.035	0.037
E-HC $^{18}\text{OOCCH}_3$	23 _{1,23} -22 _{1,22}	239045.82	146.3	22.9	239047.3	0.18	0.19
E-HC $^{18}\text{OOCCH}_3$	23 _{0,23} -22 _{0,22}	239046.13	146.3	22.9	2
A-HC $^{18}\text{OOCCH}_3$	23 _{1,23} -22 _{1,22}	239046.64	140.1	22.9	2
A-HC $^{18}\text{OOCCH}_3$	23 _{0,23} -22 _{0,22}	239046.95	140.1	22.9	2
E-HCO $^{18}\text{OCH}_3$	23 _{1,23} -22 _{1,22}	244760.37	149.9	22.9	244761.5	0.10	0.19
E-HCO $^{18}\text{OCH}_3$	23 _{0,23} -22 _{0,22}	244760.52	149.9	22.9	2
A-HCO $^{18}\text{OCH}_3$	23 _{1,23} -22 _{1,22}	244761.26	143.4	22.9	2
A-HCO $^{18}\text{OCH}_3$	23 _{0,23} -22 _{0,22}	244761.42	143.4	22.9	2
E-HC $^{18}\text{OOCCH}_3$	24 _{1,24} -23 _{1,23}	249224.59	158.7	23.9	16	...	0.19
E-HC $^{18}\text{OOCCH}_3$	24 _{0,24} -23 _{0,23}	249224.76	158.7	23.9	2

Table 7. continued.

Species	Transition J_{K_a,K_c}	Rest freq. (MHz)	E_u (K)	S_{ij}	Observed freq. (MHz)	Observed T_{MB} (K)	Modeled T_{MB} (K)
A-HC ¹⁸ OOC ₃	24 _{1,24} -23 _{1,23}	249225.35	152.1	23.9	2
A-HC ¹⁸ OOC ₃	24 _{0,24} -23 _{0,23}	249225.52	152.1	23.9	2
E-HCO ¹⁸ OCH ₃	24 _{1,24} -23 _{1,23}	255183.10	162.6	23.9	17	...	0.19
E-HCO ¹⁸ OCH ₃	24 _{0,24} -23 _{0,23}	255183.18	162.6	23.9	2
A-HCO ¹⁸ OCH ₃	24 _{1,24} -23 _{1,23}	255183.93	155.7	23.9	2
A-HCO ¹⁸ OCH ₃	24 _{0,24} -23 _{0,23}	255184.02	155.7	23.9	2
E-HC ¹⁸ OOC ₃	24 _{2,23} -23 _{2,22}	258607.91	166.3	23.6	258607.4	0.094	0.042
A-HC ¹⁸ OOC ₃	24 _{2,23} -23 _{2,22}	258612.84	162.3	23.6	258612.5 ¹⁸	0.13	0.043
E-HCO ¹⁸ OCH ₃	21 _{7,15} -20 _{7,14}	258616.51	166.6	18.5	258617.6	0.094	0.078
E-HC ¹⁸ OOC ₃	24 _{1,23} -23 _{1,22}	258616.65	166.3	23.6	2
A-HCO ¹⁸ OCH ₃	21 _{7,15} -20 _{7,14}	258619.88	166.6	18.7	258623.5	0.13	0.061
A-HC ¹⁸ OOC ₃	24 _{1,23} -23 _{1,22}	258621.56	162.2	23.6	2
E-HC ¹⁸ OOC ₃	25 _{1,25} -24 _{1,24}	259402.10	171.5	24.9	259403.9	0.16	0.19
E-HC ¹⁸ OOC ₃	25 _{0,25} -24 _{0,24}	259402.19	171.5	24.9	2
A-HC ¹⁸ OOC ₃	25 _{1,25} -24 _{1,24}	259402.80	164.5	24.9	2
A-HC ¹⁸ OOC ₃	25 _{0,25} -24 _{0,24}	259402.90	164.5	24.9	2
E-HCO ¹⁸ OCH ₃	22 _{4,19} -21 _{4,18}	262823.90	158.7	21.1	262825.5	0.064	0.039
E-HCO ¹⁸ OCH ₃	25 _{1,25} -24 _{1,24}	265604.62	175.8	24.9	265605.5	0.13	0.19
E-HCO ¹⁸ OCH ₃	25 _{0,25} -24 _{0,24}	265604.66	175.8	24.9	2
A-HCO ¹⁸ OCH ₃	25 _{1,25} -24 _{1,24}	265605.40	168.4	24.9	2
A-HCO ¹⁸ OCH ₃	25 _{0,25} -24 _{0,24}	265605.44	168.4	24.9	2
E-HCO ¹⁸ OCH ₃	21 _{4,17} -20 _{4,16}	267813.37	149.8	20.2	267815.4	0.054	0.042
E-HC ¹⁸ OOC ₃	24 _{2,22} -23 _{2,21}	268260.21	172.1	23.3	268261.2	0.14	0.041
E-HC ¹⁸ OOC ₃	26 _{1,26} -25 _{1,25}	269578.30	184.9	25.9	¹⁹	...	0.21
E-HC ¹⁸ OOC ₃	26 _{0,26} -25 _{0,25}	269578.35	184.9	25.9	2
A-HC ¹⁸ OOC ₃	26 _{1,26} -25 _{1,25}	269578.95	177.4	25.9	2
A-HC ¹⁸ OOC ₃	26 _{0,26} -25 _{0,25}	269579.00	177.4	25.9	2
E-HCO ¹⁸ OCH ₃	26 _{1,26} -25 _{1,25}	276024.88	189.4	25.9	276025.5	0.31	0.19
E-HCO ¹⁸ OCH ₃	26 _{0,26} -25 _{0,25}	276024.90	189.4	25.9	2
A-HCO ¹⁸ OCH ₃	26 _{1,26} -25 _{1,25}	276025.60	181.7	25.9	2
A-HCO ¹⁸ OCH ₃	26 _{0,26} -25 _{0,25}	276025.62	181.7	25.9	2
E-HC ¹⁸ OOC ₃	27 _{1,27} -26 _{1,26}	279753.14	198.7	26.9	279754.5 ²⁰	0.37	0.18
E-HC ¹⁸ OOC ₃	27 _{0,27} -26 _{0,26}	279753.16	198.7	26.9	2
A-HC ¹⁸ OOC ₃	27 _{1,27} -26 _{1,26}	279753.73	190.9	26.9	2
A-HC ¹⁸ OOC ₃	27 _{0,27} -26 _{0,26}	279753.76	190.9	26.9	2

Notes. Emission lines of ¹⁸O-HCOOCH₃ present in the frequency range of the 30-m Orion KL survey. Column 1 gives the species; Col. 2: line transition; Col. 3: calculated rest frequencies; Col. 4: energy of the upper level; Col. 5: line strength; Col. 6: observed frequencies; Col. 7: peak line temperature; Col. 8: main-beam temperature obtained with the model. ⁽¹⁾ Blended with the U-line. ⁽²⁾ Blended of several K-components. ⁽³⁾ Blended with H¹⁸OD. ⁽⁴⁾ Blended with SO¹⁷O. ⁽⁵⁾ Blended with SO¹⁷O and CH₃OCH₃. ⁽⁶⁾ Blended with HC₃N $\nu_7 = 4$. ⁽⁷⁾ Blended with CH₃CH₂CN b type. ⁽⁸⁾ Blended with HC₃N $\nu_6 = 1^-$. ⁽⁹⁾ Blended with HCOOH. ⁽¹⁰⁾ Blended with a wing of a CH₂CHCN line. ⁽¹¹⁾ Blended with HC₃N $\nu_7 = 2$. ⁽¹²⁾ Blended with HCOOCH₃. ⁽¹³⁾ Blended with ¹³CH₃CCH. ⁽¹⁴⁾ Blended with H₂C³³S. ⁽¹⁵⁾ Blended with a wing of a CH₂CHCN $\nu_{11} = 1$ line. ⁽¹⁶⁾ Blended with CH₃CH₂CN b type and CH₂CHCN $\nu_{15} = 1$. ⁽¹⁷⁾ Blended with ¹³CH₃OH. ⁽¹⁸⁾ Blended with CH₃¹³CH₂CN and DCOOCH₃. ⁽¹⁹⁾ Blended with CH₃CH₂CN a type. ⁽²⁰⁾ Blended with CH₃CH₂¹³CN.

and LVG codes in that line survey, see Tercero et al. 2010, 2011) as representative parameters for the different cloud components. Our modelling technique also took into account the size of each component and its offset position with respect to IRc2. Corrections for beam dilution were applied to each line depending on their frequency. The only free parameter is therefore the column density. Taking into account the compact nature of most cloud components, the contribution from the error beam is negligible except for the extended ridge, which has a small contribution for all observed lines. In addition to line opacity effects, we discussed other sources of uncertainty in Tercero et al. (2010). Owing to the weakness of the observed lines of ¹⁸O-methyl formate, we estimated the uncertainty to be 50% for the column density results.

We assumed a source size of 15'', 10'', 10'', and 120'' of diameter with uniform brightness temperature and optical depth

over this size, placed 7'', 7'', 2'', and 0'' from the pointed position for the compact ridge, the “hot” compact ridge, the hot core, and the extended ridge, respectively. The column densities we show are for each state (A, E) of both ¹⁸O-methyl formate isotopologues. Column density results were derived for each component obtaining $(4 \pm 2) \times 10^{13}$, $(1.5 \pm 0.7) \times 10^{13}$, $(2 \pm 1) \times 10^{13}$, and $(2 \pm 1) \times 10^{13}$ cm⁻² for the “hot” compact ridge, compact ridge, hot core, and extended ridge, respectively. The total column density derived for each isotologue is $\approx (1.0 \pm 0.5) \times 10^{14}$ cm⁻². Hence, no isotopic fractionation is found for the two isotopologues ¹⁸O of methyl formate. Because methyl formate is mainly emitted from the compact ridge components, we assumed a radial velocity of 7.5 km s⁻¹ for the observed frequencies given in Table 7 and Figs. 1 and 2.

Figures 1 and 2 and Table 7 show the comparisons between model and observations. The differences between the intensity of

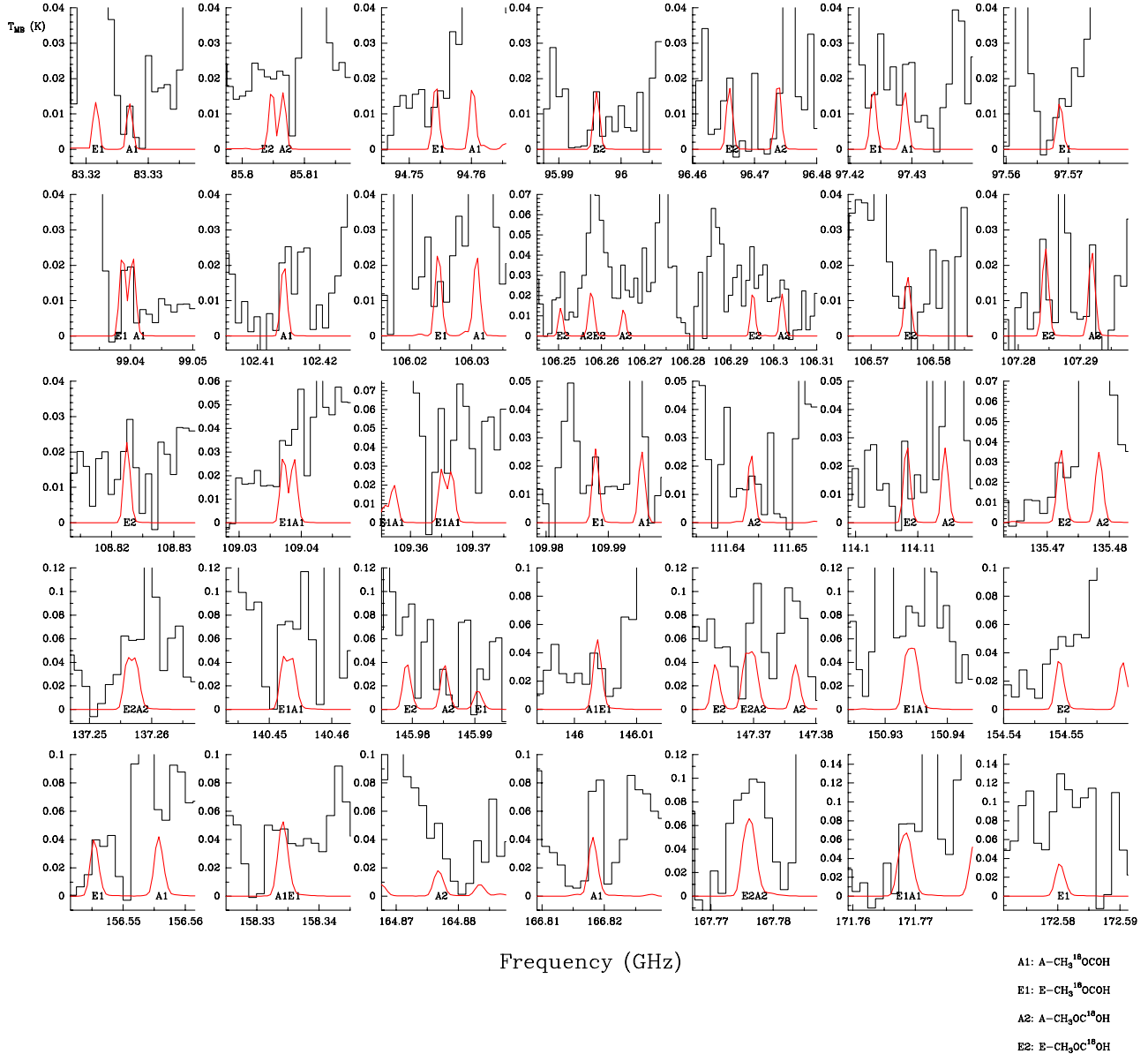


Fig. 1. Observed lines from Orion KL (histogram spectra) and model (thin curves) of ^{18}O methyl formate in the 3 and 2 mm domains. The codes A1, E1, A2, and E2 correspond to A-CH₃¹⁸OCOH, E-CH₃¹⁸OCOH, A-CH₃OC¹⁸OH, and E-CH₃OC¹⁸OH, respectively. A v_{LSR} of 7.5 km s⁻¹ is assumed.

the model and the peak intensity of the observed lines are mostly caused by the contribution of many other molecular species (the frequent overlap with other lines makes it difficult to provide a good baseline for the weak lines of ^{18}O -methyl formate). Nevertheless, the observed line intensity of isolated detected lines of ^{18}O -methyl formate agrees with the model predictions.

The complete modelling of methyl formate including the main isotopologue, the torsionally excited states, and the detected isotopologues, will be published elsewhere (López et al., in prep.).

Together with the results obtained in our previous papers concerning methyl formate (Carvajal et al. 2009; Margulès et al. 2010), we can derive the following ratios for each ^{18}O and ^{13}C methyl formate isotopologues (note that we

have obtained the same column density for both isotopologues of each ^{13}C and ^{18}O substitutions of methyl formate): $^{13}\text{C}-\text{HCOOCH}_3/\text{H}^{18}\text{O}-\text{HCOOCH}_3 \approx 13$ and $\text{HCOOCH}_3/\text{H}^{18}\text{O}-\text{HCOOCH}_3 \approx 218$ both for the compact ridge component (sum of outer and inner compact ridge). Tercero et al. (2010, 2011) derived $N(\text{O}^{13}\text{CS})/N(\text{O}^{18}\text{CS}) = 8 \pm 5$, $N(\text{O}^{16}\text{CS})/N(\text{O}^{18}\text{CS}) = 250 \pm 135$, and $N(\text{Si}^{16}\text{O})/N(\text{Si}^{18}\text{O}) \gtrsim 239$, all results agree with the ratios obtained above.

With the emission lines of the ^{18}O methyl formate isotopologues, we conclude the detection of all methyl formate isotopologues that we were able to observe in the line survey of Orion KL of Tercero and coworkers. The 80 lines found correspond to the first detection of $^{18}\text{O}-\text{HCOOCH}_3$, together with those of the two ^{13}C isotopologues of methyl formate, and those

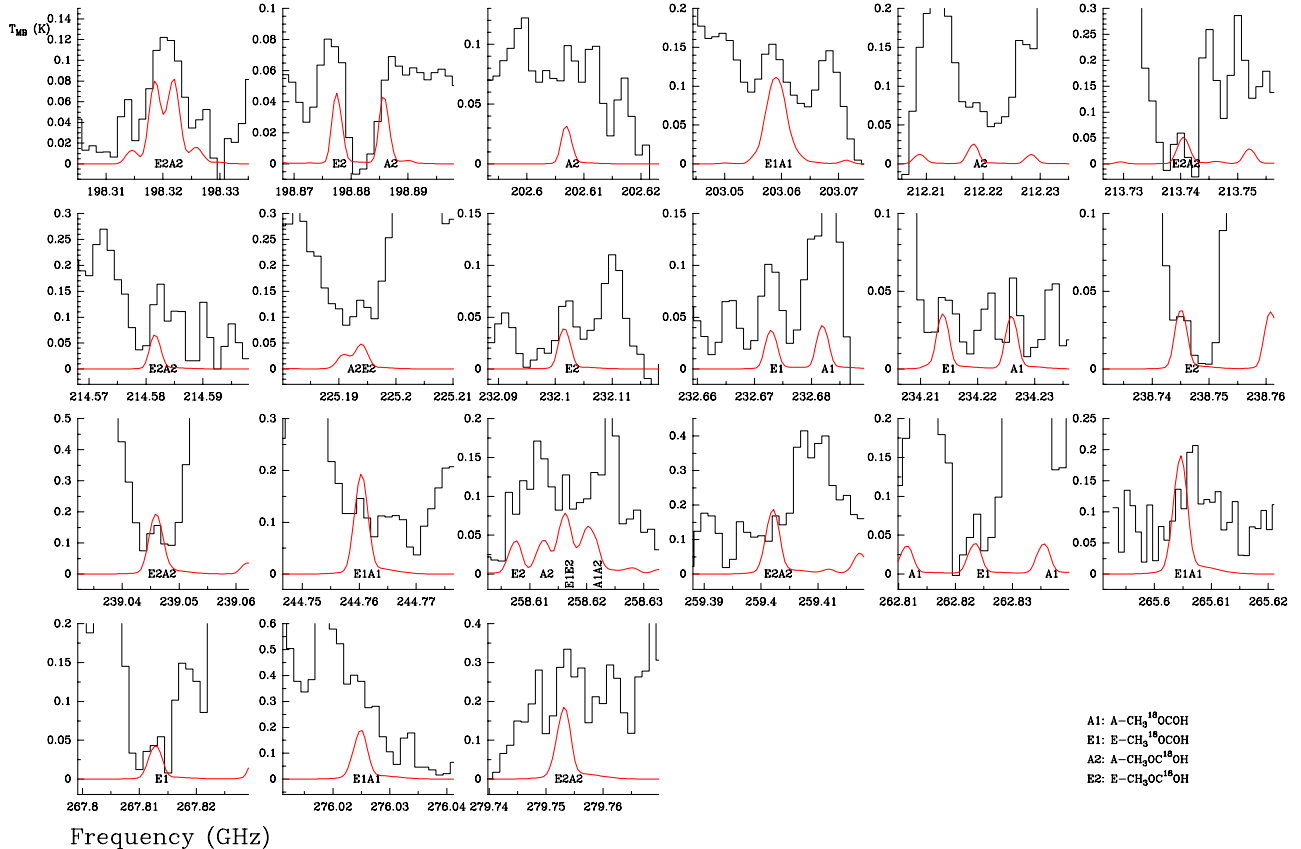


Fig. 2. Observed lines from Orion KL (histogram spectra) and model (thin curves) of ^{18}O methyl formate in the 1.3 mm domain. The codes A1, E1, A2, and E2 correspond to $\text{A}-\text{CH}_3^{18}\text{OCOH}$, $\text{E}-\text{CH}_3^{18}\text{OCOH}$, $\text{A}-\text{CH}_3\text{OC}^{18}\text{OH}$, and $\text{E}-\text{CH}_3\text{OC}^{18}\text{OH}$, respectively. A v_{LSR} of 7.5 km s^{-1} is assumed.

assigned to the tentative detection of DCOOCH_3 (Carvajal et al. 2009; Margulès et al. 2010) contribute with more than 800 lines in the 80-280 GHz domain covered by the Orion line survey of Tercero et al. (2010).

7. Conclusion

We measured and analysed the two ^{18}O isotopic species of methyl formate up to 660 GHz. We treated the internal rotation motion using the rho-axis-method and the BELGI code. We included 4430 and 3258 lines in the fits of 30 and 29 parameters for the ground torsional state for the $\text{HCO}^{18}\text{OCH}_3$ and $\text{HC}^{18}\text{OOCH}_3$ species, respectively.

Following these studies, accurate predictions of line positions and intensities were performed. The line survey of Orion KL with the IRAM 30-m telescope permitted the detection of 80 spectral features that correspond to the first detection of the $\text{HCO}^{18}\text{OCH}_3$ and $\text{HC}^{18}\text{OOCH}_3$ species.

Acknowledgements. M.C. acknowledges the financial support provided by the Andalusian Government (Spain) project number P07-FQM-03014. He also thanks Université Paris 12 for inviting him. J.C. and B.T. thank Spanish MICINN for support under grants AYA2006-14786, AYA2009-07304 and the CONSOLIDER program “ASTROMOL” CSD2009-00038. This work was supported by the Centre National d’Études Spatiales (CNES) and the Action sur Projets de l’INSU, “Physique et Chimie du Milieu Interstellaire”. This work was also done under the ANR-08-BLAN-0054.

References

- Blake, G. A., Sutton, E. C., Masson, C. R., & Philips, T. H. 1987, ApJ, 315, 621
- Blake, G. A., Mundy, L. G., Carlstrom, J. E., et al. 1996, ApJ, 472, L49
- Brown, R. D., Crofts, J. G., Gardner, F. F., et al. 1975, ApJ, 197, L29
- Churchwell, E., & Winnewisser, G. 1975, A&A, 45, 229
- Carvajal, M., Willaert, F., Demaison, J., & Kleiner, I. 2007, J. Mol. Spectrosc., 246, 158
- Carvajal, M., Margulès, L., Tercero, B., et al. 2009, A&A, 500, 1109
- Carvajal, M., Kleiner, I., & Demaison. J. 2010, ApJS, 190, 315
- Cernicharo, 1985. Internal IRAM report (Granada: IRAM)
- Chao, J., Hall, K. R., Marsh, K. N., & Wilhoit, R. C. 1986, J. Phys. Chem. Ref. Data, 15, 1369
- Comito, C., Schilke, P., Phillips, T. G., et al. 2005, ApJS, 156, 127
- Curl, R.F. 1959, J. Chem. Phys., 30, 1529
- Demaison, J., Margulès, L., Kleiner, I., & Császár, A. G. 2010, J. Mol. Spectrosc., 259, 70
- Demyk, K., Mäder, H., Tercero, B., et al. 2007, A&A, 466, 255
- Demyk, K., Włodarczak, G., & Carvajal, M. 2008, A&A, 489, 589
- Guélin, M., & Thaddeus, P. 1979, ApJ, 227, L139
- Herbst, E., Messer, J. K., De Lucia, F. C. & Helmlinger, P. 1984, J. Mol. Spectrosc., 108, 42
- Hougen, J. T., Kleiner, I., & Godefroid, M. 1994, J. Mol. Spectrosc., 163, 559
- Ilyushin, V., Alekseev, E. A., Dyubko, S. F., & Kleiner, I. 2003, J. Mol. Spectrosc., 220, 170
- Ilyushin, V., Kleiner, I., & Lovas, F. J. 2008, J. Phys. Chem. Ref. Data, 37, 97
- Ilyushin, V. V., Kryvda, A., & Alekseev, E. 2009, J. Mol. Spectrosc., 255, 32
- Johansson, L. E. B., Andersson, C., Elldér, J., et al. 1984, A&A, 130, 227
- Kassi, S., Petitprez, D., & Włodarczak, G. 2000, J. Mol. Struct., 517, 375
- Kirtman, B. 1962, J. Chem. Phys., 37, 2516
- Kleiner, I. 2010, J. Mol. Spectrosc., 260, 1
- Kobayashi, K., Ogata, K., Tsunekawa, S. & Takano, S. 2007, ApJ, 657, L17

- Langer, W. D., & Penzias, A. A. 1990, ApJ, 357, 477
 Lees, R. M., & Baker, J. G. 1968, J. Chem. Phys., 48, 5299
 Lin, C. C., & Swalen, J. D. 1959, Rev. Mod. Phys., 31, 841
 Lovas, F. J. 2004, NIST Recommended rest frequencies for observed interstellar molecular microwave transitions (Gaithersburg, NIST) <http://physics.nist.gov/cgi-bin/micro/table5/start.pl>
 Margulès, L., Coudert, L. H., Møllendal, H., et al. 2009, J. Mol. Spectrosc., 254, 55
 Margulès, L., Motiyenko, R., Demyk, K., et al. 2009, A&A, 493, 565
 Margulès, L., Huet, T. R., Demaison, J., et al. 2010, ApJ, 714, 1120
 Møllendal, H., Leonov, A., & de Meijere, A. 2005, J. Phys. Chem. A, 109, 6344
 Møllendal, H., Cole, G. C., & Guillemin, J.-C. 2006, J. Phys. Chem. A, 110, 921
 Morino, I., Odashima, H., Matsushima, F., Tsunekawa, S., & Tagaki, K. 1995, ApJ, 442, 907
 Morris, M., Palmer, P., & Zuckerman, B. 1980, ApJ, 237, 1
 Motiyenko, R. A., Margulès, L., Alekseev, E. A., Guillemin, J.-C., & Demaison, J. 2010, J. Mol. Spectrosc., 264, 94.
 Neufeld, D. A., Ashby, M. L. N., Bergin, E. A., et al. 2000, ApJ, 539, L111
 Oesterling, L. C., Albert, S., De Lucia, F. C., Sastry, K. V. L. N., & Herbst, E. 1999, ApJ, 521, 255
 Pardo, J. R., Cernicharo, J., & Serabyn, E. 2001, IEEE Trans. Antennas and Propagation, 49, 12
 Remijan, A., Shiao, Y.-S., Friedel, D. N., Meier, D. S., & Snyder, L.E. 2004, ApJ, 617, 384
 Sakai, N., Sakai, T., & Yamamoto, S. 2007, ApJ, 660, 363
 Tercero, B., Pardo, J. R., Cernicharo, & Goicoechea, J. R. 2010, A&A, 517, A96
 Tercero, B., Vincent, L., Cernicharo, J., Viti, S., & Marcelino, N. 2011, A&A, 528, A26
 Willaert, F., Møllendal, H., Alekseev, E., Carvajal, M., Kleiner, I., & Demaison, J. 2006, J. Mol. Struct., 795, 4

Appendix A: Part of the supplementary tables available at the CDS

Table A.1. Assignments, observed frequencies, calculated frequencies from the RAM fit, line strengths, and lower energy levels for ^{18}O -methyl formate ($\text{HCO}^{18}\text{OCH}_3$) microwave transitions from $v_t = 0$ torsional state included in the fit with parameters of Table 4

num ^a	v_t'	Upper State ^a				Lower State ^a				Obs. Freq. (Unc.)	Calc. Freq (Unc.)	$S(i- > f)$	Lower energy	
		J'	K_a'	K_c'	p'	v_t''	J''	K_a''	K_c''					
43674	0	52	13	40	0	51	13	39	39	647718.1067(0.050)	647718.144(0.010)	132.312	617.5730	
936	0	52	13	40	+	0	51	13	39	+	647719.279(0.050)	647719.183(0.011)	132.309	617.5762
11796	0	58	14	44	+	0	58	12	47	-		647887.350(0.119)	0.930	767.3337
63193	0	58	-14	44	0	58	12	47			647950.687(0.116)	0.931	767.3301	
914	0	52	12	41	-	0	51	12	40	-	647997.802(0.050)	647997.830(0.010)	133.472	607.9115
43651	0	52	12	41	0	51	12	40			647998.872(0.050)	647998.826(0.011)	133.473	607.9065
48149	0	60	3	58	0	59	-2	57			648062.209(0.011)	4.994	660.9676	
49446	0	60	-2	58	0	59	3	57			648062.209(0.011)	4.994	660.9676	
43413	0	60	3	58	0	59	3	57			648062.263(0.050)	648062.209(0.011)	181.830	660.9676
42838	0	60	-2	58	0	59	-2	57			648062.263(0.050)	648062.209(0.011)	181.830	660.9676
683	0	60	3	58	+	0	59	3	57	+	648068.999(0.050)	648068.989(0.011)	181.809	660.9701
91	0	60	2	58	+	0	59	2	57	+	648068.999(0.050)	648068.989(0.011)	181.809	660.9701

Table A.2. Assignments, observed frequencies, calculated frequencies from the RAM fit, line strengths, and lower energy levels for ^{18}O -methyl formate ($\text{HC}^{18}\text{OOC}_3$) microwave transitions from $v_t = 0$ torsional state included in the fit with parameters of Table 5

num ^a	v_t'	Upper state ^a				Lower state ^a				Obs. Freq. (Unc.)	Calc. Freq (Unc.)	$S(i- > f)$	Lower Energy	
		J'	K_a'	K_c'	p'	v_t''	J''	K_a''	K_c''					
81764	0	22	15	7	0	21	14	7		653662.114(0.050)	653662.108(0.005)	7.304	179.8147	
81778	0	22	15	8	0	21	14	8		653694.992(0.030)	653695.051(0.006)	7.303	179.8066	
71865	0	22	15	8	+	0	21	14	8	-		653703.123(0.004)	6.538	179.8150
71819	0	22	15	7	-	0	21	14	7	+		653703.123(0.004)	6.538	179.8150
1348	0	22	15	8	+	0	21	14	7	+	653703.117(0.030)	653703.123(0.004)	0.763	179.8150
1409	0	22	15	7	-	0	21	14	8	-	653703.117(0.030)	653703.123(0.004)	0.763	179.8150
80449	0	63	-1	62	0	62	-1	61			653877.060(0.050)	653877.075(0.013)	196.986	691.4649
81028	0	63	2	62	0	62	2	61			653877.060(0.050)	653877.075(0.013)	196.986	691.4649
84862	0	63	-1	62	0	62	2	61			653877.075(0.013)	1.888	691.4649	
83643	0	63	2	62	0	62	-1	61			653877.075(0.013)	1.888	691.4649	
64	0	63	1	62	-	0	62	1	61	-	653881.917(0.030)	653881.876(0.013)	67.659	691.4620
628	0	63	2	62	-	0	62	2	61	-	653881.917(0.030)	653881.876(0.013)	67.659	691.4620

Notes. ^a Upper and lower state quantum numbers are indicated by ' and " respectively. Torsion-rotation levels of A species have a “parity” label; levels of E species have a signed Ka value (Herbst et al. 1984). Note that for certain degenerate transitions the sum of line strengths of the degenerate transitions for a given cluster is preserved. ^(b) The first column is a line number, allowing to sort the lines by J and K sub-branches if needed. ^(c) Observed $v_t = 0$ microwave transitions in MHz, with estimated uncertainties in parentheses (in MHz). The data come from Lille-FTMW: 1–19 GHz, Lille-SMM: 150–660 GHz, Oslo: 7–80 GHz. ^(d) Calculated line frequency in MHz with calculated uncertainty in MHz. ^(e) Calculated line strengths in D**2 (for details of the calculation procedure, see text). ^(f) Lower state energy (cm^{-1}) referred to the $J = \text{Ka} = 0$ A-species energy level taken as the zero of the energy (zero-point torsional energy is 66.29250 cm^{-1} for $\text{HC}^{18}\text{OOC}_3$ and 66.27348 cm^{-1} for $\text{HCO}^{18}\text{OCH}_3$).

THz spectroscopy and first ISM detection of excited torsional states of ^{13}C -methyl formate[★]

I. Haykal¹, M. Carvajal², B. Tercero³, I. Kleiner⁴, A. López³, J. Cernicharo³, R. A. Motiyenko¹, T. R. Huet¹, J. C. Guillemin⁵, and L. Margulès¹

¹ Laboratoire de Physique des Lasers, Atomes, et Molécules, UMR CNRS 8523, Université Lille I,
59655 Villeneuve d'Ascq Cedex, France
e-mail: laurent.margulès@univ-lille1.fr

² Departamento de Física Aplicada Unidad Asociada CSIC, Facultad de Ciencias Experimentales, Universidad de Huelva,
21071 Huelva, Spain

³ Centro de Astrobiología (CSIC-INTA), Department of Astrophysics. Ctra de Ajalvir, 28850 Torrejón de Ardoz, Madrid, Spain

⁴ Laboratoire Interuniversitaire des Systèmes Atmosphériques, UMR CNRS/IPSL 7583, Université Paris 7 et Université Paris Est,
61 Av. Charles de Gaulle, 94010 Créteil Cedex, France

⁵ Institut des Sciences Chimiques de Rennes, École Nationale Supérieure de Chimie de Rennes, CNRS, UMR 6226, Allée de Beaulieu,
CS 50837, 35708 Rennes Cedex 7, France

Received 29 October 2013 / Accepted 24 April 2014

ABSTRACT

Context. An astronomical survey of interstellar molecular clouds needs a previous analysis of the spectra in the microwave and sub-mm energy range of organic molecules to be able to identify them. We obtained very accurate spectroscopic constants in a comprehensive laboratory analysis of rotational spectra. These constants can be used to predict the transitions frequencies very precisely that were not measured in the laboratory.

Aims. We present the experimental study and its theoretical analysis for two ^{13}C -methyl formate isotopologues to detect these two isotopologues for the first time in their excited torsional states, which lie at 130 cm^{-1} (200 K) in Orion-KL.

Methods. New spectra of $\text{HCOO}^{13}\text{CH}_3$ ($^{13}\text{C}_2$) methyl formate were recorded with the mm- and submm-wave spectrometer in Lille from 50 to 940 GHz. A global fit for $v_t = 0$ and 1 was accomplished with the BELGI program to reproduce the experimental spectra with greater accuracy.

Results. We analysed 5728 and 2881 new lines for $v_t = 0$ and 1 for $\text{HCOO}^{13}\text{CH}_3$. These new lines were globally fitted with 846 previously published lines for $v_t = 0$. In consequence, 52 parameters of the RAM Hamiltonian were accurately determined and the value of the barrier height ($V_3 = 369.93168(395)\text{ cm}^{-1}$) was improved. We report the detection of the first excited torsional states ($v_t = 1$) in Orion-KL for the $^{13}\text{C}_2$ and $^{13}\text{C}_1$ methyl formate based on the present analysis and previously published data. We provide column densities, isotopic abundances, and vibrational temperatures for these species.

Conclusions. Following this work, accurate prediction can be provided. This permits detecting 135 features of the first excited torsional states of ^{13}C -methyl formate isotopologues in Orion-KL in the 80–280 GHz frequency range, without missing lines.

Key words. line: identification – astronomical databases: miscellaneous – ISM: molecules – submillimeter: ISM – astrochemistry – ISM: individual objects: Orion KL

1. Introduction

Methyl formate is one of the most abundant complex organic molecules in the interstellar medium (ISM). It was identified in different sources since 1975 (Brown et al. 1975; Churchwell et al. 1975); nearly one thousand lines were detected in the ground-torsional state $v_t = 0$. Its abundance is particularly high in Orion-KL: it was detected up to 900 GHz (Comito et al. 2005) far from the maximum of absorption situated around 300 GHz; some lines from the first (Kobayashi et al. 2007), and more recently, lines from the second torsional state were detected (Takano et al. 2012). The abundance is also fairly high in W51e2, where lines from methyl formate in its first torsional states were found (Demyk et al. 2008). Molecules in the ISM can be used to

probe the physical conditions of sources, as illustrated recently by Favre et al. (2011, 2014) using methyl formate to probe the temperature structure and spatial distribution of this species in Orion-KL; depending on the molecular species, the distribution of the molecular gas can be different in this source because of its complexity (which is a result of massive star formation processes) different cloud components coexist there. Organic saturated O-rich molecules such as methyl formate generally trace the compact ridge component (for a description of the different cloud components of Orion-KL see e.g. Blake et al. 1987; Schilke et al. 2001; Persson et al. 2007; Tercero et al. 2010, 2011; Neill et al. 2013).

Around 180 molecules have been detected in the ISM or circumstellar shells, but in high mass-forming regions such as Orion-KL, 30% of the lines remain unidentified (Espluga et al. 2013a; Tercero et al. 2010). Its important to identify all the lines from the most abundant species. These molecules are often called “weeds”, and methyl formate is one of them.

* Full Table A.1 and the IRAM spectra as FITS files are only available at the CDS via anonymous ftp to cdsarc.u-strasbg.fr (130.79.128.5) or via <http://cdsarc.u-strasbg.fr/viz-bin/qcat?J/A+A/568/A58>

Identifying them is necessary in order to discover new species in the ISM without ambiguity. As shown recently by Tercero et al. (2013), the detection of methyl acetate ($\text{CH}_3\text{COOCH}_3$) and the gauche conformer of ethyl formate (g- $\text{CH}_3\text{CH}_2\text{OCOOH}$) was only possible with the assignment of 4400 lines coming from several isotopologues and vibrational levels of different weeds: $\text{CH}_3\text{CH}_2\text{CN}$, CH_2CHCN , HCOOCH_3 , and NH_2CHO .

Most of the times, accurate spectroscopic data in the millimeter and submillimeter-wave domain are not available for the isotopologues and vibrational levels. While the normal species of methyl formate were extensively studied (Ilyushin et al. 2009, and references therein) of only the two commercially available isotopologues $\text{H}^{13}\text{COOCH}_3$ (Maeda et al. 2008a,b) and DCOOCH_3 (Oesterling et al. 1995) were studied in the millimeter-wave region. Therefore we decided to investigate all the mono-isotopic species of methyl formate in the submillimeter-wave domain a few years ago. For each of them, this permits generating a new accurate prediction and allows detecting the ^{13}C species (Willaert et al. 2006; Carvajal et al. 2007, 2009, 2010), DCOOCH_3 (Margulès et al. 2010), ^{18}O species (Tercero et al. 2012) in Orion-KL and recently HCOOCH_2D (Coudert et al. 2013). This confirms the assumption that most of the U-lines come from known molecules. The lines detected for the ^{18}O species gave us the idea that it might also be possible to find lines related to the first excited torsional states that lie at 130 cm^{-1} (200 K) of the most abundant isotopologues ^{13}C .

Our motivations for studying of the first excited torsional state of $\text{HCOO}^{13}\text{CH}_3$ is also linked to a spectroscopic interest. Methyl formate, like other complex molecules, exhibits large-amplitude motion: torsion of the methyl group related to the rest of the molecules. A specific code that takes into account the interaction of the torsion and the overall rotation of the molecule is needed. Most of the codes were developed to treat data in the centimeter not in millimeter-wave domain. Recent efforts from different theoretical groups were recently made to improve the codes to reproduce the experimental accuracies with high quantum numbers that are reached at submillimeter frequencies. As shown for the normal species (Ilyushin et al. 2009) and the $^{13}\text{C}_1$ species (Carvajal et al. 2010), the global treatment of the ground- and first torsional states permits removing the high correlation between torsional parameters. This improves the quality of the fit and finally the accuracy of the predictions for the two states.

These works permit the first detection of the excited torsional state of the two ^{13}C -methyl formate isotopologues. As in Carvajal et al. (2009), we publish the spectroscopic work about $\text{HCOO}^{13}\text{CH}_3$ and the detection of the two ^{13}C isotopologues in Orion together. In the previous paper about $^{13}\text{C}_2$ (Carvajal et al. 2009), our measurements were limited to 660 GHz for the ground-torsional states. To provide an accurate prediction of this state in the ALMA range, we also reinvestigated this state up to 940 GHz.

2. Experiments

2.1. Synthesis of the methyl formate isotopologue $\text{HCOO}^{13}\text{CH}_3$

The details about synthesis and identification by NMR spectroscopy were described in Carvajal et al. (2009).

2.2. Lille – submillimeter spectra

The millimeter- and submillimeter-wave spectra were recorded using the Lille spectrometer that is based on solid-state sources

(Motiyenko et al. 2010; Haykal et al. 2013a). The sample pressure was in the range $20\text{--}30 \times 10^{-6}$ bars. Spectra were recorded at room temperature ($T = 294 \text{ K}$) in the 150–210, 225–315, 400–500, 500–630, and 780–940 GHz regions with frequency steps of 30, 36, 48, 54, and 76 kHz and an acquisition time of 35 ms per point. Absorption signals were detected either by a Schottky diodes detector (Virginia Diodes Inc.) below 315 GHz or by an InSb liquid He-cooled bolometer (QMC Instruments Ltd.) above 400 GHz, and were processed on a computer. The absolute accuracy of the line-centre frequency is estimated to be better than 30 kHz (50 kHz above 700 GHz) for isolated lines and can be as low as 100 kHz (150 kHz above 700 GHz) for blended or very weak lines.

3. Assignments and fit of the $\text{HCOO}^{13}\text{CH}_3$ spectrum

The theoretical model and the so-called RAM method (rho-axis method) used for the present spectral analyses and fits of the ground- and first torsional-excited states of $\text{HCOO}^{13}\text{CH}_3$ species have also been used previously for a number of molecules that contain an internal methyl rotor (see for example Ilyushin et al. 2003, 2008) and in particular for the normal species of the cis-methyl formate (Carvajal et al. 2007; Ilyushin et al. 2009), the two ^{13}C species (Carvajal et al. 2009, 2010), for DCOOCH_3 (Margulès et al. 2010), and for ^{18}O species (Tercero et al. 2012). The RAM Hamiltonian we used is based on previous works (Kirtman 1962; Lees & Baker 1968; Herbst et al. 1984). Because this method has been presented in great detail in the literature (Lin & Swalen 1959; Hougen et al. 1994; Kleiner 2010), we do not describe it here. The principal advantage of the RAM general approach used in our code BELGI, which is publicly available¹, is its general approach that simultaneously takes into account the A- and E-symmetry states in our fit. All the torsional levels up to a truncation limit of $v_t = 8$ are carefully tested and the interactions within the rotation-torsion energy levels are also included in the rotation-torsion Hamiltonian matrix elements (Kleiner et al. 1996). The various rotational, torsional, and coupling terms between rotation and torsion that we used for the fit of the $\text{HCOO}^{13}\text{CH}_3$ species were defined previously for the normal methyl formate species (Carvajal et al. 2007). The labelling scheme of the energy levels and transitions used for methyl formate was also described in the same reference, as was the connection with the more traditional J_{K_a, K_c} labelling.

We started with the assignment of the ground state. Predictions were provided by the BELGI program based on the set of 27 parameters previously determined in Carvajal et al. (2009). In this reference, only 658 lines were assigned from 150 to 700 GHz. Our new spectrometer has a wider coverage range than that used in 2009. Based on the previous work, we easily assigned the spectra up to $J = 63$ and $K_a = 34$ in the range 75–630 GHz. In the highest frequency range of the mm- and submm- wave spectrometer (700–940 GHz), the assignment was tentative because of the shift of the predicted lines from the experimental lines. The upper limit in frequency of the 936 previously fitted lines was 700 GHz. As a result, we assigned for the ground-state 5728 lines up to $J = 60$ and $K_a = 35$ from 50 to 940 GHz. Next, we started up again, but simultaneously including data of states $v_t = 0$ and $v_t = 1$. The fit was carried out in

¹ The source code for the fit, an example of input data file, and a readme file are available at the web site (<http://www.ifpan.edu.pl/~kisiel/introt/introt.htm#belgi>) managed by Zbigniew Kisiel. Extended versions of the code made to fit transitions with higher J and K are also available from the authors (I. Kleiner and M.C.).

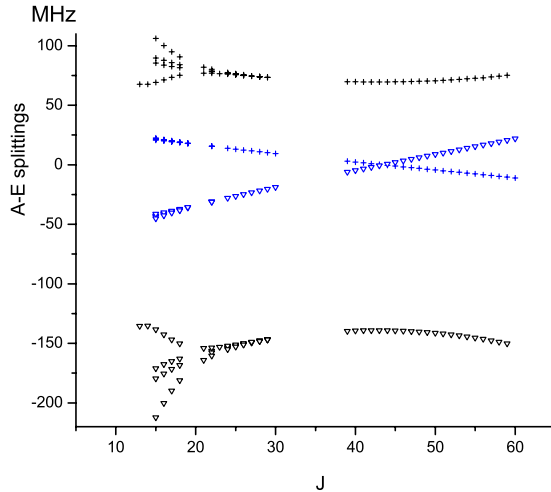


Fig. 1. A-E splitting of selected branches (R branches for $K_a = 0; 1$ in blue and $1;2$ in black) for $v_t = 1$. The x-axis represents the situation without perturbation. The A transitions (\triangledown signs) are twice as far as the E transitions (+ signs). For $K_a = 0; 1$ the A-E splitting changes sign at $J = 44$ (Ilyushin et al. 2009).

these two steps to avoid any possible misassignments. The improvement of the fit is then based on the variety and richness of the data set, and the addition of lines belonging to $v_t = 1$ is crucial. The analysis of the first excited torsional state was challenging because of a larger splitting of the A and E component by the tunnelling effect. In a recent work by Tudorie et al. (2012) the band origins ($E_A = 132.4303 \text{ cm}^{-1}$ and $E_E = 131.8445 \text{ cm}^{-1}$) for $v_t = 1$ of the parent molecule were precisely determined by a combination of microwave, mm-wave, submm-wave, and far infrared data. The value of height of the barrier was as much improved and V_3 was determined to be equal to $370.7398(58) \text{ cm}^{-1}$. In this work, for $\text{HCOO}^{13}\text{CH}_3$, the first torsional excited substates are predicted to be $E_A = 131.0565 \text{ cm}^{-1}$ and $E_E = 130.4856 \text{ cm}^{-1}$. We estimated the rotational parameters using the same difference of the ground- and the first-torsional excited states rotational parameters of the ^{12}C species. In the assignment procedure, the a-type transitions with A symmetry of R-branches were first analysed, in particular, the most intense lines with $K_a = 0$ and 1.

Methyl formate is a fairly asymmetric near-prolate top for which the dipole moment is non-zero along the a and b principle axis. For the parent specie, μ_a and μ_b were measured by Margulès et al. (2010) and their values are $1.648(8)$ and $0.706(12)$ D. We tracked these transitions based on the intensity criterion. Next we assigned the E type of transitions with the same benchmarks as those adopted for the A type of transitions. For K_a the splitting between the A transitions, as well as between the E transitions, decreases with the increase of the J quantum number. Four μ_a and μ_b rotational transitions with the same symmetry (A or E) become blended at $J = 24$. Furthermore, in the mm-wave ranges the splitting between the A and E transitions decreases with the increase of J and at a specific value of J in the submm-wave ranges this splitting changes sign (Fig. 1). Following this behaviour of the A and E type of transition for $K_a = 0$ and 1, we assigned them up to $J = 50$ at $\sim 520 \text{ GHz}$. We fitted these for $v_t = 1$ with the ERHAM (Groner 1997, 2012) program. The predictions based on this first fit were accurate enough to continue and to search for higher quantum number lines. We collected 800 A lines and 596 E lines with $K_{a,\max} = 19$

and 11 up to $J = 50$ for the A and E lines. ERHAM² treats each torsional state separately, and to proceed with the global analysis of $v_t = 0$ and 1, we used BELGI. The final data set with the upper limits of the quantum numbers and the experimental uncertainties are summarized in Table 1. The 6574 lines belonging to $v_t = 0$ and 2881 lines belonging to $v_t = 1$ were fitted with root-mean-square deviations of 38.3 and 41.9 kHz . The fit of the total of 9455 lines for $v_t = 0$ and 1 of A and E symmetries resulted in the determination of 52 parameters of the RAM Hamiltonian. Table 3 presents the values of the set of 52 newly determined parameters. In this table we also provide a comparison with the previous work. Principally, we note a striking change in the value of the barrier height. The value of the parameter V_3 changed from $407.1549(147)$ to $369.93168(395) \text{ cm}^{-1}$.

The reason for this is the fact that this parameter is an effective value. In the previous fit (Carvajal et al. 2009), the data set of lines concerned only the $v_t = 0$ state and, therefore, neither the second-order parameter (V_6) of the torsional potential function nor the kinetic parameter F could be determined. Then, F was fixed to a relatively high value estimated by ab initio methods, and in the fitting procedure, the effective value of V_3 absorbed the error of F and contained the contribution of V_6 :

$$V(\gamma) = \frac{V_3}{2} \times (1 - \cos 3\gamma) + \frac{V_6}{2} \times (1 - \cos 6\gamma) + \dots$$

The new combination of data from $v_t = 0$ and 1 improved the quality of the fit and allowed determining of 25 new parameters, particularly F and V_6 .

4. Line strengths

The intensity calculations for the two ^{13}C species of methyl formate were performed using the same method described in Hougen et al. (1994) and Ilyushin et al. (2008), that was applied for the normal species by Carvajal et al. (2007), the ^{13}C species (Carvajal et al. 2009, 2010), DCOOCH_3 (Margulès et al. 2010), and ^{18}O species (Tercero et al. 2012). For this reason we do not repeat it here. The line strength calculation for the ^{13}C species was performed using the same value for the dipole moment as for the parent methyl formate (Margulès et al. 2010). This assumption was made because the angle between the internal axis of the methyl top and the principal a-axis does not change much upon substitution (see the $\langle i, a \rangle$ angle values in Table 3). All other structural parameters such as the angle between RAM and PAM axes (θ_{RAM}) and the ρ parameter do not change much upon substitution (see Table 3). Because the changes in the structure in the various isotopomers are not important, we assumed that the dipole moment does not change considerably from one species to another. The dipole moment components of $\text{H}^{13}\text{COOCH}_3$ (Carvajal et al. 2010) and $\text{HCOO}^{13}\text{CH}_3$ in RAM axis system that we used for the intensity calculations are $\mu_a^{\text{RAM}} = 1.792 \text{ D}$; $\mu_b^{\text{RAM}} = -0.044 \text{ D}$ and $\mu_a^{\text{RAM}} = 1.793 \text{ D}$; $\mu_b^{\text{RAM}} = -0.022 \text{ D}$, respectively. We provide Table A.1, which is part of the supplementary Table S (available on CDS). It contains all included lines from our fit for the $\text{HCOO}^{13}\text{CH}_3$ methyl formate species. They show the line assignments, the observed frequencies with measurement uncertainty (in parenthesis), the computed frequencies, observed-calculated values, the line strength, and the lower-state energy relative to the $J = K = 0$ A-species level taken as zero-energy level. The prediction line-list of all transitions in $v_t = 0$ and 1 will be transmitted to the SPLATALOG and CDMS database (available at www.splatalogue.net).

² <http://www.ifpan.edu.pl/~kisiel/introt/introt.htm#erham>

Table 1. Root-mean-square (rms) deviations from the global fit^a of transitions involving $v_t = 0$ and $v_t = 1$ torsional energy levels of $^{13}\text{C}_2\text{-methyl formate}$ ($\text{HCOO}^{13}\text{CH}_3$).

Number of parameters					
Number of lines					
rms of the 6574 MW $v_t = 0-0$ lines					52
rms of the 2881 MW $v_t = 1-1$ lines					9455
rms of the 5184 A symmetry lines					0.0383 MHz
rms of the 4271 E symmetry lines					0.0419 MHz
					0.0429 MHz
					0.0349 MHz
Source ^b	Range ^c (GHz)	$v_t, J_{\max}, K_{\max}^d$	Number of lines ^e	Uncertainties ^f (MHz)	rms ^g (MHz)
AA09	4–20	0, 7, 3	27	0.005	0.0056
AA09	150–700 ^j	0, 63, 35	607	0.030	0.0252
NEW	50–940 ^k	0, 60, 35	4864	0.030	
NEW	50–940 ^k	1, 60, 26	1731	0.030	
AA09	150–700 ^j	0, 52, 27	2	0.050	
NEW	50–940 ^k	0, 52, 35	577	0.050	
NEW	50–940 ^k	1, 58, 26	814	0.050	
AA09	8–700 ^j	0, 58, 29	43	0.100 ^h	0.0644
NEW	50–940 ^k	0, 55, 33	170	0.100 ⁱ	
NEW	50–940 ^k	1, 57, 26	203	0.100 ⁱ	
AA09	8–700 ^j	0, 33, 11	122	0.150 ^h	0.1345
NEW	50–940 ^k	0, 54, 33	49	0.150 ⁱ	
NEW	50–940 ^k	1, 55, 24	68	0.150 ⁱ	
AA09	8–700 ^j	0, 58, 25	45	0.200 ^h	
NEW	50–940 ^k	0, 55, 31	68	0.200 ⁱ	
NEW	50–940 ^k	1, 55, 20	65	0.200 ⁱ	

Notes. ^(a) Parameter values are given in Table 2. The complete list of observed minus calculated residuals of $v_t = 0$ lines are given in the supplementary Table A.1. ^(b) Sources of data: AA09 stands for Carvajal et al. (2009) and NEW data come from the present work. The spectroscopic instruments are described in Sect. 2.2. ^(c) Spectral range of the measurements. ^(d) Torsional state v_t , maximum J and K_a for each group of measurements. ^(e) Number of MW lines in each uncertainty group. ^(f) Uncertainty in MHz used in the fit. ^(g) Root-mean-square deviation in MHz for each group. ^(h) The details of the accuracy of spectral measurements are given in Carvajal et al. (2009). ⁽ⁱ⁾ The accuracy of spectral measurements for the Lille spectrometer is about 0.030 MHz for isolated lines but some lines are either blended or present a poor S/N ratio and therefore their measurement accuracy is taken as either 0.100 MHz, 0.150 MHz or 0.200 MHz according to the broadening of the experimental line. ^(j) The spectrometer spectral ranges for these measurements are 8–80 GHz, 150–245 GHz, 320–350 GHz, 510–525 GHz, and 580–661 GHz (for more details, see Carvajal et al. 2009). ^(k) The spectrometer spectral ranges for the measurements of present work are: 50–100 GHz and 150–940 GHz, using a multiplication chain of solid state sources, and 100–150 GHz, using a backward wave oscillator.

5. Detection of $^{13}\text{C-HCOOCH}_3$ $v_t = 1$ in Orion KL

In this section we use the notation $^{13}\text{C-HCOOCH}_3$ when we refer to the two isotopologues. Following the procedure of our previous papers, we searched for the present species in the molecular line survey of Orion KL performed with the IRAM 30 m telescope. We detected both ^{13}C isotopologues of methyl formate in their first vibrationally excited state. In Sect. 5.1 we summarize the observations, data reduction, and overall results of this survey. We present the new detection in Sect. 5.2. In Sect. 5.3 we explain the assumed model and the excitation and radiative transfer calculations for vibrationally excited ^{13}C and ^{12}C methyl formate. We also compute our obtained $^{12}\text{C}/^{13}\text{C}$ ratio and the vibrational temperature for $^{13}\text{C-HCOOCH}_3$ $v_t = 1$.

5.1. Observations, data reduction, and overall results

The molecular line survey towards Orion KL-IRc2 ($\alpha(\text{J2000}) = 5^{\text{h}}35^{\text{m}}14.5^{\text{s}}$, $\delta(\text{J2000}) = -5^{\circ}22'30.0''$) was performed between September 2004 and January 2007 in five observing sessions with the IRAM 30 m telescope. All frequencies allowed by the A, B, C, and D receivers were covered (80–115.5, 130–178, and 197–281 GHz) with a spectral resolution of 1–1.25 MHz. System temperatures, image side-band rejections, and half-power beam widths were in the ranges 100–800 K, 27–13 dB, and 29–9'', from 80 to 281 GHz. The observations were performed in the balanced wobbler-switching mode. Pointing and focus were checked every 1–2 h on nearby quasars. The inten-

sity scale was calibrated with two absorbers at different temperatures using the ATM package (Cernicharo 1985; Pardo et al. 2001).

The data were processed using the GILDAS software³. The data reduction consisted of removing lines from the image side-band and fitting and removing baselines. We observed each frequency setting twice, with the second one shifted in frequency by 20 MHz. This allowed us to remove lines from the image side-band down to a level of 30 dB (this means that lines in the image side-band of 30 K will contribute with less than 0.03 K to the final reduced spectrum). Figures are shown in units of main-beam antenna temperature, $T_{\text{MB}} = T_{\text{A}}^{\star}/\eta_{\text{MB}}$, where η_{MB} is the main-beam efficiency ranged from 0.82 to 0.48 from the lowest to the highest frequencies. For a detailed description of the observations and data reduction procedures see Tercero et al. (2010).

Up to date, we performed a deep analysis of the data (15 papers have been already published): identifying more than 15 000 spectral features (Tercero et al. 2010; Tercero 2012), detecting new molecules in space ($\text{CH}_3\text{COOCH}_3$ and g- $\text{CH}_3\text{CH}_2\text{OCOOH}$ in Tercero et al. 2013; NH_3D^+ in Cernicharo et al. 2013; $\text{CH}_3\text{CH}_2\text{SH}$ in Kolesniková et al. 2014; also tentative detections of c- $\text{C}_6\text{H}_5\text{O}$ in Kolesniková et al. 2013 and upper limit calculations for the column density of non detected molecules –cis- $\text{CH}_2\text{CHCH}_2\text{CN}$ and cis- $\text{CH}_2\text{CHCH}_2\text{NC}$ – in Haykal et al. 2013b) and several new isotopologues and

³ <http://www.iram.fr/IRAMFR/GILDAS>

Table 2. Torsion-rotation parameters needed for the global fit of transitions involving $v_t = 0$ and $v_t = 1$ torsional energy levels of $^{13}\text{C}_2$ -methyl formate ($\text{H}^{12}\text{COO}^{13}\text{CH}_3$) provided in this work and comparison with the torsion-rotation parameters obtained in the former global fit of transitions only involving $v_t = 0$ torsional states (Carvajal et al. 2009).

nlm ^a	Operator ^b	Parameter	$v_t = 0, 1^c$	$v_t = 0^d$	nlm	Operator	Parameter	$v_t = 0, 1^c$	$v_t = 0^d$
220	$(1 - \cos 3\gamma)/2$	V_3	369.93168(395)	407.1549(147) ^g	642	$(1 - \cos 6\gamma)P^2$	N_v	$-0.312260(869) \times 10^{-3}$	0.0^f
	P_γ^2	F	5.4785214(464)	5.69168218 ^e		$(1 - \cos 6\gamma)P_a^2$	K_2	$0.84669(480) \times 10^{-3}$	0.0^f
211	$P_\gamma P_a$	ρ	0.084337567(345)	0.0845207(106)		$(1 - \cos 6\gamma)(P_b^2 - P_c^2)$	c_{11}	$-0.161265(889) \times 10^{-3}$	0.0^f
202	P_a^2	A^{RAM}	0.58658923(178)	0.5857484(245)		$(1 - \cos 6\gamma)(P_a P_b + P_b P_a)$	dd_{ab}	$-0.29738(147) \times 10^{-3}$	0.0^f
	P_b^2	B^{RAM}	0.29682136(198)	0.2959971(182)		$P_\gamma^4 P^2$	M_v	$0.7960(365) \times 10^{-8}$	0.0^f
	P_c^2	C^{RAM}	0.173496850(137)	0.1729010(134)		$2 P_\gamma^4 (P_b^2 - P_c^2)$	c_3	$0.13176(197) \times 10^{-7}$	0.0^f
	$(P_a P_b + P_b P_a)$	D_{ab}	-0.15976497(192)	-0.1573691(747)	624	$(1 - \cos 3\gamma)P^4$	f_v	$0.91080(149) \times 10^{-8}$	0.0^f
440	$(1 - \cos 6\gamma)/2$	V_6	25.40353(193)	0.0 ^f		$(1 - \cos 3\gamma)P_a^2 P^2$	k_{5J}	$0.4484(183) \times 10^{-7}$	0.0^f
422	$P_\gamma^2 P^2$	G_v	$0.27105(240) \times 10^{-5}$	$0.4682(101) \times 10^{-4}$		$(1 - \cos 3\gamma)P_a^4$	k_{5K}	$-0.21242(275) \times 10^{-6}$	0.0^f
	$2P_\gamma^2(P_b^2 - P_c^2)$	c_1	$0.10489(207) \times 10^{-5}$	0.0 ^f		$(1 - \cos 3\gamma)(P_a P_b + P_b P_a)P^2$	d_{abJ}	$0.46277(344) \times 10^{-7}$	$0.9060(708) \times 10^{-7}$
	$\sin 3\gamma(P_a P_c + P_c P_a)$	D_{ac}	0.0 ^f	-0.0040623(839)		$(1 - \cos 3\gamma)(P_a^3 P_b + P_b P_a^3)$	d_{abK}	$-0.83350(642) \times 10^{-7}$	$0.3349(260) \times 10^{-6}$
	$\sin 3\gamma(P_b P_c + P_c P_b)$	D_{bc}	0.00074120(917)	0.0010563(383)		$(1 - \cos 3\gamma)P_a^2 (P_b^2 - P_c^2)$	c_{2K}	$0.47452(372) \times 10^{-7}$	0.0^f
	$(1 - \cos 3\gamma)P^2$	F_v	-0.00229820(140)	-0.0007557(425)		$P_\gamma^2 P_a^2 P^2$	k_{2J}	$0.4462(154) \times 10^{-9}$	0.0^f
	$(1 - \cos 3\gamma)P_a^2$	k_5	0.01046256(804)	0.0124250(566)		$2P_\gamma^2 (P_a^2 (P_b^2 - P_c^2))$	c_{1K}	$0.18733(536) \times 10^{-9}$	0.0^f
	$(1 - \cos 3\gamma)(P_b^2 - P_c^2)$	c_2	$-0.3062(148) \times 10^{-4}$	0.0 ^f		$\sin 3\gamma(P_b P_c + P_c P_b)P^2$	D_{bcJ}	$-0.12682(268) \times 10^{-7}$	0.0^f
	$P_a^2 P_a^2$	k_2	$-0.43892(170) \times 10^{-4}$	0.0 ^f	606	P^6	H_J	$-0.755(12) \times 10^{-12}$	$-0.31(1) \times 10^{-13}$
	$(1 - \cos 3\gamma)P_a P_b + P_b P_a)$	d_{ab}	-0.00573380(154)	-0.013852(236)		$P_\gamma^4 P_a^2$	H_{JK}	$0.10555(83) \times 10^{-10}$	0.0^f
	$P_\gamma^2 (P_a P_b + P_b P_a)$	Δ_{ab}	0.0 ^f	$-0.16792(565) \times 10^{-3}$		$P^2 P_a^4$	H_{KJ}	$-0.34983(244) \times 10^{-10}$	0.0^f
413	$P_\gamma P_a P^2$	L_v	$0.1824(134) \times 10^{-6}$	$-0.2045(247) \times 10^{-5}$		P^6	H_K	$0.50362(252) \times 10^{-10}$	0.0^f
	$P_\gamma^2 P_a^3$	k_1	$0.127972(329) \times 10^{-4}$	0.0 ^f		$2P_\gamma^4 (P_b^2 - P_c^2)$	h_J	$-0.364(6) \times 10^{-12}$	0.0^f
	$P_\gamma \{P_a, (P_b^2 - P_c^2)\}$	c_4	$0.94726(730) \times 10^{-6}$	$0.39452(688) \times 10^{-5}$		$P^2 \{P_a^2, (P_b^2 - P_c^2)\}$	h_{JK}	$0.1996(22) \times 10^{-11}$	$0.1130(25) \times 10^{-11}$
	$P_\gamma \{P_a^2, P_b\}$	δ_{ab}	$-0.343262(938) \times 10^{-5}$	$0.1707(107) \times 10^{-4}$		$\{P_a^4, (P_b^2 - P_c^2)\}$	h_K	$-0.1811(68) \times 10^{-11}$	0.0^f
404	$-P^4$	Δ_J	$0.24016(201) \times 10^{-6}$	$0.15312(163) \times 10^{-6}$		$P^4 (P_a P_b + P_b P_a)$	D_{abJJ}	$0.2077(52) \times 10^{-11}$	0.0^f
	$-P^2 P_a^2$	Δ_{JK}	$-0.235426(785) \times 10^{-5}$	$0.21223(170) \times 10^{-5}$		$P^2 (P_a^3 P_b + P_b P_a^3)$	D_{abJK}	$-0.10787(148) \times 10^{-10}$	0.0^f
	$-P_a^4$	Δ_K	$0.576749(422) \times 10^{-5}$	$-0.17369(181) \times 10^{-5}$	615	$P_\gamma P_a^4$	l_v	$0.14903(534) \times 10^{-10}$	0.0^f
	$-2P_\gamma^2 (P_b^2 - P_c^2)$	δ_J	$0.8245(100) \times 10^{-7}$	$0.39739(813) \times 10^{-7}$					
	$-\{P_a^2, (P_b^2 - P_c^2)\}$	δ_K	$-0.41365(637) \times 10^{-7}$	$0.108794(621) \times 10^{-5}$					
	$P^2 (P_a P_b + P_b P_a)$	D_{abJ}	$-0.48884(361) \times 10^{-6}$	$0.24287(221) \times 10^{-6}$					
	$(P_a^3 P_b + P_b P_a^3)$	D_{abK}	$0.1345545(843) \times 10^{-5}$	$0.13608(491) \times 10^{-5}$					

Notes. ^(a) Notation from Ilyushin et al. (2003); $n = l+m$, where n is the total order of the operator, l is the order of the torsional part and m is the order of the rotational part. ^(b) Notation from Ilyushin et al. (2003). $\{A, B\} = AB + BA$. The product of the parameter and operator from a given row yields the term actually used in the vibration-rotation-torsion Hamiltonian, except for F , ρ and A , which occur in the Hamiltonian in the form $F(P_\gamma - \rho P_a)^2 + A^{\text{RAM}} P_a^2$. ^(c) Values of the parameters from the present fit, for the ground torsional state $v_t = 0$ and the first excited torsional state $v_t = 1$. All parameter values are in cm^{-1} except for ρ which is unitless. Statistical uncertainties are given in parentheses in units of the last quoted digit. ^(d) Values of the parameters from the fit for the ground torsional state $v_t = 0$ given by Carvajal et al. (2009). The 27 parameters were fitted for 936 MW lines from $v_t = 0$ with a root mean square of 97 kHz. All parameter values are in cm^{-1} except for ρ which is unitless. Statistical uncertainties are given in parentheses in units of the last quoted digit. ^(e) The internal rotation constant F of $\text{HCOO}^{13}\text{CH}_3$ was kept fixed to the ab initio value calculated in the equilibrium structure (see Carvajal et al. 2009). ^(f) Kept fixed. ^(g) Very large effective value obtained as a consequence of fixing F parameter to a large ab initio value and because F , V_3 and V_6 were not able to fit them at the same time only from the ground torsional state (Carvajal et al. 2009).

Table 3. Rotational constants in the principal axis system (PAM), angles between the principal axis and the methyl top axis, and internal rotation parameters upon isotopic substitution.

	HCOOCH ₃ ^a Global fit ($v_t = 0, 1$)	HCOO ¹³ CH ₃ ^b Global fit ($v_t = 0$)	HCOO ¹³ CH ₃ ^c Global fit ($v_t = 0, 1$)
A(MHz)	19 924.4249(433)	19 629.65(176)	19 707.8000(625)
B(MHz)	6947.9458(414)	6804.42(171)	6776.1833(660)
C(MHz)	5318.10685(450)	5183.442(402)	5201.30471(410)
$\angle(i, a)^d$	53.06	51.68	52.18(25)
θ_{RAM}^e	24.87951(13)	23.68	23.89824(22)
ρ	0.08427227(25)	0.0845207(106)	0.084337567(345)
F (cm ⁻¹)	5.497592(59)	5.69168218 ^f	5.4785214(464)
V_3 (cm ⁻¹)	370.7398(58)	407.1549(147)	369.93168(395)
σ^g	0.67	1.08	0.77
Nº of transitions	15 840	936	9455
Nº of fitted parameters	53	27	52

Notes. ^(a) Rotation-torsion parameters for the normal species HCOOCH₃ obtained in Tudorie et al. (2012) with the RAM-axis system, after transforming the RAM values for the A, B, C rotational parameters into PAM values following the procedure described in Carvajal et al. (2007). The RAM to PAM transformation is given in Carvajal et al. (2010). ^(b) Rotation-torsion parameters for ¹³C₂-methyl formate from Carvajal et al. (2009) transformed to the principal axis system. ^(c) Rotation-torsion parameters for ¹³C₂-methyl formate from the present work transformed into the principal axis system. ^(d) Angle in degrees between the a-principal axis and the methyl top axis (i). ^(e) The angle θ_{RAM} between the a-principal axis and the a-RAM axis is given in degrees and obtained from Eq. (1) from Carvajal et al. (2007), with the parameters A^{RAM} , B^{RAM} , C^{RAM} , and D_{ab} of Table 2. ^(f) Fixed to the ab initio value (Carvajal et al. 2009). ^(g) Unitless standard deviation.

Table 4. Kinematic parameters and physical conditions of the Orion-KL spatial components.

Parameter	Extended ridge (ER)	Compact ridge (CR)	Plateau (P)	Hot core (HC)
Source diameter (")	≈ 120 (120)	5–15 (15)	20–30 (30)	5–10 (10)
Offset (from IRc2) (")	0 (0)	7 (7)	0 (0)	2–3 (2)
$n(\text{H}_2)$ (cm ⁻³)	$\approx 10^5$	$\approx 10^6$	$\approx 10^6$	10^7 – 10^8
T_k (K)	≈ 60 (60)	80–150 (110)	100–150 (125)	150–300 (225)
Δv_{FWHM} (km s ⁻¹)	≈ 4 (4)	3–5 (4)	≈ 25 (25)	5–15 (10)
v_{LSR} (km s ⁻¹)	8–10 (8)	7–9 (7.5)	6–11 (9)	3–6 (5.5)

Notes. Parameters compiled from different authors: Blake et al. (1987); Schilke et al. (2001); Persson et al. (2007); Tercero et al. (2010); Neill et al. (2013). The values between parenthesis are those adopted for the model of HCOOCH₃ $v_t = 1$ and ¹³C-HCOOCH₃ $v_t = 0$.

vibrationally excited states of well-known molecules in this source (¹³C-CH₃CH₂CN in Demyk et al. 2007; ¹³C-HCOOCH₃ in Carvajal et al. 2009; CH₃CH₂¹⁵N, CH₃CHDCN, and CH₂DCH₂CN in Margulès et al. 2009; DCOOCH₃ in Margulès et al. 2010; ¹⁸O-HCOOCH₃ in Tercero et al. 2012; NH₂CHO $v_{12} = 1$ in Motiyenko et al. 2012; CH₃CH₂CN $v_{10} = 1$ and $v_{12} = 1$ in Daly et al. 2013; HCOOCH₂D in Coudert et al. 2013; CH₂CHCN $v_{10} = 1 \leftrightarrow (v_{11} = 1, v_{15} = 1)$ in López et al. 2014), and constraining physical and chemical parameters by means of the analysis of different families of molecules (OCS, CS, H₂CS, HCS⁺, CCS, CCCS species in Tercero et al. 2010; SiO and SiS species in Tercero et al. 2011; CH₃CH₂CN species in Daly et al. 2013; SO and SO₂ species in Esplugues et al. 2013a; HC₃N and HC₅N species in Esplugues et al. 2013b; CH₃CN in Bell et al. 2014; CH₂CHCN species and the isocyanides in López et al. 2014). In addition and to analyze some of these results, we modeled the following molecules: CH₃SH, CH₃OH, CH₃CH₂OH in Kolesniková et al. (2014), HCOOCH₃ in Margulès et al. (2010), and NH₂CHO in Motiyenko et al. (2012). Nevertheless, the study of this line survey is still open and several groups are working simultaneously based on the scope of these observations⁴.

In agreement with numerous works of this region (see e.g. Blake et al. 1987; Schilke et al. 2001; Persson et al. 2007; Neill et al. 2013), at least four cloud components could be identified in the line profiles of our low-resolution spectral lines, which are characterized by different radial velocities and line widths

(Tercero et al. 2010, 2011). Each component corresponds to specific region of the cloud that overlaps in our telescope beam. Table 4 summarizes the kinematic and physical parameters of the different components in Orion-KL.

5.2. Results

The two ¹³C isotopologues of HCOOCH₃ in their first vibrationally excited state ($v_t = 1$) have been detected in Orion-KL by means of 135 spectral features (77 of them practically unblended) without missing transitions in the range 80–280 GHz. Figure 2 shows selected detected lines of the two isotopologues together with our best model (see below). The black histogram line corresponds with the observed spectra. The model of the H¹³COOCH₃ $v_t = 1$ and HCOO¹³CH₃ $v_t = 1$ lines is shown in red and dark blue, respectively. In all boxes unblended or slightly blended detected lines of these species are depicted. The cyan blue line represents the total model compiled from our already published work (see Sect. 5.1). In Table 5 we list all detected features in our line survey. These detections are based on an inspection of the data and the modelled synthetic spectrum of the studied species and all the species already identified in our previous papers (see above). The observed main-beam temperature and the radial velocity where obtained from the peak channel of our spectra, therefore, errors in the baselines –up to ± 0.15 K for spectra at 1.3 mm due to the extremely high line density (line confusion limit) – and contribution from other species might affect the $T_{\text{mb}}^{\text{obs}}$ value. Adding species to our total model allows reducing the uncertainty in the baselines, so, in general, the $T_{\text{mb}}^{\text{obs}}$

⁴ The data of the IRAM 30 m line survey of Orion KL are available in ascii format on request to B. Tercero.

Table 5. Detected lines of $^{13}\text{C}-\text{HCOOCH}_3$ $v_t = 1$ towards Orion KL.

Spec.	J	K_a	K_c	p	J'	K'_a	K'_c	p'	Calc. freq. (MHz)	E_u (K)	$S_{ij}\mu^2$ (D ²)	Obs. freq. (MHz)	v_{LSR} (km s ⁻¹)	$T_{\text{mb}}^{\text{obs}}$ (K)	$T_{\text{mb}}^{\text{mod}}$ (K)	Blend
A- $^{13}\text{C}_1$	12	1	12	+	11	1	11	+	130 348.229	229.4	32.1	130 349.3	4.6 ± 1.2	0.06	0.03	
E- $^{13}\text{C}_1$	12	-1	12		11	-1	11		130 424.730	229.5	32.2	130 424.3	8.1 ± 1.2	0.04	0.03	
A- $^{13}\text{C}_2$	11	3	9	+	10	3	8	+	130 674.060	231.2	26.8	130 673.6	8.0 ± 1.1	0.07	0.03	$\text{CH}_3\text{CH}_2\text{C}^{15}\text{N}$
E- $^{13}\text{C}_2$	11	5	6		10	5	5		131 497.371	340.9	23.2	131 497.9	5.7 ± 1.1	0.03	0.02	
E- $^{13}\text{C}_2$	11	-3	9		10	-3	8		131 600.450	329.8	26.6	131 600.6	6.6 ± 1.1	0.03	0.02	
A- $^{13}\text{C}_2$	11	4	8	-	10	4	7	-	131 626.157	235.9	25.2	131 626.6	6.0 ± 1.1	0.07	0.02	(CH_3) ₂ CO
A- $^{13}\text{C}_2$	11	4	7	+	10	4	6	+	132 401.079	236.0	25.2	132 400.5	8.3 ± 1.1	0.04	0.02	CH_3CHDCN
A- $^{13}\text{C}_1$	11	3	9	+	10	3	8	+	132 807.823	231.8	27.4	132 806.7	9.6 ± 1.1	0.07	0.03	
A- $^{13}\text{C}_1$	11	9	2	-	10	9	1	-	132 945.107	279.3	9.86	132 946.6	3.7 ± 1.1	0.07	0.02	CCCS
A- $^{13}\text{C}_1$	11	9	3	+	10	9	2	+	132 945.107	279.3	9.86	†	3.7 ± 1.1			
E- $^{13}\text{C}_2$	11	3	8		10	3	7		136 042.486	330.6	26.8	136 042.9	6.2 ± 1.1	0.03	0.03	
E- $^{13}\text{C}_1$	11	3	8		10	3	7		138 640.538	232.8	27.6	138 640.6	6.9 ± 1.1	0.04	0.03	
A- $^{13}\text{C}_2$	13	1	13	+	12	1	12	+	138 830.565	235.5	34.0	138 829.7	8.9 ± 1.1	0.06	0.04	
E- $^{13}\text{C}_1$	12	-2	11		11	-2	10		139 241.862	234.5	31.5	139 239.2	12.6 ± 1.1	0.06	0.03	$\text{CH}_2\text{DCH}_2\text{CN}$
E- $^{13}\text{C}_1$	13	-1	13		12	-1	12		140 917.742	236.2	35.0	140 918.6	5.3 ± 1.1	0.04	0.04	
A- $^{13}\text{C}_1$	13	0	13	+	12	0	12	+	140 937.135	236.2	34.8	140 937.6	6.1 ± 1.1	0.13	0.04	CH_2DOH
E- $^{13}\text{C}_1$	13	0	13		12	0	12		141 008.471	236.2	35.0	141 007.8	8.3 ± 1.1	0.09	0.04	
E- $^{13}\text{C}_1$	12	1	11		11	1	10		141 542.530	234.2	31.6	141 543.0	6.1 ± 1.1	0.05	0.04	
A- $^{13}\text{C}_2$	12	3	10	+	11	3	9	+	142 240.894	238.0	29.5	142 240.3	8.2 ± 1.1	0.04	0.03	
E- $^{13}\text{C}_2$	12	4	8		11	4	7		144 894.428	341.8	28.2	144 895.6	4.6 ± 1.0	0.06	0.03	
E- $^{13}\text{C}_2$	12	-4	9		11	-4	8		144 984.322	341.4	28.2	144 983.7	8.4 ± 1.0	0.05	0.03	
E- $^{13}\text{C}_1$	12	7	5		11	7	4		145 262.992	266.0	21.5	145 262.9	7.1 ± 1.0	0.07	0.02	U
A- $^{13}\text{C}_1$	12	7	6	+	11	7	5	+	145 282.393	265.1	21.5	145 282.9	5.9 ± 1.0	0.07	0.04	
A- $^{13}\text{C}_1$	12	7	5	-	11	7	4	-	145 282.519	265.1	21.5	†	6.2 ± 1.0			
E- $^{13}\text{C}_1$	12	5	7		11	5	6		146 170.669	250.0	27.0	146 170.3	7.7 ± 1.0	0.15	0.03	$\text{H}^{13}\text{COOCH}_3$
E- $^{13}\text{C}_1$	12	4	8		11	4	7		147 500.782	244.1	28.9	147 501.6	5.4 ± 1.0	0.15	0.07	
E- $^{13}\text{C}_1$	12	-4	9		11	-4	8		147 501.246	243.7	28.7	†	6.3 ± 1.0			
A- $^{13}\text{C}_1$	13	2	12	-	12	2	11	-	149 734.053	241.5	34.0	149 734.5	6.0 ± 1.0	0.05	0.04	
A- $^{13}\text{C}_1$	12	2	10	+	11	2	9	+	150 951.028	237.3	31.4	150 950.6	7.9 ± 1.0	0.04	0.04	
E- $^{13}\text{C}_1$	14	0	14		13	-1	13		151 328.687	243.5	6.07	151 331.6	1.3 ± 1.0	0.11	0.05	U
A- $^{13}\text{C}_1$	14	1	14	+	13	1	13	+	151 329.124	243.4	37.5	†	2.2 ± 1.0			
E- $^{13}\text{C}_1$	14	0	14		13	0	13		151 452.158	243.5	37.7	151 451.6	8.1 ± 1.0	0.04	0.05	
E- $^{13}\text{C}_2$	13	-3	11		12	-3	10		154 267.593	344.1	32.4	154 267.7	6.8 ± 1.0	0.08	0.04	CH_3CHO
A- $^{13}\text{C}_2$	13	7	7	+	12	7	6	+	154 902.510	272.0	24.4	154 902.4	7.2 ± 1.0	0.24	0.05	$\text{SO}_2 \nu_2 = 1$
A- $^{13}\text{C}_2$	13	7	6	-	12	7	5	-	154 902.822	272.0	24.4	†	7.8 ± 1.0			
A- $^{13}\text{C}_1$	13	3	11	+	12	3	10	+	156 106.621	246.2	33.2	156 107.9	4.6 ± 1.0	0.15	0.04	$\text{HCOOCH}_3 \nu_1 = 1$
E- $^{13}\text{C}_1$	13	-3	11		12	-3	10		156 705.635	246.5	33.3	156 705.5	7.3 ± 1.0	0.11	0.04	$\text{CH}_3\text{CH}_2\text{C}^{15}\text{N}$
E- $^{13}\text{C}_1$	13	10	3		12	10	2		156 879.965	307.6	14.4	156 880.5	6.0 ± 1.0	0.05	0.01	
E- $^{13}\text{C}_1$	13	9	4		12	9	3		157 026.174	294.9	18.4	157 026.5	6.4 ± 1.0	0.09	0.02	HCOOCH_3

Notes. Emission lines of $^{13}\text{C}-\text{HCOOCH}_3$ $v_t = 1$ present in the spectral scan of Orion-KL from the IRAM 30-m radio-telescope. Column (1) indicates the species, being A- $^{13}\text{C}_1$; A- $\text{H}^{13}\text{COOCH}_3$ $v_t = 1$, E- $^{13}\text{C}_1$; E- $\text{H}^{13}\text{COOCH}_3$ $v_t = 1$, A- $^{13}\text{C}_2$; A- $\text{HCOO}^{13}\text{CH}_3$ $v_t = 1$, and E- $^{13}\text{C}_2$; E- $\text{HCOO}^{13}\text{CH}_3$ $v_t = 1$, Cols. (2)–(9) indicate the line transition, Col. (10) gives the predicted frequency obtained with the Hamiltonian parameters of this work for $^{13}\text{C}_2$ -MF and from Carvajal et al. (2010) for $^{13}\text{C}_1$ -MF, Col. (11) upper level energy, Col. (12) line strength, Col. (13) observed frequency assuming a v_{LSR} of 7 km s⁻¹, Col. (14) the radial velocity, Col. (15) observed main-beam temperature, Col. (16) modelled main-beam temperature, and Col. (17) blends. † Blended with previous line.

Table 5. continued.

Spec.	<i>J</i>	K_a	K_c	<i>p</i>	J'	K'_a	K'_c	<i>p'</i>	Calc. freq. (MHz)	E_u (K)	$S_{ij}\mu^2$ (D ²)	Obs. freq. (MHz)	v_{LSR} (km s ⁻¹)	$T_{\text{mb}}^{\text{obs}}$ (K)	$T_{\text{mb}}^{\text{mod}}$ (K)	Blend
A- ¹³ C ₁	13	10	4	–	12	10	3	–	157 221.146	306.4	14.4	157 224.1	1.4 ± 1.0	0.15	0.05	U
A- ¹³ C ₁	13	10	3	+	12	10	2	+	157 221.146	306.4	14.4	†	1.4 ± 1.0			
E- ¹³ C ₁	13	8	5		12	8	4		157 227.514	283.6	22.0	†	13.6 ± 1.0		0.02	
E- ¹³ C ₂	13	–4	10		12	–4	9		157 232.535	348.9	30.8	157 231.6	8.9 ± 1.0	0.11	0.04	CH ₃ OH
A- ¹³ C ₂	13	4	9	+	12	4	8	+	158 076.398	250.5	31.1	158 076.5	6.9 ± 0.9	0.10	0.04	
A- ¹³ C ₁	13	5	9	+	12	5	8	+	158 310.862	257.0	30.0	158 311.6	5.7 ± 0.9	0.14	0.04	¹³ CH ₃ OH
E- ¹³ C ₂	14	–2	13		13	–2	12		158 376.417	346.9	36.1	158 376.5	6.8 ± 0.9	0.07	0.05	
E- ¹³ C ₁	13	–6	8		12	–6	7		158 492.862	264.3	27.8	158 492.8	7.1 ± 0.9	0.13	0.03	U
E- ¹³ C ₁	13	–5	9		12	–5	8		159 175.181	257.1	30.1	159 175.2	6.9 ± 0.9	0.10	0.04	CH ₃ CH ₂ OOCOH
E- ¹³ C ₂	14	1	13		13	1	12		159 621.190	346.8	36.1	159 620.4	8.4 ± 0.9	0.06	0.05	CH ₃ CH ₂ OOCOH
E- ¹³ C ₁	13	–4	10		12	–4	9		159 907.354	251.3	31.4	159 906.5	8.6 ± 0.9	0.10	0.04	U
E- ¹³ C ₁	13	3	10		12	3	9		165 795.305	248.1	33.6	165 796.4	5.1 ± 0.9	0.15	0.05	CH ₃ C ¹³ CH
A- ¹³ C ₂	14	10	4	+	13	10	3	+	166 582.134	313.8	18.1	166 581.5	8.2 ± 0.9	0.08	0.04	
A- ¹³ C ₂	14	10	5	–	13	10	4	–	166 582.134	313.8	18.1	†	8.2 ± 0.9			
E- ¹³ C ₂	14	8	6		13	8	5		166 627.702	389.3	25.0	166 627.5	7.4 ± 0.9	0.08	0.03	
A- ¹³ C ₂	14	6	9	–	13	6	8	–	167 331.309	271.4	30.3	167 330.3	8.9 ± 0.9	0.12	0.04	U
A- ¹³ C ₂	14	6	8	+	13	6	7	+	167 355.684	271.4	30.3	167 356.5	5.6 ± 0.9	0.10	0.04	
E- ¹³ C ₁	14	–3	12		13	–3	11		168 050.461	254.5	36.1	168 050.1	7.7 ± 0.9	0.07	0.05	
A- ¹³ C ₂	14	5	9	–	13	5	8	–	168 269.790	264.3	32.1	168 270.3	6.1 ± 0.9	0.16	0.04	HCOO ¹³ CH ₃
A- ¹³ C ₁	14	7	8	+	13	7	7	+	169 803.580	280.8	28.4	169 802.4	9.1 ± 0.9	0.14	0.06	U
A- ¹³ C ₁	14	7	7	–	13	7	6	–	169 804.698	280.8	28.4	†	11.1 ± 0.9			
A- ¹³ C ₂	16	0	16	+	15	0	15	+	169 839.735	258.4	41.7	169 839.4	7.6 ± 0.9	0.22	0.06	CH ₃ ¹³ CH ₂ CN
E- ¹³ C ₂	16	–1	16		15	–1	15		169 881.101	356.9	42.0	169 880.5	8.1 ± 0.9	0.10	0.06	
E- ¹³ C ₂	14	2	12		13	2	11		171 156.971	351.0	35.9	171 157.6	5.9 ± 0.9	0.05	0.06	
E- ¹³ C ₂	18	–2	17		17	–2	16		200 012.238	382.3	46.5	200 011.0	8.9 ± 0.7	0.11	0.08	
E- ¹³ C ₂	16	3	13		15	3	12		200 350.331	372.6	40.9	200 351.0	5.9 ± 0.7	0.08	0.07	
E- ¹³ C ₁	17	–3	15		16	–3	14		201 246.113	281.9	44.4	201 244.8	8.9 ± 0.7	0.21	0.08	CH ₃ CH ₂ OH
A- ¹³ C ₁	16	4	12	+	15	4	11	+	202 078.548	278.5	40.7	202 078.1	7.7 ± 0.7	0.33	0.07	U
A- ¹³ C ₂	17	11	7	+	16	11	6	+	202 460.334	355.2	26.1	202 460.6	6.7 ± 0.7	0.15	0.06	
A- ¹³ C ₂	17	11	6	–	16	11	5	–	202 460.334	355.2	26.1	†	6.7 ± 0.7			
E- ¹³ C ₁	16	4	12		15	4	11		202 695.684	279.0	44.4	202 695.6	7.1 ± 0.7	0.25	0.08	U
A- ¹³ C ₂	17	9	8	–	16	9	7	–	202 701.664	328.6	32.4	202 701.7	6.9 ± 0.7	0.16	0.09	
A- ¹³ C ₂	17	9	9	+	16	9	8	+	202 701.650	328.6	32.4	†	6.9 ± 0.7			
A- ¹³ C ₁	18	1	17	–	17	1	16	–	202 854.699	285.1	47.6	202 854.4	7.5 ± 0.7	0.14	0.08	
E- ¹³ C ₁	18	1	17		17	1	16		203 103.686	285.3	47.8	203 099.3	13.5 ± 0.7	0.04	0.09	DCOOCH ₃
A- ¹³ C ₂	17	4	14	–	16	4	13	–	203 145.664	285.9	42.2	203 146.8	5.3 ± 0.7	0.25	0.07	SO ¹⁷ O HCCC ¹⁵ N
A- ¹³ C ₁	19	1	19	+	18	1	18	+	203 678.875	287.3	51.0	203 679.3	6.4 ± 0.7	0.16	0.09	U
A- ¹³ C ₁	19	0	19	+	18	0	18	+	203 682.196	287.3	51.0	203 683.2	5.6 ± 0.7	0.10	0.09	
E- ¹³ C ₁	19	–1	19		18	–1	18		203 734.744	287.4	51.3	203 733.1	9.5 ± 0.7	0.14	0.09	U
E- ¹³ C ₁	19	0	19		18	0	18		203 737.849	287.4	51.3	†	14.0 ± 0.7		0.09	
A- ¹³ C ₁	17	2	15	+	16	2	14	+	203 884.346	281.3	44.4	203 884.2	7.2 ± 0.7	0.23	0.08	HCOOCH ₃ $\nu_t = 1$

Table 5. continued.

Spec.	<i>J</i>	K_a	K_c	<i>p</i>	J'	K'_a	K'_c	<i>p'</i>	Calc. freq. (MHz)	E_u (K)	$S_{ij}\mu^2$ (D 2)	Obs. freq. (MHz)	v_{LSR} (km s $^{-1}$)	$T_{\text{mb}}^{\text{obs}}$ (K)	$T_{\text{mb}}^{\text{mod}}$ (K)	Blend
A- $^{13}\text{C}_2$	17	6	12	–	16	6	11	–	204 024.731	299.0	39.3	204 024.3	7.6 ± 0.7	0.09	0.06	H $^{13}\text{COOCH}_3$
A- $^{13}\text{C}_1$	17	10	8	–	16	10	7	–	205 972.338	342.4	30.3	205 972.2	7.2 ± 0.7	0.39	0.12	CH $_3\text{COOCH}_3$
A- $^{13}\text{C}_1$	17	10	7	+	16	10	6	+	205 972.338	342.4	30.3	†	7.2 ± 0.7			H $_2\text{CS}$
A- $^{13}\text{C}_1$	17	7	11	+	16	7	10	+	206 865.964	308.8	38.3	206 867.3	5.1 ± 0.7	0.04	0.06	CH $_3\text{COOCH}_3$
A- $^{13}\text{C}_1$	17	6	12	–	16	6	11	–	207 553.192	300.4	40.4	207 553.6	6.5 ± 0.7	0.14	0.07	U
A- $^{13}\text{C}_2$	19	2	18	–	18	2	17	–	210 097.941	293.7	48.9	210 097.2	8.0 ± 0.7	0.18	0.09	
E- $^{13}\text{C}_2$	19	–2	18		18	–2	17		210 345.827	392.4	49.2	210 346.0	6.8 ± 0.7	0.18	0.09	
A- $^{13}\text{C}_2$	20	0	20	+	19	1	19	+	211 082.205	296.0	8.83	211 087.2	0.0 ± 0.7	0.19	0.10	
A- $^{13}\text{C}_2$	20	1	20	+	19	1	19	+	211 085.095	296.0	52.3	†	4.1 ± 0.7			
A- $^{13}\text{C}_2$	20	0	20	+	19	0	19	+	211 087.344	296.0	52.3	†	7.3 ± 0.7			
A- $^{13}\text{C}_2$	20	1	20	+	19	0	19	+	211 090.234	296.0	8.83	†	11.4 ± 0.7			
E- $^{13}\text{C}_2$	20	0	20		19	–1	19		211 134.083	394.5	8.60	211 137.3	2.4 ± 0.7	0.24	0.09	NH $_2\text{CHO}$
E- $^{13}\text{C}_2$	20	–1	20		19	–1	19		211 136.716	394.5	52.6	†	6.1 ± 0.7			
A- $^{13}\text{C}_2$	17	3	14	–	16	3	13	–	211 372.277	284.0	43.3	211 376.0	1.8 ± 0.7	0.16	0.08	CH $_2\text{CH}^{13}\text{CN}/\text{U}$
E- $^{13}\text{C}_2$	18	2	16		17	2	15		211 377.266	388.8	46.0	†	8.8 ± 0.7			0.08
A- $^{13}\text{C}_1$	19	1	18	–	18	1	17	–	213 261.995	295.3	50.2	213 262.2	6.7 ± 0.7	0.13	0.09	
A- $^{13}\text{C}_1$	18	2	16	+	17	2	15	+	213 882.009	291.5	47.0	213 884.7	3.2 ± 0.7	0.23	0.09	$^{13}\text{CH}_3\text{CH}_2\text{CN}$
															CH $_2\text{CHCN } \nu_{11} = 2$	
E- $^{13}\text{C}_1$	20	0	20		19	–1	19		214 193.599	297.6	9.04	214 197.2	1.9 ± 0.7	0.34	0.13	
E- $^{13}\text{C}_1$	20	–1	20		19	–1	19		214 195.705	297.6	54.0	†	4.9 ± 0.7			
E- $^{13}\text{C}_1$	20	0	20		19	0	19		214 197.429	297.6	54.0	†	7.3 ± 0.7			
E- $^{13}\text{C}_1$	20	–1	20		19	0	19		214 199.535	297.6	9.04	†	10.2 ± 0.7			
A- $^{13}\text{C}_2$	18	10	9	–	17	10	8	–	214 572.059	351.5	32.9	214 572.2	6.8 ± 0.7	0.27	0.09	$^{13}\text{C}^{17}\text{O}$
A- $^{13}\text{C}_2$	18	10	8	+	17	10	7	+	214 572.060	351.5	32.9	†	6.8 ± 0.7			
E- $^{13}\text{C}_1$	17	3	14		16	3	13		215 322.039	286.0	44.6	215 324.7	3.3 ± 0.7	0.11	0.09	U
E- $^{13}\text{C}_2$	18	–4	15		17	–4	14		215 326.475	395.1	45.2	†	9.5 ± 0.7			0.08
E- $^{13}\text{C}_2$	18	–6	13		17	–6	12		217 440.211	408.2	42.5	217 441.0	6.0 ± 0.7	0.16	0.07	
A- $^{13}\text{C}_1$	18	4	15	–	17	4	14	–	218 060.270	297.8	46.2	218 057.1	11.4 ± 0.7	0.20	0.08	c-C $_3\text{H}_2$
E- $^{13}\text{C}_1$	18	8	10		17	8	9		218 648.438	330.1	39.3	218 647.0	8.9 ± 0.7	0.10	0.06	U
E- $^{13}\text{C}_1$	18	–9	10		17	–9	9		219 017.617	340.8	36.8	219 017.2	7.6 ± 0.7	0.10	0.06	
A- $^{13}\text{C}_2$	19	3	17	+	18	3	16	+	219 092.328	300.8	48.4	219 092.2	7.2 ± 0.7	0.13	0.09	
E- $^{13}\text{C}_2$	18	5	13		17	5	12		219 883.920	401.8	43.3	219 885.9	4.3 ± 0.7	0.13	0.08	CH $_2\text{CHCN } \nu_{11} = 2$
															U	
E- $^{13}\text{C}_1$	19	–3	17		18	–3	16		222 753.709	302.8	49.8	222 753.4	7.5 ± 0.7	0.09	0.09	U
E- $^{13}\text{C}_1$	18	5	13		17	5	12		224 161.641	305.0	44.4	224 160.9	7.9 ± 0.7	0.14	0.08	CH $_3\text{COOCH}_3$
E- $^{13}\text{C}_2$	18	4	14		17	4	13		225 917.084	397.1	45.7	225 917.1	7.0 ± 0.7	0.14	0.09	
A- $^{13}\text{C}_2$	19	10	10	–	18	10	9	–	226 614.150	362.4	36.4	226 614.6	6.4 ± 0.7	0.42	0.10	CH $_2\text{CHCN } \nu_{15} = 1$
A- $^{13}\text{C}_2$	19	10	9	+	18	10	8	+	226 614.152	362.4	36.4	†	6.4 ± 0.7			
E- $^{13}\text{C}_2$	19	–9	11		18	–9	10		227 459.769	448.7	39.1	227 459.6	7.3 ± 0.7	0.18	0.06	
A- $^{13}\text{C}_1$	18	4	14	+	17	4	13	+	229 246.345	299.9	46.5	229 247.1	6.0 ± 0.7	0.24	0.09	CH $_3\text{CH}_2\text{CN}$
E- $^{13}\text{C}_2$	19	6	13		18	6	12		229 294.250	419.7	45.2	229 294.6	6.5 ± 0.7	0.30	0.08	U
E- $^{13}\text{C}_2$	19	–6	14		18	–6	13		229 951.441	419.2	45.2	229 952.1	6.2 ± 0.7	0.11	0.08	

Table 5. continued.

Spec.	<i>J</i>	<i>K_a</i>	<i>K_c</i>	<i>p</i>	<i>J'</i>	<i>K'_a</i>	<i>K'_c</i>	<i>p'</i>	Calc. freq. (MHz)	<i>E_u</i> (K)	<i>S_{ij}μ²</i> (D ²)	Obs. freq. (MHz)	<i>v_{LSR}</i> (km s ⁻¹)	<i>T_{mb}^{obs}</i> (K)	<i>T_{mb}^{mod}</i> (K)	Blend
E- ¹³ C ₁	18	4	14		17	4	13		230 063.581	300.4	46.8	230 064.6	5.7 ± 0.7	0.21	0.10	U
A- ¹³ C ₁	19	14	6	-	18	14	5	-	230 100.629	427.4	23.6	230 100.8	6.8 ± 0.7	0.15	0.14	
A- ¹³ C ₁	19	14	5	+	18	14	4	+	230 100.629	427.4	23.6		†	6.8 ± 0.7		
E- ¹³ C ₂	19	-5	15		18	-5	14		230 101.552	412.2	46.0		†	8.0 ± 0.7		
A- ¹³ C ₁	19	9	11	+	18	9	10	+	230 720.161	351.4	40.1	230 719.6	7.7 ± 0.7	0.15	0.12	
A- ¹³ C ₁	19	9	10	-	18	9	9	-	230 720.299	351.4	40.1		†	7.9 ± 0.7		
A- ¹³ C ₂	22	0	22	+	21	1	21	+	231 708.149	317.7	9.76	231 709.6	5.2 ± 0.6	0.22	0.21	
A- ¹³ C ₂	22	1	22	+	21	1	21	+	231 709.053	317.7	57.7		†	6.3 ± 0.6		
A- ¹³ C ₂	22	0	22	+	21	0	21	+	231 709.768	317.7	57.7		†	7.3 ± 0.6		
A- ¹³ C ₂	22	1	22	+	21	0	21	+	231 710.673	317.7	9.76		†	8.4 ± 0.6		
A- ¹³ C ₁	20	2	18	+	19	2	17	+	234 053.346	313.5	52.3	234 054.0	6.2 ± 0.6	0.29	0.10	
E- ¹³ C ₁	22	0	22			21	-1	21	235 113.385	319.7	10.0	235 114.0	6.2 ± 0.6	0.35	0.24	
E- ¹³ C ₁	22	-1	22		21	-1	21		235 114.014	319.7	59.4		†	7.0 ± 0.6		
E- ¹³ C ₁	22	0	22		21	0	21		235 114.538	319.7	59.4		†	7.7 ± 0.6		
E- ¹³ C ₁	22	-1	22		21	0	21		235 115.167	319.7	10.0		†	8.5 ± 0.6		
E- ¹³ C ₂	20	-8	13		19	-8	12		240 214.055	449.0	44.6	240 213.9	7.2 ± 0.6	0.24	0.07	
A- ¹³ C ₂	22	1	21	-	21	1	20	-	241 080.593	327.0	56.9	241 082.0	5.2 ± 0.6	0.24	0.10	
E- ¹³ C ₁	20	-4	17		19	-4	16		241 374.048	320.9	51.9	241 373.5	7.7 ± 0.6	0.12	0.10	CH ₃ CH ₂ OCOH
E- ¹³ C ₁	22	-2	21		21	-2	20		244 776.097	329.3	58.6	244 774.9	8.5 ± 0.6	0.21	0.11	
E- ¹³ C ₁	22	1	21		21	1	20		244 800.362	329.3	58.6	244 799.9	7.5 ± 0.6	0.68	0.21	CH ₃ CH ₂ ¹³ CN H ¹³ COOCH ₃
A- ¹³ C ₂	21	9	13	+	20	9	12	+	251 115.944	373.3	45.4	251 115.9	7.1 ± 0.6	0.13	0.13	
A- ¹³ C ₂	21	9	12	-	20	9	11	-	251 116.550	373.3	45.4		†	7.8 ± 0.6		
A- ¹³ C ₂	24	0	24	+	23	1	23	+	252 327.721	341.5	10.7	252 327.2	7.6 ± 0.6	0.44	0.26	
A- ¹³ C ₂	24	1	24	+	23	0	23	+	252 328.505	341.5	10.7		†	8.5 ± 0.6		
A- ¹³ C ₂	24	1	24	+	23	1	23	+	252 328.001	341.5	63.0		†	7.9 ± 0.6		
A- ¹³ C ₂	24	0	24	+	23	0	23	+	252 328.225	341.5	63.0		†	8.2 ± 0.6		
A- ¹³ C ₂	21	7	14	-	20	7	13	-	252 689.210	352.5	49.4	252 689.8	6.3 ± 0.6	0.18	0.08	
E- ¹³ C ₂	21	7	14		20	7	13		252 703.017	451.8	49.4	252 704.8	4.8 ± 0.6	0.14	0.08	CH ₃ COOCH ₃
A- ¹³ C ₂	21	6	16	-	20	6	15	-	253 342.936	344.1	51.0	253 343.5	6.4 ± 0.6	0.15	0.09	
A- ¹³ C ₁	21	14	8	-	20	14	7	-	254 444.432	451.2	25.5	254 444.7	6.7 ± 0.6	0.15	0.07	
A- ¹³ C ₁	21	14	7	+	20	14	6	+	254 444.432	451.2	25.5		†	6.7 ± 0.6		
A- ¹³ C ₁	21	14	7	+	20	14	7	-	254 444.432	451.2	6.22		†	6.7 ± 0.6		
A- ¹³ C ₁	21	14	8	-	20	14	6	+	254 444.432	451.2	6.22		†	6.7 ± 0.6		
E- ¹³ C ₁	21	10	11		20	10	10		254 626.092	388.9	44.1	254 625.8	7.4 ± 0.6	0.22	0.06	
E- ¹³ C ₁	22	2	20		21	2	19		254 899.597	337.9	58.0	254 899.8	6.8 ± 0.6	0.15	0.11	
A- ¹³ C ₁	21	9	13	+	20	9	12	+	255 417.206	375.3	46.5	255 417.1	7.1 ± 0.6	0.07	0.14	
A- ¹³ C ₁	11	5	7	+	10	4	6	+	255 417.848	242.4	2.44		†	7.9 ± 0.6		
A- ¹³ C ₁	21	9	12	-	20	9	11	-	255 418.028	375.3	46.5		†	8.1 ± 0.6		
A- ¹³ C ₂	21	5	16	-	20	5	15	-	261 016.105	338.3	52.3	261 016.8	6.2 ± 0.6	0.43	0.10	
A- ¹³ C ₂	22	12	10	+	21	12	9	+	262 404.906	427.7	40.9	262 404.6	7.3 ± 0.6	0.18	0.10	
A- ¹³ C ₂	22	12	11	-	21	12	10	-	262 404.906	427.7	40.9		†	7.3 ± 0.6		
A- ¹³ C ₂	22	3	19	-	21	3	18	-	263 026.207	342.3	56.1	263 025.8	7.5 ± 0.6	0.14	0.10	
E- ¹³ C ₂	22	3	19		21	3	18		263 484.906	441.3	56.1	263 484.6	7.4 ± 0.6	0.10	0.11	

Table 5. continued.

Spec.	<i>J</i>	K_a	K_c	<i>p</i>	J'	K'_a	K'_c	<i>p'</i>	Calc. freq. (MHz)	E_u (K)	$S_{ij}\mu^2$ (D 2)	Obs. freq. (MHz)	v_{LSR} (km s $^{-1}$)	$T_{\text{mb}}^{\text{obs}}$ (K)	$T_{\text{mb}}^{\text{mod}}$ (K)	Blend
E- $^{13}\text{C}_1$	23	-3	21		22	-3	20		264 936.868	350.6	60.7	264 936.9	7.0 ± 0.6	0.13	0.12	
E- $^{13}\text{C}_1$	7	-7	1		6	-6	1		264 937.868	236.2	3.22	†	8.1 ± 0.6			
A- $^{13}\text{C}_1$	24	2	23	-	23	2	22	-	265 443.450	354.0	63.8	265 442.1	8.5 ± 0.6	0.11	0.11	DCOOCH ₃
A- $^{13}\text{C}_2$	22	6	17	-	21	6	16	-	265 640.606	356.9	53.7	265 640.8	6.8 ± 0.6	0.14	0.08	CH ₃ COOCH ₃
E- $^{13}\text{C}_1$	25	-1	25		24	0	24		266 482.702	356.6	11.5	266 483.3	6.3 ± 0.6	0.35	0.29	
E- $^{13}\text{C}_1$	25	0	25		24	0	24		266 482.602	356.6	67.6	†	6.2 ± 0.6			
E- $^{13}\text{C}_1$	25	0	25		24	-1	24		266 482.416	356.6	11.5	†	6.0 ± 0.6			
E- $^{13}\text{C}_1$	25	-1	25		24	-1	24		266 482.517	356.6	67.6	†	6.1 ± 0.6			
A- $^{13}\text{C}_1$	22	10	13	-	21	10	12	-	267 355.733	400.6	47.3	267 355.8	6.9 ± 0.6	0.19	0.13	
A- $^{13}\text{C}_1$	22	10	12	+	21	10	11	+	267 355.808	400.6	47.3	†	7.0 ± 0.6			
E- $^{13}\text{C}_2$	23	-4	20		22	-4	19		270 150.708	454.7	58.5	270 152.0	5.6 ± 0.6	0.17	0.11	
A- $^{13}\text{C}_2$	23	3	20	-	22	3	19	-	272 723.937	355.4	58.5	272 723.7	7.3 ± 0.6	0.15	0.10	
A- $^{13}\text{C}_2$	26	0	26	+	25	0	25	+	272 941.805	367.2	68.3	272 941.8	7.0 ± 0.5	0.17	0.27	
A- $^{13}\text{C}_2$	26	1	26	+	25	0	25	+	272 941.891	367.2	11.7	†	7.1 ± 0.5			
A- $^{13}\text{C}_2$	26	0	26	+	25	1	25	+	272 941.649	367.2	11.7	†	6.9 ± 0.5			
A- $^{13}\text{C}_2$	26	1	26	+	25	1	25	+	272 941.735	367.2	68.3	†	7.0 ± 0.5			
A- $^{13}\text{C}_2$	23	16	8	-	22	16	7	-	274 076.953	515.3	31.4	274 077.0	7.0 ± 0.5	0.11	0.05	
A- $^{13}\text{C}_2$	23	16	7	+	22	16	6	+	274 076.953	515.3	31.4	†	7.0 ± 0.5			
A- $^{13}\text{C}_2$	23	15	8	-	22	15	7	-	274 124.220	494.7	35.1	274 125.7	5.4 ± 0.5	0.21	0.06	U
A- $^{13}\text{C}_2$	23	15	9	+	22	15	8	+	274 124.220	494.7	35.1	†	5.4 ± 0.5			
E- $^{13}\text{C}_1$	23	-4	20		22	-4	19		274 172.892	358.8	60.0	274 173.3	6.6 ± 0.5	0.23	0.11	
A- $^{13}\text{C}_2$	23	11	12	-	22	11	11	-	274 666.966	425.6	47.0	274 666.7	7.3 ± 0.5	0.24	0.12	
A- $^{13}\text{C}_2$	23	11	13	+	22	11	12	+	274 666.961	425.6	47.0	†	7.3 ± 0.5			
A- $^{13}\text{C}_2$	23	10	14	-	22	10	13	-	274 998.925	411.7	49.4	274 998.3	7.7 ± 0.5	0.35	0.13	CH ₃ OCH ₃
A- $^{13}\text{C}_2$	23	10	13	+	22	10	12	+	274 999.054	411.7	49.4	†	7.9 ± 0.5			
E- $^{13}\text{C}_1$	23	3	20		22	3	19		276 849.213	358.5	60.1	276 849.6	6.5 ± 0.5	0.24	0.11	
E- $^{13}\text{C}_1$	26	-1	26		25	-1	25		276 936.143	369.9	70.3	276 934.7	8.5 ± 0.5	0.31	0.29	CH ₃ CH ₂ OH
E- $^{13}\text{C}_1$	26	0	26		25	0	25		276 936.189	369.9	70.3	†	8.6 ± 0.5			
E- $^{13}\text{C}_1$	26	0	26		25	-1	25		276 936.089	369.9	12.0	†	8.5 ± 0.5			
E- $^{13}\text{C}_1$	26	-1	26		25	0	25		276 936.244	369.9	12.0	†	8.7 ± 0.5			
E- $^{13}\text{C}_2$	24	-4	21		23	-4	20		280 723.536	468.2	61.1	280 722.7	7.9 ± 0.5	0.22	0.11	

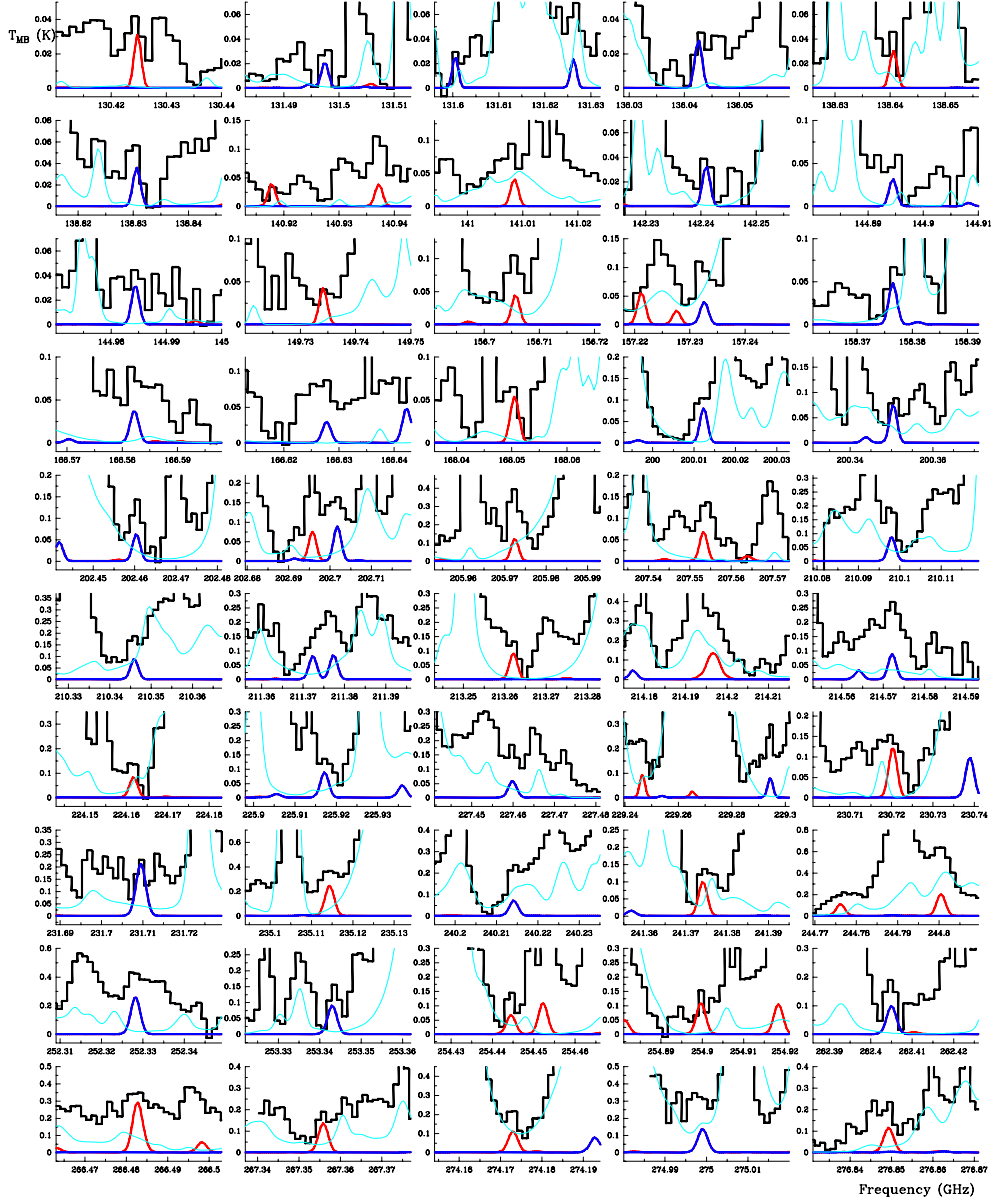


Fig. 2. Selected lines of A/E- $\text{H}^{13}\text{COOCH}_3$ $v_t = 1$ (modelled in red) and A/E- $\text{HCOO}^{13}\text{CH}_3$ $v_t = 1$ (modelled in dark blue) toward Orion-IRc2. The continuous cyan line corresponds to all lines already modelled in our previous papers except $\text{H}^{13}\text{COOCH}_3$ and $\text{HCOO}^{13}\text{CH}_3$ $v_t = 1$ (see Sect. 5.1). A v_{LSR} of 7 km s^{-1} is assumed.

has to be considered as the total intensity of the detected feature and an upper limit for the intensity of the methyl formate species in this study. Nevertheless, in Table 5 we found some values of the $T_{\text{mb}}^{\text{obs}}$ lower than those predicted by the model (synthetic spectrum $\text{HCOO}^{13}\text{CH}_3$ and $\text{H}^{13}\text{COOCH}_3$ $v_t = 1$); uncertainties in the removed baselines are the most probable source for these discrepancies. The uncertainty in the radial velocity was adopted from the spectral resolution of our data. Most unblended detected lines show a radial velocity of $\simeq 7 \text{ km s}^{-1}$, in agreement with the expected velocity for emission from the compact ridge component where organic saturated O-rich molecules have the largest abundances inside the region. In addition, most detected lines of methyl formate, its isotopologues, and its first vibrationally excited state appear at the same radial velocity (see e.g.

Carvajal et al. 2009; Margulès et al. 2010; Favre et al. 2011; Tercero et al. 2012; López et al., in prep.).

5.3. Modelling the data

To model the emission of $\text{H}^{13}\text{COOCH}_3$ and $\text{HCOO}^{13}\text{CH}_3$ $v_t = 1$ we used an excitation and radiative transfer code: MADEX (Cernicharo 2012). This time we applied LTE conditions because we lacked collisional rates for these species. Two compact ridge components ($v_{\text{LSR}} = 7 \text{ km s}^{-1}$ and $\Delta v = 3 \text{ km s}^{-1}$) are enough to model the line profiles: one at 110 K , with diameter of $15''$, and a column density of $(6 \pm 3) \times 10^{13} \text{ cm}^{-2}$ for each state (A and E) of each isotopologue, and a hotter and inner compact ridge at 250 K with a diameter of $10''$, and a column

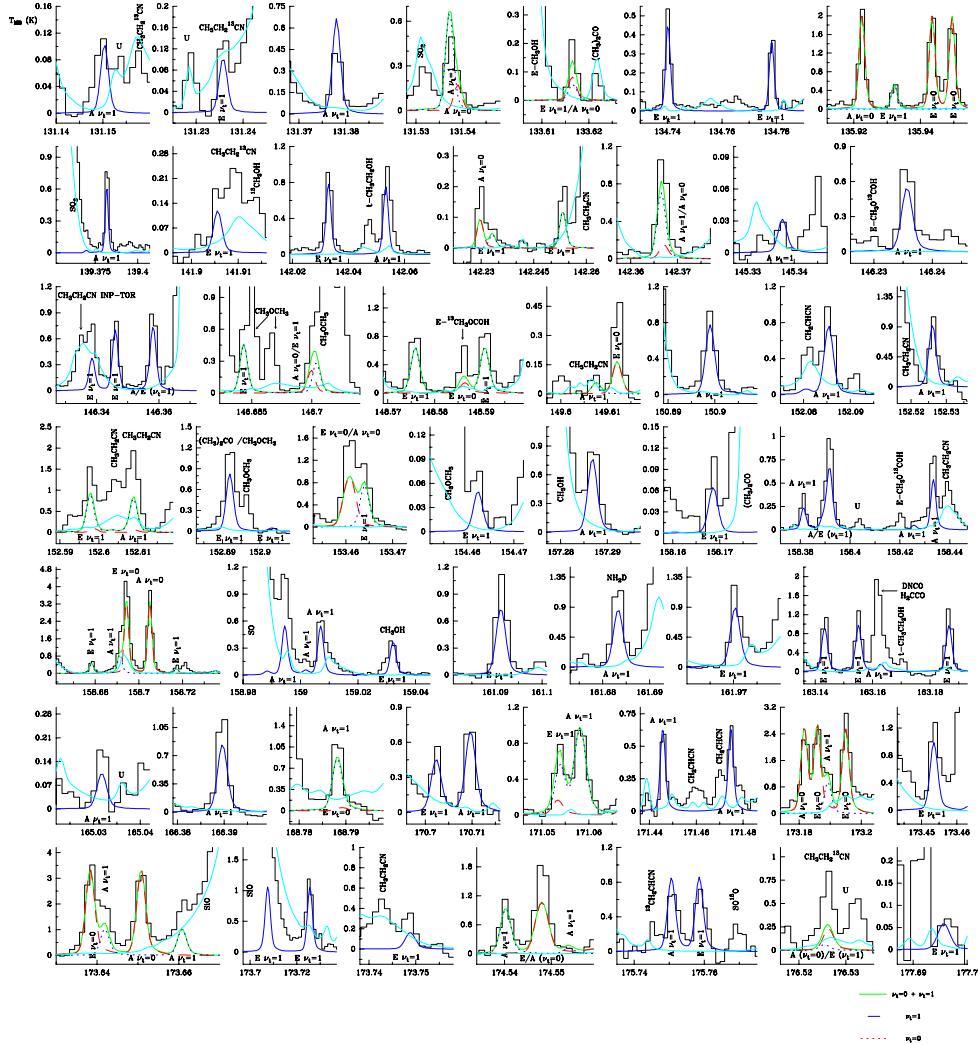


Fig. 3. Selected lines of A/E-HCOOCH₃ $\nu_t = 1$ (modelled in dark blue) toward Orion-IRc2. The dashed red line and the green continuous line correspond to methyl formate in the ground state and the sum of the emission of $\nu_t = 1$ and $\nu_t = 0$, respectively. The continuous cyan line corresponds to all lines already modelled in our previous papers except HCOOCH₃ $\nu_t = 0, 1$ (see Sect. 5.1). A v_{LSR} of 9 km s⁻¹ is assumed. The x-axis is the frequency in GHz.

density of $(6 \pm 3) \times 10^{14} \text{ cm}^{-2}$ for each state (A and E) of each isotopologue (both components are 7'' offset from the pointing position; interferometric maps show this component offset $\approx 7''$ southwest from the source I – located 0.5'' south of IRc2, Menten & Reid 1995; see e.g. Neill et al. 2013 for ALMA cycle 0 maps). The beam dilution for each line (depending on the frequency) has been also taken into account in the calculation of the emerging line intensities. The obtained synthetic spectra is shown in Fig. 2. We obtained source averaged-column densities over the source size given for each component. Uncertainties of the column density results were estimated to be between 20–30% for this line survey (see Tercero et al. 2010) taking into account errors introduced by different sources, such as the spatial overlap of the different cloud components, the modest angular resolution, or pointing errors. Nevertheless, high overlap problems add another source of uncertainty (rising to 50%) for results obtained by means of weak lines such as those of H¹³COOCH₃ and HCOO¹³CH₃ $\nu_t = 1$. All together we obtained a total column

density of $(1.4 \pm 0.7) \times 10^{15} \text{ cm}^{-2}$ for each ¹³C isotopologue of vibrationally excited methyl formate.

5.3.1. Isotope ratios

To obtain the ¹²C/¹³C ratio, we included our model for A/E-HCOOCH₃ $\nu_t = 1$ (López et al., in prep.). Figure 3 shows selected lines of methyl formate in its first vibrationally excited state in the 2 mm window (from 130 to 178 GHz). We modelled these species assuming all components listed in Table 4 and the hotter and inner compact ridge described above. The differences between the considered components with respect to the model of the ¹³C isotopologues arise because the much more stronger lines of the main isotopologue in all the spectral band (from 80 to 280 GHz) allow us to distinguish the contribution of several cloud components in the line profiles, although some of them, such as the plateau contribution, are very low. For

HCOOCH_3 $v_t = 1$ we obtained a total column density of $(1.9 \pm 0.6) \times 10^{16} \text{ cm}^{-2}$.

The column density ratio between the two vibrationally excited isotopologues (main and ^{13}C) of methyl formate yields a $^{12}\text{C}/^{13}\text{C}$ ratio between 6–35 (considering the error bars and assuming the same partition function for both species). Taking into account the weakness of the ^{13}C lines, the derived ratios are compatible with the value of $^{12}\text{C}/^{13}\text{C} \approx 35$ obtained with the column density ratios between $^{13}\text{C}-\text{HCOOCH}_3$ and HCOOCH_3 in the ground state (see Carvajal et al. 2009; Margulès et al. 2010) and agrees quite well with previous results of this ratio in Orion KL (Johansson et al. 1984; Blake et al. 1987; Demyk et al. 2007; Tercero et al. 2010; Daly et al. 2013; Esplugues et al. 2013b).

5.3.2. Vibrational temperatures

We can estimate vibrational temperatures from

$$\frac{\exp\left(-\frac{E_{v_t=1}}{T_{\text{vib}}}\right)}{f_v} = \frac{N(^{13}\text{C}-\text{HCOOCH}_3, v_t = 1)}{N(^{13}\text{C}-\text{HCOOCH}_3)}, \quad (1)$$

where $E_{v_t=1}$ is the energy of the vibrational state (187.6 K), T_{vib} is the vibrational temperature, f_v is the vibrational partition function, $N(^{13}\text{C}-\text{HCOOCH}_3, v_t = 1)$ is the column density of the vibrational state, and $N(^{13}\text{C}-\text{HCOOCH}_3)$ is the total column density of ^{13}C methyl formate. Taking into account that $N(^{13}\text{C}-\text{HCOOCH}_3) = N(\text{ground}) \times f_v$ and assuming the same partition function for these species in the ground- and the first vibrationally excited states, we only need the energy of the vibrational state and the column densities of $^{13}\text{C}-\text{HCOOCH}_3, v_t = 1$ and $^{13}\text{C}-\text{HCOOCH}_3, v_t = 0$ to derive the vibrational temperatures.

In Carvajal et al. (2009) we did not consider the hotter component of the compact ridge for column density calculations. After several works on methyl formate (Carvajal et al. 2009; Margulès et al. 2010; Tercero et al. 2012; Coudert et al. 2013; López et al., in prep.) we realize that this hotter component plays an important role in the global analysis of this molecule. In Margulès et al. (2010) we introduced a hot compact ridge to model the lines of main isotopologue of the methyl formate to properly reproduce the line profiles. After that, the study of the vibrationally excited states (this work and A. López et al., in prep.) confirms that a hot compact ridge is needed to understand the emission of this molecule. Therefore, quite strong lines such as those of $^{13}\text{C}-\text{HCOOCH}_3$ require the hot compact ridge component to obtain the best fit. Consequently, here we again modeled the emission from $\text{H}^{13}\text{COOCH}_3$ and $\text{HCOO}^{13}\text{CH}_3$ taking into account a compact ridge at a temperature of 250 K and a source size of $10''$. As in Carvajal et al. (2009), all cloud components of Table 4 were taken into account to reproduce the line profiles. Using MADEX and assuming LTE conditions, the obtained column densities for each ^{13}C isotopologue and each state (A and E) are $(2.0 \pm 0.6) \times 10^{15} \text{ cm}^{-2}$ and $(2.0 \pm 0.6) \times 10^{14} \text{ cm}^{-2}$ for the $T = 250$ K compact ridge and the $T = 110$ K compact ridge, respectively, and $(1.0 \pm 0.3) \times 10^{13} \text{ cm}^{-2}$ for the plateau, the extended ridge, and the hot core. These values yield a total column density of a factor 3 higher than obtained in Carvajal et al. (2009). This difference is mostly due to the reduced source size when we introduced the hotter component of the compact ridge.

At this point, we were ready to derive the vibrational temperatures. We assumed that both gases (ground-state and vibrationally excited) are spatially coincident, so the calculated vibrational temperatures have to be considered as lower limits. A

$T_{\text{vib}} = 156$ K was obtained for $\text{H}^{13}\text{COOCH}_3$ and $\text{HCOO}^{13}\text{CH}_3$ ($v_t = 1$) in each compact ridge component. This value is similar to the averaged kinetic temperature we adopted in this model (180 K). This result indicates that collisions are probably the main mechanism to populate the vibrationally excited levels of methyl formate.

6. Conclusion

We measured the spectra of $\text{HCOO}^{13}\text{CH}_3$ from 75 to 940 GHz. We analyzed 2881 lines from the first excited torsional states, 5728 new lines corresponding to the ground-vibrational states were also measured and added to the previous ones from Carvajal et al. (2009). The global fit of the 9455 lines, taking into account the internal rotation motion, was made using the rho-axis-method and the BELGI code. Fifty-two parameters could be determined, the global fit of both states permitted us to obtain uncorrelated values of the torsional parameters: F , V_3 , and V_6 . The value of barrier height ($V_3 = 369.93168(395) \text{ cm}^{-1}$) has been significantly improved.

Owing to this work and Carvajal et al. (2009), accurate predictions of line positions and intensities were performed. In the line survey of Orion-KL with the IRAM 30 m telescope, this permits detecting 135 spectral features in the range 80–280 GHz; there are no missing transitions in this range. This is the first detection of an excited vibrational state of a methyl formate isotopologue.

At the beginning of the line identification process of this line survey (in 2005), nearly 8000 spectral features were U lines. In 2007 we began a close collaboration between astronomers and spectroscopists to reduce the uncertainty due to unidentified lines in spectral surveys. New isotopologues of ethyl cyanide and methyl formate (Demyk et al. 2007; Margulès et al. 2009, 2010; Carvajal et al. 2009; Tercero et al. 2012; Coudert et al. 2013) and new vibrationally excited states of formamide (Motiyenko et al. 2012), ethyl cyanide (Daly et al. 2013), and vinyl cyanide (López et al. 2014) have been studied in spectroscopy laboratories and detected in Orion KL for the first time space. Altogether, we reduced 3000 of unidentified lines through these studies. At this point, we were ready to search for new molecular species, detecting methyl acetate and *gauche*-ethyl formate (Tercero et al. 2013) and *gauche*-ethyl mercaptan (Kolesniková et al. 2014) for the first time in space, and providing the tentative detection of phenol (Kolesniková et al. 2013). These new species together with the work of López et al. (in prep., about vibrationally excited CH_3OCOH and CH_3COOH) account for ≈ 1000 lines. Up to date, we have reduced 4000 of U lines in the survey of Orion KL. We expect that a large number of the still unidentified lines arise from vibrationally modes of abundant species. However, low-lying vibrationally excited states of abundant molecules such as ethyl cyanide (for example the $v_{13} = 2/v_{21} = 2$ state at $\approx 420 \text{ cm}^{-1}$) or methanol are still only poorly characterized in the laboratory, and certainly contribute to the remaining U-lines. The main goal of our studies is to provide the community with a fully analysed line survey of Orion that will constitute a template for ALMA observations of warm clouds.

Acknowledgements. M.C. acknowledges the financial support the Spanish Government through grant FIS2011-28738-C02-02, and by a joint project within the framework of a CNRS (France) and CSIC (Spain) agreement (Code No.: 2011 FR0018). J.C., A.L. and B.T. thank the Spanish MINECO for funding support from grants CSD2009-00038, AYA2009-07304, and AYA2012-32032. This work was supported by the Centre National d’Etudes Spatiales (CNES) and the Action sur Projets de l’INSU, “Physique et Chimie du Milieu Interstellaire”. This work was also performed under the ANR-08-BLAN-0054.

Appendix A: Part of the supplementary tables available at the CDS

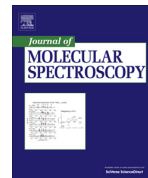
Table A.1. Assignments, observed frequencies, and calculated frequencies from the RAM fit, residuals, line strengths, and lower energy levels for methyl formate ($\text{HCOO}^{13}\text{CH}_3$) microwave transitions from $v_t = 0$ and $v_t = 1$ torsional states included in the fit with parameters of Table 2.

v'_t	Upper state ^a				Lower state ^a				Obs. Freq. (Unc.) ^b	Calc. Freq (Unc.) ^c	Obs.-Calc ^d	$S(i \rightarrow f)$ ^e	Lower energy ^f	Ref ^g	
	J'	K'_a	K'_c	p'	v'_t	J''	K''_a	K''_c							
1	50	0	50	+	1	49	0	49	+	519 745.410(30)	519 745.377(5)	0.033	137.102	560.0328	NEW B
1	51	0	51	+	1	50	0	50	+	530 000.398(30)	530 000.382(5)	0.016	22.972	577.3696	NEW B
1	52	0	52	+	1	51	0	51	+	540 252.626(30)	540 252.652(5)	-0.026	153.599	595.0485	NEW B
1	53	0	53	+	1	52	0	52	+	550 502.111(30)	550 502.133(6)	-0.022	154.358	613.0694	NEW B
1	54	0	54	+	1	53	0	53	+	560 748.773(30)	560 748.773(6)	0.000	137.761	631.4322	NEW B
1	55	0	55	+	1	54	0	54	+	570 992.512(30)	570 992.518(7)	0.003	148.615	650.1368	NEW B
1	56	0	56	+	1	55	0	55	+	581 233.298(30)	581 233.318(7)	-0.020	35.289	669.1830	NEW B
1	57	0	57	+	1	56	0	56	+	591 471.082(30)	591 471.118(8)	-0.036	181.673	688.5709	NEW B
1	58	0	58	+	1	57	0	57	+	601 705.819(30)	601 705.866(9)	-0.047	184.679	708.3002	NEW B
1	59	0	59	+	1	58	0	58	+	611 937.436(30)	611 937.510(10)	-0.074	187.823	728.3710	NEW B
1	60	0	60	+	1	59	0	59	+	622 165.944(30)	622 165.996(11)	-0.052	190.689	748.7830	NEW B
1	50	0	50		1	49	0	49		519 732.280(30)	519 732.271(5)	0.009	159.484	559.5257	NEW B
1	51	0	51		1	50	0	50		529 985.311(30)	529 985.287(6)	0.024	161.679	576.8621	NEW B
1	52	0	52		1	51	0	51		540 235.593(30)	540 235.566(6)	0.027	122.669	594.5405	NEW B
1	53	0	53		1	52	0	52		550 483.081(30)	550 483.060(6)	0.021	114.755	612.5608	NEW B
1	54	0	54		1	53	0	53		560 727.716(30)	560 727.709(6)	0.007	172.372	630.9230	NEW B
1	55	0	55		1	54	0	54		570 969.450(30)	570 969.463(7)	-0.013	175.587	649.6268	NEW B
1	56	0	56		1	55	0	55		581 208.238(30)	581 208.268(7)	-0.030	178.795	668.6723	NEW B
1	57	0	57		1	56	0	56		591 444.057(30)	591 444.072(8)	-0.015	182.011	688.0593	NEW B
1	58	0	58		1	57	0	57		601 676.811(30)	601 676.819(9)	-0.008	185.223	707.7878	NEW B
1	59	0	59		1	58	0	58		611 906.456(30)	611 906.456(9)	0.000	188.431	727.8576	NEW B
1	60	0	60		1	59	0	59		622 132.891(30)	622 132.935(10)	-0.044	191.656	748.2686	NEW B

Notes. ^(a) Upper and lower state quantum numbers are indicated by ' and " respectively. Torsion-rotation levels of A species have a "parity" label; levels of E species have a signed K_a value (Herbst et al. 1984). ^(b) Observed $v_t = 0$ and 1 microwave transitions in MHz, with estimated uncertainties in parentheses (in kHz). ^(c) Calculated line frequency in MHz with calculated uncertainty in kHz. ^(d) Differences among the experimental and computed frequencies. ^(e) Calculated line strengths in D**2 (for details of the calculation procedure, see Sect. 4). ^(f) Lower state energy (cm^{-1}) referred to the $J = K_a = 0$ A-species energy level taken as the zero of the energy (zero-point torsional energy: 71.0704 cm^{-1}). ^(g) Sources of data are explained in footnote b of Table 1. Blended lines are indicated with a capital letter B.

References

- Bell, T. A., Cernicharo, J., Viti, S., et al. 2014, *A&A*, 564, A114
- Blake, G. A., Sutton, E. C., Masson, C. R., & Philips, T. H. 1987, *ApJ*, 315, 621
- Brown, R. D., Crofts, J. G., Gardner, F. F., et al. 1975, *ApJ*, 197, L29
- Churchwell, E., & Winnewisser, G. 1975, *A&A*, 45, 229
- Carvajal, M., Willaert, F., Demaison, J., & Kleiner, I. 2007, *J. Mol. Spectrosc.*, 246, 158
- Carvajal, M., Margulès, L., Tercero, B., et al. 2009, *A&A*, 500, 1109
- Carvajal, M., Kleiner, I., & Demaison, J. 2010, *ApJS*, 190, 315
- Cernicharo 1985, Internal IRAM report (Granada: IRAM)
- Cernicharo, J. 2012, in ECLA-2011: Proc. of the European Conf. Laboratory Astrophysics, EAS Publ. Ser., eds C. Stehl, C. Joblin, & L. d'Hendecourt (Cambridge: Cambridge Univ. Press), 251
- Cernicharo, J., Tercero, B., Fuente, A., et al. 2013, *ApJ*, 771, L10
- Comito, C., Schilke, P., Phillips, T. G., et al. 2005, *ApJS*, 156, 127
- Coudert, L. H., Drouin, B. J., Tercero, B., et al. 2013, *ApJ*, submitted
- Curl, R. F. 1959, *J. Chem. Phys.*, 30, 1529
- Daly, A. M., Bermúdez, C., López, A., et al. 2013, *ApJ*, 768, 81
- Demyk, K., Mäder, H., Tercero, B., et al. 2007, *A&A*, 466, 255
- Demyk, K., Włodarczak, G., & Carvajal, M. 2008, *A&A*, 489, 589
- Esplugues, G. B., Tercero, B., Cernicharo, J., et al. 2013, *A&A*, 556, A143
- Esplugues, G. B., Cernicharo, J., Viti, S., et al. 2013, *A&A*, 559, A51
- Favre, C., Despois, D., Brouillet, N., et al. 2011, *A&A*, 532, A32
- Favre, C., Carvajal, M., Field, D., et al. 2014, *ApJ*, submitted
- Groner, P. 1997, *J. Chem. Phys.*, 107, 4483
- Groner, P. 2012, *J. Mol. Spectrosc.*, 278, 52
- Haykal, I., Motiyenko, R. A., Margulès, L., & Huet, T. R. 2013a, *A&A*, 549, A96
- Haykal, I., Margulès, L., Motiyenko, R. A., et al. 2013b, *ApJ*, 777, 120
- Herbst, E., Messer, J. K., De Lucia, F. C., & Helminger, P. 1984, *J. Mol. Spectrosc.*, 108, 42
- Hougen, J. T., Kleiner, I., & Godefroid, M. 1994, *J. Mol. Spectrosc.*, 163, 559
- Ilyushin, V., Alekseev, E. A., Dyubko, S. F., & Kleiner, I. 2003, *J. Mol. Spectrosc.*, 220, 170
- Ilyushin, V., Kleiner, I., & Lovas, F. J. 2008, *J. Phys. Chem. Ref. Data*, 37, 97
- Ilyushin, V. V., Kryvda, A., & Alekseev, E. 2009, *J. Mol. Spectrosc.*, 255, 32
- Johansson, L. E. B., Andersson, C., Elldér, J., et al. 1984, *A&A*, 130, 227
- Kirtman, B. 1962, *J. Chem. Phys.*, 37, 2516
- Kleiner, I. 2010, *J. Mol. Spectrosc.*, 260, 1
- Kleiner, I., Hougen, J. T., Grabow, J. U., et al. 1996, *J. Mol. Spectrosc.*, 179, 41
- Kobayashi, K., Ogata, K., Tsunekawa, S., & Takano, S. 2007, *ApJ*, 657, L17
- Kolesniková, L., Daly, A. M., Alonso, J. L., Tercero, B., & Cernicharo, J. 2013, *J. Mol. Spectrosc.*, 289, 13
- Kolesniková, L., Tercero, B., & Cernicharo, J. 2014, *ApJ*, 784, L7
- Lees, R. M., & Baker, J. G. 1968, *J. Chem. Phys.*, 48, 5299
- Lin, C. C., & Swalen, J. D. 1959, *Rev. Mod. Phys.*, 31, 841
- López, A., Tercero, B., Kisiel, Z., et al. 2014, *A&A*, submitted
- Maeda, A., Medvedev, I. R., De Lucia, F. C., & Herbst, E. 2008a, *ApJS*, 175, 138
- Maeda, A., De Lucia, F. C., & Herbst, E. 2008b, *J. Mol. Spectrosc.*, 251, 293
- Margulès, L., Motiyenko, R. A., Demyk, K., et al. 2009, *A&A*, 493, 565
- Margulès, L., Huet, T. R., Demaison, J., et al. 2010, *ApJ*, 714, 1120
- Menten, K. M., & Reid, M. J. 1995, *ApJ*, 445, L157
- Motiyenko, R. A., Margulès, L., Alekseev, E. A., Guillemin, J.-C., & Demaison, J. 2010, *J. Mol. Spectrosc.*, 264, 94.
- Motiyenko, R. A., Tercero, B., Cernicharo, J., & Margulès, L. 2012, *A&A*, 548, A71
- Neill, J. L., Crockett, N. R., Bergin, E. A., Pearson, J. C., & Xu, L.-H. 2013, *ApJ*, 777, 85
- Oesterling, L. C., Ferguson, D. W., Herbst, E., & De Lucia, F. C. 1995, *J. Mol. Spectrosc.*, 172, 469
- Pardo, J. R., Cernicharo, J., & Serabyn, E. 2001, *IEEE Trans. Antennas and Propagation*, 49, 12
- Persson, C. M., Olofsson, A. O. H., Koning, N., et al. 2007, *A&A*, 476, 807
- Schilke, P., Benford, C. J., Hunter, T. R., Lis, D. C., & Philips, T. G. 2001, *ApJS*, 132, 281
- Tercero, B. 2012, Ph.D., Univ. Complutense de Madrid
- Tercero, B., Pardo, J. R., Cernicharo, J. R., & Goicoechea, J. R. 2010, *A&A*, 517, A96
- Tercero, B., Vincent, L., Cernicharo, J., Viti, S., & Marcelino, N. 2011, *A&A*, 528, A26
- Tercero, B., Margulès, L., Carvajal, M., et al. 2012, *A&A*, 538, A119
- Tercero, B., Kleiner, I., Cernicharo, J., et al. 2013, *ApJ*, 770, L13
- Tudorie, M., Ilyushin, V., Vander Auwera, J., et al. 2012, *J. Chem. Phys.*, 137, 064304
- Willaert, F., Møllendal, H., Alekseev, E., et al. 2006, *J. Mol. Struct.*, 795, 4
- Takano, S., Sakai, Y., Kakimoto, S., Sasaki, M., & Kobayashio, K. 2012, *PASJ*, 64, 89



Spectroscopy of the ground, first and second excited torsional states of acetaldehyde from 0.05 to 1.6 THz



I.A. Smirnov^a, E.A. Alekseev^a, V.V. Ilyushin^{a,*}, L. Margulés^b, R.A. Motiyenko^b, B.J. Drouin^c

^a Institute of Radio Astronomy of NASU, Chernovopravorna st. 4, 61002 Kharkov, Ukraine

^b Laboratoire de Physique des Lasers, Atomes et Molécules, UMR CNRS 8523, Université de Lille 1, F-59655 Villeneuve d'Ascq, France

^c Jet Propulsion Laboratory, California Institute of Technology, 4800, Oak Grove Drive, Pasadena, CA 91109-8099, USA

ARTICLE INFO

Article history:

Received 30 September 2013

In revised form 15 November 2013

Available online 27 November 2013

Keywords:

Acetaldehyde

Submillimeter wave spectrum

THz frequency range

Methyl top internal rotation

Rho axis method

ABSTRACT

We present a new global study of the millimeter wave, submillimeter wave and THz spectra of the lowest three torsional states of acetaldehyde (CH_3CHO). New measurements have been carried out between 0.05 and 1.62 THz using three different spectrometers in IRA NASU (Ukraine), PhLAM Lille (France), and JPL (USA). The new data involving torsion–rotation transitions with J up to 66 and K_a up to 22 were combined with previously published measurements and fitted using the rho-axis-method torsion–rotation Hamiltonian. The final fit used 109 parameters to give an overall weighted root-mean-square deviation of 0.69 for the dataset consisting of 8748, 6959, and 4524 transitions belonging, respectively, to the ground, first, and second excited torsional states and 1481 $\Delta\nu_t \neq 0$ FIR transitions belonging to the torsional $\nu_t = 0 \rightarrow 1$ and $1 \rightarrow 2$ bands of the molecule. This investigation presents more than a twofold expansion in the J quantum number and almost fourfold expansion in the frequency range coverage for the acetaldehyde rotational spectrum.

© 2013 Elsevier Inc. All rights reserved.

1. Introduction

The acetaldehyde molecule (CH_3CHO) is ubiquitous in the interstellar medium of our galaxy and has been observed in the cold molecular clouds [1], translucent molecular clouds [2] as well as toward hot cores [3] and star-forming regions [4]. Recently it was also detected in the disk of a high redshift ($z = 0.89$) spiral galaxy located in front of the quasar PKS 1830-211 [5]. Due to its dense and complex spectrum, large dipole moment and a number of low-lying torsional states it is considered to be a “weed” molecule for radio astronomy observations. Previous work on the lowest three torsional states of the acetaldehyde spectrum resulted in publication of the predictions of acetaldehyde transition frequencies in the range from 900 MHz to 500 GHz with rotational quantum number cutoff of $J \leq 26$ and $K_a \leq 14$ [6]. Extension of the frequency range coverage into the submillimeter and THz frequency ranges is prompted by the new telescopes in the submillimeter wave range which opened a new domain of frequencies from 0.3 to 5 THz for radio astronomy observations. Here the three main projects are, the satellite based project Herschel (<http://astro.estec.esa.nl/hereschel/>), the airplane based project SOFIA (<http://www.sofia.usra.edu/>), and the ground based project ALMA (<http://www.eso.org/projects/alma/>) in Chile.

One more source of motivation is provided by an interesting pure spectroscopic problem of theoretical description of an isolated small-amplitude vibration state embedded in a bath of dark states. The lowest small-amplitude vibration in acetaldehyde (CH_3CHO) is ν_{10} mode at 509 cm^{-1} which is rather well separated from other small-amplitude vibrational states in acetaldehyde. Since the bath states at these energies correspond to torsion–rotation states only, the detail analysis of the ν_{10} vibrational state may provide an excellent example of an isolated small-amplitude vibration state embedded in a bath of dark states, which in fact are not so “dark” because they may be observed using methods of conventional absorption spectroscopy in view of moderate excitation energies. Whereas the first attempt to attack this spectroscopic problem using the rho-axis-method (RAM) approach provided some insight into existing difficulties the obtained fit is far from being satisfactory [7]. Since we plan to revisit this problem in the nearest future, the current study is, in part, aimed at a full understanding of the ground and lowest excited torsional states at high rotational quantum numbers. This plan will certainly help to reduce confusion for subsequent assignment of the observed spectrum of the ν_{10} vibrational state.

The rotational spectrum of the acetaldehyde molecule was the subject of a number of investigations with the first experimental work being published in 1956 [8]. We base our analysis on the results obtained by I. Kleiner and coworkers in a series of works [9–14,6] where the RAM approach was applied to the analysis of

* Corresponding author. Fax: +380 57 706 1415.

E-mail address: ilyushin@rian.kharkov.ua (V.V. Ilyushin).

the torsion–rotation spectra of acetaldehyde. Although the data up to the fourth excited torsional state were obtained [14] we limit our current work to the lowest three torsional states $\nu_t = 0, 1, 2$ of the molecule, since in our current study we are mainly interested in the expansion of the rotational quantum number range and frequency range for those torsional states which are of the primary interest for the astronomical applications.

In the current work we present a new study of the acetaldehyde spectrum that covers the frequency range from 49 GHz to 1.6 THz and the range of rotational quantum numbers up to $J \leq 66$ and $K_a \leq 22$. This presents more than a twofold expansion in the J quantum number and almost fourfold expansion in the frequency range coverage for the acetaldehyde rotational spectrum. The new dataset was analyzed using the RAM approach which was successfully applied previously to the analysis of acetaldehyde spectrum [6,13,14] and a fit within experimental error has been obtained. Rather high values of rotational quantum numbers provide an opportunity to test further the performance of the RAM approach in the case of highly excited rotational states, the question which has been addressed by us in one of our recent publications on acetic acid spectrum [15].

The rest of the paper is organized as follows. Section 2 gives a brief description of the three different spectrometers in IRA NASU (Ukraine), PhLAM Lille (France), and JPL (USA) used in our study. Section 3 provides the details on the dataset treated in our study as well as describes obtained fitting results which are then discussed in Section 4. Section 5 presents a summary of obtained results.

2. Experimental details

The absorption spectrum of acetaldehyde at the low-frequency range of current investigation (49–149.3 GHz) was recorded using the automated spectrometer of Institute of Radio Astronomy of NASU [16]. The synthesis of the frequencies in the millimeter wave range is carried out by a two-step frequency multiplication of a reference synthesizer in two phase-lock-loop (PLL) stages. The reference synthesizer is a computer-controlled direct digital synthesizer (DDS AD9851), the output is up-converted into the frequency range from 385 to 430 MHz. At the first multiplication stage a klystron operating in the 3400–5200 MHz frequency range with a narrowband (~ 1 kHz) PLL system is used. At the second multiplication stage, an Istok backward wave oscillator (BWO) is locked to a harmonic of the klystron. A set of BWOs gives an opportunity to cover the frequency range from 49 to 149 GHz. The uncertainty of the measurements was estimated to be 10 kHz for a relatively strong isolated line ($S/N > 10$), 30 kHz for weak lines ($2 < S/N < 10$) and 100 kHz for very weak lines ($S/N < 2$).

The measurements in the medium part of the range under investigation (150–950 GHz) were performed using the Lille spectrometer [16]. The frequency ranges: 150–322, 400–533 and 760–950 GHz were covered with solid state multiplied sources. The frequency of the Agilent synthesizer (12.5–17.5 GHz) was first multiplied by six and amplified by a VDI AMC-10 active sextupler, providing the output power of +14 dBm in the W-band range (75–110 GHz). This power is high enough to use passive Schottky multipliers (X2, X3, X5, X6, X9) from Virginia Diodes Inc. in the next stage of the frequency multiplication chain. In the frequency range from 580 to 660 GHz a fast scan spectrometer was applied. As a radiation source an Istok BWO is used. The BWO was phase-locked to a harmonic of Agilent E8257D synthesizer which provided large-step (~ 100 MHz) frequency sweep. A high-resolution fast frequency scan is provided by a direct digital synthesizer, which is used as a source of intermediate frequency (IF) for the BWO's

PLL. Estimated uncertainties for measured line frequencies are 30 kHz, 50 kHz, and 100 kHz depending on the observed S/N ratio and the frequency range.

Measurements from Jet Propulsion Laboratory (JPL) were done with a spectrometer utilizing a microwave synthesizer and amplifier–multiplier chains [17]. The measurements were done in a survey mode at room temperature in the following frequency windows: 950–1059.9 GHz, 1.060–1.205 THz and 1.576–1.626 THz. Estimated uncertainties are 100 kHz and 200 kHz depending on the S/N ratio observed.

3. Spectral analysis and fit

We started our analysis from the results of Refs. [6,13] where the dataset consisting of 3108 transitions with $J \leq 26$ and $K_a \leq 14$ was fitted using 48 parameters of the RAM Hamiltonian and weighted standard deviation of 1.06 was achieved. As the first step we have refitted this dataset with the RAM36 program [18] (in the previous study [6,13] BELGI code [19] was used), which implements a general expression for the RAM Hamiltonian in the following form:

$$H = \frac{1}{2} \sum_{pqkstl} B_{pqkstl} [J_x^{2p} J_z^q J_x^n J_y^l J_z^k p_z^s \cos(3t\alpha) \sin(3l\alpha) + \sin(3l\alpha) \\ \times \cos(3t\alpha) p_y^s J_y^k J_x^n J_z^q J_x^{2p}] \quad (1)$$

where the B_{pqkstl} are fitting parameters; p_z is the angular momentum conjugate to the internal rotation angle α ; J_x, J_y, J_z are projections on the x, y, z axes of the total angular momentum J . In the case of C_{3v} top and C_s frame (as it is appropriate for acetaldehyde) allowed terms in the torsion–rotation Hamiltonian must be totally symmetric in the group G_6 (and also they must be Hermitian and invariant to the time reversal operation). Whereas more detailed description of the RAM36 code can be found in [15,18] here we would like to mention the main arguments in favor of moving to the RAM36 code platform in the current study of the acetaldehyde spectrum: (i) the opportunity to choose almost any symmetry allowed term in the Hamiltonian (by choosing appropriate set of k, n, p, q, l, s, t integer indices in Eq. (1)), and (ii) enhanced calculation performance in comparison with BELGI code [19]. The latter was achieved due to special optimization of the RAM36 code [15].

One of the consequences of moving to the RAM36 code platform was a change in the quantum labeling scheme. The labeling scheme after the second diagonalization step is somewhat different from the labeling used in the previous RAM studies of acetaldehyde spectrum [6,13]. The readers are referred to Ref. [15] where the analogous change in labeling scheme is discussed in more detail for the case of the acetic acid spectrum study. In brief, our scheme begins by using eigenfunction composition to determine the torsional state to which a particular level belongs, and then uses the usual asymmetric-rotor energy ordering scheme to assign rotational K_a, K_c labels within a given torsional state. Thus we do not use a signed value of K_a for the E type levels and do not use “parity” labels for the A type levels but we do determine A_1/A_2 symmetry species in G_6 of A type levels by calculating the $(23)^*$ expectation value. Like in the case of acetic acid [15] some labeling problems were encountered due to a high level of inter-torsional interactions when even small changes in the parameter values necessitate the reassignment of several high- J transitions. The source of this problem is nearly equal mixing of different torsional basis functions in the eigenvector composition of multiple eigenstates. Almost equal mixing means that even small change in the parameter set may shift the relative maximum in eigenvector composition from one torsional state to another. Since ν_t number is determined from the relative maximum in eigenvector composi-

Table 1Statistics of the data set for the global fit to $\nu_t = 0, 1, 2$ torsional states of acetaldehyde.

Category ^a	# of transitions ^c	RMS ^d	Category ^a	# of transitions ^c	RMS ^d
$\nu_t = 0-0$	8748	0.110 MHz	$\Delta\nu_t$	1481	0.00025 cm ⁻¹
$\nu_t = 1-1$	6959	0.122 MHz	A type	9675	0.119 MHz
$\nu_t = 2-2$	4522	0.097 MHz	E type	10554	0.103 MHz
$\nu_t = 2-2$	2	0.00016 cm ⁻¹			
Unc. ^b	# of lines ^c	RMS ^d	Unc. ^b	# of lines ^c	RMS ^d
0.004 MHz	11	0.0044 MHz	0.080 MHz	55	0.0658 MHz
0.010 MHz	1423	0.0090 MHz	0.100 MHz	6534	0.0635 MHz
0.020 MHz	61	0.0231 MHz	0.150 MHz	1362	0.0960 MHz
0.030 MHz	3056	0.0183 MHz	0.200 MHz	1756	0.1618 MHz
0.040 MHz	45	0.0186 MHz	0.400 MHz	121	0.1804 MHz
0.050 MHz	3623	0.0338 MHz	0.990 MHz	377	0.5788 MHz
0.070 MHz	128	0.0617 MHz	0.00035 cm ⁻¹	678	0.00026 cm ⁻¹

^a The transitions are grouped first by torsional quantum number ν_t , and then by symmetry species. Maximum values of J and K_a included in the fit for the ground, first and second excited torsional states $J_{\max}^{\text{obs}}/K_a^{\text{max}} = 66/22, 65/19, 65/17$ respectively.

^b Data are grouped by their assigned uncertainties in the fit. Weights used for all lines in the fit are $1/(\text{unc.})^2$.

^c The number of transitions or measured lines in each category included in the least squares fit.

^d Root-mean-square deviations from the global fit.

tion the unstable ν_t determination may occur for several states. These labeling problems do not affect Hamiltonian parameter values, since after reassignment the problematic line frequencies remain in the dataset and only the energy difference between eigenvalues (with particular ordinal numbers in the diagonalized Hamiltonian matrix) is what is relevant to the parameter values.

The new measurements were assigned going up in frequency starting from the IRA NASU measurements in the 49–149 GHz frequency range. The assignments were done in parallel for all three torsional states under consideration since previous studies [6,13] provided rather good starting predictions. The Lille measurements were assigned in the second turn whereas JPL THz measurements were assigned last as they provide the highest values of rotational quantum number J accessed in the current study. Whenever it was possible we have replaced the old measurements (see [13] and references therein) with the new more accurate ones. Certainly, the assignment process included numerous cycles of refinement of the parameter set while the new data were gradually added.

As a separate step in preparation of the final dataset treated in this study we performed a special analysis of the FIR data [13] available for the torsional bands of acetaldehyde spectrum. In this process it was found that the rms deviation for the FIR data may be significantly reduced if the data set is augmented with missing transition partners in the blends. This procedure does not change the number of FIR line frequencies fitted, but it does change the number of transitions included in the fit. Since we treat blends using an intensity-weighted average of calculated (but experimentally unresolved) transition frequencies such augmenting by partners in blends provides an opportunity to better reproduce the observed spectrum and to reduce significantly the rms deviation for this group of data up to a level that let us to put original experimental uncertainty of 0.00035 cm^{-1} for all FIR measurements used in the fit [9]. In the intensity calculations used for intensity-weighted averaging of blended transition frequencies we set the temperature to be 203 K for the FIR data [9] and 300 K for the microwave data. All measured frequencies were weighted in the least squares fit (as usual) by the reciprocal of measurement uncertainty squared.

A global fit of the rotational transitions belonging to the three lowest torsional states of acetaldehyde combined with previously published data has been carried out using the RAM approach. The fit chosen as the “best” uses a model consisting of 109 parameters and provides the weighted root-mean-square deviation of 0.69 for the fit of 18552 microwave and 678 FIR line frequencies with $J \leq 66$ and $K_a \leq 22$. We note in passing that this fit was ob-

tained with 21 torsional basis functions used at the first diagonalization step and 9 torsional basis functions used at the second diagonalization step. The fitting results are summarized in Table 1. In comparison with previous results [6,13] we have expanded both the frequency range coverage by going up in frequency from 417.2 GHz to 1.6 THz and the rotational quantum number coverage by going up from $J \leq 26$ and $K_a \leq 14$ to $J \leq 66$ and $K_a \leq 22$.

Fig. 1 gives an illustration of our current understanding of the acetaldehyde spectrum around 795 GHz in which observed and predicted spectra with our current model are compared. In this region the Q series of $K_a = 9 \leftarrow 8$ transitions for different torsional substates may be easily identified as it is indicated at the top panel of the figure that corresponds to the predicted spectrum. It is seen that the majority of strong lines are assigned and well predicted by our current model although a number of rather strong unassigned lines presumably belonging to the higher excited states still may be found in the experimental spectrum.

Table 2 presents the values for the final set of torsion–rotation parameters used in our model that provide the fit of the available data set with the weighted root-mean-square (wrms) deviation of 0.69. The final set of the parameters converged perfectly in all three senses: (i) the relative change in the wrms deviation of the fit at the last iteration was about 10^{-8} ; (ii) the corrections to the parameter values generated at the last iteration are less than 10^{-4} of the calculated parameter confidence intervals; (iii) the changes generated at the last iteration in the calculated frequen-

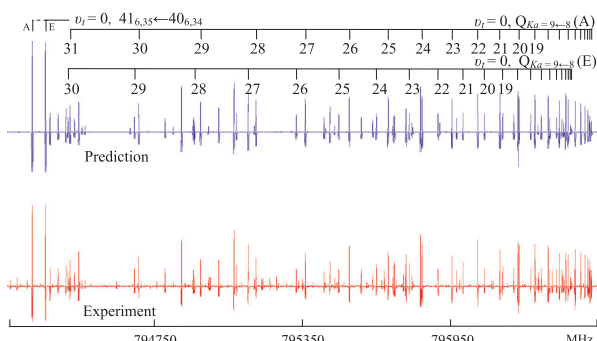


Fig. 1. Observed and predicted spectra of acetaldehyde in the range 794.1–796.5 GHz.

Table 2
Fitted parameters of the RAM Hamiltonian for acetaldehyde molecule.

Operator ^a	n_{op}	$t_{op}r_{op}$ ^b	Parameter ^c	Value ^d (cm ⁻¹)
p_x^2		2_{20}	F	7.56708175(35)
$(\frac{1}{2})(1 - \cos(3\alpha))$		2_{20}	V_3	407.59768(20)
p_aP_a		2_{11}	ρ	0.328632673(20)
P_a^2		2_{02}	A_{RAM}	1.884881309(61)
P_b^2		2_{02}	B_{RAM}	0.348706489(16)
P_c^2		2_{02}	C_{RAM}	0.3031840478(44)
$\{P_a, P_b\}$		2_{02}	D_{ab}	-0.122669037(94)
$(\frac{1}{2})(1 - \cos(6\alpha))$		4_{40}	V_6	-11.63964(50)
p_x^4		4_{40}	F_m	-0.424416(38) $\times 10^{-3}$
$p_x^2P_a$		4_{31}	ρ_m	-0.832163(52) $\times 10^{-3}$
$P^2(1 - \cos(3\alpha))$		4_{22}	V_{3J}	0.5577894(41) $\times 10^{-3}$
$P_a^2(1 - \cos(3\alpha))$		4_{22}	V_{3K}	-0.19313906(98) $\times 10^{-1}$
$(P_b^2 - P_c^2)(1 - \cos(3\alpha))$		4_{22}	V_{3bc}	0.2114597(52) $\times 10^{-3}$
$(\frac{1}{2})\{P_a, P_b\}(1 - \cos(3\alpha))$		4_{22}	V_{3ab}	0.4235363(70) $\times 10^{-2}$
$p_a^2P^2$		4_{22}	F_j	-0.291704(53) $\times 10^{-5}$
$p_a^2P_a^2$		4_{22}	F_K	-0.9824545(30) $\times 10^{-3}$
$p_a^2(P_b^2 - P_c^2)$		4_{22}	F_{bc}	0.14720(12) $\times 10^{-5}$
$(\frac{1}{2})\{P_a, P_c\}\sin(3\alpha)$		4_{22}	D_{3ac}	-0.1405503(49) $\times 10^{-1}$
$(\frac{1}{2})\{P_b, P_c\}\sin(3\alpha)$		4_{22}	D_{3bc}	0.59173(13) $\times 10^{-3}$
$p_aP_aP^2$		4_{13}	ρ_j	0.958253(42) $\times 10^{-5}$
$p_aP_a^3$		4_{13}	ρ_K	-0.571407(12) $\times 10^{-3}$
$(\frac{1}{2})\{P_a, (P_b^2 - P_c^2)\}p_z$		4_{13}	ρ_{bc}	-0.5536(12) $\times 10^{-6}$
$-P^4$		4_{04}	A_J	0.3244101(54) $\times 10^{-6}$
$-P^2P_a^2$		4_{04}	A_{JK}	-0.581770(50) $\times 10^{-5}$
$-P_a^4$		4_{04}	A_K	0.1308173(26) $\times 10^{-3}$
$-2P^2(P_b^2 - P_c^2)$		4_{04}	δ_j	0.778472(23) $\times 10^{-7}$
$\{-P_a^2, (P_b^2 - P_c^2)\}$		4_{04}	δ_K	0.94268 (17) $\times 10^{-6}$
$\{P_a, P_b\}P^2$		4_{04}	D_{abj}	0.867443(32) $\times 10^{-6}$
$\{P_a^3, P_b\}$		4_{04}	D_{abk}	0.30498(25) $\times 10^{-5}$
$(\frac{1}{2})(1 - \cos(9\alpha))$		6_{60}	V_9	-0.20318(11)
p_z^6		6_{60}	F_{mm}	-0.5066(16) $\times 10^{-6}$
$p_z^5P_a$		6_{51}	ρ_{mm}	-0.7147(34) $\times 10^{-6}$
$P^2(1 - \cos(6\alpha))$		6_{42}	V_{6J}	0.557997(73) $\times 10^{-4}$
$P_a^2(1 - \cos(6\alpha))$		6_{42}	V_{6K}	-0.37191(19) $\times 10^{-3}$
$(\frac{1}{2})\{P_a, P_b\}(1 - \cos(6\alpha))$		6_{42}	V_{6ab}	-0.13638(10) $\times 10^{-3}$
$p_z^2P^2$		6_{42}	F_{mj}	-0.1259(18) $\times 10^{-9}$
$p_z^2P_a^2$		6_{42}	F_{mk}	-0.1712(36) $\times 10^{-6}$
$p_z^2(P_b^2 - P_c^2)$		6_{42}	F_{mbc}	0.1197(22) $\times 10^{-8}$
$(\frac{1}{2})\{P_b, P_c\}\sin(6\alpha)$		6_{42}	D_{6bc}	-0.72949(57) $\times 10^{-4}$
$(\frac{1}{2})\{P_a, P_c\}\sin(6\alpha)$		6_{42}	D_{6ac}	0.46097(67) $\times 10^{-3}$
$(\frac{1}{2})\{P_a, P_c, p_z^2, \sin(3\alpha)\}$		6_{42}	D_{3acm}	-0.3178(66) $\times 10^{-5}$
$p_z^2P_a^3$		6_{33}	ρ_{mk}	0.2946(23) $\times 10^{-6}$
$p_z^2P_aP^2$		6_{33}	ρ_{mj}	-0.5306(26) $\times 10^{-8}$
$(\frac{1}{2})\{P_a, P_b, P_c, p_z, \sin(3\alpha)\}$		6_{33}	ρ_{3bc}	0.47689(54) $\times 10^{-5}$
$(\frac{1}{2})\{P_a, (P_b^2 - P_c^2)\}p_z^3$		6_{33}	ρ_{mbc}	0.4347(38) $\times 10^{-8}$
$P^4(1 - \cos(3\alpha))$		6_{24}	V_{3Jl}	-0.77602(42) $\times 10^{-8}$
$P_a^4(1 - \cos(3\alpha))$		6_{24}	V_{3KK}	0.115646(94) $\times 10^{-5}$
$p_z^2P_a^4$		6_{24}	F_{KK}	0.30324(86) $\times 10^{-6}$
$P^2(P_b^2 - P_c^2)(1 - \cos(3\alpha))$		6_{24}	V_{3bcJ}	-0.17920(30) $\times 10^{-8}$
$(\frac{1}{2})\{P_a^3, P_c\} \sin(3\alpha)$		6_{24}	D_{3acK}	0.1246(10) $\times 10^{-5}$
$p_z^2P^2P_a^2$		6_{24}	F_{jk}	-0.6904(18) $\times 10^{-8}$
$(\frac{1}{2})\{P_a, P_c\}P^2 \sin(3\alpha)$		6_{24}	D_{3acf}	0.10821(34) $\times 10^{-7}$
$(\frac{1}{2})\{P_b, P_c\}P^2 \sin(3\alpha)$		6_{24}	D_{3bcJ}	-0.7436(17) $\times 10^{-8}$
$(\frac{1}{2})\{P_a^2, P_b, P_c\} \sin(3\alpha)$		6_{24}	D_{3bcK}	0.14846(12) $\times 10^{-5}$
$(\frac{1}{2})\{(P_a, P_b^3) - \{P_a, P_b, P_c^2\}\} \cos(3\alpha)$		6_{24}	V_{3ab3}	0.38167(73) $\times 10^{-7}$
$p_z^2P_a^2(1 - \cos(3\alpha))$		6_{24}	V_{3JK}	-0.23880(36) $\times 10^{-6}$
$(\frac{1}{2})\{P_a^3, P_b\} (1 - \cos(3\alpha))$		6_{24}	V_{3abK}	0.1562(36) $\times 10^{-6}$
$(\frac{1}{2})\{P_a, P_b^2\} \sin(3\alpha)$		6_{24}	D_{3ac3}	-0.3543(24) $\times 10^{-7}$
$(\frac{1}{2})\{P_a^2, (P_b^2 - P_c^2)\}p_z^2$		6_{24}	F_{bcK}	0.7853(30) $\times 10^{-8}$
$p_z^2(P_c^4 + P_b)$		6_{24}	F_{bc2}	0.49528(94) $\times 10^{-10}$
$(P_b^4 + P_c^4) \cos 3\alpha$		6_{24}	V_{3b2c2}	-0.32294(69) $\times 10^{-8}$
$p_zP_a^5$		6_{15}	ρ_{KK}	0.12126(20) $\times 10^{-6}$
$p_zP_a^3P^2$		6_{15}	ρ_{JK}	-0.40507(54) $\times 10^{-8}$
$(\frac{1}{2})\{P_a, (P_b^2 - P_c^2)\}P^2 p_z$		6_{15}	ρ_{bcJ}	-0.15285(93) $\times 10^{-10}$
$(\frac{1}{2})\{P_a^3, (P_b^2 - P_c^2)\}p_z$		6_{15}	ρ_{bcK}	0.6381(14) $\times 10^{-8}$
$\{P_a, P_b\}P^4$		6_{06}	D_{abff}	-0.16905(91) $\times 10^{-11}$

(continued on next page)

Table 2 (continued)

Operator ^a	n_{op}	$t_{op}r_{op}$ ^b	Parameter ^c	Value ^d (cm^{-1})
$\{P_a^3, P_b\}P^2$	6 ₀₆	D_{abJK}		$0.8607(65) \times 10^{-10}$
$\{P_a^5, P_b\}$	6 ₀₆	D_{abKK}		$0.11154(82) \times 10^{-8}$
P^6	6 ₀₆	Φ_J		$0.80483(59) \times 10^{-12}$
$P^4P_a^2$	6 ₀₆	Φ_{JK}		$-0.2732(10) \times 10^{-10}$
$P^2P_a^4$	6 ₀₆	Φ_{KJ}		$-0.14266(25) \times 10^{-8}$
P_a^6	6 ₀₆	Φ_K		$0.19759(23) \times 10^{-7}$
$2P^4(P_b^2 - P_c^2)$	6 ₀₆	ϕ_J		$0.38476(25) \times 10^{-12}$
$P^2\{P_a^2, (P_b^2 - P_c^2)\}$	6 ₀₆	ϕ_{JK}		$-0.9470(55) \times 10^{-11}$
$\{P_a^4, (P_b^2 - P_c^2)\}$	6 ₀₆	ϕ_K		$0.54529(21) \times 10^{-9}$
$(\frac{1}{2})(1 - \cos(12\alpha))$	8 ₈₀	V_{12}		$0.10123(15)$
P_z^8	8 ₈₀	F_{mmmm}		$-0.8628(32) \times 10^{-8}$
$P_z^7P_a$	8 ₇₁	ρ_{mmmm}		$-0.20698(86) \times 10^{-7}$
$P^2(1 - \cos(9\alpha))$	8 ₆₂	V_{9J}		$-0.15703(56) \times 10^{-5}$
$P_a^2(1 - \cos(9\alpha))$	8 ₆₂	V_{9K}		$0.3044(14) \times 10^{-4}$
$(P_b^2 - P_c^2)(1 - \cos(9\alpha))$	8 ₆₂	V_{9bc}		$-0.11444(53) \times 10^{-5}$
$(\frac{1}{2})\{P_b, P_c\}\sin(9\alpha)$	8 ₆₂	D_{9bc}		$0.884(13) \times 10^{-6}$
$P_z^2P_a^6$	8 ₆₂	F_{mmK}		$-0.2202(11) \times 10^{-7}$
$(\frac{1}{2})\{P_a, P_b\}P_z^6$	8 ₆₂	F_{mmab}		$0.2906(29) \times 10^{-10}$
$P_a^2P_z^5$	8 ₅₃	ρ_{mmK}		$-0.13762(98) \times 10^{-7}$
$P_z^2P_a^4$	8 ₄₄	F_{mKK}		$-0.5734(57) \times 10^{-8}$
$(\frac{1}{2})P^2\{P_a, P_c\}\sin(6\alpha)$	8 ₄₄	D_{6acJ}		$-0.6552(93) \times 10^{-8}$
$(\frac{1}{2})\{P_b, P_c\}P^2\sin(6\alpha)$	8 ₄₄	D_{6bcJ}		$0.6210(71) \times 10^{-9}$
$P^4(1 - \cos(6\alpha))$	8 ₄₄	V_{6JJ}		$-0.799(16) \times 10^{-10}$
$P_a^4(1 - \cos(6\alpha))$	8 ₄₄	V_{6KK}		$0.15152(47) \times 10^{-6}$
$(\frac{1}{2})\{P_a^3, P_b\}(1 - \cos(6\alpha))$	8 ₄₄	V_{6abK}		$-0.6966(58) \times 10^{-7}$
$P_z^3P_a^5$	8 ₃₅	ρ_{mKK}		$-0.1656(23) \times 10^{-8}$
$(\frac{1}{2})\{P_a, P_b^3, P_c, p_x, \sin(3\alpha)\} - (\frac{1}{2})\{P_a, P_b, P_c^3, p_x, \sin(3\alpha)\}$	8 ₃₅	ρ_{3bc3}		$-0.2511(23) \times 10^{-10}$
$P^6(1 - \cos(3\alpha))$	8 ₂₆	V_{3Jjj}		$0.1344(25) \times 10^{-13}$
$P^4P_a^2(1 - \cos(3\alpha))$	8 ₂₆	V_{3JJK}		$0.3715(39) \times 10^{-11}$
$P^2P_a^4(1 - \cos(3\alpha))$	8 ₂₆	V_{3JCK}		$0.472(13) \times 10^{-10}$
$(\frac{1}{2})\{P_a^5, P_b\}(1 - \cos(3\alpha))$	8 ₂₆	V_{3abCK}		$-0.2031(61) \times 10^{-9}$
$(\frac{1}{2})P^2\{P_a^3, P_c\}\sin(3\alpha)$	8 ₂₆	D_{3acJK}		$-0.5470(82) \times 10^{-10}$
$(\frac{1}{2})P^2\{P_a^2, P_b, P_c\}\sin(3\alpha)$	8 ₂₆	D_{3bcJK}		$0.854(18) \times 10^{-11}$
$(\frac{1}{2})\{P_a^3, P_c^3\}\sin(3\alpha)$	8 ₂₆	D_{3ac3K}		$0.6486(74) \times 10^{-10}$
$P_z^2P_a^6$	8 ₂₆	F_{KKK}		$-0.3325(57) \times 10^{-9}$
$P_z^2P_a^7$	8 ₁₇	ρ_{KKK}		$-0.4300(86) \times 10^{-10}$
P^8	8 ₀₈	L_j		$-0.3808(46) \times 10^{-17}$
$P^4P_a^4$	8 ₀₈	L_{JK}		$0.5000(60) \times 10^{-14}$
P_a^8	8 ₀₈	L_K		$-0.2743(71) \times 10^{-11}$
$2P^6(P_b^2 - P_c^2)$	8 ₀₈	I_j		$-0.1626(22) \times 10^{-17}$
$(\frac{1}{2})P^2\{P_a, P_b\}(1 - \cos(9\alpha))$	10 ₆₄	V_{9abJ}		$-0.1960(28) \times 10^{-8}$
$(\frac{1}{2})\{P_a^5, P_b\}(1 - \cos(6\alpha))$	10 ₄₆	V_{6abKK}		$-0.585(13) \times 10^{-10}$
$P_z^2P_a^8$	10 ₂₈	F_{KKKK}		$0.1427(47) \times 10^{-14}$

^a $\{A, B, C, D\} = ABCD + DCBA$. $\{A, B, C\} = ABC + CBA$. $\{A, B\} = AB + BA$. The product of the operator in the first column of a given row and the parameter in the third column of that row gives the term actually used in the torsion-rotation Hamiltonian of the program, except for F , ρ and A_{RAM} , which occur in the Hamiltonian in the form $F(p_a + \rho p_a)^2 + A_{RAM}p_a^2$.

^b $n_{op} = t_{op} + r_{op}$, where n_{op} is the total order of the operator, t_{op} is the order of the torsional part and r_{op} is the order of the rotational part, respectively.

^c Parameter nomenclature based on the subscript procedures of [20].

^d All values are in cm^{-1} , except for ρ which is unitless. Statistical uncertainties are shown as one standard uncertainty in the units of the last two digits.

cies are less than 1 kHz. The numbers of the terms in the model distributed between the $n_{op} = 2, 4, 6, 8, 10$ orders are 7, 22, 46, 31, 3, respectively. This is consistent with the total numbers of determinable parameters of 7, 22, 50, 95, and 161 for those orders, as calculated from the differences between the total number of symmetry-allowed Hamiltonian terms of order n_{op} and the number of symmetry-allowed contact transformation terms of order $n_{op} - 1$ [21].

4. Discussion

One of the questions which arise in connection with the new set of parameters is the propriety of a rather large number of parameters included in the final fit. This question was recently discussed

in connection with acetic acid study [15] where the RAM model including 93 parameters was used to fit the rotational transitions in the three lowest torsional states with J up to 79. The main point of that discussion [15] is that studies that involve application of the RAM to the analysis of the large amplitude torsional motion in molecules only now have reached the domain of rather large rotational quantum numbers and therefore the question of what model size would be appropriate for analysis of such molecules excited to rather high J quantum states is only being addressed now. It seems natural to assume that in non-rigid molecules an expansion of Hamiltonians in powers of rotation operators will have poorer convergence in comparison with semi-rigid molecules. Nevertheless if we look at a ratio which approximately correspond to adjustable parameters per vibrational state in an ordinary molecule, we find

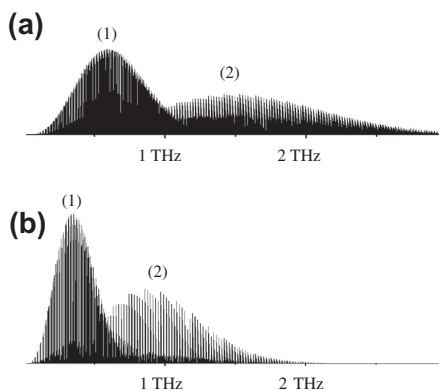


Fig. 2. Predicted rotational spectrum for the $\nu_t = 0,1,2$ torsional states of acetaldehyde at 300 K (a) and 100 K (b). In both cases maximum (1) in intensity distribution corresponds to ${}^aR_{0,1}$ -type transitions with low K_a values, whereas maximum (2) corresponds to ${}^bR_{1,\pm 1}$ type transitions with the K_a numbers approaching the J values.

for the current fit the ratio of $109/(3 * 2) = 18.2$ parameters per “asymmetric rotor spectrum”, where the 3 in the denominator represents the three torsional states under study and the 2 in the denominator arises because each vibration-rotation level splits into two components (one non-degenerate, or ‘A’ state and one doubly degenerate, or ‘E’ state). This analog of the number of parameters per vibrational state does not seem excessively large for the current rotational quantum number coverage of $0 \leq J \leq 66$ and $0 \leq K_a \leq 22$, especially taking into account that there is an interaction between the “asymmetric rotor” stacks of the levels of the same symmetry. Another metric which may be considered is the number of fitted energy levels per Hamiltonian parameter. For the current fit this number is ≈ 86 . If we look at the balance between adjustable parameters and measured frequencies in the dataset we see that the present fit is characterized by a ratio of ≈ 176 lines per adjustable parameter, which we feel is quite satisfactory, and that this ratio represents almost a factor of three improvement over the ratio of $3108/48 \approx 65$ lines/parameter obtained from the previous fit of the first three torsional states of acetaldehyde [6].

Whereas we think that the quantity of parameters used in our model is adequate it is probable that some part of these 109 parameters are needed in the model to compensate for the unmodeled effects of intertorsional perturbations in $\nu_t = 2$ torsional state of acetaldehyde already discussed in Ref. [14]. In particular the avoided crossing perturbation of the $\nu_t = 2$ $K = 9$ A type levels discussed in detail in Ref. [14] was also observed in our work. As the interacting counterpart in this case the $\nu_t = 3$ $K = 5$ A type levels were identified in Ref. [14] and in principle the RAM approach should be able to take implicitly into account such perturbations. But in practice we have a more complicated case due to the downward propagation of a perturbation from the low lying small amplitude vibration ν_{10} , which is located in vicinity of the $\nu_t = 4$ torsional excited state [7]. It should be noted that the $\nu_t = 2$ state posed the main problem in the fit and therefore to be on a safe side we decided to exclude from the fit a number of tentatively assigned high J $\nu_t = 2$ transitions whose assignments were not possible to verify by inspection of the J series.

Fig. 2 gives a general overview of acetaldehyde rotational spectrum in the frequency range up to 3 THz for the two temperatures: 100 K and 300 K. It is seen that there are two maximums in the distribution of transition intensities in the rotational spectra. The first maximum is associated with ${}^aR_{0,1}$ -type transitions with low K_a values. It is seen that at $T = 300$ the maximum in intensity is achieved at approximately 0.6 THz (this maximum corresponds to the ${}^aR_{0,1}$

transitions with J values around 30). It is seen that after reaching a maximum the intensity of these transitions begins to decrease and at about 1 THz the ${}^bR_{1,\pm 1}$ transitions with the K_a numbers approaching the J values begin to dominate in the spectrum. These transitions are responsible for the second maximum in the intensity distribution around 1.5 THz (at $T = 300$ the maximum corresponds to the ${}^bR_{1,\pm 1}$ transitions with J values around 14). Certainly, as it is seen from Fig. 2b, at lower temperatures the positions of these two maximums in the intensity distribution are shifted towards lower frequencies and towards lower rotational quantum numbers. It should be noted that in the upper frequency part of investigated range around 1.6 THz the intensities of the ${}^aR_{0,1}$ -type transitions with low K_a values appear to be too weak to be measured (around 1.2 THz namely this type of transitions provides the highest J values treated in our fit). Therefore the range of rotational quantum numbers $J \leq 66$ and $K_a \leq 22$ treated in the current study covers the majority of strong rotational transitions which may be of interest for astronomical applications in the frequency range up to 1.9 THz.

5. Conclusions

We performed a new study of the acetaldehyde spectrum in the broad frequency range from 0.05 to 1.6 THz. The new data for the $\nu_t = 0,1,2$ torsional states involving rotation transitions with J up to 66 and K_a up to 22 were analyzed using the rho-axis-method and a fit within experimental error has been achieved. Obtained results provide a firm basis for producing reliable predictions of the acetaldehyde spectrum in the frequency range up to 1.9 THz which is relevant for the Herschel and ALMA missions. Corresponding predictions and the dataset treated in our study are available as the [Supplementary material](#) with this article.

Acknowledgments

Part of this work was done within the Ukrainian-French CNRS-PICS 6051 Project. Portions of this research were carried out at the Jet Propulsion Laboratory, California Institute of Technology, under contract with the National Aeronautics and Space Administration. R.M. and L.M. acknowledge the Programme National “Physique et Chimie du Milieu Interstellaire” and the Centre National d’Etudes Spatiales (CNES).

Appendix A. Supplementary material

Supplementary data for this article are available on ScienceDirect (www.sciencedirect.com) and as part of the Ohio State University Molecular Spectroscopy Archives (http://library.osu.edu/sites/msa/jmsa_hp.htm). Supplementary data associated with this article can be found, in the online version, at <http://dx.doi.org/10.1016/j.jms.2013.11.006>.

References

- [1] H.E. Matthews, P. Friberg, W.M. Irvine, *Astrophys. J.* 290 (1985) 609–614.
- [2] B.E. Turner, R. Terzieva, E. Herbst, *Astrophys. J.* 518 (1999) 699–732.
- [3] A. Nummelin, J.E. Dickens, P. Bergman, Å. Hjalmarson, W.M. Irvine, M. Ikeda, M. Ohishi, *A&A* 337 (1998) 275–286.
- [4] S.B. Charnley, *Adv. Space Res.* 33 (2004) 23–30.
- [5] S. Muller, A. Beelen, M. Guelin, S. Aalto, J.H. Black, F. Combes, S. Curran, P. Theule, S. Longmore, *A&A* 535 (2011) A103.
- [6] I. Kleiner, F.J. Lovas, M. Godefroid, *J. Phys. Chem. Ref. Data* 25 (1996) 1113–2111.
- [7] I. Kleiner, N. Moazzzen-Ahmadi, A.R.W. McKellar, T.A. Blake, R.L. Sams, S.W. Sharpe, G. Moruzzi, J.T. Hougen, *J. Mol. Spectrosc.* 252 (2008) 214–229.
- [8] C.C. Lin, R.W. Kilb, *J. Chem. Phys.* 24 (1956) 631.
- [9] I. Kleiner, M. Godefroid, M. Herman, A.R.W. McKellar, *J. Mol. Spectrosc.* 142 (1990) 238–253.

- [10] I. Kleiner, J.T. Hougen, R.D. Suenram, F.J. Lovas, M. Godefroid, *J. Mol. Spectrosc.* 148 (1991) 38–49.
- [11] I. Kleiner, J.T. Hougen, R.D. Suenram, F.J. Lovas, M. Godefroid, *J. Mol. Spectrosc.* 153 (1992) 578–586.
- [12] W.L. Barclay Jr., M.A. Anderson, L.M. Ziurys, I. Kleiner, J.T. Hougen, *Astrophys. J. Suppl.* 89 (1993) 221–226.
- [13] S.P. Belov, M.Yu. Tretyakov, I. Kleiner, J.T. Hougen, *J. Mol. Spectrosc.* 160 (1993) 61–72.
- [14] I. Kleiner, J.T. Hougen, J.-U. Grabow, S.P. Belov, M.Yu. Tretyakov, J. Cosléou, *J. Mol. Spectrosc.* 179 (1996) 41–60.
- [15] V.V. Ilyushin, C.P. Endres, F. Lewen, S. Schlemmer, B.J. Drouin, *J. Mol. Spectrosc.* 290 (2013) 31–41.
- [16] E.A. Alekseev, R.A. Motiyenko, L. Margulès, *Radio Phys. Radio Astron.* 3 (1) (2012) 75–88.
- [17] B.J. Drouin, F.W. Maiwald, J.C. Pearson, *Rev. Sci. Inst.* 76 (2005) 093113.
- [18] V.V. Ilyushin, Z. Kisiel, L. Pszczółkowski, H. Mäder, J.T. Hougen, *J. Mol. Spectrosc.* 259 (2010) 26–38.
- [19] I. Kleiner, *J. Mol. Spectrosc.* 260 (2010) 1–18.
- [20] Xu. Li-Hong, J. Fisher, R.M. Lees, H.Y. Shi, J.T. Hougen, J.C. Pearson, B.J. Drouin, G.A. Blake, R. Braakman, *J. Mol. Spectrosc.* 251 (2008) 305–313.
- [21] K. Nakagawa, S. Tsunekawa, T. Kojima, *J. Mol. Spectrosc.* 126 (1987) 329–340.

Millimeter and submillimeter wave spectra of mono- ^{13}C -acetaldehydes*

L. Margulès¹, R. A. Motiyenko¹, V. V. Ilyushin², and J. C. Guillemin³

¹ Laboratoire de Physique des Lasers, Atomes, et Molécules, UMR CNRS 8523, Université de Lille I, 59655 Villeneuve d'Ascq Cedex, France
e-mail: laurent.margules@univ-lille1.fr

² Institute of Radio Astronomy of NASU, Chernovonopraporna 4, 61002 Kharkov, Ukraine
e-mail: ilyushin@rian.kharkov.ua

³ Institut des Sciences Chimiques de Rennes, École Nationale Supérieure de Chimie de Rennes, CNRS, UMR 6226, 11 allée de Beaulieu, CS 50837, 35708 Rennes Cedex 7, France

Received 6 December 2014 / Accepted 25 April 2015

ABSTRACT

Context. The acetaldehyde molecule is ubiquitous in the interstellar medium of our galaxy, and due to its dense and complex spectrum, large dipole moment, and several low-lying torsional states, acetaldehyde is considered to be a “weed” molecule for radio astronomy observations. Mono- ^{13}C acetaldehydes $^{13}\text{CH}_3\text{CHO}$ and $\text{CH}_3^{13}\text{CHO}$ are likely to be identified in astronomical surveys, such as those available with the very sensitive ALMA telescope. Laboratory measurements and analysis of the millimeter and submillimeter-wave spectra are the prerequisites for the successful radioastronomical search for the new interstellar molecular species, as well as for new isotopologs of already detected interstellar molecules.

Aims. In this context, to provide reliable predictions of $^{13}\text{CH}_3\text{CHO}$ and $\text{CH}_3^{13}\text{CHO}$ spectra in millimeter and submillimeter wave ranges, we study rotational spectra of these species in the frequency range from 50 to 945 GHz.

Methods. The spectra of mono- ^{13}C acetaldehydes were recorded using the spectrometer based on Schottky-diode frequency-multiplication chains in the Lille laboratory. The rotational spectra of $^{13}\text{CH}_3\text{CHO}$ and $\text{CH}_3^{13}\text{CHO}$ molecules were analyzed using the Rho axis method.

Results. In the recorded spectra we have assigned 6884 for the $^{13}\text{CH}_3\text{CHO}$ species and 6458 for $\text{CH}_3^{13}\text{CHO}$ species new rotational transitions belonging to the ground, first, and second excited torsional states. These measurements were fitted together with previously published data to the Hamiltonian models that use 91 and 87 parameters to achieve overall weighted rms deviations 0.88 for the $^{13}\text{CH}_3\text{CHO}$ species and 0.95 for $\text{CH}_3^{13}\text{CHO}$. On the basis of the new spectroscopic results, predictions of transition frequencies in the frequency range up to 1 THz with $J \leq 60$ and $K_a \leq 20$ are presented for both isotopologs.

Key words. ISM: molecules – methods: laboratory: molecular – submillimeter: ISM – molecular data – line: identification

1. Introduction

This paper is a continuation of a series of studies conducted in PhLAM Lille (France) that are devoted to the investigations of the spectra of different isotopic species of astrophysical molecules (Demyk et al. 2007; Margulès et al. 2009a,b, 2010; Carvajal et al. 2009; Tercero et al. 2012; Bouchez et al. 2012; Coudert et al. 2012, 2013; Richard et al. 2012, 2013; Haykal et al. 2013; Kutsenko et al. 2013; Nguyen et al. 2013). In particular, these works led to the first interstellar detection of HCOOCH_2D (Coudert et al. 2013), $\text{HCO}^{13}\text{CH}_3$ (Carvajal et al. 2009), $\text{HCO}^{18}\text{OCH}_3$, $\text{HC}^{18}\text{OOCCH}_3$ (Tercero et al. 2012), and CH_2DOCH_3 (Richard et al. 2013). In the current paper we focus our attention on the ^{13}C isotopologs of the ubiquitous interstellar molecule – acetaldehyde, which main isotopolog has been observed in the cold molecular clouds (Matthews et al. 1985), and translucent molecular clouds (Turner et al. 1999) toward hot cores (Nummela et al. 1998) and star-forming regions (Charnley 2004). It was recently detected in the disk of a high redshift ($z = 0.89$) spiral galaxy located in front of the quasar PKS 1830-211 (Muller et al. 2011).

* Full Tables 3–6 are only available at the CDS via anonymous ftp to cdsarc.u-strasbg.fr (130.79.128.5) or via <http://cdsarc.u-strasbg.fr/viz-bin/qcat?J/A+A/579/A46>

Rotational spectra of the parent acetaldehyde species was a subject of several investigations. The latest paper on this subject (Smirnov et al. 2014) covers the frequency range up to 1.6 THz and the range of rotational quantum numbers up to $J \leq 66$ and $K_a \leq 22$, providing a firm basis for producing reliable predictions of the acetaldehyde spectrum in the frequency range up to 1.9 THz. As concerns mono-labeled acetaldehyde isotopolog, the millimeter and submillimeter wave spectra were only studied for CH_3CDO (Martinache et al. 1989; Elkeurti et al. 2010) with the upper frequency of 376 GHz. For other mono-substituted isotopologs CH_2DCHO , $^{13}\text{CH}_3\text{CHO}$, $\text{CH}_3^{13}\text{CHO}$, and $\text{CH}_3\text{CH}^{18}\text{O}$, data available in the literature are very limited, covering the frequency range only from 8 to 40 GHz (Kilb et al. 1957; Turner & Cox 1976; Turner et al. 1981; Zaleski et al. 2012). In particular, for the $^{13}\text{CH}_3\text{CHO}$ and $\text{CH}_3^{13}\text{CHO}$ isotopologs of interest here, the dataset consisted of about 10 transitions for each of the ^{13}C isotopologs, which are evenly distributed between A-type and E-type symmetry species of the ground torsional states (Kilb et al. 1957; Zaleski et al. 2012). It is evident that for producing reliable predictions of the $^{13}\text{CH}_3\text{CHO}$ and $\text{CH}_3^{13}\text{CHO}$ spectra, these datasets should be considerably extended and a new analysis should be performed. In this context we present a new study of the $^{13}\text{CH}_3\text{CHO}$ and $\text{CH}_3^{13}\text{CHO}$ spectra with measurements and analysis extended up to 945 GHz.

2. Experiments

2.1. Synthesis

The 1-¹³C and 2-¹³C acetyl chloride were purchased from Eurisotop and used without further purification. The ¹³CH₃CHO and CH₃¹³CHO were synthesized following the preparation of Barbuy and Couturier (Barbuy et al. 1987), modified to isolate the product. In a 100 ml two-necked flask equipped with a stirring bar and a nitrogen inlet, and cooled at –20 °C were introduced under nitrogen (PPh₃)₄Pd (0.12 g, 0.1 mmol), xylene (15 ml), and ¹³C acetyl chloride (1g, 13 mmol). The flask was connected to a U-tube equipped with stopcocks and immersed in a –80 °C cold bath, and tributyl tin hydride (4.1 g, 14 mmol) was added in 2 min and the solution was then allowed to warm to room temperature. A gentle stream of nitrogen was then passed through the flask and the U-tube for 15 min. A mixture containing the labeled acetaldehyde (80%) and xylene (20%) was obtained. A very pure sample of ¹³C acetaldehyde (purity >96%) was obtained in a 78% yield (437 mg, 10 mmol) and in a 98% isotopic purity by a subsequent distillation of the solution in a vacuum line (0.1 mbar) equipped with a first U-tube cooled at –80 °C to remove the solvent and a second one immersed in a liquid nitrogen bath to selectively condense the expected product.

2.2. Lille – submillimeter spectra

The measurements in the frequency range under investigation (50–945 GHz) were performed using the Lille spectrometer (Alekseev et al. 2012). A quasi-optic dielectric hollow waveguide of 3-m length containing investigated gas at the required pressure was used as the sample cell in the spectrometer. The measurements were done at typical pressures of 10 Pa and at room temperature. The frequency ranges 50–315, 400–630, and 780–945 GHz were covered with various active and passive frequency multipliers where the Agilent synthesizer (12.5–17.5 GHz) was used as the source of radiation. Estimated uncertainties for measured line frequencies are 30 kHz and 50 kHz depending on the observed signal-to-noise ratio and the frequency range.

3. Theoretical model

Like the parent species, ¹³C acetaldehydes represent the case of near prolate ($\kappa \approx -0.95$) nonrigid molecules with the large amplitude torsional motion of the methyl top. The molecules have a plane of symmetry that means that the G_6 permutation-inversion group will be appropriate for them if internal rotation of the methyl group is taken into account. The torsional large amplitude motion of the methyl top in the molecules splits rotational transitions into two components that correspond to non-degenerate (A_1/A_2) and degenerate (E) symmetry species in G_6 . Corresponding $A - E$ splittings may already reach hundreds of MHz in the ground vibrational state. Combination of rather large rotational constants ($A \approx 56$ GHz, $B \approx 10$ GHz, $C \approx 9$ GHz) with an intermediate barrier height to internal rotation of the methyl group ($V_3 \approx 407$ cm^{–1}) and considerable dipole moment ($\mu \approx 2.734$ D) leads to an intense complex rotational spectrum expanding in THz region. The ratio of the methyl top moment of inertia to that of the rest of the molecule is rather high in these molecules, which leads to a relatively large coefficient for the coupling term between internal rotation and global rotation ($\rho \approx 0.32$). This means that the principle axis method will experience serious problems with fitting spectra of ¹³C acetaldehydes since its convergence strongly depends on the ρ value (Kleiner 2010).

The Hamiltonian used in the present work is the so-called RAM (rho axis method) internal-rotation Hamiltonian based on the work of Kirtman (Kirtman 1962), Lees and Baker (Lees & Baker 1968), and Herbst et al. (Herbst et al. 1984). Since rather complete descriptions of this method, which takes its name from the choice of axis system, have been presented several times (Hougen et al. 1994; Kleiner 2010) we do not repeat this general description here. The main advantage of the RAM Hamiltonian is its general approach that simultaneously takes into account the A- and E-symmetry species and all the torsional levels, intrinsically taking the intortorsional interactions into account within the rotation-torsion manifold of energy levels. This method was successfully applied to a number of molecules containing a C_{3v} rotor and C_s frame, including the main isotopolog of acetaldehyde (Smirnov et al. 2014). As for the main isotopolog (Smirnov et al. 2014) we employed the RAM36 (rho-axis-method for 3- and 6-fold barriers) code that uses the RAM approach for the molecules with the C_{3v} top attached to a molecular frame of C_s or C_{2v} symmetry and having 3- or 6-fold barriers to internal rotation, respectively (Ilyushin et al. 2010, 2013). The Hamiltonian in the RAM36 program is presented by the following expression:

$$\begin{aligned} H = & (1/2) \sum_{knpqrs} B_{knpqrs0} [P^{2k} P_z^n P_x^p P_y^q P_\alpha^r \cos(3s\alpha) \\ & + \cos(3s\alpha) P_\alpha^r P_y^q P_x^p P_z^n P^{2k}] \\ & + (1/2) \sum_{knpqrt} B_{knpqrt0} [P^{2k} P_z^n P_x^p P_y^q P_\alpha^r \sin(3t\alpha) \\ & + \sin(3t\alpha) P_\alpha^r P_y^q P_x^p P_z^n P^{2k}] \end{aligned} \quad (1)$$

where the B_{knpqrs} are fitting parameters; p_α is the angular momentum conjugate to the internal rotation angle α ; and P_x, P_y, P_z are projections on the x, y, z axes of the total angular momentum P . In the case of a C_{3v} top and C_s frame (as is appropriate for acetaldehyde), the allowed terms in the torsion-rotation Hamiltonian must be totally symmetric in the group G_6 (and also must be Hermitian and invariant to the time reversal operation). Since all individual operators $p_\alpha, P_x, P_y, P_z, P^2, \cos(3s\alpha)$ and $\sin(3t\alpha)$ used in Eq. (1) are Hermitian, all possible terms provided by Eq. (1) will automatically be Hermitian. The particular term to be fit is represented in the input file with a set of k, n, p, q, r, s, t integer indices that are checked by the program for conformity with time reversal and symmetry requirements, to prevent accidental introduction of symmetry-forbidden terms into the Hamiltonian.

The RAM36 computer code uses the two-step diagonalization procedure of Herbst et al. (1984). In the first step, a set of torsional calculations is performed with a relatively large torsional basis set for each symmetry species and for each value of K in the range $-J_{\max} \leq K \leq +J_{\max}$. In the current fit we used 21 torsional basis functions at the first stage. In this step only the main torsional-rotation Hamiltonian matrix elements diagonal in K are considered. In the second step a reduced torsional basis set is used, which is obtained by discarding all but the lowest several torsional eigenfunctions for a given K and symmetry species obtained from the first stage. In the current fit we used 9 torsional basis functions at the second stage. In the second step, all desired asymmetric-rotor and torsion-rotation K mixing effects are taken into account. At both stages a non-degenerate symmetry submatrix is not split into A_1/A_2 parts, which are instead treated together. A conventional weighted least-squares fit is carried out to determine the Hamiltonian parameter values

Table 1. Fitted parameters of the RAM Hamiltonian for ¹³C acetaldehyde isotopologs.

Operator ¹	n_{tr}^2	Parameter	¹² CH ₃ ¹² CHO Value ³ (cm ⁻¹)	¹³ CH ₃ ¹² CHO Value ³ (cm ⁻¹)	¹² CH ₃ ¹³ CHO Value ³ (cm ⁻¹)
p_a^2	2 ₂₀	F	7.56708175(35)	7.5652791(19)	7.5068034(55)
(1/2) (1 - cos(3 α))	2 ₂₀	V_3	407.59768(20)	407.91172(18)	407.58042(26)
$p_a P_a$	2 ₁₁	ρ	0.328632673(20)	0.328300981(35)	0.322541154(65)
P_a^2	2 ₀₂	A_{RAM}	1.884881309(61)	1.88013742(13)	1.848976496(63)
P_b^2	2 ₀₂	B_{RAM}	0.348706489(16)	0.337726802(58)	0.348720666(61)
P_c^2	2 ₀₂	C_{RAM}	0.3031840478(44)	0.294817724(11)	0.302179145(18)
{ P_a, P_b }	2 ₀₂	D_{ab}	-0.122669037(94)	-0.11817144(38)	-0.12175149(39)
(1/2) (1 - cos(6 α))	4 ₄₀	V_6	-11.63964(50)	-11.67172(20)	-11.71571(65)
p_a^4	4 ₄₀	F_m	-0.424416(38) $\times 10^{-3}$	-0.427829(96) $\times 10^{-3}$	-0.42834(12) $\times 10^{-3}$
$p_a^3 P_a$	4 ₃₁	ρ_m	-0.832163(52) $\times 10^{-3}$	-0.82821(11) $\times 10^{-3}$	-0.81162(16) $\times 10^{-3}$
$P^2 (1 - \cos(3\alpha))$	4 ₂₂	V_{3J}	0.5577894(41) $\times 10^{-3}$	0.524776(16) $\times 10^{-3}$	0.529795(22) $\times 10^{-3}$
$P_a^2 (1 - \cos(3\alpha))$	4 ₂₂	V_{3K}	-0.19313906(98) $\times 10^{-1}$	-0.1898291(17) $\times 10^{-1}$	-0.1953217(29) $\times 10^{-1}$
$(P_b^2 - P_c^2)(1 - \cos(3\alpha))$	4 ₂₂	V_{3bc}	0.2114597(52) $\times 10^{-3}$	0.192215(19) $\times 10^{-3}$	0.213208(15) $\times 10^{-3}$
(1/2){ P_a, P_b } (1 - cos(3 α))	4 ₂₂	V_{3ab}	0.4235363(70) $\times 10^{-2}$	0.405222(33) $\times 10^{-2}$	0.443922(36) $\times 10^{-2}$
$P_a^2 P^2$	4 ₂₂	F_J	-0.291704(53) $\times 10^{-5}$	-0.26533(11) $\times 10^{-5}$	-0.31536(19) $\times 10^{-5}$
$P_a^2 P_a^2$	4 ₂₂	F_K	-0.982545(30) $\times 10^{-3}$	-0.972792(46) $\times 10^{-3}$	-0.944979(89) $\times 10^{-3}$
$p_a^2 (P_b^2 - P_c^2)$	4 ₂₂	F_{bc}	0.14720(12) $\times 10^{-5}$	0.13745(31) $\times 10^{-5}$	0.16632(37) $\times 10^{-5}$
(1/2){ P_a, P_c } sin(3 α)	4 ₂₂	D_{3ac}	-0.1405503(49) $\times 10^{-1}$	-0.135881(17) $\times 10^{-1}$	-0.142957(18) $\times 10^{-1}$
(1/2){ P_b, P_c } sin(3 α)	4 ₂₂	D_{3bc}	0.59173(13) $\times 10^{-3}$	0.55489(43) $\times 10^{-3}$	0.63859(48) $\times 10^{-3}$
$P_a P_a P^2$	4 ₁₃	ρ_J	0.958253(42) $\times 10^{-5}$	0.91984(11) $\times 10^{-5}$	0.91075(15) $\times 10^{-5}$
$p_a P_a^3$	4 ₁₃	ρ_K	-0.571407(12) $\times 10^{-3}$	-0.564681(12) $\times 10^{-3}$	-0.549548(31) $\times 10^{-3}$
(1/2){ $P_a, (P_b^2 - P_c^2)$ } p_a	4 ₁₃	ρ_{bc}	-0.5536(12) $\times 10^{-6}$	-0.5763(36) $\times 10^{-6}$	-0.2887(35) $\times 10^{-6}$
- P^4	4 ₀₄	Δ_J	0.3244101(54) $\times 10^{-6}$	0.306742(20) $\times 10^{-6}$	0.325255(24) $\times 10^{-6}$
- $P^2 P_a^2$	4 ₀₄	Δ_{JK}	-0.581770(50) $\times 10^{-5}$	-0.556079(86) $\times 10^{-5}$	-0.571647(79) $\times 10^{-5}$
- P_a^4	4 ₀₄	Δ_K	0.1308173(26) $\times 10^{-3}$	0.1292582(29) $\times 10^{-3}$	0.1263888(56) $\times 10^{-3}$
- $2P^2 (P_b^2 - P_c^2)$	4 ₀₄	δ_J	0.778472(23) $\times 10^{-7}$	0.709225(70) $\times 10^{-7}$	0.786517(69) $\times 10^{-7}$
-{ $P_a^2, (P_b^2 - P_c^2)$ }	4 ₀₄	δ_K	0.94268 (17) $\times 10^{-6}$	0.105094(90) $\times 10^{-5}$	0.10255(12) $\times 10^{-5}$
{ P_a, P_b } P^2	4 ₀₄	D_{abJ}	0.867443(32) $\times 10^{-6}$	0.81273(20) $\times 10^{-6}$	0.85179(14) $\times 10^{-6}$
{ P_a^3, P_b }	4 ₀₄	D_{abK}	0.30498(25) $\times 10^{-5}$	0.29239(46) $\times 10^{-5}$	0.27116(33) $\times 10^{-5}$

Notes. ⁽¹⁾ $\{A, B\} = AB + BA$; $\{A, B, C\} = ABC + CBA$; $\{A, B, C, D\} = ABCD + DCBA$. The product of the operator in the first column of a given row and the parameter in the third column of that row gives the term actually used in the torsion-rotation Hamiltonian of the program, except for F , ρ , and A_{RAM} , which occur in the Hamiltonian in the form $F(P_a + \rho P_t)^2 + A_{\text{RAM}} P_a^2$. ⁽²⁾ $n = t + r$, where n is the total order of the operator, t is the order of the torsional part, and r the order of the rotational part. ⁽³⁾ All values are in cm⁻¹, except ρ , which is unitless. Statistical uncertainties are shown as one standard uncertainty in the units of the last two digits. A complete version up to 8th order is available in Table 7.

with a special treatment of blends where an intensity-weighted average of calculated (but experimentally unresolved) transition frequencies is put in correspondence with the measured blended-line frequency. A more detailed description of the RAM36 code can be found in Ilyushin et al. (2010, 2013).

4. Assignment and analysis of the spectra

We started our analysis of recorded spectra from the dataset of Kilb et al. (1957), which was combined with the low order torsion parameters of the main acetaldehyde isotopolog (Smirnov et al. 2014). In the initial stage the torsional parameters of the RAM Hamiltonian models were kept fixed at the values of the main isotopolog, and rotational parameters plus ρ parameters were varied to fit available transitions of ¹³CH₃CHO and CH₃¹³CHO. Obtained in this way sets of RAM Hamiltonian parameters were used to produce the initial predictions of millimeter and submillimeter wave spectra for both ¹³C isotopologs. Analysis of the recorded spectra was done in the usual iterative manner by adding new assigned lines to the fit, refining of Hamiltonian model, and producing new predictions.

Although from the point of view of future radio astronomy observations, we were mainly interested in the rotational transitions belonging to the ground torsional states of ¹³C acetaldehydes, several transitions belonging to the first and second excited torsional states have also been assigned.

The band origins of the excited torsional states are $\nu^A = 143.7836$ cm⁻¹, $\nu^E = 142.0401$ cm⁻¹ ($v_t = 1$), $\nu^A = 255.3495$ cm⁻¹, and $\nu^E = 269.2086$ cm⁻¹ ($v_t = 2$) for ¹³CH₃CHO, and $\nu^A = 143.1719$ cm⁻¹, $\nu^E = 141.4820$ cm⁻¹ ($v_t = 1$) $\nu^A = 254.6352$ cm⁻¹, and $\nu^E = 268.1986$ cm⁻¹ ($v_t = 2$) for CH₃¹³CHO. First of all the excited torsional states were added to the analysis to stabilize the fit and reduce the correlation between torsion parameters of the RAM Hamiltonian models. In addition several high- K_a series of the ground torsional state transitions were perturbed by interactions with the first and second excited torsional states, so it was necessary to get more precise information about the positions of energy levels of these states.

In total the new datasets for the rotational spectra of ¹³CH₃CHO and CH₃¹³CHO isotopologs include 6894 and 6465 measured line frequencies, respectively, with an upper value of $J = 60$. As already mentioned, both datasets include transitions belonging to the ground, first, and second excited torsional states of the ¹³C acetaldehyde isotopologs. These sets of rotational transitions were fitted to the RAM theoretical model described above. The fits adopted in the present study as the best achieved the root mean square (rms) deviations of 0.032 MHz for ¹³CH₃CHO and 0.034 MHz for CH₃¹³CHO. The weighted rms deviations for the fits were 0.88 and 0.95, respectively. The RAM Hamiltonian models include 91 parameters for ¹³CH₃CHO and 87 for CH₃¹³CHO. The values of the molecular parameters obtained from the final fits are presented in Table 1,

Table 2. Statistics of the data set for the global fit to $v_t = 0, 1, 2$ torsional states of $^{13}\text{CH}_3\text{CHO}$ and $\text{CH}_3^{13}\text{CHO}$ isotopologs of acetaldehyde molecule.

$^{13}\text{CH}_3\text{CHO}$			$\text{CH}_3^{13}\text{CHO}$		
Category ¹	# of transitions ²	rms ³	Category ¹	# of transitions ²	rms ³
$v_t = 0$ A-type	2277	0.034 MHz	$v_t = 0$ A-type	2246	0.033 MHz
$v_t = 0$ E-type	2439	0.031 MHz	$v_t = 0$ E-type	2304	0.035 MHz
$v_t = 1$ A-type	1144	0.032 MHz	$v_t = 1$ A-type	1062	0.031 MHz
$v_t = 1$ E-type	1118	0.029 MHz	$v_t = 1$ E-type	1071	0.034 MHz
$v_t = 2$ A-type	331	0.033 MHz	$v_t = 2$ A-type	296	0.033 MHz
$v_t = 2$ E-type	383	0.036 MHz	$v_t = 2$ E-type	294	0.046 MHz
Unc. ⁴	# of lines ²	rms ³	Unc. ⁴	# of lines ²	rms ³
0.030 MHz	5377	0.027 MHz	0.030 MHz	5111	0.029 MHz
0.050 MHz	1507	0.041 MHz	0.050 MHz	1347	0.047 MHz
0.100 MHz	3	0.127 MHz	0.200 MHz	4	0.231 MHz
0.200 MHz	4	0.286 MHz	0.300 MHz	2	0.067 MHz
0.300 MHz	2	0.137 MHz	0.500 MHz	1	0.262 MHz
0.500 MHz	1	0.191 MHz			

Notes. ⁽¹⁾ The transitions are grouped by symmetry and torsional quantum number v_t . ⁽²⁾ The number of transitions or measured lines in each category included in the least squares fit. Due to blending, the total number of assigned transitions differs from the total number of measured lines.

⁽³⁾ Root-mean-square deviations from the global fit. ⁽⁴⁾ Data are grouped by their assigned uncertainties in the fit. Weights used for all lines in the fit are $1/(\text{unc.})^2$.

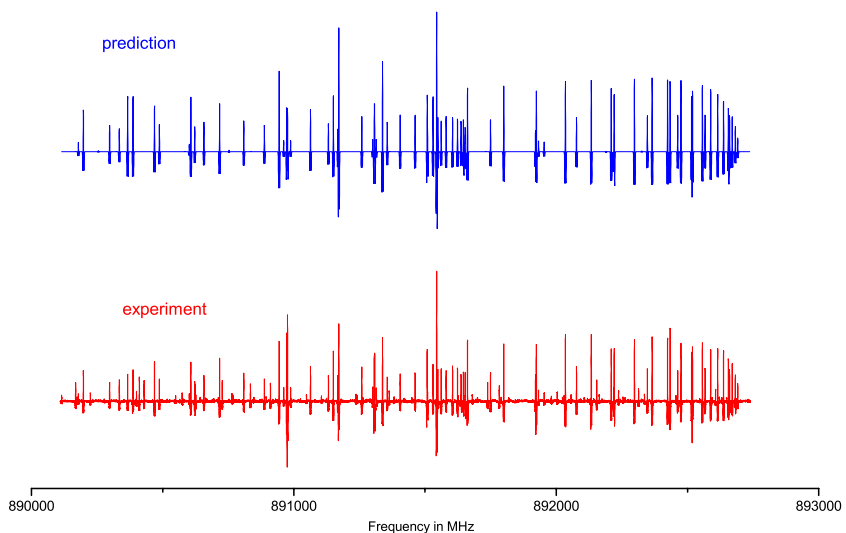


Fig. 1. Predicted (in blue) and observed (in red) rotational spectrum of $^{13}\text{CH}_3\text{CHO}$ between 891.3 and 893.2 GHz dominated by Q-type series of transitions with $K_a = 10 \leftarrow 9$. A slight inconsistency between predicted and observed spectrum, which may be visible for some strong lines, is due to source power and detector sensitivity variations.

where they are compared with the parameters of the main isotopolog Smirnov et al. (2014; owing to its significant size, the complete version of Table 1 is presented in Table 7), here only the parameters up to fourth order are given. It is seen from the comparison that up to the fourth order the RAM Hamiltonian models for the ^{13}C isotopologs are very close to the corresponding model of the main isotopolog. Starting from the sixth order, some discrepancies in the sets of parameters begin to appear. In our opinion these discrepancies are caused by the differences in the datasets. For example, the far-infrared data on the fundamental torsional band is only available for the main acetaldehyde isotopolog. The $K_a = 9 \leftarrow 8$ Q series of lines presented at Fig. 1 of Smirnov et al. (2014) may serve as one more example of such differences in the datasets: this series of transitions is present in the datasets of $^{12}\text{CH}_3^{12}\text{CHO}$ and $^{13}\text{CH}_3^{12}\text{CHO}$, but is out of range of the Lille spectrometer for $^{12}\text{CH}_3^{13}\text{CHO}$.

Table 2 summarizes the fitting results for different groups of the data. It is seen that the two main groups of data with 0.030 MHz and 0.050 MHz uncertainties are fit within the experimental error. The separate rms deviations for the A and E symmetry species are close to each other and do not differ much between torsional excited states. Figures 1 and 2, in which observed and predicted spectra are compared, give additional illustrations of our current understanding of the ^{13}C acetaldehydes spectra. The regions of the Q series of $K_a = 10 \leftarrow 9$ transitions are presented in these figures. It is seen that the majority of strong lines are assigned and predicted by our current model, although a number of rather strong unassigned lines presumably belonging to the higher excited states may still be found in the experimental spectra.

The lists of measured rotational transitions of the $^{13}\text{CH}_3\text{CHO}$ and $\text{CH}_3^{13}\text{CHO}$ isotopologs are presented in Tables 3 and 4.

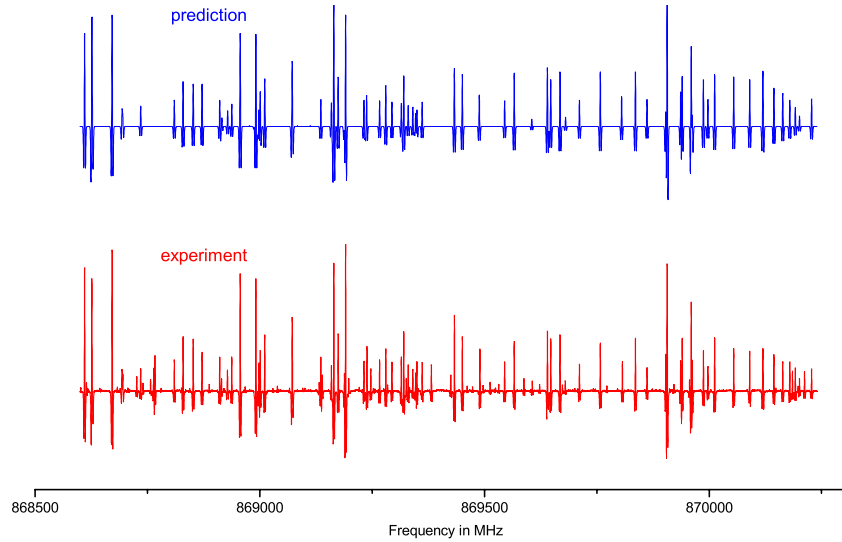


Fig. 2. Predicted (in blue) and observed (in red) rotational spectrum of $\text{CH}_3^{13}\text{CHO}$ between 869.3 and 871.0 GHz dominated by Q-type series of transitions with $K_a = 10 \leftarrow 9$. A slight inconsistency between predicted and observed spectrum, which may be visible for some strong lines, is due to source power and detector sensitivity variations.

Table 3. Assignments, measured transition frequencies, and residuals from the global fit of the microwave, millimeter-wave, and submillimeter-wave $v_t = 0, 1, 2$ data for $^{13}\text{CH}_3\text{CHO}$ acetaldehyde.

Sy	Upper level				Lower level				Position(Unc.) (in MHz)	O-C. (in MHz)	Source	Comment	
	v_t	J	K_a	K_c	Sy	v_t	J	K_a	K_c				
A1	0	3	1	2	A2	0	3	0	3	50 499.1760(0.0500)	-0.0005		
A2	0	4	1	3	A1	0	4	0	4	52 643.0560(0.0500)	0.0111		
A1	0	5	1	4	A2	0	5	0	5	55 411.1830(0.0500)	0.0129		
A2	0	6	1	5	A1	0	6	0	6	58 859.8770(0.0500)	0.0362		
A1	0	7	1	6	A2	0	7	0	7	63 052.9260(0.0500)	-0.0162		
A2	0	10	1	9	A1	0	10	0	10	80 776.1640(0.0500)	0.0373		
A1	0	13	1	12	A2	0	13	0	13	107 350.8210(0.0300)	-0.0171		
A2	0	14	1	13	A1	0	14	0	14	118 271.1660(0.0300)	0.0042		
A1	0	15	1	14	A2	0	15	0	15	130 175.9920(0.0300)	-0.0249		
A2	0	16	1	15	A1	0	16	0	16	142 998.5600(0.0300)	-0.0006		
A1	0	17	1	16	A2	0	17	0	17	156 649.3120(0.0300)	-0.0152		
A2	0	18	1	17	A1	0	18	0	18	171 020.7020(0.0300)	0.0011		
A1	0	19	1	18	A2	0	19	0	19	185 992.3500(0.0300)	-0.0246		
A2	0	20	1	19	A1	0	20	0	20	201 437.3930(0.0300)	0.0079		
A2	0	22	1	21	A1	0	22	0	22	233 243.5300(0.0300)	0.0439		
A1	0	23	1	22	A2	0	23	0	23	249 371.9770(0.0300)	0.0040		
A2	0	24	1	23	A1	0	24	0	24	265 518.1390(0.0300)	-0.0019		
A1	0	25	1	24	A2	0	25	0	25	281 604.1520(0.0300)	0.0042		
A2	0	26	1	25	A1	0	26	0	26	297 570.9590(0.0300)	0.0110		
A1	0	27	1	26	A2	0	27	0	27	313 377.6680(0.0300)	0.0153		
A1	0	33	1	32	A2	0	33	0	33	404 255.7570(0.0300)	-0.0218		
A2	0	34	1	33	A1	0	34	0	34	418 806.7790(0.0300)	0.0311		
A1	0	35	1	34	A2	0	35	0	35	433 225.8170(0.0300)	0.0342		
A2	0	36	1	35	A1	0	36	0	36	447 527.9000(0.0300)	0.0275		
A1	0	37	1	36	A2	0	37	0	37	461 726.8520(0.0300)	0.0298		
A2	0	38	1	37	A1	0	38	0	38	475 835.0620(0.0300)	0.0353		
A1	0	39	1	38	A2	0	39	0	39	489 863.4180(0.0300)	0.0186		
A2	0	40	1	39	A1	0	40	0	40	503 821.4490(0.0300)	0.0469		
A1	0	41	1	40	A2	0	41	0	41	517 717.2310(0.0300)	0.0952		
A1	0	43	1	42	A2	0	43	0	43	545 348.1920(0.0300)	0.0406		
A2	0	44	1	43	A1	0	44	0	44	559 094.0470(0.0300)	0.0473		
A1	0	45	1	44	A2	0	45	0	45	572 799.0380(0.0300)	0.0567		
A1	0	47	1	46	A2	0	47	0	47	600 098.8390(0.0300)	0.0426		
A2	0	48	1	47	A1	0	48	0	48	613 698.4900(0.0300)	0.0412		

Notes. Full table is available at the CDS: S3.

Table 4. Assignments, measured transition frequencies, and residuals from the global fit of the microwave, millimeter-wave, and submillimeter-wave $v_t = 0, 1, 2$ data for $\text{CH}_3^{13}\text{CHO}$ acetaldehyde.

<i>Sy</i>	Upper level			Lower level			Position(Unc.)	O-C	Source	Comment	
	v_t	<i>J</i>	K_a	K_c	<i>Sy</i>	v_t	<i>J</i>	K_a	K_c	(in MHz)	(in MHz)
A2	0	1	0	1	A1	0	0	0	0	19 232.4300(0.3000)	0.0062
A1	0	2	0	2	A2	0	1	0	1	38 445.3800(0.2000)	0.1300
A2	0	3	0	3	A1	0	2	0	2	57 618.9420(0.0500)	0.0162
A1	0	4	0	4	A2	0	3	0	3	76 734.0720(0.0500)	-0.0390
A2	0	5	0	5	A1	0	4	0	4	95 772.0540(0.0500)	-0.0346
A1	0	6	0	6	A2	0	5	0	5	114 715.5210(0.0500)	0.0103
A2	0	7	0	7	A1	0	6	0	6	133 549.5330(0.0500)	0.0173
A1	0	8	0	8	A2	0	7	0	7	152 263.1490(0.0500)	0.0081
A2	0	9	0	9	A1	0	8	0	8	170 850.8080(0.0500)	0.0141
A1	0	10	0	10	A2	0	9	0	9	189 313.4080(0.0500)	0.0120
A1	0	12	0	12	A2	0	11	0	11	225 900.8640(0.0500)	0.0183
A2	0	13	0	13	A1	0	12	0	12	244 058.0550(0.0500)	-0.0031
A1	0	14	0	14	A2	0	13	0	13	262 150.7570(0.0500)	0.0104
A2	0	15	0	15	A1	0	14	0	14	280 198.7740(0.0500)	0.0046
A1	0	16	0	16	A2	0	15	0	15	298 219.5590(0.0500)	0.0070
A1	0	22	0	22	A2	0	21	0	21	406 309.5330(0.0300)	0.0055
A2	0	23	0	23	A1	0	22	0	22	424 350.6000(0.0300)	0.0013
A1	0	24	0	24	A2	0	23	0	23	442 399.0100(0.0300)	0.0005
A2	0	25	0	25	A1	0	24	0	24	460 453.4140(0.0300)	-0.0043
A1	0	26	0	26	A2	0	25	0	25	478 512.4370(0.0300)	-0.0008
A2	0	27	0	27	A1	0	26	0	26	496 574.7260(0.0300)	-0.0122
A1	0	28	0	28	A2	0	27	0	27	514 639.0980(0.0300)	-0.0033
A2	0	29	0	29	A1	0	28	0	28	532 704.4390(0.0300)	-0.0043
A1	0	30	0	30	A2	0	29	0	29	550 769.8140(0.0300)	-0.0041
A2	0	31	0	31	A1	0	30	0	30	568 834.4090(0.0300)	-0.0013
A1	0	32	0	32	A2	0	31	0	31	586 897.5190(0.0300)	-0.0034
A2	0	33	0	33	A1	0	32	0	32	604 958.5620(0.0300)	0.0024
A1	0	34	0	34	A2	0	33	0	33	623 017.0230(0.0300)	0.0080
A2	0	43	0	43	A1	0	42	0	42	785 371.2800(0.0500)	0.0459
A1	0	44	0	44	A2	0	43	0	43	803 387.2720(0.0500)	0.0866
A2	0	45	0	45	A1	0	44	0	44	821 397.8580(0.0500)	0.0490
A1	0	46	0	46	A2	0	45	0	45	839 403.0260(0.0500)	0.0660
A1	0	48	0	48	A2	0	47	0	47	875 395.8740(0.0500)	-0.4172
A2	0	49	0	49	A1	0	48	0	48	893 383.8740(0.0500)	-0.3303
A1	0	50	0	50	A2	0	49	0	49	911 365.8540(0.0500)	-0.2552
A2	0	51	0	51	A1	0	50	0	50	929 341.6450(0.0500)	-0.2336

Notes. Full table is available at the CDS: S4.

They include the transition frequencies obtained in this study, as well as those available from the previous study (Kilb et al. 1957). In the first ten columns of Tables 3 and 4, the labeling for each spectral line is given: symmetry, v_t , J , K_a , and K_c . In the following columns we provide the observed transition frequencies, measurement uncertainties, residuals from the fit, and the reference in the case of Kilb et al. (1957) data (column Source). The last column Comment provides differences between the intensity-weighted average of calculated (but experimentally unresolved) transition frequencies and the observed position of the cluster of blended lines (indicated by “b” in this column). The transitions in Tables 3 and 4 are grouped in series where transitions with the same symmetry, v_t , and K_a quantum numbers are sorted in ascending order by J quantum number. Owing to their large sizes, the complete versions of Tables (S3 and S4) are presented at the CDS. Here only parts of these tables are given for illustration purposes.

The predictions for the rotational spectra of the ground and first excited torsional states of the $^{13}\text{CH}_3\text{CHO}$ and $\text{CH}_3^{13}\text{CHO}$ isotopologs up to 1 THz are given in Tables 5 and 6. The spectra

were calculated using the sets of RAM Hamiltonian parameters presented in Table 7. As in Tables 3 and 4, the first ten columns contain the labeling of transitions. The quantum numbers are followed by the columns with calculated transition frequencies and corresponding uncertainties. The next two columns contain the energy of the lower state in cm^{-1} and the product $\mu^2\text{S}$, where μ is the dipole moment of the molecule and S a transition linestrength. In our calculations of the $^{13}\text{CH}_3\text{CHO}$ and $\text{CH}_3^{13}\text{CHO}$ spectra, the values for the dipole moment components were taken to be equal to the corresponding values of the parent acetaldehyde isotopolog (Smirnov et al. 2014). In predictions we have adopted the limitations on rotational quantum numbers of $J = 65$, $K_a = 20$. In Tables 5 and 6, those transitions that match the frequency range requirement (from 1 GHz to 1 THz), whose predicted uncertainties are less than 0.1 MHz, and line strengths exceeding the limit of 0.01 are included. The complete versions of these tables will also be presented at the CDS: S5 and S6. We provide in Table 8 the rotational parts of the partition functions $Q_r(T)$ for $^{13}\text{CH}_3\text{CHO}$ and $\text{CH}_3^{13}\text{CHO}$ calculated from first principles, i.e., via direct summation over the rotational-torsional states. The maximum

Table 5. List of calculated positions and assignments of A–A and E–E transitions in the $v_t = 0,1$ torsional states of $^{13}\text{CH}_3\text{CHO}$ acetaldehyde up to $J = 65$ in the 1–1000 GHz frequency range.

Sy	Upper level				Sy	Lower level				Position	Uncert.	E_{lower}	$\mu^2 * S$
	v_t	J	K_a	K_c		v_t	J	K_a	K_c	(MHz)	(MHz)	cm $^{-1}$	D^2
A1	0	10	10	0	A2	0	10	9	2	892 691.6257	(0.0060)	161.4200	$0.112 \times 10^{+1}$
A2	0	10	10	1	A1	0	10	9	1	892 691.6257	(0.0060)	161.4200	$0.112 \times 10^{+1}$
E	0	20	10	10	E	0	20	9	12	892 743.8813	(0.0044)	258.2060	$0.951 \times 10^{+1}$
E	1	34	10	24	E	1	34	9	25	892 777.0896	(0.0279)	640.3145	$0.191 \times 10^{+2}$
E	0	19	10	9	E	0	19	9	11	892 818.1797	(0.0045)	245.7254	$0.877 \times 10^{+1}$
E	0	18	10	8	E	0	18	9	10	892 884.0773	(0.0046)	233.8688	$0.803 \times 10^{+1}$
E	0	41	10	32	E	0	42	8	35	892 904.9678	(0.0126)	664.2723	0.181×10^{-1}
E	1	20	61	4	E	1	19	5	14	892 920.7693	(0.0057)	301.0407	$0.897 \times 10^{+1}$
E	0	17	10	7	E	0	17	9	9	892 942.2879	(0.0047)	222.6363	$0.727 \times 10^{+1}$
E	0	16	10	6	E	0	16	9	8	892 993.4892	(0.0048)	212.0279	$0.649 \times 10^{+1}$
E	0	15	10	5	E	0	15	9	7	893 038.3229	(0.0050)	202.0436	$0.569 \times 10^{+1}$
E	1	16	71	0	E	1	15	6	10	893 071.5613	(0.0064)	273.2469	$0.878 \times 10^{+1}$
E	0	14	10	4	E	0	14	9	6	893 077.3943	(0.0051)	192.6833	$0.486 \times 10^{+1}$
E	0	10	8	3	E	0	9	7	3	893 089.1803	(0.0045)	105.0124	$0.882 \times 10^{+1}$
E	0	13	10	3	E	0	13	9	5	893 111.2722	(0.0053)	183.9471	$0.400 \times 10^{+1}$
E	0	12	10	2	E	0	12	9	4	893 140.4887	(0.0055)	175.8349	$0.310 \times 10^{+1}$
A2	0	48	44	5	A1	0	47	4	44	893 144.1811	(0.0044)	729.9167	$0.300 \times 10^{+3}$
E	0	11	10	1	E	0	11	9	3	893 165.5391	(0.0056)	168.3467	$0.214 \times 10^{+1}$
E	0	48	44	5	E	0	47	4	44	893 173.5666	(0.0044)	729.9087	$0.300 \times 10^{+3}$
E	0	10	10	0	E	0	10	9	2	893 186.8816	(0.0058)	161.4826	$0.112 \times 10^{+1}$

Notes. Full table is available at the CDS: S5.

Table 6. List of calculated positions and assignments of A–A and E–E transitions in the $v_t = 0,1$ torsional states of $\text{CH}_3^{13}\text{CHO}$ acetaldehyde up to $J = 65$ in the 1–1000 GHz frequency range.

Sy	Upper level				Sy	Lower level				Position	Uncert.	E_{lower}	$\mu^2 * S$
	v_t	J	K_a	K_c		v_t	J	K_a	K_c	(MHz)	(MHz)	cm $^{-1}$	D^2
A1	0	18	10	8	A2	0	18	9	10	870 012.2402	(0.0059)	233.6446	$0.788 \times 10^{+1}$
A2	0	18	10	9	A1	0	18	9	9	870 012.2402	(0.0059)	233.6446	$0.788 \times 10^{+1}$
A1	0	17	10	7	A2	0	17	9	9	870 054.6472	(0.0060)	222.0937	$0.713 \times 10^{+1}$
A2	0	17	10	8	A1	0	17	9	8	870 054.6472	(0.0060)	222.0937	$0.713 \times 10^{+1}$
E	0	45	7	38	E	0	44	7	38	870 090.1522	(0.0037)	711.3277	$0.861 \times 10^{+1}$
A1	0	16	10	6	A2	0	16	9	8	870 090.2612	(0.0062)	211.1846	$0.637 \times 10^{+1}$
A2	0	16	10	7	A1	0	16	9	7	870 090.2612	(0.0062)	211.1846	$0.637 \times 10^{+1}$
E	0	22	10	12	E	0	22	9	14	870 118.9446	(0.0053)	286.3095	$0.108 \times 10^{+1}$
A1	0	15	10	5	A2	0	15	9	7	870 119.8492	(0.0064)	200.9173	$0.558 \times 10^{+1}$
A2	0	15	10	6	A1	0	15	9	6	870 119.8492	(0.0064)	200.9173	$0.558 \times 10^{+1}$
A1	0	14	10	4	A2	0	14	9	6	870 144.1309	(0.0066)	191.2918	$0.477 \times 10^{+1}$
A2	0	14	10	5	A1	0	14	9	5	870 144.1309	(0.0066)	191.2918	$0.477 \times 10^{+1}$
A1	0	13	10	3	A2	0	13	9	5	870 163.7793	(0.0068)	182.3081	$0.392 \times 10^{+1}$
A2	0	13	10	4	A1	0	13	9	4	870 163.7793	(0.0068)	182.3081	$0.392 \times 10^{+1}$
A1	0	12	10	2	A2	0	12	9	4	870 179.4213	(0.0070)	173.9662	$0.304 \times 10^{+1}$
A2	0	12	10	3	A1	0	12	9	3	870 179.4213	(0.0070)	173.9662	$0.304 \times 10^{+1}$
A1	0	11	10	1	A2	0	11	9	3	870 191.6377	(0.0072)	166.2659	$0.210 \times 10^{+1}$
A2	0	11	10	2	A1	0	11	9	2	870 191.6377	(0.0072)	166.2659	$0.210 \times 10^{+1}$
A1	0	10	10	0	A2	0	10	9	2	870 200.9637	(0.0074)	159.2075	$0.110 \times 10^{+1}$
A2	0	10	10	1	A1	0	10	9	1	870 200.9637	(0.0074)	159.2075	$0.110 \times 10^{+1}$

Notes. Full table is available at the CDS: S6.

value of the J quantum number for the energy levels taken for calculating the partition function is 100. The vibrational part $Q_v(T)$ may be estimated in the harmonic approximation using the normal modes reported for the main isotopolog of acetaldehyde by Schimanouchi (1972). Simple formulas for calculating $Q_v(T)$ can be found elsewhere (see, for example, Gordy & Cook 1984).

5. Conclusion

A new study of the rotational spectra of the $^{13}\text{CH}_3\text{CHO}$ and $\text{CH}_3^{13}\text{CHO}$ isotopologs of the acetaldehyde molecule was carried out in a wide frequency range up to 945 GHz. The study represents more than a twenty-fold expansion in terms of frequency range coverage for the rotational spectra of mono- ^{13}C

Table 7. Fitted parameters of the RAM Hamiltonian for ^{13}C acetaldehyde isotopologs.

Operator ¹	n_{tr}^2	Parameter	$^{12}\text{CH}_3^{12}\text{CHO}$ value ³ (cm^{-1})	$^{13}\text{CH}_3^{12}\text{CHO}$ value ³ (cm^{-1})	$^{12}\text{CH}_3^{13}\text{CHO}$ value ³ (cm^{-1})
P_a^2	2 ₂₀	F	7.56708175(35)	7.5652791(19)	7.5068034(55)
(1/2) (1 - $\cos(3\alpha)$)	2 ₂₀	V_3	407.59768(20)	407.91172(18)	407.58042(26)
$\text{P}_a \text{P}_a$	2 ₁₁	ρ	0.328632673(20)	0.328300981(35)	0.322541154(65)
P_a^2	2 ₀₂	A_{RAM}	1.884881309(61)	1.88013742(13)	1.848976496(63)
P_b^2	2 ₀₂	B_{RAM}	0.348706489(16)	0.337726802(58)	0.348720666(61)
P_c^2	2 ₀₂	C_{RAM}	0.3031840478(44)	0.294817724(11)	0.302179145(18)
{ P_a, P_b }	2 ₀₂	D_{ab}	-0.122669037(94)	-0.11817144(38)	-0.12175149(39)
(1/2) (1 - $\cos(6\alpha)$)	4 ₄₀	V_6	-11.63964(50)	-11.67172(20)	-11.71571(65)
P_a^4	4 ₄₀	F_m	-0.424416(38) $\times 10^{-3}$	-0.427829(96) $\times 10^{-3}$	-0.42834(12) $\times 10^{-3}$
$\text{P}_a^3 \text{P}_a$	4 ₃₁	ρ_m	-0.832163(52) $\times 10^{-3}$	-0.82821(11) $\times 10^{-3}$	-0.81162(16) $\times 10^{-3}$
$\text{P}^2 (1 - \cos(3\alpha))$	4 ₂₂	V_{3J}	0.5577894(41) $\times 10^{-3}$	0.524776(16) $\times 10^{-3}$	0.529795(22) $\times 10^{-3}$
$\text{P}_a^2 (1 - \cos(3\alpha))$	4 ₂₂	V_{3K}	-0.19313906(98) $\times 10^{-1}$	-0.1898291(17) $\times 10^{-1}$	-0.1953217(29) $\times 10^{-1}$
$(\text{P}_b^2 - \text{P}_c^2)(1 - \cos(3\alpha))$	4 ₂₂	V_{3bc}	0.2114597(52) $\times 10^{-3}$	0.192215(19) $\times 10^{-3}$	0.213208(15) $\times 10^{-3}$
(1/2) { P_a, P_b } (1 - $\cos(3\alpha)$)	4 ₂₂	V_{3ab}	0.4235363(70) $\times 10^{-2}$	0.405222(33) $\times 10^{-2}$	0.443922(36) $\times 10^{-2}$
$\text{P}_a^2 \text{P}^2$	4 ₂₂	F_J	-0.291704(53) $\times 10^{-5}$	-0.26533(11) $\times 10^{-5}$	-0.31536(19) $\times 10^{-5}$
$\text{P}_a^2 \text{P}_a^2$	4 ₂₂	F_K	-0.982545(30) $\times 10^{-3}$	-0.972792(46) $\times 10^{-3}$	-0.944979(89) $\times 10^{-3}$
$\text{P}_a^2 (\text{P}_b^2 - \text{P}_c^2)$	4 ₂₂	F_{bc}	0.14720(12) $\times 10^{-5}$	0.13745(31) $\times 10^{-5}$	0.16632(37) $\times 10^{-5}$
(1/2) { P_a, P_c } sin(3 α)	4 ₂₂	D_{3ac}	-0.1405503(49) $\times 10^{-1}$	-0.135881(17) $\times 10^{-1}$	-0.142957(18) $\times 10^{-1}$
(1/2) { P_b, P_c } sin(3 α)	4 ₂₂	D_{3bc}	0.59173(13) $\times 10^{-3}$	0.55489(43) $\times 10^{-3}$	0.63859(48) $\times 10^{-3}$
$\text{P}_a \text{P}_a \text{P}^2$	4 ₁₃	ρ_J	0.958253(42) $\times 10^{-5}$	0.91984(11) $\times 10^{-5}$	0.91075(15) $\times 10^{-5}$
$\text{P}_a \text{P}_a^3$	4 ₁₃	ρ_K	-0.571407(12) $\times 10^{-3}$	-0.564681(12) $\times 10^{-3}$	-0.549548(31) $\times 10^{-3}$
(1/2) { $\text{P}_a, (\text{P}_b^2 - \text{P}_c^2)$ } p_a	4 ₁₃	ρ_{bc}	-0.5536(12) $\times 10^{-6}$	-0.5763(36) $\times 10^{-6}$	-0.2887(35) $\times 10^{-6}$
- P^4	4 ₀₄	Δ_J	0.3244101(54) $\times 10^{-6}$	0.306742(20) $\times 10^{-6}$	0.325255(24) $\times 10^{-6}$
- $\text{P}^2 \text{P}_a^2$	4 ₀₄	Δ_{JK}	-0.581770(50) $\times 10^{-5}$	-0.556079(86) $\times 10^{-5}$	-0.571647(79) $\times 10^{-5}$
- P_a^4	4 ₀₄	Δ_K	0.1308173(26) $\times 10^{-3}$	0.1292582(29) $\times 10^{-3}$	0.1263888(56) $\times 10^{-3}$
- $2\text{P}^2 (\text{P}_b^2 - \text{P}_c^2)$	4 ₀₄	δ_J	0.778472(23) $\times 10^{-7}$	0.709225(70) $\times 10^{-7}$	0.786517(69) $\times 10^{-7}$
-{ $\text{P}_a^2, (\text{P}_b^2 - \text{P}_c^2)$ }	4 ₀₄	δ_K	0.94268(17) $\times 10^{-6}$	0.105094(90) $\times 10^{-5}$	0.10255(12) $\times 10^{-5}$
{ P_a, P_b } P^2	4 ₀₄	D_{abJ}	0.867443(32) $\times 10^{-6}$	0.81273(20) $\times 10^{-6}$	0.85179(14) $\times 10^{-6}$
{ P_a^3, P_b }	4 ₀₄	D_{abK}	0.30498(25) $\times 10^{-5}$	0.29239(46) $\times 10^{-5}$	0.27116(33) $\times 10^{-5}$
(1/2) (1 - $\cos(9\alpha)$)	6 ₆₀	V_9	-0.20318(11)	-0.14153(11)	-0.2413(14)
P_a^6	6 ₆₀	F_{mm}	-0.5066(16) $\times 10^{-6}$	-0.8986(20) $\times 10^{-6}$	-0.7480(55) $\times 10^{-6}$
$\text{P}_a^5 \text{P}_a$	6 ₅₁	ρ_{mm}	-0.7147(34) $\times 10^{-6}$	-0.14955(33) $\times 10^{-5}$	-0.1138(11) $\times 10^{-5}$
$\text{P}^2 (1 - \cos(6\alpha))$	6 ₄₂	V_{6J}	0.557997(73) $\times 10^{-4}$	0.54132(35) $\times 10^{-4}$	0.58065(59) $\times 10^{-4}$
$\text{P}_a^2 (1 - \cos(6\alpha))$	6 ₄₂	V_{6K}	-0.37191(19) $\times 10^{-3}$	-0.37805(54) $\times 10^{-3}$	-0.33899(20) $\times 10^{-3}$
(1/2) { P_a, P_b } (1 - $\cos(6\alpha)$)	6 ₄₂	V_{6ab}	-0.13638(10) $\times 10^{-3}$	-0.12574(40) $\times 10^{-3}$	-0.12853(37) $\times 10^{-3}$
($\text{P}_b^2 - \text{P}_c^2$) (1 - $\cos(6\alpha)$)	6 ₄₂	V_{6bc}	-	0.1222(48) $\times 10^{-5}$	-0.829(29) $\times 10^{-6}$
$\text{P}_a^4 \text{P}^2$	6 ₄₂	F_{mJ}	-0.1259(18) $\times 10^{-9}$	-	-0.4837(88) $\times 10^{-8}$
$\text{P}_a^4 \text{P}_a^2$	6 ₄₂	F_{mK}	-0.1712(36) $\times 10^{-6}$	-0.8131(17) $\times 10^{-6}$	-0.5599(92) $\times 10^{-6}$
$\text{P}_a^4 (\text{P}_b^2 - \text{P}_c^2)$	6 ₄₂	F_{mbc}	0.1197(22) $\times 10^{-8}$	-	-
(1/2) { P_b, P_c } sin(6 α)	6 ₄₂	D_{6bc}	-0.72949(57) $\times 10^{-4}$	-0.6730(24) $\times 10^{-4}$	-0.7137(16) $\times 10^{-4}$
(1/2) { P_a, P_c } sin(6 α)	6 ₄₂	D_{6ac}	0.46097(67) $\times 10^{-3}$	0.4258(12) $\times 10^{-3}$	0.5301(10) $\times 10^{-3}$
(1/2) { $\text{P}_a, \text{P}_c, \text{p}_a^2$, sin(3 α)}	6 ₄₂	D_{3acm}	-0.3178(66) $\times 10^{-5}$	-	-
$\text{P}_a^3 \text{P}_a^3$	6 ₃₃	ρ_{mK}	0.2946(23) $\times 10^{-6}$	-	0.754(45) $\times 10^{-7}$
$\text{P}_a^3 \text{P}_a^2 \text{P}^2$	6 ₃₃	ρ_{mJ}	-0.5306(26) $\times 10^{-8}$	-0.3235(44) $\times 10^{-8}$	-0.968(12) $\times 10^{-8}$
(1/2) { $\text{P}_a, \text{P}_b, \text{p}_a, \text{sin}(3\alpha)$ }	6 ₃₃	ρ_{3bc}	0.47689(54) $\times 10^{-5}$	-	-
(1/2) { $\text{P}_a, (\text{P}_b^2 - \text{P}_c^2)$ } p_a^3	6 ₃₃	ρ_{mbc}	0.4347(38) $\times 10^{-8}$	-0.995(35) $\times 10^{-9}$	-
$\text{P}^4 (1 - \cos(3\alpha))$	6 ₂₄	V_{3JJ}	-0.77602(42) $\times 10^{-8}$	-0.4499(21) $\times 10^{-8}$	-0.5065(25) $\times 10^{-8}$
$\text{P}^2 \text{P}_a^2 (1 - \cos(3\alpha))$	6 ₂₄	V_{3JK}	-	-0.23620(40) $\times 10^{-6}$	-
$\text{P}_a^4 (1 - \cos(3\alpha))$	6 ₂₄	V_{3KK}	0.115646(94) $\times 10^{-5}$	0.11145(17) $\times 10^{-5}$	0.12880(30) $\times 10^{-5}$
$\text{P}_a^2 \text{P}^4$	6 ₂₄	F_{JJ}	-	0.2343(39) $\times 10^{-10}$	0.1768(58) $\times 10^{-10}$
$\text{P}_a^2 \text{P}^2 \text{P}_a^2$	6 ₂₄	F_{JK}	-0.6904(18) $\times 10^{-8}$	-0.5620(48) $\times 10^{-8}$	-0.9637(65) $\times 10^{-8}$
$\text{P}_a^2 \text{P}_a^4$	6 ₂₄	F_{KK}	0.30324(86) $\times 10^{-6}$	0.22248(28) $\times 10^{-6}$	0.2220(15) $\times 10^{-6}$
$\text{P}^2 (\text{P}_b^2 - \text{P}_c^2) (1 - \cos(3\alpha))$	6 ₂₄	V_{3bcJ}	-0.17920(30) $\times 10^{-8}$	-	-0.2040(11) $\times 10^{-8}$
(1/2) { P_a^3, P_c } sin(3 α)	6 ₂₄	D_{3acK}	0.1246(10) $\times 10^{-5}$	0.1141(18) $\times 10^{-5}$	0.171(10) $\times 10^{-6}$
(1/2) { P_a, P_c } P^2 sin(3 α)	6 ₂₄	D_{3acJ}	0.10821(34) $\times 10^{-7}$	0.7636(98) $\times 10^{-7}$	0.372(14) $\times 10^{-7}$
(1/2) { P_b, P_c } P^2 sin(3 α)	6 ₂₄	D_{3bcJ}	-0.7436(17) $\times 10^{-8}$	-0.6126(43) $\times 10^{-8}$	-0.5837(99) $\times 10^{-8}$

Notes. ⁽¹⁾ $\{A, B\} = AB + BA$; $\{A, B, C\} = ABC + CBA$; $\{A, B, C, D\} = ABCD + DCBA$. The product of the operator in the first column of a given row and the parameter in the third column of that row gives the term actually used in the torsion-rotation Hamiltonian of the program, except for F , ρ , and A_{RAM} , which occur in the Hamiltonian in the form $F(P_a + \rho P_a)^2 + A_{\text{RAM}} P_a^2$. ⁽²⁾ $n = t + r$, where n is the total order of the operator, t is the order of the torsional part, and r is the order of the rotational part, respectively. ⁽³⁾ All values are in cm^{-1} , except ρ which is unitless. Statistical uncertainties are shown as one standard uncertainty in the units of the last two digits.

Table 7. continued.

Operator ¹	<i>n</i> _{tr} ²	Parameter	¹² CH ₃ ¹² CHO value ³ (cm ⁻¹)	¹³ CH ₃ ¹² CHO value ³ (cm ⁻¹)	¹² CH ₃ ¹³ CHO value ³ (cm ⁻¹)
(1/2){P _a ² ,P _b ,P _c }sin(3α)	6 ₂₄	D _{3bcK}	0.14846(12) × 10 ⁻⁵	-0.2309(55) × 10 ⁻⁶	-0.713(55) × 10 ⁻⁷
(1/2){{P _a ,P _b ³ } - {P _a ,P _b ,P _c ² }}cos(3α)	6 ₂₄	V _{3ab3}	0.38167(73) × 10 ⁻⁷	0.5101(22) × 10 ⁻⁷	0.5078(27) × 10 ⁻⁷
P ² P _a ² (1 - cos(3α))	6 ₂₄	V _{3JK}	-0.23880(36) × 10 ⁻⁶	-	-0.28455(63) × 10 ⁻⁶
(1/2){P _a ,P _b }P ² (1 - cos(3α))	6 ₂₄	V _{3abJ}	-	-0.566(26) × 10 ⁻⁸	-
(1/2){P _a ³ ,P _b }(1 - cos(3α))	6 ₂₄	V _{3abK}	0.1562(36) × 10 ⁻⁶	0.2057(47) × 10 ⁻⁶	0.4345(43) × 10 ⁻⁶
P ² (P _b ² - P _c ²)(1 - cos(3α))	6 ₂₄	V _{3bcJ}	-	-0.1586(11) × 10 ⁻⁸	-
(1/2){P _a ² ,(P _b ² - P _c ²)}cos(3α)	6 ₂₄	V _{3bcK}	-	0.28389(89) × 10 ⁻⁶	0.2838(15) × 10 ⁻⁶
(1/2){{P _a ,P _b ³ } - {P _a ,P _b ³ }}sin(3α)	6 ₂₄	D _{3ac3}	-0.3543(24) × 10 ⁻⁷	-0.3397(69) × 10 ⁻⁷	-
(1/2){(P _b ³ ,P _c) - {P _b ,P _c ³ }}sin(3α)	6 ₂₄	D _{3bc3}	-	-0.2447(29) × 10 ⁻⁸	-0.2554(33) × 10 ⁻⁸
p _a ² (P _b ² - P _c ²)P ²	6 ₂₄	F _{bcJ}	-	-	0.1505(72) × 10 ⁻¹⁰
(1/2){P _a ² ,(P _b ² - P _c ²)}p _a ²	6 ₂₄	F _{bcK}	0.7853(30) × 10 ⁻⁸	-	-
p _a ² (P _c ⁴ +P _b ⁴)	6 ₂₄	F _{b2c2}	0.49528(94) × 10 ⁻¹⁰	-	-
(P _b ⁴ +P _c ⁴)cos3α	6 ₂₄	V _{3b2c2}	-0.32294(69) × 10 ⁻⁸	0.770(22) × 10 ⁻⁹	0.684(31) × 10 ⁻⁹
p _a P _a ⁴	6 ₁₅	ρ _{JJ}	-	-	-0.2008(54) × 10 ⁻¹⁰
p _a P _a ³ P ²	6 ₁₅	ρ _{JK}	-0.40507(54) × 10 ⁻⁸	-0.3627(21) × 10 ⁻⁸	-0.4479(25) × 10 ⁻⁸
p _a P _a ⁵	6 ₁₅	ρ _{KK}	0.12126(20) × 10 ⁻⁶	0.10832(11) × 10 ⁻⁶	0.10436(34) × 10 ⁻⁶
(1/2){P _a ,(P _b ² - P _c ²)}P ² p _a	6 ₁₅	ρ _{bcJ}	-0.15285(93) × 10 ⁻¹⁰	-	-
(1/2){P _a ³ ,(P _b ² - P _c ²)}p _a	6 ₁₅	ρ _{bcK}	0.6381(14) × 10 ⁻⁸	0.1989(33) × 10 ⁻⁸	0.1085(16) × 10 ⁻⁸
{P _a ,P _b }P ⁴	6 ₀₆	D _{abJJ}	-0.16905(91) × 10 ⁻¹¹	-0.1419(35) × 10 ⁻¹¹	-
{P _a ³ ,P _b }P ²	6 ₀₆	D _{abJK}	0.8607(65) × 10 ⁻¹⁰	0.478(19) × 10 ⁻¹⁰	0.3802(27) × 10 ⁻⁹
{P _a ⁵ ,P _b }	6 ₀₆	D _{abKK}	0.11154(82) × 10 ⁻⁸	0.888(24) × 10 ⁻⁹	0.4607(23) × 10 ⁻⁸
P ⁶	6 ₀₆	Φ _J	0.80483(59) × 10 ⁻¹²	0.6874(26) × 10 ⁻¹²	0.7043(10) × 10 ⁻¹²
P ² P _a ²	6 ₀₆	Φ _{JK}	-0.2732(10) × 10 ⁻¹⁰	-0.1630(29) × 10 ⁻¹⁰	-0.4677(31) × 10 ⁻¹⁰
P ² P _a ⁴	6 ₀₆	Φ _{KJ}	-0.14266(25) × 10 ⁻⁸	-0.12937(55) × 10 ⁻⁸	-0.17957(56) × 10 ⁻⁸
P _a ⁶	6 ₀₆	Φ _K	0.19759(23) × 10 ⁻⁷	0.18596(18) × 10 ⁻⁷	0.18908(47) × 10 ⁻⁷
2P ⁴ (P _b ² - P _c ²)	6 ₀₆	ϕ _J	0.38476(25) × 10 ⁻¹²	0.3246(12) × 10 ⁻¹²	0.34399(69) × 10 ⁻¹²
P ² {P _a ² ,(P _b ² - P _c ²)} {P _a ⁴ ,(P _b ² - P _c ²)} (1/2)(1 - cos(12α))	6 ₀₆	ϕ _K	-0.9470(55) × 10 ⁻¹¹	-0.653(13) × 10 ⁻¹¹	-0.1633(14) × 10 ⁻¹⁰
p _a ⁸	8 ₈₀	V ₁₂	0.10123(15)	-	0.1718(18)
p _a ⁷ P _a	8 ₈₀	F _{mmmm}	-0.8628(32) × 10 ⁻⁸	-	-
P ² (1 - cos(9α))	8 ₇₁	ρ _{mmmm}	-0.20698(86) × 10 ⁻⁷	-	-
P _a ² (1 - cos(9α))	8 ₆₂	V _{9J}	-0.15703(56) × 10 ⁻⁵	-0.1211(24) × 10 ⁻⁵	-0.3590(49) × 10 ⁻⁵
(P _b ² - P _c ²)(1 - cos(9α))	8 ₆₂	V _{9K}	0.3044(14) × 10 ⁻⁴	0.4013(45) × 10 ⁻⁴	-
(1/2){P _a ,P _b }(1 - cos(9α))	8 ₆₂	V _{9bc}	-0.11444(53) × 10 ⁻⁵	-0.1967(52) × 10 ⁻⁵	-
(1/2){P _a ,P _c }sin(9α)	8 ₆₂	V _{9ab}	-	-0.608(35) × 10 ⁻⁵	-0.599(34) × 10 ⁻⁵
(1/2){P _b ,P _c }sin(9α)	8 ₆₂	D _{9ac}	-	0.1409(39) × 10 ⁻⁴	-
P _a ² p _a ⁶	8 ₆₂	D _{9bc}	0.884(13) × 10 ⁻⁶	-	-0.343(10) × 10 ⁻⁵
(1/2){P _a ,P _b }p _a ⁶	8 ₆₂	F _{mmK}	-0.2202(11) × 10 ⁻⁷	-0.1406(33) × 10 ⁻⁹	-
P _a ³ p _a ⁵	8 ₅₃	F _{mmb}	0.2906(29) × 10 ⁻¹⁰	-	-
p _a ⁴ P _a ⁴	8 ₄₄	ρ _{mmK}	-0.13762(98) × 10 ⁻⁷	-	-
(1/2)P ² {P _a ,P _c }sin(6α)	8 ₄₄	F _{mKK}	-0.5734(57) × 10 ⁻⁸	-	-
(1/2){P _a ³ ,P _c }sin(6α)	8 ₄₄	D _{6acJ}	-0.6552(93) × 10 ⁻⁸	-	-
(1/2){P _b ,P _c }P ² sin(6α)	8 ₄₄	D _{6acK}	-	-	0.425(37) × 10 ⁻⁷
(1/2){P _b ³ ,P _c } - {P _b ,P _c ³ })sin(6α)	8 ₄₄	D _{6bcJ}	0.6210(71) × 10 ⁻⁹	0.748(21) × 10 ⁻⁹	-
P ⁴ (1 - cos(6α))	8 ₄₄	D _{6bc3}	-	0.5148(97) × 10 ⁻⁹	0.996(12) × 10 ⁻⁹
P _a ⁴ (1 - cos(6α))	8 ₄₄	V _{6JJ}	-0.799(16) × 10 ⁻¹⁰	-	-
(1/2){P _a ,P _b }P ² (1 - cos(6α))	8 ₄₄	V _{6KK}	0.15152(47) × 10 ⁻⁶	0.1380(11) × 10 ⁻⁶	0.1679(26) × 10 ⁻⁶
(1/2){P _a ³ ,P _b }(1 - cos(6α))	8 ₄₄	V _{6abJ}	-	-0.554(14) × 10 ⁻⁸	-
P ² (P _b ² - P _c ²)(1 - cos(6α))	8 ₄₄	V _{6abK}	-0.6966(58) × 10 ⁻⁷	-0.542(21) × 10 ⁻⁷	-
(1/2){{P _a ,P _b ³ } - {P _a ,P _b ,P _c ² }}cos(6α)	8 ₄₄	V _{6bcJ}	-	-	-0.2303(65) × 10 ⁻⁹
p _a ³ P _a ⁴	8 ₃₅	V _{6ab3}	-	-0.430(16) × 10 ⁻⁸	-
p _a ³ P _a ⁵	8 ₃₅	ρ _{mJJ}	-	-0.873(21) × 10 ⁻¹³	-
(1/2){P _a ,P _b ³ ,P _c ,p _a ,sin(3α)} - (1/2){P _a ,P _b ,P _c ³ ,p _a ,sin(3α)}	8 ₃₅	ρ _{3bc3}	-0.1656(23) × 10 ⁻⁸	-	-
P ⁶ (1 - cos(3α))	8 ₂₆	V _{3JJ}	-0.2511(23) × 10 ⁻¹⁰	-	-
P _a ⁴ P _a ² (1 - cos(3α))	8 ₂₆	V _{3JKK}	0.1344(25) × 10 ⁻¹³	-	-
P ² P _a ⁴ (1 - cos(3α))	8 ₂₆	V _{3JJK}	0.3715(39) × 10 ⁻¹¹	-	-
(1/2)P ² {P _a ³ ,P _b }(1 - cos(3α))	8 ₂₆	V _{3abJK}	0.472(13) × 10 ⁻¹⁰	0.303(11) × 10 ⁻¹⁰	-
(1/2){P _a ⁵ ,P _b }(1 - cos(3α))	8 ₂₆	V _{3abKK}	-	0.3426(55) × 10 ⁻¹⁰	-
(1/2)P ² {P _a ³ ,P _c }sin(3α)	8 ₂₆	D _{3acJK}	-0.2031(61) × 10 ⁻⁹	-	-
(1/2){P _a ⁵ ,P _c }sin(3α)	8 ₂₆	D _{3acKK}	-0.5470(82) × 10 ⁻¹⁰	-	-
(1/2){P _a ⁵ ,P _c }sin(3α)	8 ₂₆	D _{3acKK}	-	0.450(27) × 10 ⁻¹⁰	-

Table 7. continued.

Operator ¹	n_{tr}^2	Parameter	$^{12}\text{CH}_3^{12}\text{CHO}$ value ³ (cm ⁻¹)	$^{13}\text{CH}_3^{12}\text{CHO}$ value ³ (cm ⁻¹)	$^{12}\text{CH}_3^{13}\text{CHO}$ value ³ (cm ⁻¹)
$(1/2)\text{P}^2\{\text{P}_a^2, \text{P}_b, \text{P}_c\}\sin(3\alpha)$	826	D_{3bcJK}	$0.854(18) \times 10^{-11}$	—	—
$(1/2)\{\text{P}_a^4, \text{P}_b, \text{P}_c\}\sin(3\alpha)$	826	D_{3bcKK}	—	—	$-0.1697(63) \times 10^{-9}$
$(1/2)\{\text{P}_a^3, \text{P}_c^3\}\sin(3\alpha)$	826	D_{3ac3K}	$0.6486(74) \times 10^{-10}$	—	—
P_a^2P_a^6	826	F_{KKK}	$-0.3325(57) \times 10^{-9}$	—	—
$\text{P}_a\text{P}_a^3\text{P}^4$	817	ρ_{JJK}	—	—	$0.842(43) \times 10^{-13}$
P_aP_a^7	817	ρ_{KKK}	$-0.4300(86) \times 10^{-10}$	—	$-0.353(15) \times 10^{-11}$
P^8	808	L_J	$-0.3808(46) \times 10^{-17}$	$-0.358(24) \times 10^{-17}$	—
P^4P_a^4	808	L_{JK}	$0.5000(60) \times 10^{-14}$	—	$0.372(14) \times 10^{-13}$
P_a^8	808	L_K	$-0.2743(71) \times 10^{-11}$	—	$-0.1256(48) \times 10^{-11}$
$2\text{P}^6(\text{P}_b^2 - \text{P}_c^2)$	808	l_J	$-0.1626(22) \times 10^{-17}$	$-0.1332(63) \times 10^{-17}$	$-0.1426(83) \times 10^{-17}$
P_a^8P_a^2	1082	F_{mmmk}	—	$0.281(16) \times 10^{-12}$	—
$(1/2)\text{P}^2\{\text{P}_a, \text{P}_b\}(1 - \cos(9\alpha))$	1064	V_{9abJ}	$-0.1960(28) \times 10^{-8}$	—	—
$\text{P}^4\text{P}_a^2(1 - \cos(6\alpha))$	1046	V_{6JK}	—	—	$0.3164(60) \times 10^{-11}$
$\text{P}^2\text{P}_a^4(1 - \cos(6\alpha))$	1046	V_{6KK}	—	—	$-0.222(11) \times 10^{-10}$
$(1/2)\{\text{P}_a^5, \text{P}_b\}(1 - \cos(6\alpha))$	1046	V_{6abKK}	$-0.585(13) \times 10^{-10}$	—	—
P_a^2P_a^8	1028	F_{KKKK}	$0.1427(47) \times 10^{-14}$	—	—

Table 8. Torsion-rotation part $Qrt(T)$ of the total internal partition function $Q(T) = Qv(T) * Qrt(T)$, calculated from first principles using the parameter set of Table 7.

T (K)	$^{13}\text{CH}_3\text{CHO}$			$\text{CH}_3^{13}\text{CHO}$		
	Qrt (A+E)	Qrt (A)	Qrt (E)	Qrt (A+E)	Qrt (A)	Qrt (E)
10	153.249	76.8662	77.1410	150.384	75.4230	75.6797
20	431.553	215.993	216.626	423.373	211.895	212.489
30	792.543	396.437	397.413	777.474	388.897	389.814
40	1225.44	612.827	614.125	1202.20	601.205	602.429
50	1730.87	865.497	867.088	1698.28	849.196	850.700
60	2314.40	1157.23	1159.08	2271.23	1135.64	1137.39
70	2983.09	1491.56	1493.64	2928.03	1464.02	1466.00
80	3744.16	1872.08	1874.39	3675.80	1837.90	1840.09
90	4604.57	2302.29	2304.81	4521.40	2260.70	2263.10
100	5570.85	2785.43	2788.18	5471.25	2735.63	2738.24
110	6649.03			6531.29		
120	7844.64			7706.97		
130	9162.72			9003.25		
140	10 607.9			10 424.6		
150	12 184.2			11 975.2		
160	13 895.5			13 658.7		
170	15 745.0			15 478.4		
180	17 736.0			17 437.3		
190	19 871.0			19 538.1		
200	22 152.6			21 783.2		
210	24 583.1			24 174.9		
220	27 164.3			26 715.1		
230	29 898.2			29 405.7		
240	32 786.3			32 248.1		
250	35 830.2			35 243.9		
260	39 031.0			38 394.3		
270	42 390.1			41 700.5		
280	45 908.4			45 163.4		
290	49 586.8			48 784.1		
300	53 426.1			52 563.2		

Notes. For the temperatures below 100 K, the separate A and E parts of the torsion-rotation part of partition function are given, where the A and E type levels are treated as the independent subsets of energy levels. The vibrational part $Qv(T)$ (omitting the torsional vibration since it is taken into account in Qrt) may be estimated in the harmonic approximation using the vibrational frequencies reported for the parent species of acetaldehyde by Schimanouchi, Tables of Molecular Vibrational Frequencies, Vol. I: consolidated (National Bureau of Standards, Washington, DC, 1972), pp. 1160. In the calculation the states up to $J = 100$ and $vt = 8$ were included.

acetaldehydes. Using the RAM Hamiltonian models, we were able to fit the available data within experimental accuracy. The results of the present study allowed us to produce reliable predictions of rotational spectra in the ground and first excited torsional states of ¹³CH₃CHO and CH₃¹³CHO isotopologs for astrophysical purposes in the frequency range up to 1 THz for $0 < J < 65$ and $0 < K_a < 20$.

Acknowledgements. This work was done with the support of the Ukrainian-French CNRS-PICS 6051 project. The Centre National d'Etudes Spatiales (CNES) and the Action sur Projets de l'INSU, "Physique et Chimie du Milieu Interstellaire" are acknowledged for financial support. This work was also done under the ANR-08-BLAN-0054.

References

- Alekseev, E. A., Motiyenko, R. A., & Margulès, L. 2012, *Radio Physics Radio Astronomy*, **3**, 75
- Barbry, D., & Couturier, D. J. 1987, Labelled Comp. Radiopharm., XXIV, 603
- Bouchez, A., Margulès, L., Motiyenko, R. A., et al. 2012, *A&A*, **540**, A51
- Carvajal, M., Margulès, L., Tercero, B., et al. 2009, *A&A*, **500**, 1109
- Charnley, S. B. 2004, *Adv. Space Res.*, **33**, 23
- Coudert, L. H., Margulès, L., Huet, T. R., et al. 2012, *A&A*, **543**, A46
- Coudert, L. H., Drouin, B. J., Tercero, B., et al. 2013, *ApJ*, **779**, 119
- Demyk, K., Mäder, H., Tercero, B., et al. 2007, *A&A*, **466**, 255
- Elkeurti, M., Coudert, L. H., Medvedev, I. R., et al. 2010, *J. Mol. Spectr.*, **263**, 145
- Gordy, W., & Cook, R. L. 1984, *Microwave Molecular Spectra, Techniques of Chemistry*, Vol. XVIII (New York: Wiley)
- Haykal, I., Motiyenko, R. A., Margulès, L., & Huet, T. R. 2013, *A&A*, **549**, A96
- Herbst, E., Messer, J. K., De Lucia, F. C., & Helminger, P. 1984, *J. Mol. Spectr.*, **108**, 42
- Hougen, J. T., Kleiner, I., & Godefroid, M. 1994, *J. Mol. Spectr.*, **163**, 559
- Ilyushin, V. V., Kisiel, Z., Pszczołkowski, L., Mäder, H., & Hougen, J. T. 2010, *J. Mol. Spectr.*, **259**, 26
- Ilyushin, V. V., Endres, C. P., Lewen, F., Schlemmer, S., & Drouin, B. J. 2013, *J. Mol. Spectr.*, **290**, 31
- Kilb, R. W., Lin, C. C., & Wilson, E. B. 1957 *J. Chem. Phys.*, **26**, 1695
- Kirtman, B. 1962, *J. Chem. Phys.*, **37**, 2516
- Kleiner, I. 2010, *J. Mol. Spectr.*, **260**, 1
- Kutsenko, A. S., Motiyenko, R. A., Margulès, L., & Guillemin, J.-C. 2013, *A&A*, **549**, A128
- Lees, R. M., & Baker, J. G. 1968, *J. Chem. Phys.*, **48**, 5299
- Margulès, L., Motiyenko, R. A., Demyk, K., et al. 2009a, *A&A*, **493**, 565
- Margulès, L., Coudert, L. H., Möllendal, H., et al. 2009b, *J. Mol. Spectr.*, **254**, 55
- Margulès, L., Huet, T. R., Demaison, J., et al. 2010, *ApJ*, **714**, 1120
- Martinache, L., & Bauder, A. 1989, *Chem. Phys. Lett.*, **164**, 657
- Matthews, H. E., Friberg, P., & Irvine, W. M. 1985, *ApJ*, **290**, 609
- Müller, S., Beelen, A., Guelin, M., et al. 2011, *A&A*, **535**, A103
- Nguyen, L., Walters, A., Margulès, L., et al. 2013, *A&A*, **553**, A84
- Nummelin, A., Dickens, J. E., Bergman, P., et al. 1998, *A&A*, **337**, 275
- Richard, C., Margulès, L., Motiyenko, R. A., & Guillemin, J.-C. 2012, *A&A*, **543**, A135
- Richard, C., Margulès, L., Caux, E., et al. 2013, *A&A*, **552**, A117
- Schimanouchi, T. 1972, in *Tables of Molecular Vibrational Frequencies*, Vol. I: consolidated (Washington, DC: National Bureau of Standards), 89
- Smirnov, I. A., Alekseev, E. A., Ilyushin, V. V., et al. 2014, *J. Mol. Spectr.*, **295**, 44
- Tercero, B., Margulès, L., Carvajal, M., et al. 2012, *A&A*, **538**, A119
- Turner, P. M., & Cox, A. P. 1976, *Chem. Phys. Lett.*, **42**, 84
- Turner, P. M., Cox, A. P., & Hardy, J. A. 1981, *J. Chem. Soc. Faraday Trans. 2*, **77**, 1217
- Turner, B. E., Terzieva, R., & Herbst, E. 1999, *ApJ*, **518**, 699
- Zaleski, D. P., Neill, J. L., Muckle, M. T., et al. 2012, *J. Mol. Spectr.*, **280**, 68

Rotational spectroscopy, tentative interstellar detection, and chemical modeling of N-methylformamide[★]

A. Belloche¹, A. A. Meshcheryakov², R. T. Garrod³, V. V. Ilyushin², E. A. Alekseev^{2,4},
R. A. Motiyenko⁵, L. Margulès⁵, H. S. P. Müller⁶, and K. M. Menten¹

¹ Max-Planck-Institut für Radioastronomie, Auf dem Hügel 69, 53121 Bonn, Germany
e-mail: belloche@mpifr-bonn.mpg.de

² Microwave spectroscopy department, Institute of Radio Astronomy of NASU, Chernovonopraporna Str. 4, 61002 Kharkiv, Ukraine

³ Departments of Chemistry and Astronomy, University of Virginia, Charlottesville, VA 22904, USA

⁴ Quantum Radiophysics Department of V. N. Karazin Kharkiv National University, Svobody Square 4, 61022 Kharkiv, Ukraine

⁵ Laboratoire de Physique des Lasers, Atomes, et Molécules, UMR 8523, CNRS, Université de Lille 1,
59655 Villeneuve d'Ascq Cedex, France

⁶ I. Physikalisches Institut, Universität zu Köln, Zülpicher Str. 77, 50937 Köln, Germany

Received 16 September 2016 / Accepted 17 January 2017

ABSTRACT

Context. N-methylformamide, CH_3NHCHO , may be an important molecule for interstellar pre-biotic chemistry because it contains a peptide bond, which in terrestrial chemistry is responsible for linking amino acids in proteins. The rotational spectrum of the most stable *trans* conformer of N-methylformamide is complicated by strong torsion-rotation interaction due to the low barrier of the methyl torsion. For this reason, the theoretical description of the rotational spectrum of the *trans* conformer has, up to now, not been accurate enough to provide a firm basis for its interstellar detection.

Aims. In this context, as a prerequisite for a successful interstellar detection, our goal is to improve the characterization of the rotational spectrum of N-methylformamide.

Methods. We use two absorption spectrometers in Kharkiv and Lille to measure the rotational spectra over the frequency range 45–630 GHz. The analysis is carried out using the Rho-axis method and the RAM36 code. We search for N-methylformamide toward the hot molecular core Sagittarius (Sgr) B2(N2) using a spectral line survey carried out with the Atacama Large Millimeter/submillimeter Array (ALMA). The astronomical spectra are analyzed under the assumption of local thermodynamic equilibrium. The astronomical results are put into a broader astrochemical context with the help of a gas-grain chemical kinetics model.

Results. The new laboratory data set for the *trans* conformer of N-methylformamide consists of 9469 distinct line frequencies with $J \leq 62$, including the first assignment of the rotational spectra of the first and second excited torsional states. All these lines are fitted within experimental accuracy for the first time. Based on the reliable frequency predictions obtained in this study, we report the tentative detection of N-methylformamide toward Sgr B2(N2). We find N-methylformamide to be more than one order of magnitude less abundant than formamide (NH_2CHO), a factor of two less abundant than the unsaturated molecule methyl isocyanate (CH_3NCO), but only slightly less abundant than acetamide (CH_3CONH_2). We also report the tentative detection of the ^{15}N isotopolog of formamide ($^{15}\text{NH}_2\text{CHO}$) toward Sgr B2(N2). The chemical models indicate that the efficient formation of HNCO via $\text{NH} + \text{CO}$ on grains is a necessary step in the achievement of the observed gas-phase abundance of CH_3NCO . Production of CH_3NHCHO may plausibly occur on grains either through the direct addition of functional-group radicals or through the hydrogenation of CH_3NCO .

Conclusions. Provided the detection of N-methylformamide is confirmed, the only slight underabundance of this molecule compared to its more stable structural isomer acetamide and the sensitivity of the model abundances to the chemical kinetics parameters suggest that the formation of these two molecules is controlled by kinetics rather than thermal equilibrium.

Key words. line: identification – molecular data – radio lines: ISM – ISM: molecules – ISM: individual objects: Sagittarius B2(N) – astrochemistry

1. Introduction

The peptide bond is a fundamental building block of life on Earth (Kaiser et al. 2013). Therefore, peptide molecules have for a long time attracted much attention. The simplest molecule containing a peptide bond, formamide (NH_2CHO), was detected in the interstellar medium (ISM) back in the 1970s (Rubin et al. 1971). The relatively high abundance of formamide also permitted the detection of rotational lines of its first excited vibrational

state $v_{12} = 1$ in Orion KL (Motiyenko et al. 2012) and in Sagittarius (Sgr) B2(N) (Belloche et al. 2013). N-methylformamide, CH_3NHCHO , is one of the simplest derivatives of formamide and also a peptide molecule. It is of interest as a candidate for interstellar detection because its structural isomer acetamide (CH_3CONH_2) has already been detected in the ISM (Hollis et al. 2006; Halfen et al. 2011). CH_3NHCHO is the second most stable $\text{C}_2\text{H}_5\text{NO}$ isomer after acetamide (Lattelais et al. 2010).

N-methylformamide exists in two stable rotameric forms, *trans* and *cis*. Their structures are shown in Fig. 1. According to quantum chemical calculations, the *trans* conformer is more stable than *cis* by 466 cm^{-1} (666 K, Kawashima et al. 2010).

* Full Tables 2 and 3 are only available at the CDS via anonymous ftp to cdsarc.u-strasbg.fr/130.79.128.5 or via <http://cdsarc.u-strasbg.fr/viz-bin/qcat?J/A+A/601/A49>

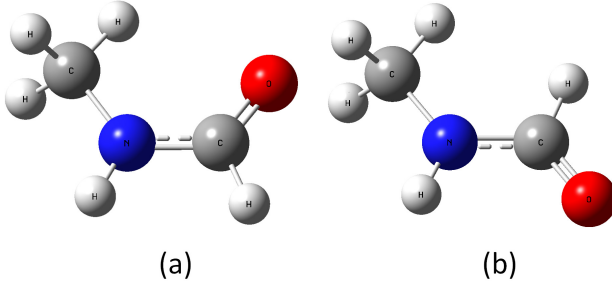


Fig. 1. Structure of *trans* (a) and *cis* (b) conformations of N-methylformamide.

The *trans* conformer is also characterized by a very low barrier to internal rotation of the methyl top. The coupling between the overall rotation of the molecule and the almost free rotation of the methyl top significantly complicates the description of the spectrum. For this reason, N-methylformamide has been the subject of extensive spectroscopic investigations, but for a long time the analysis of its microwave rotational spectrum did not yield satisfactory results. [Fantoni & Caminati \(1996\)](#) were the first to succeed in assigning rotational spectral lines belonging to the *trans* conformer in the CH_3 internal rotation ground state of A symmetry. They performed measurements between 18 and 40 GHz, but could not identify any spectral lines of the *E* species. Later, [Fantoni et al. \(2002\)](#) published results of measurements and analysis for *E* lines. The V_3 barrier of the methyl group internal rotation was determined to be $55.17 \pm 0.84 \text{ cm}^{-1}$.

Recently, [Kawashima et al. \(2010\)](#) carried out a new spectroscopic investigation of N-methylformamide. In that study, rotational spectra of both *trans* and *cis* conformers of the normal as well as deuterated CH_3NHCHO isotopologs were measured in the frequency range of 5–118 GHz. Molecular parameters including rotational constants and V_3 barriers to methyl-group internal rotation were determined for all investigated species and conformers. Owing to the relatively high barrier to internal rotation for the *cis* conformer, a good description was obtained for its 108 measured transitions. However, the low barrier and the limitations in the model used for the theoretical description of the rotational spectrum allowed these authors to fit only low J quantum number transitions ($J < 11$) for the *trans* conformer. In addition, 60 out of 467 assigned transitions of the *trans* conformer were excluded from the final fit as their residuals ranged from 1 to 67 MHz and were much higher than the experimental accuracy estimated to be 0.004–0.05 MHz.

One should note that in previous publications, two different schemes were used for naming the conformations of N-methylformamide. [Fantoni & Caminati \(1996\)](#) and [Fantoni et al. \(2002\)](#) used the dihedral angle $D(\text{H} - \text{N} - \text{C} - \text{H}')$ where H' is the carbonyl group hydrogen. The conformer with $D = 0^\circ$ was named *cis* and the conformer with $D = 180^\circ$ was named *trans*. [Kawashima et al. \(2010\)](#) used another convention widely accepted for molecules with a peptide bond. According to this convention, applied for N-methylformamide, one should use the $D^*(\text{Y} - \text{N} - \text{C} - \text{X})$ dihedral angle, where X is the carbonyl hydrogen and Y is the methyl group. *Cis* and *trans* conformers named using this convention are thus the opposite of the *cis* and *trans* conformers in [Fantoni & Caminati \(1996\)](#) and [Fantoni et al. \(2002\)](#). Here we use the naming adopted by [Kawashima et al. \(2010\)](#), that is, using the D^* dihedral angle.

In the present study, we extend the measurement and analysis of the rotational spectrum of *trans* N-methylformamide, which is of higher interest for astrophysical detection. We use the accurate frequency predictions obtained in this study to search for N-methylformamide in the ISM. We target the high mass star-forming region Sgr B2(N), one of the most prolific sources for the detection of complex organic molecules in the ISM (e.g., [Belloche et al. 2013](#)). For this, we use a spectral survey of Sgr B2(N) conducted with the Atacama Large Millimeter/submillimeter Array (ALMA) in its Cycles 0 and 1. This survey aims at exploring molecular complexity with ALMA (EMoCA, see [Belloche et al. 2016](#)).

The experimental setup is presented in Sect. 2. The analysis of the rotational spectrum of N-methylformamide and the results that follow are described in Sect. 3. A tentative detection of N-methylformamide in Sgr B2(N) is presented in Sect. 4 along with the derivation of column densities of other related molecules of interest. Chemical modeling is performed in Sect. 5 to put the observational results into a broader astrochemical context. The results are discussed in Sect. 6 and the conclusions are presented in Sect. 7.

2. Experimental setup

A sample of N-methylformamide was purchased from Sigma-Aldrich and used without further purification. The experimental investigation of the absorption spectrum of N-methylformamide was carried out over the frequency range 45–630 GHz using two microwave spectrometers. The first one is the automated millimeter wave spectrometer of the Institute of Radio Astronomy of NASU in Kharkiv, Ukraine ([Alekseev et al. 2012](#)). The second one is the terahertz spectrometer of the Laboratory of Physics of Lasers, Atoms, and Molecules in Lille, France ([Zakharenko et al. 2015](#)).

The spectrometer in Kharkiv is built according to the classical scheme of absorption spectrometers, and its detailed description can be found in [Alekseev et al. \(2012\)](#). The spectrometer was slightly upgraded with the aim of expanding the operating frequency range; a new backward-wave oscillator (BWO) unit covering frequencies from 34 to 52 GHz has been put into operation. Thus, at present, this spectrometer can record spectra between 34 and 250 GHz. In order to improve the sensitivity below 50 GHz, a new waveguide absorbing cell (a copper waveguide of $10 \times 72 \text{ mm}^2$ internal cross section and 295 cm length) was used instead of the commonly employed quasi-optic absorption cell. The measurements of N-methylformamide with the Kharkiv spectrometer were done in the frequency range 45 to 150 GHz. All measurements were performed at room temperature and with sample pressures (approximately 10 mTorr) that provided close to Doppler-limited spectral resolution. The frequency determination errors were estimated to be 10, 30, and 100 kHz depending on the measured signal-to-noise ratio.

The measurements in Lille were performed between 150 and 630 GHz at typical pressures of 10 Pa and at room temperature. The frequency determination errors were estimated to be 30 kHz and 50 kHz below and above 330 GHz, respectively. The frequencies of the lines with poor signal-to-noise ratio or distorted lineshape were measured with 50 kHz or 100 kHz accuracy.

3. Spectroscopic analysis and results

We performed the analysis using the Rho-axis method (RAM), which was already applied successfully to a number of

molecules with large-amplitude torsional motion. The method uses the axis system obtained by rotation of the principal axis system to make the new z axis parallel to the ρ vector. The coordinates of the ρ vector are calculated using the following expression:

$$\rho_g = \frac{\lambda_g I_\alpha}{I_g}, \quad (g = x, y, z),$$

where λ_g are the direction cosines of the internal rotation axis of the top in the principal axis system, I_g are the principal inertia moments, and I_α is the inertia moment of the methyl top. The RAM Hamiltonian may be written as (Kleiner 2010):

$$H_{\text{RAM}} = H_{\text{T}} + H_{\text{R}} + H_{\text{cd}} + H_{\text{int}}. \quad (1)$$

H_{T} represents the torsional Hamiltonian defined as:

$$H_{\text{T}} = F(p_\alpha - \rho J_z)^2 + V(\alpha), \quad (2)$$

where F is the internal rotation constant, p_α is the internal rotation angular momentum conjugate to the torsion angle α , and $V(\alpha)$ is the internal rotation potential function:

$$V(\alpha) = \frac{1}{2} V_3 (1 - \cos 3\alpha) + \frac{1}{2} V_6 (1 - \cos 6\alpha) + \dots \quad (3)$$

H_{R} represents the rigid rotor rotational Hamiltonian in the rho-axis system. In addition to usual A , B , and C terms, for the molecules with (xz) plane of symmetry (as is appropriate for N-methylformamide), it contains a non-diagonal term D_{xz} . In the I' coordinate representation, H_{R} has the following form:

$$H_{\text{R}} = A_{\text{RAM}} J_z^2 + B_{\text{RAM}} J_x^2 + C_{\text{RAM}} J_y^2 + D_{xz}(J_x J_z + J_z J_x). \quad (4)$$

The last two terms in Eq. (1), H_{cd} and H_{int} , are the usual centrifugal distortion and higher-order torsional-rotational interaction Hamiltonians, respectively.

To fit and predict the rotational spectra, we used the RAM36 (Rho-axis method for 3 and 6-fold barriers) program that allows one to include in the model almost any symmetry-allowed torsion-rotation Hamiltonian term up to the twelfth order (Ilyushin et al. 2010, 2013). The RAM Hamiltonian in Eq. (1) may be expressed in the following form used in the RAM36 program :

$$\begin{aligned} H = & \frac{1}{2} \sum_{knpqrs} B_{knpqrs0} [J_z^{2k} J_z^n J_x^p J_y^q p_\alpha^r \cos(3s\alpha) \\ & + \cos(3s\alpha) p_\alpha^r J_y^q J_x^p J_z^n J^{2k}] \\ & + \frac{1}{2} \sum_{knpqrt} B_{knpqrt0t} [J_z^{2k} J_z^n J_x^p J_y^q p_\alpha^r \sin(3t\alpha) \\ & + \sin(3t\alpha) p_\alpha^r J_y^q J_x^p J_z^n J^{2k}], \end{aligned} \quad (5)$$

where the B_{knpqrs} are fitting parameters. In the case of a C_{3v} top and C_s frame (as is appropriate for N-methylformamide), the allowed terms in the torsion-rotation Hamiltonian must be totally symmetric in the group G_6 (and also must be Hermitian and invariant to the time reversal operation). Since all individual operators p_α , J_x , J_y , J_z , J^2 , $\cos(3s\alpha)$, and $\sin(3t\alpha)$ used in Eq. (5) are Hermitian, all possible terms provided by Eq. (5) will automatically be Hermitian. The particular term to be fitted is represented in the input file with a set of k, n, p, q, r, s, t integer indices that are checked by the program for conformity with time reversal and symmetry requirements, to prevent accidental introduction

of symmetry-forbidden terms into the Hamiltonian. For example, $B_{0000200}$ corresponds to F in Eq. (2), $B_{0200000}$ to A_{RAM} in Eq. (4), etc. In Table 1, which presents the final set of molecular parameters, we give, instead of B_{knpqrs} , more conventional names for the parameters whose nomenclature is based on the subscript procedures of Xu et al. (2008).

The RAM36 program uses the free-rotor quantum number m to label the torsional energy levels. It is well known that the internal rotation of a methyl top attached to a molecular frame should be treated as an anharmonic vibrational motion well below the top of the barrier to internal rotation, and as a nearly free internal rotation motion well above the top of the barrier. The v_t labeling assumes that the spacings between degenerate and non-degenerate levels of the torsional Hamiltonian associated with a given v_t are much smaller than those between levels with different v_t (Lin & Swalen 1959). The *trans* conformation of N-methylformamide represents an intermediate case because of the relatively low barrier to internal rotation (Lin & Swalen 1959). Owing to the low barrier, the $A - E$ splitting in the first excited torsional state $v_t = 1$ of the *trans* conformation is comparable with the energy difference between the $v_t = 0$ and $v_t = 1$ states, whereas the $v_t = 2$ state lies well above the barrier. Because of this intermediate situation we decided to keep the quantum number labeling of torsional states m in Tables 2 and 3, which is used inside the RAM36 program.

The RAM36 code was modified to take into account the quadrupole hyperfine structure of the transitions that is present in the spectrum of N-methylformamide due to the non-zero electric quadrupole moment of the nitrogen atom. We used the standard hyperfine energy expression:

$$E_{hf} = [\chi_{aa} \langle J_a^2 \rangle + \chi_{bb} \langle J_b^2 \rangle - (\chi_{aa} + \chi_{bb}) \langle J_c^2 \rangle + \chi_{ab} \langle J_a J_b + J_b J_a \rangle] \frac{2f(I, J, F)}{J(J+1)}, \quad (6)$$

where $f(I, J, F)$ is the Casimir function. Typically, a resolved pattern of the hyperfine structure was observed as a doublet with an approximately two-to-one ratio in intensities. The stronger doublet component contains unresolved hyperfine transitions with selection rules $F = J + 1 \leftarrow F = J + 1$ and $F = J - 1 \leftarrow F = J - 1$, whereas the weaker doublet component corresponds to the $F = J \leftarrow F = J$ transition.

We started our analysis of the *trans* N-methylformamide spectrum from refitting the data available from the literature (Fantoni & Caminati 1996; Fantoni et al. 2002; Kawashima et al. 2010) using the RAM36 code. Application of the RAM36 code allowed us to fit, almost within experimental error, the data available in the literature including those lines that were previously excluded from the fits due to relatively high observed-minus-calculated values (Kawashima et al. 2010). Thus we obtained a reliable basis for assigning the newly measured lines in the 45–630 GHz range. Assigning and fitting of the new data using the RAM36 program proceeded in a fairly conventional, iterative way going up in frequency.

The complete data set treated at the final stage of the current study includes both our new data and data from the literature (Fantoni & Caminati 1996; Fantoni et al. 2002; Kawashima et al. 2010). The data set contains 12 456 A - and E -type transitions with $J \leq 62$ and $K_a \leq 21$ for *trans* N-methylformamide in the lowest three torsional states. Due to blending, these 12 456 transitions correspond to 9469 distinct line frequencies (mainly due to non-fully resolved quadrupole hyperfine structure). The fit chosen as the “best” uses a model consisting of 103 parameters. The weighted root-mean-square

Table 1. Molecular parameters of the *trans* conformer of N-methylformamide obtained with the RAM36 program.

<i>ntr</i> ^a	Parameter ^b	Operator ^c	Value ^d
220	<i>F</i>	p_α^2	5.5825023(37)
220	V_3	$\frac{1}{2}(1 - \cos 3\alpha)$	51.7199088(90)
211	ρ	$J_z p_\alpha$	0.080976579(84)
202	$A_{\text{RAM}} - 0.5(B_{\text{RAM}} + C_{\text{RAM}})$	J_z^2	0.3540036(48)
202	$0.5(B_{\text{RAM}} + C_{\text{RAM}})$	J_z^2	0.22175219(40)
202	$0.5(B_{\text{RAM}} - C_{\text{RAM}})$	$J_x^2 - J_y^2$	0.05717595(45)
202	D_{zx}	$\{J_z, J_x\}$	-0.155070742(38)
440	F_m	p_α^4	-0.67979(73) $\times 10^{-3}$
440	V_6	$\frac{1}{2}(1 - \cos 6\alpha)$	8.02866(40)
431	ρ_m	$J_z p_\alpha^3$	0.222402(74) $\times 10^{-3}$
422	F_J	$J_z^2 p_\alpha^2$	-0.1029(15) $\times 10^{-6}$
422	F_K	$J_z^2 p_\alpha^2$	-0.63309(14) $\times 10^{-4}$
422	F_{xy}	$p_\alpha^2(J_x^2 - J_y^2)$	-0.23266(15) $\times 10^{-5}$
422	F_{zx}	$\frac{1}{2}p_\alpha^2\{J_z, J_x\}$	0.226160(59) $\times 10^{-4}$
422	V_{3J}	$J_z^2(1 - \cos 3\alpha)$	-0.15939626(49) $\times 10^{-2}$
422	V_{3K}	$J_z^2(1 - \cos 3\alpha)$	0.8718486(73) $\times 10^{-2}$
422	V_{3zx}	$\frac{1}{2}(1 - \cos 3\alpha)\{J_z, J_x\}$	-0.9181495(26) $\times 10^{-2}$
422	V_{3xy}	$(J_x^2 - J_y^2)(1 - \cos 3\alpha)$	-0.194794(44) $\times 10^{-4}$
422	D_{3xy}	$\frac{1}{2}\sin 3\alpha\{J_x, J_y\}$	0.235469(41) $\times 10^{-3}$
413	ρ_J	$J_z^2 J_z p_\alpha$	0.240348(50) $\times 10^{-5}$
413	ρ_K	$J_z^3 p_\alpha$	0.112304(16) $\times 10^{-4}$
413	ρ_{zx}	$\frac{1}{2}p_\alpha\{J_z, (J_x^2 - J_y^2)\}$	-0.186678(14) $\times 10^{-4}$
413	ρ_{xy}	$\frac{1}{2}p_\alpha\{J_z, (J_x^2 - J_y^2)\}$	0.473931(43) $\times 10^{-5}$
404	D_{zxK}	$\{J_z^3, J_x\}$	0.203044(10) $\times 10^{-5}$
404	Δ_J	$-J_z^4$	0.300775(22) $\times 10^{-6}$
404	Δ_{JK}	$-J_z^2 J_z^2$	-0.83337(25) $\times 10^{-6}$
404	Δ_K	$-J_z^4$	0.302147(39) $\times 10^{-5}$
404	δ_J	$-2J_z^2(J_x^2 - J_y^2)$	0.108271(13) $\times 10^{-6}$
404	δ_K	$-\{J_z^2, (J_x^2 - J_y^2)\}$	0.367453(69) $\times 10^{-6}$
660	F_{mm}	p_α^6	-0.10119(30) $\times 10^{-4}$
660	V_9	$\frac{1}{2}(1 - \cos 9\alpha)$	2.0575(23)
651	ρ_{mm}	$p_\alpha^5 J_z$	0.26713(46) $\times 10^{-5}$
642	F_{mJ}	$J_z^2 p_\alpha^4$	0.3393(19) $\times 10^{-7}$
642	F_{mK}	$J_z^2 p_\alpha^4$	-0.6445(16) $\times 10^{-6}$
642	F_{mxy}	$p_\alpha^4(J_x^2 - J_y^2)$	0.2157(17) $\times 10^{-7}$
642	F_{mzx}	$\frac{1}{2}p_\alpha^4\{J_z, J_x\}$	-0.1406(36) $\times 10^{-7}$
642	V_{6J}	$J_z^2(1 - \cos 6\alpha)$	-0.124130(82) $\times 10^{-3}$
642	V_{6K}	$J_z^2(1 - \cos 6\alpha)$	0.4820(10) $\times 10^{-3}$
642	V_{6zx}	$\frac{1}{2}(1 - \cos 6\alpha)\{J_z, J_x\}$	-0.543394(97) $\times 10^{-3}$
642	V_{6xy}	$(1 - \cos 6\alpha)(J_x^2 - J_y^2)$	-0.20435(93) $\times 10^{-4}$
642	D_{6xy}	$\frac{1}{2}\sin 6\alpha\{J_x, J_y\}$	0.6217(56) $\times 10^{-4}$
642	D_{6zy}	$\frac{1}{2}\sin 6\alpha\{J_z, J_y\}$	-0.12563(23) $\times 10^{-3}$
633	ρ_{mJ}	$J_z^2 p_\alpha^3 J_z$	-0.3725(33) $\times 10^{-8}$
633	ρ_{mK}	$J_z^3 p_\alpha^3$	0.5362(28) $\times 10^{-7}$
633	ρ_{mxy}	$\frac{1}{2}p_\alpha^3\{J_z, (J_x^2 - J_y^2)\}$	-0.819(25) $\times 10^{-9}$
633	ρ_{mzx}	$\frac{1}{2}p_\alpha^3\{J_z^2, J_x\}$	-0.1058(18) $\times 10^{-7}$
624	F_{JJ}	$J_z^4 p_\alpha^2$	0.2173(36) $\times 10^{-10}$
624	F_{KK}	$J_z^2 p_\alpha^2$	-0.2049(35) $\times 10^{-8}$
624	F_{zxK}	$\frac{1}{2}p_\alpha^2\{J_z^3, J_x\}$	-0.1137(15) $\times 10^{-8}$
624	V_{3JJ}	$J_z^4(1 - \cos 3\alpha)$	0.131102(86) $\times 10^{-7}$
624	V_{3JK}	$J_z^2 J_z^2(1 - \cos 3\alpha)$	0.15148(95) $\times 10^{-7}$

Notes. ^(a) $n = t + r$, where n is the total order of the operator, t is the order of the torsional part and r is the order of the rotational part, respectively.

^(b) Parameter nomenclature based on the subscript procedures of Xu et al. (2008) ^(c) $\{A, B, C\} = ABC + CBA$, $\{A, B\} = AB + BA$. The product of the operator in the third column of a given row and the parameter in the second column of that row gives the term actually used in the torsion-rotation Hamiltonian of the program, except for F , ρ and A_{RAM} , which occur in the Hamiltonian in the form $F(p_\alpha - \rho P_\alpha)^2 + A_{\text{RAM}}P_\alpha^2$. ^(a) All values are in cm^{-1} (except ρ which is unitless). Statistical uncertainties are shown as one standard uncertainty in the units of the last two digits.

Table 1. continued.

<i>ntr</i> ^a	Parameter ^b	Operator ^c	Value ^d
624	V_{3KK}	$J_z^4(1 - \cos 3\alpha)$	$-0.5940(31) \times 10^{-7}$
624	V_{3zxJ}	$\frac{1}{2}J^2(1 - \cos 3\alpha)\{J_z, J_x\}$	$0.3290(72) \times 10^{-8}$
624	V_{3xyJ}	$J^2(1 - \cos 3\alpha)(J_x^2 - J_y^2)$	$-0.2988(10) \times 10^{-8}$
624	V_{3xyK}	$\frac{1}{2}(1 - \cos 3\alpha)\{J_z^2, (J_x^2 - J_y^2)\}$	$-0.1819(10) \times 10^{-7}$
624	V_{3zxK}	$\frac{1}{2}(1 - \cos 3\alpha)\{J_z^3, J_x\}$	$-0.9915(12) \times 10^{-7}$
624	V_{3zxx}	$\frac{1}{2}\cos 3\alpha\{J_z, J_x^3\}$	$-0.15343(15) \times 10^{-6}$
624	V_{3x4y4}	$\cos 3\alpha(J_x^4 + J_y^4)$	$0.7525(14) \times 10^{-8}$
624	D_{3xyJ}	$\frac{1}{2}J^2 \sin 3\alpha\{J_x, J_y\}$	$-0.6130(23) \times 10^{-8}$
624	D_{3xyK}	$\frac{1}{2}\sin 3\alpha\{J_z^2, J_x, J_y\}$	$0.23854(49) \times 10^{-6}$
624	D_{3zyJ}	$\frac{1}{2}J^2 \sin 3\alpha\{J_z, J_y\}$	$-0.6514(19) \times 10^{-7}$
624	D_{3zyK}	$\frac{1}{2}\sin 3\alpha\{J_z^3, J_y\}$	$-0.5861(61) \times 10^{-7}$
624	D_{3zyy}	$\frac{1}{2}\sin 3\alpha\{J_z, J_y^3\}$	$0.8302(24) \times 10^{-7}$
624	D_{3x3xy3}	$\frac{1}{2}\sin 3\alpha[\{J_x^3, J_y\} - \{J_x, J_y^3\}]$	$0.4008(24) \times 10^{-8}$
615	ρ_{JJ}	$J_z^4 p_\alpha$	$-0.1203(18) \times 10^{-10}$
615	ρ_{JK}	$J^2 J_z^3 p_\alpha$	$-0.6148(28) \times 10^{-9}$
615	ρ_{KK}	$J_z^5 p_\alpha$	$0.4502(53) \times 10^{-9}$
615	ρ_{zxJ}	$\frac{1}{2}J^2 p_\alpha\{J_z^2, J_x\}$	$0.475(11) \times 10^{-10}$
615	ρ_{zxK}	$\frac{1}{2}p_\alpha\{J_z^4, J_x\}$	$0.13926(45) \times 10^{-8}$
615	ρ_{x2y2}	$\frac{1}{2}p_\alpha\{J_z, J_x^2, J_y^2\}$	$0.23934(84) \times 10^{-9}$
606	D_{zxKK}	$\{J_z^5, J_x\}$	$-0.7781(20) \times 10^{-10}$
606	Φ_J	J^6	$0.4542(10) \times 10^{-12}$
606	Φ_{KJ}	$J^2 J_z^4$	$0.3394(14) \times 10^{-10}$
606	Φ_K	J_z^6	$0.2619(35) \times 10^{-10}$
606	ϕ_J	$2J^4(J_x^2 - J_y^2)$	$0.23367(53) \times 10^{-12}$
606	ϕ_{JK}	$J^2\{J_z^2, (J_x^2 - J_y^2)\}$	$-0.6207(42) \times 10^{-12}$
606	ϕ_K	$\{J_z^4, (J_x^2 - J_y^2)\}$	$0.22553(51) \times 10^{-10}$
871	ρ_{mmmm}	$J_z p_\alpha^7$	$0.7121(15) \times 10^{-7}$
862	F_{mmJ}	$J^2 p_\alpha^6$	$0.4570(73) \times 10^{-9}$
862	F_{mmK}	$J_z^2 p_\alpha^6$	$-0.19488(81) \times 10^{-7}$
862	F_{mmxy}	$p_\alpha^6(J_x^2 - J_y^2)$	$0.3816(70) \times 10^{-9}$
862	V_{9J}	$J^2(1 - \cos 9\alpha)$	$-0.15061(48) \times 10^{-3}$
862	V_{9K}	$J_z^2(1 - \cos 9\alpha)$	$0.1550(58) \times 10^{-3}$
862	V_{9xy}	$(1 - \cos 9\alpha)(J_x^2 - J_y^2)$	$-0.5022(55) \times 10^{-4}$
862	D_{9xy}	$\frac{1}{2}\sin 9\alpha\{J_x, J_y\}$	$-0.1195(32) \times 10^{-3}$
853	ρ_{mmK}	$J_z^3 p_\alpha^5$	$0.2984(20) \times 10^{-8}$
853	ρ_{mmzx}	$\frac{1}{2}p_\alpha^5\{J_z^2, J_x\}$	$-0.411(11) \times 10^{-9}$
844	F_{mJK}	$J^2 J_z^2 p_\alpha^4$	$0.980(55) \times 10^{-11}$
844	F_{mKK}	$J_z^4 p_\alpha^4$	$-0.2444(30) \times 10^{-9}$
844	F_{mxyK}	$\frac{1}{2}p_\alpha^4\{J_z^2, (J_x^2 - J_y^2)\}$	$0.1692(29) \times 10^{-10}$
844	V_{6zxx}	$\frac{1}{2}\cos 6\alpha\{J_z, J_x^3\}$	$-0.1034(16) \times 10^{-7}$
844	D_{6xyJ}	$\frac{1}{2}J^2 \sin 6\alpha\{J_x, J_y\}$	$-0.1224(35) \times 10^{-8}$
844	D_{6zyK}	$\frac{1}{2}\sin 6\alpha\{J_z^3, J_y\}$	$0.573(14) \times 10^{-7}$
835	ρ_{mKK}	$J_z^5 p_\alpha^3$	$0.1312(35) \times 10^{-10}$
826	F_{KKK}	$J_z^6 p_\alpha^2$	$-0.491(25) \times 10^{-12}$
826	V_{3JJK}	$J^4 J_z^2(1 - \cos 3\alpha)$	$-0.365(13) \times 10^{-12}$
826	V_{3KKK}	$J_z^6(1 - \cos 3\alpha)$	$-0.909(34) \times 10^{-11}$
826	V_{3zxxx}	$\frac{1}{2}\cos 3\alpha\{J_z, J_x^5\}$	$0.675(14) \times 10^{-12}$
826	D_{3xyJK}	$\frac{1}{2}J^2 \sin 3\alpha\{J_z^2, J_x, J_y\}$	$-0.1837(65) \times 10^{-11}$
826	D_{3xyKK}	$\frac{1}{2}\sin 3\alpha\{J_z^4, J_x, J_y\}$	$-0.1309(33) \times 10^{-10}$
	χ_{aa}	$0.70093(90) \times 10^{-4}$	
	χ_{bb}	$0.64466(92) \times 10^{-4}$	
	$2\chi_{ab}$	$0.1755(15) \times 10^{-4}$	

deviation of the fit of 12 456 microwave transition frequencies with $J \leq 62$ is 0.84, indicating that assumed statistical uncertainties were slightly overestimated. The largest residual of 0.293 MHz is observed in the fit for the $v_t = 0$ E -symmetry species transition $49_{9,41} \leftarrow 48_{9,40}$. The final set of molecular parameters is presented in Table 1. The final data set of fitted transitions of the N-methylformamide *trans* conformer is presented in Table 2, where we provide quantum numbers for each level, followed by observed transition frequencies, measurement uncertainties, and residuals from the fit. The complete version of Table 2 is available at the CDS; here only part of the table is presented for illustration purposes.

Comparison of the low-order parameter values from Table 1 with the corresponding parameters determined by Kawashima et al. (2010) reveals relatively significant shifts in the values on a background of a general qualitative agreement (see Table B.1). Part of these shifts come from the basic difference in the models used, although both refer to the Rho-axis method. We follow the definition of the Rho-axis method given in Hougen et al. (1994) and, in our case, the A and E species are treated together with a single set of rotational parameters. On the contrary, Kawashima et al. (2010) treated the A and E species with distinct sets of rotational parameters (see their Table 2). As a result, a direct comparison of the changes in the rotational parameters is not possible. The same is true for the centrifugal distortion constants. At the same time, the change in V_3 value is in good agreement with the prediction made in Kawashima et al. (2010) where a relatively large V_6 term in the potential function was postulated by analogy with acetamide (Ilyushin et al. 2004). The data set available in Kawashima et al. (2010) was limited to the ground torsional state transitions only and did not give the opportunity to determine the V_6 value. Thus, they examined how the V_3 potential barrier is changed when a V_6 term is added, assuming that the coupling of the vibrational modes of the NH group with the CH₃ internal rotation has an effect similar to the one observed for the NH₂ group in acetamide (Hirota et al. 2010). According to our results, the value of an index R used in Kawashima et al. (2010) to express the effect of the V_6 term quantitatively is estimated to be 26.5 which is in a relatively good agreement with the value of 23.0 obtained in Kawashima et al. (2010) on the basis of ground state data only. Thus, our results support the general analysis of the CH₃ internal rotation potential barrier in N-methylformamide provided in Kawashima et al. (2010).

A portion of the rotational spectrum of N-methylformamide measured around 133 GHz in the laboratory is shown in Fig. 2 and compared to the predicted rotational spectrum as provided by our current theoretical model. As can be seen from Fig. 2, the overall correspondence between experimental and theoretical spectra is very good. A slight inconsistency with intensity between predicted and observed spectra that may be visible for some strong lines is due to variations of source power and detector sensitivity.

The predictions of rotational transitions of *trans* N-methylformamide in the $v_t = 0, 1$, and 2 torsionally excited states resulting from the fit are presented in Table 3. They are calculated for the frequency range up to 650 GHz and for the transitions with $J \leq 65$. The table provides quantum numbers, followed by calculated transition frequencies and their uncertainties, the energy of the lower state and the product $\mu^2 S$, where μ is the dipole moment of the molecule and S is the line strength of the transition. Owing to its significant size, the complete version of Table 3 is available at the CDS.

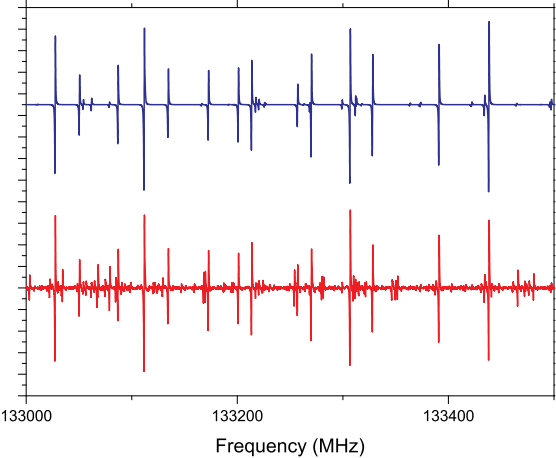


Fig. 2. Predicted (upper panel) and measured (lower panel) rotational spectrum of N-methylformamide between 133 and 133.5 GHz. The observed line shapes correspond to the first derivative of the actual line profile because frequency modulation and first harmonic lock-in detection are employed. The intensity axis is in arbitrary units.

We provide the torsional-rotational (Q_{tr}) and vibrational (Q_v) partition functions of N-methylformamide in Table 4. The values of Q_{tr} were calculated from first principles, that is, via direct summation over the rotational-torsional states. The maximum value of the J quantum number of the energy levels taken into account to calculate the partition function is 130, and excited torsional states up to $v_t = 8$ were considered. The vibrational part, Q_v , was estimated using a harmonic approximation and a simple formula that may be found in Gordy & Cook (1984, see their Eq. 3.60). The frequencies of the normal modes were obtained from DFT calculations of the harmonic force field using the B3LYP method and a 6-311++(3df, 2pd) basis set. Table 4 also lists the partition function values of acetamide that we calculated in a similar way as for N-methylformamide. The torsional-rotational part was calculated from first principles on the basis of the results presented in the paper by Ilyushin et al. (2004). To compute the Q_v values, we used, when available, vibrational frequencies reported in the literature (Kutzelnigg & Mecke 1962; Kydd & Dunham 1980), but also the results of DFT calculations with the same method and basis set as for N-methylformamide. For both molecules, the values of Q_v were calculated by taking all the vibrational modes into account except for the torsional mode which is already considered in Q_{tr} . The full partition function, Q_{tot} , is thus the product of Q_{tr} and Q_v .

4. Astronomical results

4.1. Observations

We use the full data set of the EMoCA spectral line survey obtained toward Sgr B2(N) with ALMA in its Cycles 0 and 1. The survey covers the frequency range between 84.1 and 114.4 GHz with a spectral resolution of 488.3 kHz (1.7 to 1.3 km s⁻¹). The median angular resolution is 1.6''. A detailed description of the observations, the data reduction process, and the method used to identify the detected lines and derive column densities was presented in Belloche et al. (2016). Population diagrams are constructed in the same way as in our previous work. Here, we would like to emphasize the fact that the apparent discrepancy between the synthetic populations and the fit to the observed

Table 2. Measured transitions of *trans* N-methylformamide in the $v_t = 0, 1$, and 2 states.

m'	F'^a	J'	K'_a	K'_c	m''	F''^a	J''	K''_a	K''_c	Obs. freq. (MHz)	Uncertainty (MHz)	Obs.-calc. (MHz)
-3	18	19	3	16	-3	17	18	2	16	251 285.2870	0.1000	0.0203
-3	20	19	3	16	-3	19	18	2	16	251 285.2870	0.1000	-0.0235
-3	19	19	3	16	-3	18	18	2	16	251 286.1600	0.1000	0.0037
3	21	4	17	3			20	5	16	251 379.8920	0.0500	0.0007
-2	23	3	21	-2			22	3	20	251 386.7420	0.0500	-0.0109
-2	23	3	21	-2			22	3	20	251 386.7430	0.0500	-0.0099
3	22	2	21	3			21	2	19	251 468.4440	0.0500	0.0002
0	22	8	15	0			21	8	14	251 472.2980	0.0500	-0.0016
0	22	8	14	0			21	8	13	251 493.1300	0.0500	0.0136
1	22	8	15	1			21	8	14	251 565.7320	0.0500	0.0034
0	18	19	4	16	0	17	18	3	15	251 591.3020	0.0500	0.0035
0	20	19	4	16	0	19	18	3	15	251 591.3020	0.0500	-0.0310
0	19	19	4	16	0	18	18	3	15	251 591.9750	0.0500	-0.0035

Notes. The complete table is available at the CDS. ^(a) The quantum number F is not indicated for the transitions with unresolved hyperfine structure.

Table 3. Predicted transitions of *trans* N-methylformamide in the $v_t = 0, 1$, and 2 states.

m'	F'	J'	K'_a	K'_c	m''	F''	J''	K''_a	K''_c	Calc. freq. (MHz)	Uncertainty (MHz)	E_l (cm $^{-1}$)	$\mu^2 S$ (D 2)
1	30	30	15	15	1	30	30	14	17	393 571.2045	0.0384	266.1079	20.6
1	31	30	15	15	1	31	30	14	17	393 571.2531	0.0384	266.1079	21.3
1	29	30	15	15	1	29	30	14	17	393 571.2547	0.0384	266.1079	20.0
0	24	24	5	19	0	24	24	3	22	393 583.8360	0.0055	115.5411	0.0382
0	25	24	5	19	0	25	24	3	22	393 585.7457	0.0055	115.5411	0.0398
0	23	24	5	19	0	23	24	3	22	393 585.8253	0.0055	115.5411	0.0367
0	15	15	8	8	0	15	15	6	9	393 600.5805	0.0054	62.7047	0.0364
0	16	15	8	8	0	16	15	6	9	393 600.7174	0.0054	62.7047	0.0389
0	14	15	8	8	0	14	15	6	9	393 600.7265	0.0054	62.7047	0.0342
-3	41	41	3	38	-3	40	40	3	37	393 611.4811	0.0389	337.7355	36.9
-3	42	41	3	38	-3	41	40	3	37	393 611.5587	0.0389	337.7355	37.8
-3	40	41	3	38	-3	39	40	3	37	393 611.5617	0.0389	337.7355	36.0

Notes. The complete table is available at the CDS.

populations, the former lying below the latter (see, e.g., Fig 4b), results from the fact that the model is optimized to match (i.e., not overestimate) the peak temperatures of the detected transitions while the population diagram is based on integrated intensities. Because of the high level of line confusion, the wings of the detected lines are often still partially contaminated even after removing the contribution of the other known molecules included in our complete model. Therefore, the populations derived from the integrated intensities are, most of the time, slightly overestimated.

The complete model mentioned above refers to the synthetic spectrum that includes the emission of all the molecules that we have identified in Sgr B2(N2) so far (Belloche et al. 2013, 2014, 2016; Müller et al. 2016a,b; Margulès et al. 2016); it is overlaid in green in all figures that display observed spectra.

We focus our analysis on the secondary hot core Sgr B2(N2), which is located $\sim 5''$ to the North of the main hot core Sgr B2(N1) (Belloche et al. 2016). Sgr B2(N2) has narrower linewidths ($FWHM \sim 5$ km s $^{-1}$) and thus exhibits a lower degree of line confusion than Sgr B2(N1). While some of the molecules reported below are also present on larger scales in the envelope of Sgr B2 (see, e.g., Jones et al. 2008), our interferometric observations are only sensitive to the compact emission

arising from the embedded hot cores. As shown in Fig. 3, the emission analyzed in this section is compact and the derived column densities refer to the hot core Sgr B2(N2) only.

4.2. Tentative detection of N-methylformamide (CH_3NHCHO)

We searched for emission lines of CH_3NHCHO toward Sgr B2(N2) using the spectroscopic predictions obtained in Sect. 3. We compared the observed ALMA spectrum of Sgr B2(N2) to synthetic spectra of CH_3NHCHO produced under the assumption of local thermodynamic equilibrium (LTE), which is expected to be valid given the high densities of the hot core regions probed by the EMoCA survey (Belloche et al. 2016). Figures A.1–A.3 show all the transitions of CH_3NHCHO in its ground state and its first and second torsionally excited states that are covered by our survey and are expected to contribute significantly to the detected signal for typical hot core temperatures (150–200 K). In these figures, the synthetic spectrum containing the contribution of all molecules that we have identified toward Sgr B2(N2) so far, including CH_3NHCHO , is overlaid in green on the observed spectrum, while the red spectrum shows the contribution of CH_3NHCHO only, as derived from our best-fit LTE model. Most transitions of CH_3NHCHO

Table 4. Partition functions of N-methylformamide and acetamide.

T (K)	CH ₃ NHCHO		CH ₃ CONH ₂	
	Q_{tr}^a	Q_v^b	Q_{tr}^a	Q_v^b
10	365.16247	1.00000	359.18058	1.00000
20	1189.23944	1.00000	1272.66459	1.00000
30	2488.15240	1.00000	2766.98655	1.00000
40	4317.90735	1.00008	4871.11731	1.00009
50	6701.57116	1.00058	7590.48345	1.00058
60	9648.68076	1.00224	10925.10798	1.00205
70	13164.31826	1.00592	14874.85986	1.00508
80	17251.81144	1.01233	19439.98556	1.01017
90	21913.57312	1.02193	24620.89439	1.01769
100	27151.45535	1.03496	30418.00805	1.02792
110	32966.94532	1.05150	36831.70759	1.04108
120	39361.28161	1.07156	43862.32239	1.05734
130	46335.51849	1.09509	51510.12815	1.07686
140	53890.55428	1.12204	59775.34167	1.09979
150	62027.13560	1.15237	68658.10939	1.12626
160	70745.84645	1.18606	78158.49050	1.15642
170	80047.08923	1.22311	88276.43644	1.19042
180	89931.06287	1.26356	99011.76908	1.22844
190	100397.74181	1.30747	110364.15950	1.27064
200	111446.85817	1.35493	122333.10876	1.31725
210	123077.88845	1.40605	134917.93177	1.36849
220	135290.04535	1.46097	148117.74490	1.42463
230	148082.27451	1.51987	161931.45737	1.48594
240	161453.25592	1.58293	176357.76649	1.55275
250	175401.40932	1.65036	191395.15645	1.62543
260	189924.90280	1.72242	207041.90022	1.70434
270	205021.66401	1.79936	223296.06409	1.78994
280	220689.39314	1.88148	240155.51446	1.88269
290	236925.57717	1.96908	257617.92629	1.98311
300	253727.50471	2.06251	275680.79287	2.09175
310	271092.28113	2.16213	294341.43638	2.20925
320	289016.84348	2.26834	313597.01910	2.33626
330	307497.97493	2.38156	333444.55472	2.47352

Notes. ^(a) Q_{tr} is the torsional-rotational partition function. It does not take the hyperfine splitting into account. ^(b) Q_v is the vibrational partition function. The total partition function of the molecule (without hyperfine splitting) is $Q_{\text{tr}} \times Q_v$.

are blended with lines emitted by other molecules and therefore cannot be unambiguously assigned to CH₃NHCHO. However, several lines are relatively free of contamination and match lines detected toward Sgr B2(N2), both in terms of linewidths and peak temperatures. These lines are marked with a star in Col. 11 of Tables B.2–B.4. In total, five lines can be clearly assigned to CH₃NHCHO, four within its torsional ground state and one within its first torsionally excited state. Given the small number of clearly detected lines, we consider our detection of CH₃NHCHO as tentative rather than secure.

Gaussian fits to the integrated intensity maps of four of the five detected lines indicate that the size of the emission is smaller than the beam. We obtain a size of $\sim 1.8''$ for the line at 93.41 GHz observed in setup S3 but this is also the setup with the worst angular resolution ($2.9'' \times 1.5''$); we therefore do not fully trust this size. Indeed the other lines, at 91.89, 99.69 (see Fig. 3a), and 113.61 GHz, are all unresolved, suggesting a size smaller than $1''$. We adopt a size of $0.9''$ for our LTE modeling of CH₃NHCHO. We did not attempt to fit a size to the integrated

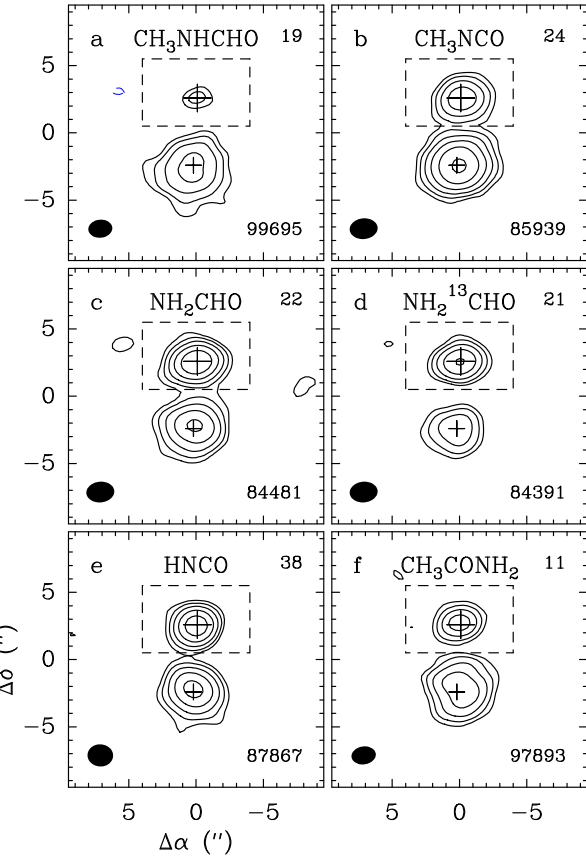


Fig. 3. Integrated intensity maps toward Sgr B2(N2) of **a)** CH₃NHCHO 9_{2,8}–8_{2,7}, **b)** CH₃NCO 10_{1,10}–9_{1,9}, **c)** NH₂CHO $v_{12} = 1$ 4_{0,4}–3_{0,3}, **d)** NH₂¹³CHO 4_{0,4}–3_{0,3}, **e)** HNCO 4_{3,1}–3_{3,0} and 4_{3,2}–3_{3,1}, and **f)** CH₃CONH₂ 9_{0,9}–8_{1,8}, 9_{1,9}–8_{1,8}, 9_{0,9}–8_{0,8}, and 9_{1,9}–8_{0,8}. The position of Sgr B2(N2) is marked with a large cross. The smaller cross indicates the position of Sgr B2(N1). Because of the different systemic velocities of the two sources, the line assignment is only valid for Sgr B2(N2), inside the dashed box. The contours start at 4σ and increase by a factor of 2 at each step. The dashed (blue) contour is at -4σ . The value of the rms noise level, σ , is given in mJy beam⁻¹ km s⁻¹ in the top right corner of each panel. The mean frequency of the integration range in MHz and the synthesized beam are shown in the bottom right and left corners of each panel, respectively.

intensity map of the fifth detected line, at 111.22 GHz, because it is somewhat more contaminated on its low-frequency side.

The population diagram of CH₃NHCHO is shown in Fig. 4. We used all detected lines plus a number of other ones that contribute significantly to detected lines and are contaminated by species that we have already identified and included in our full model. All the transitions used for the population diagram are listed in Tables B.2–B.4. Panel b of Fig. 4 shows the population diagram after correcting for the optical depth of the transitions, based on our best-fit LTE model of CH₃NHCHO, and after removing the contamination by other species, based on our full model. A fit to this diagram yields a rotational temperature of 149 ± 20 K, with a significant uncertainty (Table 5). For the LTE modeling of the spectrum, we adopt a temperature of 180 K. The best-fit parameters are listed in Table 6.

In the following sections, we derive the column density of molecules that may be related to N-methylformamide in order to

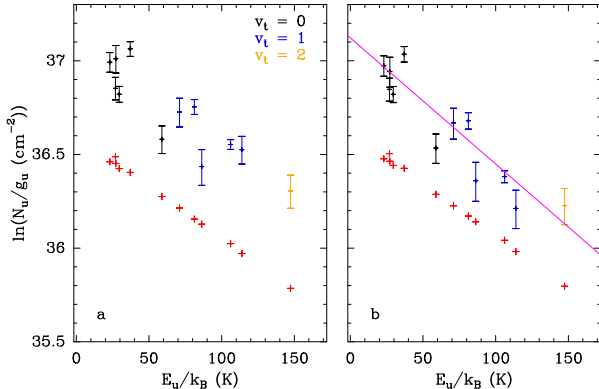


Fig. 4. Population diagram of CH_3NHCHO toward Sgr B2(N2). The observed datapoints are shown in various colors (but not red) as indicated in the upper right corner of panel a) while the synthetic populations are shown in red. No correction is applied in panel a). In panel b), the optical depth correction has been applied to both the observed and synthetic populations and the contamination by all other species included in the full model has been removed from the observed datapoints. The purple line is a linear fit to the observed populations (in linear-logarithmic space).

Table 5. Rotational temperatures derived from population diagrams of selected complex organic molecules toward Sgr B2(N2).

Molecule	States ^a	T_{fit}^b (K)
CH_3NHCHO	$v_t = 0, v_t = 1, v_t = 2$	149 (20)
CH_3NCO	$v_b = 0, v_b = 1$	140.9 (7.2)
NH_2CHO	$v = 0, v_{12} = 1$	154.8 (3.3)
$\text{NH}_2^{13}\text{CHO}$	$v = 0, v_{12} = 1$	222 (37)
HNCO	$v = 0, v_5 = 1, v_6 = 1, v_4 = 1$	220.1 (9.6)
CH_3CONH_2	$v_t = 0, v_t = 1, v_t = 2$	226 (33)

Notes. ^(a) Vibrational or torsional states that were taken into account to fit the population diagram. ^(b) The standard deviation of the fit is given in parentheses. As explained in Sect. 3 of Belloche et al. (2016), these uncertainties are purely statistical and should be viewed with caution. They may be underestimated.

put the tentative detection of this molecule into a broader astrochemical context.

4.3. Methyl isocyanate (CH_3NCO)

The first interstellar detection of methyl isocyanate was obtained toward Sgr B2(N) based on single-dish observations (Halfen et al. 2015, ; see also Cernicharo et al. 2016), shortly after its in-situ detection in the frozen surface of comet 67P/Churyumov-Gerasimenko (Goessmann et al. 2015). Here, we use the predictions available in the Cologne database for molecular spectroscopy¹ (CDMS, Müller et al. 2005) (tags 57 505 and 57 506, both version 1), which are based on measurements reported by Cernicharo et al. (2016) and Koput (1986).

Methyl isocyanate is well detected toward Sgr B2(N2) in the EMoCA spectral survey: 60 lines are clearly detected in its vibrational ground state and four in its first vibrationally excited state (Figs. A.4 and A.5). Gaussian fits to the integrated intensity maps of the detected lines indicate a median emission size

of $\sim 1.2''$ with a rms dispersion of $\sim 0.1''$ (see Fig. 3b). A fit to its population diagram shown in Fig. A.20 yields a rotational temperature of 141 ± 7 K (Table 5). We adopt a temperature of 150 K for our LTE modeling. The parameters of our best-fit model are given in Table 6. The model overestimates the peak temperature of a few transitions by ~ 30 –40% (at 87.236, 96.062, 96.120, 104.793, and 104.856 GHz) while all other transitions are well fitted; the reason for these discrepancies is unclear.

4.4. Formamide (NH_2CHO)

We use the CDMS entries for formamide in its ground and first vibrationally excited states (tags 45 512 and 45 516, versions 2 and 1, respectively) and for its ^{13}C and ^{15}N isotopologs in their ground state (tags 46 512 and 46 513, versions 2 and 1, respectively). These entries are based largely on Motiyenko et al. (2012), but also contain additional data. Laboratory data in the range of our survey were published by Kryvda et al. (2009). The entry for $v_{12} = 1$ of the ^{13}C isotopolog was prepared by one of us (HSPM) based on data from Stubgaard (1978).

Formamide is well detected toward Sgr B2(N2), with 30 lines in its vibrational ground state and 13 in its vibrationally excited state $v_{12} = 1$ (Figs. A.6 and A.7). Its ^{13}C isotopolog is also clearly detected, with 11 and 2 lines in its $v = 0$ and $v_{12} = 1$ states, respectively (Figs. A.8 and A.9). Finally, we report a tentative detection of $^{15}\text{NH}_2\text{CHO}$, with one clearly detected line consistent with a $^{14}\text{N}/^{15}\text{N}$ isotopic ratio of 300 (Fig. A.10).

We derive a median emission size of ~ 0.9 – $1.0''$ from Gaussian fits to the integrated intensity maps of the main and ^{13}C isotopologs, with a rms dispersion of $\sim 0.1''$ (see Figs. 3c and d). A number of lines of the main isotopolog are saturated and not well fitted by our simple LTE model. We selected only the transitions with an optical depth lower than 2 to build the population diagram shown in Fig. A.21. A fit to this diagram yields a rotational temperature of 155 ± 3 K (Table 5). However, we obtain a rotational temperature of 200 ± 14 K when we limit the fit to the transitions that belong to the vibrational ground state. The population diagram of the ^{13}C isotopolog is less populated (Fig. A.22) and yields a more uncertain rotational temperature of 222 ± 35 K (Table 5). We adopt a temperature of 200 K for our LTE model of all isotopologs of formamide.

We initially modeled the spectra assuming a size of $0.9''$ as derived above but, in order to fit the $v_{12} = 1$ transitions, we then had to assume a total column density of NH_2CHO much lower than the one needed to fit the ground state transitions. By reducing the size to $0.8''$, we could attenuate the discrepancy between $v = 0$ and $v_{12} = 1$, however we still need a total column density 1.4 times lower to fit $v_{12} = 1$. This is surprising because we do not face this problem for the ^{13}C isotopolog for which both states are well fitted assuming the same total column density. The discrepancy that affects the main isotopolog may be due to its higher optical depth although we do not feel that it is a satisfactory explanation.

4.5. Isocyanic acid (HNCO)

We use the CDMS entry for HNCO in its ground state (tag 43 511 version 1) by Lapinov et al. (2007) with additional measurements in the range of our survey by Hocking et al. (1975), and the JPL entry for the ^{13}C isotopolog (tag 44 008 version 1, Hocking et al. 1975). Private entries for the vibrationally excited states $v_5 = 1$, $v_6 = 1$, and $v_4 = 1$ of the main isotopolog were prepared by one of us (HSPM). They are based on

¹ <http://www.astro.uni-koeln.de/cdms/>

Table 6. Parameters of our best-fit LTE model of selected complex organic molecules toward Sgr B2(N2).

Molecule	Status ^a	N_{det}^b	Size ^c (‘‘)	T_{rot}^d (K)	N^e (cm ⁻²)	F_{vib}^f	ΔV^g (km s ⁻¹)	V_{off}^h (km s ⁻¹)	$\frac{N_{\text{ref}}^i}{N}$
$\text{CH}_3\text{NHCHO}, v_t = 0^\star$	t	4	0.9	180	1.0 (17)	1.26	5.0	0.5	1
	$v_t = 1$	t	1	0.9	180	1.0 (17)	1.26	5.0	0.5
	$v_t = 2$	t	0	0.9	180	1.0 (17)	1.26	5.0	1
$\text{CH}_3\text{NCO}, v_b = 0^\star$	d	60	1.2	150	2.2 (17)	1.00	5.0	-0.6	1
	$v_b = 1$	d	4	1.2	150	2.2 (17)	1.00	-0.6	1
$\text{NH}_2\text{CHO}, v = 0^\star$	d	30	0.8	200	3.5 (18)	1.17	5.5	0.2	1
	$v_{12} = 1$	d	13	0.8	200	2.6 (18)	1.17	5.5	0.2
$\text{NH}_2^{13}\text{CHO}, v = 0$	d	11	0.8	200	1.3 (17)	1.17	5.5	0.5	27
	$v_{12} = 1$	d	2	0.8	200	1.3 (17)	1.17	5.5	0.5
$^{15}\text{NH}_2\text{CHO}, v = 0$	t	1	0.8	200	1.2 (16)	1.17	5.5	0.5	300
$\text{HNCO}, v = 0^\star$	d	12	0.9	240	2.0 (18)	1.06	5.5	0.0	1
	$v_5 = 1$	d	4	0.9	240	2.0 (18)	1.06	5.5	0.0
	$v_6 = 1$	d	1	0.9	240	2.0 (18)	1.06	5.5	0.0
	$v_4 = 1$	t	0	0.9	240	2.0 (18)	1.06	5.5	0.0
$\text{HN}^{13}\text{CO}, v = 0$	t	0	0.9	240	1.0 (17)	1.06	5.5	0.0	20
$\text{CH}_3\text{CONH}_2, v_t = 0^\star$	d	10	0.9	180	1.4 (17)	1.23	5.0	1.5	1
	$v_t = 1$	d	8	0.9	180	1.4 (17)	1.23	5.0	1.5
	$v_t = 2$	d	5	0.9	180	1.4 (17)	1.23	5.0	1.5
	$\Delta v_t \neq 0$	t	0	0.9	180	1.4 (17)	1.23	5.0	1.5

Notes. ^(a) d: detection, t: tentative detection. ^(b) Number of detected lines (conservative estimate, see Sect. 3 of Belloche et al. 2016). One line of a given species may mean a group of transitions of that species that are blended together. ^(c) Source diameter (FWHM). ^(d) Rotational temperature. ^(e) Total column density of the molecule. $X (Y)$ means $X \times 10^Y$. An identical value for all listed vibrational/torsional states of a molecule means that LTE is an adequate description of the vibrational/torsional excitation. ^(f) Correction factor that was applied to the column density to account for the contribution of vibrationally excited states, in the cases where this contribution was not included in the partition function of the spectroscopic predictions. ^(g) Linewidth (FWHM). ^(h) Velocity offset with respect to the assumed systemic velocity of Sgr B2(N2), $V_{\text{lsr}} = 74 \text{ km s}^{-1}$. ⁽ⁱ⁾ Column density ratio, with N_{ref} the column density of the previous reference species marked with a \star .

a preliminary, unpublished analysis of the ground and the four lowest excited states and were already used in Belloche et al. (2013). The data on the excited states was summarized in Niedenhoff et al. (1996). Transition frequencies in the range of our survey were published by Yamada & Winnewisser (1977) and Yamada (1977).

Isocyanic acid is also well detected toward Sgr B2(N2), with twelve lines in its vibrational ground state, four in its vibrationally excited state $v_5 = 1$, and one in its state $v_6 = 1$ (Figs. A.11–A.13). Its state $v_4 = 1$, is not unambiguously detected but contributes significantly to the signal detected at 87.97 GHz so we have included it in our full model (Fig. A.14). The ^{13}C isotopolog is not unambiguously detected because all its significant transitions are located in the blueshifted wing of transitions of the main isotopolog, some of these suffering from absorption of the main isotopolog from the outer envelope of Sgr B2, which we have not yet taken into account in our full model (Fig. A.15). Nevertheless, the ^{13}C isotopolog contributes significantly to the signal detected at several frequencies, so we have included it in our full model, based on the model derived below for the main isotopolog and assuming a $^{12}\text{C}/^{13}\text{C}$ isotopic ratio of 20.

We derive a median size of 0.9‘‘ from Gaussian fits to the integrated intensity maps of the main isotopolog, with a dispersion of 0.2‘‘ (see Fig. 3e). The population diagram shown in Fig. A.23 uses all but three transitions that are clearly detected, plus a number of additional lines that are more contaminated but for which we have identified and modeled the contaminating species. The three transitions of the vibrational ground state that we ignore

(at 109.50, 109.91, and 110.30 GHz) have an opacity higher than 4. A fit to the population diagram yields a temperature of $220 \pm 10 \text{ K}$. However, with this temperature, the optically thick lines of the ground state would saturate with a brightness temperature that is too low. As a compromise, we use a temperature of 240 K.

The detected lines of all four states of the main isotopolog are relatively well reproduced with the same model parameters (Table 6). A few issues remain, however. First of all, the peak temperatures of the optically thick lines of $v = 0$ are slightly underestimated, except for the peak temperature of the $5_{0,5}-4_{0,4}$ transition at 109.91 GHz which is overestimated, probably because of spatial filtering of extended emission not taken into account in our model (see Fig. 6 of Jones et al. 2008). The second issue concerns two transitions with an upper energy level $E_{\text{up}} \sim 650 \text{ K}, 34_{1,34}-35_{0,35}$ at 85.37 GHz and $33_{1,33}-34_{0,34}$ at 109.96 GHz, which are both overestimated. The former is located in a frequency range affected by $\text{c-C}_3\text{H}_2$ absorption by spiral arm clouds along the line of sight to Sgr B2, so the discrepancy at this frequency may not be a problem. We note, in addition, that the model for a third transition with $E_{\text{up}} \sim 650 \text{ K}, 5_{4,1}-4_{4,0}$ at 109.78 GHz, is consistent with the detected signal. Therefore, it is unclear why our model overestimates the peak temperature of the transition at 109.96 GHz.

4.6. Acetamide (CH_3CONH_2)

We use predictions that are based on the measurements and analysis presented in Ilyushin et al. (2004) but were recomputed by

one of us (V.V.I.) with the RAM36 code. We use the partition function calculated in Sect. 3 (Table 4).

With a total of 23 lines clearly detected in its ground state and its first and second torsionally excited states toward the hot core Sgr B2(N2), acetamide can be considered as securely detected (Figs. A.16–A.19). Fits to the integrated intensity maps of three of the detected lines give a median size of $\sim 1.0''$, with a dispersion of $0.2''$ (see Fig. 3f). The emission of four other detected lines is unresolved, pointing to a smaller size. The maps of the remaining detected lines were not fitted because they are, to some level, contaminated in their wings, which could bias the size measurements. A fit to the population diagram yields a rotational temperature of 226 ± 33 K, which is not well constrained (Fig. A.24 and Table 5). We adopt a temperature of 180 K and a size of $0.9''$ for our LTE model to make the comparison to N-methylformamide more straightforward. The detected lines of the ground state ($v_t = 0$) and both torsionally excited states ($v_t = 1$ and 2), as well as lines that connect different torsional states ($\Delta v_t \neq 0$), are well reproduced with the same model parameters (Table 6). One discrepancy can be noticed in Fig. A.16; the $v_t = 0$ 25_{20.6}–25_{18.7} transition of the E species at 99.950 GHz does not have a counterpart in the observed spectrum (at the 3σ level). However it was extrapolated from a lower- J fit ($J \leq 20$) and has a frequency uncertainty of 200 kHz which means that its frequency could be off by several times this number. Indeed, the actual positions of the hyperfine components of this line, as measured in the laboratory spectrum, are 99.951.872 MHz and 99.952.331 MHz, both with an uncertainty of 10 kHz. At these frequencies, strong emission is detected toward Sgr B2(N2), which reconciles the spectrum expected for acetamide with the observed spectrum. Therefore, the discrepancy between the observed and synthetic spectra at 99.950 GHz does not pose a significant problem.

5. Chemical modeling

To investigate the production of the tentatively detected N-methylformamide in Sgr B2(N2), we use the chemical kinetics model *MAGICKAL* (Garrod 2013) with an expanded gas-grain chemical network. This network is an extension of that presented by Belloche et al. (2014), and latterly by Müller et al. (2016a), and includes formation and destruction mechanisms for both CH₃NHCHO and the related molecule CH₃NCO. The model allows for a treatment of the fully-coupled gas-phase, grain/ice-surface, and ice-mantle chemistry. The physical model follows that detailed in previous papers where a cold collapse phase to maximum density ($n_H = 2 \times 10^8 \text{ cm}^{-3}$) and minimum dust-grain temperature (8 K) is followed by a warm-up from 8 to 400 K; during this phase, the gas and dust temperatures are assumed to be well coupled. The initial chemical compositions used in the model follow those of Garrod (2013). The reader is referred to the above-mentioned publications for a more detailed discussion of the basic physical and chemical model. In the models presented here, we use the intermediate warm-up timescale, which generally produces the best match between models and observed abundances of other chemical species. The warm-up model therefore reaches a temperature of 200 K at 2×10^5 yr, reaching 400 K (and the end of the model run) at $\sim 2.85 \times 10^5$ yr.

The new network concentrates on the grain-surface production of the newly-introduced molecules. However, gas-phase destruction mechanisms for both molecules (as well as related intermediates) are included in the new network, the majority of which are ion-molecule processes or the subsequent dissociative recombination with electrons of the resultant molecular

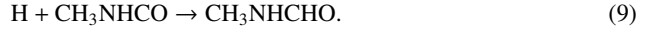
ions. Ion-molecule reactions are included for the major ionic species C⁺, He⁺, H₃⁺, H₃O⁺, and HCO⁺. Estimates for the rates of photo-dissociation of new molecules, as caused by cosmic ray-induced and (where extinction allows) external UV photons, are also included (see Garrod et al. 2008; Garrod 2013). Grain/ice-surface binding (desorption) energies for the new molecules are estimates based on interpolation/extrapolation of values for molecules with similar functional groups, following past publications. Binding energy values for CH₃NCO and CH₃NHCHO are 3575 K and 6281 K, respectively, based on the formulations [$E_{\text{des}}(\text{CH}_3) + E_{\text{des}}(\text{N}) + E_{\text{des}}(\text{C}) + E_{\text{des}}(\text{O})$] and [$E_{\text{des}}(\text{NH}_2\text{CHO}) - E_{\text{des}}(\text{H}) + E_{\text{des}}(\text{CH}_3)$]. We are not aware of any experimental determinations of these two quantities for appropriate surfaces.

In the new network, grain-surface and ice-mantle formation of CH₃NCO occurs through a single radical-addition reaction:



Each of the necessary radicals may be formed either through repetitive atomic addition or through the photo-dissociation of or chemical H-abstraction from either CH₄ or HNCO.

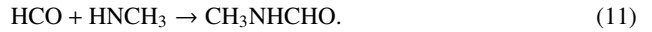
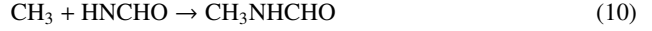
To form CH₃NHCHO, a reaction involving the addition of a hydrogen atom to CH₃NCO followed by the addition of another, presents itself as a possible route, that is,



The first of these two reactions requires the breaking of a carbon-nitrogen double bond, for which no activation energy barrier could be determined from the literature. The barrier to the similar reaction of H with HNCO has been determined experimentally in the gas phase by Nguyen et al. (1996) to be 1390 K, although the value for H + CH₃NCO could plausibly be higher or lower. The expectation, however, is that, as with most barrier-mediated atomic-H reactions on cold grains, the mechanism would involve the tunneling of the H atom through the barrier, introducing further uncertainty into the reaction rate. By default, *MAGICKAL* uses a simple rectangular-barrier treatment to determine rates for tunneling reactions, typically assuming a uniform barrier width of 1 Å; the assumed height of the energy barrier therefore absorbs all other parameters pertaining to the overall reaction rate. The ideal activation energy barrier determined for the chemical model may therefore not be fully representative of the usual high-temperature value.

Because a broad range of activation energy values could be plausible for reaction (8), in the chemical network, we initially assume that the rate for reaction (8) is negligible (models M1–M5), introducing non-zero values later.

Radical-addition reactions provide an alternative pathway to the formation of N-methylformamide, through the reactions:



The larger radicals in each of the above two reactions are produced through the addition of NH to either CH₃ or HCO. While cosmic ray-induced photo-dissociation of CH₃NH₂ and NH₂CHO may also produce the necessary radicals, the chemical abstraction of a hydrogen atom by a radical from either molecule strongly favors the production of CH₂NH₂ or NH₂CO, respectively, rather than the alternative radicals that could play a part in forming CH₃NHCHO. However, in the case of H-atom abstraction from NH₂CHO by OH, the model initially considers the

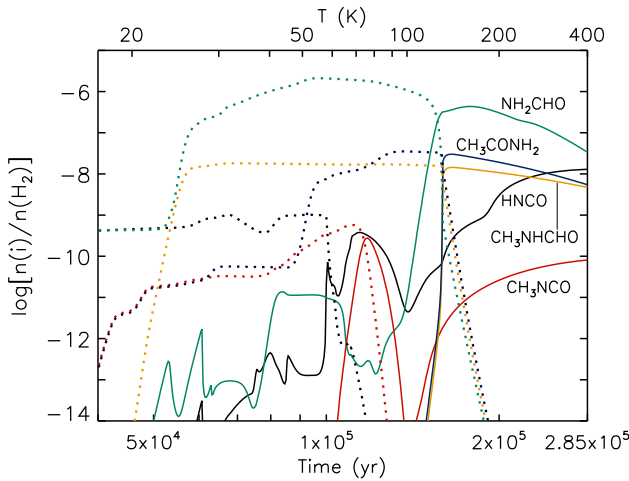


Fig. 5. Calculated abundances of selected chemical model species with respect to H_2 for model M1, during warm-up from 8 K to 400 K. Solid lines indicate gas-phase abundances; dotted lines of the same color indicate solid-phase abundances of the same species.

barriers to NH_2CO and NHCHO production to be similar (591 K versus 600 K), following the estimates used by Garrod (2013), although neither value has been determined rigorously. Consequently, the influence of the production of HNCHO through this mechanism is also examined in Sect. 5.1.

5.1. Model results

Model M1 comprises the initial model in which conversion of CH_3NCO to CH_3NHCHO via consecutive H addition (reactions (8) and (9)) is switched off.

Figure 5 shows results from model M1. Time-dependent abundances for CH_3NCO and CH_3NHCHO as well as the related species HNCO , NH_2CHO , and CH_3CONH_2 are shown. CH_3NHCHO is seen to be formed on the grains (dotted line) in abundance at approximately 25 K, coincident with a significant growth in NH_2CHO production. Its formation is dominated by reaction (10). CH_3NCO production on the grains is much more modest, and occurs only through reaction (7). Its gas-phase abundance peaks at a relatively low temperature, following its desorption from grains, and falls again, although it later begins to rise as the abundant CH_3NHCHO is photodissociated in the gas phase. CH_3CONH_2 reaches a peak abundance just a little larger than that of CH_3NHCHO , forming mainly through the addition of CH_3 and NH_2CO radicals. HNCO is formed on the grains early ($T < 20$ K) via hydrogenation of OCN, which itself is formed through the atomic addition reactions $\text{O} + \text{CN}$ and $\text{C} + \text{NO}$. The gas-phase abundance of HNCO peaks at close to 60 K as it desorbs from the grains, then falls away. It is a significant by-product of the destruction of larger molecules at later times in the model, and its abundance continues to grow until the final model temperature of 400 K is reached.

Table 7 shows the peak gas-phase abundances of the plotted species, along with the temperatures at which those peaks are reached. It may be noted that the peak abundance of CH_3NHCHO is approximately at parity with HNCO , contrary to the observed column densities shown in Table 6, where a ratio of $\sim 1:20$ is obtained. The amount of CH_3NHCHO produced in this model as compared with CH_3NCO also appears high, while the abundance of CH_3NCO is approximately one order of magnitude

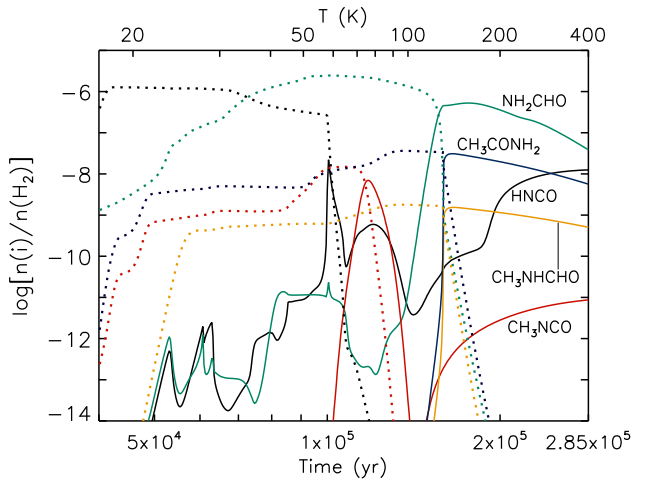


Fig. 6. As in Fig. 5 for model M4.

too low compared with HNCO . Since the sole production mechanism of CH_3NCO relies on OCN, we have also considered alternative models, in which HNCO , a possible precursor to OCN, may be more easily formed.

Models M2–M5, whose results are also tabulated in Table 7, allow the grain-surface reaction $\text{NH} + \text{CO} \rightarrow \text{HNCO}$ to occur with a lower activation energy barrier than the 2500 K first assumed by Garrod et al. (2008), an estimate based loosely on the typically assumed barrier to the H-addition reaction $\text{H} + \text{CO} \rightarrow \text{HCO}$. These models show two types of behavior, with the threshold falling somewhere between models M2 and M3, that is, an activation energy, E_A , between 2000 K and 1500 K. Below this threshold, the models move away from M1-type behavior and instead show significantly increased HNCO production on the grains, such that the desorption of HNCO into the gas phase produces the peak abundance for this molecule. Figure 6 plots abundances for model M4, for which an activation energy barrier to the $\text{NH} + \text{CO}$ reaction of 1250 K is assumed. The peak abundance of CH_3NCO is notably increased (see also Table 7) as a result of the greater HNCO abundance, which contributes to the production of OCN. Conversely, the abundance of CH_3NHCHO is found to decrease markedly in models M3–M5 as the $\text{NH} + \text{CO}$ reaction becomes competitive with the $\text{NH} + \text{HCO} \rightarrow \text{NHCHO}$ reaction at the key temperature (~ 25 K) at which CH_3 mobility makes reaction (10) important to CH_3NHCHO production. Models M3–M5 all reach within a factor of ~ 2 of the observed $\text{CH}_3\text{NHCHO}/\text{CH}_3\text{NCO}$ abundance ratio.

To investigate the importance of H-addition to CH_3NCO , we adjust the conditions assumed in model M4, taking a selection of activation energy barriers for reaction (8) to give a non-zero reaction rate. M4A assumes the same value as the reaction $\text{H} + \text{HNCO}$, while models M4B–E increase this value incrementally (see Table 8). We also switch off the H-abstraction reaction $\text{OH} + \text{NH}_2\text{CHO} \rightarrow \text{NHCHO}$, to test its influence on CH_3NHCHO production.

Model M4A demonstrates an extreme degree of conversion of CH_3NCO to CH_3NHCHO that is not borne out by the observations, while the somewhat higher barrier to hydrogenation of model M4B improves the match to the detected $\text{CH}_3\text{NHCHO}/\text{CH}_3\text{NCO}$ ratio (see also Table 9), albeit with a value greater than unity. Model M4C, as with M4, shows a modest dominance of CH_3NCO over CH_3NHCHO , in line with observations, and is similar to M4 in the quality of its overall match

Table 7. Peak gas-phase fractional abundances with respect to H₂ and temperatures at which the peak abundance values are achieved, for models with varying activation energy barriers for the grain-surface reaction NH + CO → HNCO.

Species	M1		M2		M3		M4		M5	
	$E_A = 2500$ K	$n[i]/n[H_2]$	$E_A = 2000$ K	$n[i]/n[H_2]$	T (K)	$E_A = 1500$ K	$n[i]/n[H_2]$	T (K)	$E_A = 1250$ K	$n[i]/n[H_2]$
CH ₃ NHCHO	1.4(−8)	139	1.3(−8)	139	1.6(−9)	139	1.5(−9)	139	1.5(−9)	139
CH ₃ NCO	2.8(−10)	74	1.6(−9)	74	6.9(−9)	74	6.9(−9)	74	7.0(−9)	75
NH ₂ CHO	4.3(−7)	160	4.4(−7)	160	5.3(−7)	157	5.3(−7)	157	5.4(−7)	157
HNCO	1.3(−8)	398	1.3(−8)	398	2.2(−8)	56	2.2(−8)	56	2.2(−8)	56
CH ₃ CONH ₂	3.0(−8)	138	3.0(−8)	138	3.1(−8)	138	3.1(−8)	138	3.2(−8)	138

Notes. Model M1 uses the value adopted in previous hot-core models. $X(Y)$ means $X \times 10^Y$.

Table 8. Peak gas-phase fractional abundances with respect to H₂ and temperatures at which the peak abundance values are achieved, for models based on model M4, that is, with an activation energy barrier of 1250 K for the grain-surface reaction NH + CO → HNCO.

Species	M4A		M4B		M4C		M4D		M4E	
	$E_A = 1390$ K	$n[i]/n[H_2]$	$E_A = 2000$ K	$n[i]/n[H_2]$	T (K)	$E_A = 2500$ K	$n[i]/n[H_2]$	T (K)	$E_A = 3000$ K	$n[i]/n[H_2]$
CH ₃ NHCHO	1.2(−8)	139	5.3(−9)	139	1.2(−9)	139	6.0(−10)	139	5.1(−10)	139
CH ₃ NCO	7.0(−11)	398	4.1(−9)	74	6.5(−9)	74	6.9(−9)	74	6.9(−9)	74
NH ₂ CHO	5.1(−7)	157	5.1(−7)	157	5.1(−7)	157	5.1(−7)	157	5.1(−7)	157
HNCO	2.2(−8)	56	2.2(−8)	56	2.2(−8)	56	2.2(−8)	56	2.2(−8)	56
CH ₃ CONH ₂	3.2(−8)	138	3.2(−8)	138	3.2(−8)	138	3.2(−8)	138	3.2(−8)	138

Notes. The models (M4A–E) vary from model M4 in two ways: (i) the OH + NH₂CHO → NHCHO + H₂O reaction pathway has been switched off; (ii) the reaction H + CH₃NCO → CH₃NHCO is switched on, with an activation energy barrier, E_A , as indicated. Model M4A uses the value assumed for the H + HNCO → NH₂CO reaction (1390 K, Nguyen et al. 1996), while the other models use larger values. $X(Y)$ means $X \times 10^Y$.

with observations. At the higher activation energies used in models M4D and M4E, the importance of reaction (8) diminishes. Here, the influence of the removal of the OH + NH₂CHO → NHCHO reaction becomes apparent via comparison with model M4 (Table 7); the abundance of CH₃NHCHO falls by two-thirds. For each of the models M4A–E, the behavior of HNCO, NH₂CHO, and CH₃CONH₂ are little affected in comparison to model M4.

Note that particularly in the cases of CH₃NCO and CH₃CONH₂, the temperatures at which peak abundances are attained are somewhat lower than the rotational temperatures obtained from the spectroscopic model fits to the observational data. This may be due to the imprecision of either or both of the binding energy estimates and the spectroscopic fits. The observed HNCO temperature is best represented by the late-time/high-temperature peak found in the models, rather than the brief gas-phase spike at around 60 K. The precise temperature at which the high-temperature peak is reached is dependent on the destruction rates and warm-up timescale assumed in the model. In the case of CH₃NCO, the larger spatial extent of this molecule (1.2''), as derived from the observations, compared with that of CH₃NHCHO (0.9'') is consistent with the idea that the former is released from grains at lower temperatures than the latter.

Table 9 shows ratios of the abundances of the main molecules to HNCO, as well as the CH₃NHCHO/CH₃NCO and CH₃NHCHO/CH₃CONH₂ ratios. Values are shown for the initial model M1, as well as representative models from Tables 7 and 8 that show a good match with observed values. Models M4 and M4C both show similarly good agreement with observed ratios involving CH₃NCO and CH₃NHCHO, while M4B is significantly further from the observed CH₃NHCHO/HNCO ratio. However, all four models produce an overabundance of NH₂CHO and CH₃CONH₂ by more than an order of magnitude.

Because acetamide, CH₃CONH₂, is predominantly formed as a result of H-abstraction from formamide, followed by methyl-group addition, its overabundance is related to that of NH₂CHO. The majority of the latter molecule is formed via the reaction NH₂ + H₂CO → NH₂CHO + H, which we include on the grains as well as in the gas phase, assuming the activation energy barrier determined by Barone et al. (2015) of 26.9 K. However, Song & Kästner (2016) find a substantially higher barrier that would render the reaction rate negligible (as determined for a gas-phase interaction). In order to test this possibility, we remove the NH₂+H₂CO mechanism both in the gas phase and on grains. This reduces NH₂CHO production by approximately an order of magnitude and brings the peak NH₂CHO:HNCO ratio achieved in the models to a very good match with the observed value (1.2 versus 1.8). The removal of either the gas-phase or grain-surface mechanism alone is not sufficient to reduce NH₂CHO abundance, as both contribute significantly in the present implementation. However, even the better match to observed NH₂CHO is not sufficient to bring down acetamide abundances to appropriate levels, as the alternative NH₂ + CH₃CO formation mechanism is also important to its formation. The production of acetamide in hot cores merits further detailed study.

While models M4 and M4C show similar agreement with observations in spite of the different dominant chemical pathways involved for CH₃NHCHO production, the fact that NH₂CO is a more likely product of the reaction between OH and NH₂CHO than NHCHO (judging by typical barriers to H-abstraction from an amino versus a carbonyl group) makes model M4C more plausible in this respect. The observed CH₃NHCHO/CH₃NCO ratio is bracketed by the values obtained with models M4B and M4C, indicating indeed that a mechanism of direct hydrogenation from CH₃NCO to CH₃NHCHO is capable of reproducing observations of these molecules. However, given an

Table 9. Relative abundances for a selection of chemical species, from the initial model (M1) and the three other most successful models, and from the observations toward Sgr B2(N2)

Species	M1	M4	M4B	M4C	Observations
$\text{CH}_3\text{NHCHO} / \text{HNCO}$	1.1	0.070	0.24	0.055	0.050
$\text{CH}_3\text{NCO} / \text{HNCO}$	0.021	0.32	0.19	0.30	0.11
$\text{NH}_2\text{CHO} / \text{HNCO}$	34	24	23	23	1.8
$\text{CH}_3\text{CONH}_2 / \text{HNCO}$	2.3	1.4	1.5	1.5	0.070
$\text{CH}_3\text{NHCHO} / \text{CH}_3\text{NCO}$	52	0.22	1.3	0.18	0.45
$\text{CH}_3\text{NHCHO} / \text{CH}_3\text{CONH}_2$	0.48	0.050	0.17	0.037	0.71

appropriate activation energy barrier, both reactions (8) and (10) may produce sufficient quantities of CH_3NHCHO to agree reasonably with observations.

In order to achieve observed abundances of CH_3NCO , a barrier to the reaction $\text{NH} + \text{CO} \rightarrow \text{HNCO}$ of no more than ~ 1500 K is required, allowing this to become the dominant mechanism by which HNCO is formed on grains (although its abundance in the gas phase is still dominated by its formation as a by-product of the destruction of larger species). Under such conditions, a barrier to the hydrogenation of CH_3NCO may be estimated to be approximately 2000 K to best reproduce observed abundances of N-methylformamide.

6. Discussion

The spectroscopic results obtained in Sect. 3 represent a significant improvement in the characterization of the spectrum of N-methylformamide. First of all, we have substantially expanded the frequency coverage. Second, the rotational lines belonging to the first and second excited torsional states of N-methylformamide have been assigned and fitted for the first time. Finally, the resulting best model is capable of reproducing the assigned data set within experimental error, including the lines from previous studies that were excluded from the fits due to large observed-minus-calculated values (Kawashima et al. 2010).

All the chemical models computed in the course of this work predict a substantial abundance of CH_3NHCHO compared to CH_3NCO . The smallest ratios were produced by models M4D and M4E, with $[\text{CH}_3\text{NHCHO}]/[\text{CH}_3\text{NCO}] \sim 0.07\text{--}0.09$, but all other models have $[\text{CH}_3\text{NHCHO}]/[\text{CH}_3\text{NCO}] \gtrsim 0.2$. Two of the chemical models provide values that bracket the observed ratio, thus a fine tuning of the barrier against hydrogenation of CH_3NCO would allow the observed ratio to be achieved. The chemical modeling thus gives some additional support to the tentative interstellar detection of CH_3NHCHO .

N-methylformamide, CH_3NHCHO , is a structural isomer of acetamide, CH_3CONH_2 . As mentioned in Sect. 1, CH_3NHCHO is the second most stable $\text{C}_2\text{H}_5\text{NO}$ isomer, CH_3CONH_2 being the most stable one (Lattelais et al. 2010). In Sect. 4, we found that, provided its detection is confirmed, N-methylformamide is slightly less abundant than acetamide in Sgr B2(N2), which, at first sight, appears to be in agreement with the minimum energy principle initially put forward by Lattelais et al. (2009). This principle states that the most abundant isomer of a given generic chemical formula should be the most stable one thermodynamically. Lattelais et al. (2009) found a correlation between the observed abundance ratios of isomers of several generic chemical formulae as a function of their zero-point energy difference. According to this relation, N-methylformamide should be approximately 3.5 times less abundant than acetamide while it is only

a factor 1.4 less abundant in Sgr B2(N2). The discrepancy is only slightly larger than a factor of two, but it tends to suggest that N-methylformamide does not follow this correlation closely. In addition, the range of kinetic parameters explored in the chemical models presented here produce variations in the abundance of CH_3NHCHO of more than one order of magnitude. In the case of acetamide, while the models all produce an excess over the abundance of N-methylformamide, variations in other model parameters within a plausible range can produce variations in CH_3CONH_2 abundance that are comparable with those of CH_3NHCHO . The availability of key precursor radicals at the optimal temperature for diffusion is one of the key influences on the production of such molecules, and one that is unlikely to be controlled purely by the thermodynamic properties of the products. Therefore, the abundance ratio of the two isomers has most likely an origin based on kinetics, rather than a simple thermal equilibrium. A similar conclusion was obtained by Loomis et al. (2015) and Loison et al. (2016) based on observations of the isomers of $\text{C}_3\text{H}_2\text{O}$, whose abundance ratios are not consistent with the minimum energy principle.

A further test would be to measure the abundance of the next $\text{C}_2\text{H}_5\text{NO}$ isomer, acetimidic acid, $\text{CH}_3\text{C}(\text{OH})\text{NH}$, which has a slightly higher zero-point energy than N-methylformamide (Lattelais et al. 2010). This would require laboratory measurements to characterize the rotational spectrum of this molecule and produce spectroscopic predictions suitable for an astronomical search. The dipole moment of this molecule, however, is more than a factor of 2 smaller than the ones of acetamide and N-methylformamide (Lattelais et al. 2009), making its detection more challenging.

7. Conclusions

The rotational spectrum of the *trans* conformer of N-methylformamide was studied in the laboratory in the frequency range from 45 to 630 GHz using two different spectrometers in Kharkiv and Lille. The new data provides significant expansion both in frequency range (from 118 GHz to 630 GHz) and quantum number coverage (from $J = 11$ to $J = 62$), including the first assignment of the rotational spectra of the first and second excited torsional states of N-methylformamide. The final data set contains 12 456 *A*- and *E*-type transitions in the ground, first, and second excited torsional states of the *trans* conformer. Our theoretical model fits the available data with a weighted root-mean-square deviation of 0.84, that is, within experimental error. The obtained results provide a firm basis for reliable predictions of the N-methylformamide spectrum in the millimeter and submillimeter wavelength range for the needs of radio astronomy.

Using the spectroscopic predictions obtained here, we report the first tentative interstellar detection of N-methylformamide. The main results of this study can be summarized as follows:

1. Five transitions of N-methylformamide are coincident with spectral lines detected toward the hot molecular core Sgr B2(N2). These lines are not contaminated by other species, and their intensities are well reproduced by our LTE model of N-methylformamide. This suggests that the molecule may be present in this source.
2. We derive a column density of $\sim 1 \times 10^{17} \text{ cm}^{-2}$ for N-methylformamide. The molecule is more than one order of magnitude less abundant than formamide, twice less abundant than methyl isocyanate, and only slightly less abundant than acetamide.
3. Our gas-grain chemical kinetics model is able to reproduce the abundance ratio of N-methylformamide to methyl isocyanate using kinetic parameters within a plausible range, supporting the tentative detection of the former.
4. The chemical models indicate that the efficient formation of HNCO via $\text{NH} + \text{CO}$ on grains is a necessary step in the achievement of the observed gas-phase abundance of CH_3NCO .
5. Production of CH_3NHCHO may plausibly occur on grains either through the direct addition of functional-group radicals or through the hydrogenation of CH_3NCO .
6. We also report the tentative detection of the ^{15}N isotopolog of formamide toward Sgr B2(N2) with a $^{14}\text{N}/^{15}\text{N}$ isotopic ratio of 300.

Provided the detection of N-methylformamide is confirmed, the only slight underabundance of this molecule compared to its more stable structural isomer and the sensitivity of the model abundances to the variations of the model parameters suggest that the formation of these two molecules is controlled by kinetics rather than thermal equilibrium. The interstellar detection of the next stable isomer of the $\text{C}_2\text{H}_5\text{NO}$ family, $\text{CH}_3\text{C}(\text{OH})\text{NH}$, may therefore become possible once its rotational spectrum has been measured in the laboratory.

Acknowledgements. This paper makes use of the following ALMA data: ADS/JAO.ALMA#2011.0.00017.S, ADS/JAO.ALMA#2012.1.00012.S. ALMA is a partnership of ESO (representing its member states), NSF (USA), and NINS (Japan), together with NRC (Canada), NSC and ASIAA (Taiwan), and KASI (Republic of Korea), in cooperation with the Republic of Chile. The Joint ALMA Observatory is operated by ESO, AUI/NRAO, and NAOJ. The interferometric data are available in the ALMA archive at <https://almascience.eso.org/aq/>. Part of this work was done within the Ukrainian-French CNRS-PICS # 6051 project. This work has been in part supported by the Deutsche Forschungsgemeinschaft (DFG) through the collaborative research grant SFB 956 “Conditions and Impact of Star Formation”, project area B3. Our research benefited from NASA’s Astrophysics Data System (ADS).

References

- Alekseev, E., Motiyenko, R., & Margulès, L. 2012, *Radio Physics and Radio Astronomy*, **3**, 75
- Barone, V., Latouche, C., Skouteris, D., et al. 2015, *MNRAS*, **453**, L31
- Belloche, A., Müller, H. S. P., Menten, K. M., Schilke, P., & Comito, C. 2013, *A&A*, **559**, A47
- Belloche, A., Garrod, R. T., Müller, H. S. P., & Menten, K. M. 2014, *Science*, **345**, 1584
- Belloche, A., Müller, H. S. P., Garrod, R. T., & Menten, K. M. 2016, *A&A*, **587**, A91
- Cernicharo, J., Kisiel, Z., Tercero, B., et al. 2016, *A&A*, **587**, L4
- Fantoni, A., & Caminati, W. 1996, *J. Chem. Soc., Faraday Trans.*, **92**, 343
- Fantoni, A. C., Caminati, W., Hartwig, H., & Stahl, W. 2002, *J. Mol. Struct.*, **612**, 305
- Garrod, R. T. 2013, *ApJ*, **765**, 60
- Garrod, R. T., Widicus Weaver, S. L., & Herbst, E. 2008, *ApJ*, **682**, 283
- Goesmann, F., Rosenbauer, H., Bredehoff, J. H., et al. 2015, *Science*, **349**, aab0689
- Gordy, W., & Cook, R. L. 1984, *Microwave Molecular Spectra, Techniques of Chemistry*, Vol. XVIII (New York: Wiley)
- Halfen, D. T., Ilyushin, V., & Ziurys, L. M. 2011, *ApJ*, **743**, 60
- Halfen, D. T., Ilyushin, V. V., & Ziurys, L. M. 2015, *ApJ*, **812**, L5
- Hirota, E., Kawashima, Y., Usami, T., & Seto, K. 2010, *J. Mol. Spectr.*, **260**, 30
- Hocking, W. H., Gerry, M. C. L., & Winnewisser, G. 1975, *Can. J. Phys.*, **53**, 1869
- Hollis, J., Lovas, F. J., Remijan, A. J., et al. 2006, *ApJ*, **643**, L25
- Hougen, J. T., Kleiner, I., & Godefroid, M. 1994, *J. Mol. Spectr.*, **163**, 559
- Ilyushin, V. V., Alekseev, E. A., Dyubko, S. F., Kleiner, I., & Hougen, J. T. 2004, *J. Mol. Spectr.*, **227**, 115
- Ilyushin, V. V., Kisiel, Z., Pszczółkowski, L., Mäder, H., & Hougen, J. T. 2010, *J. Mol. Spectr.*, **259**, 26
- Ilyushin, V. V., Endres, C. P., Lewen, F., Schlemmer, S., & Drouin, B. J. 2013, *J. Mol. Spectr.*, **290**, 31
- Jones, P. A., Burton, M. G., Cunningham, M. R., et al. 2008, *MNRAS*, **386**, 117
- Kaiser, R., Stockton, A., Kim, Y., Jensen, E., & Mathies, R. 2013, *ApJ*, **765**, 111
- Kawashima, Y., Usami, T., Suenram, R. D., Golubiatnikov, G. Y., & Hirota, E. 2010, *J. Mol. Spectr.*, **263**, 11
- Kleiner, I. 2010, *J. Mol. Spectr.*, **260**, 1
- Koput, J. 1986, *J. Mol. Spectr.*, **115**, 131
- Kryvda, A. V., Gerasimov, V. G., Dyubko, S. F., Alekseev, E. A., & Motiyenko, R. A. 2009, *J. Mol. Spectr.*, **254**, 28
- Kutzelnigg, W., & Mecke, R. 1962, *Spectrochim. Acta*, **18**, 549
- Kydd, R. A., & Dunham, A. R. C. 1980, *J. Mol. Struct.*, **69**, 79
- Lapinov, A. V., Golubiatnikov, G. Y., Markov, V. N., & Guarnieri, A. 2007, *Astron. Lett.*, **33**, 121
- Lattelais, M., Pauzat, F., Ellinger, Y., & Ceccarelli, C. 2009, *ApJ*, **696**, L133
- Lattelais, M., Pauzat, F., Ellinger, Y., & Ceccarelli, C. 2010, *A&A*, **519**, A30
- Lin, C. C., & Swalen, J. D. 1959, *Rev. Mod. Phys.*, **31**, 841
- Loison, J.-C., Agúndez, M., Marcelino, N., et al. 2016, *MNRAS*, **456**, 4101
- Loomis, R. A., McGuire, B. A., Shingledecker, C., et al. 2015, *ApJ*, **799**, 34
- Margulès, L., Belloche, A., Müller, H. S. P., et al. 2016, *A&A*, **590**, A93
- Motiyenko, R., Tercero, B., Cernicharo, J., & Margulès, L. 2012, *A&A*, **548**, A71
- Müller, H. S. P., Schlöder, F., Stutzki, J., & Winnewisser, G. 2005, *J. Mol. Struct.*, **742**, 215
- Müller, H. S. P., Belloche, A., Xu, L.-H., et al. 2016a, *A&A*, **587**, A92
- Müller, H. S. P., Walters, A., Wehres, N., et al. 2016b, *A&A*, **595**, A87
- Nguyen, M. T., Sengupta, D., Vereecken, L., Peeters, J., & Vanquickenborne, L. G. 1996, *J. Phys. Chem.*, **100**, 1615
- Niedenhoff, M., Yamada, K. M. T., & Winnewisser, G. 1996, *J. Mol. Spectr.*, **176**, 342
- Rubin, R., Swenson Jr, G., Benson, R., Tigelaar, H., & Flygare, W. 1971, *ApJ*, **169**, L39
- Song, L., & Kästner, J. 2016, *Phys. Chem. Chem. Phys.*, **18**, 29278
- Stubgaard, M. 1978, Ph.D. Thesis, Københavns Universitet, Denmark
- Xu, L.-H., Fisher, J., Lees, R., et al. 2008, *J. Mol. Spectr.*, **251**, 305
- Yamada, K. 1977, *J. Mol. Spectr.*, **68**, 423
- Yamada, K., & Winnewisser, M. 1977, *J. Mol. Spectr.*, **68**, 307
- Zakharenko, O., Motiyenko, R. A., Margulès, L., & Huet, T. R. 2015, *J. Mol. Spectr.*, **317**, 41

Torsion-rotation-vibration effects in the ground and first excited states of methacrolein, a major atmospheric oxidation product of isoprene

O. Zakharenko,¹ R. A. Motiyenko,¹ J.-R. Aviles Moreno,¹ A. Jabri,^{2,3} I. Kleiner,² and T. R. Huet^{1,a)}

¹Laboratoire de Physique des Lasers, Atomes et Molécules, UMR8523 CNRS – Université Lille 1, Bâtiment P5, F- 59655 Villeneuve d'Ascq Cedex, France

²Laboratoire Inter-universitaire des Systèmes Atmosphériques, CNRS - Universités Paris Est Créteil et Paris Diderot, 61 Avenue du Général de Gaulle, 94010 Créteil Cedex, France

³Institute for Physical Chemistry, RWTH Aachen University, Aachen, Germany

(Received 20 October 2015; accepted 22 December 2015; published online 11 January 2016)

Methacrolein is a major oxidation product of isoprene emitted in the troposphere. New spectroscopy information is provided with the aim to allow unambiguous identification of this complex molecule, characterized by a large amplitude motion associated with the methyl top. State-of-the-art millimeter-wave spectroscopy experiments coupled to quantum chemical calculations have been performed. For the most stable *s-trans* conformer of atmospheric interest, the torsional and rotational structures have been characterized for the ground state, the first excited methyl torsional state (v_{27}), and the first excited skeletal torsional state (v_{26}). The inverse sequence of A and E tunneling sub-states as well as anomalous A-E splittings observed for the rotational lines of $v_{26} = 1$ state clearly indicates a coupling between methyl torsion and skeletal torsion. A comprehensive set of molecular parameters has been obtained. The far infrared spectrum of Durig *et al.* [Spectrochim. Acta, Part A **42**, 89–103 (1986)] was reproduced, and a Fermi interaction between v_{25} and $2v_{27}$ was evidenced. © 2016 AIP Publishing LLC. [<http://dx.doi.org/10.1063/1.4939636>]

I. INTRODUCTION

Air pollution is the subject of many studies because of its impact on the public health, on the global chemistry, and on climate. The major part of the biogenic gases produced by the biosphere is volatile organic compounds (VOCs).¹ The emission of biogenic VOCs such as isoprene (C_5H_8) and terpenes (C_5H_8)_n ($n > 1$) is much higher, about 10 times, than the emission of the anthropogenic VOCs and represents a source of atmospheric contaminants. Isoprene constitutes between 30% and 50% of the total emission of biogenic VOCs. Methacrolein (MAC, $H_2C=C(CHO)-CH_3$) and methyl vinyl ketone (MVK, butenone $CH_3-C(O)CH=CH_2$) are major oxidation products of isoprene but they can also originate from primary emissions such as fuel evaporation or combustion (vehicular emissions) in urban environments.

The VOCs have attracted a lot of attention in recent years. Measurements of the ratio of isoprene and its oxidation products, such as MVK/MAC and [MVK + MAC]/isoprene, have been used in many studies to investigate the magnitude and location of isoprene sources.^{2,3} In particular, Cheung *et al.*³ have studied the diurnal profiles of isoprene, MAC, and MVK in Hong Kong. They noticed that in urban areas with strong anthropogenic sources, the use of MVK/MAC ratio might not be reliable to estimate the isoprene oxidation rate due to the primary emissions of MVK and MAC. Indeed, these compounds remaining in the gas phase are highly

reactive in the atmosphere. The reaction with OH radicals during daytime and with O_3 and NO_3 radicals at night is the principal removal pathway of isoprene.^{3,4} In areas where the three species originate from biogenic emissions the oxidant chemistry destroys isoprene and produces and destroys MAC and MVK during daytime.³ The tropospheric lifetimes are estimated to be 1.7 h for isoprene, 8.6 h and 6.1 h for MVK and MAC, respectively.⁵

The biogenic VOCs make a significant contribution on the tropospheric ozone O_3 and on secondary organic aerosols formation.^{6,7} These air pollutants can influence the Earth's radiation balance and have adverse effects on the human health. However, the effect of organic aerosols on climate is still not completely studied, we need a better understanding of their sources, chemical formation, and physical and chemical characteristics.⁸ Therefore, it is important to study their spectroscopic properties in laboratory in order to better understand their formation, composition, and transformation. In this paper, we focus on the analysis of the rotational spectra of the ground state and the lowest excited vibrational states of methacrolein, providing some remeasurements and new measurements of the molecular spectrum in the microwave and millimeter wave ranges. The main goal of our study is to provide for the first time accurate torsion-rotational parameters in order to allow high resolution investigations in the infrared atmospheric window.

Methacrolein is a prolate asymmetric top molecule with a methyl group. The investigation of its rotational spectrum is complicated by internal rotation of the methyl top that interacts with the overall rotation of the molecule. The internal rotation is hindered by the threefold torsional potential with three

^{a)}Author to whom correspondence should be addressed. Electronic mail: Therese.Huet@univ-lille1.fr. Tel.: +33(0)320.33.64.60.

identical minima and maxima. Due to the tunneling effect, the energy levels are split into one sub-level of A symmetry and two degenerated sub-levels of E symmetry.

The microwave spectrum of MAC was first measured in 1971 by Suzuki and Kozima in the range of 7.6–25 GHz.⁹ They were able to observe and assign the rotational transitions due to the *s-trans* conformer. The lines of the *s-cis* conformer were carefully searched but none of them had been found. Thus, the *s-trans* conformer was established to be the most stable. The investigation of the internal rotation splittings in the rotational lines of the ground vibrational state allowed to obtain an approximate value of the barrier to internal rotation of the methyl group: 467 cm⁻¹.⁹ Later, the far infrared (FIR) spectra of gaseous methacrolein (parent and deuterated species) were recorded and analyzed in the region 50–3500 cm⁻¹ by Durig *et al.*¹⁰ In this study both the *s-trans* and *s-cis* conformers were observed. By combining the microwave and FIR data for the *s-trans* conformer the authors determined the barrier to internal rotation to be 444 ± 3 cm⁻¹, whereas the corresponding barrier for *s-cis* conformer determined only from the FIR data is 441 ± 2 cm⁻¹. In addition, the LCAO-MO-SCF restricted Hartree-Fock calculations employing 6-31G* basis set carried out in Ref. 10 yielded the energy difference between *s-trans* and *s-cis* conformers to be 1057 cm⁻¹. Low Boltzmann factor (0.006 at room temperature) for the *s-cis* conformer may thus explain the difficulties to identify its rotational lines in the spectra.

In the present study we measured and analyzed the rotational spectrum of MAC in the ranges 150–465 GHz and 2–40 GHz. The experimental work was prepared and completed by quantum chemical calculations at different levels of theory, density functional theory (DFT) and *ab initio*, to model the structure of the two conformers and the large amplitude motion associated with the methyl top. The present spectroscopic characterization of MAC will allow the detailed analysis of the infrared spectra recorded by Fourier transform infrared (FTIR) spectroscopy at high resolution. Indeed a lot of efforts are put into the development of remote sensing spectrometers, and it is a duty to provide spectroscopic information on various gas traces of atmospheric interest, either for probing air quality or to develop more accurate chemistry models.

II. QUANTUM CHEMICAL CALCULATIONS

All the calculations were performed using the Gaussian 09 (G09), Revision D.01, software package.¹¹ The molecular parameters and the harmonic force field have been evaluated using different methods, and we retained the DFT (M06-2X¹²) and the Møller-Plesset second order theory (MP2)¹³ with different Pople and Dunning's basis sets.¹⁴ We have focused our attention to the calculation of most stable geometries, relative energies, and rotation barriers of the methyl group.

First, a scan of the potential energy surface (PES) of MAC, at the MP2/6-311++G(d,p) level of theory along the D7 dihedral angle (H10C9C4C1), was performed in order to characterize the two possible conformers of MAC, as

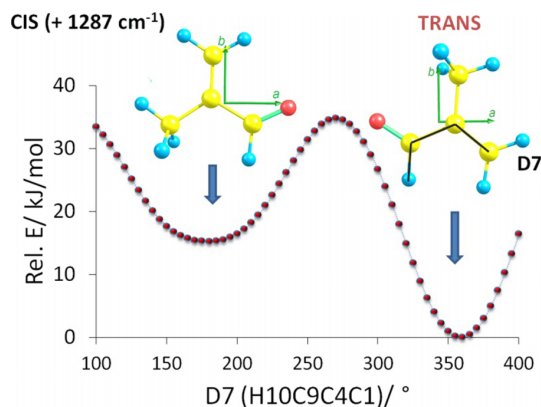


FIG. 1. Scan of the potential energy surface of methacrolein at the MP2/6-311++G(d,p) level of theory along the D7 dihedral angle (H10C9C4C1). The relative energy is issued from the MP2/aug-cc-pVQZ equilibrium geometry.

presented in Fig. 1. The scan revealed two stable conformers in good agreement with Refs. 9 and 10.

Second, the structural parameters were obtained in order to provide an accurate equilibrium geometry. The equilibrium structures were evaluated at the M06-2X/6-311++G(2df,p) level of theory. Moreover, equilibrium geometry calculations were performed at the MP2 level with the aug-cc-pVTZ and aug-cc-pVQZ basis sets. This last equilibrium structure (Cartesian coordinates) is presented in Table I and the main associated structural parameters are shown in Fig. 2. No remarkable change was observed between MP2 equilibrium geometries with aug-cc-pVTZ and aug-cc-pVQZ basis sets, and the results are in good agreement with the optimized M06-2X/6-311++G(2df,p) structure. In addition, the Gaussian-3¹⁵ and Gaussian-4¹⁶ methodologies were applied in order to better estimate the relative energy between the *s-cis* and *s-trans* conformers of MAC. Both Gaussian-3 (G3) and Gaussian-4 (G4) methodologies perform accurate energies by the calculation of several pre-defined steps on a starting molecular geometry. Then, this calculated equilibrium energy is corrected in terms of zero point, electronic correlation, and basis size contributions (see Refs. 15 and 16 for more details). This method is known to give accurate relative energies. The results are presented in Table II. The G4 value (1080 cm⁻¹) is in good agreement with the previous published value of Ref. 10 (1057 cm⁻¹). Finally, the equilibrium and ground state molecular parameters (coming from the harmonic and anharmonic calculations, respectively) were evaluated at the MP2/aug-cc-pVTZ and M06-2X/6-311++G(d,p) levels, respectively.

At the end, we have performed calculations of the rotation barriers of the methyl group at M06-2X/6-311++G(2df,p) and MP2/aug-cc-pVTZ levels of theory. Two ways were followed for the calculation of the barriers: (i) the quadratic synchronous transit QST3 methodology (quadratic synchronous transit calculation starting from the geometry of two minima and the optimization of a transition state geometry between these two minima) implemented in G09^{17,18} was used for the calculation of the structure and relative energy of the transition states structures involved in the rotation of the CH₃

TABLE I. Calculated equilibrium structures in Cartesians coordinates (angstroms) of the *s-trans* and *s-cis* conformers of methacrolein at the MP2/aug-cc-pVQZ level of theory.

Atom	<i>s-trans</i>			<i>s-cis</i>		
	X	Y	Z	Atom	X	Y
C1	-0.0025	-0.0001	-0.0016	C1	-0.0030	-0.0000
H2	-0.0028	0.0001	1.0805	H2	-0.0051	-0.0001
H3	0.9535	0.0002	-0.5051	H3	0.9430	-0.0000
C4	-1.1590	-0.0004	-0.6772	C4	-1.1644	-0.0001
C5	-1.2870	-0.0006	-2.1630	C5	-1.2916	-0.0000
H6	-0.3106	-0.0005	-2.6393	H6	-0.3149	-0.0002
H7	-1.8475	-0.8734	-2.4924	H7	-1.8405	-0.8767
H8	-1.8478	0.8719	-2.4926	H8	-1.8405	0.8767
C9	-2.4016	-0.0007	0.1158	C9	-2.4321	-0.0001
H10	-2.2597	-0.0005	1.2117	H10	-3.3538	0.0000
O11	-3.5154	-0.0010	-0.3732	O11	-2.5041	0.0000

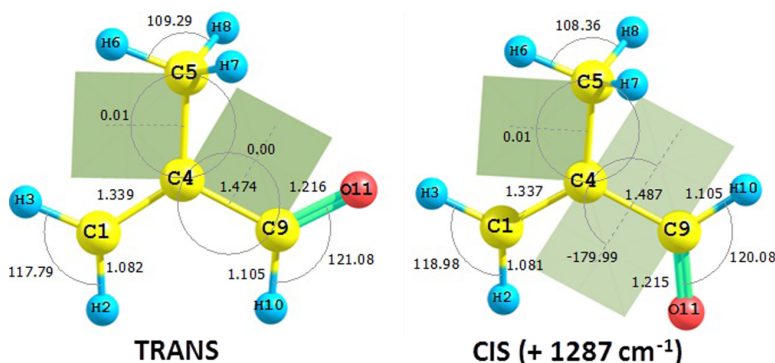


FIG. 2. Equilibrium geometries calculated at the MP2/aug-cc-pVQZ level of the theory for the most stable *s-trans* and *s-cis* conformers of methacrolein. Some structural parameters are shown (distances in Å and angles in degrees).

TABLE II. Relative energy (kJ/mol) between the higher in energy *s-cis* conformer and the lower in energy *s-trans* conformer of methacrolein at different levels of theory (DFT and *ab initio*).

Method ^a	Value
HF/6-31G ^b	13.2
M06-2X/6-311++G(2df,p)	13.6
MP2/aug-cc-pVTZ	14.4
MP2/aug-cc-pVQZ	15.4
G3	13.7
G4	13.5

^aM06-2X/6-311++G(2df,p) and MP2/aug-cc-pVTZ are zero point corrected energies; MP2/aug-cc-pVQZ is equilibrium energy.

^bValue from Ref. 10.

group; (ii) moreover, relaxed scans (the geometry is optimized in each point of the scan) of the potential energy surface were performed for the calculation of the CH₃ rotation barriers with steps of 5° for the rotation angle (along the D5 dihedral angle H6C5C4C1). Those scans were fitted according to the following equation:

$$V(\alpha) = \frac{V_3}{2} (1 - \cos 3\alpha) + \frac{V_6}{2} (1 - \cos 6\alpha),$$

where α is the internal rotation angle. The V_3 and V_6 values were determined, they are presented in Table III.

III. EXPERIMENTAL DETAILS

Methacrolein (95% purity) was purchased from Sigma Aldrich and used without further purification.

The microwave rotational spectrum was recorded by using the two Fourier transform microwave spectrometers (MB-FTMW) in Aachen. The first one is operating in the frequency range 2–26.5 GHz¹⁹ and the second spectrometer covers the spectral range between 26.5 and 40 GHz.²⁰ A mixture of 20 mbar of methacrolein completed with helium, as carried gas, to a total pressure of 2 bars was prepared. Thus, a 1% mixture of methacrolein in helium at a stagnation pressure of 100 kPa for the pulsed jet was used to record all the microwave spectra. The frequency of the spectral lines was directly measured in the high resolution mode of the spectrometer, as the average of the two Doppler components. The accuracy for an isolated line is 2 kHz, but since a number of lines are blended, we safely weighted all microwave lines at a value of 5 kHz in the fit. As detailed in Fig. 3, the A and E lines are well resolved. The A lines exhibit a fine structure due to the nuclear spin-spin interaction between hydrogen atoms. It has been modelled in detail in methyl formate²¹ and in methanol,²² and this effect was not further considered in the present work. First, values for the overall-rotation parameters A, B, C, D_J, D_K, D_{JK}, δ_J, δ_K, and for the rotation-coupling parameter ρ (related to the ratio of the methyl top moment of inertia to that of the rest of the molecule) as well as for

TABLE III. Calculated internal rotation barrier V_3 and V_6 terms (cm^{-1}) for the methyl group of the *s-trans* and *s-cis* conformers of methacrolein at different levels of theory, and experimental results.

Method	<i>s-trans</i>		<i>s-cis</i>
	V_3	V_6	V_3
QST3	M06-2X/6-311++G(2df,p)	479.3	484.2
	MP2/aug-cc-pVTZ	476.5	480.1
Relaxed PES	M06-2X/6-311++G(2df,p)	481.9 (2.1)	-9.1 (2.1)
	MP2/aug-cc-pVTZ	476.8 (1.8)	-10.8 (1.8)
Experimental	This work g. s., $v_{27}=1$	491.574 (24)	-33.302 (22)
	Reference 9 g. s.	469 (7)	
	Reference 10 IR	444 (3)	441 (2)

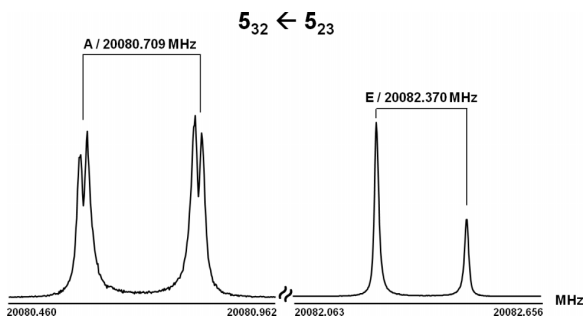


FIG. 3. Example of two high resolution FTMW signals of the *s-trans* conformer of methacrolein. The weak b-type $J_{\text{KaKc}} = 5_{32}-5_{23}$ transition of the ground state is shown, with the two A and E components associated with the internal rotation of the methyl top. A typical nuclear spin-spin structure was observed on a few A lines.

the internal rotation barrier height V_3 were optimized for the rotational lines from Ref. 9 using XIAM code.²³ This set of parameters was sufficient to easily measure new rotational transitions in the frequency range between 2 and 40 GHz for the A species. Because of the large value of the μ_a component, we first searched and easily found the very strong a-type transitions for R- and Q-branches. In a next step, another prediction was carried out with the updated spectroscopic parameters in order to determine a-type transitions for the E species. Finally, b-type transitions for A and E species were measured on high resolution mode of the two Fourier transform microwave spectrometers. At the end, a microwave data set of a total of 144 rotational lines was measured between 2 and 40 GHz for the ground state. The values of the rotation quantum numbers J and K_a are limited to 9 and 4, respectively, because of the cooled molecular beam ($T_{\text{rot}} \sim 2 \text{ K}$).

The millimeter-wave spectra were recorded in the spectral range 150–465 GHz, at room temperature and at a pressure of about 0.02 mbar, using the Lille spectrometer.²⁴ The frequency ranges, 150–322 and 400–465 GHz, were covered with solid state multiplied sources. The frequency of the Agilent synthesizer (12.5–17.5 GHz) was first multiplied by six and amplified by a VDI AMC-10 active sextupler, providing the output power of +15 dBm (~32 mW) in the W-band range (75–110 GHz). This power is high enough to use passive Schottky multipliers ($\times 2$, $\times 3$, $\times 5$) from Virginia Diodes, Inc. in the next stage of the frequency multiplication chain. Estimated uncertainties for measured line frequencies

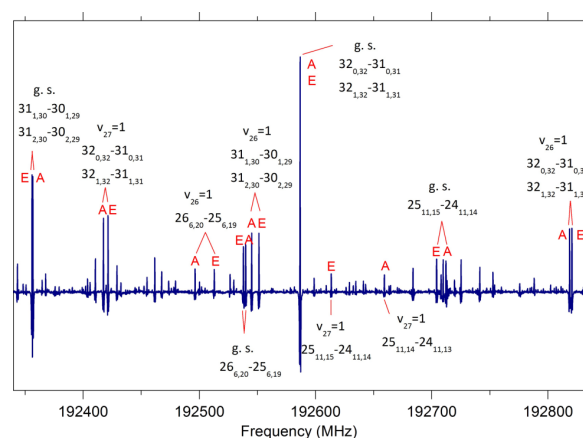


FIG. 4. A portion of the spectrum of methacrolein, showing pure rotation lines of the *s-trans* isomer in the ground state, and in $v_{27}=1$ and $v_{26}=1$. The internal rotation splittings are not observable for the ground state for the quantum number $K_a = 0/1$.

are 30 kHz, 50 kHz, and 100 kHz depending on the observed S/N ratio and the frequency range. A portion of the rotational spectrum of MAC is shown in Fig. 4. As explained hereafter, more than 4000 lines were assigned and fitted, namely, up to $J, K_a = 76, 19$ for the ground state.

IV. THEORETICAL MODEL AND SPECTRUM ANALYSIS

For the analysis of the spectrum, we used the Rho-axis-method (RAM) Hamiltonian.^{25–27} This approach has been already successfully applied for different molecules containing an internal rotor as well with high as with low barriers.^{29,30} Also the advantage of this method is its ability to fit simultaneously both the A- and E-symmetry transitions belonging to several torsional states, producing thus a single set of rotational constants.²⁸ For fitting and predicting the rotational spectra, we used the RAM36 code (rho-axis-method for 3 and 6 fold barriers).²⁹

The RAM Hamiltonian may be written as

$$H_{\text{RAM}} = H_R + H_{cd} + H_T + H_{int},$$

where H_T is a torsional Hamiltonian, H_R a rotational Hamiltonian, H_{cd} the usual centrifugal distortion Hamiltonian,

and H_{int} contains higher-order torsional–rotational interaction terms. The RAM Hamiltonian is defined in the system of axes, which is different from principal axis system (PAM) originally used to treat the overall molecular rotation. In the case of MAC, the transformation from PAM to RAM is obtained via rotation by an angle called θ_{RAM} about the *c* out-of-plane axis. This leads to different form of the rotational Hamiltonian, which now has in addition a non-diagonal D_{ab} term,

$$H_R = A_{RAM}P_a^2 + B_{RAM}P_b^2 + C_{RAM}P_c^2 + D_{ab}(P_aP_b + P_bP_a).$$

There are six different ways (representations) to identify the (*x*, *y*, *z*) reference system with the (*a*, *b*, *c*) axis system. Typically, for prolate asymmetric tops like *s-trans* conformer of MAC, the I^r representation (*a*, *b*, *c*) = (*z*, *x*, *y*) is used. From the calculated structure of the *s-trans* conformer, we determined that in the I^r representation the angle θ_{RAM} is 80.794°. However, the rotation over 80.794° in the *ab* plane yields new set of rotational constants with *B* > *A*. Therefore, for correct treatment using the RAM Hamiltonian defined in the code, its pure rotational part for the *s-trans* conformer should be set in the II^r representation (*a*, *b*, *c*) = (*x*, *z*, *y*). In this case, the angle θ_{RAM} is only 9.206° and the correct order of the rotational constants (*A* > *B*) is retained. The dipole moment components that were previously determined in the principal axis frame ($\mu_a = 2.67$ D, $\mu_b = 0.84$ D from Ref. 9) were also recalculated in the rho axis frame.^{27,28}

In the millimeter-wave range, the analysis of the ground state rotational spectrum was carried out in a usual “bootstrap” manner starting from the results of the fit of the data obtained in lower frequency range. Assigned lines were included in the least-squares fit by series in K_a quantum number starting from a pair of $\Delta J = 1$ transitions with $K_a = 0$ and $K_a = 1$. New transitions allowed to improve the values of Hamiltonian parameters and to provide reliable frequency predictions for the transitions in the next series with higher K_a values.

Room-temperature absorption spectra also contain the rotational lines from the lowest excited vibrational states, and our next logical step was an attempt to assign these lines. Methacrolein has 27 normal modes of vibration. The three low-lying vibrational modes are the CH₃ torsion (v_{27} , 130.8 cm⁻¹), the antisymmetric C1C4C9 out-of-plane bending vibration (v_{26} , 169.82 cm⁻¹), and the symmetric C1C4C9 in-plane bending vibration (v_{25} , 266 cm⁻¹) classified according to the symmetry species (A' and A'') of C_s point group as shown in Fig. 5. The energies of levels were taken from Ref. 10. Our first target was the first excited state of the methyl torsion mode. Vibrational excitation does not lead to any considerable variation of the rotational constant values; therefore, the rotational lines in excited vibrational states typically form a series of satellites close to the ground state lines, and with the intensities proportional to Boltzmann factors of the excited states. The rotational transitions of $v_{27} = 1$ state were predicted using the RAM36 program on the basis of the parameters set obtained from the fit of the ground state transitions. The initial predictions were only slightly shifted in comparison with experimental lines, making the assignment process rather simple. The same procedure was applied to predict and assign the lines of the $v_{27} = 2$ state,

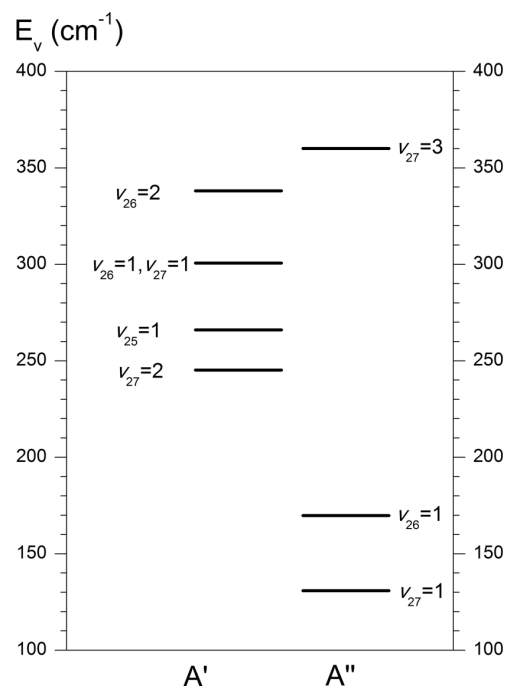


FIG. 5. The lowest vibrational states in the *s-trans* conformer of methacrolein. The experimental energy values are taken from Ref. 10.

when the results of the common fit of the $v = 0$ and $v_{27} = 1$ states were used to make the initial predictions.

In the vicinity of $\Delta J = 1$ $K_a = 0$ and 1 doublet line with unresolved A-E splitting, besides the transitions in $v_{27} = 1$ and $v_{27} = 2$ states we found several corresponding satellites, all with much broader and thus resolved splittings due to internal rotation. The most intense series of transitions after $v_{27} = 1$ state was attributed to the first excited state of the skeletal torsion mode, $v_{26} = 1$. The vibrational assignment of others lines was complicated due to resonances between excited vibrational and lack of the data.

V. RESULTS AND DISCUSSION

A. CH₃ torsion

The spectroscopic constants obtained as a results of the joint fit of $v = 0$ and $v_{27} = 1$ states are reported in Table IV. The RAM model is highly non-linear and rather strongly dependent on dataset. Also there may be strong correlations, for example, between D_{ab} , and the *A* and *B* parameters, or between *F*, and rho and V_3 parameters. In the present study, the set of rotational transitions in the two-states fit did not allow to vary the internal rotation *F* constant. When *F* was varied, it caused strong correlations and poor determinacy of the main parameters describing the internal rotation. Therefore, in the final fit, the *F* constant was fixed to the value calculated from the *ab initio* structural parameters, whereas 27 others parameters were allowed to vary. Note that because the value of *F* was fixed, no further attempt to fit *F* and $2F\rho$ as separate parameters was performed.^{31,32}

TABLE IV. List of the RAM Hamiltonian parameters for the *s-trans* conformer of methacrolein obtained in the joint fit of the ground state with $v_{27} = 1$, and of $v_{26} = 1$.

Operator	n_{tr} ^a	Parameter	(g.s. and $v_{27} = 1$) cm^{-1}	$(v_{26} = 1) \text{ cm}^{-1}$
p_α^2	2 ₂₀	F	5.489 93 fixed	5.489 93 fixed
$p_\alpha P_a$	2 ₁₁	ρ	0.279 633(41) $\times 10^{-1}$	0.282 48(45) $\times 10^{-1}$
$(1/2)(1 - \cos(3\alpha))$	2 ₂₀	V ₃	0.491 574(24) $\times 10^3$	0.623 64(28) $\times 10^3$
$(1/2)(1 - \cos(6\alpha))$	4 ₄₀	V ₆	-0.333 02(22) $\times 10^2$	0 fixed
P_a	2 ₀₂	A	0.284 428 0(23)	0.281 599(14)
P_b	2 ₀₂	B	0.150 161 0(25)	0.153 139(43)
P_c	2 ₀₂	C	0.989 374 0(45) $\times 10^{-1}$	0.989 779(17) $\times 10^{-1}$
$\{P_a, P_b\}$	2 ₀₂	D _{ab}	-0.211 33(9) $\times 10^{-1}$	-0.280 89(28) $\times 10^{-1}$
$-P^4$	4 ₀₄	D _J	0.115 029(11) $\times 10^{-6}$	0.105 20(13) $\times 10^{-6}$
$-P^2 P_a^2$	4 ₀₄	D _{JK}	-0.260 8(29) $\times 10^{-7}$	-0.108 4(46) $\times 10^{-7}$
$-P_a^4$	4 ₀₄	D _K	-0.390 10(29) $\times 10^{-7}$	-0.597 5(38) $\times 10^{-7}$
$-2P^2(P_b^2 - P_c^2)$	4 ₀₄	d _J	0.051 926(6) $\times 10^{-6}$	0.470 3(7) $\times 10^{-7}$
$-\{P_a^2(P_b^2 - P_c^2)\}$	4 ₀₄	d _K	0.067 74(16) $\times 10^{-6}$	0.056 65(13) $\times 10^{-6}$
$P^2(1 - \cos(3\alpha))$	4 ₂₂	V _{3J}	-0.129 23(49) $\times 10^{-2}$	-0.201 2(15) $\times 10^{-2}$
$P_a^2(1 - \cos(3\alpha))$	4 ₂₂	V _{3K}	0.751 1(61) $\times 10^{-3}$	0.172 4(75) $\times 10^{-2}$
$(P_b^2 - P_c^2)(1 - \cos(3\alpha))$	4 ₂₂	V _{3bc}	-1.420 6(34) $\times 10^{-3}$	-0.426 2(32) $\times 10^{-2}$
$(1/2)\{P_a, P_b\}(1 - \cos(3\alpha))$	4 ₂₂	V _{3ab}	-0.587 60(60) $\times 10^{-2}$	-0.611 6(64) $\times 10^{-2}$
$p_\alpha^2 P^2$	4 ₂₂	F _J	-0.101 01(88) $\times 10^{-4}$	
$p_\alpha^2 (P_b^2 - P_c^2)$	4 ₂₂	F _{bc}	-0.113 01(52) $\times 10^{-4}$	
$(1/2)\{P_a, (P_b^2 - P_c^2)\} p_\alpha$	4 ₁₃	ρ_{bc}	0.152 3(10) $\times 10^{-5}$	
$(1/2)\{P_b, P_c\} \sin(3\alpha)$	4 ₂₂	D _{3bc}	0.533 43(27) $\times 10^{-2}$	
$p_\alpha P_a P^2$	4 ₁₃	ρ_J	0.574(10) $\times 10^{-6}$	
$P^4 P_a^2$	6 ₀₆	Φ_{JK}	0.385 6(66) $\times 10^{-13}$	
$P^2 P_a^4$	6 ₀₆	Φ_{KJ}	-0.163 9(32) $\times 10^{-12}$	
P_a^6	6 ₀₆	Φ_K	0.147 6(32) $\times 10^{-12}$	
$P^2(1 - \cos(6\alpha))$	6 ₄₂	V _{6J}	0.150 2(30) $\times 10^{-3}$	
$(1/2)\{P_a, P_b\}(1 - \cos(6\alpha))$	6 ₄₂	V _{6ab}	0.139 6(12) $\times 10^{-2}$	
$(1/2)\{P_a, (P_b^2 - P_c^2)\} p_\alpha^3$	6 ₃₃	ρ_{mbc}	0.508 36(76) $\times 10^{-8}$	
	N lines		2429	835
	rms (MHz)		0.031 8	0.037 6
	wrms		0.776	0.843

^a $n = t + r$, where n is the total order of the operator, t is the order of the torsional part, and r is the order of the rotational part, respectively.

To estimate the quality of the fit with the restriction on F, we compared the results of the fit to experimental observations of the $v_{27} = 1-0$ torsional band in Ref. 10. It is well known (see, for example, Ref. 32) that pure rotational spectra contain only indirect data on the torsional motion, and important information is obtained from the torsional bands. In Ref. 10, the FIR spectra of MAC were measured at a resolution of 0.125 cm^{-1} and did not allow to observe any resolved rotational structure, but only to determine the band center at 130.8 cm^{-1} . Obviously, this information is not sufficient to use in the least squares fit with high-resolution microwave spectra. However it may give a general evaluation of the correctness of the fit. A comparison between the FIR spectrum from Ref. 10 and the spectrum simulated on the basis of the two-states fit at the resolution of the experiment is shown in Fig. 6. As one may see, a very good agreement between experiment and theory is achieved for $v_{27} = 1-0$ torsional band origin. The observed $v_{27} = 1-0$ band center is at 130.8 cm^{-1} , whereas it is predicted at 131 cm^{-1} on the basis of the parameters from the final fit. Thus, with the F parameter fixed to a reasonable value, the quality of the two-states fit is confirmed.

One may also notice a shift of approximately 9.5 cm^{-1} between observed and predicted $v_{27} = 2-1$ torsional bands on Fig. 6. Besides the fact that the $v_{27} = 2-1$ band was predicted without $v_{27} = 2$ pure rotational transitions in the dataset, another plausible explanation for this shift is Fermi and *c*-type Coriolis interactions between $v_{27} = 2$ and $v_{25} = 1$. It may be seen from Fig. 5 that the two vibrational levels are close and belong to the same symmetry species (A') of C_s point group. In the analysis of pure rotational spectra, the transitions in $v_{27} = 1$ state were first predicted on the basis of the ground state fit. For the low- K_a transitions, the difference between predicted and observed $v_{27} = 1$ rotational transitions did not exceed 1 or 2 MHz. We also expected the same quality of predictions for the rotational transitions of $v_{27} = 2$ state on the basis of the fit of $v = 0$ and $v_{27} = 1$ states. However, the observed transitions were shifted by more than 10 MHz from the predicted ones. Also, we could not obtain a fit within experimental accuracy by adding the assigned lines of $v_{27} = 2$ state to the existing dataset. Finally, we were able to provide a firm assignment only for rotational transitions with $K_a < 5$. Thus, symmetry and vibrational energy considerations, as well as perturbations in rotational and rovibrational spectra

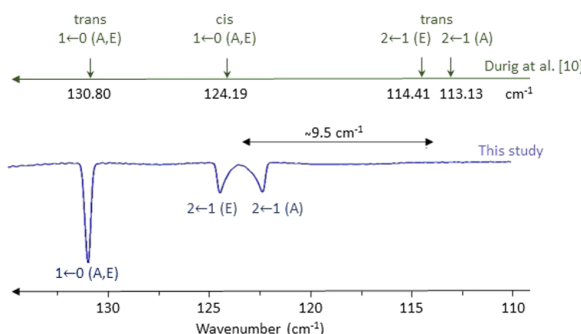


FIG. 6. The FIR spectrum of methacrolein simulated for the *s-trans* conformer on the basis of the two-states fit, at the resolution of the experimental spectrum of Ref. 10.

support the assumption of interaction between $v_{27} = 2$ and $v_{25} = 1$ states.

As mentioned in Ref. 28, another issue of importance for fitting parameters for internal rotors is that in many cases the large number of rotational, torsional, and torsion-rotational terms allowed by symmetry in the Hamiltonian is not all simultaneously determinable in least-squares fits of experimental data. Using contact transformation techniques, it can be shown that the coefficients of some of these terms can be set to zero, giving rise to so-called reduced Hamiltonians. Several authors (Lees *et al.*,³³ Duan *et al.*,³⁴ and Nakagawa *et al.*³⁵) discussed reduced Hamiltonians, usually to the fourth orders in the case of methyl top molecules of C_s point-group symmetry, and they were quite successful in applying the reduced Hamiltonians to methanol and its isotopologues. An important point is that while the number of adjustable parameters is fixed by the contact transformation, exactly which terms should be eliminated or kept is more a question of choice. In the present work, we did not investigate further this aspect, and we fit the parameters according to the reduction of Hamiltonian used in RAM36.³¹

It is interesting to compare the experimental values of the molecular parameters to their corresponding *ab initio* or DFT values. For the rotational and centrifugal distortion parameters of the ground state, a good agreement between theory and experiment was achieved. The calculated M06-2X values ($A = 8651$ MHz, $B = 4438$ MHz, $C = 2987$ MHz) differ by less than 1% with the PAM experimental rotational constants of the present work ($A = 8624.304$ MHz, $B = 4404.346$ MHz, $C = 2966.069$ MHz), after the RAM to PAM transformation.²⁸ Also the angles in degrees between the principal axis (a , b , c) and the methyl top axis (i) obtained from our fitting ($85.512(5)^\circ$, $4.488(5)^\circ$, 90°) and calculated (85.260° , 4.740° , 90°) are in very good agreement. It should be mentioned that calculated values of the quartic centrifugal distortion parameters in the I^1 representation ($D_J = 3.296$ kHz, $D_{JK} = -1.259$ kHz, $D_K = -0.585$ kHz, $\delta_J = 1.486$ kHz, $\delta_K = 1.210$ kHz) were used with success to predict the spectrum of the ground state in the millimeter-wave region, in order to facilitate the assignments. Finally, the results obtained from the fit of the relaxed scans of the PES at the M06-2X/6-311++G(2df,p) and MP2/aug-cc-pVTZ levels of theory for the CH_3 rotation barriers are in good agreement

with the experimental ones (see Table III). For the *s-trans* conformer, the calculated V_3 value is underestimated by only 3%. Concerning the V_6 barrier, the best result in terms of sign and order of magnitude is obtained with the MP2/aug-cc-pVTZ method.

B. Skeletal torsion

In the frequency range of the experiment, for the $K_a = 0$ ground state rotational transitions the A-E tunneling splittings were too small (<0.2 MHz) to be observed under Doppler-limited resolution of the spectrometer. For the same transitions of $v_{27} = 1$ state, the splittings were about 30 times higher and easily distinguishable. In the $v_{26} = 1$ state, the $K_a = 0$ transitions also exhibited A-E splittings much higher than in the ground vibrational state.

In addition to anomalously high splittings in $v_{26} = 1$ state, the order of A and E tunneling sublevels and also the order of rotational lines in the spectrum is inverted compared to the typical order of transitions in the ground state. When a given vibrational mode is not coupled to the torsional mode, the order of the rotational transition tunneling components should be the same as in the ground state that is the E-type component is shifted into lower frequencies, whereas the A-type component is shifted into higher frequencies with respect to unsplit pure rotational transition frequency. In the case of $v_{26} = 1$ state of MAC, the order of A-E components is inverted, as it may be clearly seen in Fig. 4. Several a-type transitions at high K_a values also showed a particular behavior in terms of resolved methyl torsion splittings, as illustrated in Fig. 7. Owing to Coriolis coupling two K_a transitions of E symmetry component are split, whereas two K_a transitions of A symmetry are almost degenerate and represented by single line of double intensity. This kind of anomalous A-E sequence was previously observed in several studies of molecules with one^{36–38} or two methyl tops³⁹ and explained by kinetic or potential energy coupling between the methyl and skeletal torsional modes. In Refs. 36 and 37, a two-dimensional flexible model was developed to account for this kind of interaction. The calculations performed using the model showed a good agreement with experimental data on torsional energy levels and A-E energy splittings.

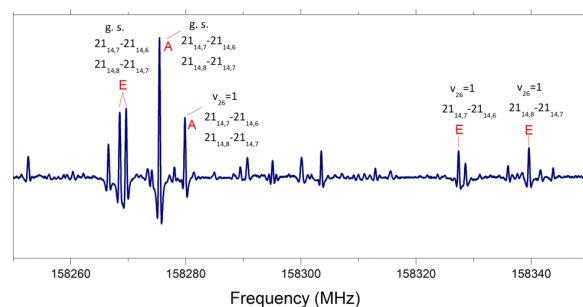


FIG. 7. A portion of the millimeter-wave spectrum of methacrolein. A few assignments are shown for the *s-trans* conformer. The inverse sequence of the rotational splittings of high K_a transitions in the v_{26} state is illustrated.

TABLE V. Relative displacements (angstroms) of the atoms for the v_{27} and v_{26} modes of the *s-trans* conformer of methacrolein obtained with the MP2/aug-cc-pVTZ calculations. The atoms of the methyl top are C5, H6, H7, and H8.

Atom	v_{27}			v_{26}		
	X	Y	Z	X	Y	Z
C1	0.00	0.00	0.04	0.00	0.00	0.13
H2	0.00	0.00	0.00	0.00	0.00	0.13
H3	0.00	0.00	0.15	0.00	0.00	0.32
C4	0.00	0.00	-0.05	0.00	0.00	-0.08
C5	0.00	0.00	-0.03	0.00	0.00	-0.03
H6	0.00	0.00	0.50	0.00	0.00	-0.45
H7	0.46	-0.03	-0.31	-0.38	0.06	0.22
H8	-0.46	0.03	-0.31	0.38	-0.06	0.22
C9	0.00	0.00	-0.09	0.00	0.00	-0.17
H10	0.00	0.00	-0.29	0.00	0.00	-0.48
O11	0.00	0.00	0.11	0.00	0.00	0.12

In order to elucidate the mechanism of the coupling between the methyl and skeletal torsions in MAC, one may use the results of the harmonic force field calculations. Table V represents the relative displacements of the atoms for the v_{27} and v_{26} modes obtained with the MP2/aug-cc-pVTZ calculation. From the analysis of the results it follows that both vibrations involve the displacements of exactly the same coordinates but in different proportions depending on vibrational mode. The methyl torsional motion is described by significant changes of X and Z coordinates of the methyl top hydrogens (H6–H8), and relatively small out-of-plane displacements of other atoms. In the case of skeletal torsion, the methyl top hydrogens are also involved but in smaller extent, although the out-of-plane displacement of other atoms is higher than for v_{27} mode. Thus, both normal modes may be represented as a mixture of pure methyl top torsion, and out-of-plane motion of other atoms, or in other words, the coupling consists in mixing the methyl top and skeletal torsional motions. What one may also notice from the relative displacements presented in Table V is the antiphase character for v_{27} and v_{26} . Two-dimensional PES for methyl and skeletal torsions would thus show the two motions with opposite sign. In the frame of the flexible model for intramolecular motions developed by Meyer,^{36–38} the interaction that may be accounted for using potential energy coupling terms is called gearing type coupling. Indeed, the results of *ab initio* calculations show that one of the vibrational motions, for example, methyl torsion, gears the second one, skeletal torsion, and vice versa.

To account for unusual A-E sequence in the $v_{26} = 1$ state, we assigned it as a virtually first excited state of the methyl torsional mode, and hence, the RAM Hamiltonian could then be used in fitting the observed transitions. The applied “method of virtual state” was successful as it allowed fitting all the $v_{26} = 1$ lines within experimental accuracy. The results of the fit are given in the last column of Table IV. The value of the V_6 parameter was fixed to zero, as it could not be fitted for a single torsional state because of its high correlation with V_3 . One should note that the fit is purely effective and, for example, the internal rotation parameters

such as V_3 have no physical meaning because they are not global parameters. Nevertheless, there is a general agreement between the parameters from the two-states fit and the fit of the $v_{26} = 1$ state.

VI. CONCLUSION

Current analysis of the rotational spectrum of *s-trans* MAC as well as quantum chemical calculations at high level of theory represents a significant advance in the knowledge on the molecular structure and dynamics, and on the low-lying excited vibrational states. The experimentally determined value of the barrier to internal rotation is relatively high, $491.574(24) \text{ cm}^{-1}$, but the A-E splittings in the ground vibrational state were resolved for the majority of the lines even at Doppler limited resolution. This value was obtained as a result of the joint analysis of the ground and first excited torsional states using the RAM Hamiltonian and RAM36 code. It compares well with the results of *ab initio* calculations. The results of the two-states fit are also in good agreement with FIR observations, as they predict well the $v_{27} = 1\text{-}0$ torsional band center. The study of the methyl torsional mode is limited by $v_{27} = 1$ state because we found that $v_{27} = 2$ state is perturbed by Fermi-type interaction with $v_{25} = 1$ state. In addition to the methyl torsion, we analyzed the first excited vibrational state of the skeletal torsional mode v_{26} . The anomalous A-E splittings and unusual sequence of A-E transitions in the $v_{26} = 1$ state were attributed to gearing coupling between methyl and skeletal torsional modes. The interesting point is that in this case the potential energy coupling could be qualitatively predicted from the harmonic force field calculations without direct analysis of the potential energy surface.

From the atmospheric application point of view, the results of the present study of MAC provide precise ground state molecular constants essential as a foundation (by using the ground state combination differences method) for the analysis of high resolution spectrum, recorded from 600 to 1600 cm^{-1} using high resolution FTIR spectrometer coupled to the far infrared beamline AILES of the SOLEIL synchrotron. The infrared range can be then refitted using appropriate Hamiltonian parameters.

ACKNOWLEDGMENTS

The present work was funded by the French ANR “Labex CaPPA” through the PIA under Contract No. ANR-11-LABX-0005-01, by the Regional Council “Nord-Pas de Calais,” and by the European Funds for Regional Economic Development (FEDER). O.Z. also acknowledges the support of CNRS-INP and of CPER IRENI for her Ph.D. thesis. A.J. gratefully acknowledges Professor Dr. W. Stahl for making his spectrometers available for the present project during his stay in Aachen.

APPENDIX: SUPPLEMENTARY DATA

A list of assignments⁴⁰ fitted in the current study with a RAM Hamiltonian, is provided as supplementary material.

- ¹A. Guenther, T. Karl, P. Harley, C. Wiedinmyer, P. I. Palmer, and C. Geron, *Atmos. Chem. Phys.*, **6**, 3181 (2006).
- ²J. Peeters and J. F. Müller, *Phys. Chem. Chem. Phys.*, **12**, 14227 (2010).
- ³K. Cheung, H. Guo, J. M. Ou, I. J. Simpson, B. Barletta, S. Meinardi, and D. R. Blake, *Atmos. Environ.*, **84**, 323 (2014).
- ⁴S. S. Brown, J. A. Degouw, C. Warneke, T. B. Ryerson, W. P. Dube, E. Atlas, R. J. Weber, R. E. Peltier, J. A. Neuman, J. M. Roberts, A. Swanson, F. Flocke, S. A. McKeen, J. Brioude, R. Sommariva, M. Trainer, F. C. Fehsenfeld, and A. R. Ravishankara, *Atmos. Chem. Phys.*, **9**, 3027 (2009).
- ⁵M. Karl, H.-P. Dorn, F. Holland, R. Koppmann, D. Poppe, L. Rupp, A. Schaub, and A. Wahner, *J. Atmos. Chem.*, **55**, 167 (2006).
- ⁶S. N. Matsunaga, C. Wiedinmyer, A. B. Guenther, J. J. Orlando, T. Karl, D. W. Toohey, J. P. Greenberg, and Y. Kajii, *Atmos. Chem. Phys. Discuss.*, **5**, 11143 (2005).
- ⁷Y. Fu and H. Liao, *Atmos. Environ.*, **59**, 170 (2012).
- ⁸D. S. Jo, R. J. Park, M. J. Kim, and D. V. Spracklen, *Atmos. Environ.*, **81**, 230 (2013).
- ⁹M. Suzuki and K. Kozima, *J. Mol. Spectrosc.*, **38**, 314 (1971).
- ¹⁰J. R. Durig, J. Qiu, B. Dehoff, and T. S. Little, *Spectrochim. Acta, Part A*, **42**, 89 (1986).
- ¹¹M. J. Frisch *et al.*, 09, Revision D.01, Gaussian, Inc., Wallingford, CT, 2009.
- ¹²Y. Zhao and D. G. Truhlar, *Theor. Chem. Acc.*, **120**, 215 (2008).
- ¹³C. Møller and M. S. Plesset, *Phys. Rev.*, **46**, 618 (1934).
- ¹⁴T. H. Dunning, Jr., *J. Chem. Phys.*, **90**, 1007 (1989).
- ¹⁵L. A. Curtiss, K. Raghavachari, P. C. Redfern, V. Rassolov, and J. A. Pople, *J. Chem. Phys.*, **109**, 7764 (1998).
- ¹⁶L. A. Curtiss, P. C. Redfern, and K. Raghavachari, *J. Chem. Phys.*, **126**, 084108 (2007).
- ¹⁷C. Peng and H. B. Schlegel, *Isr. J. Chem.*, **33**, 449 (1993).
- ¹⁸C. Peng, P. Y. Ayala, H. B. Schlegel, and M. J. Frisch, *J. Comput. Chem.*, **17**, 49 (1996).
- ¹⁹J.-U. Grabow, W. Stahl, and H. Dreizler, *Rev. Sci. Instrum.*, **67**, 4072 (1996).
- ²⁰I. Merke, W. Stahl, and H. Dreizler, *Z. Naturforsch., A*, **49**, 490 (1994).
- ²¹M. Tudorie, L. H. Coudert, T. R. Huet, D. Jegouso, and G. Sedes, *J. Chem. Phys.*, **134**, 074314 (2011).
- ²²L. H. Coudert, C. Gutlé, T. R. Huet, J.-U. Grabow, and S. A. Levshakov, *J. Chem. Phys.*, **143**, 044304 (2015).
- ²³H. Hartwig and H. Dreizler, *Z. Naturforsch., A*, **51**, 923 (1996).
- ²⁴E. A. Alekseev, R. A. Motiyenko, and L. Margulès, *Radio Phys. Radio Astron.*, **3**(1), 75 (2012).
- ²⁵B. Kirtman, *J. Chem. Phys.*, **37**, 2516 (1962).
- ²⁶R. M. Lees and J. G. Baker, *J. Chem. Phys.*, **48**, 5299 (1968).
- ²⁷J. T. Hougen, I. Kleiner, and M. Godefroid, *J. Mol. Spectrosc.*, **163**, 559 (1994).
- ²⁸I. Kleiner, *J. Mol. Spectrosc.*, **260**, 1 (2010).
- ²⁹V. Ilyushin, E. A. Alekseev, S. F. Dyubko, I. Kleiner, and J. T. Hougen, *J. Mol. Spectrosc.*, **227**, 115 (2004).
- ³⁰J. L. Alonso, A. Lesarri, J. C. Lopez, S. Blanco, I. Kleiner, and J. Demaison, *Mol. Phys.*, **91**, 731 (1997).
- ³¹V. V. Ilyushin, Z. Kisiel, L. Pszczółkowski, H. Mäder, and J. T. Hougen, *J. Mol. Spectrosc.*, **259**, 26 (2010).
- ³²M. Tudorie, V. Ilyushin, J. Vander auwera, O. Pirali, P. Roy, and T. R. Huet, *J. Chem. Phys.*, **137**, 064304 (2012).
- ³³R. Lees, *J. Chem. Phys.*, **59**, 2690 (1973).
- ³⁴Y. B. Duan, L. Wang, I. Mukhopadhyay, and K. Takagi, *J. Chem. Phys.*, **110**, 927 (1999).
- ³⁵K. Nakagawa, S. Tsunekawa, and T. Kojima, *J. Mol. Spectrosc.*, **126**, 329 (1987).
- ³⁶A. C. Fantoni, W. Caminati, and R. Meyer, *Chem. Phys. Lett.*, **133**, 27 (1987).
- ³⁷R. Meyer and A. Bauder, *J. Mol. Spectrosc.*, **94**, 136 (1982).
- ³⁸R. Meyer, W. Caminati, and H. Hollenstein, *J. Mol. Spectrosc.*, **137**, 87 (1989).
- ³⁹K. Kobayashi, T. Matsui, N. Mori, S. Tsunekawa, and N. Ohashi, *J. Mol. Spectrosc.*, **251**, 301 (2008).
- ⁴⁰See supplementary material at <http://dx.doi.org/10.1063/1.4939636> for the list of assignments fitted in the current study with a RAM Hamiltonian.

Chapitre 3

Spectroscopie de molécules avec la vibration de type inversion

3.1 Introduction

Le mouvement de vibration de type inversion est caractéristique pour les molécules ayant deux configurations équivalentes en terme d'énergie, qui ne peuvent pas être superposées par la rotation de la molécule dans l'ensemble. Un exemple de mouvement d'inversion est la rotation du groupement OH dans l'hydroxyacetonitrile. La fonction d'énergie potentielle de la molécule est présentée sur la Fig. 12. La conformation gauche de l'hydroxyacetonitrile possède deux configurations équivalentes $G+$ et $G-$ séparées par une barrière dont la hauteur est de 425 cm^{-1} . L'effet tunnel entre les configurations sépare les niveaux de vibration en deux sous-niveaux : $0+$ et $0-$. Notons également l'existence de la seconde conformation trans représentée par un seul minimum sur la courbe de l'énergie potentielle. De même façon, la substitution isotopique de H par D sur le groupement CH_3 dans le formiate de méthyle casse la symétrie C_{3v} de la toupie et entraîne l'apparition de deux conformations : l'une avec deux configurations équivalentes lorsque le deutérium se trouve en dehors du plan de symétrie, minimas 1 et 2 sur la Fig. 13a, et l'autre lorsque le deutérium se trouve dans le plan de symétrie, minimum 3 sur la Fig. 13a. Ainsi, au lieu d'une séparation de chaque niveau d'énergie en deux sous niveaux dans le cas du formiate de méthyle HCOOCH_3 on obtient la séparation de chaque niveau d'énergie en trois sous niveaux comme il est illustré sur la Fig. 13b. Notons, que dans le cas du formiate de méthyle doublement déuteré, HCOOCHD_2 , il s'agit du même phénomène de séparation en trois sous niveaux. Cependant à cause des effets d'énergie de point zero la conformation avec l'atome de deutérium hors du plan de symétrie est plus stable énergétiquement.

Parmi les différentes approches utilisées pour traiter le problème de l'effet tunnel

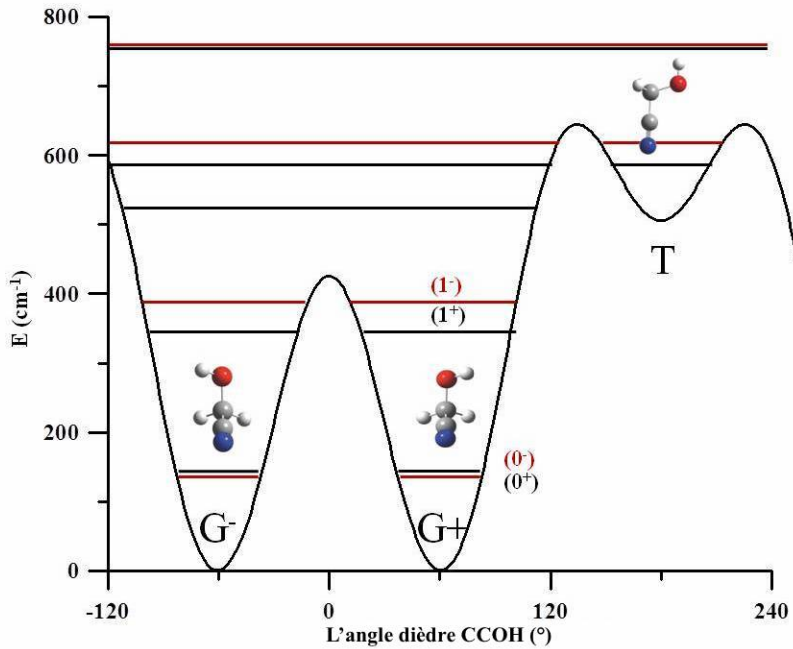


FIGURE 12: L'énergie potentielle du 2-hydroxyacétonitrile en fonction de l'angle dièdre CCOH obtenu par les calculs ab initio CCSD(T)-F12.

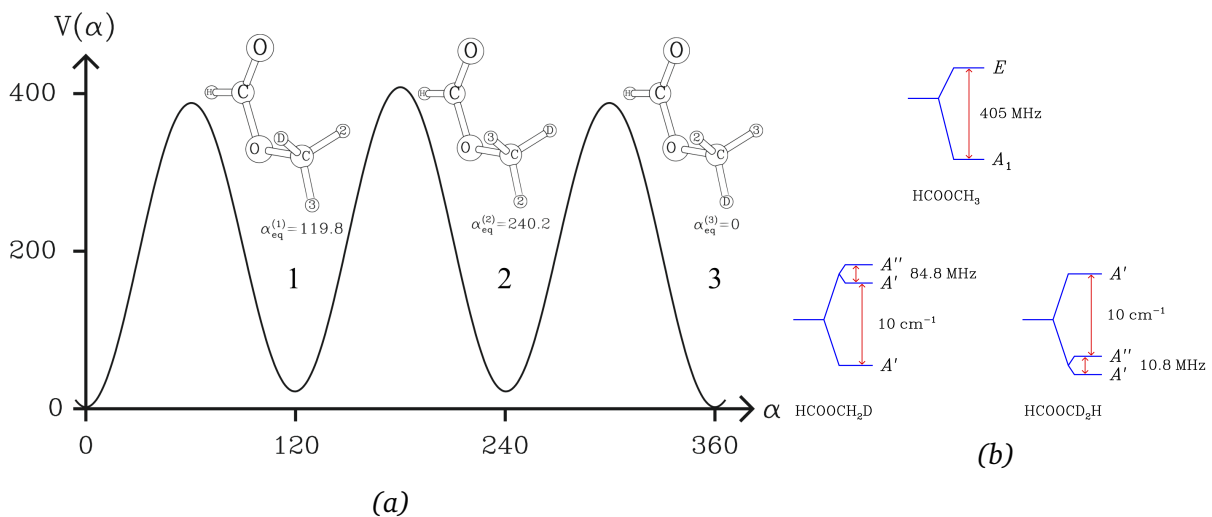


FIGURE 13: (a) La fonction de potentiel de rotation interne $V(\alpha)$ pour le formiate de méthyle mono déuteré HCOOCH_2D [Margulès et al. 2009]. Les trois configurations non superposables sont indiquées avec le nombre n égal à 1, 2 ou 3. Les configurations 1 et 2 sont isoénergétiques avec l'atome D en dehors du plan de symétrie. La configuration 3 est caractérisée par la symétrie C_s avec l'atome D dans le plan. (b) Les séparations d'un niveau d'énergie à cause de l'effet tunnel pour le formiate de méthyle. La valeur de 405 MHz pour l'espèce normale a été obtenue dans [Ilyushin et al. 2009].

dans le cas de l'inversion, les plus efficaces en terme de précision de l'ajustement sont celles basées sur la méthode d'axes internes. Premièrement, il faut évoquer le formalisme de l'effet tunnel à haute barrière développée par Jon Hougen et ses collaborateurs dans les années 1980 [Hougen and DeKoven 1983 ; Hougen 1985 ; Ohashi and Hougen 1985]. L'idée principale du formalisme est de considérer le système moléculaire comme un ensemble de configurations équivalentes, chacune accessible via l'effet tunnel. Pour chaque voie de l'effet tunnel l'on peut établir son propre système local d'axes internes dans le but d'annuler le moment angulaire issu de l'effet tunnel. Chaque configuration possède une fonction d'onde de vibration dont la forme analytique reste généralement inconnue, ce qui pose évidemment un problème pour le traitement avec les méthodes numériques. Le formalisme développé par Hougen et collaborateurs permet de contourner ce problème. Le formalisme se base sur le fait que les probabilités de l'effet tunnel entre les différentes configurations sont proportionnelles aux intégrales de recouvrement entre les fonctions d'ondes individuelles. En même temps, les probabilités de l'effet tunnel sont directement liées aux séparations des niveaux d'énergie. Au final, dans le cadre du formalisme, les niveaux d'énergie sont présentés comme une expansion en série selon les séparations qui jouent le rôle de paramètres à ajuster.

Un exemple de paramétrisation des niveaux d'énergie est présenté dans l'article [Hougen and DeKoven 1983] pour une molécule possédant 9 minimas équivalents. On pose d'abord : $\psi_0, \psi_1, \dots, \psi_8$ les fonctions d'onde individuelles associées avec 9 minimas. L'étape suivante consiste à introduire des intégrales de recouvrement comme les paramètres $X_1 = \langle \psi_i | H | \psi_{i+1} \rangle, X_2 = \langle \psi_i | H | \psi_{i+2} \rangle$ etc. (suite au caractère cyclique : $H_{i,i\pm j} = H_{i,i\pm(n-j)} = X_j$ et $0 \leq j \leq n/2$) qui expriment l'interaction entre les différents minimas. Dans l'article [Hougen and DeKoven 1983] il est démontré que l'on peut exprimer les valeurs propres (les niveaux d'énergie) de l'hamiltonien via les paramètres X_j :

$$E_r = X_0 + 2 \sum_{j=1}^4 X_j \cos \left(\frac{2\pi jr}{9} \right) + (-1)^r X_{n/2} \quad (3.1)$$

De manière générale, on somme pour tous les $0 \leq j < n/2$ et le terme $X_{n/2}$ est possible lorsque le nombre de minimas n est paire. C'est ainsi que les éléments de matrice $X_j = \langle \psi_i | H | \psi_{i+j} \rangle$ deviennent les paramètres à ajuster à partir des données expérimentales. Dans le cas d'une haute barrière à l'effet tunnel, la contribution principale dans E_r vient de quelques premiers termes X_j avec $j = 0, 1, 2, \dots$ et le développement en série dans l'Eq. 3.1 converge assez rapidement.

D'un côté cette approche permet d'analyser le spectre de rotation avec une très bonne précision. De l'autre côté les paramètres issus de l'analyse spectrale n'ont pas de sens

physique direct. Notamment, le formalisme ne permet pas d'obtenir de façon explicite les paramètres de la fonction d'énergie potentielle. Cependant, la fonction d'énergie potentielle peut être retrouvée de façon indirecte en utilisant la valeur de séparation d'énergie entre les sous-états, ainsi que l'information sur les niveaux de vibrations les plus bas que l'on peut obtenir par les calculs de chimie quantique ou par l'étude des spectres de vibration. Le formalisme a été appliqué avec succès dans l'analyse des spectres de rotation et de vibration de plusieurs molécules manifestant un ou deux MVGA, y compris pour la rotation interne d'un toupie C_{3v} . Ce dernier problème est traité à l'aide du formalisme décrit ci-dessus dans le code ERHAM, qui permet d'analyser les spectres des molécules avec une ou deux toupies C_{3v} [[Groner 1992](#); [Groner 1997](#)]. En ce qui concerne le mouvement de vibration de type inversion, la réalisation du formalisme de l'effet tunnel à haute barrière pouvant traiter ce cas est souvent appelée « le formalisme du dimère de l'eau » [[Coudert and Hougen 1988](#)], car initialement il a été appliquée pour analyser les deux MVGA du dimère de l'eau.

Une autre limitation du formalisme est son applicabilité au cas de hautes barrières à l'effet tunnel. La condition de haute barrière suggère que la plupart du temps le système est soumis à des oscillations rapides autour de la configuration d'équilibre de la molécule et de temps en temps le système subit un effet tunnel pour passer d'une configuration à une autre. Du point de vue de la mécanique quantique, cela signifie que les fonctions d'onde sont bien localisées et que la séparation des niveaux d'énergie à cause de l'effet tunnel est faible par rapport à la différence caractéristique entre les niveaux de vibration de la molécule. La situation se complique pour les molécules avec des faibles barrières. Dans ce cas les fonctions d'onde ne peuvent plus être bien localisées dans les minima d'énergie potentielle et à cause de grandes probabilités à l'effet tunnel même entre les configurations éloignées, la convergence de la méthode diminue significativement. Le formalisme de l'effet tunnel à haute barrière est une méthode « locale » et pour cette raison elle est difficile à appliquer dans le cas d'interactions vibrationnelles même s'il s'agit de vibrations de même type.

En second lieu il faut également évoquer la méthode de système d'axes réduits (SAR) proposée par Pickett [[Pickett 1972](#)] et permettant de traiter particulièrement les cas de vibration de type inversion. L'idée principale de la méthode reste la même : introduire un système d'axes internes dans le but d'annuler le moment angulaire généré par le MVGA. Dans le cas de la méthode SAR, l'inversion est traitée en tant qu'une perturbation à l'hamiltonien principal. Il a été démontré que la méthode SAR est équivalente au « formalisme du dimère de l'eau » [[Christen et al. 2002](#)]. L'avantage de l'application de la méthode SAR est que celle-ci est réalisé dans le code SPFIT/SPCAT [[Pickett 1991](#)] bien connu parmi les spectroscopistes. De ce fait, comme le modèle MAR et le code RAM36,

le modèle SAR n'a pas des limitations particulières en terme d'ordre de grandeur des opérateurs de l'hamiltonien, ce qui facilite son application.

3.2 L'étude du formiate de méthyle déuteré

3.2.1 L'application du « formalisme du dimère de l'eau » au formiate de méthyle déuteré

L'application du « formalisme du dimère de l'eau » commence par l'établissement des voies de l'effet tunnel entre les configurations non superposables. La contribution de chaque voie à l'élément de matrice de l'hamiltonien est contenue dans la fonction de Wigner $D^{(J)}(\chi_{pn}, \theta_{pn}, \phi_{pn})$, où trois angles χ_{pn} , θ_{pn} et ϕ_{pn} dépendent de la voie considérée et les indices p et n désignent la voie de l'effet tunnel. La fonction d'onde de référence pour une configuration n est donnée comme le produit de la fonction d'onde de vibration $\psi_n(\alpha)$ et la fonction d'onde de rotation $|JK\gamma\rangle$, avec $K \geq 0$ et $\gamma = \pm 1$ défini comme : $|JK\gamma\rangle = \sqrt{2} [|J, K\rangle + \gamma |J, -K\rangle]$.

Dans le cas du formiate de méthyle déuteré HCOOCH_2D , il existe trois configurations non superposables correspondant aux trois minima de la fonction d'énergie potentielle représentée sur la Fig. 13a. D'après le formalisme, on cherche à déterminer les éléments de matrice entre deux fonctions de référence : $H_{JK\gamma m; JK'\gamma'n} = \langle \Psi_{JK\gamma m} | H | \Psi_{JK'\gamma'n} \rangle$. Les trois éléments non-tunnels de la matrice, lorsque $m = n$ correspondent à l'énergie purement ro-vibrationnelle. En appliquant les règles de symétrie dans le cas du formiate de méthyle déuteré les éléments tunnels $m \leftrightarrow n$ de la matrice sont : $H_{JK\gamma 1; JK'\gamma'2} = \pm H_{JK\gamma 2; JK'\gamma'1}$ et $H_{JK\gamma 1; JK'\gamma'3} = \pm H_{JK\gamma 3; JK'\gamma'1}$. L'élément $1 \leftrightarrow 2$ décrit l'effet tunnel entre les configurations 1 et 2 avec la rotation du groupement méthyle par 120.4° . D'après le formalisme la dépendance en terme de rotation de cet élément est paramétrisée par trois angles χ_2 , θ_2 et ϕ_2 qui sont les paramètres à ajuster dans l'analyse spectrale. L'élément $1 \leftrightarrow 3$ décrit le passage de la configuration 1 à la configuration 3 via la rotation du groupement méthyle par -119.8° . Comme dans le cas du passage $1 \leftrightarrow 2$, la dépendance en terme de rotation de cet élément est paramétrisée par trois angles χ_3 , θ_3 et ϕ_3 . Cependant, lors de l'analyse des spectres de rotation l'on n'a pas pu mettre en évidence les effets dûs aux termes $H_{JK\gamma 1; JK'\gamma'3}$. En conséquence, les niveaux de rotation de la configuration avec l'atome D dans le plan de symétrie de la molécule pouvaient être traités séparément comme un état de vibration isolé. Les niveaux de rotation de la configuration avec D hors plan de symétrie ont été traités avec les termes tunnels $H_{JK\gamma 1; JK'\gamma'2}$. Dans la base des fonctions d'onde de référence, l'hamiltonien correspondant à l'effet tunnel entre les configurations 1 et 2 s'écrit comme :

$$H_{JK\gamma_1;JK'\gamma'_2} = h_2 \langle JK\gamma | D | JK'\gamma' \rangle \quad (3.2)$$

où D est l'opérateur dont les éléments de matrice peuvent être obtenus à l'aide de résultats de [Coudert and Hougen 1988]. L'hamiltonien 3.2 prend en compte la dépendance de séparations des niveaux d'énergie en fonction de nombres quantiques de rotation, mais il ne contient aucune contribution de la distorsion centrifuge. En rajoutant les opérateurs de la distorsion, l'hamiltonien 3.2 devient :

$$H_{JK\gamma_1;JK'\gamma'_2} = \frac{1}{2} \langle JK\gamma | \{h_2 + h_{2j}P^2 + h_{2k}P_z^2 + f_2(P_+^2 + P_-^2) + \dots, D\} | JK'\gamma' \rangle \quad (3.3)$$

avec h_{2j} , h_{2k} et f_2 les paramètres de distorsion. De même, on peut inclure la dépendance en distorsion centrifuge pour les trois angles χ_2 , θ_2 , et ϕ_2 en multipliant ceux-ci par les opérateurs P^2 , P_z^2 , $P_+^2 + P_-^2$ etc.

3.2.2 Résultats

Le modèle décrit ci-dessus a été appliqué dans l'analyse des spectres du formiate de méthyle déuteré CH_2D et CHD_2 dans le cas des conformations avec deux configurations équivalentes : deux atomes H ou D en dehors du plan de symétrie. Pour la conformation avec un seul atome H ou D dans le plan de symétrie, on a utilisé indépendamment le modèle standard de l'hamiltonien de Watson. Globalement, les écarts types pondérés des ajustements des fréquences de raies spectrales pour les deux espèces isotopiques de valeurs de 1.5 pour HCOOCH_2D [Coudert *et al.* 2013] et de 1.6 pour HCOOCHD_2 [Coudert *et al.* 2012] indiquent que le modèle théorique appliqué ne décrit pas le spectre et le phénomène de la rotation interne avec la précision de l'expérience. Alors que, les écarts types individuels montrent que les conformations « dans le plan » pour lesquelles on a utilisé l'hamiltonien de Watson sont mieux ajustés. Ce résultat peut être expliqué par le fait que l'interaction entre les deux conformations n'a pas été prise en compte. En termes du modèle, il s'agit des éléments $H_{JK\gamma_1;JK'\gamma'_3}$ de la matrice de l'effet tunnel. Cependant, le « formalisme du dimère de l'eau » est un modèle non linéaire. Notamment, les paramètres h et les paramètres de l'opérateur D : χ , θ et ϕ sont corrélés. La meilleure façon d'enlever la corrélation entre ces paramètres est d'attribuer dans le spectre et de prendre en compte dans l'analyse les transitions qui connectent les sous niveaux différents. Ainsi, les paramètres h_2 et h_3 peuvent être déterminés avec une très grande précision. Dans le cas du formiate de méthyle déuteré, l'attribution de telles raies s'avère une tâche extrêmement fastidieuse car les moments dipolaires induits par la rotation interne sont très faibles, de l'ordre de 0.1 D. En conséquence, les intensités de telles

transitions sont souvent en dessous de la limite de sensibilité de notre spectromètre et noyées dans les transitions de rotation des états excités de vibration non attribués.

Les résultats de l'ajustement de données spectrales de ces deux espèces déuterées du formiate de méthyle sont devenus une bonne base pour les observations dans le milieu interstellaire. Cependant, pour éviter le problème de la propagation d'erreur, dans la base des données des deux espèces CH₂D et CHD₂, pour les raies spectrales dont les incertitudes de la fréquence calculées sont supérieures à 10 kHz, on utilise leurs fréquences expérimentales. Notamment, grâce aux résultats de notre dernière étude concernant l'espèce CH₂D du formiate de méthyle, celle-ci a pu être détectée dans Orion KL [Coudert *et al.* 2013].

3.3 La méthode d'axes réduits

3.3.1 Modèle théorique

Comme il était indiqué ci-dessus la méthode SAR consiste à choisir un système d'axes dans lequel le moment angulaire produit par MVGA soit annulé. Ceci a pour conséquence l'apparition des termes non-diagonaux dans l'hamiltonien. Puisque l'analyse avec la méthode SAR implique le traitement de deux sous-états, il est pratique d'écrire l'hamiltonien en forme matricielle. Dans la base de fonctions d'onde individuelles |0⁺-

$$H_{SAR} = \begin{pmatrix} H_R^{0+} & H_I \\ H_I & H_R^{0-} + E \end{pmatrix} \quad (3.4)$$

ou également :

$$H_{SAR} = \begin{pmatrix} H_{R'} - H_\Delta & H_I \\ H_I & H_{R'} + H_\Delta \end{pmatrix} \quad (3.5)$$

Notons que les deux formes de l'hamiltonien H_{SAR} contiennent la même contribution non-diagonale H_I , représentant les termes d'interaction. H_I peut contenir de un à trois termes $H_{I,mn}$ en fonction du système d'axes réduits ou en fonction d'axes d'interaction :

$$\begin{aligned} H_{I,mn} = & F_{mn}(P_m P_n + P_n P_m) + \frac{1}{2} \{ F_{mn,J} P^2 + \\ & F_{mn,K} P_z^2 + F_{2mn}(P_+^2 + P_-^2) + \dots, P_m P_n + P_n P_m \} \end{aligned} \quad (3.6)$$

avec $mn = ab, ac$ ou bc .

Dans le cas de l'Eq. 3.4, les termes diagonaux H_R^{0+} et H_R^{0-} représentent les hamiltoniens de la rotation pure et E est la différence d'énergie entre les sous-états $0+$ et $0-$. Ainsi, chaque sous-état possède son propre ensemble de paramètres de rotation. Dans la plupart de cas, la différence d'énergie E est relativement faible et par conséquent les valeurs des constantes de rotation des deux sous-états sont très proches. Pour cette raison, il est convenable d'introduire un seul ensemble de paramètres de rotation pour les deux sous-états $H_{R'}$ et des termes de correction H_Δ pour chaque sous-état dans l'Eq. 3.5. L'hamiltonien H_Δ prend la forme suivante :

$$H_\Delta = E^* + E_J P^2 + E_J P_z^2 + E_2 (P_+^2 + P_-^2) + \dots \quad (3.7)$$

où le terme E^* est défini comme $2E^* = E$. Les termes de H_Δ sont symétrisés :

$$H_\Delta^{0+} = -H_\Delta^{0-} \quad (3.8)$$

et dans l'ajustement des données expérimentales seuls les paramètres de l'un des deux sous-états sont variés, les paramètres de l'autre étant fixés pour respecter la condition 3.8. L'utilisation de l'hamiltonien de SAR sous la forme de l'Eq. 3.5 nécessite généralement moins de paramètres à ajuster, ce qui améliore la convergence de la méthode. Un seul ensemble de paramètres de rotation dans l'hamiltonien 3.5 représente un autre avantage, car cela permet une comparaison directe avec les résultats des calculs de chimie quantique.

La partie H_Δ de l'hamiltonien 3.5 est similaire à la partie correspondante de l'hamiltonien du « formalisme du dimère de l'eau » 3.3. Cependant, il ne s'agit pas de la correspondance exacte entre les paramètres en raison des différences dans les systèmes d'axes. De même, on peut établir la similitude (mais pas la correspondance) entre les termes F_{mn} de l'Eq. 3.6 et les angles χ_{pn} , θ_{pn} et ϕ_{pn} dans la fonction de Wigner $D^{(J)}$. Ainsi les angles de rotation entre le système d'axes principaux d'inertie et le système d'axes réduits sont définis par les paramètres F_{mn} . Par exemple [Pickett 1972] :

$$F_{bc} = \frac{1}{2} \sin 2\theta (B_{PAM} - C_{PAM}) \quad (3.9)$$

où θ est l'angle de la rotation autour de l'axe z (représentation I^r) effectuée pour annuler le moment angulaire produit par MVGA. La similitude entre les termes des hamiltoniens des deux modèles peut être également observée via la comparaison des valeurs des paramètres respectifs. Par exemple, le spectre de rotation de l'éthylène glycol a été analysé avec les deux méthodes présentées ci-dessus [Christen *et al.* 1995 ; Christen and Müller 2003]. La comparaison des valeurs des paramètres de Table V dans [Christen

[et al. 1995](#)] et de paramètres de Table 3 dans [[Christen and Müller 2003](#)] indique bien la similitude entre les termes h_{2v} , h_{2j} , h_{2k} , f_2 du « formalisme du dimère de l'eau » et respectivement E^* , E_J , E_J , E_2 de la méthode SAR.

3.3.2 2-hydroxyacétonitrile

Le 2-hydroxyacétonitrile (HOCH_2CN , 2-HAN) est une molécule de 7 atomes que l'on peut former facilement en laboratoire par l'addition du cyanure de l'hydrogène (HCN) sur formaldéhyde (H_2CO) en présence de l'eau. Le 2-HAN présente un intérêt astrophysique car il peut jouer un rôle assez important dans la chimie pré-biotique et peut être à l'origine de la formation de plusieurs molécules organiques simples dans MIS. La possibilité de la formation du 2-HAN dans MIS via la même voie de synthèse que dans les conditions terrestres ($\text{HCN}^+\text{H}_2\text{CO}$ en présence de l'eau) a été évaluée [[Danger et al. 2012](#); [Danger et al. 2014](#)]. D'autres voies de la synthèse de 2-HAN, via le bombardement du cyanure de formyle (HCOCN) par les atomes de H, ou via la réaction des radicaux CN ou OH avec respectivement H_2COH ou CH_2CN sont possibles, mais elles n'ont pas été étudiées dans les conditions du MIS. La photochimie du 2-HAN conduit à la formation de HCOCN , HCN , H_2CCNH , H_2CO , CO , et CO_2 [[Danger et al. 2013](#)]. La plupart de ces composés chimiques, les précurseurs et les produits de décomposition ont été détectés dans le MIS ce qui rend le 2-HAN un candidat intéressant pour les observations astrophysiques.

Comme il a été indiqué ci-dessus, la conformation la plus stable du 2-HAN possède deux configurations équivalentes séparées par une barrière de 425 cm^{-1} . Cela a pour conséquence l'apparition dans le spectre de rotation de dédoublements pour chaque transition. Le spectre du 2-HAN a été enregistré dans une large gamme de fréquence entre 50 et 660 GHz, ce qui m'a permis d'appliquer la technique des diagrammes Loomis-Wood pour l'attribution de transitions ainsi que pour l'analyse de l'interaction entre la rotation de la molécule et le mouvement d'inversion. Un exemple de diagramme Loomis-Wood pour une série de transitions ${}^aR_{0,1} K_a = 0$ est présenté sur la Fig. 14. Le diagramme est centré sur les transitions de l'état 0^+ . Sur le diagramme l'on voit clairement apparaître une série de mêmes transitions (indiquées par les cercles rouges) de l'état 0^- . Ceci permet d'attribuer les transitions sans ambiguïté, surtout dans le cas où les raies de deux sous états se trouvent très proches. Dans le présent cas, le comportement non-linéaire de la série de transitions de l'état 0^- avec le croisement entre les deux séries indique bien une interaction entre les deux sous-états. Typiquement, dans le cas du mouvement de type inversion, l'interaction la plus forte a lieu entre les niveaux d'énergie avec les faibles valeurs du nombre quantique K_a .

A l'étape initiale de l'ajustement des données expérimentales souvent l'on n'a que des

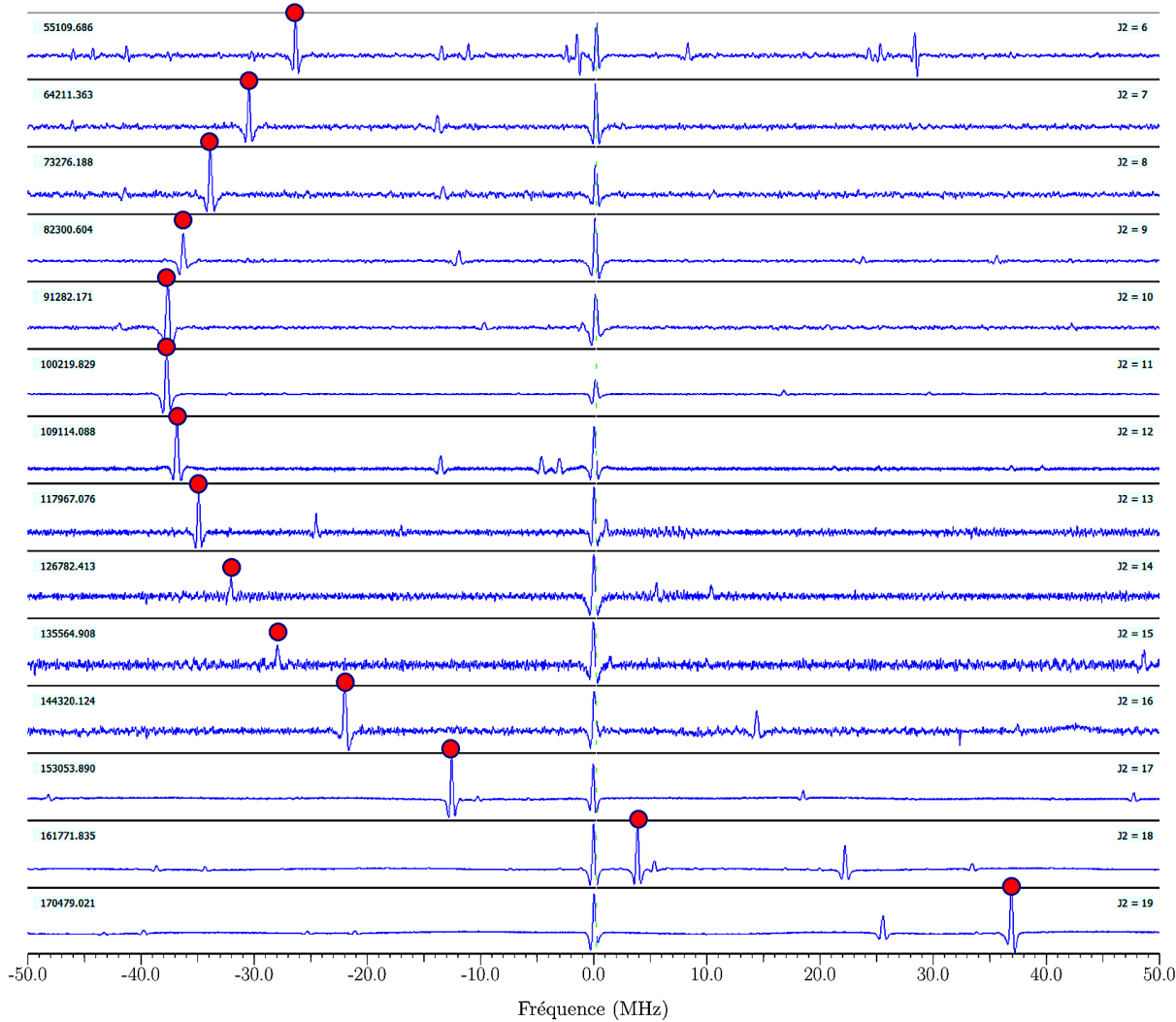


FIGURE 14: Diagramme de Loomis-Wood pour la série de transitions ${}^aR_{0,1} K_a = 0$ et $6 \leq J \leq 19$ du 2-hydroxyacétonitrile. Le diagramme est centré sur les transitions de l'état 0^+ . Les transitions correspondantes de l'état 0^- sont indiquées par les cercles rouges.

transitions entre les niveaux de rotation de même sous-état $0^+ \leftrightarrow 0^+$ et $0^- \leftrightarrow 0^-$, qui ne comportent ainsi aucune information sur la valeur du paramètre E ou E^* correspondant à la séparation entre les deux sous-états. Cependant, les termes d'interaction F_{mn} et la différence d'énergies E dans le modèle de SAR sont très corrélés, d'où la nécessité de fixer l'un de deux paramètres à l'étape initiale. Dans ce cas, j'ai adopté la stratégie suivante pour l'obtention de la solution globale :

1. fixer le paramètre E à plusieurs valeurs différentes
2. laisser varier le paramètre d'interaction
3. chercher la déviation standard minimale en fonction de E

Une fois que le minimum de la déviation standard est trouvé, l'on peut laisser varier également le paramètre E pour affiner sa valeur. Cette stratégie appliquée à l'analyse

du spectre de rotation du 2-HAN m'a permis dans un premier temps de trouver la solution globale avec la valeur approximative de la différence d'énergies E . Par la suite, en se basant sur les prévisions améliorées, il a été possible d'attribuer les transitions de rotation avec les règles de sélection $0^+ \leftrightarrow 0^-$ et de déterminer ainsi avec une très grande précision la valeur de $E = 112672.5526(30)$ MHz. Au final, l'analyse globale du spectre de rotation du 2-HAN a conduit à l'attribution de plus de 5000 raies. Toutes les raies avec les valeurs maximales de $J_{max} = 75$ et $K_{a,max} = 25$ ont été ajustées avec un modèle de SAR comprenant 47 paramètres et avec l'écart type pondéré de 0.93. Le nombre de paramètres du modèle reste toujours raisonnable avec 23.5 paramètres par état ou également plus de 100 raies pour un paramètre déterminé. Ainsi, grâce à l'étude approfondi du spectre de 2-HAN en utilisant le modèle approprié de l'hamiltonien l'on a obtenu des prévisions fiables des raies de rotation de cette molécule dans la gamme de fréquences jusqu'à 1 THz [Margulès et al. 2017]. Le 2-HAN n'a pas été détecté dans la source froide de Sgr B2(N) en se basant sur les observations publiquement disponibles des projets GBT PRIMOS, IRAM 30 m et Herschel HEXOS. En ce qui concerne le 2-HAN dans les sources chaudes, la question reste ouverte et les limites de la densité de colonne ont été établies.

3.3.3 1,3-propanediol

Les propanediols présentent un intérêt astrophysique, en étant les dérivés de l'éthylène-glycol ($\text{CH}_2\text{OHCH}_2\text{OH}$) qui a été détecté dans le nuage moléculaire interstellaire Sgr B2 (N-LMH) [Hollis et al. 2002]. Le 1,3-propanediol $\text{CH}_2\text{OHCH}_2\text{CH}_2\text{OH}$ possède plusieurs conformations stables. Les spectres des deux conformations les plus stables, I et II, manifestent des dédoublement de raies à cause de l'effet tunnel associé avec une rotation (inversion) concertée des deux groupements OH [Plusquellec et al. 2009]. Dans la dernière étude du 1,3-propanediol [Plusquellec et al. 2009], on a appliqué le modèle qui tient compte de la séparation de chaque niveau d'énergie de rotation en deux sous-niveaux 0^+ et 0^- , or l'interaction entre la rotation globale de la molécule et le mouvement d'inversion n'a pas été pris en compte. Cependant, cette interaction a bien lieu entre les niveaux avec les faibles valeurs de K_a , qui sont les plus intéressants de point de vue d'observations astrophysiques.

La Fig. 15 démontre l'importance du choix de modèle correcte de l'hamiltonien dans l'analyse et dans l'extrapolation de prévisions spectrales. Les résultats des études précédentes permettent de trouver une correspondance assez approximative avec le spectre observé comme on peut constater en comparant le spectre théorique sur la Fig.15a avec le spectre expérimental sur la Fig.15b. Le spectre théorique sur la Fig. 15a représente un multiplet composé de deux séries de deux raies intenses avec deux raie de plus faible

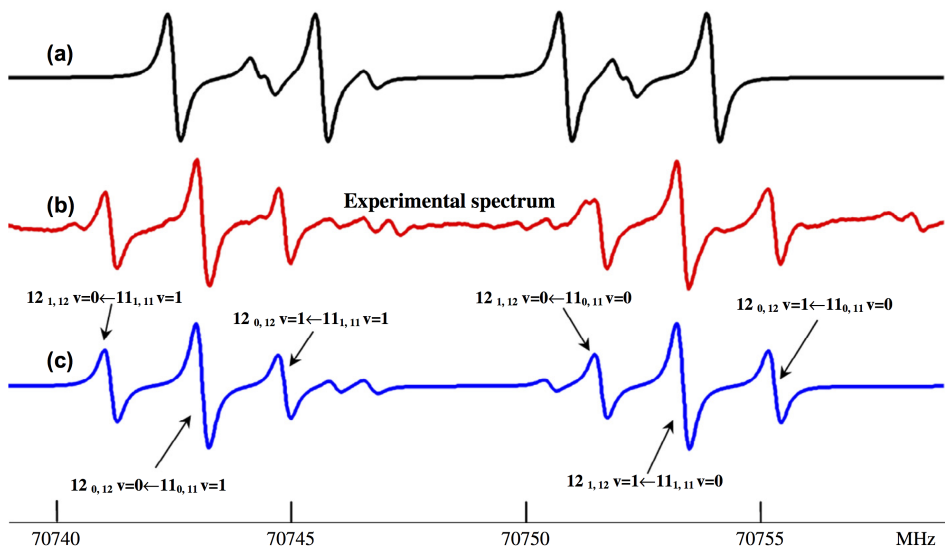


FIGURE 15: Le spectre de 1,3-propanediol autour de 70.7 GHz enregistré en dérivée première du profile d'absorption. (a) Le spectre de la conformation I calculé sur la base de paramètres obtenus dans l'étude précédente [Plusquellec et al. 2009] et qui ne tient pas compte de l'interaction entre la rotation et l'inversion; (b) Le spectre expérimental; (c) Le spectre de a conformation I calculé sur la base de notre étude avec le modèle de SAR.

intensité au milieu. Le spectre expérimental représente un multiplet de forme quelque peu différente. Alors que les décalages dans les positions de raies peuvent s'expliquer par des erreurs d'extrapolation, la répartition des intensités entre les composants du multiplet pose un problème. L'analyse détaillée de la situation a montré que la source du problème est l'interaction entre les deux sous-états 0^+ et 0^- . Dans les études précédentes [Caminati et al. 1995 ; Plusquellec et al. 2009], l'interaction a été négligée et les transitions perturbées ont été exclues des ajustements. Étant donné que le nombre de transitions perturbées dans les ensembles de données des études précédentes était plutôt faible et que la perturbation observée à basse fréquence a une faible influence sur la fréquence de transition, une telle approche semblait plutôt raisonnable. Néanmoins, à des fréquences plus élevées, où des distorsions considérables dans le spectre sont causées par l'interaction, la prise en compte de celle-ci devient obligatoire. La présence d'une telle perturbation conduit non seulement à des changements de fréquence de certaines raies, mais aussi à une redistribution d'intensité entre les transitions et modifie ainsi l'aspect caractéristique des motifs spectraux spécifiques. Comme le montre la Fig.15c, notre modèle de l'hamiltonien de SAR [Smirnov et al. 2013], où nous avons pris en compte l'interaction reproduit très bien le multiplet observé expérimentalement dans Fig.15b. Ici, il convient de noter que le problème a été rencontré pour les transitions de type ${}^aR_{0,1}$ les plus intenses (comme on peut le voir à partir des attributions de transitions données sur la Fig.15c) pour lesquelles une bonne précision d'extrapolation est

habituellement attendue et qui, de façon générale sont utilisées dans la recherche de nouvelles molécules interstellaires.

Par conséquent, ces résultats montrent encore une fois l'importance de l'étude expérimentale approfondie en laboratoire du spectre moléculaire dans une large gamme de fréquences ainsi que l'importance du choix de modèle de l'hamiltonien approprié en amont, avant des recherches radio-astronomiques. Ainsi, dans le cas de molécules manifestant des MVGA, une simple extrapolation de prévision spectrales peut être erronée et doit être utilisée dans les observations astrophysiques avec beaucoup de précaution.

3.4 Publications

1. L. Coudert, L. Margulès, T. Huet, R. Motiyenko, H. Mollendal & J.-C. Guillemin. **The submillimeter-wave spectrum of the doubly deuterated species of methyl formate HCOOCD₂H.** *Astronomy & Astrophysics*, 543, A46, 2012.
2. L. Coudert, B. Drouin, B. Tercero, J. Cernicharo, J.-C. Guillemin, R. A. Motiyenko & L. Margulès. **The First Astrophysical Detection, Terahertz Spectrum, and Database for the Monodeuterated Species of Methyl Formate HCOOCH₂D.** *The Astrophysical Journal*, 779, 119, 2013.
3. L.Margulès, B.McGuire, M.Senent, R.Motiyenko, A.Remijan & J.-C. Guillemin. **Submillimeter spectra of 2-hydroxyacetonitrile (glycolonitrile ; HOCH₂CN) and its searches in GBT PRIMOS observations of Sgr B2 (N).** *Astronomy & Astrophysics*, 601, A50, 2017.
4. I. Smirnov, E. Alekseev, V. Piddyachiy, V. Ilyushin & R. Motiyenko. **1,3-Propanediol millimeter wave spectrum : Conformers I and II.** *J. Mol. Spec.*, 293, 33–37, 2013.

The submillimeter-wave spectrum of the doubly deuterated species of methyl formate HCOOCD₂H*

L. H. Coudert¹, L. Margulès², T. R. Huet², R. A. Motiyenko², H. Møllendal³, and J.-C. Guillemin⁴

¹ LISA, UMR 7583 CNRS – Universités Paris Est Créteil et Paris Diderot, 61 avenue du Général de Gaulle, 94010 Créteil, France
e-mail: laurent.coudert@lisa.u-pec.fr

² Laboratoire de Physique des Lasers, Atomes et Molécules, UMR 8523 CNRS – Université Lille I, Bât. P5,
59655 Villeneuve d’Ascq Cedex, France

³ Centre for Theoretical and Computational Chemistry (CTCC), Department of Chemistry, University of Oslo,
PO Box 1033 Blindern, 0315 Oslo, Norway

⁴ Sciences Chimiques de Rennes, UMR 6226 CNRS – ENSCR, Avenue du Général Leclerc, CS 50837, 35708 Rennes Cedex 7,
France

Received 27 February 2012 / Accepted 17 April 2012

ABSTRACT

Context. Astronomical surveys of interstellar molecules, such as those that will be available with the very sensitive ALMA telescope, require preliminary laboratory investigations of the microwave and submillimeter-wave spectra of new molecular species to identify these in the interstellar media.

Aims. We build a linelist that should allow us to detect HCOOCD₂H, provided it is present in the interstellar media in a suitable concentration.

Methods. The experimental spectra of HCOOCD₂H have been recorded in the microwave and submillimeter-wave energy range. Line frequencies were analyzed using an internal axis method-like treatment taking into account the CD₂H internal rotation.

Results. 5933 lines of HCOOCD₂H have been assigned and their frequencies were reproduced with a unitless standard deviation** of 1.6. A linelist with calculated frequencies and intensities was built and spans the 50–660 GHz spectral region. The frequency accuracy is better than 0.1 MHz.

Conclusions. The pure rotation spectrum of the CD₂H-methyl formate isotopolog (HCOOCD₂H) has been observed in laboratory for the first time.

Key words. methods: data analysis – surveys – catalogs – molecular data – techniques: spectroscopic

1. Introduction

Deuterated molecules are important for studying and understanding the surface chemistry that takes place in interstellar clouds because they provide us with a tool to measure the D/H ratio. For this reason, the abundance of deuterated species have been retrieved for many molecular species. For instance, the mono-deuterated (Saito et al. 2000; Shah & Wootton 2001), bideuterated (Roueff et al. 2000), and triply deuterated (Lis et al. 2002; van der Tak et al. 2002) species for the ammonia molecule have all been detected and their abundance determined. In this context, a linelist for the doubly deuterated species of methyl formate (HCOOCD₂H) is built in this investigation. Because this molecule is non-rigid, it displays a fairly congested spectrum and its transitions should be observed in the extensive line surveys that will be carried out with the ALMA telescope, which will lead to its detection in the interstellar medium (ISM).

Methyl formate (HCOOCH₃) is a non-rigid complex organic molecule of astrophysical relevance (Nummelin et al. 2000; Koyabashi et al. 2007) that displays a rich microwave spectrum

that has been the subject of extensive laboratory studies (Curl Jr 1959; Brown et al. 1975; Bauder 1979; Demaison et al. 1983; Plummer et al. 1984, 1986; Oesterling et al. 1999; Karakawa et al. 2001; Ogata et al. 2004; Carvajal et al. 2007; Ilyushin et al. 2009; Demaison et al. 2010; Tudorie et al. 2011) that led to an accurate determination of its spectroscopic parameters including the height of the potential barrier that hinders the internal rotation of the methyl group.

Many investigations have also been carried out on the rotational spectrum of the isotopic species of methyl formate with a symmetrical CH₃ methyl group. The two ¹³C containing species H¹³COOCH₃ and HCOO¹³CH₃ have been analyzed and detected in the ISM by Carvajal et al. (2009, 2010). The microwave spectrum of the deuterium containing species DCOOCH₃ has also been observed and analyzed and tentatively detected in Orion (Margulès et al. 2010) and in the protostellar IRAS 16293-2422 (Demyk et al. 2010). The two ¹⁸O containing species HC¹⁸OOCCH₃ and HCO¹⁸OCH₃ were also analyzed and detected in the ISM by Tercero et al. (2011).

Fewer investigations, however, have been carried out on the isotopic species with an asymmetrical partially deuterated methyl group. The spectrum of the mono-deuterated species HCOOCH₂D has been recorded and analyzed by Margulès et al. (2009), but this isotopic variant has not yet been detected in the ISM. The microwave spectrum of the doubly deuterated species HCOOCD₂H has not been studied yet.

Experimental and theoretical investigations of the microwave spectrum of HCOOCD₂H are undertaken in this paper

* Tables 3, 6, and 10 are available at the CDS via anonymous ftp to cdsarc.u-strasbg.fr (130.79.128.5) or via

<http://cdsarc.u-strasbg.fr/viz-bin/qcat?J/A+A/543/A46>

** The unitless standard deviation χ is such that $\chi^2 = \sum_{i=1}^N [(F_i^{\text{obs}} - F_i^{\text{cal}})/u_i^{\text{obs}}]^2/(N - P)$ where F_i^{obs} , F_i^{cal} , and u_i^{obs} are observed frequencies, calculated frequencies, and experimental uncertainties, respectively, in MHz; N is the number of lines; and P is the number of varied parameters.

to build a linelist for astrophysical purposes. The microwave spectrum was recorded using Fourier transform, conventional Stark modulation, and submillimeter-wave microwave spectroscopy. Line frequencies were analyzed using the approach developed for the HCOOCH₂D mono-deuterated species (Margulès et al. 2009). The hyperfine structure of 18 transitions was also analyzed to obtain components of the effective quadrupole coupling tensors of the two deuterium atoms. The linelist spans the 50 to 660 GHz region.

2. Experimental

The sample used for the measurements was synthesized as follows: formic acid and sulfuric acid (reagent grade, 95–98%) were purchased from Aldrich, dideuteromethyl alcohol was purchased from Cambridge Isotope Laboratories, Inc. Formic acid (2 g, 43 mmol) and dideuteromethyl alcohol (1.02 g, 30 mmol) were introduced in a one-necked cell equipped with a stirring bar and a stopcock. The solution was cooled around –80 °C and sulfuric acid (0.3 g, 3 mmol) was added. The mixture was then cooled in a liquid nitrogen bath and evacuated in vacuo. The stopcock was closed, the solution was heated up to 40 °C and stirred overnight at this temperature. The cell was then adapted to a vacuum line equipped with two traps and the solution was distilled. High boiling compounds were trapped in the first trap immersed in a bath cooled at –70 °C. Dideuterated methyl formate (1.8 g, 29 mmol) was condensed in the second trap immersed in a liquid nitrogen bath (–196 °C). The yield of the reaction was 97% and should only lead to trace amounts of the other doubly deuterated species DCOOCH₂D. Identification by nuclear magnetic resonance (NMR) spectroscopy of HCOOC₂D yield: ¹H NMR (CDCl₃, 400 MHz) 3.73 (d.quint, ¹H, ⁴J_{HH} = 0.7 Hz, ²J_{HD} = 0.9 Hz, CHD₂); 8.08 (d, ¹H, ⁴J_{HH} = 0.7 Hz, CHO), ¹³C NMR (CDCl₃, 100 MHz) 50.2 (¹J_{CD} = 22.5 Hz (quint)); 161.2 (CHO). Three sets of measurements were carried out with this sample.

Set A was performed using the new molecular beam Fourier transform microwave spectrometer in Lille that spans the 2–20 GHz spectral range (Tudorie et al. 2011). Methyl formate vapors at a pressure of 30 mbar were mixed with neon carrier gas at a backing pressure of 1.3 bar, and a frequency domain signal was obtained just as in Tudorie et al. (2011). With this spectrometer, which allows us to reach a temperature as low as 2 K, each molecular line gives rise to a Doppler doublet. A total of 28 transitions were recorded and we were able to resolve the tunneling splitting due to a tunneling motion in the lowest lying configuration, as described in Sect. 3.2. For 18 lines, the quadrupole coupling hyperfine structure was also resolved. A typical example of the signal associated with the non-tunneling component of the $J_{K_a K_c} = 1_{01} \leftarrow 0_{00}$ rotational transitions is displayed in Fig. 1, where a calculated hyperfine pattern is also shown. The analysis of the hyperfine patterns, described in Sect. 3.4, provided us with useful information about the conformation structures and with 18 accurate center frequencies.

Set B was carried out in the 7–80 GHz region using the Stark-modulated spectrometer of the University of Oslo. Details of the construction and operation of this spectrometer have been given elsewhere (Møllendal et al. 2005, 2006). The spectrum was recorded at room temperature, or at roughly –20 °C, at a pressure of approximately 10 Pa, employing a Stark field strength of about 1100 V/cm. The frequency of 87 individual transitions was measured with an estimated accuracy of 0.1 MHz.

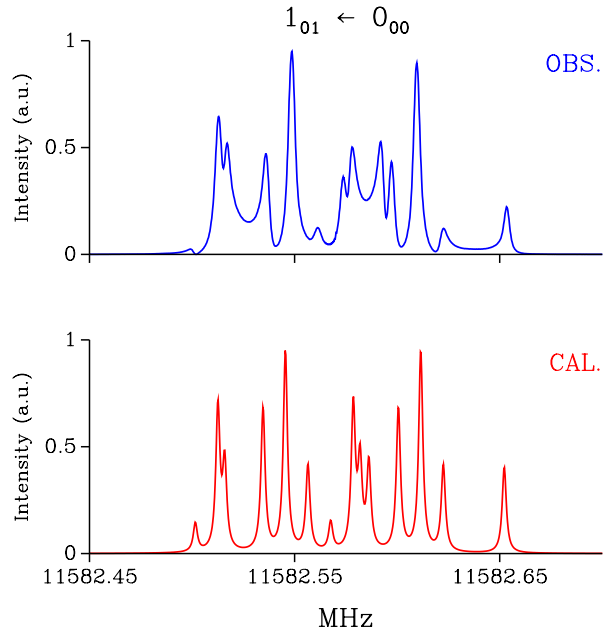


Fig. 1. Non-tunneling component of the $1_{01} \leftarrow 0_{00}$ rotational transition of doubly deuterated methyl formate recorded with the Fourier transform microwave spectrometer of Set A measurements. The quadrupole hyperfine structure associated with the two deuterium atoms can clearly be seen in the observed spectrum displayed in the upper part of the figure. The lower part of the figure shows the calculated spectrum. A Lorentzian lineshape with a half width at half height of 1.2 kHz was assumed for each hyperfine component. The experimental Doppler splitting due to the molecular beam spectrometer was taken to be equal to 66 kHz. The labeling of the transitions is presented in Sect. 3.1 and the hyperfine patterns are analyzed in Sect. 3.4.

The submillimeter-wave measurements of Set C were performed from 150 to 660 GHz using the Lille spectrometer (Motiyenko et al. 2010). In the frequency ranges 150–322 and 400–533 GHz, a solid state frequency multiplication chain was used as source of radiation. The spectra in the 580 to 660 GHz frequency range were recorded using our new fast-scan spectrometer (Alekseev et al. 2012). It is based on an Istok backward wave oscillator (BWO) locked to a harmonic of the Agilent synthesizer E8257D (8–18 GHz). A high-resolution fast frequency scan (up to 100 GHz/h) was obtained by a direct digital synthesizer used as a reference source of BWO's phase locked loop (PLL). As a detector we used an InSb liquid He-cooled bolometer from QMC instruments Ltd. The absorption cell was a stainless steel tube (6 cm diameter, 220 cm long). The sample pressure during measurements was about 2.5 Pa and the linewidth was limited by Doppler broadening. The measurement accuracy for an isolated line is estimated to be better than 30 kHz. However if the lines were blended or with a poor signal-to-noise ratio, an experimental uncertainty of 100 or even 200 kHz was assumed. A typical trace obtained with this experimental setup is shown in Fig. 2.

3. Assignment and analysis of the spectrum

3.1. Theoretical model

The rotation-torsion energy levels of doubly deuterated methyl formate were calculated using the model developed for the mono-deuterated species (Margulès et al. 2009). Owing to

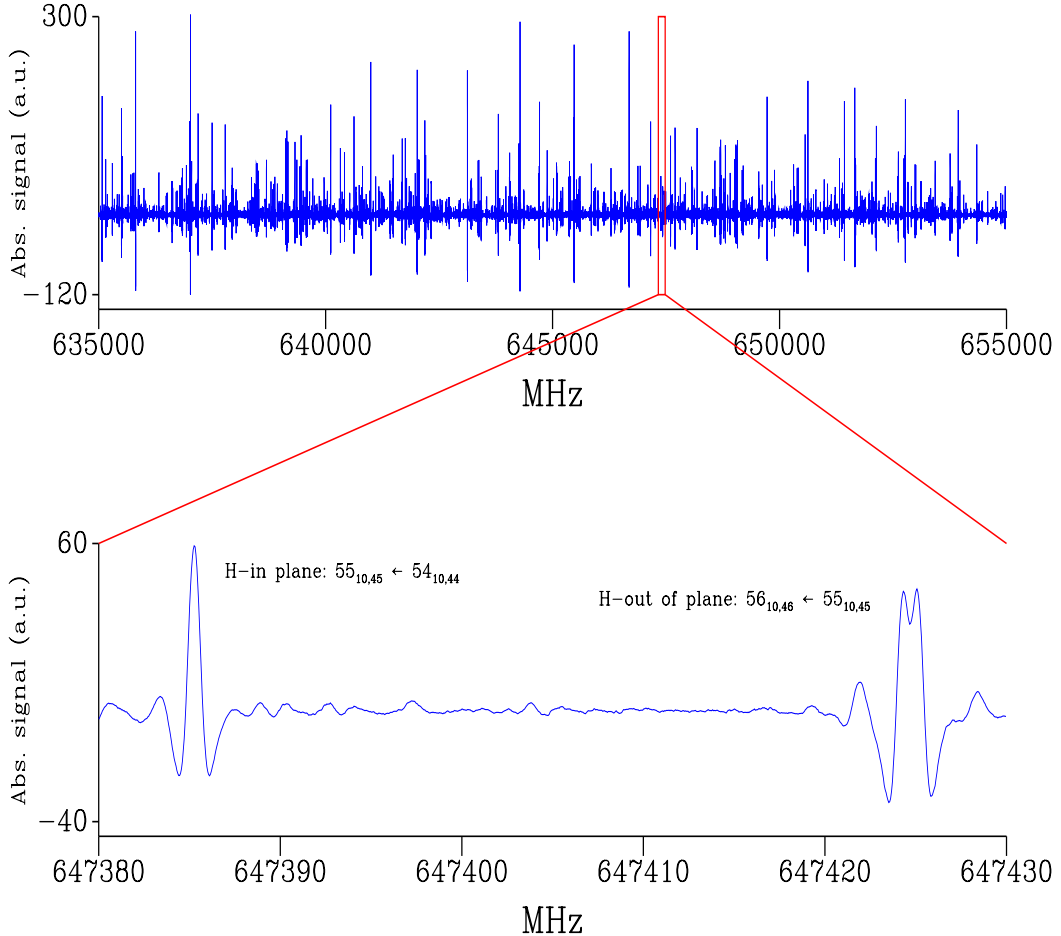


Fig. 2. Two portions of the submillimeter-wave spectrum recorded with the Set C experimental setup are shown. Both traces are the second derivative of the actual spectrum profile due to signal demodulation at $2F$. The x -axis is the frequency in MHz, the y -axis is the absorption signal in arbitrary units. The upper part of the figure shows the portion from 635 to 655 GHz where R -type lines can be seen that are likely candidates for an astrophysical detection. The lower part shows the smaller portion of the spectrum from 647 380 to 647 430 MHz where two transitions are labeled. The tunneling splitting can be seen for the transition corresponding to the H-out-of-plane configurations.

zero-point energy effects, the energy level diagram of HCOOCD₂H is qualitatively different from that of HCOOCH₂D, as shown in Fig. 3. In HCOOCD₂H, the isolated sublevel of A' symmetry has the highest energy. This sublevel corresponds to the so-called H-in-plane configuration such that the only hydrogen atom of the methyl group lies in the molecular symmetry plane. The rotational levels arising from this configuration can be calculated using a Watson-type Hamiltonian. The two close-lying sublevels, of symmetry A' and A'' , below the isolated sublevel, are tunneling sublevels arising from hindered rotation of the methyl group. The torsional motion can connect the two so-called H-out-of-plane configurations with the only hydrogen atom of the methyl group above or below the plane that contains the HCOO atoms. The internal axis method (IAM) approach (Hougen 1985; Coudert & Hougen 1988) developed for the mono-deuterated species (Margulès et al. 2009) allows us to calculate the rotational energies arising from these two configurations because it accounts for the rotational dependence of the tunneling splitting. Rotational levels arising from the H-in-plane configuration are labeled using the usual asymmetric top rotational quantum numbers J , K_a , and K_c . Rotational levels corresponding to the two H-out-of-plane configurations will be labeled using these rotational quantum numbers and the +

or – sign depending on whether the level arises from the lower or upper tunneling sublevel, respectively.

3.2. Transitions assignment

The Set A centimeter-wave spectrum was assigned first. Strong, low J , a -type transitions were identified starting from spectroscopic constants calculated from the structure. Using a bootstrap approach, a preliminary line frequency analysis was carried out and new transitions were predicted and searched for. This procedure was repeated and allowed us to also assign a -type transitions in Sets B and C. When enough of those were available, b -type transitions were also assigned for all measurement sets. For the H-out-of-plane configurations, a few c -type transitions could be assigned. Table 1 gives the number of assigned transitions for configuration along with maximum values of J and K_a .

3.3. Line frequency analysis

The microwave data recorded in our investigation were analyzed calculating the tunneling-rotational energy with the theoretical approach developed for the mono-deuterated species

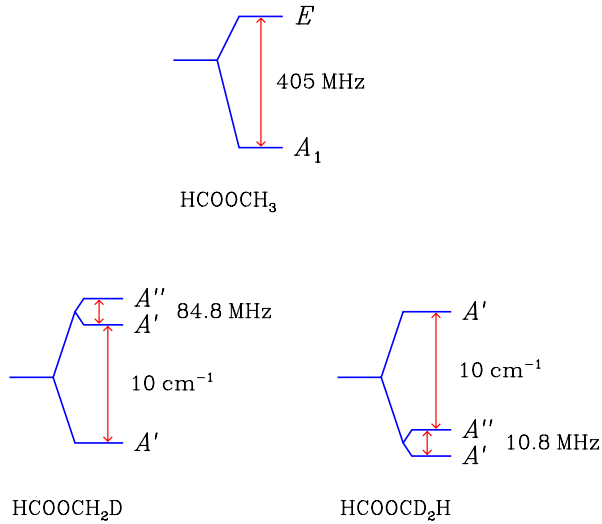


Fig. 3. Torsional energy pattern of HCOOCH_3 , HCOOCH_2D , and HCOOCDOH . The energy pattern consists of two sublevels, 405 MHz apart, for the lighter symmetrical species (Ilyushin et al. 2009) which belong to the A_1 and E symmetry species of C_{3v} . For the mono-deuterated species, three nondegenerate sublevels arise. Two close-lying A' and A'' levels, only 80 MHz apart, can be seen about 10 cm^{-1} above an A' isolated sublevel (Margulès et al. 2009). For the doubly deuterated species, the pair of close-lying levels is about 10 cm^{-1} below the isolated sublevel. For this species, the tunneling splitting is 10.8 MHz as obtained in this work.

Table 1. Number of assigned transitions for the various configurations.

Configuration	N	a -type	b -type	c -type	$J(\text{Max})$	$K_a(\text{Max})$
H-in-plane	2295	1191	1104		0	60
H-out-of-plane	3638	1956	1565		65	60
Both	5933	3147	2669		65	60

(Margulès et al. 2009). Experimental frequencies were introduced in a least-squares fit procedure where they were given a weight equal to the inverse of the square of their experimental uncertainty. Unresolved doublets were treated as follows: assuming that such a doublet corresponds to the two transitions $J'K'_{a1}K''_{c1}, \pm \leftarrow J''K'_{a1}K''_{c1}, \pm$ and $J'K'_{a2}K'_{c2}, \pm \leftarrow J''K''_{a2}K''_{c2}, \pm$ with calculated frequencies F_1 and F_2 , respectively. The doublet was treated in the analysis as a single data point with a calculated frequency equal to $(F_1 + F_2)/2$. In the present data set, usual unresolved K -type doublets arise for all configurations. For the H-out-of-plane configurations, doublets also arise because of unresolved tunneling components. Quartets are also observed and are due to unresolved K -type and tunneling components.

For the 5933 fitted transitions, the root-mean-square (rms) value of the observed minus calculated residual is 0.047 MHz and the unitless standard deviation is 1.6. For the 2295 (3638) transitions corresponding to the H-in-plane configuration (H-out-of-plane configurations) only, the rms value is 0.039 MHz (0.051 MHz). Table 2 lists assignments, observed frequencies, and observed minus calculated differences for the 40 lowest frequency transitions. Table 3, available at the CDS, lists the same quantities for all transitions. These quantities are displayed using 12 columns. Columns 1 to 4 (5 to 8) give the assignment of the upper (lower) level in terms of J , K_a , K_c , and the configuration label. The latter is blank for the H-in-plane configuration and + or - for the H-out-of-plane configurations

(see Sect. 3.1). Column 9 is the observed frequency in MHz with its uncertainty given in parentheses in kHz; Col. 10 is the observed minus calculated residual in kHz; Col. 11 indicates whether the line belongs to a doublet or to a quartet, and Col. 12 describes the measurement set from which the transition was taken using the labeling of Sect. 2. Tables 4 and 5 give the values and the uncertainties of the parameters determined in the analysis for the H-in-plane and H-out-of-plane configurations, respectively.

3.4. Hyperfine structure analysis

The hyperfine splittings observed for several transitions in Set A are caused by quadrupole coupling arising from both deuterium atoms. Numbering these two atoms 2 and 3 as in Margulès et al. (2009), their nuclear momentum will be I_2 and I_3 , respectively. The matrix of the effective quadrupole coupling Hamiltonian, as given in Eq. (1) of Coudert et al. (1989), is set-up using the $|(I_2, I_3)IJFM_F\rangle$ basis set that corresponds to the coupling scheme $\mathbf{I} = \mathbf{I}_2 + \mathbf{I}_3$ and $\mathbf{F} = \mathbf{I} + \mathbf{J}$. Since $I_2 = I_3 = 1$, the quantum number for the total nuclear spin angular momentum I is 0, 1, or 2; and the quantum number for the total angular momentum F takes the five values $J - 2$, $J - 1$, J , $J + 1$, and $J + 2$, for $J \geq 2$. For $J = 1$, F only takes the four values 0, 1, 2, and 3; and for $J = 0$, F only takes the three values 0, 1, and 2. Matrix elements of the effective quadrupole coupling Hamiltonian with this coupling scheme were derived by Robinson & Cornwell (1953). These results show that nine hyperfine levels arise for $J \geq 2$, seven for $J = 1$, and only three for $J = 0$.

The hyperfine patterns were analyzed using a least-squares fit procedure in which the hyperfine energy is computed as outlined in the previous paragraph. For the H-in-plane configuration, the following components of the effective quadrupole coupling tensors were determined:

$$eQq_{xx}^2 = eQq_{xx}^3, \quad eQq_{yy}^2 = eQq_{yy}^3, \quad (1)$$

where superscripts 2 and 3 identify the two deuterium atoms. For the H-out-of-plane configurations, only the following linear combinations of effective quadrupole coupling tensor components could be determined because of the tunneling averaging:

$$(eQq_{xx}^2 + eQq_{xx}^3)/2, \quad (eQq_{yy}^2 + eQq_{yy}^3)/2, \quad (2)$$

where superscripts 2 and 3 have the same meaning as in Eq. (1). Table 6, available at the CDS and displaying 12 columns, gives the transition assignment (Cols. 1 to 8), the center frequency (Col. 9), its uncertainty in kHz (Col. 10), the number of hyperfine components (Col. 11), and the rms deviation (Col. 12) for the fitted hyperfine patterns. The center frequencies can also be found in Table 2. Fitted components of the effective quadrupole coupling tensors are listed in Table 7 where they are compared to values obtained through ab initio calculations (Demaison 2009, priv. comm.; Demaison et al. 2010).

4. Intensity calculation

Line strengths were calculated using the values for the dipole moment components listed in Table 8, retrieved from those of the normal species. The values reported for the latter species by Curl Jr (1959) were $\mu_a = 1.63$, $\mu_b = 0.68$, and $\mu_{\text{tot}} = 1.77$ D, without quoted uncertainties. Measurements carried out recently by Margulès et al. (2010) led to the more accurate values $\mu_a = 1.648(8)$, $\mu_b = 0.706(12)$, and $\mu_{\text{tot}} = 1.793(11)$ D. The partition

Table 2. Assignments, observed frequencies, and observed minus calculated differences in the microwave spectrum of HCOOC₂H.

J'	K'_a	K'_c	\pm	J''	K''_a	K''_c	\pm	Obs ^a	Diff ^c	Set ^d	J'	K'_a	K'_c	\pm	J''	K''_a	K''_c	\pm	Obs ^a	Diff ^c	Set ^d
2	1	1	+	2	1	2	+	4130.528(30)	-3	A	4	1	3	-	4	1	4	-	13 728.493(2) ^b	3	A
6	2	4	+	6	2	5	+	6861.507(30)	8	A	4	1	3	+	4	1	4	+	13 729.199(2) ^b	12	A
3	1	2	-	3	1	3	-	8254.912(30)	0	A	2	1	1	2	0	2	0	2	13 884.674(1) ^b	1	A
3	1	2	+	3	1	3	+	8255.339(30)	5	A	18	5	13	18	5	14	14 882.480(150)-171	B			
2	0	2	+	1	1	1	+	9959.041(1) ^b	-1	A	4	1	3	4	1	4	14 922.583(1) ^b	-1	A		
2	0	2	-	1	1	1	-	9959.310(1) ^b	1	A	2	1	1	-	2	0	2	-	15 084.586(1) ^b	0	A
1	0	1	-	0	0	0	-	11 145.210(1) ^b	10	A	2	1	1	+	2	0	2	+	15 085.130(1) ^b	6	A
1	0	1	+	0	0	0	+	11 145.267(1) ^b	-1	A	34	9	25	34	9	26	15 319.840(150)-331	B			
7	1	7	+	6	2	4	+	11 401.310(30)	-31	A	22	6	16	22	6	17	15 589.120(150)-107	B			
7	1	7	-	6	2	4	-	11 403.493(30)	-4	A	26	7	19	26	7	20	15 840.000(150)	3	B		
7	2	5	-	7	2	6	-	11 514.713(30)	7	A	3	1	2	3	0	3	16 611.700(1) ^b	-2	A		
7	2	5	+	7	2	6	+	11 515.400(30)	15	A	3	1	2	-	3	0	3	-	17 513.025(3) ^b	0	A
1	0	1	0	0	0	0	0	11 582.571(1) ^b	-1	A	3	1	2	+	3	0	3	+	17 513.691(3) ^b	7	A
1	1	0	1	0	1	1	1	12 239.931(1) ^b	-6	A	11	3	8	11	3	9	18 090.260(150)	22	B		
2	0	2	1	1	1	1	1	12 277.561(1) ^b	-4	A	15	4	11	15	4	12	20 664.460(150)-294	B			
4	1	3	+	3	2	2	+	12 425.644(30)	2	A	4	1	3	4	0	4	20 672.400(150)	127	B		
4	1	3	-	3	2	2	-	12 426.284(30)	3	A	2	1	2	1	1	1	21 666.090(150)-367	B			
1	1	0	-	1	0	1	-	13 597.872(1) ^b	-9	A	19	5	14	19	5	15	22 323.440(150)	328	B		
1	1	0	+	1	0	1	+	13 598.344(1) ^b	-4	A	2	0	2	1	0	1	23 018.640(150)-240	B			
14	4	10	14	4	11	13	609.710(150)	-47	B	23	6	17	23	6	18	23 236.730(150)-219	B				

Notes. Transitions are assigned with the usual rotational quantum numbers of the upper and lower levels. For transitions within the H-out-of-plane configurations, the + or - signs identify tunneling sublevels. Only the 40 lowest frequency transitions appear in this table. ^(a) Obs is the observed frequency in MHz. The uncertainty is given in parentheses in kHz. ^(b) Obtained in the hyperfine structure analysis of Sect. 3.4. ^(c) Diff is the observed minus calculated difference in kHz. ^(d) The measurement set as defined in Sect. 2 is given.

Table 4. Spectroscopic parameters for the H-in-plane configuration.

Parameter	Value	Parameter	Value
A	17 281.949 265(420)	$H_{KJJ} \times 10^9$	-210.249(540)
B	6540.604 314(110)	$H_{JJJ} \times 10^9$	2.332(19)
C	5041.990 952(120)	$h_{KK} \times 10^9$	-601.454(3897)
		$h_{KJ} \times 10^9$	330.458(839)
$\Delta_{KK} \times 10^3$	41.404 648(2200)	$h_{JJ} \times 10^9$	1.322(7)
$\Delta_{KJ} \times 10^3$	-7.932 466(660)		
$\Delta_{JJ} \times 10^3$	5.806 476(90)	$L_{KKKK} \times 10^{12}$	-14.173(2998)
$\delta_K \times 10^3$	-5.786 705(1000)	$L_{KKKJ} \times 10^{12}$	4.787(720)
$\delta_J \times 10^3$	1.787 297(26)	$L_{KJJJ} \times 10^{12}$	-4.897(72)
		$l_{KKJ} \times 10^{12}$	4.777(839)
$H_{KKK} \times 10^9$	123.268(4797)	$l_{KJJ} \times 10^{12}$	7.766(162)
$H_{KKJ} \times 10^9$	611.220(1469)		

Notes. Parameters are in MHz. Numbers in parentheses are one standard deviation in the same units as the last digit. These parameters are involved in the pure rotational Hamiltonian in the second of Eqs. (10) of Margulès et al. (2009).

function Q_{rot} was computed for several temperatures taking a degeneracy factors equal to $(2J+1)$. The energy of the $0_{00}, +$ level corresponding to the H-out-of-plane configurations was taken to be equal to zero, that of the 0_{00} level of the H-in-plane configuration was set to 10 cm^{-1} as in Sect. 3.1. Table 9 gives the values thus obtained for the partition functions.

The linelist was built calculating the frequencies of the allowed transitions characterized by a lower and an upper rotational quantum number J smaller than 60. Integrated intensities were calculated in $\text{nm}^2 \text{ MHz}$ units at 300 K using the results given in Tables 8 and 9. Just as in the JPL (Pickett et al. 1998) data bases, the selected transitions are those with an intensity in $\text{nm}^2 \text{ MHz}$ units at 300 K larger than

$$10^{\text{LOGSTR0}} + (F/300\,000)^2 \times 10^{\text{LOGSTR1}}, \quad (3)$$

Table 5. Spectroscopic parameters for the H-out-of-plane configurations.

Parameter	Value	Parameter	Value
θ_2	6.655 648(2600)	$H_{KKK} \times 10^9$	1195.553(5096)
ϕ_2	81.578 313(5700)	$H_{KKJ} \times 10^9$	-461.461(1289)
		$H_{KJJ} \times 10^9$	-34.508(420)
h_2	-5.394 756(8600)	$H_{JJJ} \times 10^9$	-1.833(54)
$h_{2k} \times 10^6$	2914.209(47967)	$h_{KK} \times 10^9$	357.691(5396)
$h_{2j} \times 10^6$	-1184.396(10193)	$h_{KJ} \times 10^9$	101.726(510)
$f_2 \times 10^6$	-213.732(4497)	$h_{JJ} \times 10^9$	-0.878(5)
A	18 482.353 793(330)	$L_{KKKK} \times 10^{12}$	-114.585(14390)
B	6261.052 643(100)	$L_{KKKJ} \times 10^{12}$	159.564(21585)
C	4884.201 398(110)	$L_{KKJJ} \times 10^{12}$	-55.071(7495)
		$L_{KJJJ} \times 10^{12}$	-5.095(48)
$\Delta_{KK} \times 10^3$	57.573 479(2000)	$L_{JJJJ} \times 10^{12}$	-0.058(8)
$\Delta_{KJ} \times 10^3$	-13.498 154(360)	$l_{KKK} \times 10^{12}$	-308.607(59958)
$\Delta_{JJ} \times 10^3$	5.036 334(120)		
$\delta_K \times 10^3$	1.622 568(630)		
$\delta_J \times 10^3$	1.540 159(21)		

Notes. Parameters are in MHz except for θ_2 and ϕ_2 , which are in degrees. Numbers in parentheses are one standard deviation in the same units as the last digit. Parameters are defined in Eqs. (12), (13), and (22) of Margulès et al. (2009) or are involved in the pure rotational Hamiltonian in the first of Eqs. (10) of the same reference.

where F is the frequency in MHz, and LOGSTR0 and LOGSTR1 are two dimensionless constants set to -9 and -7, respectively. The uncertainty on the calculated frequency was retrieved from the analysis results.

The linelist is given in Table 10, available at the CDS. It is formatted in the same way as the catalog line files of the JPL data base (Pickett et al. 1998) and has 16 columns. The first, second, and third columns contain the line frequency (FREQ) in MHz, the error (ERR) in MHz, and the base 10 logarithm of the line

Table 7. Effective quadrupole coupling tensors components in MHz.

Component	Value ^a	Ab initio ^b
$eQq_{xx}^2 = eQq_{xx}^3$	-0.0087(14)	-0.0071
$eQq_{yy}^2 = eQq_{yy}^3$	0.0819(17)	0.0935
$(eQq_{xx}^2 + eQq_{yy}^2)/2$	-0.0311(10)	-0.0305
$(eQq_{xx}^3 + eQq_{yy}^3)/2$	0.0063(14)	-0.0106

Notes. Superscripts 2 and 3 identify the deuterium atoms. The two first (last) lines correspond to the H-in-plane configuration (H-out-of-plane configurations). ^(a) Fitted values obtained in Sect. 3.4 are reported. Numbers in parentheses are one standard deviation in the same units as the last digit. ^(b) From Demaison (2009, priv. comm.), Demaison et al. (2010).

Table 8. Numerical values, in Debye, used for the dipole moment components matrix elements in the line intensity calculation.

Configuration	μ_x	μ_y	μ_z
H-in-plane	0.792	0.0	1.608
H-out-of-plane	0.763	0.011	1.622

Notes. Dipole moment components were retrieved from those of the normal species (Margulès et al. 2010).

Table 9. Partition function Q_{rot} of HCOOCD₂H for several values of the temperature T in Kelvin.

T/K	Q_{rot}	T/K	Q_{rot}
9.375	455	150.000	37 839
18.750	1424	225.000	69 294
37.500	4372	300.000	104 036
75.000	13 020		

Notes. The energy of the $J = 0, A'$ sublevel of the H-out-of-plane configurations was taken to be equal to zero; that of the $J = 0, A'$ level of the H-in-plane configuration was taken to be equal to 10 cm^{-1} (see Fig. 3).

intensity (LGINT) in nm² MHz at 300 K. The fourth, fifth, and sixth columns give the degrees of freedom of the rotational partition function (DR), the lower state energy (ELO) in cm⁻¹, and the upper state degeneracy (GUP), respectively. The seventh and eighth columns contain the species tag (TAG) and format number (QNFMFT), respectively. Finally, Cols. 9 to 12 (13 to 16) give the assignment of the upper (lower) level in terms of J , K_a , K_c , and the configuration label. The latter is 0 or 1 for the + and - levels of the H-out-of-plane configurations and 2 for the H-in-plane configuration. When the calculated error (ERR) was smaller than 10 kHz, it was set to that value. For observed unblended microwave lines, the line frequency (FREQ) and the error (ERR) were replaced by their experimental values. This is then indicated by a negative species tag (TAG).

5. Conclusion

The pure rotation spectrum of HCOOCD₂H was observed in laboratory up to 660 GHz. Almost six thousand lines were

assigned to the H-in-plane and H-out-of-plane configurations. The large amplitude torsional motion of the partially deuterated CD₂H methyl group was accounted for in the energy level calculation. The spectroscopic constants given in Tables 4 and 5 were determined and allowed us to reproduce the observed frequencies with an accuracy better than 100 kHz. The linelist built using the results of this analysis should allow the detection of HCOOCD₂H, provided it is present in the ISM in a suitable concentration.

Acknowledgements. This work was supported by the French program Action sur Projets de l'INSU "Physique et Chimie du Milieu Interstellaire" and by the contracts ANR-08-BLAN-0054 and ANR-08-BLAN-0225.

References

- Alekseev, E. A., Motiyenko, R. A., & Margulès, L. 2012, Radio Phys. Radio Astron., 3, 75
- Bauder, A. 1979, J. Phys. Chem. Ref. Data, 8, 583
- Brown, R. D., Crofts, J. G., Gardner, F. F., et al. 1975, ApJ, 197, L29
- Carvajal, M., Willaert, F., Demaison, J., & Kleiner, I. 2007, J. Mol. Spectrosc., 246, 158
- Carvajal, M., Margulès, L., Tercero, B., et al. 2009, A&A, 500, 1109
- Carvajal, M., Kleiner, I., & Demaison, J. 2010, ApJS, 190, 315
- Coudert, L. H., & Hougen, J. T. 1988, J. Mol. Spectrosc., 130, 86
- Coudert, L. H., Hougen, J. T., & Suenram, R. D. 1989, J. Mol. Spectrosc., 135, 314
- Curl, Jr, R. F. 1959, J. Chem. Phys., 30, 1529
- Demaison, J., Boucher, D., Dubrulle, A., & van Ejck, B. P. 1983, J. Mol. Spectrosc., 102, 260
- Demaison, J., Margulès, L., Kleiner, I., & Császár, A. G. 2010, J. Mol. Spectrosc., 259, 70
- Demyk, K., Bottinelli, S., Caux, E., et al. 2010, A&A, 517, A17
- Hougen, J. T. 1985, J. Mol. Spectrosc., 114, 395
- Ilyushin, V., Kryvda, A., & Alekseev, E. 2009, J. Mol. Spectrosc., 255, 32
- Karakawa, Y., Oka, K., Odashima, H., Takagi, K., & Tsunekawa, S. 2001, J. Mol. Spectrosc., 210, 196
- Koyabashi, K., Ogata, K., Tsunekawa, S., & Takano, S. 2007, ApJ, 657, L17
- Lis, D. C., Roueff, E., Gerin, M., et al. 2002, ApJ, 571, L55
- Margulès, L., Coudert, L. H., Möllendal, H., et al. 2009, J. Mol. Spectrosc., 254, 55
- Margulès, L., Huet, T. R., Demaison, J., et al. 2010, ApJ, 714, 1120
- Möllendal, H., Leonov, A., & de Meijere, A. 2005, J. Phys. Chem. A, 109, 6344
- Möllendal, H., Cole, G. C., & Guillemin, J.-C. 2006, J. Phys. Chem. A, 109, 921
- Motiyenko, R. A., Margulès, L., Alekseev, E. A., Guillemin, J.-C., & Demaison, J. 2010, J. Mol. Spectrosc., 264, 94
- Nummelin, A., Bergman, P., Hjalmarson, A., et al. 2000, ApJS, 128, 213
- Oesterling, L. C., Albert, S., De Lucia, F. C., Sastry, K. V. L. N., & Herbst, E. 1999, ApJ, 521, 255
- Ogata, K., Odashima, H., Takagi, K., & Tsunekawa, S. 2004, J. Mol. Spectrosc., 225, 14
- Pickett, H. M., Poynter, R. L., Cohen, E. A., et al. 1998, J. Quant. Spectrosc. Radiat. Transf., 60, 883
- Plummer, G. M., Herbst, E., De Lucia, F. C., & Blake, G. A. 1984, ApJS, 55, 633
- Plummer, G. M., Herbst, E., De Lucia, F. C., & Blake, G. A. 1986, ApJS, 60, 949
- Robinson, G. W., & Cornwell, C. D. 1953, J. Chem. Phys., 21, 1436
- Roueff, E., Tiné, S., Coudert, L. H., et al. 2000, A&A, 354, L63
- Saito, S., Ozeki, H., Ohishi, M., & Yamamoto, S. 2000, ApJ, 535, 227
- Shah, R. Y., & Wootten, A. 2001, ApJ, 554, 933
- Tercero, B., Margulès, L., Carvajal, M., et al. 2011, A&A, 538, A119
- Tudorie, M., Coudert, L. H., Huet, T. R., Jegouso, D., & Sedes, G. 2011, J. Chem. Phys., 134, 074314
- van der Tak, F. F. S., Schilke, P., Müller, H. S. P., et al. 2002, A&A, 388, L53

THE FIRST ASTROPHYSICAL DETECTION, TERAHERTZ SPECTRUM, AND DATABASE FOR THE MONODEUTERATED SPECIES OF METHYL FORMATE HCOOCH₂D

L. H. COUDERT¹, B. J. DROUIN², B. TERCERO³, J. CERNICHARO³, J.-C. GUILLEMIN⁴, R. A. MOTIYENKO⁵, AND L. MARGULÈS⁵

¹ LISA, UMR 7583 CNRS-Universités Paris Est Créteil et Paris Diderot, 61 Avenue du Général de Gaulle, F-94010 Créteil, France; laurent.coudert@lisa.u-pec.fr

² Jet Propulsion Laboratory, California Institute of Technology, Pasadena, CA 91109, USA

³ Centro de Astrobiología (CSIC-INTA), Laboratory of Molecular Astrophysics, Department of Astrophysics,

Ctra de Ajalvir, Km 4, E-28850 Torrejón de Ardoz, Madrid, Spain

⁴ Institut des Sciences Chimiques de Rennes, UMR 6226 CNRS-ENSCR, 11 Allée de Beaulieu, CS 50837, F-35708 Rennes Cedex 7, France

⁵ Laboratoire de Physique des Lasers, Atomes et Molécules, UMR 8523 CNRS-Université Lille I, Bât. P5, F-59655 Villeneuve d'Ascq Cedex, France

Received 2013 July 10; accepted 2013 October 13; published 2013 December 2

ABSTRACT

Based on new measurements carried out in the laboratory from 0.77 to 1.2 THz and on a line-frequency analysis of these new data, along with previously published data, we build a line list for HCOOCH₂D that leads to its first detection in the Orion KL nebula. The observed lines, both in space and in the laboratory, involve the *cis* D-in-plane and *trans* D-out-of-plane conformations of HCOOCH₂D and the two tunneling states arising from the large-amplitude motion connecting the two *trans* configurations. The model used in the line position calculation accounts for both *cis* and *trans* conformations, as well as the large-amplitude motion.

Key words: astronomical databases: miscellaneous – ISM: individual objects (Orion KL) – ISM: molecules – line: identification – methods: data analysis – methods: laboratory: molecular – submillimeter: ISM

Online-only material: color figures, machine-readable tables

1. INTRODUCTION

Methyl formate (HCOOCH₃) is a non-rigid complex organic molecule of astrophysical relevance displaying a rich microwave spectrum that has been the subject of extensive laboratory studies (Curl 1959; Brown et al. 1975; Bauder 1979; Demaison et al. 1983; Plummer et al. 1984, 1986; Oesterling et al. 1999; Karakawa et al. 2001; Ogata et al. 2004; Carvajal et al. 2007; Ilyushin et al. 2009; Demaison et al. 2010; Tudor et al. 2011). The normal species of methyl formate was first detected as early as 1975 by Brown et al. (1975) in Sgr B2. It was later detected in the hot cores of giant molecular clouds, in star-forming regions, and in comets (Blake et al. 1986; Nummelin et al. 2000; Kobayashi et al. 2007; Demyk et al. 2008). Due to the importance of deuterium fractionation (Herbst 1992), detections of its monodeuterated isotopic variants have also been attempted. The monodeuterated species DCOOCH₃, with a deuterated carbonyl group, has been tentatively detected in Orion (Margulès et al. 2010) and in the protostar IRAS 16293-2422 (Demyk et al. 2010). However, no attempt has been made to detect the monodeuterated species HCOOCH₂D, with a deuterated methyl group, although its microwave spectrum has already been investigated (Margulès et al. 2009a).

In this paper, following the strategy of our previous papers devoted to methyl formate (Carvajal et al. 2009; Margulès et al. 2010; Tercero et al. 2012), we report the first detection of the monodeuterated species HCOOCH₂D in space by means of 66 unblended lines found in the Orion KL nebula's line survey performed with the IRAM 30 m telescope (Tercero et al. 2010, 2011). In this paper, we also build an astrophysical database for this isotopic species that is computed using the results of a line-frequency analysis of new terahertz transitions, recorded in the present investigation in the 0.77–1.2 THz region, along with previously published submillimeter-wave transitions (Margulès et al. 2009a). The database is formatted like the catalog line files of the Jet Propulsion Laboratory (JPL) and, thanks to the extended frequency range of the new dataset, spans the 50 GHz to 1.2 THz region.

2. DATASETS AND LINE ASSIGNMENTS

The laboratory spectra measured in this work were recorded using the Frequency Multiplied Submillimeter Spectrometer (FMSS; Drouin et al. 2005) at JPL. The FMSS was scanned through the 0.77–0.85 THz and 0.95–1.2 THz ranges with three separate multiplier chains. The sample of deuterated methyl formate, previously used by Margulès et al. (2009a), was shipped to JPL and transferred into a sealed 10 cm diameter, 3 m length quartz tube for scans at pressures of 30 mTorr, except for the last scan, from 0.95 to 1.06 THz, which was scanned with a lower pressure of 8 mTorr due to a limited amount of sample. Spectra were recorded with a fine step size of 108–144 kHz and detected in direct absorption using a Schottky diode detector built by Virginia Diodes (WR1.2 ZBD). The voltage rectified at the diode detector was amplified immediately with an Analog Modules pre-amplifier (321A-2-4.7-NI) with a 1.4 kΩ input impedance. Following the pre-amplification, the frequency-modulated source signal was demodulated at twice the modulation rate for a second harmonic detection of the absorption with reduced background fluctuations. Nearly identical conditions were utilized for similar isotopic scans of ¹³C substituted methyl formate and the other deuterated form of methyl formate (DCOOCH₃). The raw spectra are archived at JPL and are available upon request to the authors.

The center frequencies of the isolated and blended features were measured from the raw spectra such as the single spectrum shown in Figure 1, which shows a portion of the spectrum recorded at JPL in the 840000–840400 MHz frequency range. The highest frequency sweep, from 1.06 to 1.20 THz, is shown in Figure 2. That the large features are cut off of the intensity scale is due to partially and fully deuterated water, which appears as an impurity in all scans. The source power, as well as atmospheric absorption near 1.10, 1.11, 1.53, and 1.63 THz, produce the broad variations in the signal across the band, which has roughly equal intensity strong lines in every 1 GHz segment. The line density decreases with increasing frequency, with 20 lines GHz⁻¹ detected in

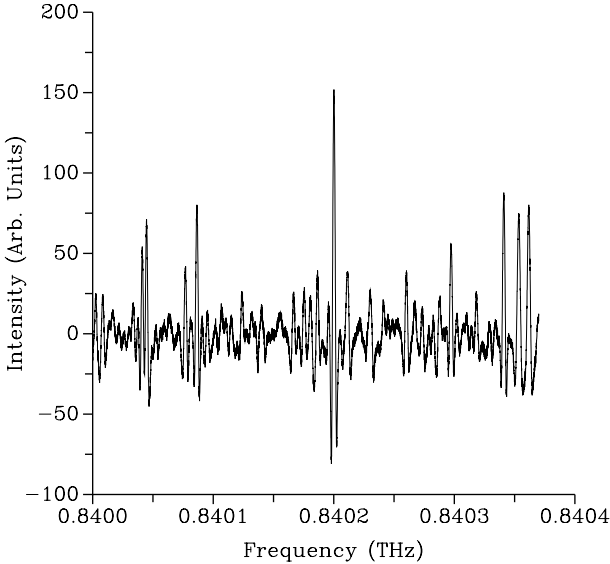


Figure 1. Portion of the spectrum recorded using the JPL experimental setup. The experimental line at 0.8402 THz is a singlet line belonging to the D-in-plane conformation. The two experimental lines at 0.84035 and 0.84036 THz belong to CH₂DOH.

this (highest frequency) sweep. However, the asymmetric-top patterns are all intermixed with only the mid- K ranges of b -type branches readily detected. With little pattern recognition available, the broadband coverage and the slowly varying source power enable confident assignments and permit some ability to judge the character of potentially blended features. Assigned lines were given a 100 kHz uncertainty. Strong isolated lines are significantly more accurate, but the spectrum is dominated by overlapping lines.

The HCOOCH₂D species of methyl formate displays two conformations that are a few cm⁻¹ apart. The lower lying one

Table 1
Number of Assigned Transitions^a for Each Conformation and for Each Dataset

Dataset	D-in-plane	D-out-of-plane	Both Conformations
Margulès et al. (2009a)	433	739	1172
This work	765	885	1650
All	1198	1624	2822

Note. ^a The number of lines assigned in the experimental spectra is given. The actual number of lines is larger as both datasets include unresolved multiplets.

corresponds to the D-in-plane configuration and the upper lying one corresponds to the two energetically equivalent D-out-of-plane configurations (Coudert et al. 2012, Figure 3). Both conformations give rise to a - and b -type transitions. Due to the internal rotation motion taking place for the D-out-of-plane conformation, transitions within this conformation are split into two tunneling components and weak c -type transitions between the two tunneling sublevels can also be observed (Margulès et al. 2009a).

The assignment of the transitions measured at JPL was initiated using predictions based on the results of Margulès et al. (2009a) and strong a -type transitions could be identified. Using a bootstrap approach, a preliminary line frequency analysis was carried out and new transitions were predicted and searched for. This procedure was repeated and allowed us to also assign all a -type transitions. Afterward, b -type transitions were then assigned for both conformations. The total number of assigned experimental lines is 2822 and corresponds to 5279 transitions as many lines are unresolved multiplets depending on whether the K -type and/or the tunneling splittings were resolved. Table 1 gives the number of assigned lines for each conformation. In the present dataset, the maximum J - and K_a -values are 84 and 41, respectively. The assigned lines include 1466, 1321, and 28 a -, b -, and c -type transitions, respectively. About seven rotation-tunneling transitions with $\Delta K_a = \Delta K_c = 0$, which are allowed by symmetry, were also measured.

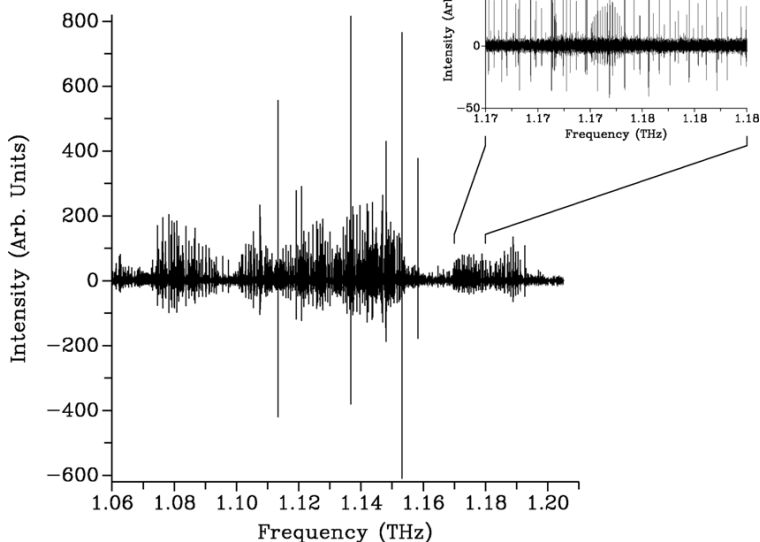


Figure 2. Spectrum recorded between 1.06 and 1.20 THz; the inset shows detail including an unidentified band that is likely to belong to an excited vibrational state of deuterated methyl formate.

Table 2
Assignments^a, Observed Frequencies^b, and Observed Minus Calculated Differences^c in the Microwave Spectrum^d of HCOOCH₂D

J'	K'_a	K'_c	\pm	J''	K''_a	K''_c	\pm	Obs.	Diff.	Multiplet	Ref.
24	18	6		23	17	7		770424.549(100)	-1	<i>D</i>	This work
34	14	20		33	13	21		770446.590(100)	37	<i>D</i>	This work
63	16	48	+	62	16	47	+	770452.291(100)	8	<i>D</i>	This work
76	1	75		75	1	74		770621.252(100)	12	<i>Q</i>	This work
30	17	13	+	29	16	14	+	770922.224(100)	20	<i>Q</i>	This work
66	16	50		65	16	49		771016.995(100)	2		This work
29	16	13		28	15	14		771059.780(100)	22	<i>D</i>	This work
64	13	51		63	13	50		771122.780(100)	-125		This work
67	23	44		66	23	43		771199.377(100)	-331	<i>D</i>	This work
72	3	69	+	71	3	68	+	771287.711(100)	-40	<i>Q</i>	This work

Notes.

^a Transitions are assigned with the usual rotational quantum numbers of the upper and lower levels. For transitions of the D-out-of-plane conformation, the + or - signs identify tunneling sublevels. Only the 10 lowest frequency transitions measured in this work appear.

^b Observed frequency in MHz is given in the column titled “Obs.” Experimental uncertainties are given in parentheses in kHz.

^c Observed minus calculated residuals in kHz are given in the column titled “Diff.”

^d A blank space or the letters *D*, *T*, or *Q*, in the column titled “Multiplet” indicate that the line is a singlet, a doublet, a triplet, or a quadruplet, respectively. The reference to which the line belongs to is given in the column titled “Ref.”

(This table is available in its entirety in a machine-readable form in the online journal. A portion is shown here for guidance regarding its form and content.)

3. LINE-FREQUENCY ANALYSIS

The microwave data were analyzed calculating the tunneling-rotational energy with the theoretical approach accounting for the large-amplitude torsional motion proposed by Margulès et al. (2009a). Experimental frequencies were introduced in a least-squares fit procedure where they were given a weight equal to the inverse of the square of their experimental uncertainty. Unresolved multiplets were treated taking for their calculated frequency the average of the calculated frequency of all members of the multiplet.

For the 2822 fitted lines, the root mean square (rms) value of the observed minus calculated residual is 0.16 MHz and the unitless standard deviation is 1.6. For the 1198 (1624) transitions corresponding to the D-in-plane (D-out-of-plane) conformation, the rms value is 0.112 MHz (0.191 MHz). Table 2 lists assignments, observed frequencies, and observed minus calculated differences. Tables 3 and 4 give the values and the uncertainties of the parameters determined in the analysis for the D-in-plane and D-out-of-plane conformations, respectively.

4. THE DATABASE

Line strengths were calculated using the values for the dipole moment components listed in Table 5, retrieved from those of the normal species (Margulès et al. 2010). The partition function Q_{rot} was computed for several temperatures taking the degeneracy factors to be equal to $(2J+1)$. The energy of the 0_{00} level of the D-in-plane conformation was taken to be equal to zero and that of the $0_{00}, +$ level of the D-out-of-plane conformation was set to 10 cm^{-1} , in agreement with Coudert et al. (2012). Table 6 gives the values thus obtained for the partition functions.

The line list was built calculating the frequencies of the allowed transitions characterized by a rotational quantum number J smaller than 80. Integrated intensities were calculated in $\text{nm}^2 \cdot \text{MHz}$ units at 300 K using the results given in Tables 5 and 6. Just as in the JPL database (Pickett et al. 1998) catalog

Table 3
Spectroscopic Parameters^a for the D-in-plane Conformation

Parameter	Value	Parameter	Value
A	19921.587 052(980)	$H_{KIJ} \times 10^9$	20.859(480)
B	6415.266 933(180)	$H_{III} \times 10^9$	2.127(7)
C	5004.268 277(200)	$h_{KK} \times 10^9$	269.470(4797)
$\Delta_{KK} \times 10^3$	77.885 125(4400)	$h_{KJ} \times 10^9$	79.308(600)
$\Delta_{KJ} \times 10^3$	-19.418 282(1000)	$h_{JJ} \times 10^9$	1.309(3)
$\Delta_{JJ} \times 10^3$	4.926 657(66)	$L_{KKKK} \times 10^{12}$	-57.549(4797)
$\delta_K \times 10^3$	3.543 944(1900)	$L_{KKKJ} \times 10^{12}$	39.543(1019)
$\delta_J \times 10^3$	1.481 254(26)	$L_{KKJJ} \times 10^{12}$	-10.698(291)
$H_{KKK} \times 10^9$	1734.492(8094)	$L_{KJJJ} \times 10^{12}$	-1.919(30)
$H_{KKJ} \times 10^9$	-714.476(2129)	$I_{KJJ} \times 10^{12}$	0.686(57)

Note. ^a Parameters are in MHz. The numbers in parentheses are one standard deviation in the same units as the last digit. These parameters are involved in the pure rotational Hamiltonian in Equation (10) of Margulès et al. (2009a).

line files, the selected transitions are those with an intensity in $\text{nm}^2 \cdot \text{MHz}$ units at 300 K larger than

$$10^{\text{LOGSTR0}} + (F/300,000)^2 \times 10^{\text{LOGSTR1}}, \quad (1)$$

where F is the frequency in MHz and LOGSTR0 and LOGSTR1 are two dimensionless constants set to -9 and -7, respectively. The line list, given in Table 7, is formatted in the same way as the catalog line files of the JPL database (Pickett et al. 1998) and gives the line frequency in MHz and the error in MHz, retrieved from the line frequency analysis results, and the base 10 logarithm of the line intensity in $\text{nm}^2 \cdot \text{MHz}$ at 300 K. Also given are the degrees of freedom of the rotational partition function, the lower state energy in cm^{-1} , the upper state degeneracy, and the species tag and format number. The assignment of the transition is given in the remaining columns in terms of J, K_a, K_c , and the tunneling label. When the calculated error was smaller than 10 kHz, it was set to that value. For observed unblended

Table 4
Spectroscopic Parameters^a for the D-out-of-plane Conformation

Parameter	Value	Parameter	Value
θ_2	4.796 110(3000)	$f_{2kkk} \times 10^{12}$	49.753(2009)
ϕ_2	85.248 000(5700)	$f_{2kj} \times 10^{12}$	-13.810(779)
		$f_{2jj} \times 10^{12}$	-0.512(96)
h_2	-42.837 517(77000)	A	18516.681 258(830)
$h_{2k} \times 10^6$	22572.466(1199170)	B	6730.195 643(190)
$h_{2j} \times 10^6$	-1565.485(236836)	C	5164.955 356(180)
$f_2 \times 10^6$	499.174(80944)	$\Delta_{KK} \times 10^3$	57.893 618(2000)
$s_{2xz} \times 10^6$	-6270.914(164886)	$\Delta_{KJ} \times 10^3$	-14.761 884(1000)
$h_{2kk} \times 10^6$	-107.451(8094)	$\Delta_{JJ} \times 10^3$	6.207 069(120)
$h_{2kj} \times 10^6$	15.664(2428)	$\delta_K \times 10^3$	1.572 356(2500)
$h_{2jj} \times 10^6$	-1.771(246)	$\delta_J \times 10^3$	1.968 600(66)
$f_{2k} \times 10^6$	-11.012(1289)	$H_{KKK} \times 10^9$	821.395(2338)
$f_{2j} \times 10^6$	0.461(66)	$H_{KKJ} \times 10^9$	-9.303(3897)
$h_{2kkk} \times 10^9$	306.733(18287)	$H_{KJJ} \times 10^9$	-69.780(1109)
$h_{2kkj} \times 10^9$	13.391(8394)	$H_{JJJ} \times 10^9$	-3.541(42)
$h_{2kjj} \times 10^9$	-9.135(989)	$h_{KK} \times 10^9$	87.160(11692)
$h_{2jjj} \times 10^9$	0.533(75)	$h_{KJ} \times 10^9$	140.310(899)
$f_{2kk} \times 10^{12}$	-18669.944(3597509)	$h_{JJ} \times 10^9$	-1.601(21)
$f_{2kj} \times 10^{12}$	8445.556(659543)	$L_{KKJ} \times 10^{12}$	-6.053(450)
$f_{2jj} \times 10^{12}$	-84.167(11092)	$L_{KJJ} \times 10^{12}$	-0.370(147)
$h_{2kkk} \times 10^{12}$	-160.823(12591)	$L_{JJJ} \times 10^{12}$	-0.175(4)
$h_{2kkj} \times 10^{12}$	-54.501(5396)	$l_{KKK} \times 10^{12}$	54.829(2608)
$h_{2kjj} \times 10^{12}$	19.125(1319)	$l_{KKJ} \times 10^{12}$	77.674(1589)
$h_{2jjj} \times 10^{12}$	0.349(168)	$l_{KJJ} \times 10^{12}$	5.828(87)
$h_{2jjj} \times 10^{12}$	-0.046(7)	$l_{JJJ} \times 10^{12}$	-0.079(2)

Note. ^a Parameters are in MHz except θ_2 and ϕ_2 , which are in degrees. Numbers in parentheses are one standard deviation in the same units as the last digit. Parameters are defined in Equations (12), (13), and (22) of Margulès et al. (2009a) or are involved in the pure rotational Hamiltonian in Equation (10) of the same reference.

microwave lines, the line frequency and the error were replaced by their experimental values. This is indicated by a negative species tag.

5. DETECTION OF HCOOCH₂D IN ORION KL

We report the first detection of HCOOCH₂D in space by means of 66 unblended lines. The lines of the D-in-plane and the D-out-of-plane configurations were searched for in the Orion KL's line survey performed with the IRAM 30 m telescope (Tercero et al. 2010, 2011).

5.1. Observations and Overall Results

Five observing sessions (two in 2004 September, two in 2005 April, and the last one in 2007 January) have been used to complete the line survey toward the Orion KL nebula in all the frequency ranges available with the IRAM 30 m telescope. The 3.0, 2.0, and 1.3 mm windows (80–115.5 GHz, 130–178 GHz, and 197–281 GHz, respectively) were observed with 1 MHz of spectral resolution. System temperatures were in the range 100–800 K from the lowest to the highest frequencies. We reached the line confusion limit at 1.3 mm where the line density in Orion is extremely high. The spectra were calibrated in antenna temperature using the atmospheric transmission model package (Cernicharo 1985; Pardo et al. 2001). All the observations were performed using the Wobbler Switching mode. The 30 m beam size at the observing frequency ranges from 29'' to 9'' from 80 GHz to 280 GHz. Pointing and focus were checked every 1–2 hr on nearby pointing sources. We

Table 5
Dipole Moment Components

Conformation	μ_a	μ_b	μ_c
D-in-plane	1.640	0.724	0.0
D-out-of-plane	1.628	0.751	0.008

Notes. Numerical values for the dipole moment components, in Debye, used in the line intensity calculation were retrieved from those of the normal species (Margulès et al. 2010).

Table 6
Partition Function Q_{rot} for Several Values of the Temperature T in Kelvin.

T/K	Q_{rot}	T/K	Q_{rot}	T/K	Q_{rot}	T/K	Q_{rot}
9.375	276	37.500	3619	150.000	34489	300.000	100582
18.750	1047	75.000	11474	225.000	64705		

Notes. In agreement with Coudert et al. (2012), the energy of the 0_{00} level of the D-in-plane conformation was taken equal to zero; that of the $0_{00}, +$ level of the D-out-of-plane conformation was assumed to be 10 cm⁻¹.

pointed toward Orion-IRc2 at $\alpha_{2000.0} = 5^{\text{h}}35^{\text{m}}14\overset{\text{s}}{.}5$, $\delta_{2000.0} = -5^{\circ}22'30''.0$. All frequency settings were repeated at a slightly shifted frequency (10–20 MHz; new tuning was not necessary) in order to remove all possible contributions coming from the image side band. After processing of the data, at least all features in our survey above a 0.05 K threshold are coming from the signals in band. (For a detailed explanation of the observations and data analysis, see Tercero et al. 2010).

During the interpretation of the line survey, we had to deal with more than 15000 spectral features, of which 3600 are still unidentified. Thanks to the close collaboration between spectroscopists and astronomers, around 4400 of these lines have been successfully assigned to several isotopologues of CH₃CH₂CN, CH₂CHCN, HCOOCH₃, their vibrational levels and those of abundant molecules (NH₂CHO), and to the recently detected molecules methyl acetate (CH₃COOCH₃) and the gauche conformer of ethyl formate (G-CH₃CH₂OCHO) in this source (Demeky et al. 2007; Carvajal et al. 2009; Margulès et al. 2009b, 2010; Motiyenko et al. 2012; Tercero et al. 2012, 2013; Daly et al. 2013; A. López et al. 2013, in preparation; Haykal et al. 2013a). We also provided tentative detections (phenol c-C₆H₅OH, Kolesniková et al. 2013) and/or upper limit calculations for the column density of non-detected species (allyl-isocyanide CH₂CHCH₂NC, Haykal et al. 2013b). In a parallel work, the study of the survey was divided in the analysis of different families of molecules; this way, we have consistently analyzed these groups of molecules: CS-bearing species (Tercero et al. 2010), silicon-bearing molecules (Tercero et al. 2011), SO and SO₂ (Esplugaes et al. 2013a), methyl cyanide (Bell et al. 2013), ethyl cyanide (Daly et al. 2013), HCN, HNC, and HCO⁺ (N. Marcelino et al. 2013, in preparation), HC₃N and HC₅N (Esplugaes et al. 2013b), and vinyl cyanide (A. López et al. 2013, in preparation). Nevertheless, the analysis of this survey is still open and several works are in progress.

5.2. Results and Astronomical Modeling

Figure 3 shows selected lines from the D-in-plane and D-out-of-plane conformations of HCOOCH₂D present in our Orion data, together with our best model (explained below). All depicted lines are mostly free of blending with other species and in all boxes we observe a significant contribution from the studied species. No unblended lines of either conformation are missing

Table 7
Line List^a for the Microwave Spectrum^b of HCOOCH₂D

FREQ	ERR	LGINT	ELO	J'	K' _a	K' _c	±	J''	K'' _a	K'' _c	±
50041.7982	0.5000	-6.1442	44.1007	12	3	9	-	12	2	10	-
50044.2220	0.5000	-7.9394	143.9912	25	3	22	+	24	5	19	+
50046.6345	0.5000	-6.1442	44.0989	12	3	9	+	12	2	10	+
50046.6994	0.5000	-7.4039	232.0113	25	15	11	-	26	14	12	-
50046.6994	0.5000	-7.4039	232.0113	25	15	10	-	26	14	13	-
50053.4958	0.5000	-7.3976	232.0120	25	15	11	+	26	14	12	+
50053.4958	0.5000	-7.3976	232.0120	25	15	10	+	26	14	13	+
50070.5600	0.5000	-7.9389	143.9905	25	3	22	-	24	5	19	-
50071.4186	0.5000	-8.2617	98.7511	20	3	17	-	21	2	20	-
50078.3048	0.5000	-8.3046	207.2301	31	6	26		32	4	29	

Notes.

^a Columns FREQ, ERR, LGINT, and ELO contain the line frequency in MHz, the error, also in MHz, the base 10 logarithm of the line intensity in nm² · MHz at 300 K, and the lower level energy (ELO) in cm⁻¹. The eight remaining columns contain the line assignment in terms of J, K_a, K_c, and the tunneling label ±. The latter is + or - for the two tunneling sublevels of the D-out-of-plane conformation and blank for the D-in-plane conformation.

^b The line list is built using the results of the line-frequency analysis reported in this work.

(This table is available in its entirety in a machine-readable form in the online journal. A portion is shown here for guidance regarding its form and content.)

Table 8
Physical and Chemical Parameters Derived for Different Species

Parameter	HCOOCH ₂ D	DCOOCH ₃	HCOOCH ₃	¹³ C-HCOOCH ₃ <i>v_t = 1</i>	CH ₃ CH ₂ OCOH	CH ₃ CH ₂ CN
<i>d</i> ('')	15	15	15	15	15	4–10
off ('')	7	7	7	7	7	5
<i>T</i> _{rot} (K)	110	110–250	110–250	110–250	150	110–275
Δ <i>v</i> _{FWHM} (km s ⁻¹)	4	4	4	3	3	5–13
<i>v</i> _{LSR} (km s ⁻¹)	7.5	7.5	7.5	7	8	3–5
Component	Comp. ridge	Comp. ridge	Comp. ridge	Comp. ridge	Comp. ridge	Hot core
<i>N</i> _{comp} (cm ⁻²)	5.0 × 10 ¹⁴	5.0 × 10 ¹⁴	1.2 × 10 ¹⁶	6.6 × 10 ¹⁴	4.5 × 10 ¹⁴	3.8 × 10 ¹⁶
<i>N</i> _{tot} (cm ⁻²)	5.0 × 10 ¹⁴	7.8 × 10 ¹⁴	2 × 10 ¹⁶	6.6 × 10 ¹⁴	4.5 × 10 ¹⁴	4.1 × 10 ¹⁶

Notes. Parameters are compiled from Margulès et al. (2010), Tercero et al. (2013), Daly et al. (2013), and Haykal et al. (2013a). Column density values are given for each conformation, conformer, or state.

in the 168 GHz wide bandwidth covered. In order to model this emission, rotational constants of the D-out-of-plane conformation derived from this study, a fit to all the transitions of the D-in-plane conformation provided by Margulès et al. (2009a), and dipole moment from Curl (1959) have been implemented in the MADEX code (Cernicharo 2012). The D-in-plane conformation and the two tunneling substates of the D-out-of-plane conformation have been considered to be an independent molecular species for the calculation of line intensities. Owing to the lack of collisional rates for this molecule, the synthetic spectrum of these deuterated isotopologues of methyl formate was calculated assuming local thermodynamic equilibrium conditions. Only one component from this source (see, e.g., Blake et al. 1987; Schilke et al. 2001; Tercero et al. 2010 for Orion KL's components information), the compact ridge, has been necessary to properly model all lines arising from these species. We have adopted a size of 15'' and an offset 7'' from the pointing position (IRc2) of the compact ridge component (see, e.g., Favre et al. 2011). Beam dilution for each line has been taken into account in the calculation of the emerging line intensities. The physical/chemical parameters derived by the model are a kinetic temperature of 110 ± 20 K, a local standard of rest (LSR) velocity of the cloud of 7.5 km s⁻¹, a line width of 4 km s⁻¹, and a column density for each conformation of (5.0 ± 1.0) × 10¹⁴ cm⁻².

In this paper, we simplify the models used in Margulès et al. 2010 and Tercero et al. 2012. In these previous papers, we used the cloud components detected and modeled for the strong methyl formate lines. However, all these contributions are difficult to distinguish in the weak lines of both conformations of HCOOCH₂D, as the contribution from the compact ridge is mainly responsible for the observed line profiles. Besides, in spite of the need to include several components of Orion KL to properly fit the line profiles of methyl formate, both the main species and the ¹³C isotopologues, and vibrationally excited methyl formate (Haykal et al. 2013a), the compact ridge component also appears to be the main contribution to the emission. In Table 8, we compare several observed and derived physical and chemical parameters obtained for different species. We include the values of the calculated column density in the shown component and the total column density in all the components considered when we analyzed the emission of the corresponding species. For methyl formate and ¹³C-HCOOCH₃, *v_t = 1*, a temperature gradient of the compact ridge is required for fitting all lines arising in our survey. The line profiles of DCOOCH₃ could probably be fit properly using a single rotational temperature. However, in Margulès et al. (2010), we used the same components that those obtained for HCOOCH₃ in order to assess the detection of the deuterated species. For ethyl formate (CH₃CH₂OCOH), a single rotational

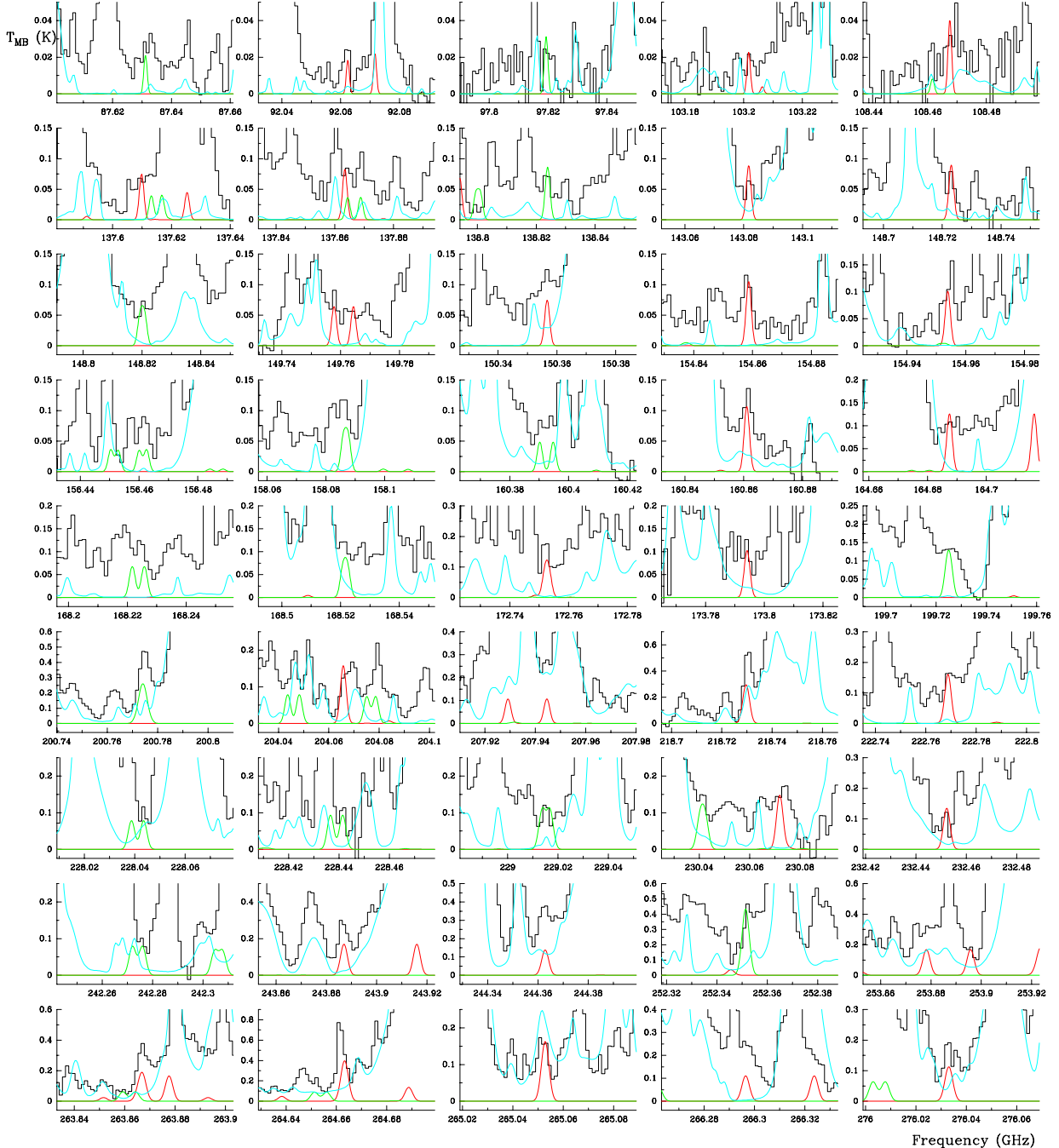


Figure 3. Selected lines of the D-out-of-plane (green) and D-in-plane (red) conformations of HCOOCH_2D toward Orion-IRc2. The solid cyan line corresponds to all lines already modeled in our previous papers (see the text).

(A color version of this figure is available in the online journal.)

temperature (150 K) yields good fits between the data and a synthetic spectrum (Tercero et al. 2013). Finally, we included ethyl cyanide ($\text{CH}_2\text{CH}_3\text{CN}$; Daly et al. 2013) in Table 8 for contrasting the parameters obtained for molecules with high abundances in the compact ridge with one high-abundance molecule in the hot core.

We have obtained consistent results in all the works related to methyl formate. Both column density ratios, $N(\text{D-out-of-plane conformation})/N(\text{HCOOCH}_3)$ and $N(\text{D-in-plane}$

conformation)/ $N(\text{HCOOCH}_3)$ (see Margulès et al. 2010 for column density results of methyl formate), give a value of 0.04 ± 0.02 for the compact ridge (taking into account both compact ridge components considered for HCOOCH_3), in agreement with that obtained for $N(\text{DCOOCH}_3)/N(\text{HCOOCH}_3)$ by Margulès et al. (2010), who derived 0.06 and 0.02 for the hot compact ridge and compact ridge, respectively. Similar abundance ratios have been found by different authors in the compact ridge component: $N(\text{HDO})/N(\text{H}_2\text{O}) = 0.03$

Table 9
Detected Lines of HCOOCH₂D

J	K _a	K _c	±	J'	K' _a	K' _c	±	Predicted Freq. (MHz)	Error (MHz)	E _u (K)	S _{ij} (D ²)	Observed Freq. (MHz)	Obs. v _{LSR} (km s ⁻¹)	T _{mb} ^a (K)	Blend
8	0	8	—	7	0	7	—	87631.062	0.005	15.2	20.8	87631.0	7.7 ± 1.7	0.02	
8	0	8	+	7	0	7	+	87631.593	0.005	15.2	20.8	†	9.5 ± 1.7		
8	2	7	—	7	2	6	—	90089.776	0.002	22.3	19.8	90089.3	9.1 ± 1.7	0.02	
8	4	5	—	7	4	4	—	92062.615	0.002	30.7	15.9	92062.9	6.6 ± 1.6	0.03	
9	1	9	—	8	1	8	—	97329.436	0.006	20.0	23.4	97330.0	5.8 ± 1.5	0.05	
9	1	9	+	8	1	8	+	97329.987	0.006	20.0	23.4	†	7.5 ± 1.5		
9	0	9	—	8	0	8	—	97819.262	0.006	19.9	23.4	97819.0	8.3 ± 1.5	0.02	
9	0	9	+	8	0	8	+	97819.764	0.006	19.9	23.4	†	9.8 ± 1.5		
9	7	3	—	8	7	2	—	103201.885	0.002	58.1	9.46	103201.9	7.5 ± 1.5	0.02	
9	7	2	—	8	7	1	—	103201.886	0.002	58.1	9.46	†	7.5 ± 1.5		
9	6	4	—	8	6	3	—	103296.342	0.002	49.3	13.9	103296.0	8.5 ± 1.5	0.02	
9	6	3	—	8	6	2	—	103296.420	0.002	49.3	13.9	†	8.7 ± 1.5		
9	4	5	—	8	4	4	—	103857.559	0.002	35.7	19.2	103857.0	9.1 ± 1.4	0.03	
9	3	6	—	8	3	5	—	105527.227	0.002	31.1	21.3	105529.0	2.5 ± 1.4	0.06	HCOOCH ₃ ν _t = 1
9	3	7	—	8	3	6	—	107931.645	0.005	27.1	21.2	107933.5	2.3 ± 1.4	0.05	CH ₃ CH ₂ OCHO
9	3	7	+	8	3	6	+	107934.070	0.005	27.1	21.2	†	9.1 ± 1.4		
9	4	6	—	8	4	5	—	108317.278	0.008	31.3	18.9	108318.0	5.5 ± 1.4	0.04	
9	4	6	+	8	4	5	+	108318.144	0.006	31.3	19.1	†	7.9 ± 1.4		
9	2	7	—	8	2	6	—	108467.754	0.002	28.4	22.8	108468.0	6.8 ± 1.4	0.03	
9	4	5	—	8	4	4	—	108619.766	0.007	31.3	19.1	108620.9	4.4 ± 1.4	0.03	
9	4	5	+	8	4	4	+	108620.764	0.009	31.3	18.9	†	7.1 ± 1.4		
10	2	9	—	9	2	8	—	111650.695	0.002	32.5	25.4	111651.9	4.3 ± 1.3	0.06	
10	7	4	—	9	7	3	—	114734.301	0.002	63.6	13.6	114734.9	5.9 ± 1.3	0.09	CH ₂ CHCN ν ₁₅ = 1
10	7	3	—	9	7	2	—	114734.304	0.002	63.6	13.6	†	5.9 ± 1.3		
10	6	5	—	9	6	4	—	114865.222	0.002	54.8	17.0	114866.9	3.1 ± 1.3	0.11	U
10	6	4	—	9	6	3	—	114865.513	0.002	54.8	17.0	†	3.9 ± 1.3		
11	0	11	—	10	0	10	—	114872.867	0.003	34.0	29.0	114871.9	10.0 ± 1.3	0.11	HCOOCH ₃ ν _t = 2
10	4	7	—	9	4	6	—	115395.477	0.002	41.2	22.3	115395.9	6.4 ± 1.3	0.12	CH ₃ CH ₂ OCHO
11	4	7	+	10	4	6	+	133953.756	0.005	43.5	25.3	133953.8	7.4 ± 1.1	0.07	
13	1	13	—	12	1	12	—	134638.258	0.003	46.5	34.3	134638.8	6.3 ± 1.1	0.25	CH ₃ CH ₂ CN ν ₁₃ /ν ₂₁
12	1	11	—	11	1	10	—	135401.324	0.003	44.4	31.1	135398.0	14.9 ± 1.1	0.07	CH ₃ CHO ν _t = 1
12	3	10	—	11	3	9	—	137610.084	0.003	49.1	29.8	137609.8	8.1 ± 1.1	0.07	
11	2	9	—	10	2	8	—	137613.363	0.005	37.7	28.1	137612.8	8.7 ± 1.1	0.07	HCOOCH ₃
12	7	6	—	11	7	5	—	137863.652	0.003	76.3	21.0	137864.9	4.8 ± 1.1	0.08	
12	7	5	—	11	7	4	—	137863.709	0.003	76.3	21.0	†	4.9 ± 1.1		
11	3	8	—	10	3	7	—	137864.659	0.006	40.0	27.1	†	7.0 ± 1.1		
11	3	8	+	10	3	7	+	137869.082	0.005	40.0	27.1	137869.8	5.9 ± 1.1	0.11	U
13	1	13	—	12	1	12	—	138823.866	0.007	43.6	34.0	138823.9	7.4 ± 1.1	0.07	
13	1	13	+	12	1	12	+	138824.329	0.007	43.6	34.0	†	8.4 ± 1.1		
13	0	13	—	12	0	12	—	138883.386	0.007	43.6	34.0	138883.8	6.6 ± 1.1	0.23	U
13	0	13	+	12	0	12	+	138883.830	0.007	43.6	34.0	†	7.6 ± 1.1		
12	4	8	—	11	4	7	—	139847.915	0.003	54.1	28.4	139846.8	9.9 ± 1.1	0.07	CH ₃ COOCH ₃
13	2	12	—	12	2	11	—	143081.943	0.003	51.6	33.5	143081.8	7.8 ± 1.0	0.06	
13	3	11	—	12	3	10	—	148723.308	0.003	56.3	32.7	148722.8	8.5 ± 1.0	0.07	
13	1	12	—	12	1	11	—	148819.613	0.006	48.7	33.3	148820.9	4.9 ± 1.0	0.07	
13	1	12	+	12	1	11	+	148821.114	0.006	48.7	33.3	†	7.9 ± 1.0		
14	1	14	—	13	1	13	—	149157.880	0.007	50.8	36.7	149158.1	7.1 ± 1.0	0.10	
14	1	14	+	13	1	13	+	149158.320	0.008	50.8	36.7	†	7.9 ± 1.0		
13	9	5	—	12	9	4	—	149158.892	0.003	105.2	18.0	†	9.1 ± 1.0		
13	9	4	—	12	9	3	—	149158.892	0.003	105.2	18.0	†	9.1 ± 1.0		
14	0	14	—	13	0	13	—	149191.398	0.007	50.8	36.7	149190.7	8.9 ± 1.0	0.43	HCOOCH ₃ (CH ₃) ₂ CO
14	0	14	+	13	0	13	+	149191.825	0.008	50.8	36.7	†	9.8 ± 1.0		
13	6	8	—	12	6	7	—	149758.006	0.003	74.7	27.1	149758.8	5.9 ± 1.0	0.10	
13	6	7	—	12	6	6	—	149764.600	0.003	74.7	27.1	149764.9	6.9 ± 1.0	0.06	
13	5	8	—	12	5	7	—	150356.939	0.003	67.3	29.5	150356.8	7.8 ± 1.0	0.12	
15	1	15	—	14	1	14	—	154678.384	0.004	60.8	39.6	154678.7	6.9 ± 1.0	0.17	CH ₃ CH ₂ ¹³ CN
14	1	13	—	13	1	12	—	154858.948	0.003	58.8	36.1	154857.7	9.9 ± 1.0	0.12	CH ₃ OCH ₃
14	1	13	+	13	1	12	+	154858.948	0.003	58.8	36.1	†	9.9 ± 1.0		HCOOCH ₃
13	2	11	—	12	2	10	—	154954.147	0.003	54.8	33.5	154955.7	4.5 ± 1.0	0.15	U
13	8	6	+	12	8	5	+	155774.954	0.006	86.5	21.4	155775.7	6.1 ± 1.0	0.08	CH ₂ ¹³ CHCN
13	8	5	+	12	8	4	+	155774.958	0.006	86.5	21.4	†	6.1 ± 1.0		
13	3	10	—	12	3	9	—	156388.308	0.003	57.5	32.7	156389.3	5.6 ± 1.0	0.07	
13	6	8	—	12	6	6	—	156460.298	0.020	69.8	25.9	156461.8	4.6 ± 1.0	0.07	
13	6	7	—	12	6	6	—	156462.818	0.009	69.8	26.9	†	9.5 ± 1.0		
14	2	13	—	13	2	12	—	158086.241	0.006	56.4	35.9	158086.2	7.6 ± 0.9	0.12	
14	2	13	+	13	2	12	+	158087.889	0.006	56.4	35.9	†	10.0 ± 0.9		
14	1	13	—	13	1	12	—	158894.305	0.006	56.3	35.9	158894.8	6.6 ± 0.9	0.11	
14	1	13	+	13	1	12	+	158895.777	0.006	56.3	35.9	†	9.3 ± 0.9		

Table 9
(Continued)

J	K _a	K _c	±	J'	K' _a	K' _c	±	Predicted Freq. (MHz)	Error (MHz)	E _u (K)	S _{ij} (D ²)	Observed Freq. (MHz)	Obs. v _{LSR} (km s ⁻¹)	T _{mb} ^a (K)	Blend
14	3	12	—	13	3	11	—	159698.558	0.003	63.9	35.3	159699.7	5.4 ± 0.9	0.08	
13	4	9	—	12	4	8	—	160390.473	0.006	58.3	31.2	160390.5	7.4 ± 0.9	0.08	
13	4	9	+	12	4	8	+	160395.030	0.005	58.3	31.2	160394.3	8.9 ± 0.9	0.08	
14	8	7	—	13	8	6	—	160861.326	0.003	101.4	25.1	160861.7	6.8 ± 0.9	0.13	CH ₂ ¹³ CHCN
14	8	6	—	13	8	5	—	160861.337	0.003	101.4	25.1	†	6.8 ± 0.9		
15	1	14	—	14	1	13	—	164606.241	0.004	66.7	38.8	164605.7	8.5 ± 0.9	0.11	
16	1	16	—	15	1	15	—	164687.734	0.004	68.7	42.2	164688.7	5.7 ± 0.9	0.10	
14	4	10	—	13	4	9	—	164866.756	0.003	69.3	34.3	164866.7	7.6 ± 0.9	0.10	CH ₃ CH ₂ OCHOH
14	8	7	—	13	8	6	—	167890.903	0.006	94.6	25.0	167889.7	9.6 ± 0.9	0.23	(CH ₃) ₂ CO
14	8	6	—	13	8	5	—	167890.915	0.006	94.6	25.0	†	9.7 ± 0.9		
14	7	8	—	13	7	7	—	168221.588	0.006	85.6	27.8	168224.3	2.7 ± 0.9	0.12	DCOOCH ₃
14	7	7	—	13	7	6	—	168222.376	0.006	85.6	27.8	†	4.1 ± 0.9		
14	7	8	+	13	7	7	+	168225.681	0.006	85.6	27.9	†	10.0 ± 0.9		
14	7	7	+	13	7	6	+	168226.470	0.006	85.6	27.8	†	11.4 ± 0.9		
15	2	14	—	14	2	13	—	168521.077	0.006	64.5	38.5	168521.8	6.2 ± 0.9	0.12	
15	2	14	+	14	2	13	+	168522.677	0.006	64.5	38.5	†	9.1 ± 0.9		
14	4	11	—	13	4	10	—	169016.309	0.005	66.0	34.0	169015.5	8.9 ± 0.9	0.20	U
15	1	14	—	14	1	13	—	169033.485	0.006	64.4	38.6	169035.6	3.7 ± 0.9	0.24	HC ¹⁸ OOC ₃
15	1	14	+	14	1	13	+	169034.944	0.006	64.4	38.6	†	6.3 ± 0.9		
15	7	9	—	14	7	8	—	172752.270	0.003	99.5	31.1	172752.6	6.9 ± 0.9	0.17	
15	7	8	—	14	7	7	—	172753.589	0.003	99.5	31.7	†	9.2 ± 0.9		
15	5	11	—	14	5	10	—	173794.446	0.003	83.4	35.3	173794.7	7.1 ± 0.9	0.12	
18	1	17	—	17	1	16	—	199724.700	0.006	91.7	46.5	199727.6	3.1 ± 0.8	0.15	U
18	1	17	+	17	1	16	+	199726.122	0.006	91.7	46.5	†	5.3 ± 0.8		
16	3	14	—	15	2	13	—	199921.119	0.006	80.8	3.19	199921.4	7.1 ± 0.8	0.03	
19	1	19	—	18	1	18	—	200773.519	0.008	94.0	49.9	200775.2	5.0 ± 0.7	0.49	CH ₃ CH ₂ OH
19	1	19	+	18	1	18	+	200773.843	0.008	94.0	49.9	†	5.5 ± 0.7		
19	0	19	—	18	0	18	—	200775.163	0.008	94.0	49.9	†	7.4 ± 0.7		
19	0	19	+	18	0	18	+	200775.485	0.008	94.0	49.9	†	7.9 ± 0.7		
17	9	9	—	16	9	8	—	204043.999	0.006	132.4	32.5	204047.2	2.8 ± 0.7	0.14	H ¹³ COOCH ₃
17	9	8	—	16	9	7	—	204043.999	0.006	132.4	32.5	†	2.8 ± 0.7		
17	9	9	+	16	9	8	+	204048.616	0.006	132.4	32.5	†	9.6 ± 0.7		
17	9	8	+	16	9	7	+	204048.616	0.006	132.4	32.5	†	9.6 ± 0.7		
19	1	18	—	18	1	17	—	204066.071	0.004	103.1	49.4	204069.6	2.3 ± 0.7	0.16	HCOO ¹³ CH ₃
17	4	14	—	16	4	13	—	204075.369	0.005	93.8	42.4	204079.7	1.1 ± 0.7	0.20	H ¹³ CCCN ν ₇ = 2
17	4	14	+	16	4	13	+	204078.908	0.005	93.8	42.4	†	6.3 ± 0.7		
18	10	9	—	17	10	8	—	206850.006	0.003	162.2	33.2	206847.6	11.0 ± 0.7	0.15	CH ₃ CH ₂ CN ν ₁₃ /ν ₂₁
18	10	8	—	17	10	7	—	206850.006	0.003	162.2	33.2	†	11.0 ± 0.7		
6	6	1	—	5	5	0	—	209621.621	0.013	29.5	3.01	209621.4	7.8 ± 0.7	0.15	HCOOCH ₃ ν _t = 1
6	6	0	—	5	5	1	—	209621.634	0.013	29.5	3.01	†	7.8 ± 0.7		
6	6	1	+	5	5	0	+	209622.126	0.013	29.5	3.11	†	8.5 ± 0.7		
6	6	0	+	5	5	—	+	209622.139	0.013	29.5	3.11	†	8.6 ± 0.7		
17	5	12	—	16	5	11	—	209716.882	0.006	99.7	41.2	209718.9	4.6 ± 0.7	0.22	H ¹³ COOCH ₃
17	5	12	+	16	5	11	+	209722.127	0.006	99.7	41.2	†	12.1 ± 0.7		
19	1	18	—	18	1	17	—	210004.925	0.006	101.8	49.1	210005.0	7.4 ± 0.7	0.53	(CH ₃) ₂ CO
19	1	18	+	18	1	17	+	210006.329	0.006	101.8	49.1	†	9.4 ± 0.7		
20	1	20	—	19	1	19	—	211091.566	0.008	104.2	52.6	211096.3	0.8 ± 0.7	0.45	CH ₃ OH
20	1	20	+	19	1	19	+	211091.865	0.009	104.2	52.6	†	1.2 ± 0.7		
20	0	20	—	19	0	19	—	211092.448	0.008	104.2	52.6	†	2.0 ± 0.7		
20	0	20	+	19	0	19	+	211092.747	0.009	104.2	52.6	†	2.5 ± 0.7		
18	5	13	—	17	5	12	—	211553.756	0.004	112.1	44.1	211552.5	9.3 ± 0.7	0.10	
19	3	17	—	18	3	16	—	212534.733	0.004	109.9	48.9	212536.2	5.4 ± 0.7	0.18	
20	2	19	—	19	2	18	—	213887.260	0.004	113.3	52.1	213885.0	10.7 ± 0.7	0.26	¹³ CH ₃ CH ₂ CN
18	4	14	—	17	4	13	—	216782.819	0.004	107.2	45.7	216782.5	7.9 ± 0.7	0.38	(CH ₃) ₂ CO
19	9	11	—	18	9	10	—	218729.508	0.003	159.8	39.1	218731.2	5.2 ± 0.7	0.58	CH ₂ CHCN ν ₁₅ = 1
19	9	10	—	18	9	9	—	218729.557	0.003	159.8	39.1	†	5.2 ± 0.7		
19	4	16	—	18	4	15	—	218730.506	0.004	116.1	48.1	†	6.5 ± 0.7		
20	1	19	—	19	1	18	—	220296.238	0.006	112.4	51.8	220297.5	5.8 ± 0.7	0.39	CH ₃ ¹³ CN
20	1	19	+	19	1	18	+	220297.622	0.006	112.4	51.8	†	7.7 ± 0.7		
7	6	2	—	6	5	1	—	221560.202	0.012	33.5	3.01	221560.0	7.8 ± 0.7	0.07	
7	6	1	—	6	5	2	—	221560.342	0.012	33.5	3.01	†	8.0 ± 0.7		
7	6	2	+	6	5	1	+	221561.002	0.013	33.5	3.11	†	8.9 ± 0.7		
7	6	1	+	6	5	2	+	221561.142	0.013	33.5	3.11	†	9.0 ± 0.7		
20	3	18	—	19	3	17	—	222769.101	0.004	120.6	51.5	222770.0	6.3 ± 0.7	0.17	
22	1	22	—	21	1	21	—	224689.136	0.005	126.3	58.2	224690.0	6.3 ± 0.7	0.31	
22	0	22	—	21	0	21	—	224690.264	0.005	126.3	58.2	†	7.9 ± 0.7		
19	9	11	—	18	9	9	+	228441.909	0.006	153.7	39.1	228442.4	6.9 ± 0.7	0.11	
19	9	11	+	18	9	10	+	228441.928	0.006	153.7	39.1	†	6.9 ± 0.7		

Table 9
(Continued)

<i>J</i>	<i>K_a</i>	<i>K_c</i>	±	<i>J'</i>	<i>K'_a</i>	<i>K'_c</i>	±	Predicted Freq. (MHz)	Error (MHz)	<i>E_u</i> (K)	<i>S_{ij}</i> (D ²)	Observed Freq. (MHz)	Obs. <i>v_{LSR}</i> (km s ⁻¹)	<i>T_{mb}</i> ^a (K)	Blend
19	8	11	+	18	8	11	—	229013.808	0.011	143.6	40.8	229015.1	5.8 ± 0.7	0.12	
19	8	11	—	18	8	10	—	229014.351	0.008	143.6	41.2	†	6.5 ± 0.7		
19	8	12	+	18	8	11	+	229016.905	0.008	143.6	41.2	†	9.9 ± 0.7		
19	8	12	—	18	8	10	+	229017.452	0.011	143.6	40.8	†	10.6 ± 0.7		
19	4	15		18	4	14		229518.326	0.004	118.2	48.4	229519.3	6.2 ± 0.7	0.14	
20	11	10		19	11	9		229839.213	0.004	198.0	37.2	229837.5	9.7 ± 0.7	0.37	
20	11	9		19	11	8		229839.213	0.004	198.0	37.2	†	9.7 ± 0.7		
19	7	13	—	18	7	12	—	229841.076	0.008	134.8	43.1	†	12.2 ± 0.7		
19	7	13	+	18	7	12	+	229843.578	0.008	134.8	43.3	†	15.4 ± 0.7		
19	7	12	—	18	7	11	—	229964.664	0.008	134.8	43.3	229966.1	5.6 ± 0.7	0.22	CH ₂ CHCN <i>v</i> ₁₁ = 3
19	7	12	+	18	7	11	+	229967.228	0.009	134.8	43.1	†	9.0 ± 0.7		
20	2	18	—	19	2	17	—	230040.745	0.006	119.7	51.1	230042.4	5.3 ± 0.7	0.15	
20	2	18	+	19	2	17	+	230042.772	0.006	119.7	51.1	†	8.0 ± 0.7		
20	10	11		19	10	10		230072.391	0.003	183.8	39.9	230071.1	9.2 ± 0.7	0.15	
20	10	10		19	10	9		230072.394	0.003	183.8	39.9	†	9.2 ± 0.7		
20	9	12		19	9	11		230398.724	0.003	170.9	42.5	230397.4	9.2 ± 0.7	0.27	CH ₂ CHCN <i>v</i> ₁₅ = 1
20	9	11		19	9	10		230398.847	0.003	170.9	42.5	†	9.4 ± 0.7		
19	6	14	—	18	6	13	—	230761.120	0.006	127.3	45.4	230766.2	0.9 ± 0.7	0.22	U
19	6	14	+	18	6	13	+	230764.944	0.006	127.3	45.4	†	5.9 ± 0.7		
20	8	13		19	8	12		230870.631	0.003	159.4	44.6	230868.7	10.0 ± 0.6	0.40	CH ₂ ¹³ CHCN
20	8	12		19	8	11		230873.895	0.003	159.4	44.6	†	14.3 ± 0.6		
20	7	14		19	7	13		231568.004	0.004	149.4	46.8	231569.8	5.2 ± 0.6	0.12	
20	6	15		19	6	14		232452.669	0.004	140.8	48.4	232452.4	7.8 ± 0.6	0.12	
20	5	16		19	5	15		232572.679	0.004	133.6	49.7	232573.9	5.9 ± 0.6	0.23	CH ₃ ¹³ CH ₂ CN
21	2	19		20	2	18		234054.276	0.004	131.7	54.2	234054.3	7.5 ± 0.6	0.31	
20	3	17		19	3	16		236549.822	0.004	126.0	51.5	236547.7	10.2 ± 0.6	0.31	DCOOCH ₃
21	3	19	—	20	3	18	—	239765.256	0.005	131.3	53.7	239766.3	6.2 ± 0.6	0.27	
21	3	19	+	20	3	18	+	239767.464	0.006	131.3	53.7	239768.3	6.5 ± 0.6	0.26	
20	5	16	+	19	5	15	+	242276.461	0.006	132.5	49.6	242276.4	7.6 ± 0.6	0.10	
23	2	22		22	2	21		243887.433	0.005	147.0	60.0	243886.3	8.9 ± 0.6	0.30	³⁴ SHD
21	6	16		20	6	15		244363.298	0.004	152.5	51.3	244363.4	7.4 ± 0.6	0.38	U
24	0	24		23	1	23		244678.199	0.005	149.3	10.3	244680.3	4.9 ± 0.6	0.44	
24	1	24		23	1	23		244678.682	0.005	149.3	63.5	†	5.5 ± 0.6		
24	0	24		23	0	23		244679.051	0.005	149.3	63.5	†	6.0 ± 0.6		
24	1	24		23	0	23		244679.534	0.005	149.3	10.3	†	6.6 ± 0.6		
22	3	20	—	21	3	19	—	250108.540	0.006	143.3	56.4	250111.3	4.2 ± 0.6	0.22	U
22	3	20	+	21	3	19	+	250110.680	0.006	143.3	56.4	†	6.8 ± 0.6		
24	0	24	—	23	1	23	—	252351.616	0.010	149.6	12.7	252352.6	6.3 ± 0.6	0.48	
24	1	24	—	23	1	23	—	252351.693	0.010	149.6	63.2	†	6.4 ± 0.6		
24	0	24	—	23	0	23	—	252351.763	0.010	149.6	63.2	†	6.5 ± 0.6		
24	0	24	+	23	1	23	+	252351.810	0.010	149.6	12.7	†	6.6 ± 0.6		
24	1	24	—	23	0	23	—	252351.840	0.010	149.6	12.7	†	6.6 ± 0.6		
24	1	24	+	23	1	23	+	252351.888	0.010	149.6	63.2	†	6.7 ± 0.6		
24	0	24	+	23	0	23	+	252351.958	0.010	149.6	63.2	†	6.7 ± 0.6		
24	1	24	+	23	0	23	+	252352.035	0.010	149.6	12.7	†	6.8 ± 0.6		
24	2	23		23	2	22		253878.590	0.005	159.2	62.7	253878.2	8.0 ± 0.6	0.31	CH ₃ CH ₂ ¹³ CN
24	1	23		23	1	22		253896.118	0.005	159.2	62.7	253896.3	7.3 ± 0.6	0.19	
22	8	15		21	8	14		254451.934	0.004	183.3	50.7	254455.0	3.9 ± 0.6	0.27	H ¹³ COOCH ₃ <i>v</i> _t = 1
22	8	14		21	8	13		254465.903	0.004	183.3	50.7	254466.3	7.0 ± 0.6	0.28	U
22	12	11	+	21	12	10	+	263859.673	0.007	227.7	41.0	263860.3	6.8 ± 0.6	0.04	
22	12	10	+	21	12	9	+	263859.673	0.007	227.7	41.0	†	6.8 ± 0.6		
22	12	11	—	21	12	10	—	263864.631	0.007	227.7	41.0	263867.2	4.6 ± 0.6	0.39	
22	12	10	—	21	12	9	—	263864.631	0.007	227.7	41.0	†	4.6 ± 0.6		
23	16	8		22	16	7		263865.858	0.005	326.0	31.6	†	6.0 ± 0.6		
23	16	7		22	16	6		263865.858	0.005	326.0	31.6	†	6.0 ± 0.6		
25	2	24		24	2	23		263867.437	0.005	171.9	65.4	†	7.8 ± 0.6		
22	5	17		21	5	16		264078.565	0.004	159.0	55.5	264078.8	7.2 ± 0.6	0.18	CH ₂ DCH ₂ CN
7	7	1		6	6	0		264638.757	0.008	48.8	2.99	264639.2	7.0 ± 0.6	0.11	
7	7	0		6	6	1		264638.758	0.008	48.8	2.99	†	7.0 ± 0.6		
26	0	26		25	1	25		264663.455	0.006	174.2	11.2	264662.1	9.0 ± 0.6	0.79	CH ₃ CH ₂ OH CH ₂ ¹³ CHCN
26	1	26		25	1	25		264663.609	0.006	174.2	68.8	†	9.2 ± 0.6		
26	0	26		25	0	25		264663.728	0.006	174.2	68.8	†	9.3 ± 0.6		
26	1	26		25	0	25		264663.883	0.006	174.2	11.2	†	9.5 ± 0.6		
23	10	14		22	10	13		265053.256	0.004	220.2	49.7	265053.8	6.9 ± 0.6	0.16	
23	10	13		22	10	12		265053.313	0.004	220.2	49.7	†	6.9 ± 0.6		
21	5	16	+	20	5	15	+	265136.706	0.008	146.6	52.8	265136.3	8.0 ± 0.6	0.13	
22	8	15	—	21	8	14	—	266193.006	0.009	180.2	49.9	266197.5	2.4 ± 0.6	0.15	CH ₃ OH
22	8	15	+	21	8	14	+	266195.626	0.010	180.2	49.9	†	5.4 ± 0.6		

Table 9
(Continued)

J	K _a	K _c	±	J'	K' _a	K' _c	±	Predicted Freq. (MHz)	Error (MHz)	E _u (K)	S _{ij} (D ²)	Observed Freq. (MHz)	Obs. v _{LSR} (km s ⁻¹)	T _{mb} ^a (K)	Blend
23	8	16	—	22	8	15	—	266296.865	0.004	196.1	53.7	266296.3	8.1 ± 0.6	0.26	
24	2	22	—	23	2	21	—	270832.373	0.006	168.8	61.6	270834.2	5.5 ± 0.6	0.15	
24	2	22	+	23	2	21	+	270834.338	0.006	168.8	61.6	†	7.7 ± 0.6		
25	1	24	—	24	2	23	—	271802.831	0.007	172.7	11.6	271807.1	2.8 ± 0.6	0.31	
25	1	24	+	24	2	23	+	271804.105	0.007	172.7	11.6	†	4.2 ± 0.6		
25	2	24	—	24	2	23	—	271805.499	0.007	172.7	65.0	†	5.7 ± 0.6		
25	2	24	+	24	2	23	+	271806.769	0.007	172.7	65.0	†	7.1 ± 0.6		
25	1	24	—	24	1	23	—	271807.685	0.007	172.7	65.0	†	8.1 ± 0.6		
25	1	24	+	24	1	23	+	271808.953	0.007	172.7	65.0	†	9.5 ± 0.6		
25	2	24	—	24	1	23	—	271810.352	0.007	172.7	11.6	†	11.1 ± 0.6		
25	2	24	+	24	1	23	+	271811.618	0.007	172.7	11.6	†	12.5 ± 0.6		
24	4	21	—	23	4	20	—	271820.670	0.004	176.3	61.4	271822.1	5.9 ± 0.6	0.26	CH ₃ CHO
26	0	26	—	25	1	25	—	272973.976	0.011	175.3	13.8	272974.1	7.4 ± 0.5	0.30	DCOOCH ₃
26	1	26	—	25	1	25	—	272973.997	0.011	175.3	68.5	†	7.4 ± 0.5		
26	0	26	—	25	0	25	—	272974.017	0.011	175.3	68.5	†	7.4 ± 0.5		
26	1	26	—	25	0	25	—	272974.038	0.011	175.3	13.8	†	7.4 ± 0.5		
26	0	26	+	25	1	25	+	272974.116	0.011	175.3	13.8	†	7.5 ± 0.5		
26	1	26	+	25	1	25	+	272974.137	0.011	175.3	68.5	†	7.5 ± 0.5		
26	0	26	+	25	0	25	+	272974.156	0.011	175.3	68.5	†	7.6 ± 0.5		
26	1	26	+	25	0	25	+	272974.177	0.011	175.3	13.8	†	7.6 ± 0.5		
24	14	11	—	23	14	10	—	275628.745	0.005	298.5	42.0	275629.1	7.1 ± 0.5	0.22	
24	14	10	—	23	14	9	—	275628.745	0.005	298.5	42.0	†	7.1 ± 0.5		
24	12	13	—	23	12	12	—	276033.561	0.004	263.2	47.8	276033.6	7.5 ± 0.5	0.20	
24	12	12	—	23	12	11	—	276033.561	0.004	263.2	47.8	†	7.5 ± 0.5		

Notes. Emission lines of HCOOCH₂D present in the spectral scan of Orion KL from the IRAM 30 m radio telescope. Columns 1–8 give the line assignment. + or – in Columns 4 and 8 identify the two tunneling sublevels of the D-out-of-plane conformation; a blank entry indicates a transition of the D-in-plane conformation. Column 9 gives the predicted frequency in the laboratory. Column 10 gives the uncertainty of frequency predictions. Column 11 is the upper level energy. Column 12 is the line strength. Column 13 is the observed frequency assuming a v_{LSR} of 7.5 km s⁻¹. Column 14 is the observed radial velocity, Column 15 the main beam temperature, and Column 16 gives blends. A † in Column 13 means that line is blended with a previous line.

^a This value has to be considered an upper limit.

and N(HDCO)/N(H₂CO) = 0.01 by Persson et al. (2007), N(DCN)/N(HCN) = 0.01–0.06 by Schilke et al. (1992), and N(HDCS)/N(H₂CS) = 0.040 ± 0.012 by Tercero et al. (2010).

The full census of detected lines is provided in Table 9, where we list 66 unblended lines as well as 56 lines moderately blended with other species. Owing to the weakness of these features, the main beam antenna temperature and the radial velocity have been obtained from the peak channel of our spectra. Therefore, errors in the baselines and contribution from other species could affect the T_{mb} value, which has to be considered to be the total intensity of the detected feature and an upper limit on the intensity of deuterated methyl formate in this study. The uncertainty in the radial velocity has been adopted from the spectral resolution of our data. Line widths are not included in Table 9 due to the difficulty of obtaining this parameter from the data (overlap problems and/or weak lines). This identification is based on a whole inspection of the data and the modeled synthetic spectrum of the studied species and all the species already identified in our previous papers (see above). We consider blended lines to be those that are close enough to other stronger features. No missing lines were found in unblended frequencies of the spectra.

Rotational diagrams were included in order to judge the quality of the detection. The following equation relates the molecular parameters with the observed ones (see, e.g., Turner 1991; Goldsmith & Langer 1999; Persson et al. 2007 for a detailed discussion of the derivation):

$$\ln\left(\frac{N_u}{g_u}\right) = \ln\left(\frac{8\pi k v^2 W}{hc^3 A_{ul} g_u b}\right) = \ln\left(\frac{N}{Q_{rot}}\right) - \frac{E_{upp}}{k T_{rot}}, \quad (2)$$

where N_u is the column density in the upper state (cm⁻²), g_u is the statistical weight in the upper level, W (K cm s⁻¹)

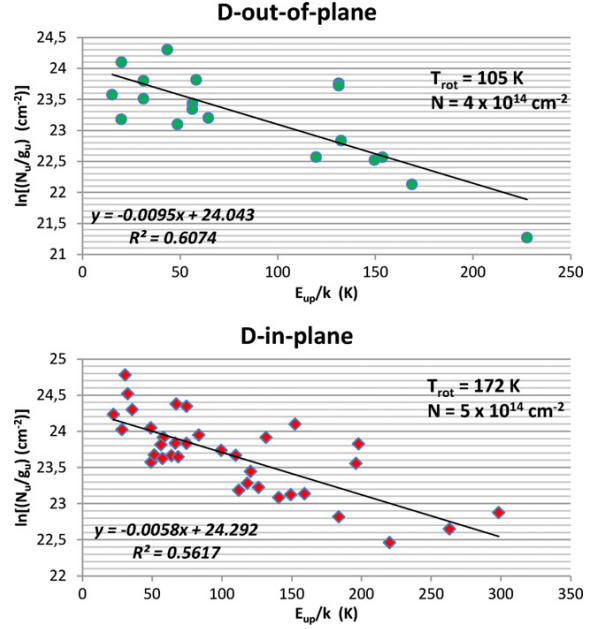


Figure 4. Rotational diagrams for both conformations of HCOOCH₂D.
(A color version of this figure is available in the online journal.)

is the integrated line intensity (in main beam temperature), A_{ul} is the Einstein A-coefficient of spontaneous emission, N (cm⁻²) is the total column density, Q_{rot} is the rotational partition function, E_{upp} (K) is the upper level energy, T_{rot} (K) is the rotational temperature, and b is the beam dilution factor.

The upper state column densities divided by the statistical weight are plotted as a function of the upper level energies for both conformations of HCOOCH₂D in Figure 4, setting the line width to 4 km s⁻¹. The rotational temperature and the total column density can be derived from these plots by performing a linear least squares fit to the points. For the out-of-plane conformation, we used 20 transitions with upper level energies ranging from 15.2 to 227.7 K, while for the in-plane conformation we considered 35 transitions with energies between 22.3–298.5 K. We derived the rotational temperatures and column densities, $T_{\text{rot}} = 105 \pm 50$ K and $N = (4 \pm 2) \times 10^{14}$ cm⁻² and $T_{\text{rot}} = 172 \pm 70$ K and $N = (5 \pm 2) \times 10^{14}$ cm⁻², for the out-of-plane and in-plane conformations, respectively. These results are in agreement with the values obtained in our model (see above), confirming the detection of HCOOCH₂D.

6. CONCLUSIONS

The pure rotational spectrum of HCOOCH₂D was recorded in the laboratory from 0.77 to 1.2 THz. 1650 lines were assigned to the D-in-plane and D-out-of-plane conformations. A line-frequency analysis of the present dataset and of previously published transitions (Margulès et al. 2009a) was performed accounting for the large-amplitude torsional motion of the partially deuterated CH₂D methyl group taking place in the D-out-of-plane conformation. The experimental frequencies were reproduced with an rms of 0.16 MHz and the spectroscopic constants thus obtained are given in Tables 3 and 4. The line list built using the results of this analysis allowed us to detect HCOOCH₂D in Orion KL. 66 unblended lines, as well as 56 lines that were moderately blended with other species, could be observed from both conformations. These detections, the good agreement between model and observations, and the consistent results between model and rotational diagrams ensure the detection of both conformations of HCOOCH₂D in Orion. In addition, the observed deuteration enhancement is consistent with that obtained for other species in this source.

Portions of this paper present research carried out at the Jet Propulsion Laboratory, California Institute of Technology, under contract with the National Aeronautics and Space Administration. Government sponsorship is acknowledged. This work was also supported by the French program Action sur Projets de l'INSU "Physique et Chimie du Milieu Interstellaire" (PCMI) and by the contracts ANR-08-BLAN-0054 and ANR-08-BLAN-0225. J.C. and B.T. thank the Spanish MINECO for funding support from grants CSD2009-00038, AYA2009-07304, and AYA2012-32032.

REFERENCES

- Bauder, A. 1979, JPCRD, **8**, 583
 Bell, T. A., Cernicharo, J., Viti, S., et al. 2013, A&A, submitted
- Blake, G. A., Sutton, E. C., Masson, G. R., & Phillips, T. G. 1986, ApJS, **60**, 357
 Blake, G. A., Sutton, E. C., Masson, C. R., & Phillips, T. G. 1987, ApJ, **315**, 621
 Brown, R. D., Crofts, J. G., Godfrey, P. D., et al. 1975, ApJL, **197**, L29
 Carvajal, M., Margulès, L., Tercero, B., et al. 2009, A&A, **500**, 1109
 Carvajal, M., Willaert, F., Demaison, J., & Kleiner, I. 2007, JMoSp, **246**, 158
 Cernicharo, J. 1985, Internal IRAM Report (Granada: IRAM)
 Cernicharo, J. 2012, in ECLA-2011: Proc. of the European Conf. on Laboratory Astrophysics, EAS Publication Series, 2012, ed. C. Stehl, C. Joblin, & L. d'Hendecourt (Cambridge: Cambridge Univ. Press), 251
 Coudert, L. H., Margulès, L., Huet, T. R., et al. 2012, A&A, **543**, A46
 Curl, R. F. 1959, JChPh, **30**, 1529
 Daly, A. M., Bermúdez, C., López, A., et al. 2013, ApJ, **768**, 81
 Demaison, J., Boucher, D., Dubrulle, A., & van Eijck, B. P. 1983, JMoSp, **102**, 260
 Demaison, J., Margulès, L., Kleiner, I., & Császár, A. G. 2010, JMoSp, **259**, 70
 Demyk, K., Bottinelli, S., Caux, E., et al. 2010, A&A, **517**, A17
 Demyk, K., Mäder, H., Tercero, B., et al. 2007, A&A, **466**, 255
 Demyk, K., Włodarczak, G., & Carvajal, M. 2008, A&A, **489**, 589
 Drouin, B. J., Maiwald, F. W., & Pearson, J. C. 2005, RScI, **76**, 093113
 Esplugues, G. B., Cernicharo, J., Viti, S., et al. 2013b, A&A, **559**, 51
 Esplugues, G. B., Tercero, B., Cernicharo, J., et al. 2013a, A&A, **556**, 143
 Favre, C., Despois, D., Brouillet, N., et al. 2011, A&A, **532**, A32
 Goldsmith, P. F., & Langer, W. D. 1999, ApJ, **517**, 209
 Haykal, I., Carvajal, M., Tercero, B., et al. 2013a, A&A, submitted
 Haykal, I., Margules, L., Huet, T. R., et al. 2013b, ApJ, **777**, 120
 Herbst, E. 1992, in Isotope Effects in Gas Phase Chemistry, ed. J. A. Kaye (Washington, DC: American Chemical Society), 358
 Ilyushin, V., Kryvda, A., & Alekseev, E. 2009, JMoSp, **255**, 32
 Karakawa, Y., Oka, K., Odashima, H., Takagi, K., & Tsunekawa, S. 2001, JMoSp, **210**, 196
 Kobayashi, K., Ogata, K., Tsunekawa, S., & Takano, S. 2007, ApJL, **657**, L17
 Kolesniková, L., Daly, A. M., Alonso, J. L., Tercero, B., & Cernicharo, J. 2013, JMoSp, **289**, 13
 Margulès, L., Coudert, L. H., Møllendal, H., et al. 2009a, JMoSp, **254**, 55
 Margulès, L., Huet, T. R., Demaison, J., et al. 2010, ApJ, **714**, 1120
 Margulès, L., Motienko, R., Demyk, K., et al. 2009b, A&A, **493**, 565
 Motienko, R. A., Tercero, B., Cernicharo, J., & Margulès, L. 2012, A&A, **548**, A71
 Nummelin, A., Bergman, P., Hjalmarson, A., et al. 2000, ApJS, **128**, 213
 Oesterling, L. C., Albert, S., De Lucia, F. C., Sastry, K. V. L. N., & Herbst, E. 1999, ApJ, **521**, 255
 Ogata, K., Odashima, H., Takagi, K., & Tsunekawa, S. 2004, JMoSp, **225**, 14
 Pardo, J. R., Cernicharo, J., & Serabyn, E. 2001, ITAP, **49**, 1683
 Persson, C. M., Olofsson, A. O. H., Koning, N., et al. 2007, A&A, **476**, 807
 Pickett, H. M., Poynter, R. L., Cohen, E. A., et al. 1998, JQSRT, **60**, 883
 Plummer, G. M., Herbst, E., De Lucia, F. C., & Blake, G. A. 1984, ApJS, **55**, 633
 Plummer, G. M., Herbst, E., De Lucia, F. C., & Blake, G. A. 1986, ApJS, **60**, 949
 Schilke, P., Benford, D. J., Hunter, T. R., Lis, D. C., & Phillips, T. G. 2001, ApJS, **132**, 281
 Schilke, P., Walmsley, C. M., Pineau Des Forets, G., et al. 1992, A&A, **256**, 595
 Tercero, B., Cernicharo, J., Pardo, J. R., & Goicoechea, J. R. 2010, A&A, **517**, A96
 Tercero, B., Kleiner, I., Cernicharo, J., et al. 2013, ApJL, **770**, L13
 Tercero, B., Margulès, L., Carvajal, M., et al. 2012, A&A, **538**, A119
 Tercero, B., Vincent, L., Cernicharo, J., Viti, S., & Marcelino, N. 2011, A&A, **528**, A26
 Tudorie, M., Coudert, L. H., Huet, T. R., Jegouso, D., & Sedes, G. 2011, JChPh, **134**, 074314
 Turner, B. E. 1991, ApJS, **76**, 617

Submillimeter spectra of 2-hydroxyacetonitrile (glycolonitrile; HOCH₂CN) and its searches in GBT PRIMOS observations of Sgr B2(N)[★]

L. Margulès¹, B. A. McGuire², M. L. Senent³, R. A. Motiyenko¹, A. Remijan², and J. C. Guillemin⁴

¹ Laboratoire de Physique des Lasers, Atomes, et Molécules, UMR CNRS 8523, Université de Lille I, 59655 Villeneuve d'Ascq Cedex, France

e-mail: laurent.margules@univ-lille1.fr

² National Radio Astronomy Observatory, Charlottesville, VA 22903, USA

³ Departamento de Química y Física Teóricas, Instituto de Estructura de la Materia, IEM-C.S.I.C., Serrano 121, 28006 Madrid, Spain

⁴ Institut des Sciences Chimiques de Rennes, École Nationale Supérieure de Chimie de Rennes, CNRS, UMR 6226, 11 allée de Beaulieu, CS 50837, 35708 Rennes Cedex 7, France

Received 18 March 2016 / Accepted 10 October 2016

ABSTRACT

Context. Recent experimental works have studied the possible formation of hydroxyacetonitrile on astrophysical grains. It was formed from hydrogen cyanide (HCN) and formaldehyde (H₂CO) in the presence of water under interstellar medium conditions. Because these precursor molecules are abundant, hydroxyacetonitrile is an excellent target for interstellar detection.

Aims. Previous studies of the rotational spectra were limited to 40 GHz, resulting in an inaccurate line list when predicted up to the millimeter-wave range. We measured and analyzed its spectra up to 600 GHz to enable its searches using cutting-edge millimeter and submillimeter observatories.

Methods. The molecule 2-hydroxyacetonitrile exhibits large amplitude motion that is due to the torsion of the hydroxyl group. The analysis of the spectra was made using the RAS formalism available in the SPFIT program with Watson's S-reduction Hamiltonians.

Results. The submillimeter spectra of hydroxyacetonitrile, an astrophysically interesting molecule, were analyzed. More than 5000 lines were fitted with quantum number values reaching 75 and 25 for J and K_a , respectively. An accurate line list and partition function were provided. A search for hydroxyacetonitrile in publicly available GBT PRIMOS project, IRAM 30 m, and *Herschel* HEXOS observations of the Sgr B2(N) high-mass star-forming region resulted in a non-detection; upper limits to the column density were determined.

Key words. ISM: molecules – methods: laboratory: molecular – submillimeter: ISM – molecular data – line: identification

1. Introduction

More than 30 nitriles (organic cyanides) have been observed to date in the interstellar medium (ISM). Among these are the well-known family of cyanopolyyynes, and isopropyl cyanide, the first branched hydrocarbon detected in the ISM (Belloche et al. 2014). This large dataset is useful in constraining models of nitrile formation in the ISM, and in predicting which other nitrile species might be present and detectable. However, many simple nitriles have yet to be detected. These non-detections could be due to a weak or null dipolar moment (for example cyanogen NCCN or 2-butyne-1,4-dinitrile NC–C≡C–CN) or to the lack of recorded microwave spectra caused by unknown or difficult syntheses of the target products. With the advent of state-of-the-art millimeter and submillimeter facilities like the Stratospheric Observatory for Infrared Astronomy (SOFIA) and the Atacama Large Millimeter/submillimeter Array (ALMA), laboratory studies of rotational spectra in this frequency range are critical for advancing the field. Such work will have to be followed by attempts, both in the laboratory and through theoretical

models, to understand formation processes and observed interstellar abundances (or upper limits).

The simplest cyanohydride, 2-hydroxyacetonitrile (glycolonitrile; HOCH₂CN), is readily formed in the lab by the addition of hydrogen cyanide (HCN) to formaldehyde (H₂CO) in water (Gaudry 1955). It is thought to play an important role in prebiotic chemistry, and could lead to the formation of a number of simpler organic molecules (Arrhenius et al. 1994). The formation of 2-hydroxyacetonitrile in astrophysical ices was first studied from a theoretical point of view (Woon 2001). Recently, its formation and photolytic decomposition on interstellar grains have been experimentally evaluated. These studies show that under these conditions, HCN reacts with H₂CO in the presence of H₂O to form HOCH₂CN (Danger et al. 2012, 2014). Although not studied, the hydrogen-atom bombardment of formyl cyanide (HC(=O)CN) could also lead to the formation of HOCH₂CN, as could do the reaction of CN or OH with H₂COH or CH₂CN, respectively. Photochemistry of pure HOCH₂CN leads to the formation of HC(=O)CN, HCN, ketenimine (H₂C=C=NH), H₂CO, CO, and CO₂ (Danger et al. 2013). It should be noted that most of the compounds cited as possible precursors or as photoproducts have been detected in the ISM.

* Hydroxyacetonitrile fit is only available at the CDS via anonymous ftp to cdsarc.u-strasbg.fr (130.79.128.5) or via <http://cdsarc.u-strasbg.fr/viz-bin/qcat?J/A+A/601/A50>

The gas-phase, infrared spectrum of HOCH₂CN has been recently reinvestigated (Chrostowska et al. 2015), while the microwave spectrum of HOCH₂CN has not been treated since it was first observed by Cazzoli et al. (1973) from 8–40 GHz. The gauche rotamer has been observed. Doublets of the rotational transitions were observed arising from tunneling between the two equivalent gauche rotamers. The rotational constants indicate that the angle between the HOC and OCC planes at the potential minima is approximately 123° from the *trans* position, while the rotational constants calculated from a molecular model, and the potential functions, indicate that this angle is likely closer to 116°.

New spectra were measured in Lille in the range 150–600 GHz, and combined with high-level ab initio calculations for an accurate analysis. A search of the publicly available GBT PRIMOS project, IRAM 30 m, and *Herschel* HEXOS observations of Sgr B2(N) for the molecule found no evidence for a cold population of the species, and upper limits were established.

2. Experiments

2.1. Synthesis

HOCH₂CN has been prepared as previously reported (Gaudry 1947, 1955).

2.2. Lille – submillimeter spectra

The measurements from 50–660 GHz were performed using the Lille spectrometer (Zakharenko et al. 2015). A quasi-optic dielectric hollow waveguide, 3 m in length, containing HOCH₂CN was used as the sample cell in the spectrometer. The measurements were typically performed at pressures of 10 Pa and at room temperature. The frequency ranges of 50–315 and 400–550 GHz were covered with various active and passive frequency multipliers where an Agilent synthesizer (12.5–18.25 GHz) was used as the source of radiation. Estimated uncertainties for measured line frequencies are 30 kHz and 50 kHz depending on the observed signal-to-noise ratio and the frequency range.

3. Theoretical calculations

High-level ab initio calculations were used to determine the geometries of the two conformers, *gauche* and *trans*, and to compute low-energy torsional levels. Electronic structure calculations were performed using both the MOLPRO (Werner et al. 2012) and GAUSSIAN packages (Frisch et al. 2009). The torsional energy levels were determined by variational calculations using the procedure previously employed for other non-rigid species (Senent 2004).

The equilibrium structures, *gauche* and *trans*, of HOCH₂CN, as well as the most relevant spectroscopic parameters (equilibrium rotational constants and the one-dimensional potential energy surface, 1D-PES, for the hydroxyl torsion) were computed using explicitly correlated coupled cluster theory with single and double substitutions augmented by a perturbative treatment of triple excitations (CCSD(T)-F12b) (Knizia et al. 2009; Werner et al. 2007) with an aug-cc-pVTZ basis set (Kendall et al. 1992). Second-order Möller-Plesset theory (MP2) was employed to determine vibrational corrections for the potential energy surface and the α_j^r vibration-rotation constants. For the explicitly correlated calculations, the MOLPRO default options were selected.

Table 1. Calculated ground-state rotational constants (MHz), energies and conformational barriers (cm^{-1}), and dipole moments (Debye) for HOCH₂CN.

Parameter	<i>gauche</i> -HOCH ₂ CN	<i>trans</i> -HOCH ₂ CN
A_0	33 621.46	35 519.53
B_0	4828.88	4833.28
C_0	4370.77	4369.98
ΔE		506.3
$V(\text{gauche-gauche})$		425.8
$V(\text{gauche-trans})$		645.4
μ	2.94	
μ_a	2.32	
μ_b	1.31	
μ_c	1.23	

The ground vibrational state rotational constants of the two conformers were determined from the equilibrium parameters using Eq. (1) (cf. Senent et al. 2015)

$$B_0 = B_e + \Delta B_e^{\text{core}} + \Delta B_{\text{vib}}, \quad (1)$$

where ΔB_e^{core} represents the core-valence correlation correction and ΔB_{vib} is the vibrational contribution to the rotational constants derived from the vibration-rotation interaction parameters. The results are shown in Table 1.

The low torsional energy levels were calculated using a variational solution to the Hamiltonian given in Eq. (2) (Senent 1998a,b):

$$\hat{H}(\alpha) = -\left(\frac{\partial}{\partial \alpha}\right) B_\alpha \left(\frac{\partial}{\partial \alpha}\right) + V^{\text{eff}}(\alpha). \quad (2)$$

Here, α is the OH torsional coordinate, B_α are the kinetic energy parameters, and $V^{\text{eff}}(\alpha)$ is the vibrationally corrected 1D-PES (Császár et al. 2004) shown in Fig. 1.

The ground vibrational state splits into two components $E(0^-)$ and $E(0^+)$ because of tunneling in the $V(\text{gauche-gauche})$ barrier. Ab initio calculations predict a splitting of 96 563.148 MHz (3.2210 cm^{-1}). In addition, the first excited vibrational state shows two components lying at 223.05 cm^{-1} (1^+) and 261.27 cm^{-1} (1^-) over the ground state. The first *trans* level lies at 459 cm^{-1} (0).

4. Analysis of the spectra

We have analysed the spectra of the *gauche* conformer, which is the more stable of the two. This analysis was not trivial because the *gauche* rotamer exhibits one large amplitude motion (LAM) with a symmetric two minima potential due to the two equivalent gauche rotamers. As a result of tunneling through the barrier to OH-group torsion, the ground state is split into two substates: 0^- and 0^+ . This rotamer is very close to a symmetric prolate rotor with an asymmetry parameter $\kappa = -0.968$. Like other nitriles, the dipole moment is large; the values we determined from MP2/aug-cc-pVTZ ab initio calculations and are given in Table 1. The component along the *c*-axis of the dipole moment is linked to torsional motion, giving rise to transitions between the two torsional substates 0^- and 0^+ .

An initial prediction of the spectra was made for the two substates 0^- and 0^+ separately with Watson's Hamiltonian in the I' representation using the rotational parameters from

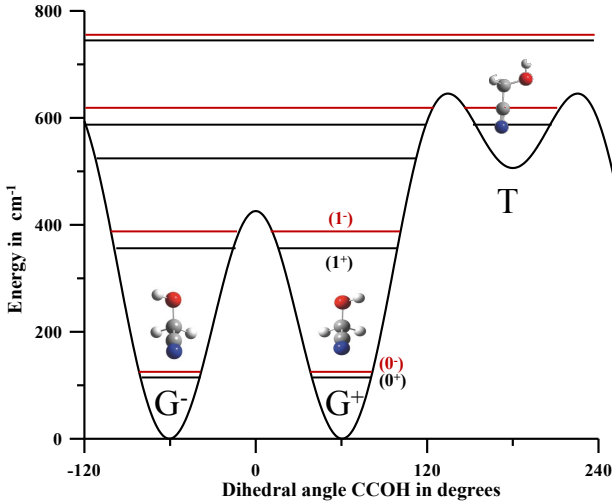


Fig. 1. CCSD(T)-F12 potential energy as a function of the hydroxyl group internal rotation coordinate.

Cazzoli et al. (1973) and the quartic centrifugal distortion constants obtained from the harmonic force field at the MP2/aug-cc-pVTZ level of theory. We first assign the A-type, R-branch transitions, which are the brightest in our spectra. Owing to the rather strong interaction between these two sublevels, it was not possible to assign and fit data even for $K_a = 0$ and 1 transitions in the lower range of the spectra 150–315 GHz. Some less perturbed levels were found above 400 GHz, and an assignment and fit was possible by treating the two sublevels separately for K_a values up to 2 in the 400–500 GHz range, improving the values of the rotational and the centrifugal distortion constants. The two sublevels were then merged in a unique fit, using the energy difference between the 0^- and 0^+ levels determined by Cazzoli et al. (1973) as the starting point. We note that this value, 110 700 MHz, is close to the one we determined, 112 672.5526(30) MHz.

For the global fit, a model based on the reduced axis system (RAS) approach proposed by Pickett (1972) was implemented in the widely used SPFIT/SPCAT programs for fitting and predicting molecular spectra. We have successfully employed this method in previous studies showing the same kind of double minimum LAM (Motiyenko et al. 2010, 2015; Smirnov et al. 2013). It has been shown by Christen et al. (2002) that the RAS formalism is equivalent to the IAM approaches developed by Hougen and coworkers for molecules with several large amplitude motions (Hougen 1985; Couder & Hougen 1988).

The perturbation terms in the RAS Hamiltonian are equivalent in this case to off-diagonal Coriolis coupling terms; the Hamiltonian used has the form given in Eq. (3):

$$H = H_R + H_C. \quad (3)$$

More details about the exact expression of the Hamiltonian can be found in Christen & Müller (2003). In that work, they also proposed the use of average rotational constants for both substates introducing a Hamiltonian for centrifugal distortion corrections, given in Eq. (4),

$$H_R = H_S + H_\Delta, \quad (4)$$

where H_R is the standard Watson S-reduction Hamiltonian in the I' coordinate representation and H_Δ defined in Eq. (5),

$$H_\Delta = E^* + E^* J^2 + E_K^* J_z^2 + E_2^* (J_+^2 + J_-^2) + \dots, \quad (5)$$

where E^* is a half energy difference between two A or B levels ($\Delta E = 2E^*$), and J , J_z , and $J_\pm = J_x \pm iJ_y$ are the rotational angular momentum operator and its components. This procedure has two main advantages. First, a unique set of rotational and centrifugal distortion parameters permits an easier comparison with ab initio calculations. Second, this method is more robust and avoids correlations between different rotational and Coriolis coupling parameters.

Including the F_{2ac} parameter slightly decreases the standard deviation of fit from 29.2 kHz (wrms: 0.931) to 28.5 kHz (wrms: 0.907), and it seems to be determined: $-0.0967(82)$. Looking closely, however, including F_{2ac} has several negative consequences on the fit. Ten lines were rejected from the fit after including F_{2ac} . We also notice a strong influence on F_{acK} : its values change from 0.009943(25) to 0.00304(59) when fitting F_{2ac} . This influence is confirmed by looking at the correlation coefficient; there is almost full correlation with F_{ac} , F_{acJ} , and F_{acK} , with coefficients of -0.996 , -0.990 , and 0.999 , respectively. We have thus decided to keep F_{2ac} fixed to zero in the final fit. The final set of parameters obtained are in Table 2. In total, 5128 distinct lines were assigned with maximum values for J and K_a of 75 and 25, respectively. Part of the new measurements are in Table 3. Owing to its large size, the complete version of the global fit Table (S1) is supplied at the CDS¹. The fitting files .lin (S2), .par (S3), and the prediction .cat (S4) are also available at CDS.

5. Observations

We have conducted a search of the publicly available Prebiotic Interstellar Molecular Survey (PRIMOS) project observations of the high-mass star-forming region Sgr B2(N) for a signal from HOCH₂CN. PRIMOS is a near-frequency continuous, 1–50 GHz broadband molecular line survey conducted with the Robert C. Byrd Green Bank Telescope (GBT), and centered on the Large Molecular Heimat at (J2000) $\alpha = 17^\text{h}47^\text{m}19^\text{s}8$, $\delta = -28^\circ22'17''$. Full observational and data-reduction details are given in Neill et al. (2012); the entire dataset is accessible online². The PRIMOS observations vary in RMS noise level from $\sim 3\text{--}8$ mK across the band; however, we find no evidence for emission or absorption from HOCH₂CN in the survey. Below, we establish upper limits to the column density for a variety of physical conditions, and briefly discuss the possibilities for future searches for this molecule.

We follow the convention of Hollis et al. (2004) using Eq. (6) to calculate an upper limit to column density N_T , given a rotational partition function Q , upper state energy E_U , rotational temperature T_r , transition frequency v , intrinsic line strength $S\mu^2$, observed intensity ΔT_A^* , linewidth ΔV , telescope efficiency η_B , and background temperature T_{bg} :

$$N_T = \frac{QE_u/kT_r}{\frac{8\pi^3}{3k}vS\mu^2} \times \frac{\frac{1}{2}\sqrt{\frac{\pi}{\ln(2)}}\frac{\Delta T_A^*\Delta V}{\eta_B}}{1 - \frac{e^{hv/kT_r}-1}{e^{hv/kT_{bg}}-1}}. \quad (6)$$

The structure of Sgr B2(N) is complex, with a compact ($\sim 5''$) hot molecular core surrounded by a more extended, colder molecular shell (Hollis et al. 2007). The background continuum structure against which molecules in this shell absorb is $\sim 20''$ in diameter (see, e.g., Fig. 3b of Mehringer et al. 1993). For the purposes of this study, we assume these same source sizes for warm molecular material and cold molecular material and explicitly calculate

¹ <http://cdsweb.u-strasbg.fr/A+A.htm>

² www.cv.nrao.edu/PRIMOS

Table 2. Spectroscopic parameters of the *gauche* conformer of 2-hydroxyacetonitrile.

Parameters in MHz	This work	Cazzoli et al. ^a	Theory ^b
Rotational and centrifugal distortion constants			
<i>A</i>	33 609.53194(27) ^c	0 ⁻ : 33 605.57(22) 0 ⁺ : 33 611.68(22)	33 621.46
<i>B</i>	4838.014347(41)	0 ⁻ : 4840.44(4) 0 ⁺ : 4835.51(4)	4828.88
<i>C</i>	4377.304462(40)	0 ⁻ : 4377.60(3) 0 ⁺ : 4376.44(3)	4370.77
$D_J * 10^3$	3.093051(44)	2.7 (0.8)	3.079
$D_{JK} * 10^3$	-63.89803(34)	-81 (5)	-65.329
$D_K * 10^3$	969.2208(61)		958.548
$d_1 * 10^3$	-0.695725(10)		-0.68705
$d_2 * 10^3$	-0.041757(18)		-0.03659
$H_J * 10^6$	0.0107392(81)		
$H_{JK} * 10^6$	-0.16090(71)		
$H_{KJ} * 10^6$	-3.6005(17)		
$H_K * 10^6$	82.883(56)		
$h_1 * 10^6$	0.0044035(40)		
$h_2 * 10^6$	0.0005288(27)		
$h_3 * 10^6$	0.00007335(95)		
$L_K * 10^9$	-3.14(17)		
$L_{KKJ} * 10^9$	0.3292(25)		
$L_{JK} * 10^9$	-0.04864(29)		
$L_{JJK} * 10^9$	0.001496(12)		
$L_J * 10^9$	-0.00005190(75)		
$l_1 * 10^9$	-0.00002619(46)		
$l_2 * 10^9$	-0.00000544(39)		
$l_3 * 10^9$	-0.00000236(17)		
Tunneling splitting constants			
<i>E</i>	112 672.5526(30)	110 700 fixed	96563.148 ^d
E_J	1.0954348(39)		
E_K	-13.606157(53)		
$E_{JJ} * 10^3$	-0.00749(11)		
$E_{JK} * 10^3$	-0.19132(72)		
$E_{KK} * 10^3$	0.44739(78)		
E_2	0.331606(22)		
$E_{2J} * 10^3$	-0.0073918(30)		
$E_{2K} * 10^3$	1.339(22)		
$E_{2JJ} * 10^9$	0.07826(71)		
$E_{2JK} * 10^9$	-21.80(20)		
$E_4 * 10^6$	-5.215(60)		
$E_{4J} * 10^9$	0.1756(13)		
Coriolis coupling constants			
F_{bc}	-5.7926(14)		
$F_{bcK} * 10^3$	43.41(74)		
$F_{bcJ} * 10^3$	-0.113411(86)		
$F_{bcKK} * 10^6$	-19.08(43)		
$F_{bcJK} * 10^6$	0.4789(72)		
$F_{2bc} * 10^6$	86.5(14)		
F_{ac}	75.52596(18)		
$F_{acI} * 10^3$	-0.05771(28)		
$F_{acK} * 10^3$	9.943(25)		
$F_{acJK} * 10^6$	0.485(16)		
$F_{acKK} * 10^6$	-9.229(30)		
Number of distinct lines			5128
Number of parameters			47
$J''_{\max}, K''_{a,\max}$			75, 25
Standard deviation of the fit (in kHz)			29.2
Weighted deviation of fit			0.931

Notes. ^(a) Cazzoli et al. (1973). ^(b) Calculated using CCSD(T)-F12 theory and the MP2/aug-cc-pVTZ anharmonic force field. ^(c) Number in parentheses is one standard deviation in unit of the last digit. ^(d) Calculated by solving variationally the Hamiltonian, see text for details.

Table 3. Measured frequencies of the *gauche* conformer of 2-hydroxyacetonitrile and residuals from the fit (full fit is available at the CDS: S1).

J''	Upper level		v''^a	J'	Lower level		Frequency(Unc.)	o.-c.
	K''_a	K''_c			K'_a	K'_c	(in MHz)	(in MHz)
75	0	75	1	74	1	74	657 112.073(0.030)	-0.0230
75	1	75	1	74	0	74	657 112.073(0.030)	-0.0230
18	9	9	1	17	8	10	657 168.387(0.030)	0.041
18	9	10	1	17	8	9	657 168.387(0.030)	0.041
44	10	35	1	44	9	35	657 260.517(0.030)	0.002
43	10	34	1	43	9	34	657 600.923(0.030)	0.027
12	8	4	1	11	7	4	658 010.623(0.030)	0.035
12	8	5	1	11	7	5	658 010.623(0.030)	0.035
36	10	27	1	36	9	27	659 576.402(0.030)	0.057
28	14	15	0	28	13	15	659 608.388(0.030)	-0.059
35	10	26	1	35	9	26	659 806.414(0.030)	0.017
25	6	19	1	24	5	19	659 980.141(0.030)	-0.022

Notes. ^(a) Following SPFIT format the torsional substate 0^- and 0^+ are labeled 0 and 1, respectively.

the spatial overlap of these regions with the GBT beam as its size varies across the frequency coverage.

Hollis et al. (2007) establish the background continuum temperature at 85 points across the PRIMOS frequency coverage. These continuum measurements range from more than 100 K at low frequencies to just above the CMB at the higher frequencies, although these measurements are not corrected for any assumed source geometry or beam dilution effects. The authors attribute this to non-thermal continuum in the source. We adopt their measurements of the continuum for these calculations, but correct them for the overlap of the assumed source size of the continuum-emitting region with the GBT beam in the PRIMOS observations.

The tabulated values for the partition function are given in Table 4, with $Q_{\text{tot}}(T) = Q_{\text{vib}}(T)Q_{\text{rot}}(T)$. The rotational partition function is calculated at each temperature by direct state counting according to Eq. (7) (Gordy & Cook 1984):

$$Q_r = \frac{1}{\sigma} \sum_{J=0}^{J=\infty} \sum_{K=-J}^{K=J} (2J+1)e^{-E_{J,K}/kT_{\text{ex}}} \quad (7)$$

The vibrational partition function was calculated with respect to the zero-point level using the expression:

$$Q(T)_{\text{vib}} = \prod_{i=1}^{3N-6} \frac{1}{1 - e^{-E_i/kT}} \quad (8)$$

The four lowest vibrational excited states levels were considered. The remaining ones above 885 cm^{-1} were found to have no influence on the partition function calculations. Their frequencies are respectively 228 cm^{-1} (328 K), 246 cm^{-1} (354 K), 343 cm^{-1} (494 K), and 576 cm^{-1} (829 K); these values were taken from Chrostowska et al. (2015).

Finally, we assume that the excitation of all HOCH₂CN can be described by a single rotational temperature. We do not, however, make the assumption that this temperature is described by local thermodynamic equilibrium (LTE), meaning that the excitation temperature is not thermalized to the kinetic temperature of the gas. This approach has previously proven to be successful in modeling both the emission and absorption of molecules in PRIMOS observations (Hollis et al. 2004; Loomis et al. 2013; McGuire et al. 2016). We note, however,

that several other molecules exhibit populations which cannot be described by a single excitation temperature (McGuire et al. 2012; Faure et al. 2014), and thus care should be taken to examine any single-excitation temperature results on a case-by-case basis.

In addition to the PRIMOS observations, we have also examined publicly available surveys of Sgr B2(N) from Belloche et al. (2013) [IRAM 30 m: 80–116 GHz] and Neill et al. (2014) [Herschel HEXOS: 480–600 GHz]. No compelling evidence for HOCH₂CN is found in either survey. With the exception of the warm (200 K), extended (200'') population, the upper limits established by the PRIMOS data are not changed by more than ~10% due to greater noise in the higher-frequency data, compared to PRIMOS.

Table 5 shows the upper limits calculated here for several different common populations of species. The given values represent the best limits achievable across all three datasets. It is immediately clear that the PRIMOS observations are most sensitive to cold populations of HOCH₂CN, with the established upper limits several orders of magnitude lower than for warmer excitation conditions. This occurs because for relatively large, complex species such as HOCH₂CN, which have large partition functions, any significant level of excitation pushes the Boltzmann peak into the mm and sub-mm regimes, resulting in low spectral intensities in the region of PRIMOS coverage. Our searches at higher frequencies suffered greatly from more heavily line-confusion-limited spectra; ALMA observations of the region are likely the only method for spatially filtering this confusion.

The first detection of methyl isocyanate (CH₃NCO), a structural isomer of HOCH₂CN, has recently been reported in Sgr B2(N) by Halfen et al. (2015) in a cold, extended population ($T_r \sim 26 \text{ K}$, $N_T \sim 2 \times 10^{13} \text{ cm}^{-2}$) in two velocity components. A second warmer population ($T_r \sim 200 \text{ K}$, $N_T \sim 4 \times 10^{17} \text{ cm}^{-2}$) was subsequently identified by Cernicharo et al. (2016) in two velocity components. For comparison, we have calculated upper limits for HOCH₂CN under these excitation conditions, as well.

For the warm population of Cernicharo et al. (2016), the CH₃NCO:HOCH₂CN ratio is $>1000:1$. The ratio for the colder population of Halfen et al. (2015) is, conversely, $>1:1$. If the same formation pathways are in effect for both the warm and cold populations, the upper limit established for the cold

Table 4. Rotational and vibrational partition functions at various temperatures.

T (K)	$Q(T)_{\text{rot}}$	$Q(T)_{\text{vib}}$
300	65 208.5016	2.8710
225	42 282.4022	1.8981
150	22 866.7336	1.2971
75	7939.2463	1.0233
37.5	2713.8889	1.0002
18.75	901.1494	1.0000
9.375	285.4325	1.0000

Table 5. Upper limits to HOCH₂CN column density in PRIMOS, IRAM, and *Herschel* HEXOS observations toward Sgr B2(N) for several common conditions.

T_r (K)	Source size (")	Upper limit column density (cm^{-2})
8	20	8×10^{12}
18	20	8×10^{13}
26 ^b	200 ^b	2×10^{13}
80	5	2×10^{15}
130	5	4×10^{15}
200	5	8×10^{15}
200 ^b	200 ^b	7×10^{14}

Notes. ^(a) We estimate the uncertainties in the upper limits to be ~30%, largely arising from absolute flux calibration and pointing uncertainties. ^(b) Values were chosen for comparison to CH₃NCO detection from Halfen et al. (2015) and Cernicharo et al. (2016). A source size of 200" follows the assumption that the source completely fills the beam.

population is likely closer to $\sim 10^{10} \text{ cm}^{-2}$. In this case, the best-case scenario for detection is likely through masering action in low-frequency transitions. Such emission enhancement has been seen in this source (Faure et al. 2014), and has indeed been used to detect extremely low-abundance species (e.g., carbodiimide, HNCNH; McGuire et al. 2012).

6. Conclusion

The spectra of 2-hydroxyacetonitrile, a molecule expected to have a role in prebiotic chemistry, were measured and analyzed up to 600 GHz. The assignment of the spectra was not obvious owing to large amplitude motion of the OH group, but was aided by high-level ab initio calculations. With the newly constrained constants, the fit and predictions are now accurate throughout the millimeter and submillimeter regions. These results enabled its search in the GBT PRIMOS survey toward Sgr B2(N). No cold population was detectable; however, the possibility of a warmer population remains, and upper limits were established.

Acknowledgements. This work was supported by the Programme National "Physique et Chimie du Milieu Interstellaire" and the Centre National d'Études

Spatiales (CNES). This work was also done under ANR-13-BS05-0008-02 IMO-LABS. B.A.M. is a Jansky Fellow of the National Radio Astronomy Observatory. The National Radio Astronomy Observatory is a facility of the National Science Foundation operated under cooperative agreement by Associated Universities, Inc.

References

- Arrhenius, T., Arrhenius, G., & Paplawsky, W. 1994, *Origins of life and evolution of the biosphere*, 24, 1
- Belloche, A., Garrod, R. T., Müller, H. S. P., & Menten, K. M. 2014, *Science*, 345, 1584
- Cazzoli, G., Lister, D. G., & Mirri, A. M. 1973, *J. Chem. Soc., Faraday Trans. 2*, 69, 569
- Christen, D., & Müller, H. S. P. 2003, *Phys. Chem. Chem. Phys.*, 5, 3600
- Christen, D., Müller, H. S. P., & Coudert, L. H. 2002, 57th International Symposium on Molecular Spectroscopy, TB03
- Chrostowska, A., Darrigan, C., Dargelos, A., Benidar, A., & Guillemin, J.-C. 2015, *Chem. Phys. Chem.*, 16, 3660
- Coudert, L. H., & Hougen, J. T. 1988, *J. Mol. Spectr.*, 130, 86
- Császár, A. G., Szalay, V., & Senent, M. L. 2004, *J. Chem. Phys.*, 120, 1203
- Danger, G., Duvernay, F., Theulé, P., Borget, F., & Chiavassa, T. 2012, *ApJ*, 756, 11
- Danger, G., Duvernay, F., Theulé, P., et al. 2013, *A&A*, 549, A7
- Danger, G., Rimola, A., Abou Mrad, N., et al. 2014, *Phys. Chem. Chem. Phys.*, 16, 3360
- Faure, A., Remijan, A. J., Szalewicz, K., & Wiesenfeld, L. 2014, *ApJ*, 783, 72
- Frisch, M., Trucks, G., Schlegel, H., et al. 2009, Gaussian software, version 09, revision D01
- Gaudry, R. 1947, *Organic Syntheses*, 27, 41
- Gaudry, R. 1955, *Organic Syntheses*, Coll. 3, 436
- Gordy, W., & Cook, R. L. 1984, Microwave molecular spectra, 3rd edn. (New York: Wiley)
- Hollis, J., Jewell, P., Remijan, A. J., & Lovas, F. 2007, *ApJ*, 660, L125
- Hollis, J. M., Jewell, P., Lovas, F., & Remijan, A. 2004, *ApJ*, 613, L45
- Hougen, J. T. 1985, *J. Mol. Spectr.*, 114, 395
- Kendall, R. A., Dunning Jr, T. H., & Harrison, R. J. 1992, *J. Chem. Phys.*, 96, 6796
- Knizia, G., Adler, T. B., & Werner, H.-J. 2009, *J. Chem. Phys.*, 130, 054104
- Loomis, R. A., Zaleski, D. P., Steber, A. L., et al. 2013, *ApJ*, 765, L9
- McGuire, B. A., Loomis, R. A., Charness, C. M., et al. 2012, *ApJ*, 758, L33
- McGuire, B. A., Carroll, P. B., Loomis, R. A., et al. 2016, *Science*, 352, 1449
- Mehringer, D. M., Palmer, P., Goss, W., & Yusef-Zadeh, F. 1993, *ApJ*, 412, 684
- Motiyenko, R. A., Margulès, L., Goubet, M., et al. 2010, *J. Phys. Chem. A*, 114, 2794
- Motiyenko, R. A., Margulès, L., Alekseev, E. A., & Guillemin, J.-C. 2015, *J. Phys. Chem. A*, 119, 1048
- Neill, J. L., Muckle, M. T., Zaleski, D. P., et al. 2012, *ApJ*, 755, 153
- Pickett, H. M. 1972, *J. Chem. Phys.*, 56, 1715
- Senent, M. 1998a, *J. Mol. Spectr.*, 191, 265
- Senent, M. 1998b, *Chem. Phys. Lett.*, 296, 299
- Senent, M. 2004, *J. Phys. Chem. A*, 108, 6286
- Senent, M., Dalbouha, S., Cuisset, A., & Sadovskii, D. 2015, *J. Phys. Chem. A*, 119, 9644
- Smirnov, I., Alekseev, E., Piddyachiy, V., Ilyushin, V., & Motiyenko, R. 2013, *J. Mol. Spectr.*, 293, 33
- Werner, H., Knowles, P., Knizia, G., et al. 2012, MOLPRO, version 2012.1, a package of ab initio programs, see <http://www.molpro.net>
- Werner, H.-J., Adler, T. B., & Manby, F. R. 2007, *J. Chem. Phys.*, 126, 164102
- Woon, D. E. 2001, *Icarus*, 149, 277
- Zakharenko, O., Motiyenko, R. A., Margulès, L., & Huet, T. R. 2015, *J. Mol. Spectr.*, 317, 41



1,3-Propanediol millimeter wave spectrum: Conformers I and II



I.A. Smirnov^a, E.A. Alekseev^a, V.I. Piddyachiy^a, V.V. Ilyushin^{a,*}, R.A. Motienko^b

^aInstitute of Radio Astronomy of NASU, Chervonopraporna St., 4, 61002 Kharkov, Ukraine

^bLaboratoire de Physique des Lasers, Atomes et Molécules, UMR CNRS 8523, Université de Lille 1, F-59655 Villeneuve d'Ascq, France

ARTICLE INFO

Article history:

Received 6 August 2013

In revised form 18 September 2013

Available online 18 October 2013

Keywords:

1,3-Propanediol

Millimeter wave spectrum

Coriolis coupling

Tunneling splittings

ABSTRACT

We present a new study of the millimeter wave spectrum of the lowest two conformers of the 1,3-propanediol ($\text{CH}_2\text{OHCH}_2\text{CH}_2\text{OH}$) molecule. The new measurements involving rotational transitions with J up to 65 and K_a up to 30 for conformer I and J up to 59 and K_a up to 29 for conformer II have been carried out between 49 and 237 GHz using the Kharkov millimeter wave spectrometer. The new data were combined with previously published measurements and fitted using a model that assumes a symmetric potential energy surface with two minima between which the system tunnels. The final fit included 19 parameters for conformer I and 23 parameters for conformer II with weighted root-mean-square deviations of 0.81 and 0.73 achieved for datasets consisting of 3384 and 2947 line frequencies belonging to the ground states of conformer I and conformer II, respectively. The millimeter wave spectra of both conformers reveal a rather strong influence of the Coriolis type perturbation, which previously was not taken into account in the analysis of the 1,3-propanediol spectrum.

© 2013 Elsevier Inc. All rights reserved.

1. Introduction

Propanediols attract spectroscopic attention as possible new candidates for interstellar detection since they are the derivatives of ethylene glycol ($\text{CH}_2\text{OHCH}_2\text{OH}$), which was detected towards the interstellar molecular cloud in Sgr B2 (N-LMH) [1]. The two forms of propanediol, namely, 1,2-propanediol and 1,3-propanediol, have been recently studied using FTMW spectroscopy methods [2,3] with the upper frequency limit of these investigations being 25 GHz. Earlier studies of both propanediol forms provide data with the upper frequencies of 40 GHz for 1,2 propanediol [4] and 78 GHz for 1,3-propanediol [5]. An interstellar search for the 1,3-propanediol conformer I was made as a part of the Green Bank Telescope (GBT) Prebiotic Interstellar Molecule Survey (PIMOS) Legacy Project and no transitions were detected beyond the 1-sigma rms noise limit [3]. The present study is aimed at extending the investigated frequency range for 1,3-propanediol and providing a reliable basis for further interstellar searches of this molecule at higher frequencies and in hot cores.

1,3-Propanediol exists in a form of several low-energy conformers [3,5] and in the present study we concentrated our attention on the two most stable conformers I and II (see Fig. 1). Rotational spectra of both conformers show additional splittings due to tunneling between two structurally chiral forms which is associated with the concerted rotation of the two OH groups [3]. Possible pathways for such interconversions in 1,3-propanediol molecule

were analyzed in Ref. [3] based on high level ab initio calculations. Analogous interconversion between structurally chiral forms was observed for example in ethylene glycol molecule [6–8] or in conformer V of glycerol [9]. To accommodate additional splittings observed in the spectrum, a model assuming a symmetric double minimum potential surface was used where the lowest two inversion substates O^+ and O^- are split by some amount [3]. Although a considerable Coriolis interaction between the two tunneling substates may be expected from the studies of related ethylene glycol molecule [8] this coupling was not taken into account in the theoretical models used in previous studies of 1,3-propanediol spectrum. Our current results show that the Coriolis interaction between the two tunneling substates in the spectra of the two most stable conformers I and II of 1,3-propanediol is very important and may affect the results of astronomical search for this molecule.

1.1. Experimental details

1,3-Propanediol sample has been purchased from Fluka and used without further purification. To provide sufficient vapor pressure the sample was heated up to 75 °C. The new measurements for 1,3-propanediol spectrum were made in the frequency range from 49 to 149 GHz and from 202 to 237 GHz using the automated millimeter wave spectrometer of IRA NASU [10]. The synthesis of the frequencies in the millimeter wave range is carried out by a two-step frequency multiplication of the reference synthesizer in two phase-lock-loop (PLL) stages. As the reference synthesizer a computer-controlled direct digital synthesizer (DDS AD9851) is

* Corresponding author. Fax: +380 57 706 1415.

E-mail address: ilyushin@rian.kharkov.ua (V.V. Ilyushin).

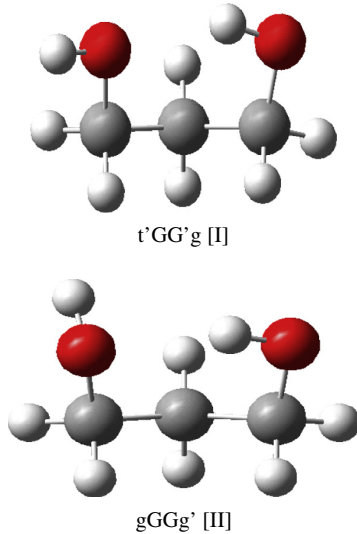


Fig. 1. The structures of conformer I and conformer II of the 1,3-propanediol molecule that were studied in our work (adapted from Ref. [3]).

employed whose output is up-converted into the frequency range from 385 to 430 MHz. At the first multiplication stage a klystron operating in the 3400–5200 MHz frequency range with a narrow-band (~ 1 kHz) PLL system is used. At the second multiplication stage, a set of Istok backward wave oscillators (BWO) locked to a harmonic of the klystron is used. The set of available BWO's covers the frequency range from 49 to 149 GHz. For the measurements from 202 to 237 GHz a self-made Shottky diode frequency doubler was used. The uncertainty of the measurements was estimated to be 10 kHz for a relatively strong isolated line ($S/N > 10$), 30 kHz for weak lines ($2 < S/N \text{ ratio} < 10$) and 100 kHz for very weak lines ($S/N < 2$).

1.2. Spectral analysis and fit

Our initial analysis was based on the results of the previous work [3] which gave an opportunity to make first tentative assignments of observed spectrum for both conformers relatively

easy. As it was already shown in Refs. [3,5] the a-type transitions of the conformer I and II are split because of tunneling between two equivalent configurations, whereas b- and c-type transitions have very little splitting or do not have it at all. Thus, a model assuming a symmetric potential energy surface with two minima between which the system tunnels was necessary for the analysis of the observed spectrum. The tunneling between two equivalent configurations is related to the concerted rotation of OH groups in the molecule [3]. Following Ref. [3] the system was modeled by two inversion substates O^+ and O^- split by some amount where b- and c-type transitions were assigned as rotational transitions within each inversion substate and a-type transitions were assigned as transitions that crossed between the inversion substates. As in Ref. [3] we used Pickett's SPFIT/SPCAT programs for spectral analysis [11] and at the initial stage of our study we used separate sets of rotational parameters for each inversion substate.

First, we decided to concentrate our efforts on conformer I since this is the lowest energy conformer of the molecule and the strongest transitions observed in the spectrum belong to this conformer. Although the results of the previous studies [3,5] made it possible to find some correspondence between predicted and observed line positions, assignment problems were encountered already for low K_a transitions. These problems are illustrated in Fig. 2, where a fragment of the recorded spectrum of 1,3-propanediol is compared with predictions obtained for conformer I using the results of Ref. [3] (Fig 2a) and our results (Fig 2c). As it can be seen from Fig. 2 there is a specific multiplet observed in the spectrum (curve 2b) that consists of two triplets of lines. At the same time the predictions based on the results of Ref. [3] (see curve 2a) assume a multiplet of somewhat different form. Whereas the shifts in line positions may be explained by extrapolation errors the distribution of intensities between the components of the multiplet posed a problem. Careful consideration of the situation showed that the source of the problem is Coriolis interaction between the two tunneling substates. In both Refs. [3,5] the Coriolis interaction was neglected and perturbed transitions were excluded from the fits [3,5]. Since the number of perturbed transitions in the datasets of [3,5] was rather small and since observed Coriolis perturbation at low frequencies gives relatively small frequency shifts such an approach seemed quite reasonable. Nevertheless, at higher frequencies, where considerable distortions in the spectrum are caused by Coriolis interaction, it was not possible to neglect this

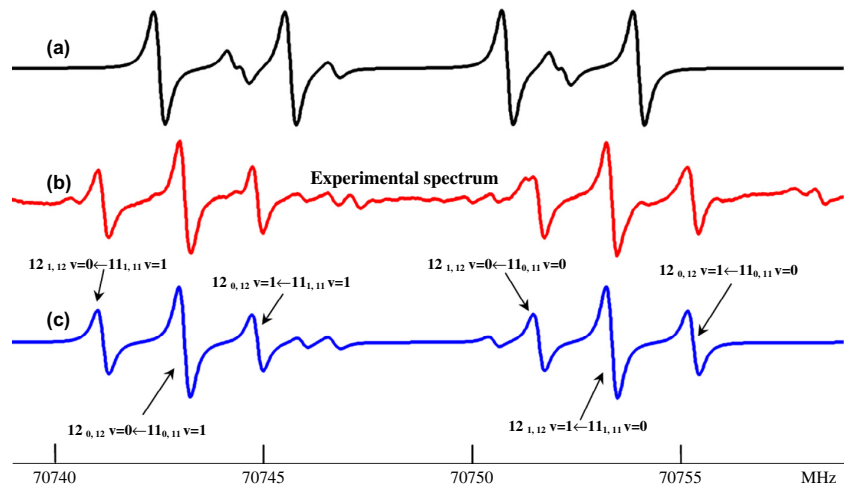


Fig. 2. Fragment of the 1,3-propanediol conformer I spectrum near 70.7 GHz. (a) Predicted spectrum based on the results of Ref. [3]; (b) experimental spectrum obtained in this work using the automated spectrometer of IRA NASU; and (c) predictions of the spectrum based on the results of our investigation. $v = 0$ and $v = 1$ stand for the two inversion substates splitted by the tunneling in the 1,3-propanediol spectrum. Note that because of the frequency modulation and first harmonic detection the form of the lines correspond to the first derivative of the actual lineshape.

interaction anymore. Presence of such perturbation leads not only to frequency shifts of some lines, but also to intensity redistribution between transitions that change the characteristic appearance of the specific spectral patterns to be searched. As can be seen from Fig. 2c our model where we took into account Coriolis interaction reproduces very well the experimentally observed multiplet in Fig. 2b. Here it should be noted that the problem was encountered for the most intense low K_a R-type transitions (as it can be seen from the transition assignments given in Fig. 2c) for which rather good accuracy of extrapolation is usually expected and which as a rule are used in the searches of new interstellar molecules. Therefore, these results show the importance of comprehensive experimental laboratory study of molecular spectrum in a wide frequency range prior to the radio astronomy searches of a molecule of interest.

As it was mentioned at the initial stage of our study of conformer I, we followed the model choice of Ref. [3] where separate sets of rotational parameters were used for each inversion substate. Inclusion of the Coriolis interaction terms in the model gave us an opportunity to assign many rotational transitions in the frequency range from 49 to 149 GHz but some problems with fitting low K_a transitions above 200 GHz were encountered. At this point, looking for a possible solution of the problem we had changed to the model used in Ref. [8] for the structurally similar molecule ethylene glycol, where the same (i.e. averaged for the two substates) set of rotational parameters is used for both inversion substates augmented by the Coriolis coupling and splitting parameters. This model is based on the reduced axis system (RAS) approach proposed by Pickett [12]. This approach seemed to be more robust to possible correlation problems between different rotational and Coriolis coupling parameters and indeed gave us an opportunity to find and correct several misassignments of some perturbed transitions which were made at the initial stage of our study. After several more cycles of assignment and fitting we got satisfactory fit within experimental error for the dataset consisting of 3384 line frequencies that correspond to the ground state transitions with J up to 65 and K_a up to 30 of conformer I. In the final dataset the old measurements from Ref. [5] were replaced by our new more accurate measurements. The experimental data set was considerably extended both in frequency coverage (237 GHz versus 78 GHz in [3,5]) and rotational quantum number coverage ($J \leq 65$ and $K_a \leq 30$ versus $J \leq 13$ and $K_a \leq 8$ in [3,5]). The final set of parameters for the ground state of conformer I is presented in Table 1. The details for the effective A-reduction Hamiltonian in use can be found in [8]. The total number of transitions included

in the fit was 6195 which due to blending correspond to 3384 measured line frequencies. The achieved weighted root mean square deviation of the fit was 0.81. The full dataset for the conformer I ground state rotational spectrum treated in this work is available as a *Supplementary material* for this article.

After the fit within experimental error was achieved for conformer I we moved to conformer II spectral analysis. We did not encounter the problems found in the spectrum of conformer I during the assignment process presumably because Coriolis perturbation is weaker for conformer II. Thus in a usual iteration manner of adding new assignments to the fit and updating predictions we get a satisfactory fit for the experimental data consisting of 4824 ground state transitions of conformer II with J up to 59 and K_a up to 29 (due to blending these 4824 transitions correspond to 2947 line frequencies). In the final dataset the measurement results from Ref. [3] are also included. The parameter values resulting from the final fit for conformer II are presented in Table 2. The weighted root-mean-square deviation of the fit was 0.73. The full dataset for the conformer II ground state rotational spectrum treated in this work is available as the *Supplementary material* for this article.

Fig. 3 gives an overview of the observed millimeter wave spectrum of 1,3-propanediol around 130 GHz. In Fig. 3a the simulation of the room temperature spectrum of conformers I and II of 1,3-propanediol based on our current results is given. As it may be expected from comparison of the dipole moments of conformer I ($\mu_a = 2.917(1)$ D, $\mu_b = 1.465(16)$ D, $\mu_c = 1.024(16)$ D) and conformer II (ab initio, $\mu_a = 1.80$ D, $\mu_b = 2.13$ D, $\mu_c = -0.65$ D) [3], as well as from the energy difference between two conformers (ab initio, 1.28 kJ/mol) [3], the strongest lines in the observed spectrum correspond to ${}^aR_{0,1}$ transitions of conformer I which appear as clearly distinguished doublets splitted by the tunneling motion in the molecule (conformer I transitions are marked by a '1' in Fig. 3). For the conformer II spectrum the strong lines correspond to ${}^aR_{0,1}$ and ${}^bQ_{1,-1}$ transitions (conformer II transitions are marked by a '2' in Fig. 3). Although rather high J and K_a quantum numbers were included in the fit and therefore in predictions it is seen from comparison with experimental spectrum that a lot of rather strong lines remain unassigned. This gives us a hope to find in the experimental spectrum the lines belonging to several higher energy conformers of 1,3-propanediol predicted using ab initio calculations in Ref. [3]. This work is in progress now, and we have some preliminary assignments for a rotational spectrum which looks very similar to the conformer I ground state spectrum and therefore presumably correspond to the low lying vibration state of conformer I.

Table 2
Rotational, tunneling splitting and Coriolis coupling parameters of conformer II of the 1,3-propanediol molecule.

Parameter ^a	Value ^b	Parameter ^a	Value ^b
A (MHz)	7698.6443(11)		
B (MHz)	3893.5572(11)		
C (MHz)	2854.8845(13)	ΔE (MHz)	5.42284(38)
ΔJ (kHz)	2.378565(47)	E_J (kHz)	-0.03509(64)
ΔJ_K (kHz)	0.170885(79)	E_K (kHz)	-0.2157(20)
ΔK (kHz)	2.10270(26)		
δ_J (kHz)	0.7519082(93)	F_{ab} (MHz)	92.819(22)
δ_K (kHz)	4.138505(64)	F_{ac} (MHz)	39.976(84)
ϕ_J (Hz)	-0.006853(20)		
ϕ_{JK} (Hz)	0.072298(52)	N_{lines}	3384
ϕ_{KJ} (Hz)	-0.16999(22)	rms (MHz)	0.0207
ϕ_K (Hz)	0.12245(30)	wrms	0.81
ϕ_J (Hz)	-0.0030051(24)		
ϕ_K (Hz)	0.03809(34)		

^a RAS Hamiltonian in A reduction form in the I' representation is used.

^b Numbers in parentheses are one standard deviation in units of the last significant digits.

^a RAS Hamiltonian in A reduction form in the I' representation is used.

^b Numbers in parentheses are one standard deviation in units of the last significant digits.

Parameter ^a	Value ^b	Parameter ^a	Value ^b
A (MHz)	7586.5999(22)	ΔE (MHz)	39.22430(38)
B (MHz)	3881.73578(11)	E_J (kHz)	1.2568(85)
C (MHz)	2847.0134(22)	E_K (kHz)	-1.5281(82)
ΔJ (kHz)	2.511358(63)	E_2 (kHz)	0.7166(41)
ΔJ_K (kHz)	-1.41273(24)		
ΔK (kHz)	3.21783(41)	F_{ab} (MHz)	10.123(19)
δ_J (kHz)	0.801121(24)	F_{abJ} (kHz)	-0.278(15)
δ_K (kHz)	3.87717(15)	F_{abK} (kHz)	-9.789(24)
ϕ_J (Hz)	-0.007523(19)	F_{ac} (MHz)	18.83(28)
ϕ_{JK} (Hz)	0.06652(20)		
ϕ_{KJ} (Hz)	-0.07066(32)		
ϕ_J (Hz)	-0.0031012(58)	N_{lines}	2947
ϕ_{JK} (Hz)	-0.00488(13)	rms (MHz)	0.0164
ϕ_K (Hz)	0.06332(63)	wrms	0.73
L_{JK} (mHz)	0.000363(18)		

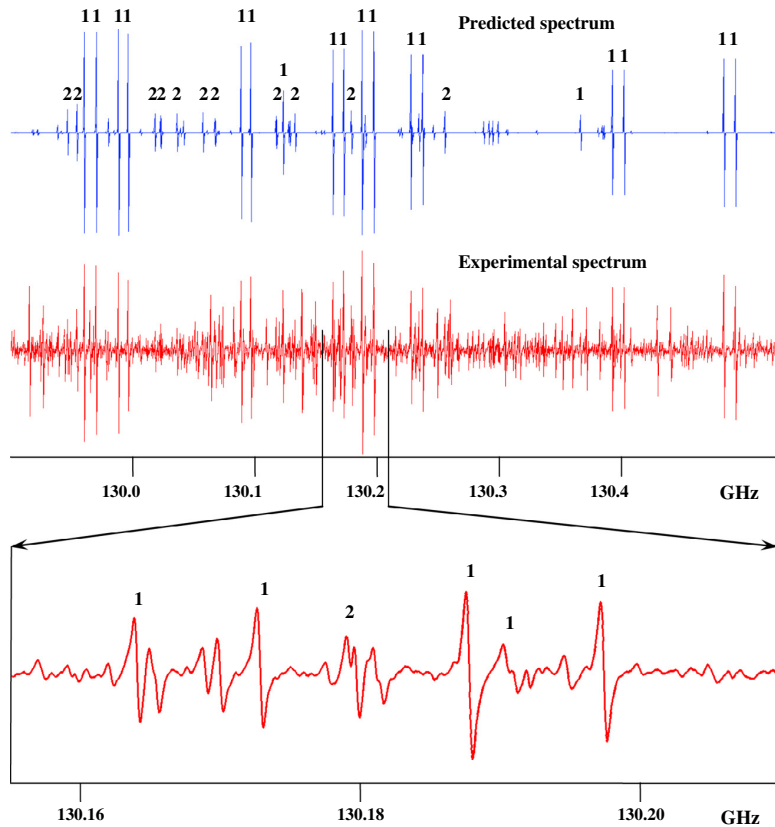


Fig. 3. Fragment of the room temperature 1,3-propanediol spectrum near 130 GHz: (a) predictions of the conformer I (transitions marked by a '1') and conformer II (transitions marked by a '2') ground state rotational spectra based on our current results (only the strongest transitions are marked in the figure); (b and c) experimental spectrum recorded in our work. Note that because of the frequency modulation and first harmonic detection the form of the lines correspond to the first derivative of the actual lineshape.

2. Discussion

If we compare our new values for the rotational and splitting parameters with corresponding values from Ref. [3] we find that the values for the splittings ΔE coincide very well for both conformers despite the inclusion of J and K dependences for this quantity in the current model and using one set of averaged rotational parameters for both inversion substates. The slight discrepancy in the values of the rotational constants (somewhat larger for conformer I) disappear if one recalculates the values from the reduced axis system to principal axis system. So, here we also have good agreement with the previous results [3] as well as for the quartic centrifugal distortion parameters. It should be noted that for conformer I almost the same quality of the fit may be achieved when F_{ac} is replaced by E_2 and L_{JK} , whereas in the conformer II fit an attempt to omit the F_{ac} parameter and compensate its effect by some other parameters leads to about 15% increase in rms deviation. Therefore, although inclusion of F_{ac} parameter in the parameter sets to some extent increases the correlation between the Coriolis coupling parameters and rotational parameters (which is quite understandable since F_{ab} and F_{ac} give a rotation from the principal axis system to the RAS), as the final fits we took those with the F_{ac} parameter since here we get better rms deviations with a smaller number of floated parameters.

The reduced axis system approach of Pickett [12] employed in our work is closely related to a number of internal-axis-method (IAM) type models developed by Hougen and coworkers for

molecules with several large amplitude motions [13–17]. Moreover, the first analysis of the tunneling splittings in ethylene glycol (a molecule structurally similar to 1,3-propanediol), was based on the IAM type formalism developed for the ethylene glycol case by Coudert and coworkers [6,7]. The equivalence of the RAS- and IAM-type approaches has been shown by Coudert et al. [18] and the main reason why one would like to switch from the IAM to the RAS approach was related to the convenience of including the higher order Hamiltonian terms provided by the SPFIT and SPCAT programs [11]. Indeed, both approaches consider the problem in terms of a phenomenological Hamiltonian and a set of splittings which arise from tunneling of the system between equivalent non-superimposable configurations of the molecule and both allow taking into account the Coriolis interaction between the tunneling motion and the overall rotation of the molecule. The close correspondence between the RAS approach and the IAM type approach gives an opportunity to validate the applicability of the RAS approach in the case of 1,3-propanediol ground state spectra. The IAM type approach is based on the high barrier tunneling formalism which assumes that vibrational eigenfunctions of equivalent non-superimposable configurations of the molecule are well localized. Therefore we may assume that the same requirement of the high barrier case is applicable to the RAS formalism. Consideration of possible tunneling paths made in Ref. [3] gives an opportunity to make the following estimations for the order of magnitude for the barrier heights: 1883 cm^{-1} for conformer I and 1520 cm^{-1} for conformer II [3]. These values together with rather small splittings

between inversion substates of both conformers indicate that the requirement of the high barrier is indeed satisfied which in turn substantiates employment of the RAS approach for the analysis of the 1,3-propanediol spectrum. The fits within experimental error obtained here for both conformers give additional confidence in the validity of the chosen theoretical approach.

3. Conclusions

We have undertaken the new study of the 1,3-propanediol spectrum for the two lowest conformers in the frequency range from 49 to 237 GHz. Analysis was performed using RAS Hamiltonian with the model that assumes two substates between which the system tunnels. The fits, within experimental error, were obtained for 6195 rotational transitions with $J \leq 65$ and $K_a \leq 30$ of conformer I and for 4824 transitions with $J \leq 59$ and $K_a \leq 29$ of conformer II. The analysis of the new measurements revealed significant influence of the Coriolis interaction between tunneling motion and overall rotation of a molecule in 1,3-propanediol. Our results provide a firm basis for the radioastronomical search of the lowest energy conformers I and II of 1,3-propanediol at the frequencies below 300 GHz where the present spectroscopic parameters should yield reliable predictions.

Acknowledgments

The authors would like to thank Dr. F.J. Lovas for a number of corrections of the English in the manuscript. Part of this work was done within the Ukrainian–French CNRS–PICS 6051 project.

Appendix A. Supplementary material

Supplementary data associated with this article can be found, in the online version, at <http://dx.doi.org/10.1016/j.jms.2013.10.001>.

References

- [1] J.M. Hollis, F.J. Lovas, P.R. Jewell, L.H. Coudert, *Astrophys. J. Lett.* 571 (2002) L59–L62.
- [2] D.F. Plusquellic, F.J. Lovas, B.H. Pate, J.L. Neill, M.T. Muckle, A.J. Remijan, *J. Mol. Spectrosc.* 257 (2009) 82–93.
- [3] D.F. Plusquellic, F.J. Lovas, B.H. Pate, J.L. Neill, M.T. Muckle, A.J. Remijan, *J. Phys. Chem. A* 113 (2009) 12911–12918.
- [4] W. Caminati, *J. Mol. Spectrosc.* 86 (1981) 193–201.
- [5] W. Caminati, S. Melandri, P.G. Favero, *J. Mol. Spectrosc.* 171 (1995) 394–401.
- [6] D. Christen, L. Coudert, R. Suenram, F.J. Lovas, *J. Mol. Spectrosc.* 172 (1995) 57–77.
- [7] D. Christen, L.H. Coudert, J.A. Larsson, D. Cremer, *J. Mol. Spectrosc.* 205 (2001) 185–196.
- [8] D. Christen, H.S.P. Müller, *Phys. Chem. Chem. Phys.* 5 (2003) 3600–3605.
- [9] V.V. Ilyushin, R.A. Motiyenko, F.J. Lovas, D.F. Plusquellic, *J. Mol. Spectrosc.* 251 (2008) 129–137.
- [10] E.A. Alekseev, R. Motiyenko, L. Margulès, *Radio Phys. Radio Astron.* 3 (1) (2012) 75–88.
- [11] H.M. Pickett, *J. Mol. Spectrosc.* 148 (1991) 371–377.
- [12] H.M. Pickett, *J. Chem. Phys.* 56 (1972) 1715–1723.
- [13] J.T. Hougen, *J. Mol. Spectrosc.* 114 (1985) 395–426.
- [14] L.H. Coudert, J.T. Hougen, *J. Mol. Spectrosc.* 130 (1988) 86–119.
- [15] J.T. Hougen, *J. Mol. Spectrosc.* 89 (1981) 296–327.
- [16] N. Ohashi, J.T. Hougen, *J. Mol. Spectrosc.* 112 (1985) 384–400.
- [17] N. Ohashi, J.T. Hougen, *J. Mol. Spectrosc.* 121 (1987) 474–501.
- [18] D. Christen, H.S.P. Mueller, L.H. Coudert, 57th International Symposium on Molecular Spectroscopy, Ohio State University, Paper TB03, 2002.

Chapitre 4

Études des molécules manifestant deux mouvements de vibration de grande amplitude de nature différentes

4.1 Introduction

Les méthodes théoriques appliquées aux spectres des molécules manifestant deux MVGA sont basées sur le formalisme de l'effet tunnel à haute barrière. Cependant, par rapport aux études présentées ci-dessus, l'analyse de deux MVGA nécessite un traitement assez particulier à l'aide des groupes de symétrie moléculaire. Les molécules peuvent posséder de la symétrie structurelle que l'on peut décrire à l'aide des opérations de rotation suivant un axe et de réflexion par rapport à un plan. L'ensemble de ces opérations constitue le groupe de symétrie ponctuel. Ce genre de groupe peut être appliqué dans la description des niveaux d'énergie des molécule rigides. Pour les molécules non-rigides, il est nécessaire d'introduire des groupes de symétrie moléculaire dont les opérations sont les permutations avec et sans inversion des noyaux identiques. Pour cela on commence par établir le groupe complet composé de toutes les opérations de permutation-inversion des noyaux identiques. Par la suite, le groupe de symétrie moléculaire est construit en excluant les opérations qui ne sont pas réalisables, c.à.d. les opération que l'on ne peut reproduire à l'aide de MVGA. Il faut également noter que l'on peut considérer un groupe de permutation-inversion pour une molécule rigide. Dans ce cas, les opérations du groupe de permutation-inversion correspondent un à un aux opérations de rotation et de réflexion du groupe de symétrie ponctuelle.

La question de symétrie a été déjà brièvement abordée dans le Chapitre 2 où les sous-niveaux de torsion ont été caractérisés selon les types de symétrie *A* et *E* du groupe ponctuel C_{3v} . En effet, la rotation interne d'une toupie, dont la symétrie structurelle est

C_{3v} est décrite à l'aide des opérations de permutation-inversion qui constituent le groupe de symétrie moléculaire G_6 . Ce groupe de symétrie moléculaire est isomorphe au groupe ponctuelle C_{3v} et pour cette raison l'on utilise les espèces de symétrie de celui-ci. De même, pour le mouvement de type inversion auquel l'on a consacré le Chapitre 3, on peut introduire le groupe de symétrie G_2 qui est isomorphe aux groupes ponctuels C_s ou C_2 . Ainsi, les sous états 0^+ et 0^- peuvent être également caractérisés selon le espèces de symétrie de l'un de ces deux groupes ponctuels.

Les molécules manifestants deux MVGA nous amènent à des cas plus compliqués avec des groupes de symétrie moléculaires plus larges ou bien à des cas où l'on doit introduire un groupe de symétrie moléculaire pour une molécule ne possédant aucune symétrie structurelle. Un autre aspect important lié aux opérations de permutation des noyaux équivalents est l'influence de la statistique de spin sur les intensités de raies. Cet aspect est également important pour les molécules rigides et semi-rigides possédant une symétrie ponctuelle.

Pour calculer les poids statistiques en fonction du type de symétrie, l'on doit d'abord déterminer les caractères χ de la représentation Γ du groupe de symétrie moléculaire pour chaque opération de permutation P à l'aide de la formule suivante [Bunker and Jensen 2006] :

$$\chi^\Gamma(P) = 2 \prod (2I_a + 1)(-1)^{2I_a(n_a - 1)} \quad (4.1)$$

Pour les opérations de permutation-inversion, les caractères correspondants $\chi^\Gamma(P^*)$ sont égaux à zéro. Chaque facteur du produit dans l'Eq.4.1 correspond à l'ensemble de n_a noyaux équivalents permuts par l'opération P (avec $n_a = 1$ dans le cas où l'opération laisse le noyaux inchangés). De manière générale, la représentation Γ obtenue à l'aide de l'Eq.4.1 est réductible en une combinaison de représentations irréductibles Γ^* du groupe de symétrie moléculaire : $\Gamma = \sum a_i \Gamma_i^*$, où a_i sont les poids statistiques de chaque type de symétrie. Pour déterminer les coefficients a_i on peut utiliser la formule suivante :

$$a_i = \frac{1}{h} \sum_P \chi^\Gamma(P) \chi^{\Gamma_i^*}(P) \quad (4.2)$$

où h est l'ordre du groupe et la somme porte sur toutes les opérations de permutation sans l'inversion car $\chi^\Gamma(P^*) = 0$.

Les poids statistiques a_i déterminent le nombre de fonctions de spin des noyaux ψ_n pour chaque type de symétrie Γ^* . La fonction d'onde complète Ψ_c est le produit de fonctions d'onde individuelles : des électrons ψ_e , de vibration ψ_v , de rotation ψ_r et de ψ_n : $\Psi_c = \psi_e \psi_v \psi_r \psi_n$. Pour déterminer les poids statistiques par rapport aux fonctions d'ondes individuelles, il faut d'abord déterminer les représentations irréductibles de

Ψ_c par rapport aux permutations paires et impaires des fermions : $P_{\text{paire}}\Psi_c = +\Psi_c$ et $P_{\text{impaire}}\Psi_c = -\Psi_c$. Dans le cas où les opérations du groupe de symétrie moléculaire ne concernent que les bosons, Ψ_c appartient à la représentation complètement symétrique. Par la suite, en utilisant la table de multiplication du groupe, l'on peut déduire des différents combinaisons des fonctions d'onde individuelles dont le produit appartient à la même représentation que Ψ_c : $\Gamma_c = \Gamma_e \otimes \Gamma_v \otimes \Gamma_r \otimes \Gamma_n$.

4.2 Étude du spectre de la méthylamine

4.2.1 Modèle théorique

Comme dans le cas de l'étude des espèces déutérées du formiate de méthyle, l'application du formalisme de l'effet tunnel à haute barrière commence par l'établissement des configurations équivalentes et des voies de l'effet tunnel entre elles. La molécule de la méthylamine est caractérisée par trois configurations équivalentes du groupement méthyle accessibles par la rotation de celui-ci par 120° , ainsi que par deux configurations équivalentes du groupement NH_2 liées par le mouvement de type inversion. Il faut également noter que l'inversion du NH_2 doit être suivie par une rotation du CH_3 par 60° . Au total, la méthylamine possède six configurations, chacune étant associée à un minimum sur la surface d'énergie potentielle sur la Fig. 16. La surface est présentée en fonction de deux coordonnées caractéristiques des MVGA : les angles de torsion τ et de l'inversion γ .

L'étape suivante consiste à introduire un groupe de symétrie moléculaire pour caractériser les MVGA. Les voies de l'effet tunnel entre les configurations équivalentes peuvent être représentés par les opérations de permutation des atomes. L'ensemble des ces permutations forme un groupe de symétrie moléculaire. Dans le cas de la méthylamine, six opérations de permutation, présentées sur la Fig. 17 en combinaison avec les opération d'inversion (réflexion dans le plan pour le groupe ponctuel C_s) forment le groupe de symétrie G_{12} . Ainsi, les fonctions d'onde de tous le minima peuvent être exprimées par l'application des opérations du groupe G_{12} à la fonction d'onde dans le premier minimum sur la Fig. 16 caractérisé par l'opération E . Les niveaux d'énergie de la méthylamine sont définis via les nombres quantiques classiques J et $K = K_a$ et via les représentations irréductibles du groupe de permutation-inversion G_{12} : $A_1, A_2, B_1, B_2, E_1, E_2$. Les niveaux de symétrie E_1 et E_2 doublement dégénérés ont une définition supplémentaire ± 1 pour distinguer entre deux niveaux avec les même J et K_a . Les niveaux avec $K_a = 0$ sont définis comme $E_{1,2} + 1$. Les poids statistiques calculés pour chaque espèce de symétrie sont : 1 pour A_1, A_2 et E_2 et 3 pour B_1, B_2 et E_1 .

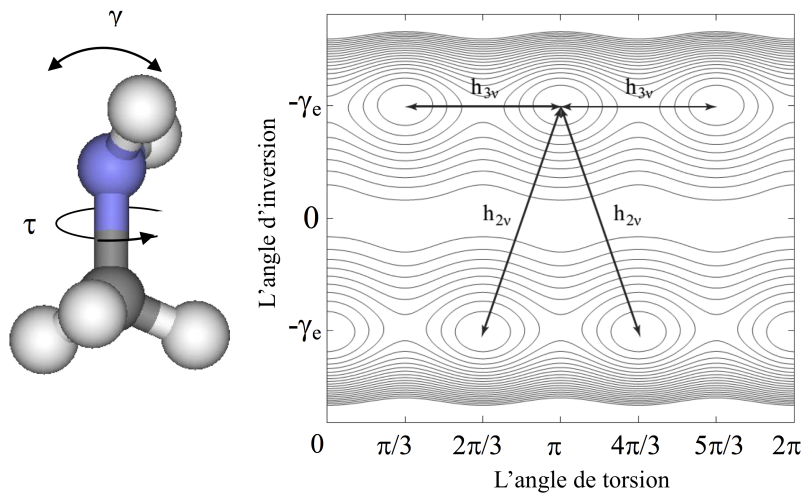


FIGURE 16: La structure de la méthylamine et la surface d'énergie potentielle en fonction de l'angle de torsion τ et d'inversion γ . Le mouvement de torsion du groupement méthyle (h_{3v}) et le mouvement d'inversion du groupement aminé (h_{2v}) sont indiqués par les flèches. L'inversion du NH_2 doit être suivie par la rotation du CH_3 par $\frac{\pi}{3}$ ce qui couple d'avantage les deux MVGA.

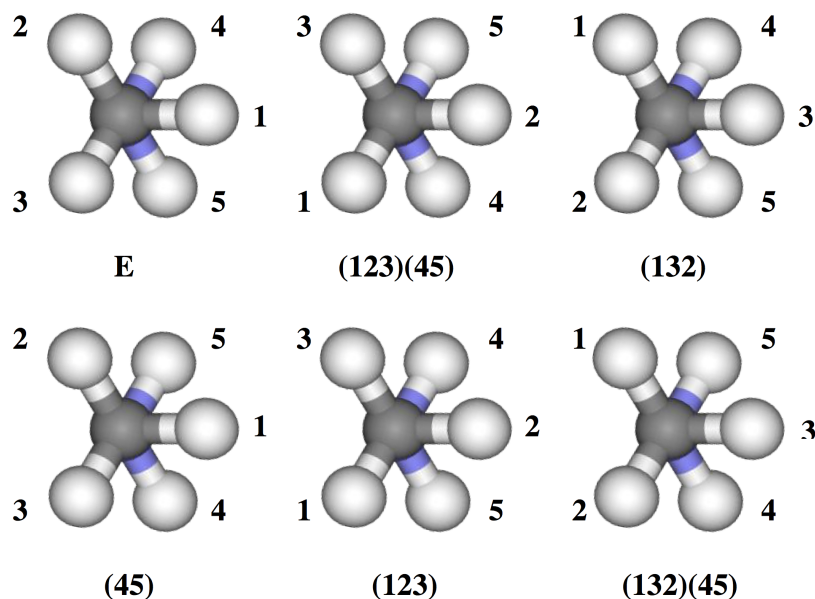


FIGURE 17: Six configurations non-superposables de la méthylamine liées par l'effet tunnel et les opérations de permutation du groupe de symétrie moléculaire G_{12} qui correspondent aux effets tunnels à partir de la configuration initiale (en haut à gauche).

Le modèle de l'hamiltonien pour la méthylamine comprend également une application de la méthode partielle d'axes internes. La méthode est dite « partielle » car elle ne compense que le moment angulaire produit par la torsion de CH₃. Ainsi dans l'hamiltonien pour la méthylamine on introduit le paramètre ρ qui décrit le couplage entre la rotation interne du groupement CH₃ et la rotation globale de la molécule. Cependant, l'introduction d'axes internes pose un problème du point de vue du groupe de symétrie moléculaire et nécessite une extension du groupe par un facteur $m \in \mathbb{Z}$, dont la valeur dépend de ρ . Par conséquent, la méthode partielle d'axes interne entraîne l'apparition de $6m$ configurations équivalentes et la matrice de l'hamiltonien est construite dans la base de $6m$ fonctions d'onde de vibration [Ohashi and Hougen 1987].

L'hamiltonien pour la méthylamine est défini de façon suivante :

$$\begin{aligned} H = & h_v + h_j P^2 + h_k P_z^2 + (f_+ P_+^2 + f_- P_-^2) + q J_z + (r_+ P_+ + r_- P_-) \\ & + [s_+(P_+ P_z + P_z P_+) + s_-(P_- P_z + P_z P_-)] + (f_+^{(2)} P_+^4 + f_-^{(2)} P_-^4) \\ & + \text{termes d'ordre supérieur} \end{aligned} \quad (4.3)$$

où les « termes d'ordre supérieur » représentent les corrections de la distorsion centrifuge ainsi que les dépendances en J et K de différents paramètres de l'effet tunnel. Les éléments de la matrice de l'hamiltonien 4.3 sont exprimés comme une expansion en série de Fourier de manière similaire à l'Eq. 3.1. Dans la série, le terme j correspond à l'effet tunnel entre la configuration $|1\rangle$ et la configuration $|j\rangle$. Dans le cas de la méthylamine, les configurations sont numérotées de façon à ce que les valeurs de j paires $j = 2, 4, 6, \dots$ correspondent au mouvement d'inversion et les valeurs de j impaires, à l'exception de 1, $j = 3, 5, 7, \dots$ correspondent au mouvement de torsion. Les termes avec $j = 1$ décrivent le cas du mouvement sans l'effet tunnel, c.a.d. la rotation pure de la molécule.

Le sens physique des différents termes de l'hamiltonien 4.3 est le suivant. Les paramètres h_v représentent l'énergie de vibration du système. Dans l'expansion des éléments de la matrice de l'hamiltonien 4.3, les termes h_v avec $j = 2, 3, 4, 5, \dots$ représentent les séparations entre des niveaux d'énergie à cause de l'effet tunnel suivant chaque chemin unique du système. Les paramètres non-tunnels ($j = 1$) h_j , h_k et f correspondent aux combinaisons de paramètres du rotateur rigide $\frac{1}{2}(B + C)$, $A - \frac{1}{2}(B + C)$ et $\frac{1}{4}(B - C)$ respectivement. Les mêmes paramètres avec $j > 1$ correspondent aux corrections des paramètres de rotateur rigide à cause de l'effet tunnel. Le paramètre $f^{(2)}$ décrit les contributions non-tunnel et tunnel des termes $\Delta K = 4$. Les termes linéaires q et r correspondent à l'interaction des composantes du moment angulaire total avec les moments angulaires générés par les deux MVGA dans le système d'axes moléculaires. Suite à leur définitions, seuls les termes linéaires q et r tunnels ($j > 1$) sont permis. Le terme s non-tunnel quadratique est permis suite à l'application de la méthode partielle d'axes

internes et de ce fait il est similaire aux termes D_{zx} ou D_{zy} de l'Eq. 2.5.

4.2.2 Analyse du spectre

Ma contribution dans l'étude du spectre de rotation de la méthylamine peut être séparée en deux parties. Premièrement, j'ai enregistré et analysé le spectre de l'espèce isotopique principale de la molécule. Ceci a été fait dans le but d'étendre la gamme spectrale par rapport aux études précédentes. La dernière analyse critique de tous les résultats précédents sur le spectre de l'état fondamental de CH_3NH_2 [Ilyushin and Lovas 2007] couvrait la gamme de fréquence jusqu'à 0.5 THz. La méthylamine est une molécule relativement légère et son spectre est dominé par les transitions μ_c . Le maximum d'absorption dans le spectre de la méthylamine à la température caractéristique du MIS de 150 K se trouve autour de 1.5 THz et le maximum se décale vers 0.8 THz à 50 K. Dans notre nouvelle étude [Motiyenko et al. 2014], les mesures spectrales dans la gamme 0.5 – 0.945 THz effectuées au Laboratoire PhLAM ont été combinées avec les mesures dans la gamme de 1 à 2.6 THz effectuées au JPL. Cela représente une extension par facteur 5 par rapport aux mesures précédentes et par un facteur 2.3 en nombre de raies spectrales attribuées. L'application de l'hamiltonien du formalisme de l'effet tunnel à haute barrière a permis d'ajuster les fréquences de toutes les raies à une précision expérimentale avec l'écart type pondéré de 0.87 et d'obtenir des prévisions spectrales fiables jusqu'à 3 THz et pour toutes les transitions avec $0 < J < 50$ et $0 < K_a < 20$.

En second lieu, j'ai également enregistré et analysé le spectre de l'espèce isotopique ^{13}C de la méthylamine [Motiyenko et al. 2016]. Ce travail a été accompli dans le cadre de la série d'études des espèces isotopiques des molécules très abondantes dans le MIS. L'analyse initiale du spectre de $^{13}\text{CH}_3\text{NH}_2$ s'est basée sur l'hypothèse que la substitution isotopique de ^{12}C par ^{13}C affecte peu le MVGA de la torsion-inversion et de ce fait l'allure des multiplets produits par le MVGA pour les deux espèces isotopiques est quasi-identique. Ainsi, dans les ajustements initiaux des raies attribuées de l'espèce ^{13}C de la méthylamine, les paramètres tunnels ont été fixés aux valeurs des paramètres correspondants de l'espèce ^{12}C et seul les paramètres non-tunnels ont été variés. Les prévisions spectrales obtenues de cet ensemble de paramètres issus de l'ajustement initial ont permis de continuer l'analyse du spectre de $^{13}\text{CH}_3\text{NH}_2$ de manière standard itérative et de libérer progressivement les termes tunnels de l'hamiltonien 4.3. Au final, l'hypothèse sur la faible variation des paramètres tunnels suite à la substitution isotopique $^{12}\text{C} \rightarrow ^{13}\text{C}$ s'est avérée plausible, comme l'on peut constater en comparant les paramètres correspondants de deux espèces isotopique de la méthylamine dans Table 2 [Motiyenko et al. 2016]. Les résultats de l'analyse du spectre de $^{13}\text{CH}_3\text{NH}_2$ ont permis d'obtenir des prévisions fiables dans la gamme de fréquences jusqu'à 1 THz et pour toutes les

transitions avec $0 < J < 50$ et $0 < K_a < 20$.

Un autre aspect commun à l'étude des deux espèces isotopiques est la structure hyperfine due au moment quadrupolaire non-nul de l'atome ^{14}N . Puisque l'hamiltonien 4.3 et le code informatique utilisés pour ajuster les fréquences de raies par défaut n'incluent pas la contribution d'interaction responsable de la structure hyperfine, celle-ci a été traitée séparément de la manière suivante. La fréquence de chaque composante dans le multiplet de la structure hyperfine f_{hf} peut être exprimée comme :

$$f_{hf} = f_{rot} + \frac{E_{hf}(I, J'', F'') - E_{hf}(I, J', F')}{h} \quad (4.4)$$

où f_{rot} est la fréquence de transition de rotation-torsion-inversion que l'on peut calculer à l'aide de l'hamiltonien 4.3. L'énergie quadrupolaire E_{hf} est exprimée comme :

$$E_{hf}(I, J, F) = \left[\frac{1}{2}\chi_+ \langle P_x^2 + P_y^2 - 2P_z^2 \rangle - \frac{1}{2}\chi_- \langle P_x^2 - P_y^2 \rangle + \chi_{xz} \langle P_x P_z + P_z P_x \rangle \right] \frac{2f(I, J, F)}{J(J+1)} \quad (4.5)$$

où $\chi_+ = -\chi_{zz}$, $\chi_- = \chi_{yy} - \chi_{xx}$ [Kreglewski *et al.* 1992], $\langle P_x^2 \rangle$, $\langle P_y^2 \rangle$, $\langle P_z^2 \rangle$ et $\langle P_x P_z + P_z P_x \rangle$ sont les valeurs propres des opérateurs correspondants dans le système d'axes de l'hamiltonien 4.3 et $f(I, J, F)$ est la fonction de Casimir [Gordy and Cook 1984].

Pour déterminer les fréquences f_{rot} on a ajusté toutes les composantes hyperfines au modèle de l'Eq. 4.4 avec un ensemble de paramètres composé de toutes les fréquences f_{rot} ainsi que de trois constantes d'interaction hyperfine χ_+ , χ_- et χ_{xz} . Les fréquences f_{rot} ont été ensuite utilisées dans l'ajustement global pour déterminer les paramètres de l'hamiltonien 4.3.

Comme l'on peut constater, l'application du formalisme de l'effet tunnel à haute barrière permet d'obtenir la description théorique du spectre de l'état fondamental de la méthylamine à la précision expérimentale. Un bon accord entre la théorie et l'expérience est illustré sur la Fig. 18 où l'on compare les spectres observés et les spectres calculés autour de 0.9 THz pour les deux espèces isotopiques de la méthylamine. Sur l'échelle du milieu de chaque graphique on a mis les attributions de symétrie pour l'origine de chaque bande de transitions de type Q . Ceci est fait dans le but de mettre en évidence l'effet des deux MVGA sur l'allure du spectre. Les deux MVGA sont responsables des séparations entre les bandes qui peuvent atteindre plusieurs dizaines de GHz. A l'aide de spectres sur la Fig. 18, on peut également vérifier l'influence de la statistique de spin en fonction de type symétrie de chaque bande.

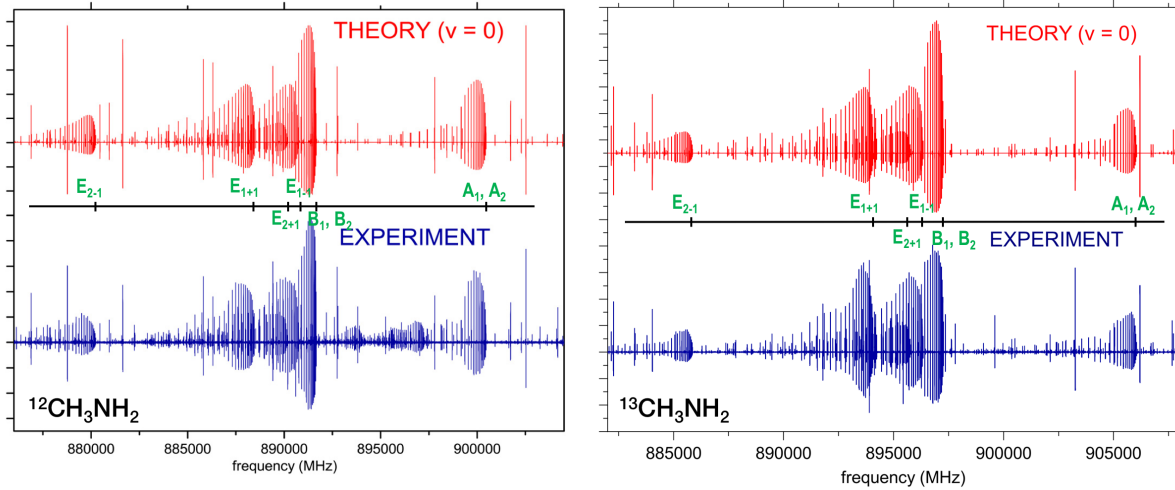


FIGURE 18: Les spectres théoriques (en rouge) et expérimentales (en bleu) de la méthylamine. Une légère incohérence entre les deux spectres peut avoir lieu à cause de variation de la puissance de la source de rayonnement THz et de la sensibilité du détecteur.

4.3 Étude du spectre de l'aminomalononitrile

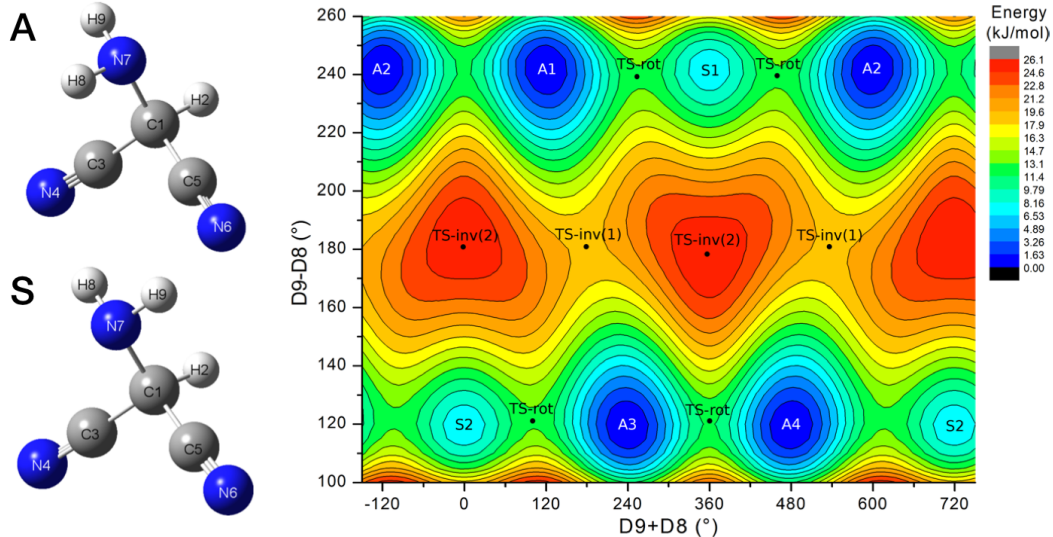


FIGURE 19: La structure de deux conformations A et S et la surface d'énergie potentielle de l'aminomalononitrile en fonction de deux coordonnées indépendantes $D_9 - D_8$ et $D_9 + D_8$. Voir le texte pour la définition des coordonnées.

L'aminomalononitrile (AMN, $\text{H}_2\text{NCH}(\text{CN})_2$) est le trimère du cyanure d'hydrogène HCN. Celui-ci a été détecté depuis longtemps dans le MIS [Snyder and Buhl 1971], dans l'atmosphère du Titan [Hanel *et al.* 1981] et dans les comètes [Schloerb *et al.* 1988]. L'AMN est le produit intermédiaire de la synthèse de l'adénine, le composé oligomérique avec la formule $(\text{HCN})_5$ faisant partie de l'ADN, l'ARN et de différents coenzymes et étant

ainsi considéré comme l'un des composés clés de la période pré-biotique de la Terre. Pour l'instant l'adénine n'a pas été détectée dans le MIS, cependant l'E-cyanométhanamine, le composé avec la formule $(HCN)_2$ et également le produit intermédiaire dans la synthèse de l'adénine a été détecté récemment [Zaleski *et al.* 2013]. L'addition du HCN sur le cyanométhanamine conduit à la formation de l'AMN. La détection de ce dernier pourrait aider à améliorer la compréhension de la chimie d'hydrogène dans le MIS.

Du point de vue de la structure moléculaire, l'AMN peut être considéré comme un dérivé de la méthylamine avec un remplacement de deux atomes d'hydrogène du groupement méthyle par deux groupements fonctionnels CN. La rotation de la molécule est compliquée par les mêmes MVGA que dans le cas de la méthylamine : la torsion et l'inversion. Par rapport à la méthylamine, la symétrie moléculaire de l'AMN est réduite et la surface d'énergie potentielle tracée en fonction de deux coordonnées représentant les MVGA est un peu différente notamment suite à l'apparition de deux conformations *A* (asymétrique) et *S* (symétrique, car possède un plan de symétrie) correspondant à deux et quatre minima, voir Fig. 19. La conformation *A* est beaucoup plus stable et représente un plus grand intérêt pour les recherches dans le MIS.

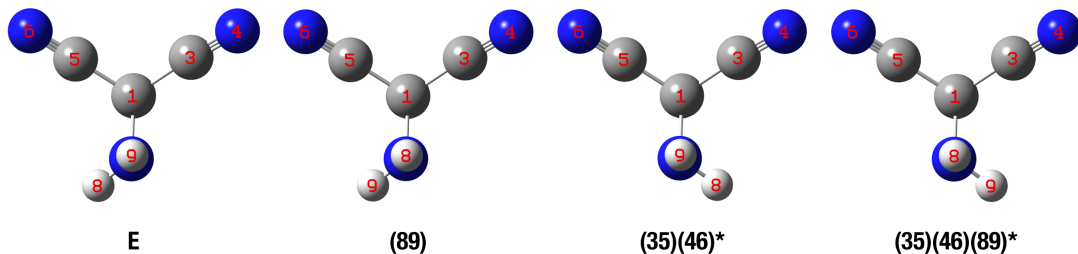


FIGURE 20: Quatre configurations non-superposables de l'aminomalononitrile et les opérations de permutation-inversion du groupe de symétrie moléculaire G_4 qui correspondent aux effets tunnels à partir de la configuration initiale (à gauche).

La conformation *A* possède la symétrie minimale C_1 , cependant pour traiter les deux MVGA et leurs effets sur l'allure du spectre de rotation, un groupe de symétrie doit être introduit. Les quatre configurations équivalentes de la conformation *A* sont liées par les opérations de permutation-inversion : *E*, (89) , $(35)(46)^*$ et $(35)(46)(89)^*$ (voir Fig. 20). Ici l'opération $(35)(46)^*$ est réalisable suite à l'inversion, l'opération $(35)(46)(89)^*$ est réalisable suite à la torsion et l'opération (89) correspond à la combinaison de deux MVGA. Les quatre opérations constituent le groupe de symétrie G_4 , ayant quatre représentations irréductibles : A_1 , A_2 , B_1 et B_2 . Par conséquent, chaque niveau d'énergie de la conformation *A* a une dégénérescence de quatre et en plus des nombres quantiques standards J , K_a , K_c doit être caractérisé selon l'un des quatre types de symétrie. Les opérations du groupe G_4 permutent deux atomes d'azote ayant le spin $I = 1$ et deux atomes d'hydrogène ayant le spin $I = \frac{1}{2}$. Ainsi, on peut calculer que les poids statistiques

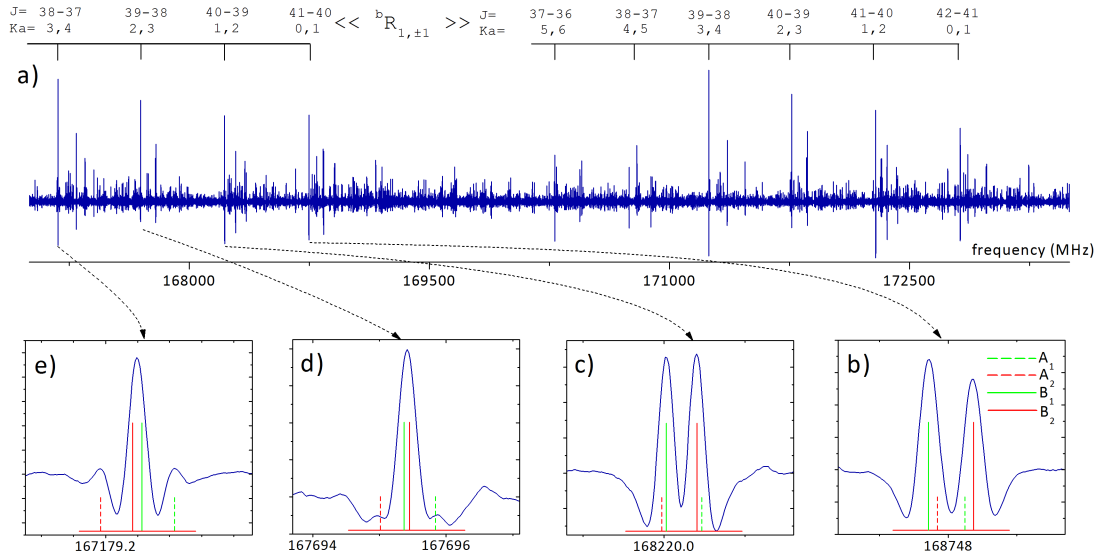


FIGURE 21: (a) Le spectre expérimental de l'aminomalononitrile dans la gamme de fréquences 167 - 173 GHz illustrant les séries des raies intenses de type ^bR_{1,±1}. (b-e) Les vues détaillées sur quelques raies intense chacune représentant un multiplet à cause de deux MVGA. L'attribution de chaque composante de multiplet suivant le type de symétrie du groupe G₄ ainsi que les intensités relatives sont indiquées.

de représentations irréductibles : A₁, A₂, B₁ et B₂ sont respectivement 1, 1, 3 et 3.

L'influence de la statistique de spin sur les intensités des raies est illustrée sur la Fig.21. Chaque transition de rotation est séparée en quatre composantes, deux intenses et deux plus faibles, avec un rapport approximatif de 3 sur 1. L'inversion de la séquence de composantes spectrales en fonction de nombres quantiques K_a est un indicateur de perturbation. Pour traiter l'interaction entre la rotation de la molécule et les MVGA, dans un premier temps j'ai adopté la méthode de SAR qui au final s'est avérée suffisante pour ajuster les transitions attribuées à la précision expérimentale. En effet, les calculs de chimie quantique montrent que la hauteur de la barrière à la torsion est environ 1.5 plus faible que la hauteur de la barrière à l'inversion. Ainsi, l'on peut supposer que la plupart du temps la molécule se trouve dans les configurations A1 et A2 ou A3 et A4 sur la Fig. 19 et que le MVGA dominant est la torsion, entraînant l'effet tunnel A1 ↔ A2 ou A3 ↔ A4. En termes de symétrie de l'hamiltonien, il s'agit de séparer les niveaux de symétrie A et les niveaux de symétrie B et de ne pas traiter les interactions entre les niveaux A et les niveaux B.

En tenant compte du traitement séparé des niveaux de symétrie A et B, dans la base de fonctions d'onde individuelles |ψ(A₁)⟩, |ψ(A₂)⟩, |ψ(B₁)⟩ et |ψ(B₂)⟩, l'hamiltonien de

4.4. Étude du spectre du Diméthyléther deutéré

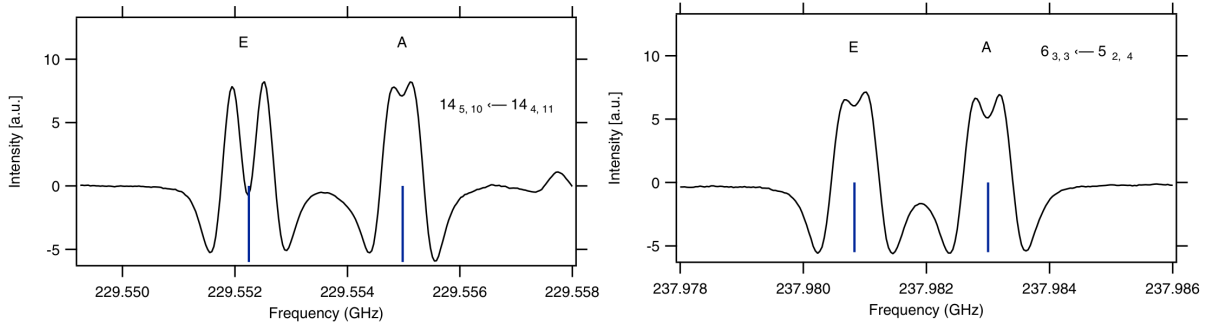


FIGURE 22: Exemple de raies de la conformation A du diméthyleéther déutéré manifestant les deux MVGA. Chaque transition est séparé en deux composantes A et E à cause de la torsion du groupement méthyle non-substitué. Chaque composante est à son tour séparé en deux sous-composantes à cause de mouvement de l'inversion du deutérium.

la méthode SAR prend la forme suivante :

$$H = \begin{pmatrix} H_{\text{rot}} - H_{\Delta}^A & H_{\text{I}}^A & 0 & 0 \\ H_{\text{I}}^A & H_{\text{rot}} + H_{\Delta}^A & 0 & 0 \\ 0 & 0 & H_{\text{rot}} - H_{\Delta}^B & H_{\text{I}}^B \\ 0 & 0 & H_{\text{I}}^B & H_{\text{rot}} + H_{\Delta}^B \end{pmatrix} \quad (4.6)$$

où les hamiltoniens H_{Δ} et H_{I} sont donnés dans Eq. 3.6 et Eq. 3.7 respectivement. L'application de l'hamiltonien 4.6 a permis d'ajuster les fréquences d'environ 1400 raies spectrales à la précision expérimentale et avec un écart-type pondéré de 0.68 [Motiyenko *et al.* 2015]. L'ensemble de données comprend les transitions avec les nombres quantiques : $10 \leq J \leq 74$ et $0 \leq K_a \leq 23$. On peut constater que le modèle qui utilise le traitement séparé des niveaux de symétrie A et B est suffisant pour obtenir une bonne description du spectre de l'AMN à la résolution limitée par l'effet Doppler. Pour la molécule de l'AMN cette approche est également suffisante en ce qui concerne la préparation de la base de données pour les observations dans le MIS.

4.4 Étude du spectre du Diméthyléther deutéré

Pour marquer les limites théoriques actuelles en ce qui concerne les MVGA à deux dimensions, je voudrais évoquer le cas du diméthyléther deutéré ($\text{CH}_3\text{OCH}_2\text{D}$, DME-d). L'espèce isotopique principale de cette molécule a été détectée pour la première fois dans les années 1970 [Snyder *et al.* 1974]. La molécule est abondante dans les « hot cores » qui sont les précurseurs des étoiles de grande masses [Ikeda *et al.* 2001] ainsi que dans les « corinos » qui forment les étoiles de faible masse [Cazaux *et al.* 2003 ; Bottinelli *et al.* 2004]. Le mécanisme de formation du DME n'est pas bien connu et pour

cette raison l'étude et la détection de l'espèce déutérée peuvent fournir une information sur la chimie de cette molécule dans le MIS.

L'espèce isotopique principale du DME possède deux groupements méthyle, dont le mouvement de torsion est limité par une barrière de 900 cm^{-1} environ. Dans ce cas il s'agit de deux MVGA de même nature. La deutération de l'un des atomes d'hydrogène entraîne l'apparition de deux conformations comme dans le cas du formiate de méthyle deutéré : symétrique (*S*, car celle-ci possède un plan de symétrie) et asymétrique (*A*). La rupture de symétrie entraîne également la séparation des MVGA et pour le DME-d l'on a deux MVGA de natures différentes : la torsion du groupement méthyle non-deutéré et l'inversion de l'atome de deutérium. L'effet tunnel à travers la barrière à la torsion conduit au dédoublement de chaque transition en deux composantes de symétrie *A* et *E*. L'inversion de l'atome de deutérium dans la conformation *A* conduit au dédoublement supplémentaire de chacune des composantes en 0^+ et 0^- . Dans l'expérience en laboratoire à la température ambiante quelques dizaines des quartets des raies sont particulièrement bien résolus pour des transitions avec des valeurs de nombres quantiques $J < 15$ et $K_a < 5$ assez petits. Ce cas est illustré sur la Fig. 22.

A ce jour, il n'existe pas de codes pouvant traiter de façon efficace et à la précision expérimentale la torsion et l'inversion dans le cas de DME-d. Le code qui traite le cas similaire de la méthylamine a été développé spécialement pour cette molécule et tient compte de la symétrie particulière de l'hamiltonien. En plus, la deutération ne varie pas la hauteur de la barrière à l'inversion de façon significative et pour cette raison, il est impossible de séparer les deux MVGA et appliquer la méthode RAS comme cela a été fait pour l'aminomalononitrile. Comme l'on peut constater à partir de la Fig. 22, les séparations *A* – *E* sont bien supérieures par rapport aux séparations $0^+ - 0^-$ pour chacune de composantes *A* et *E*. Ce fait, ainsi que le fait que les séparations $0^+ - 0^-$ ont été observées pour environ 10 % de raies attribuées de la conformation *A*, nous ont permis de ne pas traiter l'inversion et d'appliquer le modèle qui traite uniquement la torsion pour les deux conformations du DME-d. Le code ERHAM et par conséquent le formalisme de l'effet tunnel à haute barrière ont été choisis pour les raisons suivantes. Tout d'abord ce code a été utilisé dans l'analyse de l'espèce isotopique principale du DME. La relativement haute valeur de la barrière à la rotation interne justifie bien le choix de la méthode. En plus, la conformation *A* ne possède pas de plan de symétrie ce qui limite le choix de codes disponibles (par exemple, on ne peut pas utiliser le code RAM36 qui traite les molécules de symétrie C_s). Pour pouvoir comparer correctement les résultats pour les deux conformations on doit également utiliser le même modèle.

Le code ERHAM a été utilisé pour ajuster et calculer les prévisions spectrales pour les deux conformations. En ce qui concerne les séparations $0^+ - 0^-$ pour la conformation

4.4. Étude du spectre du Diméthyléther deutéré

A, pour chaque doublet on a calculé la fréquence moyenne de ces composantes et on a utilisé cette fréquence comme la fréquence d'une composante de symétrie *A* ou *E* suivant le cas. Pour tenir compte de l'imperfection du modèle dans l'ajustement, les fréquences moyennes ont été pondérées par l'incertitude de 0.1 MHz qui est deux à trois fois supérieur par rapport à l'incertitude de mesure de notre spectromètre térahertz. Au final, les fréquences de plus de 1200 raies pour chaque conformation ont été ajustées avec les écarts-types pondérés proches de 1. Les valeurs des écarts-types de 0.091 MHz pour la conformation *S* et de 0.104 MHz pour la conformation *A* sont un peu élevées par rapport à la précision de mesure du spectromètre. Cela peut davantage signifier la nécessité de l'application d'un modèle qui tient compte de deux MVGA. Néanmoins, la précision des résultats obtenus dans notre étude a été suffisante pour calculer les prévisions spectrales du DME-d et de détecter cette espèce isotopique dans le MIS dans la région de la protoétoile de faible masse IRAS 16293-2422 [[Richard et al. 2013](#)].

4.5 Publications

1. R. Motiyenko, V. Ilyushin, B. Drouin, S. Yu & L. Margulès. **Rotational spectroscopy of methylamine up to 2.6 THz.** *Astronomy & Astrophysics*, 563, A137, 2014.
2. R. Motiyenko, L. Margulès, V. Ilyushin, I. Smirnov, E. Alekseev, D. Halfen & L. M. Ziurys. **Millimeter and submillimeter wave spectra of ^{13}C methylamine.** *Astronomy & Astrophysics*, 587, A152, 2016.
3. R. A. Motiyenko, L. Margulès, E. A. Alekseev & J.-C. Guillemin. **High-Resolution Millimeter Wave Spectroscopy and Ab Initio Calculations of Aminomalononitrile.** *The Journal of Physical Chemistry A*, 119, 1048–1054, 2015.
4. C. Richard, L. Margulès, E. Caux, C. Kahane, C. Ceccarelli, J.-C. Guillemin, R. A. Motiyenko, C. Vastel & P. Groner. **Mono-deuterated dimethyl ether : laboratory spectrum up to 1 THz-Torsion-rotational spectrum within the vibrational ground-state for the symmetric and asymmetric conformers and first detection in IRAS 16293-2422.** *Astronomy & Astrophysics*, 552, A117, 2013.

Rotational spectroscopy of methylamine up to 2.6 THz[★]

R. A. Motiyenko¹, V. V. Ilyushin², B. J. Drouin³, S. Yu³, and L. Margulès¹

¹ Laboratoire de Physique des Lasers, Atomes, et Molécules, UMR CNRS 8523, Université de Lille 1,
59655 Villeneuve d'Ascq Cedex, France

e-mail: roman.motienko@univ-lille1.fr

² Institute of Radio Astronomy of NASU, Chernonopraporna, 4, 61002 Kharkov, Ukraine

³ Jet Propulsion Laboratory, California Institute of Technology, 4800 Oak Grove Drive, Pasadena CA 91109-8099, USA

Received 4 December 2013 / Accepted 20 January 2014

ABSTRACT

Context. Methylamine (CH_3NH_2) is the simplest primary alkylamine that has been detected in the interstellar medium. The molecule is relatively light, with the 50 K Boltzmann peak appearing near 800 GHz. However, reliable predictions for its rotational spectrum are available only up to 500 GHz. Spectroscopic analyses have been complicated by the two large-amplitude motions: internal rotation of the methyl top and inversion of the amino group.

Aims. To provide reliable predictions of the methylamine ground state rotational spectrum above 500 GHz, we studied its rotational spectrum in the frequency range from 500 to 2650 GHz.

Methods. The spectra of methylamine were recorded using the spectrometers based on Schottky diode frequency multiplication chains in the Lille laboratory (500–945 GHz) and in JPL (1060–2660 GHz). The analysis of the rotational spectrum of methylamine in the ground vibrational state was performed on the basis of the group-theoretical high barrier tunneling Hamiltonian developed for methylamine by Ohashi and Hougen.

Results. In the recorded spectra, we have assigned 1849 new rotational transitions of methylamine. They were fitted together with previously published data, to a Hamiltonian model that uses 76 parameters with an overall weighted rms deviation of 0.87. On the basis of the new spectroscopic results, predictions of transition frequencies in the frequency range up to 3 THz with $J \leq 50$ and $K_a \leq 20$ are presented.

Key words. ISM: molecules – methods: laboratory: molecular – submillimeter: ISM – molecular data – line: identification

1. Introduction

Methylamine (CH_3NH_2) is a seven-atom organic molecule and the simplest primary alkylamine. Methylamine is considered as a precursor of the simplest amino acid glycine. Recent experimental studies have shown several reaction pathways to forming glycine in water containing ices starting from CH_3NH_2 and CO_2 subjected to high energy electrons (Holton et al. 2005) or UV radiation (Bossa et al. 2009; Lee et al. 2009). Under similar conditions glycine can decompose to yield methylamine and CO_2 (Ehrenfreund et al. 2001). Interstellar methylamine was first detected toward Sgr B2 at 3.5 cm (Fourikis et al. 1974) and at 3 mm (Kaifu et al. 1974). Recently, methylamine has been detected in a spiral galaxy with a high redshift of 0.89 located in front of the quasar PKS 1830-211 (Muller et al. 2011). It was also observed in cometary samples of the Stardust mission (Glavin et al. 2008).

Despite its astrophysical importance, the current knowledge of the rotational spectrum of methylamine is limited in terms of frequency coverage and in assignments of the J quanta. The limitation was caused by the complexity of theoretical treatment that involved the two large amplitude motions present in the molecule: the torsional (internal rotation) motion of the methyl moiety and the wagging (inversion) motion of the amino group. Both motions are hindered by barriers of intermediate height

(23.2 kJ/mol (2796 K) for the wagging, and 8.6 kJ/mol (1033 K) for the torsion, see Kreglewski 1989), but thanks to the leading role of light hydrogen atoms in the tunneling process, the tunneling splittings observed in the rotational spectra are large (up to several tens of GHz). Earlier studies of methylamine were performed mostly in cm-wave range (Lide 1954; Shimoda et al. 1954; Hirakawa et al. 1956; Nishikawa 1957) and in the lower part of the mm-wave range below 100 GHz (Takagi & Kojima 1971, 1973) as a support for astrophysical observations. All these measurements were summarized by Ohashi et al. (1987) and complemented with new far-infrared rotational transitions and ground-state combination differences determined from the fundamental torsional band.

Later publications represent the extension of the methylamine data set further into millimeter- and submillimeter-wave ranges (Kreglewski & Włodarczak 1992; Ilyushin et al. 2005), as well as high resolution measurements for accurately determining of hyperfine constants (Kreglewski et al. 1992). The most recent critical review of all previously available data on the rotational spectrum of methylamine in the ground vibrational state by Ilyushin & Lovas (2007) covers the frequency range up to 500 GHz and includes the calculated transition frequencies for $J < 30$. At the same time, methylamine is a rather light molecule with the maximum in intensity distribution of the rotational transitions lying near 2 THz for $T = 300$ K. In the interstellar medium, the temperatures are typically lower so the absorption maximum is shifted to lower frequencies. For example, toward

* Full Tables 2 and 3 are only available at the CDS via anonymous ftp to [cdsarc.u-strasbg.fr 130.79.128.5](http://cdsarc.u-strasbg.fr/130.79.128.5) or via <http://cdsarc.u-strasbg.fr/viz-bin/qcat?J/A+A/563/A137>

Sgr B2(N) the rotational temperature of methylamine was recently determined to be 159(39) K by [Halfen et al. \(2013\)](#), and a temperature of 100 K was suggested by [Belloche et al. \(2013\)](#) for the same source. In addition, in the survey by [Belloche et al. \(2013\)](#) methylamine was observed towards Sgr B2(M) with a rotational temperature around 50 K. According to our estimations for $T = 150$ K, the absorption maximum of rotational spectrum of methylamine is at 1.5 THz, and it is shifted down to 0.8 THz for $T = 50$ K. Therefore there is a clear interest in the reliable predictions of the methylamine rotational spectrum above 500 GHz especially regarding the sub-THz coverage of the ALMA project. Simple extrapolation of frequency predictions for molecules exhibiting large amplitude motions may be unreliable in view of the high level of nonrigidity. In this context we present here a new study of the methylamine spectrum with measurements and analysis extended up to 2.6 THz.

2. Experiments

In the frequency range 500–945 GHz we recorded the rotational spectrum of methylamine using the Lille spectrometer based on solid-state sources. We used a commercial sample of methylamine with 99% purity. The optimum gas pressure in the absorption cell providing the best signal-to-noise ratio of the recorded spectra was between 60–70 μbar , with higher pressures preferred in the higher frequency range. Under this condition the observed molecular absorption line shapes were described well with a Voigt profile in which the Doppler and pressure broadening contributions are related as 2 to 1. Owing to additional line broadening caused by unresolved (or partially resolved) quadrupole hyperfine structure, the estimated measurement uncertainty for the strong isolated lines was conservatively taken to be 60 kHz which is somewhat higher compared to the value of 30 kHz usually provided by the Lille spectrometer. The frequencies of the lines with poor signal-to-noise ratio and distorted line shape were estimated to have uncertainties of 100–200 kHz.

Measurements from Jet Propulsion Laboratory (JPL) utilized a modular frequency multiplication spectrometer built from a microwave synthesizer and amplifier-multiplier components ([Drouin et al. 2005](#); [Pearson et al. 2011](#)). Measurements were done at room temperature in the following frequency windows: 1.061–1.093 THz, 1.575–1.625 THz and 2.560–2.660 THz at pressures ranging from 25–140 μbar . Estimated uncertainties are 100 kHz, 200 kHz and 500 kHz depending on the width of the observed lines and distortions in the lineshapes.

3. Assignment and analysis of the spectrum

3.1. Theoretical model

The phenomenological Hamiltonian used in the present study is based on the group-theoretical high-barrier tunneling formalism developed for methylamine by [Ohashi & Hougen \(1987\)](#). The formalism appeared to be the most successful in fitting the rotational spectrum of methylamine in the ground state as well as in the first excited torsional state. The Hamiltonian operator is defined as

$$\begin{aligned} H = & h_v + h_j J^2 + h_k J_z^2 + (f_+ J_+^2 + f_- J_-^2) + q J_z \\ & + (r_+ J_+ + r_- J_-) + [s_+(J_+ J_z + J_z J_+)] \\ & + s_-(J_- J_z + J_z J_-) + (f_+^{(2)} J_+^4 + f_-^{(2)} J_-^4) \\ & + \text{higher order terms} \end{aligned} \quad (1)$$

where “higher order terms” represent ordinary centrifugal distortion terms as well as the J and K dependences of the various tunneling splitting parameters. Hamiltonian matrix elements of the various operators are expanded in Fourier series whose n th term represents a tunneling process from molecular framework 1 to molecular framework n (see the paper [Ohashi & Hougen 1987](#), for definition of the frameworks in methylamine). In the notation adopted, the subscript $n = 1$ corresponds to nontunneling motion. The even subscripts $n = 2, 4, 6, \dots$ designate tunneling involving inversion of the amine group. The odd subscripts $n = 3, 5, 7, \dots$ refer to tunneling involving only torsional motion of the methyl group. Thus, the tunneling from framework 1 to framework 2 corresponds to the inversion of amino group followed by 60° internal rotation of the methyl group, whereas the tunneling from framework 1 to framework 3 corresponds to the internal rotation of the methyl group by 120°. Corresponding to this approach the coefficients h_m , h_{nJ} , q_n etc. ($n \neq 1$), which appear in the table of molecular constants refer to different tunneling processes in the molecule, while the coefficients with $n = 1$ are represented by usual asymmetric rotor Hamiltonian.

In the Hamiltonian (1) the nontunneling value of h_v corresponds to an absolute energy offset for all levels, but the tunneling values of h_v represent the tunneling frequencies in the non-rotating molecule for each symmetrically inequivalent tunneling path. The nontunneling values of h_j , h_k , and f correspond physically to the usual asymmetric-rotor rotational constants $\frac{1}{2}(B+C)$, $A - \frac{1}{2}(B+C)$, and $\frac{1}{4}(B-C)$, while the tunneling values of h_j , h_k , and f correspond to tunneling corrections to these rotational constants. The $f^{(2)}$ parameters correspond to tunneling and nontunneling contributions to the asymmetric-rotor $\Delta K = 4$ term of the Hamiltonian. The linear terms q and r in Eq. (1) correspond physically to the interaction of components of the total angular momentum with any angular momentum generated in the molecule-fixed axis system by the two large amplitude motions in the molecule. Only tunneling contributions for these linear terms are allowed in the Hamiltonian. The nontunneling quadratic s term allows physically for the fact that the molecule-fixed components J_x , J_y , and J_z of the total angular momentum J are not expressed in the principal-axis system of the molecule since partial internal axis method is used to set up the Hamiltonian.

According to the energy level labeling scheme adopted for methylamine in [Ohashi et al. \(1987\)](#), each energy level is labeled by the value of the usual quantum numbers J and $K = K_a$ and by an overall torsion-wagging-rotation symmetry species Γ corresponding to an irreducible representation of the permutation-inversion group $G_{12}: A_1, A_2, B_1, B_2, E_1, E_2$. The symmetry labels of doubly degenerate levels E_1 and E_2 have additional ± 1 labels to distinguish between two levels with the same J and K_a (see discussion by [Ohashi et al. 1987](#)). For the $K_a = 0$ levels, the $+1$ and -1 labels have no meaning since there is only one E_1 or E_2 level. Since the choice is arbitrary, we have designated all $K_a = 0$ E levels as $+1$ levels.

The computer fitting program used in the present analysis of the rotational spectrum of methylamine was developed by N. Ohashi ([Ohashi et al. 1987](#)) and previously modified by V. Ilyushin who added new Hamiltonian terms ([Ilyushin et al. 2005](#)) and provided the line strength calculations ([Ilyushin & Lovas 2007](#)). In the present study the program was subjected to a number of further modifications. In addition to expanding different array dimensions with the aim of providing calculations for J quantum numbers above $J = 30$ and a number of modifications undertaken with the aim of speeding up the code, new higher

order centrifugal distortion corrections to the ρ parameter (ρ_{JJ} , ρ_{JK} , and ρ_{KK}) were included into the program code. From these parameters ρ_{JJ} , and ρ_{JK} are determined in the current study. Also we have used a new labeling procedure in the program since the previous labeling procedure was based on searching for the dominant component in basis-set composition of eigenvectors and not for all eigenstates above $J = 30$ it was possible to find such a component. Therefore the labeling scheme based on searching for similarities in basis-set composition in eigenvectors belonging to adjacent J values described by Ilyushin (2004) was used.

Methylamine has two nonzero dipole moment components $\mu_a = -0.307$ D and $\mu_c = 1.258$ D. The symmetry selection rules are the following: $A_1 \leftrightarrow A_2$, $B_1 \leftrightarrow B_2$, $E_1 \leftrightarrow E_1$, $E_2 \leftrightarrow E_2$. Whereas in the framework of the high-barrier tunneling formalism used for methylamine there are both tunneling and nontunneling contributions to the dipole moment matrix elements, we do not have any information on the tunneling contributions and therefore the calculations were done taking only non-tunneling contributions into account (permanent dipole moment components). It should be noted that the observed line intensities are reproduced rather well by nontunneling contributions of dipole moment matrix elements.

3.2. Assignment and analysis

The assignment procedure was rather straightforward because of relatively sparse spectra, good signal-to-noise ratio for the majority of the ground state lines, and good predictions obtained for the frequency range above 500 GHz from the set of parameters in the paper by Ilyushin & Lovas (2007). First we proceeded with the assignment of all the lines with $J < 30$, which was the upper J limit of the previous work (Ilyushin & Lovas 2007). Most of these rotational transitions were predicted within the 0.5 MHz vicinity of the actual line positions. Only a few transitions, with $J = 26 \dots 30$, exhibited initial “obs-calc” deviations up to 1.2 MHz. As the next step, we extended our analysis to transitions involving higher values of $J > 30$. Indeed, after the $J < 30$ assignment was complete the observed spectra still contained many strong unassigned lines that could be attributed to the ground vibrational state. This was especially evident in the case of ^cQ -type transitions. A new prediction with $J \leq 50$ was generated and the transitions with J up to 45 were assigned in the recorded spectra. Additionally, several $J > 30$ rotational transitions were assigned in the millimeter-wave spectra records obtained in the previous study of methylamine (Ilyushin et al. 2005). A portion of the observed rotational spectrum of methylamine around 890 GHz is shown in Fig. 1 and compared to the predicted rotational spectrum in the ground vibrational state. As can be seen from Fig. 1 the overall correspondence between experimental and theoretical spectra is very good. Particularly in this spectral region, the observed spectrum is dominated by ^cQ -type series of transitions with $K_a = 6 \leftarrow 5$, but also another Q -type series, presumably in the first excited torsional state (268 cm⁻¹ above the ground state), can be distinguished.

The relatively narrow linewidths below 1 THz enable resolution of nuclear quadrupole hyperfine splittings for more than 200 rotational transitions. The hyperfine structure was resolved even for relatively high- J transitions up to $J = 44$. Only the most intense hyperfine components with the $\Delta F = \Delta J$ selection rule were observed. Typically a resolved pattern of the hyperfine structure was observed as a doublet with an approximately 2-to-1 ratio in intensities. The stronger doublet component contains unresolved hyperfine transitions with selection rules $F = J+1 \rightarrow F' = J' + 1$ and $F = J - 1 \rightarrow F' = J' - 1$, whereas the weaker

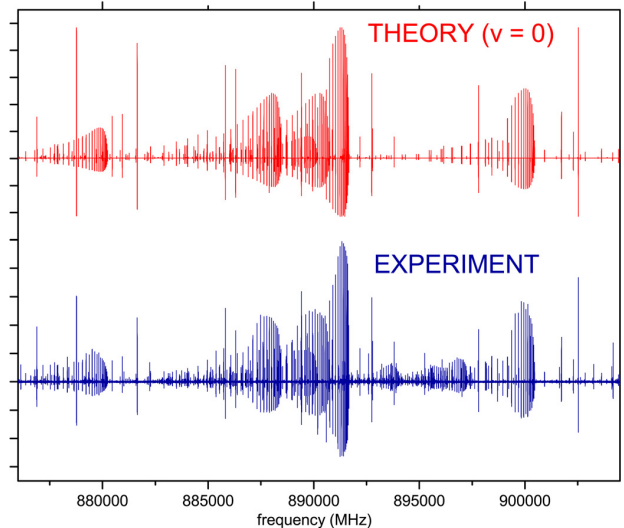


Fig. 1. Predicted (in red) and observed (in blue) rotational spectrum of methylamine between 876 and 905 GHz dominated by ^cQ -type series of transitions with $K_a = 6 \leftarrow 5$. A slight inconsistency between predicted and observed spectrum, that may be visible for some strong lines, is due to source power and detector sensitivity variations.

doublet component corresponds to the $F = J \rightarrow F' = J'$ transition. To provide hyperfine-free frequencies used in our analysis of the rotation-torsion-wagging spectrum of the ground state of methylamine, we fit the frequencies of the individual hyperfine components using the model described in the paper by Ilyushin et al. (2005). In the fit we also used previously available data on the methylamine quadrupole hyperfine splittings (Ilyushin et al. 2005). The quadrupole hyperfine parameters χ_+ , and χ_- obtained from the fitting of the hyperfine patterns of the rotational transitions are presented in Table 1.

In total, the new dataset for the rotational spectrum of the ground state of methylamine includes 2558 microwave and 785 far-infrared transitions. Here we use terms “microwave” and “far infrared” to distinguish between the measurements obtained using the methods of conventional absorption spectroscopy and Fourier transform spectroscopy, although in fact the frequency range of our current “microwave” measurements overlap with “far infrared” measurements of the previous paper (Ilyushin & Lovas 2007), and we were able to remeasure 65 far infrared transitions in our current work improving thus the measurement accuracy for these transitions by at least two orders of magnitude. Compared to the previous paper by Ilyushin & Lovas (2007), 1849 new microwave transitions were included in the dataset as a result of the present study. The details of the weighting scheme of the previous measurements are described in papers by Ilyushin et al. (2005) and Ilyushin & Lovas (2007).

The set of 3343 rotational transitions in the ground vibrational state of methylamine was fitted to the theoretical model described above. The fit adopted in the present study as the “best” achieved the rms deviation of 0.094 MHz for microwave transitions and 0.00029 cm⁻¹ for FIR transitions. The weighted rms deviation of the fit was 0.87. It was obtained with 76 parameters, whereas 53 parameters were used in the last two previous studies. The values of the molecular parameters obtained from the final fit are presented in Table 1. Comparison of Table 1 in Ilyushin & Lovas (2007) and Table 1 here shows that the new parameters correspond to the higher order centrifugal distortion

Table 1. Molecular parameters of the ground torsional state of methylamine.

	Rotational	Inversion	Torsional
B	22 169.36697(12)	h_2	-1549.18492(70)
$A - B$	80 986.38521(57)	h_4	2.72760(86)
$B - C$	877.88368(10)	h_{2J}	0.1019324(54)
Δ_J	$3.946663(19) \times 10^{-2}$	h_{2K}	1.738763(87)
Δ_{JK}	0.1710869(21)	h_{4J}	$-6.81(39) \times 10^{-5}$
Δ_K	0.701310(14)	h_{4K}	$-4.083(26) \times 10^{-3}$
δ_J	$1.757561(60) \times 10^{-3}$	h_{2JJ}	$-4.218(19) \times 10^{-6}$
δ_K	-0.336039(16)	h_{2KK}	$-9.640(16) \times 10^{-4}$
Φ_J	-1.9145(91) $\times 10^{-8}$	h_{2JK}	-1.4939(20) $\times 10^{-4}$
Φ_{JK}	3.728(13) $\times 10^{-6}$	h_{2JKK}	1.004(18) $\times 10^{-7}$
Φ_{KJ}	-1.1185(60) $\times 10^{-5}$	h_{2KKK}	3.442(88) $\times 10^{-7}$
Φ_K	$3.837(13) \times 10^{-5}$	q_2	21.54649(37)
ϕ_J	-1.059(37) $\times 10^{-9}$	q_4	$-2.700(16) \times 10^{-2}$
ϕ_{JK}	1.626(14) $\times 10^{-6}$	q_{2J}	$-3.6839(20) \times 10^{-3}$
ϕ_K	3.677(17) $\times 10^{-4}$	q_{2K}	$-1.9484(12) \times 10^{-2}$
L_{JK}	4.867(50) $\times 10^{-9}$	q_{2JJ}	$6.56(13) \times 10^{-7}$
L_{KKJ}	-2.035(13) $\times 10^{-8}$	q_{2JK}	1.006(49) $\times 10^{-6}$
L_K	1.021(38) $\times 10^{-8}$	q_{2KK}	8.632(74) $\times 10^{-6}$
		q_{2JKK}	1.122(36) $\times 10^{-9}$
ρ	0.649759856(98)	f_2	-9.6036(16) $\times 10^{-2}$
ρ_J	-1.954(56) $\times 10^{-8}$	f_4	3.445(21) $\times 10^{-4}$
ρ_K	-1.1548(30) $\times 10^{-6}$	f_{2J}	5.540(28) $\times 10^{-6}$
ρ_{JJ}	-3.93(19) $\times 10^{-11}$	f_{2K}	2.972(75) $\times 10^{-4}$
ρ_{JK}	6.376(91) $\times 10^{-10}$	f_{2JJ}	$-2.56(14) \times 10^{-10}$
		$f_{2JK}^{(2)}$	-4.154(12) $\times 10^{-6}$
		$f_{2JKK}^{(2)}$	3.76(28) $\times 10^{-8}$
Hyperfine		$f_{2J}^{(2)}$	3.328(91) $\times 10^{-10}$
χ_+	-2.4129(12)	$f_{2J}^{(2)}$	10.628(33)
χ_-	6.0697(25)	r_2	
		r_{2J}	-1.067(42) $\times 10^{-3}$

Notes. All parameters are in MHz, except for ρ , ρ_J , ρ_K , ρ_{JJ} , and ρ_{JK} which are unitless. The structural parameter ρ describes the coupling between the internal rotation of the methyl top and the overall rotation of the molecule as a whole.

Table 2. Measured rotational transitions of methylamine in the ground vibrational state (a part of the table available at the CDS).

J'	K'_a	Γ'	J''	K''_a	Γ''	Obs. freq. (MHz)	Uncertainty (MHz)	Obs.-calc. (MHz)	Ref.
8	3	E2+1	9	2	E2+1	6857.0000	0.5000	-0.0130	8
26	1	E2-1	26	0	E2+1	7515.5600	0.5000	0.2446	4
30	1	E1-1	30	0	E1+1	7727.7400	0.5000	0.1575	2
						...			
26	1	A1	25	2	A2	937 775.1550	0.1000	-0.0528	1
26	1	E2+1	25	2	E2-1	938 406.5120	0.1000	-0.0832	1
33	3	E1-1	32	4	E1-1	938 488.7230	0.1000	0.0283	1
12	3	E2+1	11	2	E2+1	938 520.8920	0.0600	0.0265	1
32	2	E2+1	31	3	E2+1	938 870.3740	0.1000	-0.1167	1
32	2	E1-1	31	3	E1+1	940 305.5990	0.1000	0.0354	1
12	3	E2-1	11	2	E2+1	940 874.0690	0.1000	-0.0028	1
26	1	E1+1	25	2	E1+1	940 900.0500	0.0600	-0.0182	1
						...			

References. (1) This study; (2) Shimoda et al. (1954); (3) Lide (1954); (4) Hirakawa et al. (1956); (5) Nishikawa (1957); (6) Takagi & Kojima (1971); (7) Takagi & Kojima (1973); (8) Ohashi et al. (1987); (9) Kreglewski et al. (1992); (10) Kreglewski & Włodarczak (1992); (11) Ilyushin et al. (2005).

corrections of the rotational and torsional-wagging tunneling parameters, as might be expected a priori.

The list of measured rotational transitions of the ground vibrational state of methylamine is presented in Table 2. It includes the rotational transition frequencies obtained in this study as well as those available from previous studies. In the first six columns of Table 2, the quanta for each spectral line are given: J , K_a , and

symmetry label Γ . In the following columns we provide the observed transition frequencies, measurement uncertainties, residuals from the fit, and the reference from which the measurements were obtained. Only hyperfine free rotational frequencies that were used in the final fit are presented in Table 2 for the observed transitions. Table 3 predicts the ground state rotational spectrum of methylamine up to 3 THz. The spectrum was calculated taking

Table 3. Predicted transitions of methylamine in the ground vibrational state (a part of the table available at the CDS).

J'	K'_a	Γ'	F'	J''	K''_a	Γ''	F''	Calc. freq. (MHz)	Uncertainty (MHz)	$\mu^2 S$ (D ²)	W_{st}	E_l cm ⁻¹
16	6	E1-1	15	15	5	E1-1	15	1 598 784.9732	0.0116	0.015	3	245.110
16	6	E1-1	16	15	5	E1-1	15	1 598 785.5067	0.0116	3.853	3	245.110
16	6	E1-1	17	15	5	E1-1	16	1 598 785.5734	0.0116	4.102	3	245.110
16	6	E1-1	15	15	5	E1-1	14	1 598 785.5800	0.0116	3.618	3	245.110
16	6	E1-1	16	15	5	E1-1	16	1 598 786.0754	0.0116	0.015	3	245.110
27	2	B1	27	26	1	B2	26	1 599 370.4898	0.0357	2.832	3	515.248
27	2	B1	28	26	1	B2	27	1 599 371.6159	0.0357	2.939	3	515.248
27	2	B1	26	26	1	B2	25	1 599 371.6610	0.0357	2.729	3	515.248
28	5	E2-1	27	28	2	E2-1	27	1 599 595.1420	0.0279	0.009	1	614.251
28	5	E2-1	29	28	2	E2-1	29	1 599 595.1714	0.0279	0.009	1	614.251
28	5	E2-1	28	28	2	E2-1	28	1 599 595.9938	0.0279	0.009	1	614.251

nuclear quadrupole hyperfine structure into account. Therefore each energy level in Table 3 is labeled by four quantum numbers: J , K_a , Γ , and total angular momentum F . The quantum numbers are followed by the columns with calculated transition frequencies and corresponding uncertainties. The next two columns contain the product $\mu^2 S$, and the nuclear spin statistical weight which is equal to 1 for A_1 , A_2 and E_2 species and equal to 3 for B_1 , B_2 and E_1 species. The next column represents the energy of the lower state. Owing to their significant sizes, the complete versions of Tables 2 and 3 are presented at the CDS. Here only parts of Tables 2 and 3 are given for illustration purposes.

Since the highest J and K_a values accessed in our experimental study were $J = 45$ and $K_a = 19$, the limitation of $J = 50$, $K_a = 20$ was adopted for our prediction. We have included in the calculation the rotational transitions with rotational selection rules $J = 0, \pm 1$ and $K_a = 0, \pm 1, \pm 2, \pm 3$. In Table 3, those transitions that match the frequency range requirement (from 1 GHz to 3 THz) and whose predicted uncertainties are less than 1 MHz, and line strength exceeds the limit of 0.01 are included. Also, to limit the size of Table 3, we have only presented the most intense hyperfine quadrupole components for which the relative intensities exceeded 0.1% of the total intensity of the rotation transition (i.e., mainly with the selection rule $\Delta F = \Delta J$). In addition we provide the rotational part of the partition function $Q_r(T)$ of methylamine calculated from first principles (Table 4), i.e. via direct summation over the rotational-tunneling states. The maximum value of the J quantum number for the energy levels taken for calculating the partition function is 100. The vibrational part $Q_v(T)$ may be estimated in the harmonic approximation using the normal modes reported by Shimanouchi (1972). Simple formulas for calculating $Q_v(T)$ can be found elsewhere (see, for example, Gordy & Cook 1984).

To get an estimate of how the observed deviations from the predicted positions may correlate with predicted uncertainties we compared the predicted uncertainties and transition frequencies calculated using the Hamiltonian parameters of Ilyushin & Lovas (2007) with actual line positions for the new lines measured in our current work. The highest obs.-calc. value (about 34 MHz) was found for the 44 3 B2 \rightarrow 44 2 B1 transition which frequency was predicted (based on the results of Ilyushin & Lovas 2007) with the uncertainty of 3.2 MHz thus giving a ratio of ten between observed deviation and predicted uncertainty. Comparison for other newly measured transitions more or less satisfies this upper limit on the correlation between observed deviations and predicted uncertainties. The gap between predicted uncertainties and actual deviations from the prediction is quite understandable since the uncertainties do not account

Table 4. Rotation part $Q_r(T)$ of the total internal partition function $Q(T) = Q_v(T) \times Q_r(T)$, calculated from first principles using the parameter set of Table 1.

Temperature (K)	$Q_r(T)$
300	31 179.43
200	16 960.43
150	11 011.92
50	2116.56
10	188.94

for the extension of the model needed to describe higher J and K_a transitions adequately. Presumably, the value of this gap is determined by the extrapolation distance and by a level of non-rigidity of a molecule. The extrapolation from $J = 45$ to $J = 50$ in our current spectrum prediction is less strained than the example considered above of extrapolation from $J = 30$ to $J = 45$, and therefore we might expect better correspondence between predicted uncertainties and actual deviations for the newly predicted transition frequencies.

4. Conclusions

A new study of the ground state rotational spectrum was carried out in a wide frequency range up to 2.6 THz. The study represents an almost fivefold expansion in terms of frequency range coverage for the rotational spectrum of methylamine. Although we have not discovered any significant discrepancies between the ground state spectra observed and predicted on the basis of the last results by Ilyushin and Lovas, 21 new parameters of the Hamiltonian were added into the model in order to achieve the fit within experimental accuracy. The inclusion of new parameters is explained by the extension of the model for transitions involving $J > 30$, and also by the fact that a number of far-infrared transitions were remeasured with microwave precision. The results of the present study allow us to produce reliable predictions of the ground state transition frequencies of the methylamine molecule for astrophysical purposes in the frequency range up to 3 THz for $0 < J < 50$ and $0 < K_a < 20$.

Acknowledgements. The authors are indebted to Dr. N. Ohashi for providing his fitting program for methylamine. This work was done with the support of the Ukrainian-French CNRS-PICS 6051 project. Portions of this research were carried out at the Jet Propulsion Laboratory, California Institute of Technology, under contract with the National Aeronautics and Space Administration.

References

- Belloche, A., Müller, H. S. P., Menten, K., Schilke, P., & Comito, C. 2013, A&A, 559, A47
- Bossa, J.-B., Duvernay, F., Theulé, P., et al. 2009, A&A, 506, 601
- Drouin, B. J., Maiwald, F. W., & Pearson, J. C. 2005, Rev. Sci. Instrum., 76, 093113
- Ehrenfreund, P., Bernstein, M. P., Dworkin, J. P., Sandford, S. A., & Allamandola, L. J. 2001, ApJ, 550, L95
- Fourikis, N., Takagi, K., & Morimoto, M. 1974, ApJ, 191, L139
- Glavin, D. P., Dworkin, J. P., & Sandford, S. A. 2008, Met. Planet. Sci., 43, 399
- Gordy, W., & Cook, R. L. 1984, Microwave Molecular Spectra, Techniques of Chemistry, Vol. XVIII (New York: Wiley)
- Halfen, D. T., Iyushin, V. V., & Ziurys, L. M. 2013, ApJ, 767, 66
- Hirakawa, H., Miyahara, A., & Shimoda, K. 1956, J. Phys. Soc. Jpn., 11, 334
- Holtom, P. D., Bennett, C. J., Osamura, Y., Mason, N. J., & Kaiser, R. I. 2005, ApJ, 626, 940
- Iyushin, V. V. 2004, J. Mol. Spec., 227, 140
- Iyushin, V., & Lovas, F. J. 2007, J. Phys. Chem. Ref. Data, 36, 1141
- Iyushin, V. V., Alekseev, E. A., Dyubko, S. F., Motiyenko, R. A., & Hougen, J. T. 2005, J. Mol. Spectr., 229, 170
- Kaifu, N., Morimoto, M., Nagane, K., et al. 1974, ApJ, 191, L135
- Kreglewski, M. 1989, J. Mol. Spectr., 133, 10
- Kreglewski, M., & Włodarczak, G. 1992, J. Mol. Spectr., 156, 383
- Kreglewski, M., Stahl, W., Grabow, J.-U., & Włodarczak G. 1992, Chem. Phys. Lett., 196, 155
- Lee, C.-W., Kim, J.-K., Moon, E.-S., Minh, Y. C., & Kang, H. 2009, ApJ, 697, 428
- Lide, Jr., D. R. 1954, J. Chem. Phys., 22, 1613
- Muller, S., Beelen, A., Guelin, M., et al. 2011, A&A, 535, A103
- Nishikawa, T. 1957, J. Phys. Soc. Jpn., 12, 668
- Ohashi, N., & Hougen, J. T. 1987, J. Mol. Spec., 121, 474
- Ohashi, N., Takagi, K., Hougen, J. T., Olson, W. B., & Lafferty, W. J. 1987, J. Mol. Spectr., 126, 443
- Pearson, J. C., Drouin, B. J., Maestrini, A., et al. 2011, Rev. Sci. Instrum., 82, 093105
- Schimanouchi, T. 1972, in Tables of Molecular Vibrational Frequencies, Vol. I: consolidated (Washington, DC: National Bureau of Standards), 67
- Shimoda, K., Nishikawa, T., & Itoh, T. 1954, J. Phys. Soc. Jpn., 9, 974
- Takagi, K., & Kojima, T. 1971, J. Phys. Soc. Jpn., 30, 1145
- Takagi, K., & Kojima, T. 1973, ApJ, 181, L91

Millimeter and submillimeter wave spectra of ^{13}C methylamine[★]

R. A. Motiyenko¹, L. Margulès¹, V. V. Ilyushin², I. A. Smirnov², E. A. Alekseev², D. T. Halfen³, and L. M. Ziurys³

¹ Laboratoire de Physique des Lasers, Atomes, et Molécules, UMR CNRS 8523, Université de Lille 1,
59655 Villeneuve d'Ascq Cedex, France

e-mail: roman.motienko@univ-lille1.fr

² Institute of Radio Astronomy of NASU, Chernovonopraporna, 4, 61002 Kharkov, Ukraine

³ Departments of Chemistry and Astronomy, Arizona Radio Observatory and Steward Observatory, University of Arizona,
Tucson, AZ 85721, USA

Received 9 July 2015 / Accepted 7 December 2015

ABSTRACT

Context. Methylamine (CH_3NH_2) is a light molecule of astrophysical interest, which has an intensive rotational spectrum that extends in the submillimeter wave range and far beyond, even at temperatures characteristic for the interstellar medium. It is likely for ^{13}C isotopologue of methylamine to be identified in astronomical surveys, but there is no information available for the $^{13}\text{CH}_3\text{NH}_2$ millimeter and submillimeter wave spectra.

Aims. In this context, to provide reliable predictions of $^{13}\text{CH}_3\text{NH}_2$ spectrum in millimeter and submillimeter wave ranges, we have studied rotational spectra of the ^{13}C methylamine isotopologue in the frequency range from 48 to 945 GHz.

Methods. The spectrum of ^{13}C methylamine was recorded using conventional absorption spectrometers. The analysis of the rotational spectrum of ^{13}C methylamine in the ground vibrational state was performed on the basis of the group-theoretical high-barrier tunneling Hamiltonian that was developed for methylamine. The available multiple observations of the parent methylamine species toward Sgr B2(N) at 1, 2, and 3 mm using the Submillimeter Telescope and the 12 m antenna of the Arizona Radio Observatory were used to make a search for interstellar $^{13}\text{CH}_3\text{NH}_2$.

Results. In the recorded spectra, we have assigned 2721 rotational transitions that belong to the ground vibrational state of the $^{13}\text{CH}_3\text{NH}_2$. These measurements were fitted to the Hamiltonian model that uses 75 parameters to achieve an overall weighted rms deviation of 0.73. On the basis of these spectroscopic results, predictions of transition frequencies in the frequency range up to 950 GHz with $J \leq 50$ and $K_a \leq 20$ are presented. The search for interstellar ^{13}C methylamine in available observational data was not successful and therefore only an upper limit of $6.5 \times 10^{14} \text{ cm}^{-2}$ can be derived for the column density of $^{13}\text{CH}_3\text{NH}_2$ toward Sgr B2(N), assuming the same source size, temperature, linewidth, and systemic velocity as for parent methylamine isotopic species.

Key words. ISM: molecules – methods: laboratory: molecular – submillimeter: ISM – molecular data – line: identification

1. Introduction

This paper is a part of a series of studies conducted in PhLAM Lille (France) that are devoted to the investigations of the spectra of different isotopic species of astrophysical molecules (Demyk et al. 2007; Margulès et al. 2009a,b, 2015; Carvajal et al. 2009; Tercero et al. 2012; Bouchez et al. 2012; Coudert et al. 2012; Richard et al. 2012, 2013; Haykal et al. 2013; Kutsenko et al. 2013; Nguyen et al. 2013). In particular these works led to the first interstellar detection of HCOOCH_2D (Coudert et al. 2013), $\text{HCO}^{13}\text{CH}_3$ (Carvajal et al. 2009), $\text{HCO}^{18}\text{OCH}_3$, $\text{HC}^{18}\text{OOCCH}_3$ (Tercero et al. 2012), CH_2DOCH_3 (Richard et al. 2013). In the current paper we focus our attention on the ^{13}C isotopologue of the methylamine molecule. Interstellar methylamine was first detected toward Sgr B2 at 3.5 cm (Fourikis et al. 1974) and at 3 mm (Kaifu et al. 1974). Later surveys conducted by Turner (1989) toward Sgr B2(OH) and Nummeling et al. (1998) in Sgr B2(N) also found spectral lines of CH_3NH_2 . Recently, methylamine has been detected in a spiral galaxy with a high redshift of 0.89, located in front of the quasar PKS 1830-211 (Muller et al. 2011). Also Fourikis et al. (1977) reported probable detection of deuterated methyl amine (CH_3NHD) in the southern region of Sgr B2.

The rotational spectrum of the parent methylamine species has been the subject of a number of investigations. The latest paper on this issue (Motiyenko et al. 2014) covers the frequency range up to 2.6 THz and the range of rotational quantum number J up to 45, which provides reliable predictions of the methylamine spectrum in the frequency range up to 3 THz. Also a number of deuterated isotopologues were studied by means of microwave spectroscopy: CH_3ND_2 (Takagi & Kojima 1971), CD_3NH_2 (Sastry 1960; Kreglewski et al. 1990b), CD_3ND_2 (Lide 1954; Kreglewski et al. 1990a), CH_3NHD (Ohashi et al. 1991), and CH_2DNH_2 (Tamagake & Tsuboi 1974). To our knowledge, there has been no previous spectroscopic study of $^{13}\text{CH}_3\text{NH}_2$ isotopologue of methylamine in the microwave range. In this context, we present here an experimental study of the $^{13}\text{CH}_3\text{NH}_2$ ground state rotational spectrum in the frequency range from 48 to 945 GHz. Based on the results obtained, a search for interstellar ^{13}C methylamine was made using available data from our recent observations of methanimine (CH_2NH) and methyl amine (CH_3NH_2) toward Sgr B2(N) (Halfen et al. 2013).

2. Experiments

The measurements in Lille were done with a ^{13}C enriched sample of methylamine purchased from Sigma-Aldrich, which was used without further purification. The measurements in the frequency ranges 150–315, 400–630 and 775–945 GHz were

* Full Tables 3 and 4 are only available at the CDS via anonymous ftp to cdsarc.u-strasbg.fr (130.79.128.5) or via <http://cdsarc.u-strasbg.fr/viz-bin/qcat?J/A+A/587/A152>

covered using the Lille spectrometer with solid state multiplied sources. The frequency of the Agilent synthesizer (12.5–17.5 GHz) was used as a reference source of radiation, which was further multiplied using various active and passive multipliers. Estimated uncertainties for measured line frequencies are 30 kHz, 60 kHz, and 100 kHz, depending on the observed S/N ratio and the frequency range. The measurements in Kharkov were made using a sample with a natural abundance of ^{13}C isotopologue of methylamine. The measurements were performed in the frequency range from 48 to 148 GHz using the automated spectrometer of Institute of Radio Astronomy of NASU (Alekseev et al. 2012). An initial search for the $^{13}\text{CH}_3\text{NH}_2$ ground state rotational transitions was made using the spectrum records from our previous study (Ilyushin et al. 2005). Later a number of transitions were remeasured with an increased signal accumulation to provide a better S/N ratio. The estimated uncertainties for the measured line frequencies are 30 kHz and 100 kHz, depending on the observed S/N ratio.

3. Assignment and analysis of the spectrum

3.1. Theoretical model

In our current study, we used the phenomenological Hamiltonian model, which is based on the group-theoretical high-barrier tunneling formalism that was developed for methylamine by Ohashi & Hougen (1987). Since rather complete descriptions of this formalism and its implementation in the case of the methylamine molecule have been already presented several times in the literature (Ohashi & Hougen 1987; Ohashi et al. 1987; Ilyushin et al. 2005; Ilyushin & Lovas 2007; Motiyenko et al. 2014), we do not repeat a general description here. The formalism appeared to be the most successful for fitting the rotational spectrum of methylamine in the ground state, as well as in the first excited torsional state, and therefore it was chosen for the analysis of the $^{13}\text{CH}_3\text{NH}_2$ ground state rotational spectrum.

The Hamiltonian operator is defined as

$$\begin{aligned} H = & h_v + h_j J^2 + h_k J_z^2 + (f_+ J_+^2 + f_- J_-^2) + q J_z \\ & + (r_+ J_+ + r_- J_-) + [s_+(J_+ J_z + J_z J_+)] \\ & + s_-(J_- J_z + J_z J_-)] + (f_+^{(2)} J_+^4 + f_-^{(2)} J_-^4) \\ & + \text{higher order terms}, \end{aligned} \quad (1)$$

where “higher order terms” represent ordinary centrifugal distortion terms as well as the J and K dependences of the various tunneling splitting parameters. The physical meaning of different parameters in Hamiltonian (1) was briefly discussed in Motiyenko et al. (2014). The computer fitting program used in the present analysis of the rotational spectrum of ^{13}C methylamine was developed by N. Ohashi (Ohashi et al. 1987) and previously modified by V. Ilyushin, who added new Hamiltonian terms (Ilyushin et al. 2005; Motiyenko et al. 2014) and provided the line strength calculations (Ilyushin & Lovas 2007). As in the case of the main isotopologue (Ilyushin et al. 2005; Motiyenko et al. 2014) we have made a separate analysis of the quadrupole hyperfine structure of ^{13}C methylamine transitions, which is present because of the nonzero nuclear quadrupole moment of nitrogen ^{14}N . We used the following hyperfine energy expression, which permits the calculation of the hyperfine splittings for each rotational transition:

$$\begin{aligned} E_{hf}(I, J, F) = & \left[\frac{1}{2} \chi_+ \langle J_x^2 + J_y^2 - 2J_z^2 \rangle - \frac{1}{2} \chi_- \langle J_x^2 - J_y^2 \rangle \right. \\ & \left. + \chi_{xz} \langle J_x J_z + J_z J_x \rangle \right] \frac{2f(I, J, F)}{J(J+1)}, \end{aligned} \quad (2)$$

where $\chi_+ = -\chi_{zz}$, $\chi_- = \chi_{yy} - \chi_{xx}$ (Kreglewski et al. 1990a); $\langle J_x^2 \rangle$, $\langle J_y^2 \rangle$, $\langle J_z^2 \rangle$, $\langle J_x J_z + J_z J_x \rangle$ are the expectation values of the operators in the axis system of the effective Hamiltonian (1) used, and $f(I, J, F)$ is the Casimir function (Gordy & Cook 1984). As in the case of the main methylamine isotopologue, the analysis of observed hyperfine structure produced a set of “hyperfine free” rotational transition frequencies which were further analyzed using the effective Hamiltonian (1).

3.2. Assignment and analysis

We started our analysis of recorded spectra from a search of $K_a = 0$ R -type transitions which, because of torsion-wagging large amplitude motion in the molecule, form a characteristic quartet of lines. This search was based on the assumption that the substitution of ^{13}C will not affect significantly the tunneling splittings in the molecule (in comparison to the main methylamine isotopologue) and that the corresponding quartets of $K_a = 0$ R -type transitions will have a similar appearance in $^{13}\text{CH}_3\text{NH}_2$ and $^{12}\text{CH}_3\text{NH}_2$ spectra. The tentative assignment of the first such quartet at 173.2 GHz that corresponds to the $K_a = 0$ $J = 4 \leftarrow 3$ transitions gave us an opportunity to assign the whole series of this kind of transitions and get an initial approximation for the rotational constants of $^{13}\text{CH}_3\text{NH}_2$ (at this stage the tunneling parameters were kept fixed at the values of the main methylamine isotopologue, Motiyenko et al. 2014). Obtained in this way, the initial model allowed us to continue assigning the spectra in a usual iterative manner by adding new assigned lines to the fit, refining the Hamiltonian model, and producing new predictions.

The Doppler-limited resolution of our spectrometers provided an opportunity to resolve nuclear quadrupole hyperfine splittings for 898 rotational transitions. Typically, as for the main methylamine isotopologue, a resolved pattern of the hyperfine structure was observed as a doublet with an approximately 2-to-1 ratio in intensities. The stronger doublet component contains unresolved hyperfine transitions with selection rules $F = J+1 \rightarrow F' = J'+1$ and $F = J-1 \rightarrow F' = J'-1$, whereas the weaker doublet component corresponds to the $F = J \rightarrow F' = J'$ transition. At the same time, a number of hyperfine components with selection rules $\Delta F \neq \Delta J$ were also assigned. To provide the hyperfine-free frequencies we used in our analysis of the rotation-torsion-wagging spectrum of the ground state of ^{13}C methylamine, we fitted the frequencies of the individual hyperfine components using the model described above. The quadrupole hyperfine parameters χ_+ , and χ_- that we obtained from the fitting of the hyperfine patterns of the rotational transitions are presented in Table 1.

In total, the dataset for the rotational spectra of $^{13}\text{CH}_3\text{NH}_2$ in the ground vibrational state includes 2721 rotational transitions with an upper value of $J = 43$. This set of rotational transitions was fitted to the effective Hamiltonian of the group-theoretical high-barrier tunneling formalism that was developed for methylamine by Ohashi & Hougen (1987). The fit adopted in the present study as the “best” achieved the root-mean-square (rms) deviation of 0.039 MHz that corresponds to the weighted rms deviation of 0.73. The Hamiltonian model includes 75 parameters. The values of the molecular parameters obtained from the final fit are presented in Table 1. In Table 2, the main rotational and torsion-wagging splitting parameters for $^{13}\text{CH}_3\text{NH}_2$ and $^{12}\text{CH}_3\text{NH}_2$ (Motiyenko et al. 2014) are compared. From the comparison we see that the values of the main tunneling splitting parameters in both isotopologues of

Table 1. Molecular parameters of the ground torsional state of $^{13}\text{CH}_3\text{NH}_2$.

	Rotational	Inversion	Torsional
\bar{B}	21 661.952564(88)	h_2	-1546.22791(71)
$A - \bar{B}$	81 496.38707(41)	h_4	2.72870(73)
$B - C$	838.138853(57)	h_{2J}	$9.97182(41) \times 10^{-2}$
Δ_J	$3.806084(18) \times 10^{-2}$	h_{2K}	1.737675(73)
Δ_{JK}	0.1668639(18)	h_{4J}	$-8.57(24) \times 10^{-5}$
Δ_K	0.706766(12)	h_{4K}	$-4.400(40) \times 10^{-3}$
δ_J	$1.660274(31) \times 10^{-3}$	h_{2JJ}	$-3.674(11) \times 10^{-6}$
δ_K	-0.322295(13)	h_{2KK}	$-9.256(11) \times 10^{-4}$
Φ_J	$-1.901(11) \times 10^{-8}$	h_{2JK}	$-1.5092(20) \times 10^{-4}$
Φ_{JK}	3.420(14) $\times 10^{-6}$	h_{JKK}	1.157(21) $\times 10^{-7}$
Φ_{KJ}	-1.0297(59) $\times 10^{-5}$	q_2	21.53616(27)
Φ_K	$3.8535(94) \times 10^{-5}$	q_4	$-2.858(16) \times 10^{-2}$
ϕ_J	$-9.25(34) \times 10^{-10}$	q_{2J}	$-3.5835(14) \times 10^{-3}$
ϕ_{JK}	1.392(15) $\times 10^{-6}$	q_{2K}	$-1.9767(11) \times 10^{-2}$
ϕ_K	3.540(18) $\times 10^{-4}$	q_{2JJ}	$4.955(84) \times 10^{-7}$
L_{JK}	$4.589(48) \times 10^{-9}$	q_{JK}	$2.201(23) \times 10^{-6}$
L_{KKJ}	$-1.730(18) \times 10^{-8}$	q_{2KK}	$8.58(11) \times 10^{-6}$
ρ	0.649733019(68)	f_2	$-9.22031(89) \times 10^{-2}$
ρ_J	$-1.952(59) \times 10^{-8}$	f_4	$3.341(15) \times 10^{-4}$
ρ_K	$-1.1731(22) \times 10^{-6}$	f_{2J}	$5.087(14) \times 10^{-6}$
ρ_{JJ}	$-4.04(16) \times 10^{-11}$	f_{2K}	$2.007(47) \times 10^{-4}$
ρ_{JK}	$6.12(13) \times 10^{-10}$	f_{4K}	$-2.98(13) \times 10^{-6}$
		f_{2JJ}	$-1.738(62) \times 10^{-10}$
		$f_{2K}^{(2)}$	$-3.9049(86) \times 10^{-6}$
		$f_4^{(2)}$	$4.14(15) \times 10^{-8}$
		$f_{2J}^{(2)}$	$3.023(56) \times 10^{-10}$
χ_+	-2.4154(33)	r_2	10.584(26)
χ_-	6.0704(32)	r_{2J}	$-1.067(53) \times 10^{-3}$
		r_{2K}	-0.324(14)
Hyperfine			

Notes. All parameters are in MHz, except for $\rho, \rho_J, \rho_K, \rho_{JJ}$, and ρ_{JK} which are unitless. The structural parameter ρ describes the coupling between the internal rotation of the methyl top and the overall rotation of the molecule as a whole. $\bar{B} = (B + C)/2$.

Table 2. Main rotational and torsion-wagging splitting parameters (all in MHz except of ρ which is unitless) of the ground torsional state of ^{13}C and ^{12}C methylamines.

Parameter ^a	$^{13}\text{CH}_3\text{NH}_2$	$^{12}\text{CH}_3\text{NH}_2$
B	21 661.952564(88)	22 169.36697(12)
$A - \bar{B}$	81 496.38707(41)	80 986.38521(57)
$B - C$	838.138853(57)	877.88368(10)
Δ_J	$3.806084(18) \times 10^{-2}$	$3.946663(19) \times 10^{-2}$
Δ_{JK}	0.1668639(18)	0.1710869(21)
Δ_K	0.706766(12)	0.701310(14)
δ_J	$1.660274(31) \times 10^{-3}$	$1.757561(60) \times 10^{-3}$
δ_K	-0.322295(13)	-0.336039(16)
h_2	-1546.22791(71)	-1549.18492(70)
h_3	-2488.87759(96)	-2493.5110(12)
h_4	2.72870(73)	2.72760(86)
h_5	2.87728(52)	2.88853(58)
q_2	21.53616(27)	21.54649(37)
f_2	$-9.22031(89) \times 10^{-2}$	$-9.6036(16) \times 10^{-2}$
f_3	-0.165432(10)	-0.173725(15)
ρ	0.649733019(68)	0.649759856(98)

Notes. ^(a) $\bar{B} = (B + C)/2$.

methylamine are quite close. Since the $A - \bar{B}$ is slightly larger in $^{13}\text{CH}_3\text{NH}_2$ than in $^{12}\text{CH}_3\text{NH}_2$, the strong Q -type series of lines in $^{13}\text{CH}_3\text{NH}_2$ are shifted up in frequency compared with the main isotopologue as it is seen, for example, from Fig. 1, which presents the same $K_a = 6 \leftarrow 5$ cQ series of transitions as

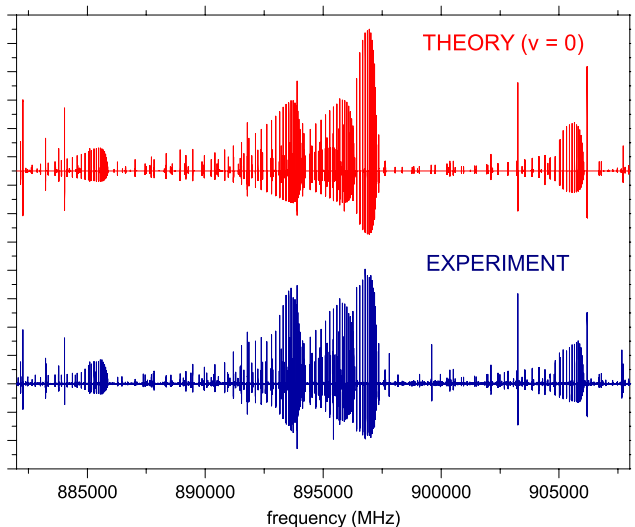


Fig. 1. Predicted (in red) and observed (in blue) rotational spectrum of ^{13}C methylamine between 882 and 908 GHz dominated by cQ -type series of transitions with $K_a = 6 \leftarrow 5$. A slight inconsistency between predicted and observed spectrum, which may be visible for some strong lines, is due to source power and detector sensitivity variations. Weak unassigned lines are due to higher excited vibrational states.

in Fig. 1 of Motiyenko et al. (2014). A portion of the observed rotational spectrum of ^{13}C methylamine around 890 GHz, compared in Fig. 1 to the predicted rotational spectrum in the ground

Table 3. Measured rotational transitions of $^{13}\text{CH}_3\text{NH}_2$ in the ground vibrational state.

J'	K'_a	Γ'	J''	K''_a	Γ''	Obs. freq. (MHz)	Uncertainty (MHz)	Obs.-calc. (MHz)
13	1	B1	13	0	B2	48 242.931	0.030	-0.0271
12	1	E2-1	12	0	E2+1	48 567.327	0.100	0.0139
13	1	E1-1	13	0	E1+1	50 719.336	0.030	-0.0006
					...			
31	5	E2+1	30	6	E2+1	448 438.474	0.030	0.0174
20	2	A2	19	3	A1	449 166.832	0.060	-0.0405
24	2	E1+1	24	1	E1-1	449 464.830	0.030	0.0117
26	3	A1	26	2	A2	449 514.293	0.030	-0.0305
13	7	E1-1	14	6	E1-1	449 739.006	0.060	0.0465
31	5	E1+1	30	6	E1+1	450 025.342	0.030	-0.0234
13	7	E1+1	14	6	E1+1	450 125.555	0.060	-0.0034
					...			

Notes. The full table is available at the CDS.

Table 4. Predicted transitions of ^{13}C methylamine in the ground vibrational state.

J'	K'_a	Γ'	F'	J''	K''_a	Γ''	F''	Calc. freq. (MHz)	Uncertainty (MHz)	$\mu^2 S$ (D ²)	W_{st}	E_l cm ⁻¹
18	1	B1	17	17	0	B2	17	945 375.3582	0.0126	0.011	3	220.416
18	1	B1	18	17	0	B2	17	945 375.4011	0.0124	3.432	3	220.416
18	1	B1	19	17	0	B2	18	945 376.9962	0.0124	3.629	3	220.416
18	1	B1	18	17	0	B2	18	945 377.0368	0.0126	0.011	3	220.416
18	1	B1	17	17	0	B2	16	945 377.0903	0.0124	3.246	3	220.416
34	3	E1-1	34	33	4	E1-1	33	945 404.9932	0.0237	3.703	3	853.710
34	3	E1-1	35	33	4	E1-1	34	945 405.4807	0.0237	3.814	3	853.710
34	3	E1-1	33	33	4	E1-1	32	945 405.4956	0.0237	3.596	3	853.710
33	2	E2+1	32	32	3	E2+1	31	945 502.5113	0.0310	3.362	1	786.807
33	2	E2+1	34	32	3	E2+1	33	945 502.5288	0.0310	3.572	1	786.807
33	2	E2+1	33	32	3	E2+1	32	945 503.1308	0.0310	3.465	1	786.807

Notes. The full table is available at the CDS.

vibrational state, illustrates an overall very good correspondence between experimental and theoretical spectra. The majority of strong lines are assigned (and correspond mainly to eQ -type transitions with $K_a = 6 \leftarrow 5$) and are well predicted by our current model, although a number of rather strong unassigned lines, presumably belonging to the higher excited states, may still be found in the experimental spectrum.

The list of measured rotational transitions of the ground vibrational state of ^{13}C methylamine is presented in Table 3. In the first six columns of Table 3, the quanta for each spectral line are given: J , K_a , and symmetry label Γ . In the following columns we provide the observed transition frequencies, measurement uncertainties, and residuals from the fit. Only hyperfine free rotational frequencies that were used in the final fit are presented in Table 3 for the observed transitions. Table 4 gives the prediction of the ground state rotational spectrum of ^{13}C methylamine up to 950 GHz. The spectrum was calculated taking nuclear quadrupole hyperfine coupling into account. Therefore each energy level in Table 4 is labeled by four quantum numbers: J , K_a , Γ , and total angular momentum F . The quantum numbers are followed by the columns with calculated transition frequencies and corresponding uncertainties. The next two columns contain the product $\mu^2 S$ (where μ is the dipole moment of the molecule and S is transition linestrength), and the nuclear spin statistical weight which is equal to 1 for A_1 , A_2 , and E_2 species and equal to 3 for B_1 , B_2 , and E_1 species. The next column represents the energy of the lower state. In our calculations of the $^{13}\text{CH}_3\text{NH}_2$ spectrum, the values for the dipole moment components were taken to be equal to the corresponding values of the parent methylamine isotopologue $\mu_a = -0.307$ D and

$\mu_c = 1.258$ D (Motiyenko et al. 2014). Owing to their significant sizes, the complete versions of Tables 3 and 4 are presented at the CDS. Here only parts of Tables 3 and 4 are provided for illustration purposes.

In our predictions of the ground state rotational spectrum, we have adopted the limitation of $J_{\max} = 50$, $K_{a,\max} = 20$. In the calculation, we have included the rotational transitions with rotational selection rules $\Delta J = 0, \pm 1$ and $\Delta K_a = 0, \pm 1, \pm 2, \pm 3$. In Table 4, those transitions that match the frequency range requirement (from 1 GHz to 950 GHz), whose predicted uncertainties are less than 1 MHz and whose line strength exceeds the limit of 0.01, are included. Also, to limit the size of Table 4, we have only presented the most intense hyperfine quadrupole components for which the relative intensities exceeded 0.1% of the total intensity of the rotation transition (i.e., mainly with the selection rule $\Delta F = \Delta J$). In addition, we provide the rotational part of the partition function $Q_r(T)$ of ^{13}C methylamine calculated from first principles (Table 5), i.e. via direct summation over the rotational-tunneling states. The maximum value of the J quantum number for the energy levels taken for calculating the partition function is 100. The vibrational part $Q_v(T)$ may be estimated in the harmonic approximation using the normal modes reported by Schimanouchi (1972) for the main methylamine isotopologue. Simple formulas for calculating $Q_v(T)$ can be found elsewhere (see, for example Gordy & Cook 1984).

4. Astronomical observations

The spectral records used to search for $^{13}\text{CH}_3\text{NH}_2$ here are a part of a complete spectral-line survey of the 1, 2, and 3 mm

Table 5. Rotation part $Q_r(T)$ of the total internal partition function $Q(T) = Q_v(T) \times Q_r(T)$, calculated from first principles using the parameter set of Table 1.

Temperature (K)	$Q_r(T)$
300	31908.65
200	17356.87
150	11269.17
50	2165.81
10	193.24

windows toward Sgr B2(N). The data were recorded during the period September 2002 to March 2013 using the Arizona Radio Observatory (ARO) 12 m telescope on Kitt Peak and the Submillimeter Telescope (SMT) on Mount Graham.

The receivers employed were dual-polarization, SIS mixers covering the 3 and 2 mm bands (68–116 and 130–172 GHz). The single-sideband mixers were tuned to reject the image sideband of a level typically ≥ 18 dB. Data were also obtained with a new dual-polarization receiver using ALMA Band 3 (83–116 GHz) sideband-separating (SBS) mixers. With these devices, the image rejection was usually ≥ 16 dB, attained within the mixer architecture. The temperature scale was determined by the chopper wheel method, corrected for forward spillover losses, and is given as T_{R}^* . The radiation temperature T_{R} , assuming the source

only fills the main beam, is $T_{\text{R}} = \frac{T_{\text{R}}^*}{\eta_c}$, where η_c is the main beam efficiency, corrected for forward spillover losses. The spectrometer backend utilized for the measurements was a millimeter autocorrelator (MAC) with either 390 kHz or 781 kHz resolution, and a bandwidth of 600 MHz channel $^{-1}$. The spectra were smoothed using a cubic spline routine to a 1 MHz resolution.

At the SMT, observations in the frequency range 210–280 GHz (1 mm) were taken with a dual-polarization receiver, utilizing ALMA Band 6 SBS mixers with rejection of at least 16 dB of the image sideband. The temperature scale was determined by the chopper wheel method, and is given as T_{A}^* . The radiation

temperature T_{R} is $T_{\text{R}} = \frac{T_{\text{A}}^*}{\eta_b}$, where η_b is the main beam efficiency. A 2048 channel filter bank with 1 MHz resolution was utilized as the spectrometer backend, split into parallel mode (2×1024). The beam size ranged from $87''$ to $37''$ at the 12 m and $36''$ to $23''$ at the SMT. All observations were conducted toward Sgr B2(N) ($\alpha = 17^{\text{h}}44^{\text{m}}09.5^{\text{s}}$; $\delta = -28^{\circ}21'20''$; B1950.0, or $\alpha = 17^{\text{h}}47^{\text{m}}19.2^{\text{s}}$; $\delta = -28^{\circ}22'22''$; J2000.0: NED¹) in position switching mode with a $+30'$ OFF position in azimuth. A 10–20 MHz local oscillator shift and direct observation of the image sideband were employed to identify any image contamination. The pointing accuracy is estimated to be $\pm 5''$ – $10''$ at the 12 m and $\pm 2''$ at the SMT. The telescope pointing was determined by observations of planets.

5. Column density upper limit toward Sgr B2(N)

We searched for the transitions of $^{13}\text{CH}_3\text{NH}_2$ in our complete spectral-line survey of the 1, 2, and 3 mm windows toward Sgr B2(N). The search was conducted in a systematic way by modeling the expected emission in the local thermodynamic equilibrium (LTE) approximation, which is certainly valid for the rotational transitions in the vibrational ground state. There are a number of non-LTE effects which may affect our results. We may overestimate a total column density of $^{13}\text{CH}_3\text{NH}_2$ gas if the

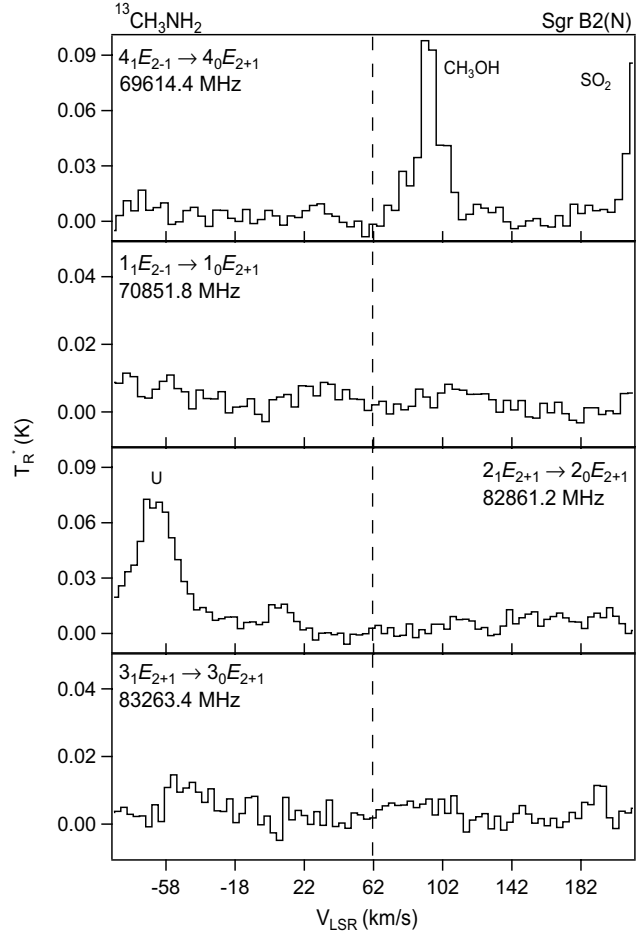


Fig. 2. Results of an interstellar search for the selected rotational transitions of $^{13}\text{CH}_3\text{NH}_2$.

density is not sufficient to thermally populate the vibrationally excited states via collisions (the partition function of ^{13}C methylamine includes the contribution of excited vibrational states in the LTE approximation). At the same time, we may underestimate the total column density because infrared excitation may also contribute to the population of the vibrationally excited states (e.g., Nummelin & Bergman 1999). Also we cannot exclude that radiative decay, involving rovibrational transitions, may affect the rotational populations of the vibrational ground state. Since there is no easy way to correct for these possible non-LTE effects, we restrained our analysis to the LTE assumption. Within the frequency ranges of our survey, we have looked for 69 transitions of ^{13}C methylamine that are predicted to be the most prominent spectral features of the molecule under the physical parameters of our model. We assumed the same source size, temperature, linewidth, and systemic velocity as for parent isotopic species of methylamine (Halfen et al. 2013). The physical parameters of the $^{13}\text{CH}_3\text{NH}_2$ model are $T_{\text{rot}} = 159$ K, $\Delta V_{1/2} = 15$ km s $^{-1}$, and $V_{\text{LSR}} = 64$ km s $^{-1}$ with the assumption that the source fills the beam. Among checked transitions, only eight are found to be relatively free of contamination, and these are listed in Table 6. All other transitions of $^{13}\text{CH}_3\text{NH}_2$ are heavily blended with transitions of other species and cannot be detected with our single-dish data. The LTE modeled spectrum for the four selected contamination-free transitions of $^{13}\text{CH}_3\text{NH}_2$ is compared to the observed spectrum in Fig. 2. It

¹ <http://ned.ipac.caltech.edu/forms/calculator.html>

Table 6. Uncontaminated transitions of ^{13}C methylamine in Sgr B2(N).

J'	K'_a	Γ'	J''	K''_a	Γ''	Frequency (MHz)	η_c	T_R^* (K)	E_u (K)	$\mu^2 S$ (D 2)
4	1	E2-1	4	0	E2+1	69 614.44	0.94	<0.005	24.72	5.75
2	1	E2-1	2	0	E2+1	70 741.04	0.94	<0.004	10.22	2.40
1	1	E2-1	1	0	E2+1	70 851.75	0.94	<0.003	6.06	1.27
6	1	E1-1	6	0	E1+1	73 461.33	0.93	<0.005	47.62	10.61
2	1	B2	2	0	B1	78 707.52	0.92	<0.004	10.32	3.98
3	1	E1-1	3	0	E1+1	78 740.49	0.92	<0.004	16.70	4.79
2	1	E2+1	2	0	E2+1	82 861.25	0.92	<0.003	10.80	1.58
3	1	E2+1	3	0	E2+1	83 263.42	0.92	<0.003	17.06	1.71

is seen that, at the typical noise level of this survey, we have the apparent non-detection of these $^{13}\text{CH}_3\text{NH}_2$ transitions toward Sgr B2(N). Therefore only an upper limit on the column density of $^{13}\text{CH}_3\text{NH}_2$ can be deduced from our current observational data which, for the assumed physical parameters of our model, is $<6.5 \times 10^{14} \text{ cm}^{-2}$.

6. Conclusions

The first study of the rotational spectra of the ^{13}C isotopologue of methylamine molecule was carried out in the frequency range from 48 to 945 GHz. Using the effective Hamiltonian model based on the group-theoretical high-barrier tunneling formalism developed for methylamine by Ohashi & Hougen (1987), we were able to fit the available data within experimental accuracy. The results of the present study allow us to produce reliable predictions of rotational spectra in the ground vibrational state of $^{13}\text{CH}_3\text{NH}_2$ for astrophysical purposes in the frequency range up to 950 GHz for $0 < J < 50$ and $0 < K_a < 20$. An attempt to detect interstellar $^{13}\text{CH}_3\text{NH}_2$ toward Sgr B2(N) using available observational data from a spectral-line survey of the 1, 2, and 3 mm windows using the Arizona Radio Observatory (ARO) 12 m telescope on Kitt Peak and the Submillimeter Telescope (SMT) on Mount Graham was not successful and resulted in the determination of the $^{13}\text{CH}_3\text{NH}_2$ column density upper limit of $<6.5 \times 10^{14} \text{ cm}^{-2}$. The ratio of $^{12}\text{CH}_3\text{NH}_2$ to $^{13}\text{CH}_3\text{NH}_2$, using the column density of $^{12}\text{CH}_3\text{NH}_2$ from Halfen et al. (2013), is >7.7 . This value can be compared to those from other species, such as HC_3N and CH_2CHCN , in Sgr B2(N) of ~ 20 (Belloche et al. 2013, Halfen et al., in prep.). Thus, the upper limit for $^{13}\text{CH}_3\text{NH}_2$ in Sgr B2(N) could be approximately $2.5 \times 10^{14} \text{ cm}^{-2}$, about a factor of three less than the current limit, and below the current detection limit. We hope that the new observations toward Sgr B2(N) using the very sensitive ALMA telescope will provide an opportunity to detect $^{13}\text{CH}_3\text{NH}_2$ in the interstellar medium.

Acknowledgements. The authors are indebted to Dr. N. Ohashi for providing his fitting program for methylamine. This work was done with the support of the Ukrainian-French CNRS-PICS 6051 project. This research was supported by NSF grants AST-1140030 and AST-1211502. The SMT and Kitt Peak 12 m are operated by the Arizona Radio Observatory (ARO), Steward Observatory, University of Arizona, with support from the NSF University Radio Observatories program (URO: AST-1140030).

References

- Alekseev, E. A., Motyienko, R. A., & Margulès, L. 2012, *Radio Physics and Radio Astronomy*, **3**, 75
- Belloche, A., Müller, H. S. P., Menten, K. M., Schilke, P., & Comito, C. 2013, *A&A*, **559**, A47
- Bouchez, A., Margulès, L., Motyienko, R. A., et al. 2012, *A&A*, **540**, A51
- Carvajal, M., Margulès, L., Tercero, B., et al. 2009, *A&A*, **500**, 1009
- Demaison, J., Włodarczak, G., Huet, T. R., et al. 2009, *A&A*, **500**, 1009
- Coudert, L. H., Margulès, L., Huet, T. R., et al. 2012, *A&A*, **543**, A46
- Coudert, L. H., Drouin, B. J., Tercero, B., et al. 2013, *ApJ*, **779**, A119
- Demyk, K., Mäder, H., Tercero, B., et al. 2007, *A&A*, **466**, 255
- Fourikis, N., Takagi, K., & Morimoto, M. 1974, *ApJ*, **191**, L139
- Fourikis, N., Takagi, K., & Saito, S. 1977, *ApJ*, **212**, L33
- Gordy, W., & Cook, R. L. 1984, Molecular Spectra, Techniques of Chemistry, Vol. XVIII (New York: Wiley)
- Halfen, D. T., Ilyushin, V. V., & Ziurys, L. M. 2013, *ApJ*, **767**, 66
- Haykal, I., Motyienko, R. A., Margulès, L., & Huet, T. R. 2013, *A&A*, **549**, A96
- Ilyushin, V., & Lovas, F. J. 2007, *J. Phys. Chem. Ref. Data*, **36**, 1141
- Ilyushin, V. V., Alekseev, E. A., Dyubko, S. F., Motyienko, R. A., & Hougen, J. T. 2005, *J. Mol. Spec.*, **229**, 170
- Kaifu, N., Morimoto, M., Nagane, K., et al. 1974, *ApJ*, **191**, L135
- Kreglewski, M., Stryjewski, D., & Dreizler, H. 1990a, *J. Mol. Spec.*, **139**, 182
- Kreglewski, M., Jäger, W., & Dreizler, H. 1990b, *J. Mol. Spec.*, **144**, 334
- Kutsenko, A. S., Motyienko, R. A., Margulès, L., & Guillemin, J.-C. 2013, *A&A*, **549**, A128
- Lide, Jr., D. R. 1954, *J. Chem. Phys.*, **22**, 1613
- Margulès, Motyienko, R., Demyk, K., Tercero, B. 2009a, *A&A*, **493**, 565
- Margulès, L., Coudert, L. H., Møllendal, H., et al. 2009b, *J. Mol. Spec.*, **254**, 55
- Margulès, L., Motyienko, R. A., Ilyushin, V. V., & Guillemin, J.-C. 2015, *A&A*, **579**, A46
- Motyienko, R. A., Ilyushin, V. V., Drouin, B. J., Yu, S., & Margulès, L. 2014, *A&A*, **563**, A137
- Muller, S., Beelen, A., Guelin, M., et al. 2011, *A&A*, **535**, A103
- Nguyen, L., Walters, A., Margulès, L., et al. 2013, *A&A*, **553**, A84
- Nummelin, A., & Bergman, P. 1999, *A&A*, **341**, L59
- Nummelin, A., Bergman, P., Hjalmarson, A., et al. 1998, *ApJS*, **117**, 427
- Ohashi, N., & Hougen, J. T. 1987, *J. Mol. Spec.*, **121**, 474
- Ohashi, N., Takagi, K., Hougen, J. T., Olson, W. B., & Lafferty, W. J. 1987, *J. Mol. Spec.*, **126**, 443
- Ohashi, N., Oda, M., & Takagi, K. 1991, *J. Mol. Spec.*, **145**, 180
- Richard, C., Margulès, L., Motyienko, R. A., & Guillemin, J.-C. 2012, *A&A*, **543**, A135
- Richard, C., Margulès, L., Caux, E., et al. 2013, *A&A*, **552**, A117
- Sastray, K. V. L. N. 1960, *Proc. Indian Acad. Sci. Sect. A*, **51**, 301
- Schimanouchi, T. 1972, in Tables of Molecular Vibrational Frequencies, Vol. I: consolidated (Washington, DC: National Bureau of Standards), 67
- Takagi, K., & Kojima, T. 1971, *J. Phys. Soc. Jpn.*, **30**, 1145
- Tamagake, K., & Tsuboi, M. 1974, *J. Mol. Spec.*, **53**, 204
- Tercero, B., Margulès, L., Carvajal, M., et al. 2012, *A&A*, **538**, A119
- Turner, B. E. 1989, *ApJS*, **70**, 539

High-Resolution Millimeter Wave Spectroscopy and Ab Initio Calculations of Aminomalononitrile

Roman A. Motiyenko,*[†] Laurent Margulès,[†] Eugen A. Alekseev,[‡] and Jean-Claude Guillemin[¶]

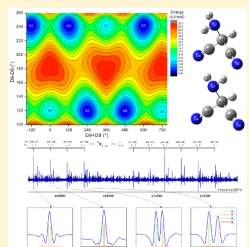
[†]Laboratoire de Physique des Lasers, Atomes et Molécules, UMR CNRS 8523, Université de Lille 1, F-59655 Villeneuve d'Ascq Cedex, France

[‡]Institute of Radio Astronomy of NASU, Chervonopraporna 4, 61002 Kharkiv, Ukraine

[¶]Ecole Nationale Supérieure de Chimie de Rennes, CNRS, UMR 6226, 11 Allée de Beaulieu, CS 50837, F-35708 Rennes Cedex 7, France

S Supporting Information

ABSTRACT: The HCN trimer aminomalononitrile ($\text{H}_2\text{NCH}(\text{CN})_2$, AMN) is considered as a key compound in prebiotic chemistry and a potential candidate for detection in the interstellar medium. In this view, we studied the rotational spectrum of AMN in the 120–245 GHz frequency range. The spectroscopic work was augmented by high-level ab initio calculations. The calculations showed that between two existing rotamers, symmetric and asymmetric, the most stable is the asymmetric conformation, and it is the only conformation observed in the recorded spectra. The symmetric conformation is 6.7 kJ/mol higher in energy and thus has a very low Boltzmann factor. The analysis of the rotational spectra of the A conformation has shown that the observed lines exhibit a doublet or quartet structure owing to two large-amplitude motions, C–N torsion and amino group inversion. To study the large-amplitude motions in detail, we calculated a two-dimensional potential energy surface and determined the barrier heights for the torsion and inversion, $V_t = 12.5 \text{ kJ/mol}$ and $V_i = 19.1 \text{ kJ/mol}$. About 2500 assigned rotational transitions in the ground vibrational state were fitted within experimental accuracy using the reduced axes system Hamiltonian. The set of obtained spectroscopic parameters allows accurate calculation of transition frequencies and intensities for an astrophysical search of AMN.



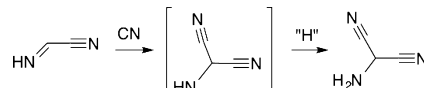
INTRODUCTION

Hydrogen cyanide (HCN) has been detected for a long time in the interstellar medium (ISM),¹ in the atmosphere of Titan,² and in comets.³ Adenine, an oligomeric compound of HCN with the $(\text{HCN})_5$ formula, is a constituent of DNA, RNA, and many coenzymes and can be easily formed in water starting from HCN.⁴ Adenine is thus often considered as a key compound of the prebiotic period of the Primitive Earth.^{4–6} Attempts to detect it in the ISM are unsuccessful up to date but the *E*-cyanomethanimine ($\text{HN}=\text{CH}-\text{CN}$), a compound with $(\text{HCN})_2$ formula and an intermediate often postulated in the synthesis of adenine in prebiotic conditions,^{4,7–9} has been recently detected.¹⁰ In the hypothesis of the formation of adenine in one or both of these media by subsequent additions of HCN monomer on cyanomethanimine, the first step should give a compound with a $(\text{HCN})_3$ formula. Even if several isomers with a $\text{C}_3\text{H}_3\text{N}_3$ formula can be drawn, the aminomalononitrile (aminopropanedinitrile, AMN) is often considered as the most likely derivative issued from the addition of HCN on cyanomethanimine.^{5,11,12} Furthermore, in all of the mechanistic studies on the synthesis of adenine from HCN, AMN has been postulated as an intermediate,^{5,6,9} and several reactions starting from the latter have given adenine.^{5,7–9,11} On the other hand, AMN is a useful intermediate in the synthesis of many heterocyclic systems.^{13–19} Such properties designate AMN as a key compound in prebiotic chemistry and an attractive candidate for the ISM. Its detection in the ISM, after

HCN and the cyanomethanimine, would be a determinant to improve our understanding of the chemistry of HCN in the Universe.

How could AMN be synthesized in the ISM? The formation of cyanomethanimine in significant amounts by gas-phase synthetic routes is considered as not compatible with low-temperature interstellar environments even for acid-catalyzed reaction pathways.^{20,21} However, even if the cyanomethanimine is formed in the solid phase, it has been detected in the gas phase, and it could react on the grain surfaces or in the gas phase after vaporization to form AMN. The reaction pathway could involve the radical addition of CN on cyanomethanimine, followed by abstraction of a radical hydrogen from another molecule or reaction with a hydrogen radical if the energy of the reaction can be released; see Scheme 1.

Scheme 1. Proposed Reaction Pathway in the Synthesis of AMN from Cyanomethanimine



Received: December 18, 2014

Revised: January 15, 2015

Published: January 20, 2015

The identification of a species in the ISM requires that its spectrum has first been assigned in the laboratory. We present here the results of the analysis of the AMN rotational spectrum as a support for future astrophysical observations. Our experimental work has been augmented by high-level quantum chemical calculations, which were undertaken to obtain information for use in assigning the rotational spectrum and investigating properties of the potential energy hypersurface. Two stable conformations, symmetric (S) and asymmetric (A), exist for AMN. Their structure and atom numbering are illustrated in Figure 1. The two conformations differ by

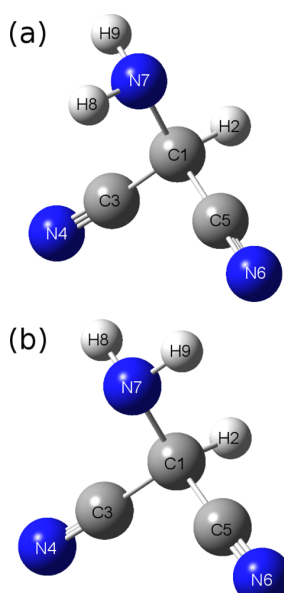


Figure 1. Calculated structure and atom numbering of A (a) and S (b) conformations of AMN.

orientation of the NH_2 group. In the S conformation, both hydrogens (H_8 and H_9) of the amino group are in syn configuration ($\pm 60^\circ$) relative to the H_2 hydrogen. The S conformation has a plane of symmetry and thus belongs to the C_s symmetry point group. In the A conformation, one of the amino group hydrogens is in anti configuration (180°), and the other hydrogen is in a skew position relative to the H_2 hydrogen. The rotation around the C–N bond connects the S and A conformations. Because of the large-amplitude character of the C–N torsion and NH_2 wagging, the amino H atoms are symmetry-equivalent, and there are four equivalent configurations for the A conformation. A similar problem of two large-amplitude motions (LAMs) that complicate the rotational spectra exists for methylamine,²² ethylamine,²³ and protonated methanol.²⁴

■ EXPERIMENTAL SECTION

Preparation of AMN. AMN was prepared as previously reported²⁵ starting from AMN *p*-toluenesulfonate. The latter compound was purchased from Aldrich and used without further purification. The synthesis details are presented in Appendix A of the Supporting Information.

^1H NMR (400 MHz, CDCl_3) δ 2.18 (d brd, 2H, $^3J_{\text{HH}} = 8.9$ Hz, NH_2); 4.78 (t, 1H, $^3J_{\text{HH}} = 8.9$ Hz, CH). ^{13}C NMR (100 MHz, CDCl_3) δ 34.3 (d, $^1J_{\text{CH}} = 151.1$ Hz, CH); 115.6 (s, CN).

Conventional Absorption Spectroscopy Experiment.

Owing to the relatively high kinetic instability of AMN, the major part of experimental measurements of its rotational spectrum has been performed using the Lille BWO-based fast scan spectrometer²⁶ and in the so-called “flow mode”. During the experiment, the absorption cell, which consisted of 1.2 m Pyrex glass tube with Teflon windows, was kept at room temperature, whereas the sample was cooled at a temperature of about -15°C and evaporated outside of the cell. Then, the sample was continuously injected through a side opening at one end of the cell and pumped out through another side opening at the other end. The optimum gas pressure in the cell was kept close to 20 Pa. Using the fast-scan spectrometer, the spectral region of 120–180 GHz was covered by the measurements. In addition, we recorded the rotational spectrum of AMN in a relatively narrow frequency range of 225–242 GHz using the spectrometer based on solid-state sources. The major impurity observed in the recorded spectrum was the HCN monomer, but for the spectral analysis, this compound does not cause any problem because it has only one strong triplet line in the frequency range of the experiment at 177.261 GHz. We did not find any other significant impurity, at least not any having a permanent dipole moment, because all of the strongest lines observed were assigned to AMN. The recorded spectrum of AMN is very dense, which may be explained by relatively small values of rotational constants, as well as by a large partition function, owing, in particular, to five excited vibrational states lying below 300 cm^{-1} .

■ QUANTUM CHEMICAL METHODS

The present quantum chemical calculations were performed using the Gaussian 09 suite of programs.²⁷ The geometries were fully optimized using the “tight” convergence option, and the vibrational frequencies were calculated at the MP2 level. Peterson and Dunning’s correlation-consistent aug-cc-pVTZ basis set, which is of triple- ζ quality and includes both diffuse and polarized functions, was used. To analyze the LAMs in AMN, we computed a two-dimensional optimized potential energy surface (PES). Such calculation is rather costly; therefore, it was computed also at the MP2 level but with a smaller 6-311++G(2p, 2d) basis set. There are multiple ways to define LAM coordinates. For example, in the case of a similar problem for methylamine, the torsional angle may be defined as a simple dihedral angle²⁸ involving a hydrogen atom of the methyl group or an average of six dihedral angles²⁴ involving hydrogen atoms of both amino and methyl groups. In this case, the inversion angle for methylamine may be defined as the angle between the NH_2 plane and the extension of the C–N bond.²⁴ In the present study, we define LAM coordinates in a simpler way especially from the point of view of quantum chemical calculations. To describe two LAMs, we used two dihedral angles D_8 ($\text{H}_2-\text{C}_1-\text{N}_7-\text{H}_8$) and D_9 ($\text{H}_2-\text{C}_1-\text{N}_7-\text{H}_9$). For the computation, the angle D_9 was varied from 0 to 355° with a step of 5° , and the angle D_8 was varied from $D_9 - 100^\circ$ to $D_9 + 100^\circ$ also with a step of 5° . During the computations, both dihedral angles were kept fixed, whereas all others’ structural parameters (dihedrals, angles, and bond lengths) were optimized.

Relative energies of the conformations and transition states (TSs) as a result of ab initio calculations are presented in Table 1. Calculated geometrical parameters and harmonic vibrational frequencies for both conformers are given, respectively, in Tables S1 and S2 in the Supporting Information. The resultant

Table 1. Relative Energies with Respect to the A Conformer of AMN^a

conformation	ΔE_a (kJ/mol)
A	0.0
S	6.72 (6.25)
TS-rot	12.5 (12.2)
TS-inv (1)	19.1 (18.8)
TS-inv (2)	21.5 (20.4)

^aThe ZPE-corrected energies are reported in parentheses. For the definition of TSs, see the text and Figure 2.

PES is shown in Figure 2. For a convenient graphical representation, the PES is plotted as a function of two

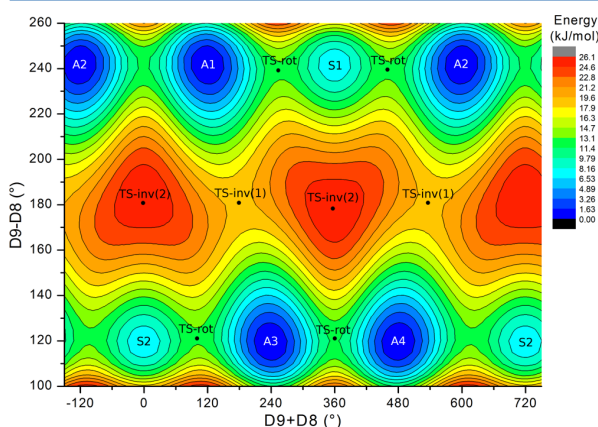


Figure 2. Calculated PES for AMN as a function of two independent coordinates $D_9 + D_8$ and $D_9 - D_8$. See the text for the definition of the coordinates.

independent coordinates $D_9 + D_8$ and $D_9 - D_8$, and it is repeated over 720° for the $D_9 + D_8$ coordinate. As follows from the analysis of Table 1 and Figure 2, the A conformer is the most stable one. For both A and S conformations, only positive vibrational frequencies were obtained, indicating that they correspond to a minimum (stable conformation) on the potential energy hypersurface. The S conformation is less stable than the A by about 6.7 kJ/mol (zero-point energy (ZPE)-corrected value: 6.2 kJ/mol).

The calculated PES contains six distinct minima; four of them correspond (A1, A2, A3, and A4) to the A conformation and two others (S1 and S2) to the S conformation. In the adopted coordinate system, the internal rotation around the C_1-N_7 bond keeps fixed the $D_9 - D_8$ coordinate either at 120° or at 240° and varies the $D_9 + D_8$ coordinate. Thus, it connects two A configurations and one S configuration. The TSs related to the C_1-N_7 internal rotation (TS-rot) were characterized using the "QST3" procedure implemented in the Gaussian 09 software package at the MP2 level of theory and using the aug-cc-pVTZ basis set. Two saddle points, exhibiting only one imaginary frequency, have been found. The calculations showed that both TSs have the same energy of 12.5 kJ/mol (ZPE-corrected value: 12.2 kJ/mol) with respect to the most stable A conformation. The TSs that correspond to the inversion of amino group hydrogens (TS-inv) were searched for using the "TS" procedure of the Gaussian 09. As a result, two different saddle point geometries were obtained. The first-order TS is characterized by planar orientation of all hydrogen atoms with

respect to the C_1-N_7 bond. On the calculated PES, there are two equivalent first-order saddle points that have the following values of dihedral angles: $D_8 = 0^\circ$, $D_9 = 180^\circ$ or $D_8 = 180^\circ$, $D_9 = 0^\circ$. The harmonic force field calculation for the TS-inv state provides one imaginary frequency. Two equivalent second-order inversion TSs are characterized by the dihedrals $D_8 = 90^\circ$, $D_9 = 270^\circ$ or $D_8 = 270^\circ$, $D_9 = 90^\circ$. It is interesting to note that in the case of amino group inversion in methylamine, the values of the first- and second-order inversion barriers are very close²⁹ and do not allow one to clearly determine the preferable tunneling pathway. The calculation performed for methylamine at the MP2 level and using the 6-311G++ basis set yielded the values of $V_i^{(1)} = 27.6$ kJ/mol and $V_i^{(2)} = 27.9$ kJ/mol, and the DFT/B3LYP calculations with the same basis set yielded the values of $V_i^{(1)} = 21.4$ kJ/mol and $V_i^{(2)} = 21.7$ kJ/mol. In the present case, the symmetry break for AMN leads to two distinctive barriers with rather different heights $V_i^{(1)} = 19.1$ kJ/mol and $V_i^{(2)} = 21.5$ kJ/mol. Thus, in the case of AMN, the inversion through the first-order TS, which directly connects two minima of the A conformation, is preferred.

■ GROUP THEORY

Four equivalent configurations of the A conformation may lead to complications in the description of its rotational spectrum. The A conformation of AMN does not possess any symmetry; however, for the description of tunneling motions, a molecular symmetry group may be used. By labeling the atoms from 1 to 9, as shown in Figure 1, one can see that the following permutation-inversion operations, E, (89), (35)(46)*, (35)(46)(89)*, are feasible owing to the tunneling through the barriers of finite height. The (35)(46)(89)* operation is feasible owing to the torsional tunneling, the (35)(46)* operation corresponds to the tunneling through inversion barrier, and finally, the (89) is the product of two others operations mentioned above, that is, it corresponds to the combination of torsional and inversion motions. These four permutation-inversion operations represent G_4 molecular symmetry group having four irreducible representations, A_1 , A_2 , B_1 , and B_2 .

Thus, from a molecular symmetry group point of view, owing to four structurally equivalent configurations, each rotational level of the A conformation of AMN has four-fold degeneracy, which may be removed by tunneling through torsion and inversion barriers. Therefore, in addition to usual quantum numbers, the rotational levels of AMN may be now labeled according to the irreducible representations of the G_4 group. For the parent isotopic species of AMN, the elements of the G_4 group for AMN exchange are two nitrogen nuclei having spin $I_N = 1$, two carbon nuclei having zero spin, and two hydrogen nuclei having spin $I_H = 1/2$. Our calculations show that in this case, the statistical weights for the irreducible representations A_1 , A_2 , B_1 , and B_2 are correspondingly 1, 1, 3, and 3.

According to the ab initio calculations, the A conformation of AMN has three nonzero dipole moment components, $\mu_a = 1.1$ D, $\mu_b = 3.3$ D, and $\mu_c = 1.0$ D. The operations of the G_4 group that contain the inversion of coordinates change the sign of only the μ_a projection, keeping the signs of μ_b and μ_c . Therefore, in the ground vibrational state, the electric dipole transitions owing to μ_b can occur only between two sublevels having the same symmetry, that is, $A_1 \leftrightarrow A_1$, $A_2 \leftrightarrow A_2$, $B_1 \leftrightarrow B_1$, and $B_2 \leftrightarrow B_2$. Consequently, the a- and c-type transitions have the following selection rules, $A_1 \leftrightarrow A_2$ and $B_1 \leftrightarrow B_2$, and the transitions between A and B levels are forbidden.

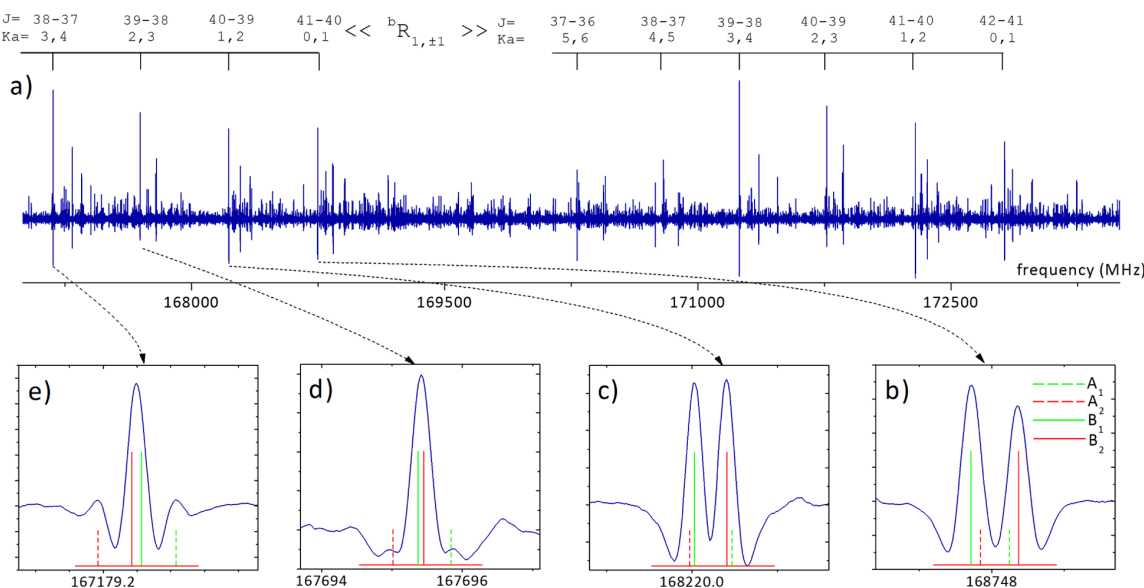


Figure 3. A part of the experimental spectrum of AMN in the 167–173 GHz frequency range showing (a) the intense series of ${}^bR_{1,\pm 1}$ transitions and (b–e) a detailed view of selected transitions exhibiting torsion-inversion splittings. For these transitions, the assignment according to irreducible representations of the G_4 molecular symmetry group and the relative intensities are also indicated.

In the study of the rotational spectrum of *gauche*-ethylamine, Fischer and Botskor²³ used different symmetry labeling for a similar problem of two LAMs connecting four equivalent minima. Starting from geometrically equivalent localized total wave functions for each of the four minima, they combined them first to produce symmetrical (S) and antisymmetrical (A) wave functions with respect to the torsional motion. Then, to treat the inversion, they combined the wave functions of the same torsional symmetry to obtain even (e) and odd (o) functions for the inversion. From a group theory point of view, in ref 23, the produced delocalized wave functions having symmetry labeling se, so, ae, and ao belong correspondingly to A_1 , A_2 , B_1 , and B_2 irreducible representations of the G_4 molecular symmetry group introduced in this paper.

■ ASSIGNMENT AND RESULTS

The assignment started with the search for the most intense lines. In the frequency range of the experiment, these were expected to be μ_b -type transitions with $\Delta J = \pm 1$ selection rule (see Figure 3a). First, on the basis of the predictions obtained from ab initio rotational and centrifugal distortion constants, we searched for $K_a = 0$ and 1 and $K_c = J {}^bR_{\pm 1,1}$ transitions because they are less subjected to centrifugal distortion correction and, thus, they are usually better predicted. These transitions form a series of easily distinguishable doublets with splittings that reduce with J increasing. In the recorded spectra, we located and assigned such transitions with the values of the J quantum number ranging from 32 to 42. The predicted $K_a = 0 \leftarrow 1$ and $K_a = 1 \leftarrow 0$ splittings for these transitions were much smaller than the Doppler-limited resolution of the experiment; therefore, the doublet structure observed (see Figure 3b) was attributed to tunneling effects. By taking the central frequency of each doublet, we fitted the observed transitions to the Watson A-reduction Hamiltonian in the I' coordinate representation, and we produced the first experimental set of rotational parameters containing B and C constants (the A rotational constant was kept fixed to its ab initio value), as well

as Δ_p and δ_J centrifugal distortion terms. The frequency predictions calculated on the basis of the experimental parameters allowed the assignment of the next series of quartets with the same selection rules and $K_a = 1$ and 2 and $K_c = J - 1$. These series of transitions also exhibited doublet structure (Figure 3c) that was attributed to tunneling effects. In a similar manner, the series of transitions with $K_a = 2$ and 3 and $K_c = J - 2$ was assigned. This series, in contrast to the two previous ones, had a barely resolvable quartet structure that provided important information on symmetry assignment. The quartet consisted of two unresolved strong transitions in the center and two weaker transitions on each side. The relative intensities of strong and weak transitions 3 to 1 correspond to statistical weights of the G_4 group irreducible representations. Thus, one can assign the strong lines as belonging to B symmetry species and weaker ones to A symmetry species. The fact that no A lines were resolved for $K_a = 0,1$ and $K_a = 1,2$ series may be explained by the inverse order of B and, correspondingly, A lines for $K_a = 2,3$ and other series (see the assignment of the lines on Figure 3a). The corresponding A symmetry species transitions for $K_a = 0,1$ and $K_a = 1,2$ are therefore mixed with B species transitions, and they are not distinguished under the Doppler-limited resolution of our experiment.

The inversion in the order of B lines is an indicator of a perturbation, and an appropriate model should be used to treat correctly this problem. In the present study, we used the model based on the reduced axis system (RAS) approach proposed by Pickett.³⁰ It is well-suited for molecules having one or two LAMs with a double minimum-potential. In the case of AMN, the S conformer is considerably higher in energy than the A conformer. Thus, the C–N torsion in the A conformer may be considered as a LAM between only two equivalent minima at least for the ground vibrational state. As has been shown by Coudert,³¹ the RAS method is equivalent to the internal axis method developed and successfully used by Hougen and co-workers for molecules with several LAMs.^{22,32–34} The

Table 2. Spectroscopic Constants of the A Conformer of AMN

parameters	rotation		torsion-inversion		
	ground state	theory ^a	parameters	B species	A species
A (MHz)	5742.99822(40) ^b	5731.39	E* (MHz)	2981.563(35)	3362.1(65)
B (MHz)	2884.81743(23)	2874.87	E _J * (MHz)	0.004855(13)	
C (MHz)	2037.38599(21)	2035.42	E _K * (MHz)	0.05513(20)	0.05597(46)
Δ _J (kHz)	1.39923(12)	1.418	E _{JK} * (kHz)	-0.001643(74)	
Δ _{JK} (kHz)	-6.65593(57)	-6.916	E _{KK} * (kHz)	0.00339(24)	
Δ _K (kHz)	21.9327(15)	22.51	F _{ab} (MHz)	5.6258(34)	5.516(49)
δ _J (kHz)	0.552005(27)	0.5589	F _{abj} (kHz)	0.0759(30)	
δ _K (kHz)	1.41647(36)	1.355	F _{abK} (kHz)	-0.729(54)	
Φ _J (Hz)	0.005616(20)		F _{ac} (MHz)	17.7973(61)	17.808(13)
Φ _{JK} (Hz)	-0.032406(98)		F _{ack} (kHz)	-0.5635(84)	-0.502(12)
Φ _K (Hz)	0.01784(59)				
Φ _J (Hz)	0.1724(17)				
ϕ _J (Hz)	0.0026531(48)				
ϕ _{JK} (Hz)	-0.001611(84)				
ϕ _K (Hz)	0.11947(36)				
N ^c	1405				
σ (MHz) ^d	0.027				
σ _w ^e	0.68				

^aMP2/aug-cc-pVTZ calculations. ^bNumbers in parentheses are two standard deviations in the same units as the last digit. ^cNumber of distinct frequency lines. ^dRoot-mean-square deviation of the fit. ^eWeighted root-mean-square deviation of the fit.

perturbation terms in the RAS Hamiltonian are equivalent in this case to off-diagonal Coriolis coupling terms. The choice of the RAS method is also determined by the fact that it is implemented in widely used SPFIT/SPCAT programs for fitting and predicting molecular spectra.

We applied the RAS method to treat the perturbations connecting two *B* levels and connecting two *A* levels or in terms of the labeling scheme introduced by Fischer and Botskor for ethylamine, “between the levels of different torsional parity but belonging to the same inversion state”. As was discovered during the spectral analysis, no perturbation terms connecting *A* and *B* levels were needed to fit the observed spectra within experimental accuracy. The Hamiltonian used has the following form

$$H = \begin{pmatrix} H_{\text{rot}} - H_{\Delta}^A & H_{\text{I}}^A & 0 & 0 \\ H_{\text{I}}^A & H_{\text{rot}} + H_{\Delta}^A & 0 & 0 \\ 0 & 0 & H_{\text{rot}} - H_{\Delta}^B & H_{\text{I}}^B \\ 0 & 0 & H_{\text{I}}^B & H_{\text{rot}} + H_{\Delta}^B \end{pmatrix} \quad (1)$$

where H_{rot} is the standard Watson A-reduction Hamiltonian in the I' coordinate representation and H_{I}^A and H_{I}^B are perturbation terms respectively for *A* and *B* symmetry species. In addition, the pure rotational part of the Hamiltonian is defined in such a way that it allows one to fit averaged rotational and centrifugal distortion constants for both tunneling substates.³⁵ This procedure seemed to be more robust to possible correlation problems between different rotational and Coriolis coupling parameters. Fitting averaged constants is achieved by introducing H_{Δ}^A and H_{Δ}^B terms, which may be defined as

$$H_{\Delta} = E^* + E_J^* J^2 + E_K^* J_z^2 + E_2^* (J_+^2 + J_-^2) + \dots \quad (2)$$

where E^* is a half-energy difference between two *A* or *B* levels ($\Delta E = 2E^*$) and J , J_z , and $J_{\pm} = J_x \pm iJ_y$ are the rotational angular

momentum operator and its components. One may also notice that in the present study, we fit a single set of pure rotational and centrifugal distortion parameters for all four tunneling substates. Indeed, such an approach seems to be reasonable because in the case of ethylamine, the average values of rotational constants for *A* and *B* states are almost identical.²³

In total, in the rotational spectrum of AMN, we assigned about 1400 distinct frequency lines with $10 \leq J \leq 74$ and $0 \leq K_a \leq 23$ that correspond to about 2500 rotational transitions of the *A* conformation. About 80% of the assigned lines are of *B* symmetry species because their intensities are favored by spin statistics. Due to extreme density of the spectrum and lower intensities caused by statistical weights, the assignment of *A* species lines was more difficult. The correctness of the assignment of *B* symmetry perturbed transitions was confirmed by the identification of weak μ_a -type lines. As was mentioned before, the recorded rotational spectrum of AMN is very dense. Owing to their strong intensities the μ_b -type lines were thus easily assigned. The intensities of the μ_a -type transitions calculated using the ab initio value of the μ_a dipole moment component are much weaker and, in comparison with the experimental spectrum, are at the confusion limit of the experiment. The μ_a -type lines connect B_1 and B_2 levels; therefore, their frequencies depend on the energy difference ΔE_B between these two levels. The ΔE_B term is usually highly correlated with Coriolis coupling terms. Incorrect assignment of μ_b -type transitions would produce incorrect values of Coriolis coupling parameters, thus making impossible the assignment of transitions, whose frequencies depend on the energy difference ΔE_B . One should note that the extreme density of the rotational spectrum of AMN does not allow simple recognition of a pattern for such a series of transitions, which would be possible in the case of less dense and more intense spectrum. Thus, the correct assignment of μ_a -type transitions was made only on the basis of correct frequency predictions obtained from the analysis of the perturbed μ_b -type transitions.

The whole data set of the assigned transitions was fitted within experimental accuracy using a RAS Hamiltonian consisting of 31 parameters. The frequencies of assigned rotational transitions are presented in Table S2 of the Supporting Information. The rotational parameters obtained as the result of the fit are listed in Table 2. The unique set of rotational constants allows more straightforward comparison with corresponding ab initio values that are also listed in Table 2. As follows from the analysis of the parameters in Table 2, in addition to the rotational constants, we determined the full set of quartic and sextic centrifugal distortion constants. All of them agree well with corresponding values from ab initio calculations.

The final results of the fit allowed us to perform the correct assignment of the tunneling substates. For this purpose, we applied the energy splittings scheme made for ethylamine by ref 23 (see Figure 5 of ref 23), and we used the energy differences ΔE_A and ΔE_B from our fit. The assumption of the scheme validity for AMN is supported by the fact that the values of the barriers to torsion and inversion motions in ethylamine and AMN are relatively close.

CONCLUSIONS

The results of the present study have shown that two conformations exist for the AMN molecule. Quantum chemical calculations indicate that the A conformer is preferred over the S conformer by 6.7 kJ/mol. This assumption is in general agreement with the experimental spectrum, where only the A conformer was observed. Quantum chemical calculations and spectroscopic analysis also show evidence for two LAMs in the AMN molecule. The analysis of the calculated two-dimensional PES indicates that four equivalent configurations exist for the A conformation of the molecule. The torsional motion along the C–N bond, the amino group inversion, or a combination of two motions may interconnect these four configurations. From ab initio calculations, the barriers to torsion and inversion are estimated to be, respectively, 12.5 and 19.1 kJ/mol.

Notwithstanding relatively high barriers, we observed the tunneling splittings in the millimeter wave rotational spectrum of the A conformation measured with Doppler-limited resolution. One should also note that for the S conformation of AMN, there are two equivalent configurations that may be interconnected via tunneling motions. Thus, each rotational energy level of the S conformation is split into two sublevels, and one could also observe tunneling splittings in the rotational spectrum. The analysis of the observed transitions performed using the RAS approach allowed us to fit all of the observed transitions within experimental accuracy. As a result, the set of Hamiltonian parameters may be used to accurately predict frequencies and intensities of AMN rotational lines beyond the frequency range of the experiment and for transitions with $J \leq 75$ and $K_a \leq 23$. Thus, the spectroscopic information obtained in this study provides a solid basis for the astrophysical detection of AMN.

ASSOCIATED CONTENT

Supporting Information

Synthesis of AMN, calculated molecular structure and harmonic vibrational frequencies, rotational line assignments, measured frequencies, experimental uncertainties, and deviations from the final fit. This material is available free of charge via the Internet at <http://pubs.acs.org>.

AUTHOR INFORMATION

Corresponding Author

*E-mail: roman.motienko@univ-lille1.fr. Phone: +33(0) 230434490. Fax: +33(0)20337020.

Notes

The authors declare no competing financial interest.

ACKNOWLEDGMENTS

The Centre National d'Études Spatiales (CNES), the Action sur Projets de l'INSU, "Physique et Chimie du Milieu Interstellaire", and ANR-13-BS05-0008-02 IMOLABS are acknowledged for financial support.

REFERENCES

- (1) Snyder, L. E.; Buhl, D. Observations of Radio Emission from Interstellar Hydrogen Cyanide. *Astrophys. J., Lett.* **1971**, *163*, L48.
- (2) Hanel, R.; et al. Infrared Observations of the Saturnian System from Voyager 1. *Science* **1981**, *212*, 192–200.
- (3) Schloerb, F. P.; Kinzel, W. M.; Swade, D. A.; Irvine, W. M. Observations of HCN in Comet P/Halley. *Astron. Astrophys.* **1987**, *187*, 475–480.
- (4) Oró, J. Mechanism of Synthesis of Adenine from Hydrogen Cyanide under Possible Primitive Earth Conditions. *Nature* **1961**, *191*, 1193–1194.
- (5) Hudson, J. S.; Eberle, J. F.; Vachhani, R. H.; Rogers, L. C.; Wade, J. H.; Krishnamurthy, R.; Springsteen, G. A Unified Mechanism for Abiotic Adenine and Purine Synthesis in Formamide. *Angew. Chem. Int. Ed.* **2012**, *124*, 5224–5227.
- (6) Wang, J.; Gu, J.; Nguyen, M. T.; Springsteen, G.; Leszczynski, J. From Formamide to Adenine: A Self-Catalytic Mechanism for an Abiotic Approach. *J. Phys. Chem. B* **2013**, *117*, 14039–14045.
- (7) Ferris, J. P.; Orgel, L. Aminomalononitrile and 4-Amino-5-cyanoimidazole in Hydrogen Cyanide Polymerization and Adenine Synthesis. *J. Am. Chem. Soc.* **1965**, *87*, 4976–4977.
- (8) Sanchez, R. A.; Ferbis, J. P.; Orgel, L. E. Studies in Prebiotic Synthesis: II. Synthesis of Purine Precursors and Amino Acids from Aqueous Hydrogen Cyanide. *J. Mol. Biol.* **1967**, *30*, 223–253.
- (9) Roy, D.; Najafian, K.; von Ragué Schleyer, P. Chemical Evolution: The Mechanism of the Formation of Adenine under Prebiotic Conditions. *Proc. Natl. Acad. Sci. U.S.A.* **2007**, *104*, 17272–17277.
- (10) Zaleski, D. P.; et al. Detection of E-Cyanomethanimine toward Sagittarius B2(N) in the Green Bank Telescope PRIMOS Survey. *Astrophys. J., Lett.* **2013**, *765*, L10.
- (11) Ferris, J. P.; Orgel, L. Studies in Prebiotic Synthesis. I. Aminomalononitrile and 4-Amino-5-cyanoimidazole. *J. Am. Chem. Soc.* **1966**, *88*, 3829–3831.
- (12) Ferris, J.; Edelson, E. Chemical Evolution. 31. Mechanism of the Condensation of Cyanide to Hydrogen Cyanide Oligomers. *J. Org. Chem.* **1978**, *43*, 3989–3995.
- (13) Johnson, T. B.; Nicolet, B. H. Researches on Pyrimidines. LXVI. The Formation of Pyrimidines from Diethyl Aminomalonate and Amino Malonicnitrile. *J. Am. Chem. Soc.* **1914**, *36*, 345–355.
- (14) Rayner, B.; Tapiero, C.; Imbach, J. Synthetic Nucleosides. IX. Some α -Ribofuranonucleosides. *J. Carbohydr., Nucleosides, Nucleotides* **1976**, *3*, 1–14.
- (15) Hosmane, R. S.; Lim, B. B.; Burnett, F. N. Rearrangements in Heterocyclic Synthesis: A Novel Translocation of an (N-Amino-N-methylamino) methylene Group from a Heterocyclic N-Amino-N-methylformamidine Side Chain to the Vinylogous Nitrile Function. *J. Org. Chem.* **1988**, *53*, 382–386.
- (16) Birkett, P. R.; Chapleo, C. B.; Mackenzie, G. Synthesis of Novel Imidazotriazepines and Their Conversion to 9-(2-Ethylaminoethyl) adenine and 9-(2-Ethylaminoethyl) hypoxanthine. *Synthesis* **1991**, *1991*, 822–824.

- (17) Corelli, F.; Summa, V.; Brogi, A.; Monteagudo, E.; Botta, M. Chiral Azole Derivatives. 2. Synthesis of Enantiomerically Pure 1-Alkylimidazoles. *J. Org. Chem.* **1995**, *60*, 2008–2015.
- (18) Brieden, W.; Fuchs, R. *Process for the Production of 3-Alkoxy-5-alkylpyrazin-2-amines*. Eur. Pat. Appl. EP 820993 A2 19980128, 1998.
- (19) Shibata, K.; Yoshida, M.; Doi, T.; Takahashi, T. Derivatization of a Tris-oxazole Using Pd-Catalyzed Coupling Reactions of a 5-Bromooxazole Moiety. *Tetrahedron Lett.* **2010**, *51*, 1674–1677.
- (20) Smith, I.; Talbi, D.; Herbst, E. The Production of HCN Dimer and More Complex Oligomers in Dense Interstellar Clouds. *Astron. Astrophys.* **2001**, *369*, 611–615.
- (21) Yim, M. K.; Choe, J. C. Dimerization of HCN in the Gas Phase: A Theoretical Mechanistic Study. *Chem. Phys. Lett.* **2012**, *538*, 24–28.
- (22) Ohashi, N.; Hougen, J. T. The Torsional-Wagging Tunneling Problem and the Torsional-Wagging-Rotational Problem in Methylamine. *J. Mol. Spectrosc.* **1987**, *121*, 474–501.
- (23) Fischer, E.; Botskor, I. The Microwave Spectrum of *gauche*-Ethylamine. *J. Mol. Spectrosc.* **1984**, *104*, 226–247.
- (24) Bhatta, R. S.; Gao, A.; Perry, D. S. A Comparative Ab Initio Study of Torsion–Inversion Coupling in CH_3NH_2 , CH_3OH_2^+ and $\text{CH}_3\text{CH}_2^\bullet$. *J. Mol. Struct.: THEOCHEM* **2010**, *941*, 22–29.
- (25) Moser, R.; Claggett, A.; Matthews, C. Peptide Formation from Aminomalononitrile (HCN Trimer). *Tetrahedron Lett.* **1968**, *9*, 1605–1608.
- (26) Alekseev, E.; Motiyenko, R.; Margulès, L. Millimeter- and Submillimeter-Wave Spectrometers on the Basis of Direct Digital Frequency Synthesizers. *Radio Phys. Radio Astron.* **2012**, *3*, 75–88.
- (27) Frisch, M. J. et al. *Gaussian 09*, revision D.01; Gaussian Inc.: Wallingford, CT, 2009.
- (28) Smeyers, Y. G.; Villa, M.; Senent, M.-L. *Ab Initio* Determination of the Torsion-Wagging and Wagging-Bending Infrared Band Structure Spectrum of Methylamine. *J. Mol. Spectrosc.* **1998**, *191*, 232–238.
- (29) Kim, H.-W.; Zeroka, D. Internal-Rotation and Inversion Potential Energy Surfaces for Methylamine and Methylphosphine. *Int. J. Quantum Chem.* **2008**, *108*, 974–982.
- (30) Pickett, H. M. Vibration–Rotation Interactions and the Choice of Rotating Axes for Polyatomic Molecules. *J. Chem. Phys.* **1972**, *56*, 1715–1723.
- (31) Christen, D.; Müller, H. S.; Coudert, L. The g'Ga Conformer of Ethylene Glycol: A Test Case for Tunneling-Rotation Approaches Developed for Non-Rigid Molecules. *57th International Symposium on Molecular Spectroscopy*; Ohio State University, 2002; TB03.
- (32) Hougen, J. T. A Generalized Internal Axis Method for High Barrier Tunneling Problems, as Applied to the Water Dimer. *J. Mol. Spectrosc.* **1985**, *114*, 395–426.
- (33) Ohashi, N.; Hougen, J. T. The Torsional-Wagging Tunneling Problem and the Torsional-Wagging-Rotational Problem in Hydrazine. *J. Mol. Spectrosc.* **1985**, *112*, 384–400.
- (34) Coudert, L.; Hougen, J. Tunneling Splittings in the Water Dimer: Further Development of the Theory. *J. Mol. Spectrosc.* **1988**, *130*, 86–119.
- (35) Christen, D.; Müller, H. S. The Millimeter Wave Spectrum of aGg' Ethylene Glycol: The Quest for Higher Precision. *Phys. Chem. Chem. Phys.* **2003**, *5*, 3600–3605.

Mono-deuterated dimethyl ether: laboratory spectrum up to 1 THz

Torsion-rotational spectrum within the vibrational ground-state for the symmetric and asymmetric conformers and first detection in IRAS 16293-2422*

C. Richard¹, L. Margulès¹, E. Caux^{2,3}, C. Kahane⁴, C. Ceccarelli⁴, J.-C. Guillemin⁵, R. A. Motiyenko¹,
C. Vastel^{2,3}, and P. Groner⁶

¹ Laboratoire de Physique des Lasers, Atomes et Molécules, CNRS UMR 8523, Université Lille 1, 59655 Villeneuve d'Ascq Cedex, France
e-mail: cyril.richard@phlam.univ-lille1.fr, laurent.margules@univ-lille1.fr

² Université de Toulouse, UPS-OMP, IRAP, Toulouse, France

³ CNRS, Institut pour la Recherche en Astrophysique et Planétologie, 9 Av. Colonel Roche, BP 44346, 31028 Toulouse Cedex 4, France

⁴ UJF-Grenoble 1/CNRS-INSU, Institut de Planétologie et d'Astrophysique de Grenoble (IPAG) UMR 5274, 38041 Grenoble, France

⁵ Institut des Sciences Chimiques de Rennes, UMR 6226 CNRS – ENSCR, Avenue du Général Leclerc, CS 50837, 35708 Rennes Cedex 7, France

⁶ Department of Chemistry, University of Missouri-Kansas City, Kansas City, MO 64110-2499, USA

Received 30 November 2012 / Accepted 25 February 2013

ABSTRACT

Context. Dimethyl ether is one of the most abundant complex organic molecules (COMs) in star-forming regions. Like other COMs, its formation process is not yet clearly established, but the relative abundances of its deuterated isotopomers may provide crucial hints in studying its chemistry and tracing the source history. The mono-deuterated species (CH_2DOCH_3) is still a relatively light molecule compared to other COMs. Its spectrum is the most intense in the THz domain in the 100–150 K temperature regime, tracing the inner parts of the low-mass star-forming region. Therefore, it is necessary to measure and assign its transitions in this range in order to be able to compute accurate predictions required by astronomical observations, in particular with the telescope operating in the submm range, such as ALMA.

Aims. We present the analysis of mono-deuterated dimethyl ether in its ground-vibrational state, based on an effective Hamiltonian for an asymmetric rotor molecules with internal rotors. The analysis covers the frequency range 150–990 GHz.

Methods. The laboratory rotational spectrum of this species was measured with a submillimeter spectrometer (50–990 GHz) using solid-state sources. For the astronomical detection, we used the IRAM 30 m telescope to observe a total range of 27 GHz, in 4 frequency bands from 100 GHz to 219 GHz.

Results. New sets of spectroscopic parameters have been determined by a least squares fit with the ERHAM code for both conformers. These parameters have permitted the first identification in space of both mono-deuterated DME isomers via detection of twenty transitions in the solar-type protostar IRAS 16293-2422 with the IRAM 30 m telescope. The DME deuteration ratio in this source appears as high as observed for methanol and formaldehyde, two species known to play an important role in the COMs formation history.

Key words. line: identification – methods: laboratory – molecular data – techniques: spectroscopic – submillimeter: ISM – ISM: molecules

1. Introduction

Dimethyl ether (DME) is a large complex organic molecule (COM) detected for the first time in the interstellar medium (ISM) by Snyder et al. (1974). Abundant in the hot cores, which are the precursors of high-mass stars (Ikeda et al. 2001), DME is also one of the main COMs in hot corinos, forming low-mass stars, such as IRAS 16293-2422 (Cazaux et al. 2003; Bottinelli et al. 2004). In both types of sources, the commonly adopted scenario is that grain surface chemistry plays a crucial role in the formation of COMs in the early, cold prestellar stage of star

formation; subsequently, during the warm up phase corresponding to the hot cores and hot corinos stages, the icy grain mantles evaporate and inject the products of grain surface chemistry into the molecular gas (Herbst & van Dishoeck 2009, and references therein). However, the relative importance of cold grain surface and post-evaporation warm gas-phase processes in the formation of DME is under debate (see e.g. Peeters et al. 2006; Brouillet et al. 2013). Furthermore, DME has been recently detected in a cold prestellar core, L1689B, (Bacmann et al. 2012), where the warm-up phase has not yet taken place. At least for DME, the COM formation scenario in protostars needs further investigations. Many hydrogenated molecules observed in hot corinos such as IRAS 16293-2422 show remarkably high D/H abundance ratios, significantly higher than observed in hot cores. This so-called super-deuteration phenomenon (Ceccarelli et al. 2007) is thought to be linked to molecular depletion on the grain

* Full Tables A.1, A.2, B.1, and B.2, which respectively give the measured (in laboratory) and predicted frequencies, are only available at the CDS via anonymous ftp to cdsarc.u-strasbg.fr (130.79.128.5) or via <http://cdsarc.u-strasbg.fr/viz-bin/qcat?J/A+A/552/A117>

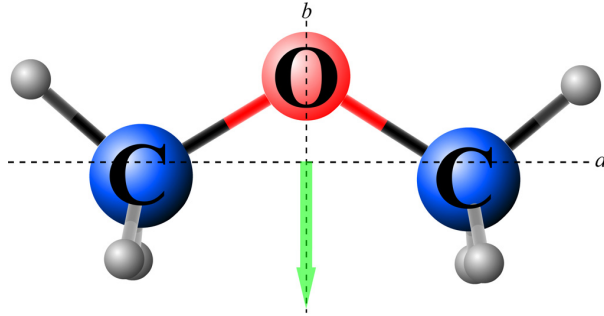


Fig. 1. Representation of the DME and of its electric dipole moment in the principal inertial axes. The dipole moment arrow is drawn from the negative to positive charge.

surface during the cold prestellar phase. However, deuterium chemistry in hot cores might be significantly different as shown by the distinct methanol deuterated species relative abundances (Ratajczak et al. 2011). Thus, measuring the deuteration ratio of DME in different types of sources is likely to provide constraints on this species chemistry and formation history. Even though dimethyl ether is such an abundant interstellar molecule, up to now, the mono-deuterated isotopologue has not been observed.

DME is a near-prolate asymmetric top ($\kappa = -0.922$ MHz) with only a b -dipole moment component, $\mu_b = 1.302$ D (Blukis et al. 1963). Figure 1 represents the molecule and its electronic dipole moment pointing from the negative to the positive poles along the b -axis. Previous laboratory investigations have been conducted for DME up to 2.1 THz (Groner et al. 1998; Endres et al. 2009). Upon partial deuteration on one of the methyl groups, the DME molecule can exist in one of two different conformations, each with a single CH_3 internal rotor. The symmetric conformation is characterized by the D atom located in the C-O-C plane, and thus by C_s symmetry. When the D atom is located outside of the C-O-C plane the corresponding conformation is called asymmetric. The asymmetric conformation has two equivalent configurations with a possible tunneling motion between them. In summary, one can expect to observe in the rotational spectrum of deuterated DME the typical A - E splittings due to the nonsubstituted methyl top internal rotation for both conformations, and additional doublet splitting of A and E lines of the asymmetric conformation due to tunneling of the CH_2D group.

The rotational spectrum of mono-deuterated DME in the vibrational ground-state (see simulated spectra at different temperatures in Fig. 2) was studied for the first time by Blukis et al. (1963). They measured a few transitions for several isotopic species in the centimeter-wave range (8.2–50 GHz) and determined the rotational constants. The starting point of our study was the analysis carried out in the same frequency range with better accuracy for almost all isotopic species by Niide & Hayashi (2003). In the present study, the set of assigned transitions was thus greatly extended to 1 THz, and data from this current investigation were combined with published data into a global fit for each conformer. At the same time, two new accurate sets of parameters were derived from the fits performed with the ERHAM code (Groner 1997, 2012). These new data are thus now precise enough to allow an astrophysical detection in the ISM.

This paper presents our laboratory investigation and analysis of mono-deuterated DME, as well as a detection in the solar-type protostar IRAS 16293-2422 using the IRAM 30 m telescope.

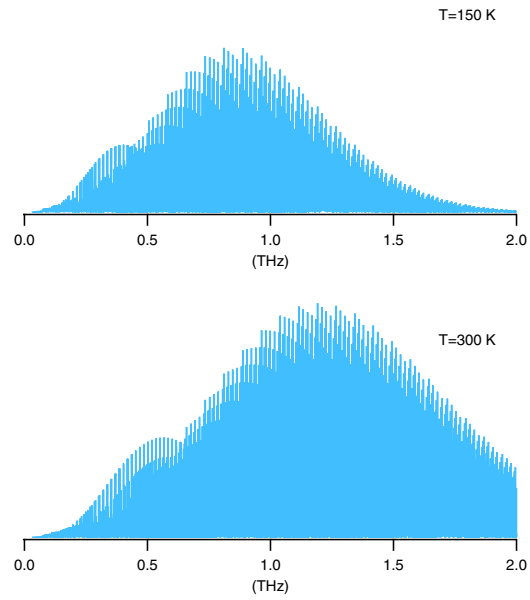


Fig. 2. Stick spectrum of mono-deuterated DME (symmetric conformer) in its vibrational ground state at 150 K (above) and 300 K (below). This figure illustrates the importance of the analysis around 1 THz. Although the dense ISM is generally colder, such temperatures exist in the warm inner regions of the collapsing protostars (see for instance Ceccarelli et al. 2000). The spectrum intensity scale is arbitrary.

2. Experimental details

2.1. Preparation of mono-deuterated dimethyl ether

The synthesis of mono-deuterated DME has already been reported by Shtarev et al. (1999) and has been modified as follows. Lithium aluminum deuteride (420 mg, 10 mol) and tetraglyme (20 mL) were introduced into a 100 mL two-necked flask equipped with a stirring bar, a stopcock, and a septum. The flask was fitted to a vacuum line equipped with two traps. The flask was immersed in a cold bath (-25 °C) and degassed. The stopcock was then closed. Bromomethyl methyl ether (2.5 g, 20 mmol) diluted in tetraglyme (5 mL) was added slowly with a syringe through the septum. At the end of the addition, the mixture was stirred for 30 min at room temperature. The first trap was then immersed in a -80 °C cold bath and the second one in a liquid nitrogen bath (-196 °C). The stopcock of the cell was opened slowly. Residual bromomethyl methyl ether and high boiling impurities were condensed in the first trap, and mono-deuterated DME was selectively condensed in the second trap. The yield was 80% based on the starting brominated ether.

2.2. Lille – submillimeter wave spectrometer

The submillimeter-wave measurements were performed with the Lille spectrometer (150–990 GHz) (Motiyenko et al. 2010). The sources are only solid-state devices. The frequency of the Agilent synthesizer (12.5–17.5 GHz) was first multiplied by six and amplified by a Spacek active sextupler providing the output power of +15 dBm in the W-band range (75–110 GHz). This power is high enough to use passive Schottky multipliers ($\times 2$, $\times 3$, $\times 5$, $\times 2 \times 3$, $\times 3 \times 3$) from Virginia Diodes Inc. in the next stage of the frequency multiplication chain. As a detector we used an InSb liquid He-cooled bolometer from QMC Instruments Ltd. to improve the sensitivity of the spectrometer; the source

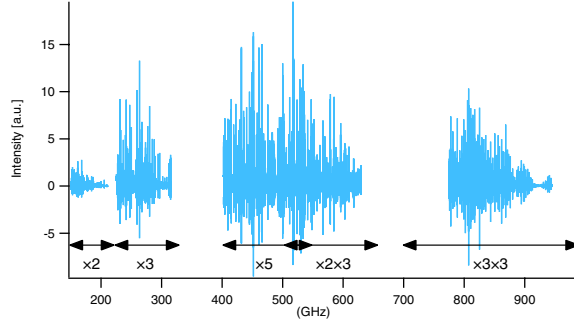


Fig. 3. Spectrum of mono-deuterated DME recorded at Lille is represented with each multiplier range ($\times 2$, $\times 3$, $\times 5$, $\times 2 \times 3$, $\times 3 \times 3$), which cover most of the frequencies up to 990 GHz. The spectrum intensity scale is arbitrary.

was frequency-modulated at 10 kHz. The absorption cell was a stainless-steel tube (6 cm diameter, 220 cm long). The sample pressure during measurements was about 1.5 Pa (15 μ bar), and the linewidth was limited by Doppler broadening. These measurements were performed at room temperature. The measurement accuracy for isolated lines is estimated to be better than 30 kHz up to 630 GHz and 50 kHz at higher frequencies owing to the Doppler effect. However, if the lines were blended or had a poor signal-to-noise ratio, they were assigned an uncertainty of 100 or even 200 kHz. The spectrum of mono-deuterated DME recorded at Lille appears in its entirety in Fig. 3.

3. Spectral analysis

This analysis of the spectrum of mono-deuterated DME was undertaken to extend the work of Niide & Hayashi (2003). Previous parameters and assigned transitions were used for the initial prediction with the ERHAM code (Groner 1997, 2012) in Watson's A reduction (Watson 1977). Then, the prediction was improved step by step with the addition of new identified lines. The XIAM program (Hartwig & Dreizler 1996) was also used for comparisons, but owing limitations in the program for blended transitions, fits results were poorer so are not presented in this paper except for the barrier height for rotation of the methyl group, V_3 .

Mono-deuterated DME shows a very complex spectrum, and there are a lot of unassigned lines due to the excited torsional states about 200–240 cm^{-1} above the ground state (values given by Endres et al. (2010) for the parent species). In addition, many lines are blended or distorted. As a rule, lines with residuals higher than 4σ were excluded from the fit. Since the principal axes in mono-deuterated DME have almost the same orientation with respect to the molecular frame as in normal DME, the dipole moment in mono-deuterated DME is almost parallel to the b axis; in consequence, the spectrum contains mainly b -transitions. However, Groner et al. (1998) report that “forbidden” c -transitions can occur when pseudo-quantum numbers K_a and K_c do not represent the wave functions very well in the case of mixing or level crossing. In our analysis, a few c -transitions have been assigned especially at high frequency. Transitions without intense torsional-rotational interaction obey b -type asymmetric top selection rules: $\Delta J = 0, \pm 1$; $\Delta K_a = \pm 1, 3, \dots$; $\Delta K_c = \pm 1, 3, \dots$ (Gordy & Cook 1984). The spin weight for both substates A and E is 4. The spectroscopic parameters and their uncertainties are presented in Table 1 for both conformers.

Table 1. Spectroscopic constants of the ground-vibrational state of mono-deuterated DME for the two different conformers.

Parameters	Symmetric conformer	Asymmetric conformer
ρ	0.216545(71)	0.19175(13)
β (deg)	7.545(9)	9.718(24)
α (deg)	0.0 ^a	0.0 ^b
A (MHz)	38 281.53382(35)	34 764.30530(33)
B (MHz)	9309.18796(13)	9642.41649(12)
C (MHz)	8277.96648(11)	8537.25156(12)
Δ_J (kHz)	7.06511(11)	8.97763(10)
Δ_{JK} (kHz)	-20.32475(64)	-18.29447(56)
Δ_K (kHz)	297.4899(30)	245.4877(22)
δ_J (kHz)	1.281232(37)	1.835770(33)
δ_K (kHz)	-8.9793(21)	-9.3752(32)
Φ_J (Hz)	0.004839(35)	0.006426(25)
Φ_{JK} (Hz)	0.0925(23)	0.1800(22)
Φ_{KJ} (Hz)	-3.2546(79)	-3.5559(73)
Φ_K (Hz)	10.078(11)	9.5379(70)
ϕ_J (Hz)	0.002403(15)	0.003130(11)
ϕ_{JK} (Hz)	0.1716(15)	0.2760(11)
ϕ_K (Hz)	1.649(89)	4.446(71)
ϵ_1 (MHz)	-2.9882(33)	-2.5032(60)
$[A - (B + C)/2]_1$ (kHz)	0.951(42)	0.663(55)
$[(B + C)/2]_1$ (kHz)		-0.0281(79)
$[(B - C)/4]_1$ (kHz)	0.1349(33)	0.1140(46)
V_3^c (cm^{-1})	906.61(75)	905.84(121)
Lines ^d	1253	1286
$J(\max), K_a(\max)$	54, 15	55, 19
L_{worst}^e	3.5	-3.8
n^f	20	21
σ_{fit}^g (MHz)	0.091	0.104
σ_w^h	1.06	1.12

Notes. Numbers in parentheses are one standard deviation in the same units as the last digit. ^(a) By symmetry. ^(b) Assumed, see Sect. 4.

^(c) Barrier height for rotation of the methyl group determined with XIAM. This parameter is not considered in the ERHAM fit. ^(d) Number of distinct lines in the fit. ^(e) $(o. - c.)/\sigma$ of the poorest-fit line.

^(f) Number of free parameters used in the fit. ^(g) Standard deviation of the fit. ^(h) Weighted standard deviation (dimensionless).

For the symmetric conformer, the fit includes 1255 distinct lines (1219 new lines). The lines were fitted with J up to 54 and K_a up to 15. A total of 20 spectroscopic parameters were determined by the least-squares method and are listed in Table 1. The fifteen nontunneling parameters correspond to the rotational and distortion constants. In addition, two internal rotation parameters (ρ and β), one energy tunneling parameter (ϵ_1) and two rotational constant tunneling parameters ($[A - (B + C)/2]_1$ and $[(B - C)/4]_1$) were determined. The notation used in this paper was developed in detail by Groner (1997). The weighted (dimensionless) standard deviation of the fit is of 1.06, while the rms (for the unweighted frequencies) is of 91 kHz.

Then, 1286 distinct lines (1251 new lines) were assigned and included in the fit for the asymmetric conformer. Three lines from the previous study (Niide & Hayashi 2003) were removed from the final fit because of higher residuals (more than 4σ). In addition, three other microwave lines originally assigned to the *A* state by Niide & Hayashi (2003) were attributed to the *E* state, and another tunneling coefficient was determined ($[(B+C)/2]_1$). The total of the transitions was fitted with $0 \leq J \leq 55$ and a K_a value up to 19. Table 1 presents the 21 parameters determined. The fit gives a weighted standard deviation of 1.12 and an rms of 104 kHz.

4. Discussion

The ground-vibrational state rotational spectrum of mono-deuterated DME (CH_2DOCH_3) was measured and analyzed in the frequency range up to 1 THz for both conformers. All experimental frequencies given in Tables A.1 and A.2 are available in their entirety in electronic form at the CDS. Only 17 and 19 frequencies for the symmetric and asymmetric conformers, respectively, deviated by more than 3σ . In both cases, lines with residuals greater than 4σ were assigned but not included in the fit, and these frequencies are reported in Tables A.1 and A.2 with an uncertainty of 0.

It seems that somewhat better results were obtained for symmetric conformer in the least-squares fit. Indeed, in the case of asymmetric conformer, tunneling between two equivalent configurations leads to Coriolis-type perturbations in the spectra that cannot be accounted for in the present ERHAM code. Moreover, some series of *A* and *E* lines of asymmetric conformer exhibit additional doublet structure due to the tunneling. This effect was particularly visible within the first members of *Q* branches and at low frequency, i.e., for the lines with low K_a (≤ 5) and J (≤ 15). Indeed, the splitting increases as J decreases as shown in Fig. 4. Another example of the quartets for *R* lines is given in Fig. 5. In all these cases, the center frequency of the doublet was entered as the transition frequency in the ERHAM fit, and an uncertainty of 0.1 MHz was assumed. This method has been used for 89 lines between 150 and 290 GHz. Fortunately for the present investigation, most of the lines showed doublets (twice as intense as for the symmetric conformer); therefore, it was possible to use the one-top approximation for the CH_3 group as long as no quartets were included in the fit. The correct treatment of such additional doubling requires inclusion of new Coriolis-type terms in the model.

Unlike the symmetric conformation, the asymmetric conformer does not have a symmetry plane. Therefore at the beginning, α , the angle of the ρ axis with regard to *ab* principal plane, was set to an arbitrary value of 10° . The subsequent least-squares fit resulted in an extremely low value for α , much less than 1° . As a consequence, α was set to zero for the final fit.

Another interesting quantity reported in Table 1 is the barrier height V_3 , which was derived with the XIAM code and, therefore, not used in the fit of the free spectroscopic parameters listed in the table. Its value, either for the symmetric or the asymmetric configuration, is in good agreement with earlier work (Durig et al. 1976; Lovas et al. 1979) for the parent species.

5. Prediction

The newly derived sets of spectroscopic constants shown in Table 1 have permitted predictions of transition frequencies for the symmetric and asymmetric conformers up to 1.2 THz.

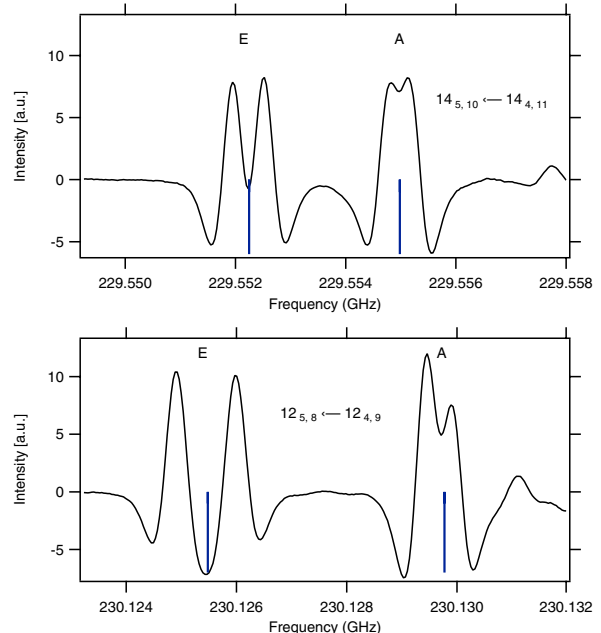


Fig. 4. Rotational transitions $J_{K_a,K_c} = 14_{5,10} \leftarrow 14_{4,11}$ and $J_{K_a,K_c} = 12_{5,8} \leftarrow 12_{4,9}$ of asymmetric mono-deuterated DME in the vibrational ground state at 230 GHz. Stick spectrum below experimental lines represents the prediction given by ERHAM. The internal motion of the CH_2D group is observed through the *A* and *E* components, which are split into two substates. It is also noticeable that this separation increases as J decreases and it is more intense in the *E* component. The experimental measurements are peaked in the center of the doublet. The spectrum intensity scale is arbitrary.

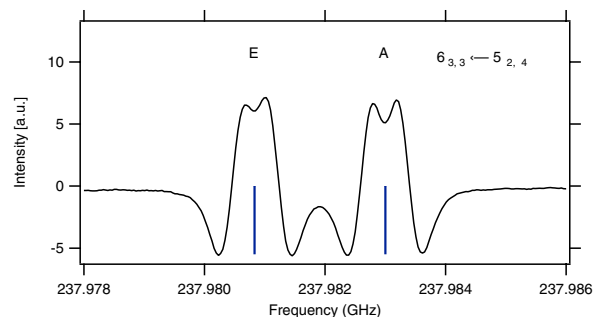


Fig. 5. Rotational transition $J_{K_a,K_c} = 6_{3,3} \leftarrow 5_{2,4}$ of asymmetric mono-deuterated DME in the vibrational ground state at 238 GHz. In the case of an *R* line, the splitting of the *A* and *E* states is nearly identical unlike in the *Q* line as represented in Fig. 4. The spectrum intensity scale is arbitrary.

Two short examples are provided in Tables B.1 and B.2 from 301.6 GHz to 303.5 GHz. The complete tables are available through the CDS. Calculated frequencies for both torsional substates *A* and *E* (symmetry numbers 0 and 1, respectively) are given with their line strength S for the μ_b component. To obtain the proper transition intensity, S must be multiplied by the square of μ_b and by the spin weight. Lines with $S < 0.1$, uncertainty ≥ 0.2 MHz, and $J > 60$ were removed from the predictions in order to keep only those lines that could be relevant for an astrophysical detection. In addition, a modified version of ERHAM provided predictions in the format of the JPL catalog (Pickett 1991).

Table 2. Rotational partition function for the symmetric and asymmetric conformers of mono-deuterated DME in the ground vibrational state computed for nine different temperatures.

Temperature	2.275 K	5 K	9.375 K	18.75 K	37.5 K	75 K	150 K	225 K	300 K
Symmetric conformer									
A state	58.6	142.5	361.4	1015.2	2861.7	8082.2	22 850.4	41 941.2	64 256.6
E state	58.6	142.5	361.4	1015.2	2861.7	8082.2	22 850.4	41 941.2	64 256.6
Total	117.2	285.0	722.8	2030.4	5723.5	16 164.3	45 700.8^a	83 882.3^b	128 513.1^b
Approx. ^c	111.7	277.6	712.8	2016.0	5702.2	16 164.3	45 617.5	83 804.6	129 025.6
Ratio	1.049	1.027	1.014	1.007	1.004	1.002	1.002	1.001	0.996
Asymmetric conformer									
A state	119.2	289.6	734.2	2061.8	5811.8	16 413.5	46 407.7	85 201.7	130 629.7
E state	119.1	289.5	734.1	2061.8	5811.8	16 413.5	46 407.7	85 201.7	130 629.7
Total	238.3	579.1	1468.3	4123.7	11 623.5	32 826.9	92 815.4^a	170 403.4^b	261 259.3^b
Approx. ^c	226.8	563.7	1447.4	4093.7	11 578.8	32 749.9	92 630.6	170 173.4	261 999.0
Ratio	1.051	1.027	1.014	1.007	1.004	1.002	1.002	1.001	0.997

Notes. The data presented in bold are the results used for the astrophysical detection in Sect. 7. This table is given for the rotational degrees of freedom; the contributions from vibrational excited states are ignored. ^(a) The sum of states did not converge completely, error for total <20 for the symmetric conformation, <40 for asymmetric. ^(b) The sum of states has not converged (this is the reason for ratio <1 at 300 K). ^(c) These values are computed with the rigid asymmetric rotor approximation.

Numerical values of the overall partition function were computed for nine different temperatures and listed in Table 2 in order to derive column densities. The results for the asymmetric conformation are multiplied by two because of the additional degeneracy discussed in Sect. 4. However, the intensity calculation in ERHAM for the JPL catalog format file does not consider this additional degeneracy. To arrive at the proper overall intensity for the asymmetric conformer, one needs to multiply the catalog intensity by two or divide the quoted sum of states by two.

6. Observations

We have successfully searched for the deuterated DME lines in the nearby low-mass protostar IRAS 16293-2422 (hereinafter IRAS 16293). Located in the Ophiuchi complex at 120 pc from the Sun (Loinard et al. 2008), IRAS 16293 has played a similar role to a prototype for low-mass protostars in astrochemical studies, such as Sgr B2 or Orion KL for high-mass protostars. Many complex organic molecules (COMs) have been detected towards IRAS 16293 including DME (Cazaux et al. 2003; Caux et al. 2011), with abundances comparable to those found in high-mass protostars. Because the level of molecular deuteration is considerably higher in low-mass protostars than in their massive counterparts (Ceccarelli et al. 2007), IRAS 16293 is thus the best candidate to look for deuterated DME. The data presented here come from recent observations, performed in March 2012 in four selected frequency ranges at 3, 2, and 1 mm, with the new broad band EMIR receivers at the IRAM 30 m telescope. IRAS 16293 hosts in a common colder envelope, two hot corinos, A (south-east) and B (northwest), separated by about 4'' (Wooten 1989).

Our observations, performed in DBS (double-beam-switch) observing mode with a 90'' throw, were centered on the B component at $\alpha(2000.0) = 16^{\mathrm{h}}32^{\mathrm{m}}22.6^{\mathrm{s}}$, $\delta(2000.0) = -24^{\circ}28'33''$. The pointing and focus were checked every two hours on nearby planets or on continuum radio sources (1741-038 or 1730-130). The pointing accuracy was better than 2'', and even at the highest frequencies, the A and B components were both inside the beam of our observations so that the observed emission includes the contributions from both cores. Interferometric observations show that the molecular lines emitted by core B are much narrower than those emitted by core A (Bottinelli et al. 2004)

Table 3. Observational parameters.

Frequency (GHz)	HPBW (")	Spectral resolution (MHz)	RMS (mK)
100.5–109.8	23	0.195	3–4.8
146.7–150.8	16	0.195	7.1–9.1
165.7–169.8	14	0.195	18.7–22.7
209.5–218.8	12	0.195	15.2–19.7

and that DME lines emitted by core B are at least as strong as DME lines emitted by core A (Jørgensen et al. 2011). The TIMASSS survey (The IRAS 16293-2422 Millimeter And Submillimeter Spectral Survey, Caux et al. 2011) performed with the IRAM 30 m telescope and JCMT telescopes confirms that narrow DME lines from B are easily detected when contributions from both sources are simultaneously observed. This represents an additional favorable factor for identifying of deuterated DME lines in the spectrum from IRAS 16293, since it reduces the risk of blending by nearby lines from other species.

Comparison of the line intensities with those of the TIMASSS survey (Caux et al. 2011) shows that the calibration is accurate within 15%. Table 3 summarizes the observed bands and the details of the observations. Several representative spectra are plotted in Fig. 6.

7. Results: mono-deuterated DME identification in IRAS 16293

Thanks to the spectral resolution and the sensitivity of our IRAM 30 m observations, we were able to identify the 20 brightest lines of both forms of mono-deuterated DME, eight lines for the symmetric conformer and 12 lines for the asymmetric one (see Table 4) in the 27 GHz wide frequency range covered by our spectra. As for most complex molecules, mono-deuterated DME shows a very large number of transitions between 100 GHz and 220 GHz, and many of them were expected to be very faint. The identification was therefore checked using thresholds on both the upper energy level of the lines, restricted to $E'_{\max} \leq 100$ K and their Einstein coefficient, restricted to $A_{ij} \geq 10^{-5}$.

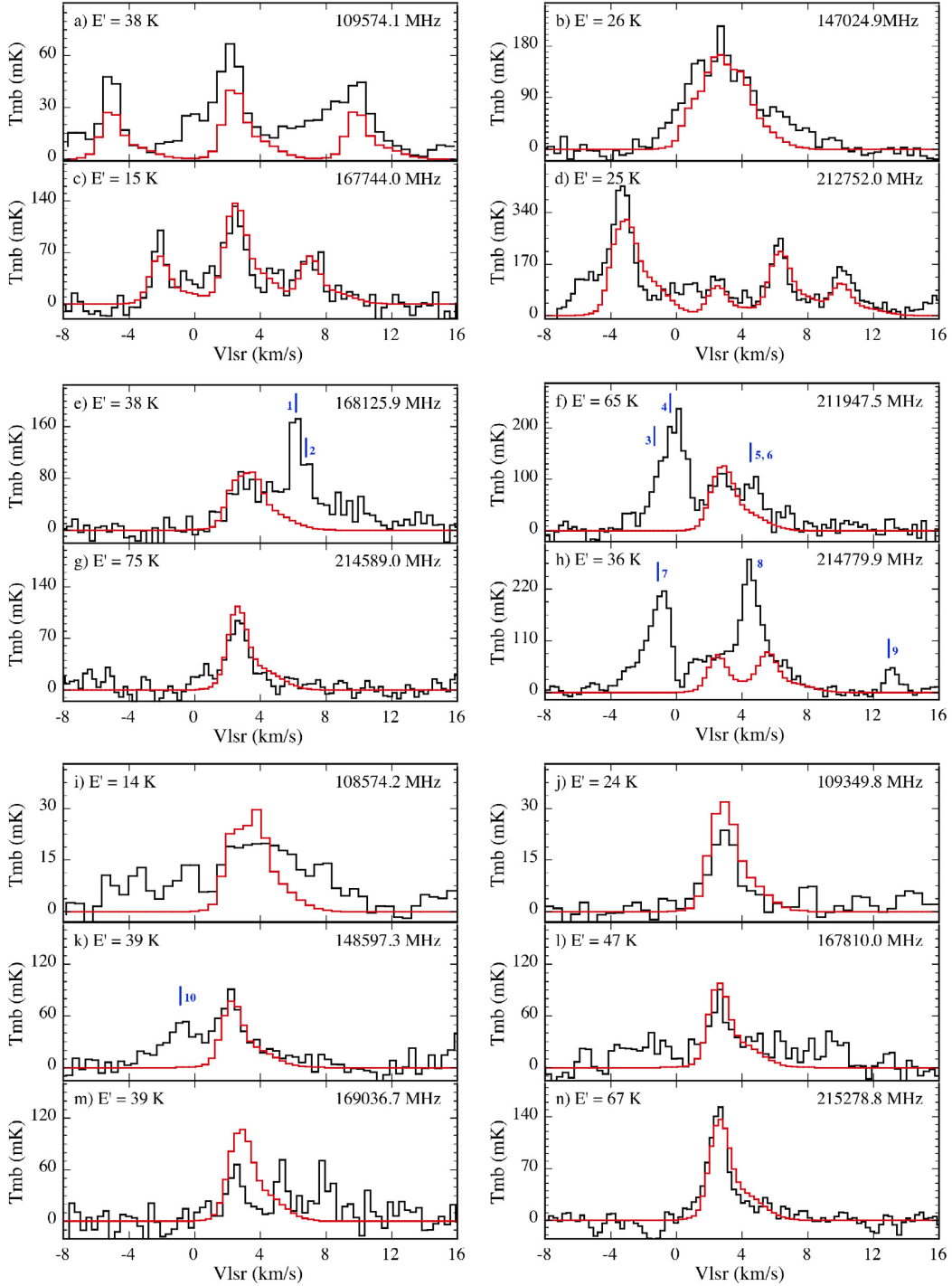


Fig. 6. Some observed transitions of DME and DME-1D (black) and the computed LTE model (red) using the CASSIS software. E values are the upper energy level of the observed lines. The notation E refers to the notation used in Table 1. The LTE model has been computed in bins of the same spectral resolution as the observations. Other transitions from other species are also present in these spectra. Panels a) to d): some observed transitions of DME. Panels e) to h): all detected transitions of DME-1D-sym. Panel e) DME-1D-sym ($9_{1,9}-8_{0,8}$) E and A lines. The blended lines are 1: OC^{33}S (14–13) and 2: $\text{C}_2\text{H}_5\text{OH}$ (10–9). Panel f) DME-1D-sym ($12_{1,12}-11_{0,11}$) E and A lines. The blended lines are 3: HCOOCH_3 (17–16) and 4, 5, 6: CH_3CHO (11–10) transitions. Panel g) DME-1D-sym ($13_{1,13}-12_{1,12}$) E and A lines. Panel h) DME-1D-sym ($8_{2,7}-7_{1,6}$) E and A lines. The blended lines are 7: HCOOCH_3 (18–17), 8: $\text{H}_2\text{C}^{18}\text{O}$ ($3_{1,2}-2_{1,1}$) and one unidentified line (9; around 13 km s^{-1}). Panels i) to n): All detected transitions of DME-1D-asym. Panel i) DME-1D-asym ($5_{1,5}-4_{0,4}$) E and A lines. Panel j) DME-1D-asym ($7_{0,7}-6_{1,6}$) E and A lines. Panel k) DME-1D-asym ($9_{0,9}-8_{1,8}$) E and A lines. The blended line is 10: HC(O)NH_2 ($7_{4,4}-6_{4,3}$). Panel l) DME-1D-asym ($10_{0,10}-9_{1,9}$) E and A lines. Panel m) DME-1D-asym ($9_{1,9}-8_{0,8}$) E and A lines. Panel n) DME-1D-asym ($12_{1,12}-11_{0,11}$) E and A lines.

Table 4. Mono-deuterated DME observed lines for both conformations.

$N^{(a)}$	$\sigma^{(b)}$	J'	K'_a	K'_c	J''	K''_a	K''_c	Frequency (MHz)	E' (K)	A_{ij} (s^{-1})	rms (mK)	δV ($km\ s^{-1}$)	ΔV ($km\ s^{-1}$)	$T_{mb}\Delta V$ ($mK\ km\ s^{-1}$)	Detected		
Symmetric conformer																	
1	1	7	0	7	6	1	6	101 503.8	23	2.83×10^{-5}	5.6	0.55	[−2, 8]	30	64	65	no
2	0	7	0	7	6	1	6	101 503.2									
3	1	7	2	6	7	1	7	103 200.3	29	2.43×10^{-5}	3.7	0.55	[0, 7]	0	24	36	no
4	0	7	2	6	7	1	7	103 197.7	29	2.43×10^{-5}	3.7	0.55	[0, 7]	2	24	36	no
5	1	14	1	13	14	0	14	107 329.6	92	2.03×10^{-5}	3.7	0.55	[0, 7]	0	5	36	no
6	0	14	1	13	14	0	14	107 331.6	92	2.03×10^{-5}	3.7	0.55	[0, 7]	12	5	36	no
7	1	8	2	7	8	1	8	107 480.9	36	2.62×10^{-5}	3.6	0.55	[0, 7]	31	23	35	no
8	0	8	2	7	8	1	8	107 478.3	36	2.62×10^{-5}	3.6	0.55	[0, 7]	19	23	35	no
9	1	9	1	9	8	0	8	168 125.3	38	1.52×10^{-4}	14.2	0.35	[0, 6]	269	254	61	yes ^(e)
10	0	9	1	9	8	0	8	168 125.9									
11	1	12	1	12	11	0	11	211 947.1	65	3.05×10^{-4}	13.4	0.27	[1, 7]	397	283	85	yes ^(f)
12	0	12	1	12	11	0	11	211 947.5									
13	1	13	0	13	12	1	12	214 588.8	75	3.16×10^{-4}	8.4	0.27	[0, 8]	224	226	62	yes ^(g)
14	0	13	0	13	12	1	12	214 589.0									
15	1	8	2	7	7	1	6	214 777.7	36	1.77×10^{-4}	11.1	0.27	[1, 4]	200	180	50	yes ^(h)
16	0	8	2	7	7	1	6	214 779.9	36	1.77×10^{-4}	11.1	0.27	[1, 4]	412	180	50	yes ^(h)
Asymmetric conformer																	
17	1	9	2	8	9	1	9	102 689.8	44	1.04×10^{-5}	4.0	0.55	[0, 6]	35	18	36	no
18	0	9	2	8	9	1	9	102 691.7	44	1.04×10^{-5}	4.0	0.55	[0, 6]	26	18	36	no
19	1	10	0	10	9	1	9	108 481.1	53	1.14×10^{-5}	4.0	0.55	[0, 6]	24	17	36	no
20	0	10	0	10	9	1	9	108 483.0	53	1.14×10^{-5}	4.0	0.55	[0, 6]	12	17	36	no
21	1	5	1	5	4	0	4	108 573.7	14	1.04×10^{-5}	3.7	0.55	[0, 8]	100	103	58	yes ⁽ⁱ⁾
22	0	5	1	5	4	0	4	108 574.2									
23	1	7	0	7	6	1	6	109 349.5	24	1.85×10^{-5}	3.7	0.55	[0, 8]	51	93	39	yes ^(j)
24	0	7	0	7	6	1	6	109 349.8									
25	1	9	0	9	8	1	8	148 597.1	39	5.13×10^{-5}	7.2	0.40	[1, 8]	214	192	60	yes ^(k)
26	0	9	0	9	8	1	8	148 597.3									
27	1	10	0	10	9	1	9	167 809.8	47	7.61×10^{-5}	14.4	0.35	[0, 6]	153	237	104	yes ^(l)
28	0	10	0	10	9	1	9	167 810.0									
29	1	9	1	9	8	0	8	169 036.3	39	7.94×10^{-5}	14.7	0.35	[0, 8]	228	288	123	yes ^(m)
30	0	9	1	9	8	0	8	169 036.7									
31	1	12	1	12	11	0	11	215 278.6	67	1.67×10^{-4}	10.2	0.27	[0, 8]	297	328	75	yes ⁽ⁿ⁾
32	0	12	1	12	11	0	11	215 278.8									

Notes. Parameters of the mono-deuterated DME observed lines: δV is the spectral resolution, ΔV is the velocity interval on which the intensities have been integrated for each line. It varies with the frequency and is tuned to minimize the contribution of blending lines from other species (see Fig. 6). The columns “ $T_{mb}\Delta V$ ” give the integrated intensities over these ΔV intervals for the observations (obs.), for the model (mod.) and for the 5σ (5σ) detection limit in these intervals ($1\sigma = \text{rms} \times \sqrt{\delta V \times \Delta V}$). Lines for which the integrated intensity is greater than 5σ are considered as detected and are presented in Fig. 6 (the ⁽ⁱ⁾ in the column “detected” refers to Fig. 6 panels). For lines too close in frequency to be separated, the integrated intensities is given for both lines merged. ^(a) Numbering of the transitions; ^(b) symmetry number: 0(A), 1(E).

The lines listed in Table 4 are detected with an S/N higher than 5 (see Fig. 6). Other rotational transitions from both forms of mono-deuterated DME lie in the observed frequency range. According to the predictions of the LTE (local thermodynamic equilibrium) model based on the detected lines (see below), the intensities of these transitions are weak, and their non-detection is coherent with the noise of our observations.

In the same frequency range, several transitions of the main DME isotopomer are present as well (see Fig. 6). To derive the DME main and deuterated isotopomers column densities, we have assumed that emission from all three species were in LTE.

As mentioned above, both source A and source B contribute to the observed emission. The ALMA interferometric

observations obtained during the Science Verification program, allow the central velocity V_{lsr} and the linewidth FWHM of each contribution to be estimated precisely (Pineda et al. 2012), and we used these values as fixed parameters in our LTE modeling of the DME lines.

In contrast, the source sizes, as determined by the interferometric observations, cannot directly be used to model single-dish observations because a fraction of the extended emission collected in the single-dish spectra is partly lost in the interferometric observations. We therefore adjusted the size of the two components in the LTE modeling, and we estimate that the uncertainties on the sizes of the two components adjusted in the LTE modeling are ~50% so that it introduces an uncertainty

Table 5. Physical parameters of the DME species adopted and derived from the LTE modeling.

Core	V_{lsr} (km s $^{-1}$)	$FWHM$ (km s $^{-1}$)	Size (")	T_{rot} (K)	N^a (10 15 cm $^{-2}$)	N_a^b (10 14 cm $^{-2}$)	N_s^c (10 14 cm $^{-2}$)	D/H (%)
A	3.8	3.0	1.2	30(±10)	5.0(±2)	2.5	5.0	~15
B	2.6	1.2	2.0	30(±10)	20.0(±5)	10.0	20.0	~15

Notes. This model is displayed in Fig. 6. The values in parenthesis are 1σ uncertainties. ^(a) Column density of DME. ^(b) Column density of symmetric conformation of mono-deuterated DME. ^(c) Column density of asymmetric conformation of mono-deuterated DME.

of about a factor 2 on the derived column densities. In the following, we used the CASSIS software¹ and computed synthetic spectra over a large grid of column densities and rotation temperatures [N, T_{rot}] for each of the two cores assuming LTE². We then performed a χ^2 minimization of the model line profiles using the corresponding [N, T_{rot}] values, compared to the observed lines, as

$$\chi^2 = \sum_{i=1}^{n_{\text{lin}}} \sum_{j=1}^{n_{\text{chan}}} \frac{(I_{\text{obs},ij} - I_{\text{mod},ij})^2}{(\text{rms}_i)^2}, \quad (1)$$

where n_{lin} is the number of lines i , n_{chan} the number of channels j for each line, $I_{\text{obs},ij}$ and $I_{\text{mod},ij}$ the intensities observed and predicted by the model respectively in the channel j of the line i , and rms _{i} the rms of the line i (Coutens 2012). This minimization therefore gives the best-fit column densities and rotational temperature, as well as their corresponding uncertainties, which best reproduce our observations of DME. These values are listed in Table 5.

For the mono-deuterated DME species, we assumed, for each core, the same linewidth, central velocity, source size, and rotation temperature as for the main DME species and we have only adjusted the column densities to obtain the best fit to the observed lines. The resulting column densities are listed in Table 5.

The asymmetric conformation of mono-deuterated DME appears to be two times more abundant than the symmetric conformation of mono-deuterated DME on both sources. This result is simply the consequence of the statistical redistribution of D atoms due to a substitution of an H atom by a D atom in the main DME isotopomer. The total DME deuteration ratio is given by the fraction $[N_a + N_s]/N$. It is ~15% for both A and B components, so much higher than the cosmic D/H value of 1.5×10^{-5} (Linsky 2003) and comparable to “super-deuteration” ratios measured in IRAS 16293 for H₂CO and CH₃OH (Loinard et al. 2000; Parise et al. 2002). This result represents a strong constraint for the chemical modeling of the DME formation and deuteration processes.

8. Conclusion

The torsion-rotational spectrum of mono-deuterated dimethyl ether (CH₃OCH₂D) was observed in the laboratory up to 1 THz. More than 2500 distinct lines were assigned to the symmetric and asymmetric conformers. The spectroscopic parameters given in Table 1 were determined for both species, and it allowed us to reproduce measurements with a standard deviation better

than 105 kHz. They also have permitted transitions to be predicted up to 1.2 THz. Thanks to these frequency predictions, the symmetric and the asymmetric conformers of mono-deuterated dimethyl ether have been detected in the solar-type binary protostar IRAS 16293-2422. From an LTE modeling of these lines, together with lines from the main isotopomer, we concluded that dimethyl ether is highly deuterated in this source, with a D/H abundance ratio ~15%, as high as observed for methanol and formaldehyde, two species known to play important roles in the COMs formation history. Comparison of these species deuteration in hot cores might also contribute to a better understanding of the cold grain surface and warm gas-phase processes in the DME chemistry. A detailed and comparative study of the DME deuteration ratio in the two hot corinos of IRAS 16293, which are likely to present somewhat different evolutions due to their different masses, would provide crucial information on the chemical and physical history of the sources. With the high spatial resolution and sensitivity provided by the ALMA interferometer, such ambitious goals can be reached and will represent an important step towards understanding the history of solar-type systems like our own.

Acknowledgements. This work was supported by the CNES and the Action sur Projets de l'INSU, “Physique et Chimie du Milieu Interstellaire” and by the ANR-08-BLAN-0225 contracts.

References

- Bacmann, A., Taquet, V., Faure, A., Kahane, C., & Ceccarelli, C. 2012, A&A, 541, L12
- Blukis, U., Kasai, P. H., & Myers, R. J. 1963, J. Chem. Phys., 38, 2753
- Bottinelli, S., Ceccarelli, C., Neri, R., et al. 2004, ApJ, 617, L69
- Brouillet, N., Despois, D., Baudry, A., et al. 2013, A&A, 550, A46
- Caux, E., Kahane, C., Castets, A., et al. 2011, A&A, 532, A23
- Cazaux, S., Tielens, A., Ceccarelli, C., et al. 2003, ApJ, 593, L51
- Ceccarelli, C., Castets, A., Caux, E., et al. 2000, A&A, 355, 1129
- Ceccarelli, C., Caselli, P., Herbst, E., et al. 2007 (Tucson: University of Arizona Press), 951, 47
- Coutens, A. 2012, Water deuteration in star-forming regions: Contribution of Herschel/HIFI spectroscopic data, Ph.D. Thesis, IRAP
- Durig, J. R., Li, Y. S., & Groner, P. 1976, J. Molec. Spectrosc., 62, 159
- Endres, C. P., Drouin, B. J., Pearson, J. C., et al. 2009, A&A, 504, 635
- Endres, C. P., Müller, H. S. P., Lewen, F., et al. 2010, 65th OSU International Symposium on Molecular Spectroscopy
- Gordy, W., & Cook, R. L. 1984, Microwave Molecular Spectroscopy (New York: Wiley)
- Groner, P. 1997, J. Chem. Phys., 107, 4483
- Groner, P. 2012, J. Mol. Spectrosc., 278, 52
- Groner, P., Albert, S., Herbst, E., & De Lucia, F. C. 1998, ApJ, 500, 1059
- Hartwig, H., & Dreizler, H. 1996, Z. Naturforsch., 51, 923
- Herbst, E., & van Dishoeck, E. F. 2009, ARA&A, 47, 427
- Ikeda, M., Ohishi, M., Nummelin, A., et al. 2001, ApJ, 560, 792
- Jørgensen, J. K., Bourke, T. L., Nguyen Luong, Q., & Takakuwa, S. 2011, A&A, 534, A100
- Linsky, J. L. 2003, Space Sci. Rev., 106, 49
- Loinard, L., Castets, A., Ceccarelli, C., et al. 2000, A&A, 359, 1169
- Loinard, L., Torres, R., Mioduszewski, A., & Rodriguez, L. 2008, Proc. IAU Symp., 218
- Lovas, F. J., Lutz, H., & Dreizler, H. 1979, J. Phys. Chem. Ref. Data, 8, 1051
- Motiyenko, R. A., Margulés, L., Alekseev, E. A., Guillemin, J. C., & Demaison, J. 2010, J. Molec. Spectrosc., 264, 94
- Niide, Y., & Hayashi, M. 2003, J. Mol. Spectrosc., 148, 371
- Parise, B., Ceccarelli, C., Tielens, A., et al. 2002, A&A, 393, L49
- Peeters, Z., Rodgers, S. D., Charnley, S. B., et al. 2006, A&A, 445, 197
- Pickett, H. M. 1991, J. Mol. Spectrosc., 148, 371
- Pineda, J. E., Maury, A. J., Fuller, G. A., et al. 2012, A&A, 544, L7
- Ratajczak, A., Taquet, V., Kahane, C., et al. 2011, A&A, 528, L13
- Shtarev, A. B., Tian, F., Dolbier, W. R., Jr., & Smart, B. E. 1999, J. Am. Chem. Soc., 121, 7335
- Snyder, L. E., Buhl, D., Schwartz, P. R., et al. 1974, ApJ, 191, L79
- Watson, J. K. G. 1977, Vibrational Spectra and Structure (Amsterdam: Elsevier), 6, 1
- Wooten, A. 1989, ApJ, 337, 858

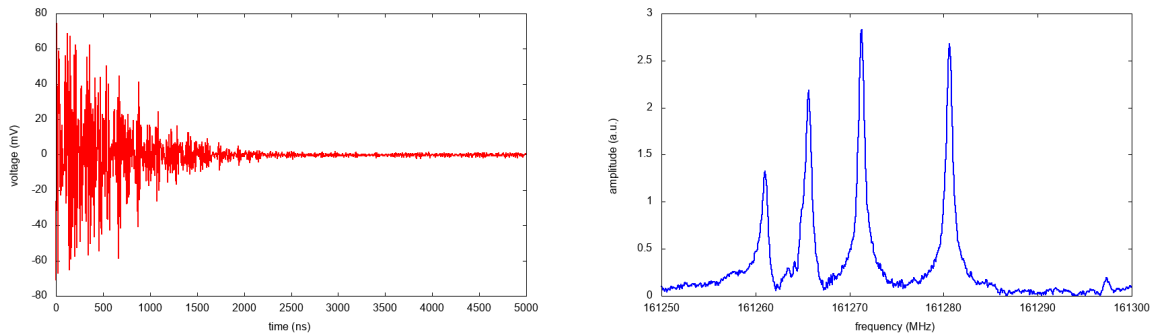
¹ The CASSIS software was developed by IRAS-UPS/CNRS (<http://cassis.irap.omp.eu/>)

² The complete LTE formalism can be found on the CASSIS webpage.

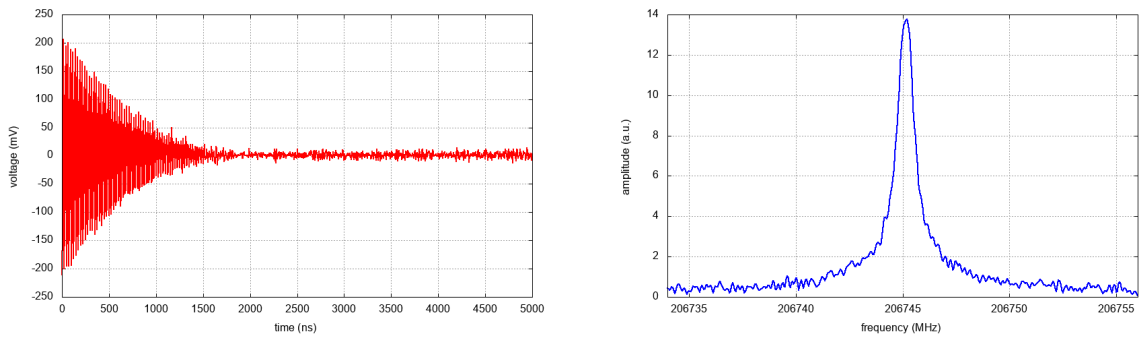
Conclusions et perspectives

En ce qui concerne la partie expérimentale, le résultat principal obtenu est la mise en place d'un spectromètre térahertz à l'état de l'art. Le spectromètre utilise les meilleures sources térahertz en terme de performances en spectroscopie à haute résolution : les chaines de multiplication de fréquence basées sur les diodes Schottky planaires. Le système à balayage rapide en fréquence que j'ai développé permet d'atteindre les limites physiques dans le taux d'enregistrement de spectre d'absorption en utilisant une modulation en fréquence de la source de rayonnement qui garantie une meilleure sensibilité. En même temps la synchronisation entre la commutation du synthétiseur à balayage rapide et la détection assure la précision de la fréquence dans chaque point du spectre et de ce fait ne détériore pas la précision de mesure de fréquence d'une raie par rapport à l'expérience en mode « classique ».

Le système avec un synthétiseur DDS à bord est une bonne analogie aux générateurs de forme d'onde arbitraire. La capacité des cartes de test DDS de générer des pulsations à dérive de fréquence pour une application dans la spectroscopie microonde a été démontré récemment [Finneran *et al.* 2013]. Par conséquent, le système à balayage rapide en fréquence ouvre la voie à la spectroscopie d'émission par transformé de Fourier dans le domaine térahertz. En ce moment je suis en train de tester le spectromètre par transformée de Fourier dans la gamme 150 – 220 GHz développé à la base du spectromètre dont le schéma est présenté sur la Fig. 5. Par rapport au schéma, seule la partie de détection a été modifiée tout en gardant la source de rayonnement térahertz. La particularité du nouveau spectromètre est que pour polariser les molécules et détecter le signal moléculaire on utilise une seule source grâce à la capacité de DDS de commuter la fréquence de façon extrêmement rapide. Ainsi, on peut générer des pulsations à fréquence unique f_u dont la bande Δ_f dépend essentiellement de la durée T_p de la pulsation : $\Delta_f = \frac{1}{T_p}$ ou la pulsation par dérive de fréquence dont la bande dépend des fréquences minimale f_{min} et maximales f_{max} de balayage et ne dépend pas de la durée de la pulsation. Par la suite, pour détecter le signal moléculaire, il suffit de commuter la fréquence de DDS à une valeur f_d différente de f_u ou en dehors de $f_{max} - f_{min}$ pour pouvoir détecter le battement entre la décroissance de la polarisation moléculaire et f_d .



(a) Le signal dans le domaine temporel (à gauche) et le spectre (à droite) de la transition $J = 17 \leftarrow 16$ de OCS. Les signaux ont été obtenus en une seule acquisition ($5 \mu\text{s}$).



(b) Le signal dans le domaine temporel (à gauche) et le spectre (à droite) de $\text{CH}_3\text{CH}_2\text{CN}$ dans la gamme $161.25 - 161.30 \text{ GHz}$ obtenus par excitation d'une impulsion par dérive de fréquence. Les raies correspondent aux transitions de la bande ${}^aR_{0,1}$, $J = 18 \leftarrow 17$ et $K_a = 7 \dots 10$. Les signaux ont été obtenus en accumulant 1024 acquisitions.

FIGURE 23: Exemples des spectres moléculaires enregistrés durant les test du nouveau spectromètre à impulsions térahertz.

Les Fig. 23a et 23b démontrent les résultats de premiers tests effectués. La Fig. 23a représente le signal de battement suite à l'excitation par une impulsion à la fréquence unique et la transformé de Fourier du signal avec une raie de la transition $J = 17 \leftarrow 16$ de OCS. Sur la Fig. 23b on présente le signal de battement et le spectre de $\text{CH}_3\text{CH}_2\text{CN}$ dans la gamme $161.25-161.30 \text{ GHz}$ obtenu via excitation par impulsion par dérive de fréquence et avec une accumulation de 1024 réalisations. Il faut noter que le temps d'enregistrement de chaque réalisation est seulement $5 \mu\text{s}$, et il pourrait être encore réduit. Par conséquent, l'avantage de cette technique par rapport à la spectroscopie d'absorption est la possibilité de détecter les phénomènes ultra-rapides à l'échelle de microseconde et de suivre, par exemple, la cinétique de réactions chimiques. Un autre avantage est la possibilité de coupler la pulsation avec un jet supersonique et d'étudier des complexes moléculaires formé dans le jet.

Dans ce mémoire j'évoque l'application de la spectroscopie térahertz aux molécules

d'intérêt astrophysique ou atmosphériques. A plus long terme il serait intéressant de poursuivre des développements instrumentaux pour des analyses chimiques générales. En effet, durant 60 dernières années on a accumulé une importante quantité des données sur pléthore de molécules différentes. Ces données sont disponibles dans les bases telles que JPL, CDMS ou HITRAN. Les avancées techniques de la dernière décennie permettent de construire les instruments spectroscopiques dans le domaine térahertz très performants en terme de sensibilité, rapidité, taille, consommation etc. Dans ce domaine, l'entreprise américaine BrightSpec créée par les spectroscopistes de l'Université de Virginie propose déjà des solutions dans l'analyse de traces de gaz ou des impuretés volatiles de substances chimiques.

En ce qui concerne les études des spectres des molécules manifestant des MVGA, dans la grande majorité des cas on a pu reproduire les données spectrales avec des modèles théoriques à la précision expérimentale au moins pour l'état fondamental de vibration. Ceci est devenu possible grâce au développement et l'application des modèles les plus performants.

La méthode la plus efficace pour traiter la rotation interne d'une ou deux toupies de symétrie C_{3v} est la MAR. Celle-ci peut être appliquée pour tous les types de problèmes indépendamment des valeurs des paramètres de couplage torsion-rotation ρ et F ainsi que de la hauteur la barrière V_3 . L'un des meilleurs codes pour analyser la rotation interne est RAM36, car il n'a pas des limitations pratiques dans le choix de termes de l'hamiltonien. Cependant, le code est limité aux molécules de symétrie C_s . Il serait très utile dans le futur de développer une version de RAM36 applicable aux molécules de symétrie minimale C_1 . Les études spectroscopiques des molécules dans le cadre de travaux présentés ici démontrent les limites de la MAR lorsque il existe une interaction entre les états excités de la torsion et d'un autre MVGA. En ce moment, Vadym Ilyushin travaille sur un modèle de la MAR incluant les termes Coriolis [Ilyushin *et al.* 2017] et permettant de résoudre le problèmes d'interactions des états excités. Les résultats que l'on a obtenu dans l'étude de la méthacroléine pourrait être un point de référence pour le modèle.

Pour les molécules manifestant la vibration de type inversion, ainsi que pour les molécules qui sont caractérisées par deux MVGA de natures différentes, à ce jour il n'existe pas de modèles aussi efficaces que la méthode « globale » MAR pour les molécules avec un rotateur interne C_{3v} . Néanmoins, les méthodes « locales », telles que le formalisme de l'effet tunnel à haute barrière et la méthode de SAR m'ont permis de traiter la grande majorité de problèmes liés à l'inversion et à la combinaison de torsion et d'inversion. La seule vraie limitation, que j'ai rencontré, était la hauteur de la barrière. Il serait cependant intéressant d'étudier la question d'une méthode « globale » pour le

mouvement d'inversion. Dans ce cas, le problème principale serait la paramétrisation de l'énergie potentielle. Pour les molécules avec une toupie de symétrie C_{3v} , grâce à la périodicité, la fonction du potentiel est présentée par un développement en série qui converge assez rapidement. L'absence de périodicité pour l'inversion complique significativement la définition de l'énergie potentielle. Ici comme exemple, on peut citer les travaux [Kreglewski 1978 ; Kreglewski *et al.* 1992 ; Kreglewski and Włodarczak 1992] sur la méthylamine, dans lesquels une méthode « globale » a été développée. Cependant, les résultats obtenus dans ces travaux n'ont pas atteint la précision expérimentale. Il faut noter que les auteurs de modèle « globale » de la méthylamine avaient également des restrictions au niveau des capacités des calculs des ordinateurs de l'époque. A l'aide de capacités informatiques actuelles il serait intéressant de revenir à ce type de modèles en introduisant des bases plus larges des fonctions d'onde de vibration. Il faut également noter qu'une approche hybride est en cours de développement en ce moment [Kleiner and Hougen 2017]. Dans cette approche la torsion est traitée à l'aide de termes de la méthode « globale » et l'inversion à l'aide de termes à l'effet tunnel.

Comme perspective à moyen terme, je voudrais évoquer un projet intégrant des développements à la fois théoriques et expérimentaux. Le projet consiste à étudier des espèces radicalaires et des molécules à couches ouvertes manifestants des MVGA. D'une part, l'obtention des telles espèces en quantité suffisante pour la spectroscopie à haute résolution est presque toujours un défi. D'autre part, l'influence de la structure électronique à couche ouverte sur MVGA reste peu étudiée. En plus, ce type de molécules présente un grand intérêt pour les études des processus chimiques dans le MIS, ainsi que dans l'atmosphère terrestre.

Bibliographie

- [Alekseev 2011] E. A. Alekseev. *Direct Digital Frequency Synthesizers : Potentialities and Limitations for Microwave Spectroscopy Applications*. Radio Phys. Radio Astron. **2**, 369–378, 2011 (cité sur la page 12).
- [Alekseev et al. 2012] E. A. Alekseev, R. A. Motiyenko et L. Margules. *Millimeter- and Submillimeter-Wave Spectrometers on the Basis of Direct Digital Frequency Synthesizers*. Radio Phys. Radio Astron. **3**, 75–88, 2012 (cité sur les pages 10, 18).
- [Belloche et al. 2017] A. Belloche, A. Meshcheryakov, R. Garrod, V. Ilyushin, E. Alekseev, R. Motiyenko, L. Margulès, H. Müller et K. Menten. *Rotational spectroscopy, tentative interstellar detection, and chemical modeling of N-methylformamide*. A&A **601**, A49, 2017 (cité sur la page 64).
- [Bottinelli et al. 2004] S. Bottinelli, C. Ceccarelli, R. Neri, J. P. Williams, E. Caux, S. Cazaux, B. Lefloch, S. Maret et A. G. Tielens. *Near-Arcsecond Resolution Observations of the Hot Corino of the Solar-Type Protostar IRAS 16293–2422*. ApJL **617**, L69, 2004 (cité sur la page 201).
- [Brown et al. 1975] R. Brown, J. Crofts, P. Godfrey, F. Gardner, B. Robinson et J. Whiteoak. *Discovery of interstellar methyl formate*. ApJ **197**, L29–L31, 1975 (cité sur la page 59).
- [Brown et al. 2008] G. G. Brown, B. C. Dian, K. O. Douglass, S. M. Geyer, S. T. Shipman et B. H. Pate. *A broadband Fourier transform microwave spectrometer based on chirped pulse excitation*. Rev. Sci. Instrum. **79**, 053103, 2008 (cité sur la page 6).
- [Bunker and Jensen 2006] P. R. Bunker et P. Jensen. *Molecular symmetry and spectroscopy*. NRC Research Press, 2006 (cité sur les pages 51, 192).
- [Caminati et al. 1995] W. Caminati, S. Melandri et P. G. Favero. *Free-Jet Absorption Microwave Spectrum of 1, 3-Propanediol*. J. Mol. Spectrosc. **171**, 394–401, 1995 (cité sur la page 156).
- [Carvajal et al. 2007] M. Carvajal, F. Willaert, J. Demaison et I. Kleiner. *Reinvestigation of the ground and first torsional state of methylformate*. J. Mol. Spectrosc. **246**, 158–166, 2007 (cité sur la page 61).
- [Carvajal et al. 2009] M. Carvajal, L. Margulès, B. Tercero, K. Demyk, I. Kleiner, J. Guillemin, V. Lattanzi, A. Walters, J. Demaison, G. Wlodarczak et al. *Rotational spectrum of $^{13}C_2$ -methyl formate ($HCOO^{13}CH_3$) and detection of the two ^{13}C -methyl formate in Orion*. A&A **500**, 1109–1118, 2009 (cité sur la page 60).
- [Cazaux et al. 2003] S. Cazaux, A. Tielens, C. Ceccarelli, A. Castets, V. Wakelam, E. Caux, B. Parise et D. Teyssier. *The Hot Core around the Low-Mass Protostar IRAS 16293–2422 : Scoundrels Rule !* ApJL **593**, L51, 2003 (cité sur la page 201).
- [Christen and Müller 2003] D. Christen et H. S. Müller. *The millimeter wave spectrum of aGg' ethylene glycol : The quest for higher precision*. Phys. Chem. Chem. Phys. **5**, 3600–3605, 2003 (cité sur les pages 152, 153).

- [Christen *et al.* 1995] D. Christen, L. Coudert, R. D. Suenram et F. J. Lovas. *The Rotational/Concerted Torsional Spectrum of the g'Ga Conformer of Ethylene Glycol*. *J. Mol. Spectrosc.* **172**, 57–77, 1995 (cité sur la page 152).
- [Christen *et al.* 2002] D. Christen, H. S. Müller et L. Coudert. *The g'Ga conformer of ethylene glycol : A test case for tunneling-rotation approaches developed for non-rigid molecules*. 57th International Symposium on Molecular Spectroscopy, Ohio State University, TB03, 2002 (cité sur la page 148).
- [Churchwell and Winnewisser 1975] E. Churchwell et G. Winnewisser. *Observations of methyl formate in the galactic center*. *A&A* **45**, 229–231, 1975 (cité sur la page 59).
- [Comito *et al.* 2005] C. Comito, P. Schilke, T. Phillips, D. Lis, F. Motte et D. Mehringer. *A molecular line survey of Orion KL in the 350 micron band*. *ApJS* **156**, 127, 2005 (cité sur la page 59).
- [Coudert and Hougen 1988] L. Coudert et J. Hougen. *Tunneling splittings in the water dimer : Further development of the theory*. *J. Mol. Spectrosc.* **130**, 86–119, 1988 (cité sur les pages 148, 150).
- [Coudert *et al.* 2012] L. Coudert, L. Margulès, T. Huet, R. Motiyenko, H. Møllendal et J.-C. Guillemin. *The submillimeter-wave spectrum of the doubly deuterated species of methyl formate HCOOCD₂H*. *A&A* **543**, A46, 2012 (cité sur la page 150).
- [Coudert *et al.* 2013] L. Coudert, B. Drouin, B. Tercero, J. Cernicharo, J.-C. Guillemin, R. A. Motiyenko et L. Margulès. *The First Astrophysical Detection, Terahertz Spectrum, and Database for the Monodeuterated Species of Methyl Formate HCOOCH₂D*. *ApJ* **779**, 119, 2013 (cité sur les pages 150, 151).
- [Curl Jr 1959] R. Curl Jr. *Microwave spectrum, barrier to internal rotation, and structure of methyl formate*. *J. Chem. Phys.* **30**, 1529–1536, 1959 (cité sur la page 60).
- [Danger *et al.* 2012] G. Danger, F. Duvernay, P. Theulé, F. Borget et T. Chiavassa. *Hydroxyacetonitrile (HOCH₂CN) Formation in astrophysical conditions. Competition with the aminomethanol, a glycine precursor*. *ApJ* **756**, 11, 2012 (cité sur la page 153).
- [Danger *et al.* 2013] G. Danger, F. Duvernay, P. Theulé, F. Borget, J.-C. Guillemin et T. Chiavassa. *Hydroxyacetonitrile (HOCH₂CN) as a precursor for formylcyanide (CHOCN), ketenimine (CH₂CNH), and cyanogen (NCCN) in astrophysical conditions*. *A&A* **549**, A93, 2013 (cité sur la page 153).
- [Danger *et al.* 2014] G. Danger, A. Rimola, N. A. Mrad, F. Duvernay, G. Roussin, P. Theule et T. Chiavassa. *Formation of hydroxyacetonitrile (HOCH₂CN) and polyoxymethylene (POM)-derivatives in comets from formaldehyde (CH₂O) and hydrogen cyanide (HCN) activated by water*. *Phys. Chem. Chem. Phys.* **16**, 3360–3370, 2014 (cité sur la page 153).
- [Demaison *et al.* 2010] J. Demaison, L. Margulès, I. Kleiner et A. Császár. *Equilibrium structure in the presence of internal rotation : A case study of cis-methyl formate*. *J. Mol. Spectrosc.* **259**, 70–79, 2010 (cité sur la page 57).
- [Drouin *et al.* 2005] B. J. Drouin, F. W. Maiwald et J. C. Pearson. *Application of cascaded frequency multiplication to molecular spectroscopy*. *Rev. Sci. Instrum.* **76**, 093113, 2005 (cité sur la page 13).
- [Dryagin 1970] Y. A. Dryagin. *A method of measuring frequency by a high-quality Fabry-Perot resonator*. *Izv. Vyss. Uchebn. Zaved. Radiofiz.* **13**, 141–145, 1970 (cité sur la page 10).

- [Fantoni and Caminati 1996] A. Fantoni et W. Caminati. *Rotational spectrum and ab initio calculations of N-methylformamide*. J. Cjem. Soc., Faraday Trans. **92**, 343–346, 1996 (cité sur la page 63).
- [Fantoni *et al.* 2002] A. C. Fantoni, W. Caminati, H. Hartwig et W. Stahl. *The very low methyl group V 3 barrier of cisN-methylformamide : A-E doubling from the free jet rotational spectrum*. J. Mol. Struct. **612**, 305–307, 2002 (cité sur la page 63).
- [Finneran *et al.* 2013] I. A. Finneran, D. B. Holland, P. B. Carroll et G. A. Blake. *Development of a Reduced-Cost Chirped Pulse Microwave Spectrometer*. In : *68th International Symposium on Molecular Spectroscopy, WH16*. 2013 (cité sur la page 237).
- [Gerecht *et al.* 2011] E. Gerecht, K. O. Douglass et D. F. Plusquellec. *Chirped-pulse terahertz spectroscopy for broadband trace gas sensing*. Opt. Express **19**, 8973–8984, 2011 (cité sur la page 6).
- [Gordy and Cook 1984] W. Gordy et R. L. Cook. *Microwave molecular spectra*. Wiley, 1984 (cité sur la page 197).
- [Goubet *et al.* 2012] M. Goubet, R. A. Motiyenko, L. Margulès et J.-C. Guillemin. *Synthesis, High-Resolution Millimeter-Wave Spectroscopy, and Ab Initio Calculations of Ethylmercury Hydride*. The Journal of Physical Chemistry A **116**, 5405–5409, 2012 (cité sur la page 12).
- [Groner 1992] P. Groner. *Large-amplitude motion tunneling parameters in effective rotational Hamiltonians from rotation-internal rotation theory*. J. Mol. Spectrosc. **156**, 164–189, 1992 (cité sur la page 148).
- [Groner 1997] P. Groner. *Effective rotational Hamiltonian for molecules with two periodic large-amplitude motions*. J. Chem. Phys. **107**, 4483–4498, 1997 (cité sur la page 148).
- [Hanel *et al.* 1981] R. Hanel, B. Conrath, F. Flasar, V. Kunde, W. Maguire, J. Pearl, J. Pirraglia, R. Samuelson, L. Herath, M. Allison et al. *Infrared observations of the Saturnian system from Voyager 1*. Science **212**, 192–200, 1981 (cité sur la page 198).
- [Hartwig and Dreizler 1996] H. Hartwig et H. Dreizler. *The microwave spectrum of trans-2, 3-dimethyloxirane in torsional excited states*. Ze. Naturforsch. A **51**, 923–932, 1996 (cité sur la page 57).
- [Haykal *et al.* 2014] I. Haykal, M. Carvajal, B. Tercero, I. Kleiner, A. López, J. Cernicharo, R. Motiyenko, T. R. Huet, J. Guillemin et L. Margulès. *THz spectroscopy and first ISM detection of excited torsional states of ¹³C-methyl formate*. A&A **568**, A58, 2014 (cité sur la page 61).
- [Herbst *et al.* 1984] E. Herbst, J. Messer, F. C. De Lucia et P. Helminger. *A new analysis and additional measurements of the millimeter and submillimeter spectrum of methanol*. J. Mol. Spectrosc. **108**, 42–57, 1984 (cité sur la page 54).
- [Herschbach 1959] D. R. Herschbach. *Calculation of Energy Levels for Internal Torsion and Over-All Rotation. III*. J. Chem. Phys. **31**, 91–108, 1959 (cité sur la page 54).
- [Hollis *et al.* 2002] J. M. Hollis, F. J. Lovas, P. R. Jewell et L. Coudert. *Interstellar antifreeze : ethylene glycol*. ApJL **571**, L59, 2002 (cité sur la page 155).
- [Hougen 1985] J. T. Hougen. *A generalized internal axis method for high barrier tunneling problems, as applied to the water dimer*. J. Mol. Spectrosc. **114**, 395–426, 1985 (cité sur la page 147).
- [Hougen and DeKoven 1983] J. T. Hougen et B. M. DeKoven. *The application of extended permutation-inversion groups to internal rotation of a symmetric rotor top in a symmetric or asymmetric rotor molecule*. J. Mol. Spectrosc. **98**, 375–391, 1983 (cité sur la page 147).

- [Hougen *et al.* 1994] J. T. Hougen, I. Kleiner et M. Godefroid. *Selection rules and intensity calculations for a Cs asymmetric top molecule containing a methyl group internal rotor*. *J. Mol. Spectrosc.* **163**, 559–586, 1994 (cité sur les pages 54, 56).
- [Ikeda *et al.* 2001] M. Ikeda, M. Ohishi, A. Nummelin, J. Dickens, P. Bergman, Å. Hjalmarson et W. M. Irvine. *Survey observations of c-C₂H₄O and CH₃CHO toward massive star-forming regions*. *ApJ* **560**, 792, 2001 (cité sur la page 201).
- [Ilyushin 2012] V. Ilyushin. *Microwave Spectroscopy of Torsion Vibrations in Molecules : Approximation of Rigid Constraint on Structural Torsional Parameters ρ and F in Rho Axis Method*. *Radio Phys. Radio Astron.* **16**, 414, 2012 (cité sur la page 61).
- [Ilyushin and Lovas 2007] V. Ilyushin et F. J. Lovas. *Microwave spectra of molecules of astrophysical interest. XXV. Methylamine*. *J. Phys. Chem. Ref. Data* **36**, 1141–1276, 2007 (cité sur la page 196).
- [Ilyushin *et al.* 2009] V. Ilyushin, A. Kryvda et E. Alekseev. *A new joint analysis of the ground and first excited torsional states of methylformate*. *J. Mol. Spectrosc.* **255**, 32–38, 2009 (cité sur la page 146).
- [Ilyushin *et al.* 2010] V. V. Ilyushin, Z. Kisiel, L. Pszczółkowski, H. Mäder et J. T. Hougen. *A new torsion–rotation fitting program for molecules with a sixfold barrier : Application to the microwave spectrum of toluene*. *J. Mol. Spectrosc.* **259**, 26–38, 2010 (cité sur les pages 57, 58).
- [Ilyushin *et al.* 2017] V. V. Ilyushin, I. Kleiner et H. J. T. *A new multi-state vibration-torsion-rotation fitting program for molecules with a C_{3v} top and C_s frame*. In : *The 25th Colloquium on High-Resolution Molecular Spectroscopy, P5.1*. 2017 (cité sur la page 239).
- [Kawashima *et al.* 2010] Y. Kawashima, T. Usami, R. D. Suenram, G. Y. Golubiatnikov et E. Hirota. *Dynamical structure of peptide molecules : Fourier transform microwave spectroscopy and ab initio calculations of N-methylformamide*. *J. Mol. Spectrosc.* **263**, 11–20, 2010 (cité sur les pages 63, 64).
- [Kirtman 1962] B. Kirtman. *Interactions between ordinary vibrations and hindered internal rotation. I. Rotational energies*. *J. Chem. Phys.* **37**, 2516–2539, 1962 (cité sur la page 57).
- [Kleiner 2010] I. Kleiner. *Asymmetric-top molecules containing one methyl-like internal rotor : Methods and codes for fitting and predicting spectra*. *J. Mol. Spectrosc.* **260**, 1–18, 2010 (cité sur les pages 52, 53, 54, 56).
- [Kleiner and Hougen 2017] I. Kleiner et J. T. Hougen. *Competition between two large amplitude motion models : new hybrid Hamiltonian versus old pure tunneling Hamiltonian*. In : *72nd International Symposium on Molecular Spectroscopy, TI08*. 2017 (cité sur la page 240).
- [Kleiner *et al.* 1996] I. Kleiner, F. J. Lovas et M. Godefroid. *Microwave spectra of molecules of astrophysical interest. XXIII. Acetaldehyde*. *J. Chem. Phys. Ref. Data* **25**, 1113–1210, 1996 (cité sur la page 62).
- [Kobayashi *et al.* 2007] K. Kobayashi, K. Ogata, S. Tsunekawa et S. Takano. *Torsionally excited methyl formate in orion KL*. *ApJL* **657**, L17, 2007 (cité sur la page 59).
- [Kreglewski 1978] M. Kreglewski. *Vibration-inversion-internal rotation-rotation Hamiltonian for methylamine*. *J. Mol. Spectrosc.* **72**, 1–19, 1978 (cité sur la page 240).
- [Kreglewski and Włodarczak 1992] M. Kreglewski et G. Włodarczak. *The rotational spectrum of methylamine in a submillimeter-wave range*. *J. Mol. Spectrosc.* **156**, 383–389, 1992 (cité sur la page 240).

- [Kreglewski *et al.* 1992] M. Kreglewski, W. Stahl, J.-U. Grabow et G. Włodarczak. *The quadrupole coupling tensor of methyl amine*. Chem. Phys. Lett. **196**, 155–158, 1992 (cité sur les pages 197, 240).
- [Kroto 1992] H. W. Kroto. *Molecular rotation spectra*. Dover, 1992 (cité sur la page 51).
- [Lewen *et al.* 1998] F. Lewen, R. Gendriesch, I. Pak, D. G. Paveliev, M. Hepp, R. Schieder et G. Winnewisser. *Phase locked backward wave oscillator pulsed beam spectrometer in the submillimeter wave range*. Rev. Sci. Instrum. **69**, 32–9, 1998 (cité sur la page 10).
- [Lin and Swalen 1959] C. C. Lin et J. D. Swalen. *Internal rotation and microwave spectroscopy*. Reviews of Modern Physics **31**, 841, 1959 (cité sur la page 53).
- [Maestrini *et al.* 2010] A. Maestrini, B. Thomas, H. Wang, C. Jung, J. Treuttel, Y. Jin, G. Chatto-padhyay, I. Mehdi et G. Beaudin. *Multiplicateurs de fréquences et mélangeurs THz utilisant des diodes Schottky*. Comptes Rendus Phys. **11**, 480–495, 2010 (cité sur la page 13).
- [Margulès *et al.* 2009] L. Margulès, L. Coudert, H. Møllendal, J.-C. Guillemin, T. Huet et R. Janečková. *The microwave spectrum of the mono deuterated species of methyl formate HCOOCH₂D*. J. Mol. Spectrosc. **254**, 55–68, 2009 (cité sur la page 146).
- [Margulès *et al.* 2015] L. Margulès, R. Motiyenko, V. Ilyushin et J. Guillemin. *Millimeter and submillimeter wave spectra of mono-¹³C-acetaldehydes*. A&A **579**, A46, 2015 (cité sur la page 63).
- [Margulès *et al.* 2017] L. Margulès, B. McGuire, M. Senent, R. Motiyenko, A. Remijan et J. Guillemin. *Submillimeter spectra of 2-hydroxyacetonitrile (glycolonitrile; HOCH₂CN) and its searches in GBT PRIMOS observations of Sgr B2 (N)*. A&A **601**, A50, 2017 (cité sur la page 155).
- [McElmurry *et al.* 2003] B. A. McElmurry, R. R. Lucchese, J. W. Bevan, I. I. Leonov, S. P. Belov et A. C. Legon. *Studies of Ar :HBr using fast scan submillimeter-wave and microwave coaxial pulsed jet spectrometers with sub-kHz precision*. J. Chem. Phys. **119**, 10687–10695, 2003 (cité sur la page 10).
- [Medvedev *et al.* 2004] I. Medvedev, M. Winnewisser, F. C. De Lucia, E. Herbst, E. Białykowska-Jaworska, L. Pszczołkowski et Z. Kisiel. *The millimeter- and submillimeter-wave spectrum of the trans-gauche conformer of diethyl ether*. J. Mol. Spectrosc. **228**, 314–328, 2004 (cité sur la page 6).
- [Meyer 1979] R. Meyer. *Flexible models for intramolecular motion, a versatile treatment and its application to glyoxal*. J. Mol. Spectrosc. **76**, 266–300, 1979 (cité sur la page 66).
- [Meyer and Bauder 1982] R. Meyer et A. Bauder. *Torsional coupling in pyruvic acid*. J. Mol. Spectrosc. **94**, 136–149, 1982 (cité sur la page 66).
- [Meyer *et al.* 1989] R. Meyer, W. Caminati et H. Hollenstein. *Torsional motions in methyl glycolate*. J. Mol. Spectrosc. **137**, 87–103, 1989 (cité sur la page 66).
- [Motiyenko *et al.* 2010a] R. A. Motiyenko, L. Margulès, M. Goubet, H. Møllendal et J.-C. Guillemin. *High Resolution Millimeter-Wave Spectroscopy of Vinyltellurol*. The Journal of Physical Chemistry A **114**, 12202–12207, 2010 (cité sur la page 12).
- [Motiyenko *et al.* 2010b] R. A. Motiyenko, L. Margulès, M. Goubet, H. Møllendal, A. Konovalov et J.-C. Guillemin. *First High Resolution Spectroscopic Studies and Ab Initio Calculations of Ethanetellurol*. The Journal of Physical Chemistry A **114**, 2794–2798, 2010 (cité sur la page 12).
- [Motiyenko *et al.* 2012a] R. A. Motiyenko, L. Margulès et J.-C. Guillemin. *The submillimeter-wave spectrum of diisocyanomethane*. Astronomy & Astrophysics **544**, A82, 2012 (cité sur la page 12).

- [Motiyenko *et al.* 2012b] R. A. Motiyenko, L. Margulès et J.-C. Guillemin. *High Resolution Millimeter-Wave Spectroscopy of Cyclopropylphosphine–Borane*. The Journal of Physical Chemistry A **116**, 1565–1570, 2012 (cité sur la page 12).
- [Motiyenko *et al.* 2014] R. Motiyenko, V. Ilyushin, B. Drouin, S. Yu et L. Margulès. *Rotational spectroscopy of methylamine up to 2.6 THz*. A&A **563**, A137, 2014 (cité sur la page 196).
- [Motiyenko *et al.* 2015] R. A. Motiyenko, L. Margulès, E. A. Alekseev et J.-C. Guillemin. *High-Resolution Millimeter Wave Spectroscopy and Ab Initio Calculations of Aminomalononitrile*. J. Phys. Chem A **119**, 1048–1054, 2015 (cité sur la page 201).
- [Motiyenko *et al.* 2016] R. Motiyenko, L. Margulès, V. Ilyushin, I. Smirnov, E. Alekseev, D. Halfen et L. M. Ziurys. *Millimeter and submillimeter wave spectra of ^{13}C methylamine*. A&A **587**, A152, 2016 (cité sur la page 196).
- [Neill *et al.* 2013] J. L. Neill, B. J. Harris, A. L. Steber, K. O. Douglass, D. F. Plusquellic et B. H. Pate. *Segmented chirped-pulse Fourier transform submillimeter spectroscopy for broadband gas analysis*. Opt. Express **21**, 19743–19749, 2013 (cité sur la page 6).
- [Ohashi and Hougen 1985] N. Ohashi et J. T. Hougen. *The torsional-wagging tunneling problem and the torsional-wagging-rotational problem in hydrazine*. J. Mol. Spectrosc. **112**, 384–400, 1985 (cité sur la page 147).
- [Ohashi and Hougen 1987] N. Ohashi et J. T. Hougen. *The torsional-wagging tunneling problem and the torsional-wagging-rotational problem in methylamine*. J. Mol. Spectrosc. **121**, 474–501, 1987 (cité sur la page 195).
- [Park *et al.* 2011] G. B. Park, A. H. Steeves, K. Kuyanov-Prozument, J. L. Neill et R. W. Field. *Design and evaluation of a pulsed-jet chirped-pulse millimeter-wave spectrometer for the 70–102 GHz region*. J. Chem. Phys. **135**, 024202, 2011 (cité sur la page 6).
- [Pearson *et al.* 2011] J. C. Pearson, B. J. Drouin, A. Maestrini, I. Mehdi, J. Ward, R. H. Lin, S. Yu, J. J. Gill, B. Thomas, C. Lee, G. Chatopadhyay, E. Schlecht, F. W. Maiwald, P. F. Goldsmith et P. Siegel. *Demonstration of a room temperature 2.48–2.75 THz coherent spectroscopy source*. Rev. Sci. Instrum. **82**, 093105, 2011 (cité sur la page 13).
- [Petkie *et al.* 1997] D. T. Petkie, T. M. Goyette, R. P. A. Bettens, S. P. Belov, S. Albert, P. Helmlinger et F. C. De Lucia. *A fast scan submillimeter spectroscopic technique*. Rev. Sci. Instrum. **68**, 1675–1683, 1997 (cité sur les pages 6, 10).
- [Pickett 1972] H. M. Pickett. *Vibration–Rotation Interactions and the Choice of Rotating Axes for Polyatomic Molecules*. J. Chem. Phys. **56**, 1715–1723, 1972 (cité sur les pages 148, 152).
- [Pickett 1991] H. M. Pickett. *The fitting and prediction of vibration-rotation spectra with spin interactions*. J. Mol. Spectrosc. **148**, 371–377, 1991 (cité sur la page 148).
- [Plusquellic *et al.* 2009] D. Plusquellic, F. Lovas, B. H. Pate, J. L. Neill, M. T. Muckle et A. J. Remijan. *Distinguishing tunneling pathways for two chiral conformer pairs of 1, 3-propanediol from the microwave spectrum*. J. Phys. Chem A **113**, 12911–12918, 2009 (cité sur les pages 155, 156).
- [Richard *et al.* 2013] C. Richard, L. Margulès, E. Caux, C. Kahane, C. Ceccarelli, J.-C. Guillemin, R. A. Motiyenko, C. Vastel et P. Groner. *Mono-deuterated dimethyl ether : laboratory spectrum up to 1 THz-Torsion-rotational spectrum within the vibrational ground-state for the symmetric and asymmetric conformers and first detection in IRAS 16293-2422*. A&A **552**, A117, 2013 (cité sur la page 203).

- [Rohart 2017] F. Rohart. *Overcoming the detection bandwidth limit in precision spectroscopy : The analytical apparatus function for a stepped frequency scan.* J. Quant. Spectrosc. Radiat. Transf. **187**, 490–504, 2017 (cité sur la page 21).
- [Rohart et al. 2014] F. Rohart, S. Mejri, P. L. T. Sow, S. K. Tokunaga, C. Chardonnet, B. Darquié, H. Dinesan, E. Fasci, A. Castrillo, L. Gianfrani et C. Daussy. *Absorption-line-shape recovery beyond the detection-bandwidth limit : Application to the precision spectroscopic measurement of the Boltzmann constant.* Phys. Rev. A **90**, 042506, 2014 (cité sur la page 21).
- [Schloerb et al. 1988] F. P. Schloerb, W. M. Kinzel, D. A. Swade et W. M. Irvine. *Observations of HCN in comet P/Halley.* In : *Exploration of Halley's Comet.* Springer, 1988, 475–480 (cité sur la page 198).
- [Smirnov et al. 2013] I. Smirnov, E. Alekseev, V. Piddyachiy, V. Ilyushin et R. Motiyenko. *I, 3-Propanediol millimeter wave spectrum : Conformers I and II.* J. Mol. Spectrosc. **293**, 33–37, 2013 (cité sur la page 156).
- [Smirnov et al. 2014] I. Smirnov, E. Alekseev, V. Ilyushin, L. Margulés, R. Motiyenko et B. Drouin. *Spectroscopy of the ground, first and second excited torsional states of acetaldehyde from 0.05 to 1.6 THz.* J. Mol. Spectrosc. **295**, 44–50, 2014 (cité sur la page 63).
- [Snyder and Buhl 1971] L. E. Snyder et D. Buhl. *Observations of radio emission from interstellar hydrogen cyanide.* ApJ **163**, L47, 1971 (cité sur la page 198).
- [Snyder et al. 1974] L. Snyder, D. Buhl, P. Schwartz, F. Clark, D. Johnson, F. Lovas et P. Giguere. *Radio detection of interstellar dimethyl ether.* ApJ **191**, L79, 1974 (cité sur la page 201).
- [Steber et al. 2012] A. L. Steber, B. J. Harris, J. L. Neill et B. H. Pate. *An arbitrary waveform generator based chirped pulse Fourier transform spectrometer operating from 260 to 295 GHz.* J. Mol. Spectrosc. **280**, 3–10, 2012 (cité sur la page 6).
- [Takano et al. 2012] S. Takano, Y. Sakai, S. Kakimoto, M. Sasaki et K. Kobayashi. *Detection of Methyl Formate in the Second Torsionally Excited State ($vt=2$) in Orion KL.* Pub. Astronom. Soc. Japan **64** 2012 (cité sur la page 59).
- [Tercero et al. 2012] B. Tercero, L. Margulès, M. Carvajal, R. A. Motiyenko, T. Huet, E. Alekseev, I. Kleiner, J.-C. Guillemin, H. Møllendal et J. Cernicharo. *Microwave and submillimeter spectroscopy and first ISM detection of 18O-methyl formate.* A&A **538**, A119, 2012 (cité sur la page 61).
- [Woods 1966] R. C. Woods. *A general program for the calculation of internal rotation splittings in microwave spectroscopy.* J. Mol. Spectrosc. **21**, 4–24, 1966 (cité sur la page 56).
- [Woods 1967] R. Woods. *A general program for the calculation of internal rotation splittings in microwave spectroscopy : Part II. The n-top problem.* J. Mol. Spectrosc. **22**, 49–59, 1967 (cité sur la page 56).
- [Xu et al. 1999] L.-H. Xu, R. M. Lees et J. T. Hougen. *On the physical interpretation of torsion-rotation parameters in methanol and acetaldehyde : Comparison of global fit and ab initio results.* J. Chem. Phys. **110**, 3835–3841, 1999 (cité sur la page 61).
- [Zakharenko et al. 2015] O. Zakharenko, R. A. Motiyenko, L. Margulès et T. R. Huet. *Terahertz spectroscopy of deuterated formaldehyde using a frequency multiplication chain.* J. Mol. Spectrosc. **317**, 41–46, 2015 (cité sur la page 18).
- [Zakharenko et al. 2016] O. Zakharenko, R. Motiyenko, J.-R. Aviles Moreno, A. Jabri, I. Kleiner et T. Huet. *Torsion-rotation-vibration effects in the ground and first excited states of methacrolein, a major atmospheric oxidation product of isoprene.* J. Chem. Phys. **144**, 024303, 2016 (cité sur la page 65).

- [Zaleski *et al.* 2012] D. P. Zaleski, J. L. Neill, M. T. Muckle, N. A. Seifert, P. Brandon Carroll, S. L. Widicus Weaver et B. H. Pate. *A Ka-band chirped-pulse Fourier transform microwave spectrometer*. *J. Mol. Spectrosc.* **280**, 68–76, 2012 (cité sur la page [6](#)).
- [Zaleski *et al.* 2013] D. P. Zaleski, N. A. Seifert, A. L. Steber, M. T. Muckle, R. A. Loomis, J. F. Corby, O. Martinez Jr, K. N. Crabtree, P. R. Jewell, J. M. Hollis et al. *Detection of E-cyanomethanimine toward Sagittarius B2 (N) in the Green Bank Telescope PRIMOS survey*. *ApJL* **765**, L10, 2013 (cité sur la page [199](#)).

Curriculum Vitae

Roman Motiyenko

Né le 8 Février 1982 à Poltava(Ukraine)

Cursus académique et professionnel

2010 à présent : Maitre de conférences, Université Lille 1, UFR de Physique, Laboratoire de Physique des Lasers Atomes et Molécules (PhLAM)

2009 – 2010 : Attaché temporaire d'enseignement et de recherche, Université Lille 1, UFR de Physique

2008 – 2009 : Stage post-doctoral, Université Lille 1, Laboratoire de Physique des Lasers Atomes et Molécules (PhLAM), responsable Pr. L. Margulès

2004 – 2008 : Thèse de Doctorat (candidat ès sciences physico-mathématiques) intitulée "*Les spectres de rotation des molécules de furfurole, glycine et uréthane dans le domaine des microondes*", soutenue à l'Université Nationale de Kharkiv V.N. Karazine le 14 mars 2008 devant le conseil scientifique spécialisé composé de 25 membres (Président du conseil : Pr. V.A. Svitich)

Encadrement

- Co-encadrant de la thèse (50%) de Olena Zakharenko. Le directeur de thèse est Prof. T. Huet. Le titre de travaux est : "*Spectroscopie THz de molécules atmosphériques. Application à l'étude de composés organiques volatils*". La soutenance a eu lieu le 01/03/2016 à l'Université Lille 1.
- Co-encadrant de la thèse (50%) de Anastasia Pienkina. Le directeur de thèse est Prof. L. Margulès (Lille 1). Le titre de travaux est "*Heterodyne receiver for interstellar molecular laboratory spectroscopy*". Thèse débutée le 07/01/2015, soutenance prévue en décembre 2017.
- Responsable de stage Master 2 (100%) de Sabath Bteich, UFR de Physique, Université Lille 1. Intitulé du stage : "*Étude de molécules organiques complexe d'intérêt astrophysique dans le domaine térahertz*". Le rapport de stage soutenu le 16/06/2014 avec mention 'bien'.
- Responsable de stage Master (100%) de Iuliia Armeeva étudiante de l'Université Nationale de Kharkiv, Ukraine dans le cadre de l'appel d'offres Bourses Stage Master lancé par RI et DIRVED de l'Université Lille 1. Intitulé du stage : "*Spectroscopie submillimétrique de nitriles et isonitriles d'intérêt astrophysique*". Le rapport de stage soutenu le 26/06/2013 avec mention 'très bien'.

Activités d'animation et de rayonnement

- Cours "*Microwave spectroscopy : lab and space*" présenté à l'École thématique internationale du CNRS HiResMIR@CAES-Fréjus-2013.

- Co-responsable de l'organisation et administrateur web du prochain colloque du programme national de l'INSU "Physique et chimie du milieu interstellaire" qui aura lieu à Lille en Octobre 2016 (environ 150 participants).

Publications et communications

- 54 publications dans des revues à comité de lecture dont 40 pour la période après la thèse
 - 66 communications orales et par affiche à des congrès français et internationaux pour la période après la thèse
1. Ilyushin, V. V., Alekseev, E. A., Dyubko, S. F., Motiyenko, R. A., Hougen, J. T. "The rotational spectrum of the ground state of methylamine" *J. Mol. Spec.*, 229 (2), pp. 170-187 (2005).
 2. Ilyushin, V. V., Alekseev, E. A., Dyubko, S. F., Motiyenko, R. A., Lovas, F. J. "Millimeter wave spectrum of glycine" *J. Mol. Spec.*, 231 (1), pp. 15-22 (2005).
 3. Baskakov, O. I., Markov, I. A., Alekseev, E. A., Motiyenko, R. A., Lohilahti, J., Horneman, V.-M., Winnewisser, B. P., Medvedev, I. R., De Lucia, F. C. "Simultaneous analysis of rovibrational and rotational data for the 4^1 , 5^1 , 6^1 , 7^2 , 8^1 , $7^{19}1$ and 9^2 states of HCOOH" *J. Mol. Struct.*, 795 (1-3), pp. 54-77 (2006).
 4. Motiyenko, R. A., Alekseev, E. A., Dyubko, S. F., Lovas, F. J. "Microwave spectrum and structure of furfural" *J. Mol. Spec.*, 240 (1), pp. 93-101 (2006).
 5. Baskakov, O. I., Alekseev, E. A., Motiyenko, R. A., Lohilahti, J., Horneman, V.-M., Alanko, S., Winnewisser, B. P., Medvedev, I. R., De Lucia, F. C. "FTIR and millimeter wave investigation of the 7^1 and 9^1 states of formic acid HCOOH and H₁₃COOH" *J. Mol. Spec.*, 240 (2), pp. 188-201 (2006) .
 6. Motiyenko, R. A., Alekseev, E. A., Dyubko, S. F. "Microwave spectroscopy of furfural in vibrationally excited states" *J. Mol. Spec.*, 244 (1), pp. 9-12 (2007).
 7. Motiyenko, R. A., Alekseev, E. A., Kryvda, A. V., Gerasimov, V. G., Dyubko, S. F. "Microwave spectrum of ^{13}C methyl iodide" *J. Mol. Spec.*, 245 (1), pp. 81-83 (2007).
 8. Ilyushin, V. V., Motiyenko, R. A., Lovas, F. J., Plusquellec, D. F. Microwave spectrum of glycerol : Observation of a tunneling chiral isomer *J. Mol. Spec.*, 251 (1-2), pp. 129-137 (2008).
 9. Margulès, L., Motiyenko, R. A., Demyk, K., Tercero, B., Cernicharo, J., Sheng, M., Weidmann, M., Gripp, J., Mäder, H., Dernaison, J. "Rotational spectrum of deuterated and ^{15}N ethyl cyanides : CH₃CHDCN and CH₂DCH₂CN and of CH₃CH₂C 15 N" *Astronomy and Astrophysics*, 493 (2), pp. 565-569 (2009).
 10. Kryvda, A. V., Gerasimov, V. G., Dyubko, S. F., Alekseev, E. A., Motiyenko, R. A. "New measurements of the microwave spectrum of formamide" *J. Mol. Spec.*, 254 (1), pp. 28-32 (2009).
 11. Goubet, M., Motiyenko, R. A., Réal, F., Margulès, L., Huet, T. R., Asselin, P., Soulard, P., Krasnicki, A., Kisiel, Z., Alekseev, E. A. "Influence of the geometry of a hydrogen bond on conformational stability : A theoretical and experimental study of ethyl carbamate" *Phys. Chem. Chem. Phys.*, 11 (11), pp. 1719-1728 (2009).

12. Margulès, L., Motiyenko, R. A., Alekseev, E. A., Demaison, J. "Choice of the reduction and of the representation in centrifugal distortion analysis : A case study of dimethylsulfoxide" *J. Mol. Spec.*, 260 (1), pp. 23-29 (2010).
13. Motiyenko, R. A., Margulès, L., Goubet, M., Møllendal, H., Konovalov, A., Guillemin, J.-C. "First high resolution spectroscopic studies and Ab Initio calculations of ethanetellurol" (2010) *J. Phys. Chem. A*, 114 (8), pp. 2794-2798.
14. Motiyenko, R. A., Margulès, L., Goubet, M., Møllendal, H., Guillemin, J.-C. "High resolution millimeter-wave spectroscopy of vinyltellurol" *J. Phys. Chem. A*, 114 (46), pp. 12202-12207 (2010).
15. Motiyenko, R. A., Margulès, L., Alekseev, E. A., Guillemin, J.-C., Demaison, J. "Centrifugal distortion analysis of the rotational spectrum of aziridine : Comparison of different Hamiltonians" *J. Mol. Spec.*, 264 (2), pp. 94-99 (2010).
16. Sironneau, V., Chelin, P., Kwabia Tchana, F., Kleiner, I., Pirali, O., Roy, P., Guillemin, J.-C., Orphal, J., Margulès, L., Motiyenko, R. A., Cooke, S. A., Youngblood, W. J., Agnew, A., Dewberry, C. T. "Reinvestigation of the microwave and new high resolution far-infrared spectra of cis-methyl nitrite, CH₃ONO : Rotational study of the two first torsional states" *J. Mol. Spec.*, 267 (1-2), pp. 92-99 (2011).
17. Møllendal, H., Margulès, L., Belloche, A., Motiyenko, R. A., Konovalov, A., Menten, K. M., Guillemin, J.-C. "Rotational spectrum of a chiral amino acid precursor, 2-aminopropionitrile, and searches for it in Sagittarius B2(N)" *Astronomy and Astrophysics*, 538, art. no. A51 (2012) .
18. Motiyenko, R. A., Margulès, L., Guillemin, J.-C. "High resolution millimeter-wave spectroscopy of cyclopropylphosphine-borane" *J. Phys. Chem. A*, 116 (6), pp. 1565-1570 (2012).
19. Tercero, B., Margulès, L., Carvajal, M., Motiyenko, R. A., Huet, T. R., Alekseev, E. A., Kleiner, I., Guillemin, J.-C., Møllendal, H., Cernicharo, J. "Microwave and submillimeter spectroscopy and first ISM detection of ¹⁸O-methyl formate" *Astronomy and Astrophysics*, 538, art. no. A119 (2012).
20. Bouchez, A., Margulès, L., Motiyenko, R. A., Guillemin, J.-C., Walters, A., Bottinelli, S., Ceccarelli, C., Kahane, C. "The submillimeter spectrum of deuterated glycolaldehydes" *Astronomy and Astrophysics*, 540, art. no. A51 (2012).
21. Møllendal, H., Margulès, L., Motiyenko, R. A., Larsen, N. W., Guillemin, J.-C. "Rotational spectrum and conformational composition of cyanoacetaldehyde, a compound of potential prebiotic and astrochemical interest" *J. Phys. Chem. A*, 116 (16), pp. 4047-4056 (2012).
22. Alekseev E. A, Motiyenko, R. A., Margulès, L. "Millimeter-and submillimeter-wave spectrometers on the basis of direct digital frequency synthesizers" *Radio Physics and Radio Astronomy*, 3 (1), pp. 75-88 (2012).
23. Goubet, M., Motiyenko, R. A., Margulès, L., Guillemin, J.-C. "Synthesis, high-resolution millimeter-wave spectroscopy, and ab initio calculations of ethylmercury hydride" *J. Phys. Chem. A*, 116 (22), pp. 5405-5409 (2012).
24. Coudert, L. H., Margulès, L., Huet, T. R., Motiyenko, R. A., Møllendal, H., Guillemin, J.-C. "The submillimeter-wave spectrum of the doubly deuterated species of methyl formate HCOOCD₂H" *Astronomy and Astrophysics*, 543, art. no. A46 (2012).

25. Guinet, M., Rohart, F., Buldyreva, J., Gupta, V., Eliet, S., Motiyenko, R. A., Margulès, L., Cuisset, A., Hindle, F., Mouret, G. "Experimental studies by complementary terahertz techniques and semi-classical calculations of N₂-broadening coefficients of CH₃³⁵Cl" *J. Quant. Spec. Rad. Trans.*, 113 (11), pp. 1113-1126 (2012).
26. Richard, C., Margulès, L., Motiyenko, R. A., Guillemin, J.-C. "Analysis of the terahertz rotational spectrum of the three mono-¹³C ethyl cyanides (¹³C-CH₃CH₂CN)" *Astronomy and Astrophysics*, 543, art. no. A135 (2012).
27. Motiyenko, R. A., Margulès, L., Guillemin, J.-C. "The submillimeter-wave spectrum of diisocyanomethane" *Astronomy and Astrophysics*, 544, art. no. A82 (2012).
28. Motiyenko, R. A., Tercero, B., Cernicharo, J., Margulès, L. "Rotational spectrum of formamide up to 1 THz and first ISM detection of its ν₁₂ vibrational state" *Astronomy and Astrophysics*, 548, art. no. A71 (2012).
29. Haykal, I., Motiyenko, R. A., Margulès, L., Huet, T. R. "Millimeter and submillimeter wave spectra of ¹³C-glycolaldehydes" *Astronomy and Astrophysics*, 549, art. no. A96 (2013).
30. Kutsenko, A. S., Motiyenko, R. A., Margulès, L., Guillemin, J.-C. "The extended spectroscopic database for deuterated species of formamide up to 1 THz" *Astronomy and Astrophysics*, 549, art. no. A128 (2013).
31. Richard, C., Margulès, L., Caux, E., Kahane, C., Ceccarelli, C., Guillemin, J.-C., Motiyenko, R. A., Vastel, C., Groner, P. "Mono-deuterated dimethyl ether : Laboratory spectrum up to 1 THz : Torsion-rotational spectrum within the vibrational ground-state for the symmetric and asymmetric conformers and first detection in IRAS 16293-2422" *Astronomy and Astrophysics*, 552, art. no. A117 (2013).
32. Nguyen, L., Walters, A., Margulès, L., Motiyenko, R. A., Guillemin, J.-C., Kahane, C., Ceccarelli, C. "Extension of the millimeter- and submillimeter-wave spectral databases of deuterated methyl cyanides (CH₂DCN and CHD₂CN)" *Astronomy and Astrophysics*, 553, art. no. A84 (2013).
33. Buldyreva, J., Margulès, L., Motiyenko, R. A., Rohart, F. "Speed dependence of CH₃³⁵Cl-O₂ line-broadening parameters probed on rotational transitions : Measurements and semi-classical calculations" *J. Quant. Spec. Rad. Trans.*, 130, pp. 304-314 (2013).
34. Smirnov, I. A., Alekseev, E. A., Piddyachiy, V. I., Ilyushin, V. V., Motiyenko, R. A. "1,3-Propanediol millimeter wave spectrum : Conformers I and II" *J. Mol. Spec.*, 293-294, pp. 33-37 (2013).
35. Motiyenko, R. A., Margulès, L., Guillemin, J.-C. "Millimeter- and submillimeter-wave spectrum of methyleneaminoacetonitrile" *Astronomy and Astrophysics*, 559, art. no. A44 (2013).
36. Coudert, L. H., Drouin, B. J., Tercero, B., Cernicharo, J., Guillemin, J.-C., Motiyenko, R. A., Margulès, L. "The first astrophysical detection, terahertz spectrum, and database for the monodeuterated species of methyl formate HCOOCH₂D" *Astrophysical Journal*, 779 (2), art. no. 119 (2013).
37. Haykal, I., Carvajal, M., Tercero, B., Kleiner, I., López, A., Cernicharo, J., Motiyenko, R. A., Huet, T. R., Guillemin, J.-C., Margulès, L. "THz spectroscopy and first ISM

- detection of excited torsional states of ^{13}C -methyl formate" *Astronomy and Astrophysics*, 568, art. no. A58 (2014).
- 38. Dudaryonok, A. S., Lavrentieva, N. N., Buldyreva, J., Margulès, L., Motiyenko, R. A., Rohart, F. "Experimental studies, line-shape analysis and semi-empirical calculations of broadening coefficients for $\text{CH}_3^{35}\text{Cl}-\text{CO}_2$ submillimeter transitions" *J. Quant. Spec. Rad. Trans.*, 145, pp. 50-56 (2014).
 - 39. Smirnov, I. A., Alekseev, E. A., Ilyushin, V. V., Margulès, L., Motiyenko, R. A., Drouin, B.J. "Spectroscopy of the ground, first and second excited torsional states of acetaldehyde from 0.05 to 1.6 THz" *J. Mol. Spec.*, 295, pp. 44-50 (2014).
 - 40. Coudert, L. H., Zemouli, M., Motiyenko, R. A., Margulès, L., Klee, S. "Analysis of the microwave, terahertz, and far infrared spectra of monodeuterated methanol CH_2DOH up to $J = 26$, $K = 11$, and o_1 " *J. Chem. Phys.*, 140 (6), art. no. 064307 (2014).
 - 41. Motiyenko, R. A., Ilyushin, V. V., Drouin, B. J., Yu, S., Margulès, L. "Rotational spectroscopy of methylamine up to 2.6 THz" *Astronomy and Astrophysics*, 563, art. no. A137 (2014).
 - 42. Motiyenko, R. A., Margulès, L., Alekseev, E. A., Guillemin, J.-C. "High-resolution millimeter wave spectroscopy and Ab initio calculations of aminomalononitrile" *J. Phys. Chem. A*, 119 (6), pp. 1048-1054 (2015).
 - 43. Margulès, L., Motiyenko, R. A., Ilyushin, V. V., Guillemin, J.-C. "Millimeter and submillimeter wave spectra of mono- ^{13}C -acetaldehydes" *Astronomy and Astrophysics*, 579, art. no. A46 (2015).
 - 44. Gupta, V., Rohart, F., Margulès, L., Motiyenko, R. A., Buldyreva, J. "Line-shapes and broadenings of rotational transitions of $\text{CH}_3^{35}\text{Cl}$ in collision with He, Ar and Kr" *J. Quant. Spec. Rad. Trans.*, 161, pp. 85-94 (2015).
 - 45. Tercero, B., Cernicharo, J., López, A., Brouillet, N., Kolesniková, L., Motiyenko, R. A., Margulès, L., Alonso, J. L., Guillemin, J.-C. "Searching for trans ethyl methyl ether in Orion KL" *Astronomy and Astrophysics*, 582, art. no. A39 (2015).
 - 46. Zakharenko, O., Motiyenko, R. A., Margulès, L., Huet, T. R. "Terahertz spectroscopy of deuterated formaldehyde using a frequency multiplication chain" *J. Mol. Spec.*, 317, pp. 41-46 (2015).
 - 47. Zakharenko, O., Motiyenko, R. A., Aviles Moreno, J.-R., Jabri, A., Kleiner, I., Huet, T. R. "Torsion-rotation-vibration effects in the ground and first excited states of methacrolein, a major atmospheric oxidation product of isoprene" *J. Chem. Phys.*, 144 (2), art. no. 024303 (2016).
 - 48. Motiyenko, R. A., Margulès, L., Ilyushin, V. V., Smirnov, I. A., Alekseev, E. A., Halfen, D. T., Ziurys, L. M. "Millimeter and submillimeter wave spectra of ^{13}C methylamine" *Astronomy and Astrophysics*, 587, art. no. A152 (2016).
 - 49. Bteich, S. B., Tercero, B., Cernicharo, J., Motiyenko, R. A., Margulès, L., Guillemin, J.-C. "Millimeter wave spectra of carbonyl cyanide" *Astronomy and Astrophysics*, 592, art. no. A43 (2016).
 - 50. Asselin, P., Berger, Y., Huet, T. R., Margulès, L., Motiyenko, R., Hendricks, R. J., Tarbutt, M. R., Tokunaga, S. K., Darquié, B. "Characterising molecules for fundamental physics : An accurate spectroscopic model of methyltrioxorhenium derived

- from new infrared and millimetre-wave measurements" *Phys. Chem. Chem. Phys.*, 19, pp. 4576-4587, (2017).
51. Belloche, A., Meshcheryakov, A. A., Garrod, R. T., Ilyushin, V. V., Alekseev, E. A., Motiyenko, R. A., Margulès, L., Müller, H.S.P., Menten, K. M. "Rotational spectroscopy, tentative interstellar detection, and chemical modeling of N-methylformamide" *Astronomy and Astrophysics*, 601, art. no. A49 (2017).
 52. Margulès, L., McGuire, B. A., Senent, M. L., Motiyenko, R. A., Remijan, A., Guillemin, J.-C. "Submillimeter spectra of 2-hydroxyacetonitrile (glycolonitrile ; HOCH₂CN) and its searches in GBT PRIMOS observations of Sgr B2(N)" *Astronomy and Astrophysics*, 601, art. no. A50 (2017).
 53. Pienkina, A. O., Margulès, L., Motiyenko, R. A., Müller, H.S.P., Guillemin, J.-C. "The millimeter and sub-millimeter rotational spectrum of triple ¹³C-substituted ethyl cyanide" *Astronomy and Astrophysics*, 601, art. no. A2 (2017).
 54. Zakharenko, O., Motiyenko, R. A., Aviles Moreno, J.-R., Huet, T. R. "Conformational Landscape and Torsion-Rotation-Vibration Effects in the Two Conformers of Methyl Vinyl Ketone, a Major Oxidation Product of Isoprene" *J. Phys. Chem. A*, 121, pp. 6420-6428 (2017).